Gas Turbine Laboratory
Department of Aeronautics and Astronautics
Massachusetts Istitute of Technology
Cambridge, MA 02139

Phase III Report on Contract Number NAS8-35018

entitled

TURBINE BLADE TIP AND SEAL CLEARANCE EXCITATION FORCES

submitted to

NASA George C. Marshall Space Flight Center
Huntsville, AL 35812

ATTN: Glenn E. Wilmer, Jr., EP62
Technical Monitor

PRINCIPAL INVESTIGATORS:

M. Martinez-Sanchez
Associate Professor, Aeronautics and Astronautics

B. Jaroux
Assistant Professor, Aeronautics and Astronautics
(now at the University of California, Santa Barbara,CA)

May 27, 1992

Acknowledgment:

In addition to the Principal Investigators mentioned in the Title Page, several graduate students have contributed in an essential way to this research. In a chronological order, these are: Yuan Qiu (M.S. 1985, Ph.D 1991), who worked on the initial part of the AFTF facility design; R.P. Gauthier (M.S.1990), who completed the drawings and developed the 2-D actuator disk theory; D.H. Loose, who helped build the AFTF and performed the first actual tests in it; K.T. Millsaps (M.S. 1987, Ph.D 1992), who built the LSTF and ran all of the seal tests; S.J. Song (Ph.D candidate), who performed most of the AFTF experiments; K.E. Leung (M.S. 1991), who extended to 3-D the actuator disk theory; S.Yoo (Ph.D candidate), who wrote the data acquistion software and extended the theory to unsteady conditions; T. Palczynski (M.S. candidate), who performed and correlated the shrouded turbine tests. This report would not have been possible without their dedication and insights.

ABSTRACT

This report describes experimental and theoretical work done as Phase III of a program sponsored by NASA (Marshall SFC) to investigate the magnitude, origin and parametric variations of destabilizing forces which arise in high power turbines due to blade-tip leakage effects. Phases I and II consisted of background research and facility development, respectively, and have been reported on separately.

The two facilities which were built for this purpose are first described. The larger one is a closed, 2 atm pressurized Freon-12 flow loop in which is installed a 1:1 replica of the SSME first stage hydrogen turbine, which can be driven by the flow, and which generates about 14 KW of power into a load-absorbing DC generator. The turbine shaft can be precisely offset along one linear axis by a fraction of the gap clearance, both statically and dynamically, by using an inertial shaker. A rotating dynamometer senses directly all components of force on the turbine. Flow instrumentation is also provided in the form of traversing directional probes on a rotatable casing, plus numerous wall taps. This instrumentation is used to investigate the disturbances caused to the flow field by the turbine offset. The smaller facility is used to measure the forces on labyrinth seals of the same type as those used in our turbine tests with a shrouded turbine. The seals can be kinematically whirled and spun (independently), and the inlet swirl can be set to a variety of values. Air is the working fluid (with atmospheric discharge) and the data are real-time pressure distributions in the seal glands.

Five different unshrouded turbine configurations were tested with static offsets, plus one with a shroud band and a two-ridge seal. The forces along and perpendicular to the offset were measured directly with the dynamometer, and were also inferred form velocity triangles and pressure distributions obtained from detailed flow surveys. These two routes yielded values in fair agreement in all cases. The cross-forces are seen to originate mainly (~2/3) from the classical Alford mechanism (nonuniform work extraction due to varying blade efficiency with tip gap) and about 1/3 from a slightly skewed hub pressure pattern. The direct forces arise mainly (75%) from this pressure pattern, the rest from a slight skewness of the Alford mechanism. The pressure nonuniformity (lower pressures near the widest gap) is seen to arise from a large-scale redistribution of the flow as it approaches the eccentric turbine.

The cross-forces are found to increase substantially when the gap is reduced from 3% to 1.9% of blade height, probably due to viscous blade-tip effects. The forces also increase when the hub gap between stator and rotor decreases. The force coefficient decreases with operating flow coefficient.

In the case of the shrouded turbine, most of the forces arise from nonuniform seal pressures. This includes about 1/2 of the transverse forces. The rest appears to come from uneven work extraction (Alford mechanism). Their level is about 50% higher than in the unshrouded cases.

The seals rig data were obtained for five seal builds, three of them with smooth stator, two with a honeycomb stator. The seals are all one-gland, straight-through. Dynamic damping is found to be an inviscid mechanism, largely independent of swirl or spin. Swirl determines strongly the static (zero whirl) cross-forces. The direct forces (restoring) are found to depend on a subtle effect, involving variation of the carry-over coefficient with gap. The honeycomb land has little effect on cross-forces, while largely eliminating direct forces.

The work on the dynamic Alford forces could not extract quantitative data. Progress was made by building and testing a dynamic shaking apparatus, but the

forces to be measured were masked by larger dynamic and vibratory forces sensed by the dynamometer. Two possible avenues are suggested for improving this situation: and (a) testing with an eccentrically mounted turbine, in which case whirl and spin speeds coincide, and dynamic disturbances should be minimal, and/or (b) Extracting the radial forces from real-time flow measurements.

Theoretical models of various degrees of complexity were developed to help interpreting and extrapolating the data. The notion of partial work done by the fluid leaking through the tip gaps was put on a quantitative basis by examining the leakage vortex roll-up dynamics. This was used to obtain a theory of the work loss due to a uniform gap. Perturbation and multiple scale arguments were then used to extend this to the case of an eccentric turbine. This yields an unsteady, 3-D theory which can predict the redistribution of the approach flow, and its effect on work defect, cross-forces, pressure patterns, and dynamic damping. The predictions agree qualitatively with the data and exhibit the correct trends, but the cross-forces are generally under-predicted.

TABLE OF CONTENTS

1.0 Introduction

1.1 Problem Statement

This report details the results of our experimental and theoretical investigation on the radial forces experienced by high power turbines when disturbed from their concentric position. These forces arise because of the non-symmetric flow disturbances caused near the blade tips by the lack of concentricity. They have been referred to in the US as "Alford" forces, after J.S. Alford, who identified their basic mechanism in a seminal paper on gas turbines [1], and also in Europe as "Thomas forces", after similar independent work on steam turbines by H.J. Thomas [2]. Although the Alford forces are relatively small in magnitude, their component at right angles to the turbine deflection is usually not resisted by any structural stiffness, and can therefore result in a dangerous buildup of whirling motion. Secondarily, their component in line with deflection can produce a noticeable shift of the rotor natural frequencies.

1.2 Structure of Research Program

Our program of research, sponsored by NASA Marshall SFC, was structured in three phases:

- **Phase I** (1983-1985) included a review of previous work on this problem, development of a simple theoretical extension of Alford's model to include flow redistribution effects, and a preliminary concept for an experimental rig. The results were documented in Ref. [3].
- **Phase II** (1985-1988) included detailed design of a test facility, construction of this facility, and acquisition of preliminary test data for facility verification. Results were described in Ref. [4].
- **Phase III** (1988-1991) constituted the main experimental phase, on which the present report will concentrate. The supporting theory developed will also be

described.

1.3 Discussion of Research Approach – Facility Design Implications

As documented in Ref. [3], the previous state of knowledge about Alford forces was deficient in several respects:

a) A small empirical data base. While some parametric variations had been studied by Ulrichs [5] and Wohlrab [6], there was insufficient basis for generalization to untested configurations or operating conditions.

b) A general lack of understanding of the detailed fluid mechanisms involved. Such understanding was needed for any attempt at a predictive theory that could extend beyond the data base.

c) An almost complete lack of data or theory about possible dynamic (i.e. velocity-dependent) Alford forces.

d) In addition, there were questions about the accuracy of some of the existing data, given the smallness of the radial forces compared to the main (tangential) turbine forces. The apparent nonlinearities exhibited by some of the data in Refs. [5], [6], and [7] could be due to these inaccuracies. There was also concern about the fact that many (but not all) of the data had been obtained in test rigs with Reynolds numbers below the range where fully turbulent conditions (prevalent in all real high power turbines) are established.

Our research program was intended to improve the situation with respect to all these concerns. Given the almost unlimited number of parameter variations that would be required to cover the range of practical turbine configurations and operating parameters, it was decided to emphasize basic understanding, both through detailed flow mapping and through supporting theory development. However, to avoid missing essential qualitatively new phenomena, a reasonable number of parameter variations were planned, covering parameters which were likely (either *a priori* or from previous

data) to be sensitive. These parameters included Reynolds number, stator-rotor gap (between blades and, separately, between hubs), radial mean clearance and presence or absence of a shroud band. In addition, the operating conditions were to be varied around the turbine nominal (best efficiency) operating point.

The concern about data contamination by operating in a laminar or transition regime led (Ref. [4]) to the adoption of a closed loop, pressurized Freon test facility. At the nominal 2 atm mean pressure, and using a 1:1 replica of the Shuttle first stage fuel turbopump turbine, the test Reynolds number based on chord and stator leaving velocity is then as high as 1.4×10^6, well above the 10^5-2×10^5 range normally associated with transition. The pressurization also added confidence that the level of the forces to be measured would be sufficient for accurate determination. This design decision, however, did lead to complications, associated mainly with the need to maintain sealing despite the several moveable casing parts required, and despite the various shaft and probe penetrations needed. These difficulties were all overcome but, in retrospect, some aspects of the program, particularly the dynamic testing, might have been more successful had we opted for a simpler, atmospheric test rig.

The concern about accurate force measurement was addressed through the adoption of a rotary dynamometer, designed according to the experience of Ref. [8]. This had several advantages: (a) the radial turbine forces were sensed at their source, avoiding the contamination associated with bearings or seals when stationary force balances are used; (b) since forces which are static in the fixed frame were read as one-per-rev varying forces, we were able to use semiconductor strain gauges, which have very high sensitivity and stiffness, but are inadequate for DC measurements because of their drift; (c) a very compact design was possible, allowing simultaneous sensing of all force and torque components. This led to some redundancy, which can be exploited in the data reduction process. This dynamometer proved successful in operation. The complication of having to extract the data through a multi-channel slip

ring assembly did imply a more laborious design and construction, but has not caused any subsequent problems.

The desire for detailed flow probing led to the adoption of a rotatable turbine casing, which would carry the flow probes for azimuthal scanning. Radial scanning was accommodated by individual micrometric traversing mechanisms in each probe. The turbine stator is rigidly supported by this casing, which means that no continuous tangential scanning is possible with respect to the stator blading. This was only a minor difficultly because, as corroborated through measurements, very little azimuthal distortion exists upstream of the stator, whereas the distortion is strong downstream of the turbine. Once again, the price to pay for the data acquisition flexibility of this arrangement was design complexity. The main difficulty was achieving good pressure sealing between the fixed and the rotatable sections of the casing, while keeping the friction forces low enough for the motor drive to operate the casing smoothly. This was accomplished successfully.

The nature of the research requires an ability to produce a precisely controllable lateral offset of the turbine, within the small limits allowed by the radial clearance (27 or 17 thousandths of an inch). This was the major driver for the mechanical design of the test rig, because the various tolerances of the subassemblies had to be tightly controlled to ensure the required precision. Two consequences were: (a) high cost of the assembly fabrication, and (b) heavy, rigid construction. The solution adopted (Ref. [4]) involved a stiff bearing support assembly, mounted inside the pressure shell, and supported by two rigid bars sliding on linear bearings with pressure seals. This did prove successful for static deflections, but the large mass of the assembly and the dry friction of the bar seals and bearings dictated the need for quite powerful shakers for dynamic deflection.

Another consequence of the requirement for small turbine shaft offsets is the need to insert a shaft section fitted through flexible joints to the sections carrying the

turbine and the downstream power takeoff, respectively. This section has a slight pivoting motion when the turbine shaft is offset, and the pressure seal required needs to act as the pivot point, making its design difficult. A double-acting hydrostatic seal was required, and it has proven satisfactory. A secondary effect of this arrangement is the introduction of harmonic shaft cross-forces due to the flex coupling deflections. These contaminate the force data sensed by the rotary dynamometer, but can be filtered out in the data reduction process (see Section 2.3.1)

The issue of time-resolved versus time-averaged measurements had to be faced in the design process. For purely static offset situations, the forces and flow distortions of interest must be steady in the fixed frame (although superimposed unsteadiness exists due to vibrations and to blade passage effects). On the other hand, for measurements with time-varying offsets, as required in studying dynamic effects, the applied disturbance frequency, at least, needs to be resolved. Given the intrinsic high band pass of the semiconductor strain gauges, and the availability of high speed data acquisition systems, time-resolving the dynamometer data presented no difficulty in principle. On the other hand, time-resolving the flow data (largely pressure readings) at the intended frequencies of up to about 50 Hz would have required careful design, with short pressure lines to the transducers and minimum volumes. Given the large number (close to 100) of such lines in our case, it was decided to opt for a low response design instead, which would be adequate for detailed mappings in the static-offset case. The exception, to be discussed more fully below, was the special labyrinth seals rig, where four flush-mounted Kulite transducers were used and time-resolved measurements were obtained. The low response design allows flexibility in routing the pressure lines and, through the use of a fast scanning device, the number of transducers and amplifiers can be reduced to two, unsteady of one per line.

As follows from the discussion so far, a large number of data channels was

required for these tests. Three different data acquisition systems were used (Ref. [4]): (a) Dynamometer data (9 sets of full bridges) were sampled 32 or 64 times per revolution (i.e. at a few kHz) by a Le Croy 8212A digitizing system. This was necessary for proper filtering, projection onto the fixed frame, and scaling. (b) Temperatures, torque, flow rate and other slowly varying signals were acquired through a separate system (a digitizing card in the AT computer). (c) Close to 100 pressure points were scanned at 4 ports/sec using a 48-channel double Scanivalve system, sensed using two transducers with reference taps connected to upstream and downstream points, respectively, and digitized by the Scanivalve data system itself. For systems (b) and (c), synchronization is not an issue, since only time-averaged measurements were intended. System (a) had to be synchronized carefully in order to obtain proper phase angles for the various forces sensed. Synchronization signals were derived from either a shaft-mounted optical encoder, from proximeter signals responding to individual blade passages, or, occasionally, from a magnetic pick-up mounted on the lower shaft. This complex data acquisition system, plus its associated data reduction software, required extensive work and constant attention, but worked generally well.

It was recognized from the beginning that dynamic, in addition to static, effects might be at work, and that their magnitude and sign would play an important role in the resulting turbine dynamics. However, it was also recognized that their accurate measurement presented problems much more difficult than those for static effects. This is, in part, due to the data acquisition problems discussed above but, more significantly, to the intrusion of inertia forces into the force sensing scheme. Unless the forces could be sensed even closer to their source (i.e. possibly by blade strain sensors), the turbine disk inertia would introduce force signals at least an order of magnitude larger than those expected from fluid sources. This is so independently of whether a shaker is used (imposed dynamic displacement) or a ring-down experiment

is done (free dynamics). Other difficulties arise from the additional vibrations introduced in the process of dynamic shaking. The decision, discussed above, to go to a pressurized system in order to increase sensitivity and Reynolds number, complicated these effects by requiring tight seals on the turbine-offsetting rods. This, plus the tight linear bearings needed for precise positioning, implied large forces to be overcome during shaking. The design adopted for dynamic testing, and the corresponding results and problems, will be more fully covered in Section 8. For the present purposes, it is sufficient to say that the design philosophy adopted was to ensure successful static results first. Allowance was made from dynamic testing, but its special features did not dictate the rig design (except, once again, for the seals test rig).

As noted above, a separate auxiliary test rig was also constructed to investigate labyrinth seal forces. This was directed especially to the shrouded turbine configuration, where earlier work [5], [6], [7], indicates that most of the Alford force can be ascribed to the sealing labyrinth. This rig, which is significantly simpler than the turbine facility, operates in open loop with air and, through a double-eccentric bearing system, can produce simultaneous spinning and whirling motions in any combination. Forces are not sensed directly, but instead, the pressure distribution in the seal cavity is measured in real time, and integrated to yield the force components (shear force effects can be estimated to be small by comparison). Because of the time resolution and the whirling motion, this rig yields both static and dynamic force effects. The results will be discussed in Section 7.

1.4 Theoretical Approach

The starting point for our understanding of the turbine radial forces was, as noted, the work of Alford [1]. His argument, which is more fully explained in Refs. [3] and [4] is that, because the efficiency of a turbine is known to decrease as tip gap

increases, an offset turbine will generate a higher tangential force on the side whose gap is reduced, and vice versa. Integration around the periphery then yields a pure cross-force, with no component aligned with displacement, and with no dynamic lag or lead. If $\beta = \frac{\partial \eta}{\partial(\delta/H)}$ is the sensitivity of turbine efficiency to (tip gap)/(blade height), Q is the torque and R the mean radius, the force F_y due to an offset e_x is found to be

$$F_y = \frac{\beta}{2} \eta \frac{Q}{R} \frac{e_x}{H} \tag{1.1}$$

One critical assumption in this derivation is that the local tip gap determines the local tangential force per unit length through the changes in local efficiency. In reality, it can be expected that the presence of the unsymmetrically placed turbine will induce a redistribution of the flow, so that a force redistribution would occur, even if the efficiency remained constant. This redistribution must occur on a scale of the order of R, and would be missed by calculations made on the blade scale. It will also be small in magnitude (of order e_x/H), and could be missed in measurements, even though its net effect may be of the same order as that yielding Eq. (1). This indicates the need for a theoretical approach that will determine the large-scale features of the flow in response to the turbine offset. Actuator disk theory is one such approach, whereby the details of the blading are condensed to a single plane, and the calculation extends to distances upstream and downstream which are larger than the blade dimensions.

This type of model was developed early in our work (Ref. [3]). The flow was radially averaged, and approximate connecting conditions were used to replace the blading. The results showed the expected effect of flow redistribution, although the numerical impact on net forces was small. An important feature that resulted was the ability to treat unsteady offsets with the prediction of relatively minor impact for the frequencies of interest.

The radial averaging in this type of model implies a loss of most of the detailed flow features associated with tip gap, and necessitates a reliance on empirical β

values. It also requires a crude set of connecting conditions, including (in our model) the assumption of perfect guidance of flow by the blading. This is tenable for the stator, but one of the strong features of the gap flow in the turbine is a large localized underturning near the tip. For these reasons, a more complete theory was felt to be needed.

This problem was approached in two steps. First, the *radial* migration effects due to the tip gap were investigated by assuming a centered turbine, and deriving an actuator disk theory which accounts for the tip gap presence. This permits the introduction of strong radial gradients, localized underturning, differential axial velocities and other physical effects due to the gap. The results explicitly give the turbine loss of work and (separately) of efficiency as functions of tip gap, with no empiricism. The theory is explained in Section 9.2.

The next step is the introduction of a non-uniform tip gap (as in an offset turbine). Since this produces azimuthal redistributions on a scale ~R, much greater than the scale (~H) for the radial redistributions treated above, a multiple-scale argument can be used, and the results of the radial redistribution theory can be locally applied at each tangential location, except with the approaching flow conditions obtained after tangential redistribution. This combination of two 2-D "actuator disk" theories effectively yields a 3-D description of the flow, which can then be compared to data. The theory is explained in Section 9.3.

As noted, these models can be extended to a time-dependent form, appropriate for studying dynamic Alford forces. This is incorporated into the theory in Sec. 9.3. Also treated is the effect of a finite axial hub gap.

2.0 Summary Description of Test Facilities

This section has two objectives: (a) to summarize, for easy reference, the description of the test facilities used in our research (a more complete discussion is in

Ref. [4]); and (b) to update Ref. [4] by discussing rig modifications and additions which occurred after January 1990.

2.1 The Alford Force Test Facility (AFTF)

As noted in the introduction, this was the major test rig, used to measure turbine forces directly and to map flow fields about eccentric turbines. It is a pressurized, Freon 12 filled loop fitted with a gas blower, heat exchanger/cooler, removable turbine test section, power extraction generator, and data system. Nominal operating conditions are 30 psia mean pressure, 4.4 kg/sec flow rate.

Figures 2.1 and 2.2 show two views of the facility. As indicated, the test section is vertical, with flow from above. Flow control is accomplished via manually adjusted valves (4 in Fig. 2.1). The bypass valve (13 in Fig. 2.1) was only used for low flow tests, mainly with the shrouded turbine. Turbine speed control is accomplished by varying the excitation current to the load-extracting DC generator (14 in Fig. 2.2). The DC power generated is dissipated in a resistor bank cooled by an air draft induced by the laboratory steam ejector. The bank can be reconfigured for additional turbine control, but this was found unnecessary, because of the excellent power regulation capabilities of the DC supplies used for generator excitation. The loop itself was constructed out of 10 inch and 12 inch diameter PVC piping, with glued flanges carrying neoprene gaskets. The blower (mounted on a platform outside the laboratory) is an upgraded 100 HP Stanley blower, fitted with a double-acting mechanical seal (for pressure and vacuum operation). The heat exchanger, rated at 52 KWth, uses city water. A commercially obtained Venturi tube is used for flow rate measurements (3 in Fig. 2.1). The loop has operated with no problems throughout the test series.

Figure 2.3 shows in more detail the test section area. The "Upper Section" of the casing (Part 12) can be rotated by ±90° by a motor-driven chain mechanism. It

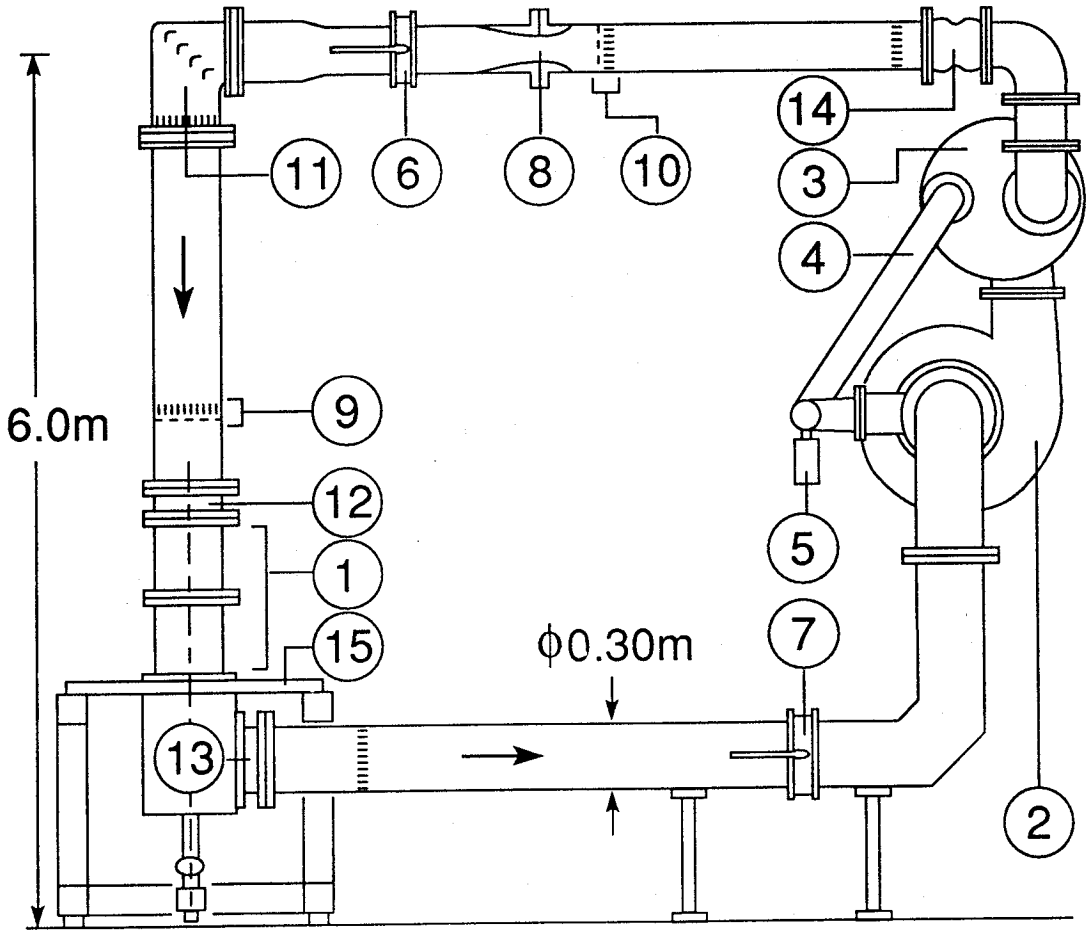

Fig. 2.1: Overall view of the Alford force test facility, front view. (1) Turbine test section. (2) Blower. (3) Heat exchanger. (4) Bypass duct. (5) Bypass valve. (6) Throttle valve (upper). (7) Throttle valve (lower). (8) Venturi flow meter. (9),(10) Flow straighteners. (11) Flow turning vanes. (12) Vibration isolator. (13) Exhaust plenum. (14) Vibration isolator. (15) Support plate.

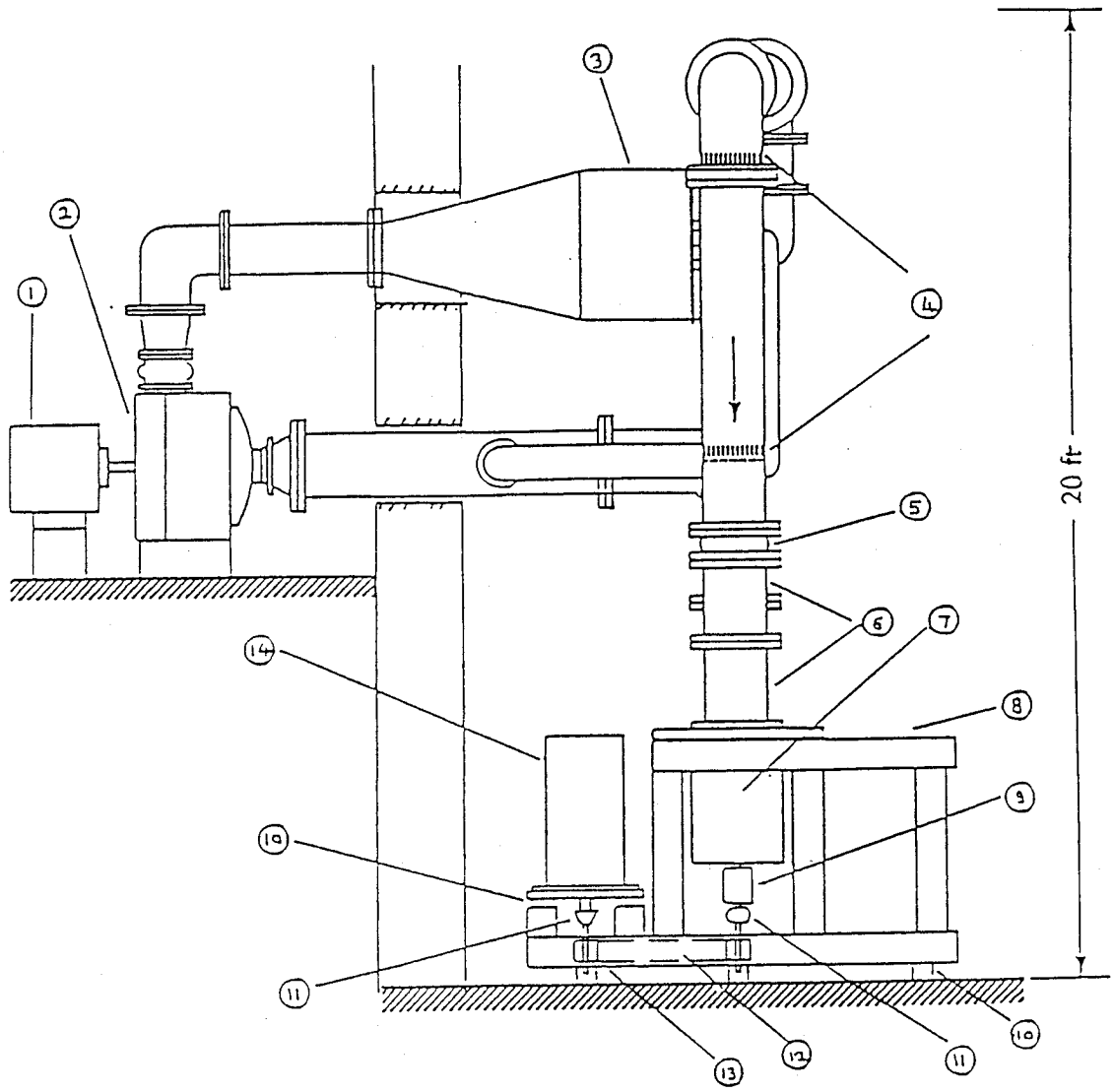

Fig. 2.2: Overall view of the Alford force test facility, side view. (1) 100 hp electric motor, (2) Compressor, (3) Heat exchanger, (4) Flow straightener, (5) Vibration isolator, (6) Test section, (7) Exhaust plenum, (8) Test stand, (9) Slipring assembly, (10) Vibration absorbing mounts, (11) Flexible shaft coupling, (12) Drive belt, (13) Pulley sprocket, (14) DC motor/generator

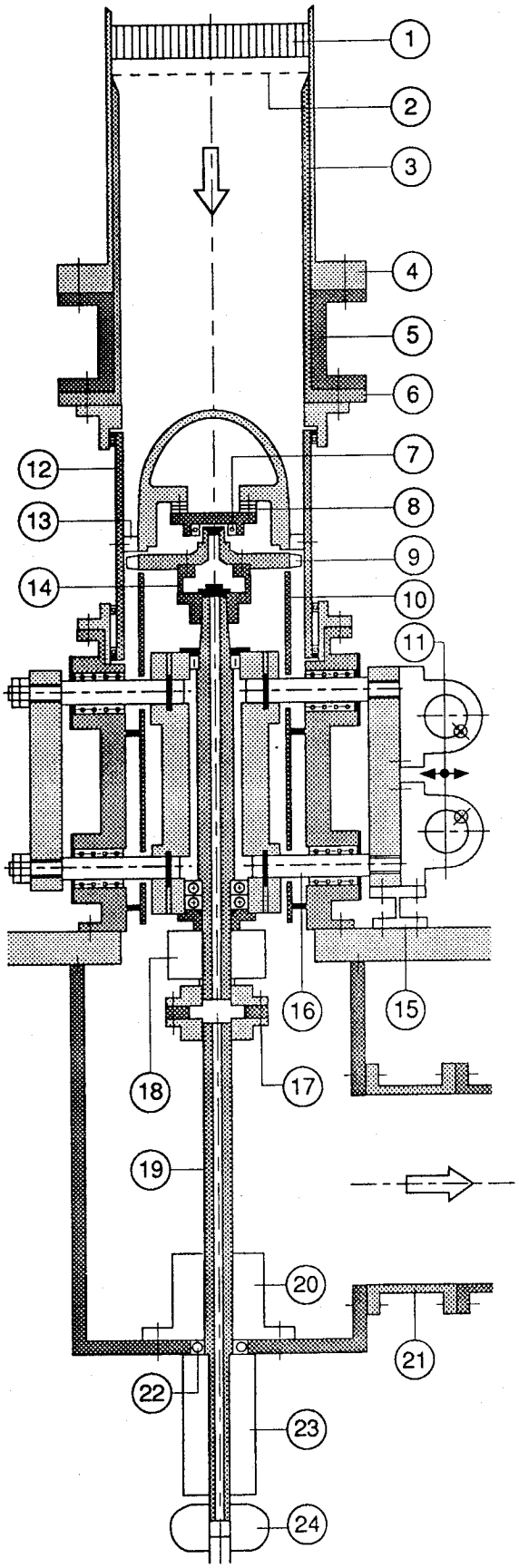

(1) Flow straightener
(2) Screen
(3) Main loop piping
(4) Flange
(5) Flexible insert
(6) Liner
(7) Snubber bearing
(8) Snubber support
(9) Test turbine
(10) Downstream flow-smoothing shield
(11) Dynamic shakers
(12) Rotatable casing
(13) Stator blades
(14) Rotating dynamometer
(15) Flexible shaker support
(16) Turbine-offsetting rods
(17) Upper flex joint
(18) Optical encoder
(19) Intermediate shaft
(20) Double-acting seal
(21) Flexible insert
(22) Pivoting bearing
(23) Slip ring assembly
(24) Lower flex joint

Fig. 2.3: Turbine test section and transmission assembly

carries the stator and hub (which is itself supported by the stator blades, attached to the casing). The turbine shaft connects to the turbine via the four-legged dynamometer (Part 14), and is supported by two bearings, of which the lower is a preloaded opposing pair which carries the axial load. The bearings themselves are carried in a heavy cylindrical structure which can be translated sideways by means of four stiff horizontal rods, two on each side. The rods slide on linear bearings, housed in the "Lower Section" of the casing (see Fig. 2.3). Static offsets are achieved by the systematic insertion and removal of calibrated metal shims between the casing and the large connecting vertical bars. For dynamic offsets, the shims are removed, and two counter-rotating synchronized rotating mass shakers (Part 11) are activated.

The test section rests on a heavy steel plate, under which hangs the flow dump plenum (a square aluminum box). The plenum connects to the downstream piping through a flexible insert, and also carries the intermediate section of the turbine shaft through a double-acting seal which allows a slight pivoting action. The optical encoder is located inside the plenum (Part 18).

By disconnecting the upper section upper flange, the lower plenum exit flange, and the lower shaft flex coupling, the entire test section can be translated sideways on rollers located under the base plate for loop opening. After this operation, and removal of the flow probes, the upper casing can be lifted, exposing the turbine. The entire operation of opening or closing the loop can be accomplished (after some practice) in about two days.

Figure 2.4 shows in detail the upper test section, including stator, turbine, dynamometer and rotatable casing. Notice the flow-smoothing cylindrical surface placed immediately downstream of the turbine, and flush with its inner radius. The stator can be mounted in three different sets of holes in the casing (16 in Fig. 2.4), allowing for adjustment of the stator-turbine axial gap. For any such mounting, the gap between the stator hub and the turbine hub can be changed by inserting appropriate

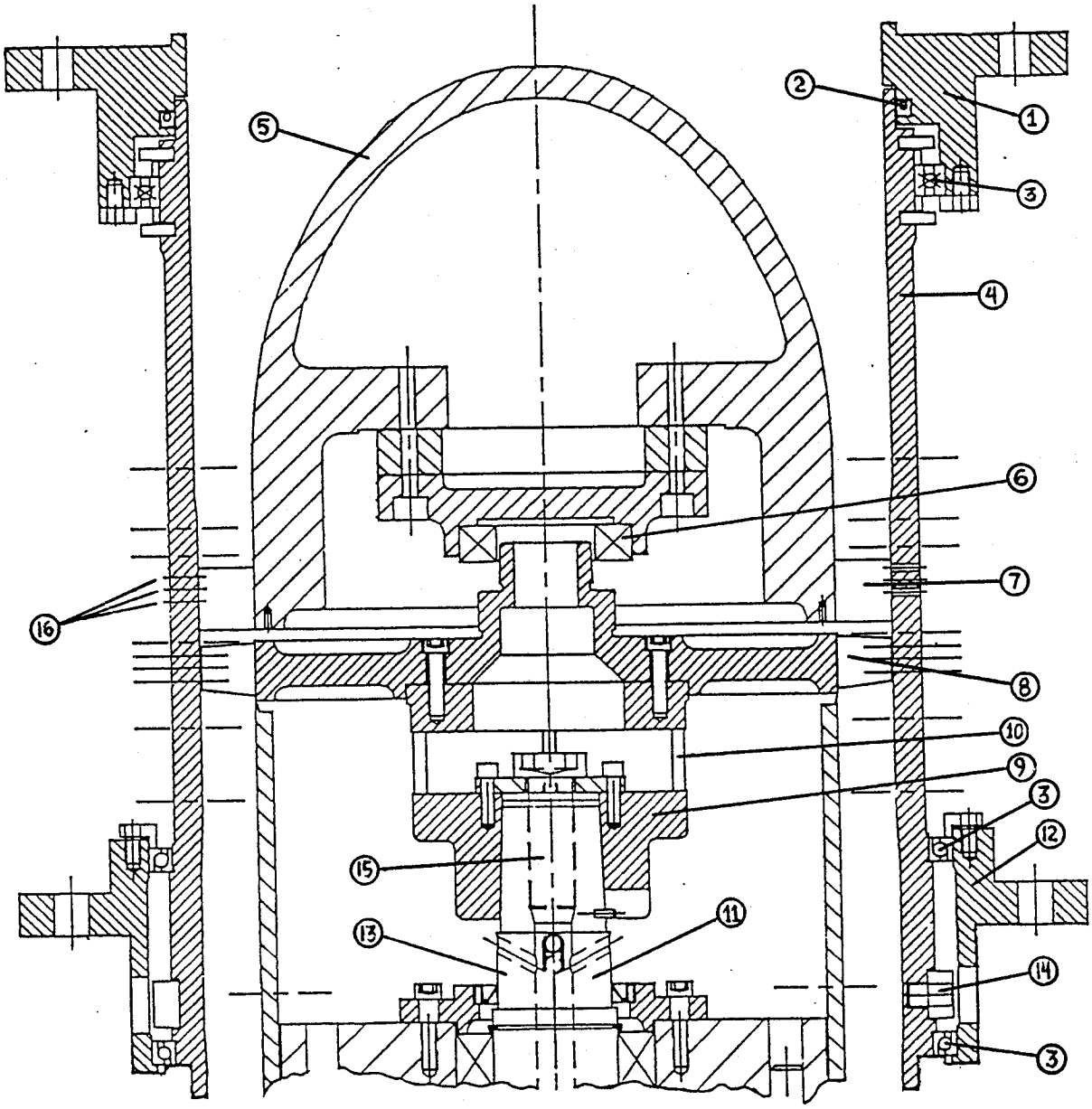

Fig. 2.4: Turbine test section, upper section. (1) Upper flange, (2) Rotatable easing seal, (3) Rotatable casing bearing, (4) Rotatable casing, (5) Ogive, (6) Electrically insulated snubber bearing, (7) Stator blades, (8) Rotor, (9) Rotating dynamometer, (10) Square posts where strain gauges are attached, (11) Upper drive shaft, (12) Lower flange, (13) Location of upper torque strain gauge bridge, (14) Chain for rotating casing, (15) Hollow shaft for instrumentation wires, (16) Three axial locations for stator retaining screws

TABLE 2.1
DESIGN PARAMETERS FOR SSME FUEL TURBOPUMP FIRST STAGE AND ALFORD FORCE TEST FACILITY TURBINE

	SSME Fuel Turbopump, First Stage	Alford Force Test Facility Turbine
Flow coefficient, ϕ	0.58	0.58
Work coefficient, ψ	1.508	1.508
Stator exit angle	70°	70°
Relative rotor inlet angle	43.9°	43.9°
Rotor exit angle	60°	60°
Absolute exit angle	-3.1°	-3.1°
Degree of reaction	0.216	0.216
Rotor mean radius, cm (in)	12.88 (5.07)	12.88 (5.07)
Number of rotor blades	63	63
Rotor blade height, cm (in)	2.17 (0.854)	2.17 (0.854)
Rotor blade chord, cm (in)	2.21 (0.870)	2.21 (0.870)
Rotation rate, rpm	34,560	3440
Axial flow vbelocity, m/s (in/s)	262 (10,300)	26 (1020)
Mass flow rate, kg/s (slug/s)	71.8 (4.92)	4.48 (0.307)
Inlet pressure, kPa (psi)	34,950 (5069)	224 (32.43)
Inlet temperature, K (°F)	1053 (1436)	300 (80)
Pressure ratio	1.192	1.231
Efficiency	0.821	0.75

rings (mounting screws shown in the figure).

The test turbine used for the unshrouded configuration tests is a 1:1 replica of the shuttle HPHTP first stage. The dimensions, nominal aerodynamic parameters, and other flow characteristics are detailed in Table 2.1 for the test turbine and for the HPHTP. As indicated in the table, all the non-dimensional flow parameters (except those related to compressibility) are duplicated. The specific heat ratio γ is substantially different, however, and so is the Mach number (0.414 maximum in the test section vs. a smaller value in the HPHTP). These differences are of no consequence, however, because at these low Mach numbers, compressibility effects play an insignificant role. The compressor exit Reynolds number is 5.6×10^6 in the HPHTP vs. 1.4×10^6 in the test turbine. This may imply some loss of efficiency in the test turbine, but no qualitative flow differences.

In contrast to the rotor, the stator differs from that of the HPFTP in that twist was eliminated, using a design with the mean blade angles of the HPFTP stator. This had a major reduction impact on cost and complexity. It was judged that the slight performance loss to be expected was unlikely to affect the value of the Alford force data because the stator has no gap and the blade height/radius ratio is small. There can be a slight shift of the best operating point towards higher speeds (lower flow coefficients) due to the local increase of the stator blade angle near the tip, but data were to be obtained over a range of flow coefficients in any case.

The modifications made to the AFTF facility for dynamic testing will be discussed in Section 8. Instrumentation and data reduction are discussed in Section 2.3.

2.2 The Labyrinth Seals Test Facility (LSTF)

This smaller facility was dedicated to a study of the static and dynamic radial forces acting on large diameter, single-cavity labyrinths similar to those used to seal

the flow around the shroud band of shrouded turbines. The relative simplicity of the geometry and construction, plus the fact that no direct force sensing is necessary, allowed a good deal of flexibility in varying several important operating parameters. Chief among these are inlet swirl angle, rotor whirling speed, rotor spin rate, gap/length ratio, and nature of the land surface.

Details of the design philosophy are given in Refs. [4], [9], and [10]. Efforts were made to place at least some of the test conditions above the laminar/turbulent transition for the knife-edge throttlings, and to avoid excessive momentum carry-over to the second throttling, by using realistic length/gap ratios. The pressure ratio was kept moderate, below choking, as is the case for the turbines in the SSME, but choked conditions can also be obtained. The working gas is air, and the main data are time-resolved pressure measurements at four points in the labyrinth gland. The driven whirl is used to ensure that each of the pressure measurement points samples the complete eccentric pressure pattern. Thus, the rig is not capable of directly measuring cases with zero whirl, but can deal with small positive or negative whirls, from which extrapolation to zero is simple. A concurrent theory development effort provided a linearized model which can be used to rationalize and extrapolate the results.

The general flow path in the facility is shown in Fig. 2.5. As indicated, operation is in open loop, with air discharging to the room through a muffler. Figure 2.6 is a side view of the test section assembly. Two drives are noted: one, in line, provides the spin motion, the other, driven by a belt, provides the whirl by producing a small satelliting motion of the shaft bearing support assembly. Air is admitted to a plenum (Fig. 2.7), from which it discharges through convergent swirl vanes or holes into the test labyrinth inlet channel. The swirl vanes can be changed to provide nominal discharge angles of 0°, 15°, 30°, 45°, and 60° (for 0° and 15°, holes are used instead of vanes).

The test seal (6 in Fig. 2.7) is mounted on one of two disks (9), the second of which serves as a balancing mass. Auxiliary axial seals are also shown in the front

Fig. 2.5: Dynamics Seals Test Facility Layout

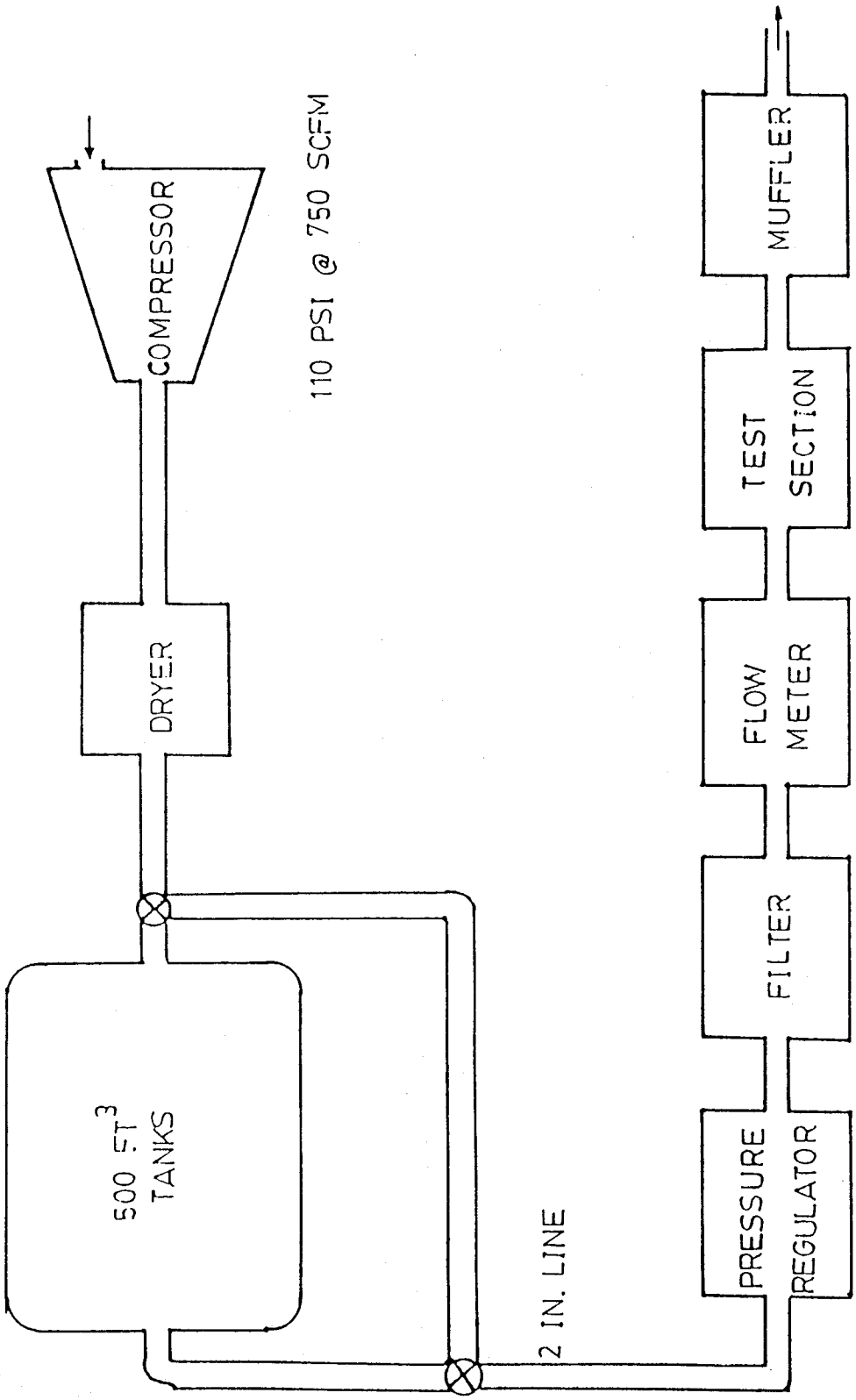

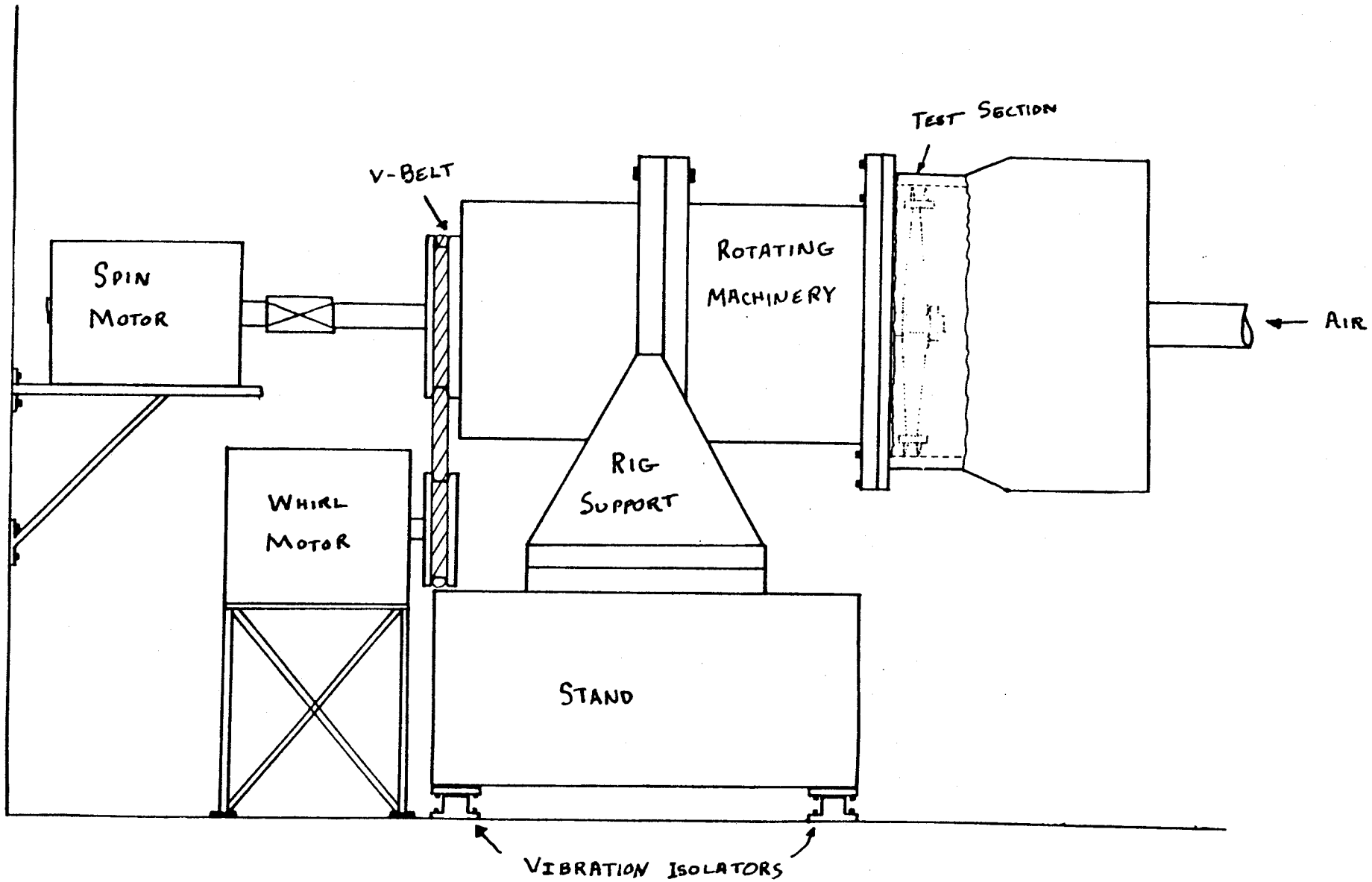

Fig. 2.6 - Side view of labyrinth seal test facility.

Fig. 2.7: **Dynamic Seals Test Section Assembly**

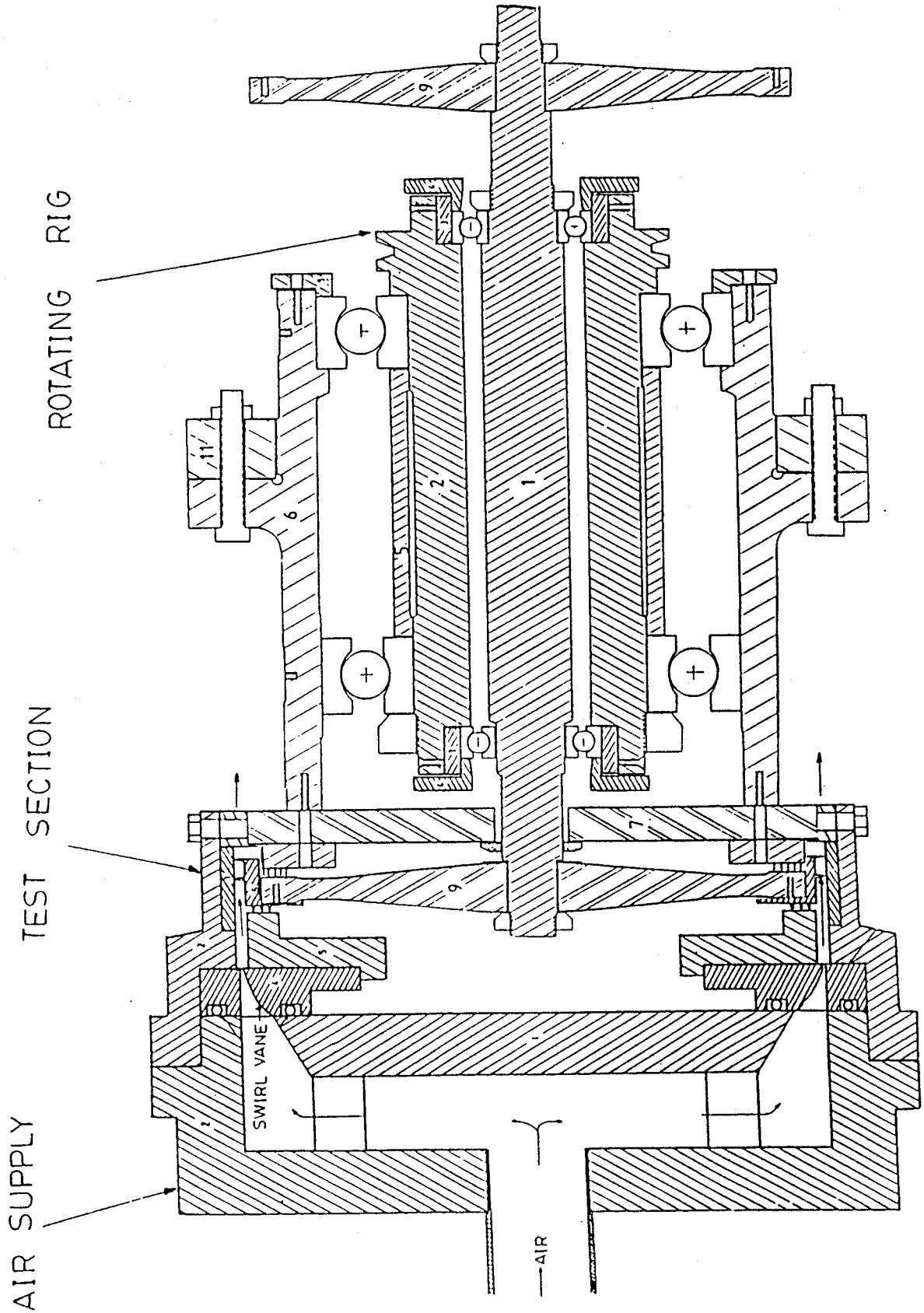

and back of the test rotor. Pressurized air is admitted to the cavity behind the test rotor for partial balancing of the axial load. Careful control of this pressure is needed to avoid either bearing seizure or axial chattering.

The right side of Fig. 2.7 details the drive mechanism. The large diameter outer bearings run concentrically inside the outer housing. The shaft bearings are mounted with a small, controllable eccentricity on the intermediate structure (part 1 in Fig. 2.7), which is belt-driven to produce whirl. Weights are placed eccentrically on the intermediate structure such that, at each eccentricity setting, the inertial axis is still near the geometric center of the outer casing.

Two different seal lengths (10 mm and 17.3 mm) were tested, each with a smooth and a honeycomb land surface. Further details will be given in the Results section.

2.3 Instrumentation and Data Acquisition (AFTF)

Figure 2.8 shows the general arrangement of the data acquisition system. As noted in the introduction, three digitizers are used: one for low frequency data (thermocouples and loop status signals), a second for the real-time recording of dynamometer data (plus torque data from a shaft-mounted bridge), and a third one directly attached to the scanivalve system. All data are transferred during each run to the hard disk of the PC-AT lab computer, and periodically loaded to diskettes for later analysis.

The major instruments and the general data reduction procedure for each of them will be next discussed. Details which are specific to the extraction of particular pieces of information will be more fully discussed in the sections dealing with the data.

2.3.1 Force Dynamometer

The rotating dynamometer (part 9 in Fig. 2.4) consists of four instrumented flexible posts which directly support the turbine. The locations of the attached strain

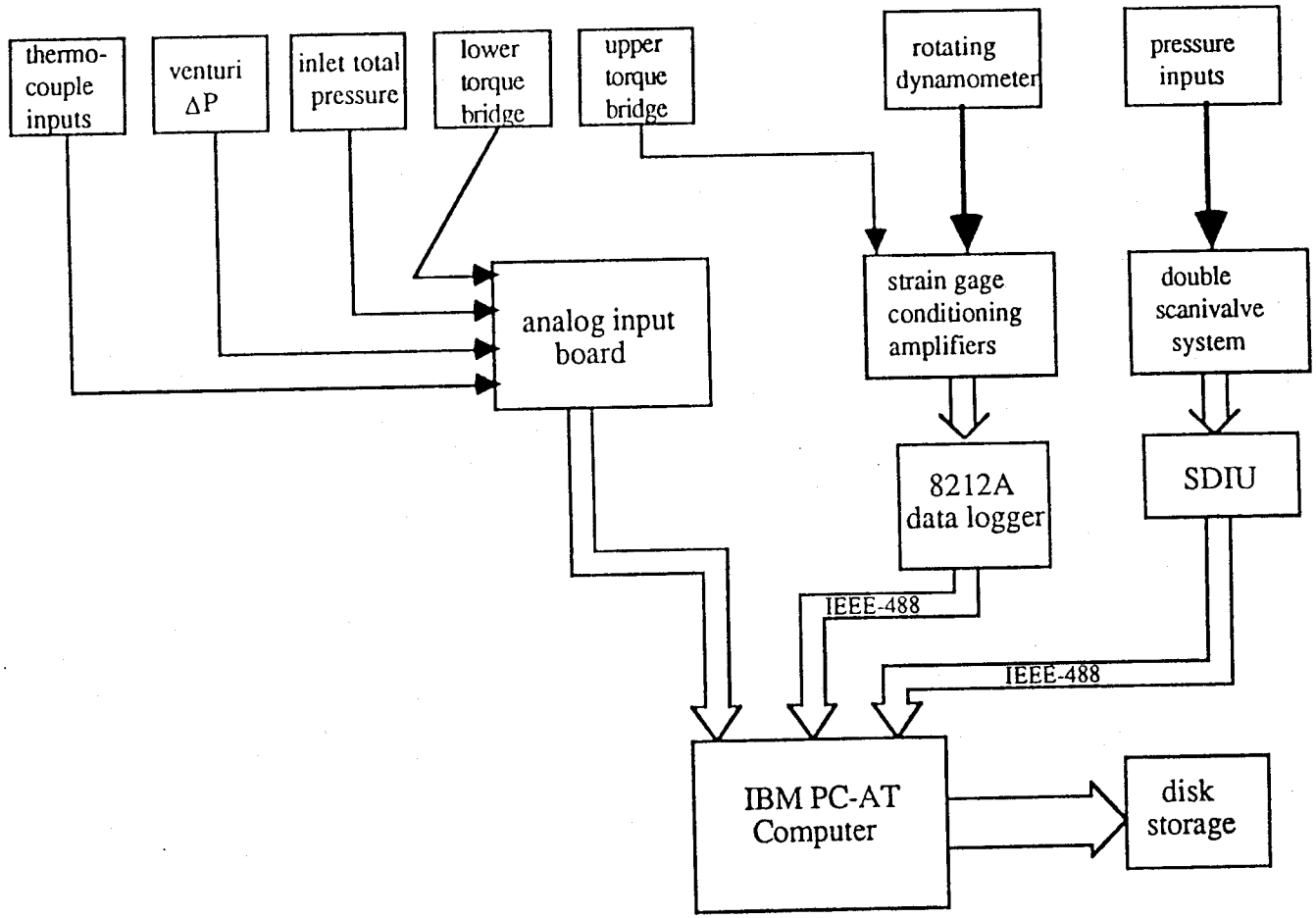

Fig. 2.8 Flow chart of data acqusition

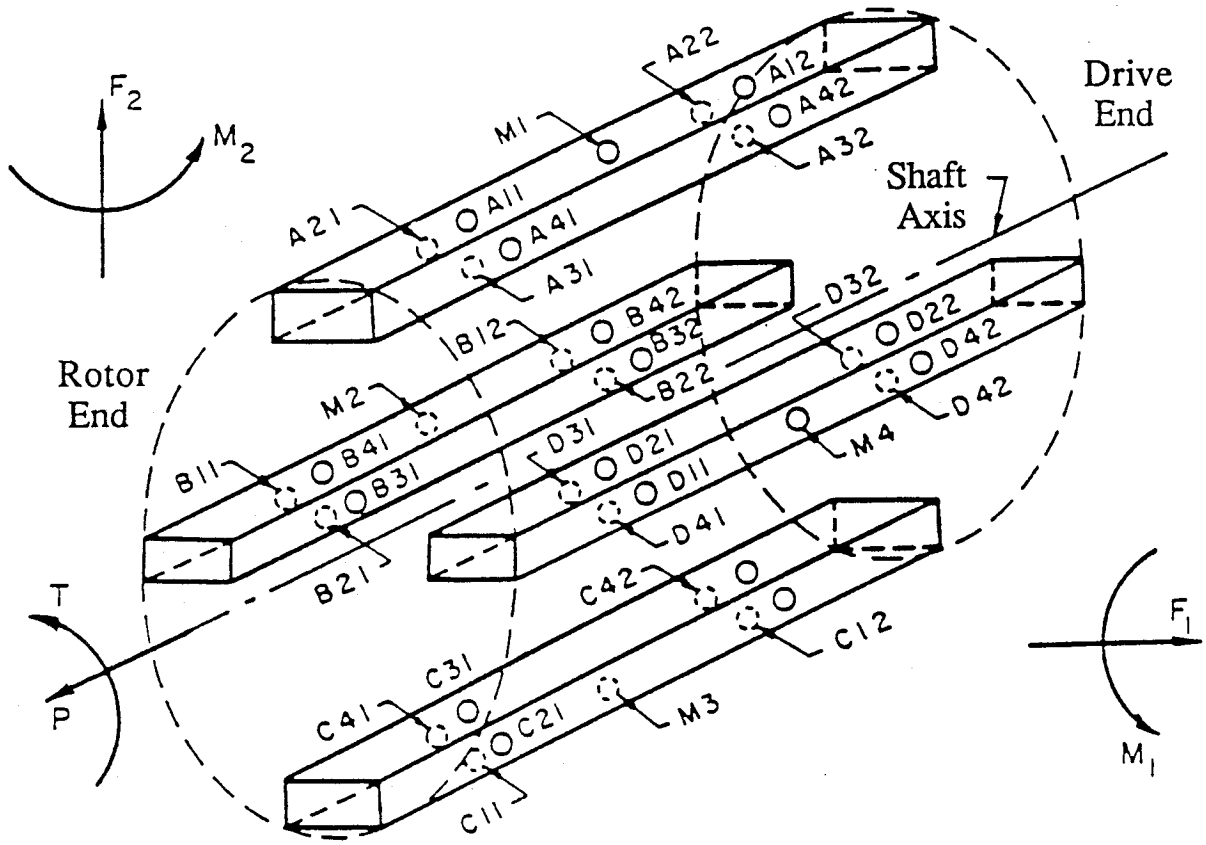

Fig. 2.9 Sketch of dynamometer measuring section consisting of four posts A, B, C and D and 9 strain gages per post: 4 at quarter length, XK1, 1 at mid-length, MK and 4 at three-quarter length, XK2. Forces and moments shown are defined as acting on the rotor, at the rotor end of the dynamometer.

gauges are shown in Fig. 2.9. As noted, all three force components (two bending, one torsion) can be extracted. The gauges are arranged into a set of 9 full wheatstone bridges, each of them yielding an output which is primarily sensitive to only two components of force or moment, and secondarily (about 2 orders of magnitude less) to the other components. The exception is Bridge 9, sensitive primarily to thrust only.

The output wires are permanently connected to the bridges and cemented in place as they exit through the hollow turbine shaft. At the other end, they connect to a set of slip rings keyed to the intermediate shaft and located outside the exit plenum, just above the removable lower flex joint (part 9 in Fig.2.2).

The six forces and moments can be extracted from a selection of six of the bridge outputs, through a calibration matrix, the elements of which are determined by a series of calibration experiments. These are described in Ref. [4], and will not be repeated here. The calibration included dynamic loadings as well, which verified the insensitivity to frequency in the desired range. The errors in reconstructing a known load through the calibration matrix were under 2% for all loadings and speeds.

The bridge data are sampled 32 or 64 times per turbine revolution using clock signals which are provided by the optical encoder. The data sequence is referred to rotor orientation by means of a once-per-turn pulse also provided by the encoder at a known turbine position. Occasionally the encoder malfunctioned, and then the clock signals were derived from the proximeter which senses the passage of each individual turbine blade (63 of them); for compatibility with the rest of the data reduction process, these data were then interpolated to a 64-per-turn format. When clocking was from the blade proximeter, a second proximeter was used to provide a once-per-turn synchronization signal by sensing passage of a protuberance attached to the lower shaft.

Low frequency fluctuations occur, due both to flow fluctuations and to low frequency system vibration. Their impact is minimized by averaging 128 or 256

consecutive revolutions (2 to 5 seconds), using the synchronization signals for proper phasing. This volume of data can be accommodated in the dynamic memory modules of the Le Croy digitizer, which is read into computer disk after each acquisition.

The type of azimuthal variation encountered, and the magnitude of the low frequency fluctuations, can be appreciated in Figs. 2.10(a), (b), and (c). Figures 2.10(a) and (b) show the raw output (in volts) of one of the strain gauge bridges. The intra-cycle pattern is recognizable from turn to turn, but there is clearly a large slow fluctuation superimposed. Averaging over 256 cycles produces the azimuthal variation shown in Fig. 2.10(b). We have verified that averaging over any number of cycles greater than about 30-60 produces negligible differences as to the averaged signal. After this is done to each bridge signal, multiplication times the calibration matrix yields force components *in the rotating frame* such as those in Fig. 2.10(c), where F_1 and F_2 are force projections on two axes fixed to the turbine at a well defined, but arbitrarily chosen, orientation.

The next step in the reduction is to project the forces onto the fixed frame (XY), where X is the direction of the turbine offset, and Y is at 90° to it. This operation requires accurate indexing to fix the time when the (1-2) and the (XY) axes coincide. The result for our example is shown in Fig. 2.11(a). It is apparent that, in addition to the average values of F_x and F_y (0^{th} harmonics), which is what one would expect from a static deflection along OX, there are strong higher harmonics, particularly a 2^{nd} harmonic. These harmonics are then eliminated by simply averaging over the revolution to extract the desired $\overline{F}_x$ and $\overline{F}_y$ averages, which are shown in Fig. 2.11(b). The harmonics appear to be related to the necessary presence of slight deflections in the flex couplings at the bottom of the shaft.

The force level shown in Fig. 2.11(b) (1-3 lbs) is typical of what is obtained for deflections of 10-15 thousandths of an inch. They are generally linear in the turbine deflection. The departures from linearity which are seen in $F_y(e)$ curves, in particular,

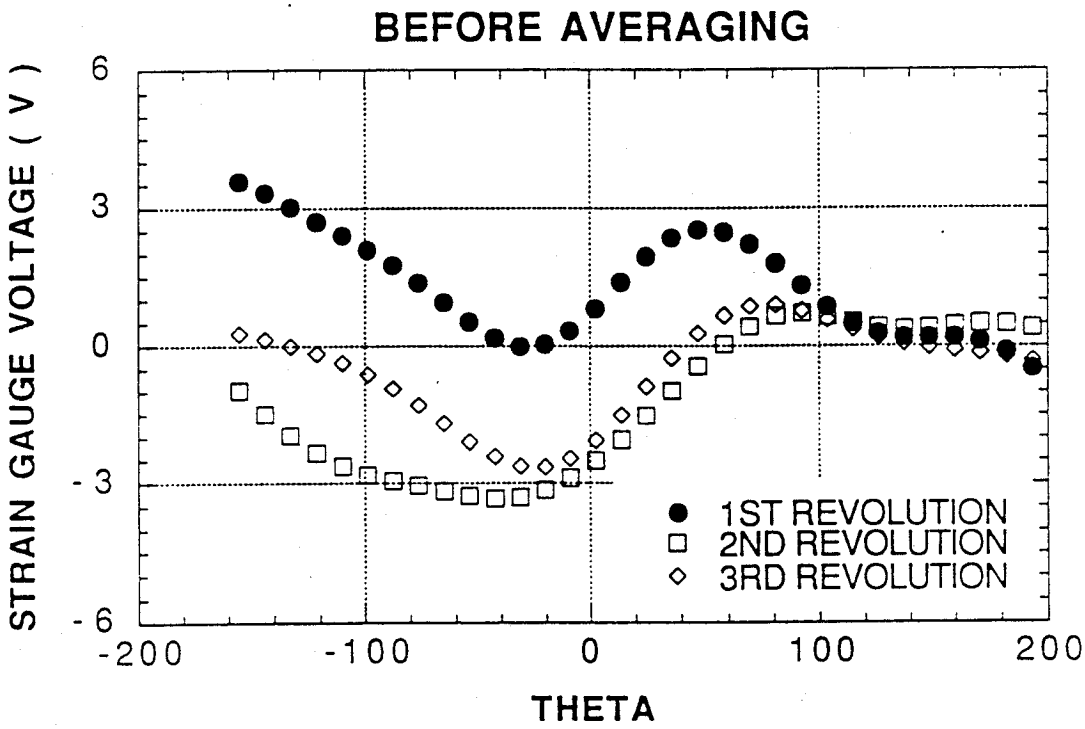

Fig. 2.10a: Raw output from one dynamometer bridge (three consecutive revolutions)

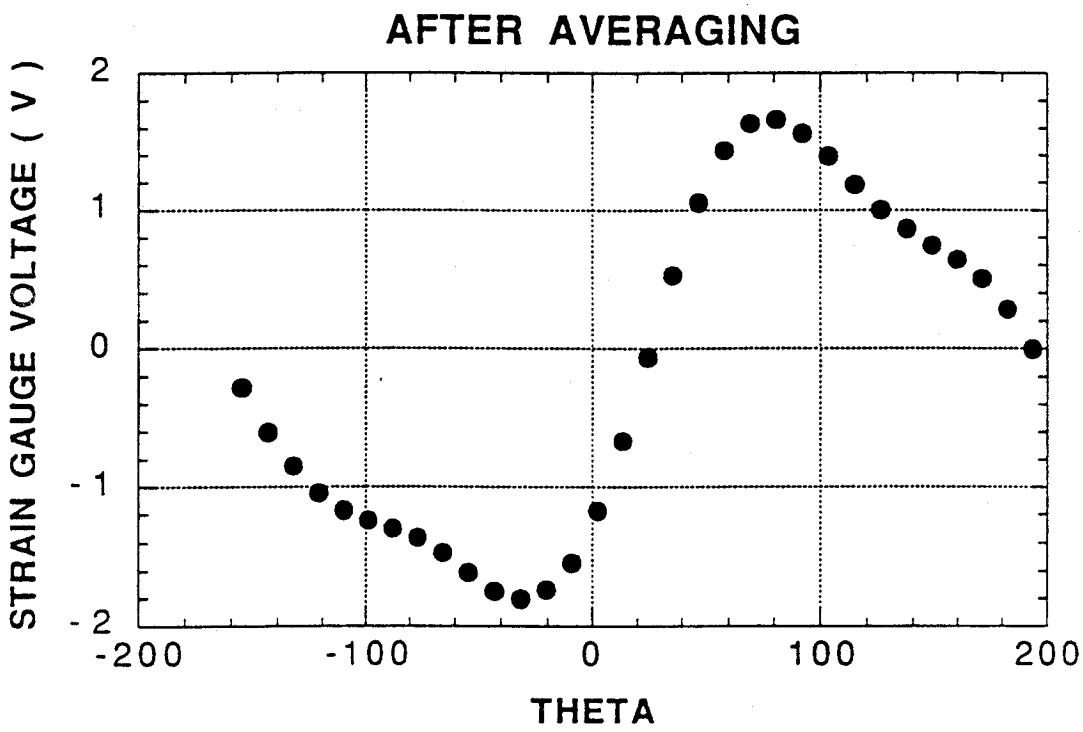

Fig. 2.10b: Ensemble average bridge signal, after phase-locked averaging

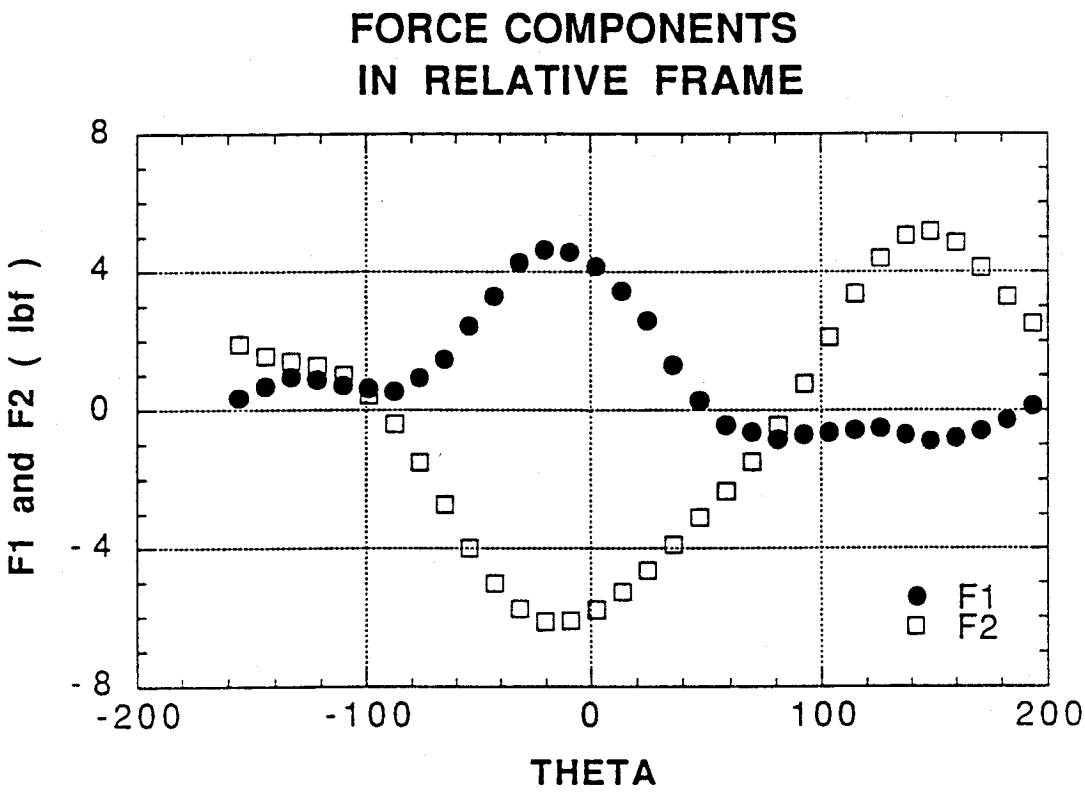

Fig. 2.10c: Force components in the rotating frame over one full revolution

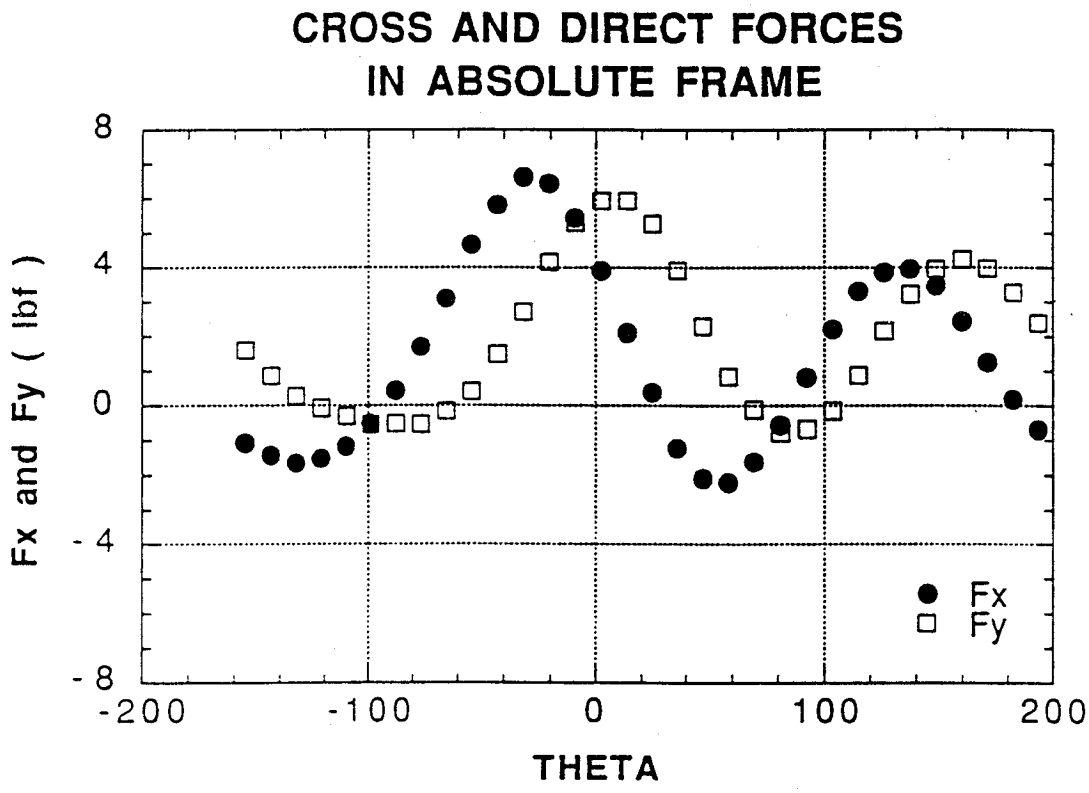

Fig. 2.11a: Force components projected onto fixed axes

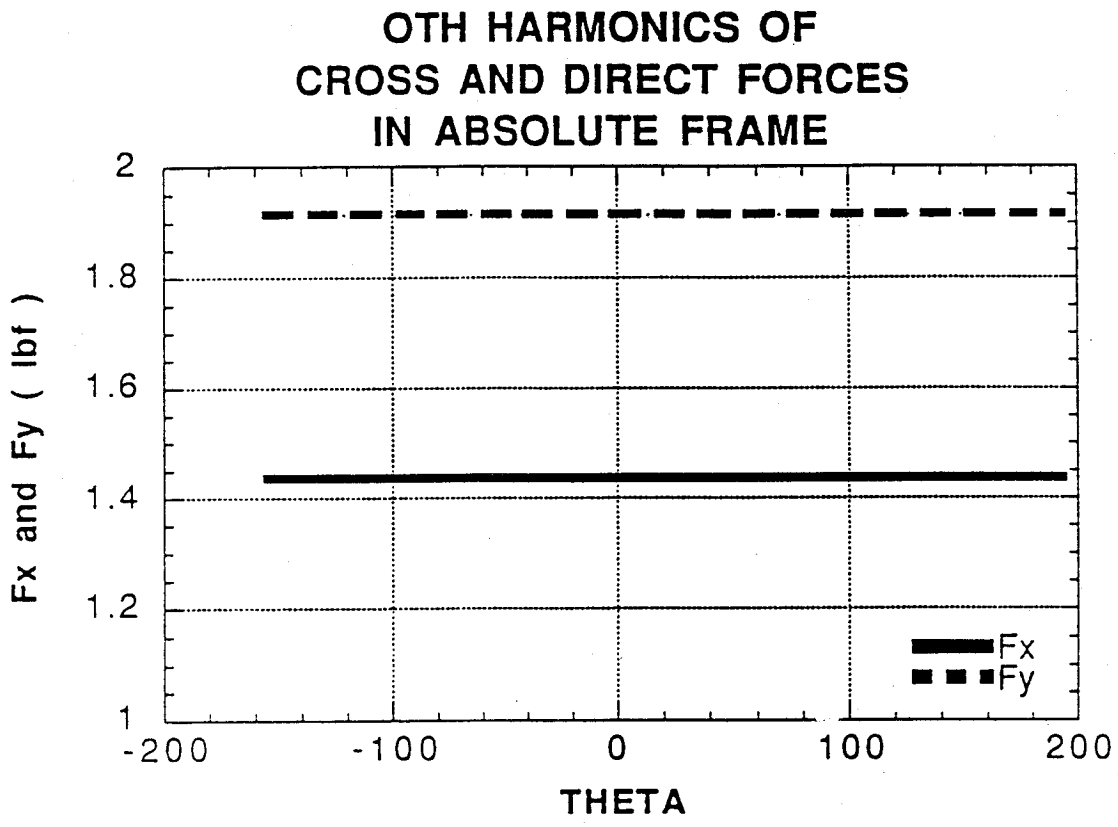

Fig. 2.11b: Time average of forces in fixed frame

do not have a repeatable pattern, and are more a measure of the residual measurement error than of any basic physics. Figures 2.12 and 2.13 are representative of the best and worst linearity in our F_y data.

Figures 2.12 and 2.13 also display the F_x ("Direct Force") component of force. Here, the slight S-shaped curve is visible, and appears to be a consistent feature in all cases. In terms of repeatability, notice that three different measurement points are given in Figs. 2.12 and 2.13 for each eccentricity. The separate symbols are nearly indistinguishable in the graphs. A fuller discussion of the dynamometer data must await Sections 4-6.

2.3.2 Instrumentation for Flow Measurements

The location of the instrument ports for flow measurements is detailed in Fig. 2.14a. The type of instrument used at each station is explained in Fig. 2.14b.

The static wall taps at stations 0, 1, 3, 4, 5, 6, 7, 8, 9, and 10 are simple 0.5 mm holes drilled through the wall, backed by 1/8" brass tubes to which several meter lengths of flexible plastic tubing attach. This tubing ends at separate ports on the Scanivalve pressure multiplexer.

The three-hole probes (two each in stations 1 and 9) are wedge-shaped, with one central and two lateral holes, to measure the magnitude and yaw angle of the relative flow, plus a thermocouple for total temperature sensing. The five-hole probes (two each at stations 2 and 8) are similar, but have additional slanted surfaces with two more holes for sensing flow pitch angle. The probe diameter is about 3 mm.

Subsequent to the issuance of Ref. [4], all of the three- and five-hole probes were mounted on traversing devices which allow radial scanning, as well as rotation about the probe axis (yawing). These devices are as shown in Fig. 2.15. The five-hole probes have their sensing holes displaced by 16 mm from the probe tip, with the result that only the outer 7 mm of the flow passage can be scanned. This is not a serious

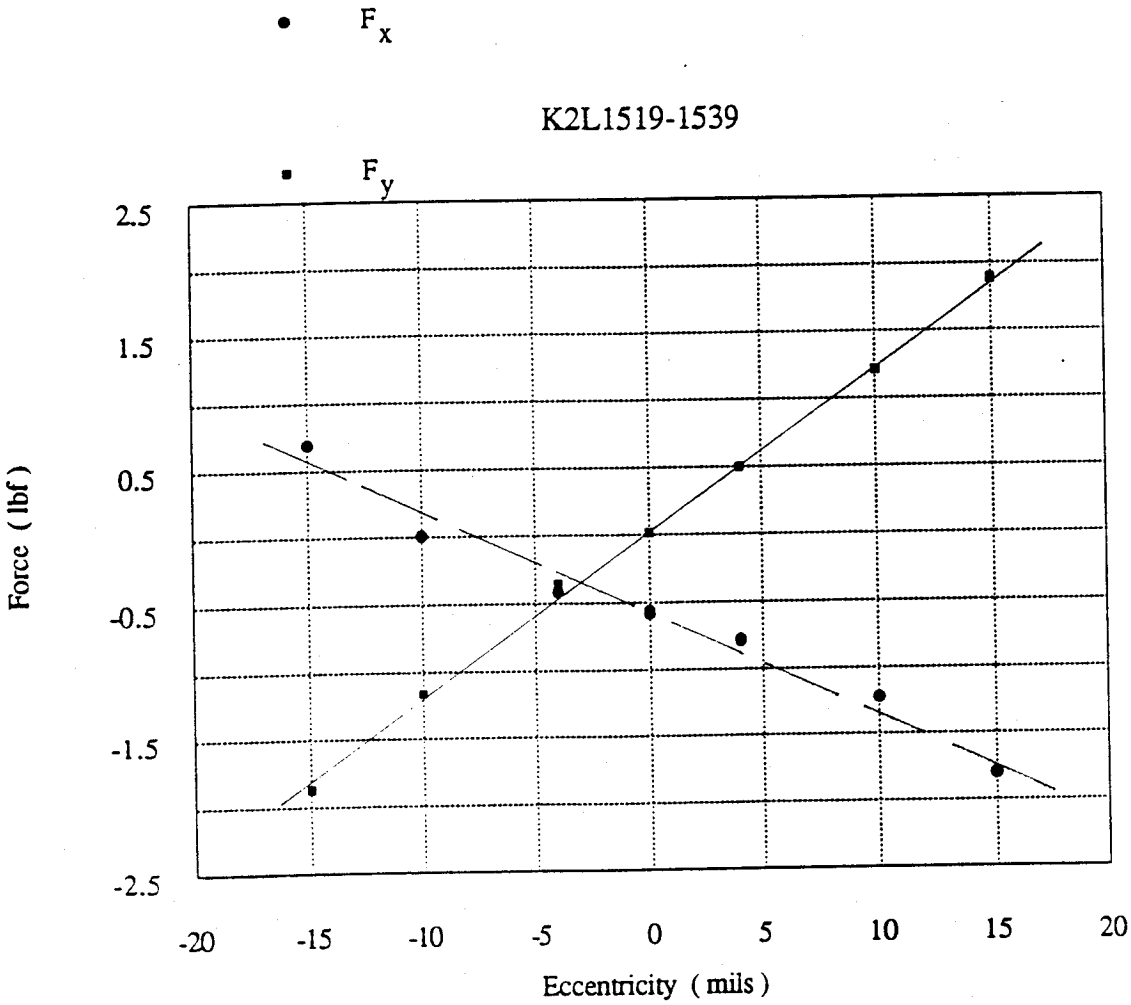

Fig. 2.12 Direct and Cross-Force vs. Eccentricity, with linear curve fits.
Off design condition 2L (70% speed, See table 3.1)

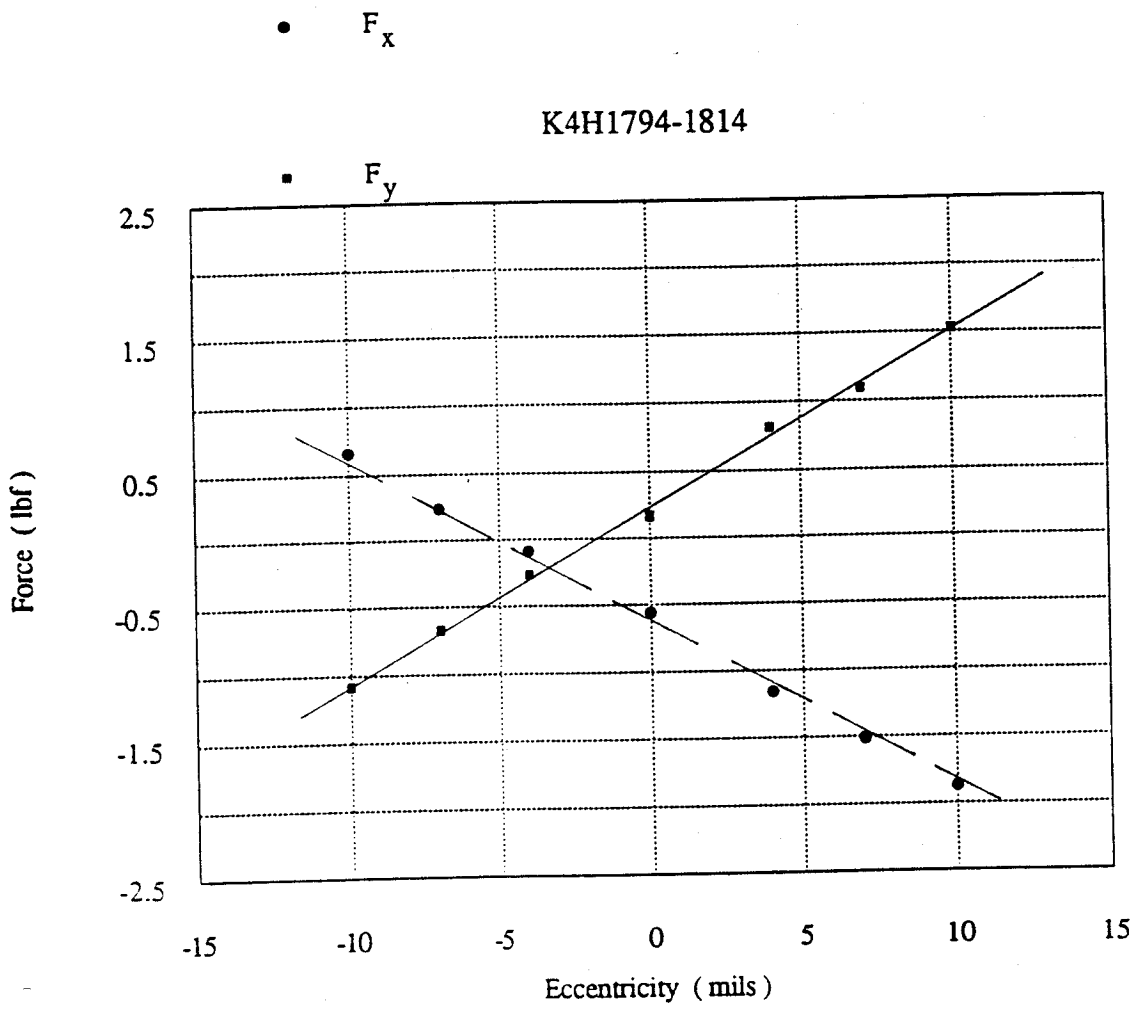

Fig. 2.13 Direct and Cross-Force vs. Eccentricity, with linear curve fits.
Off-design condition 4H (110% speed, See table 3.1)

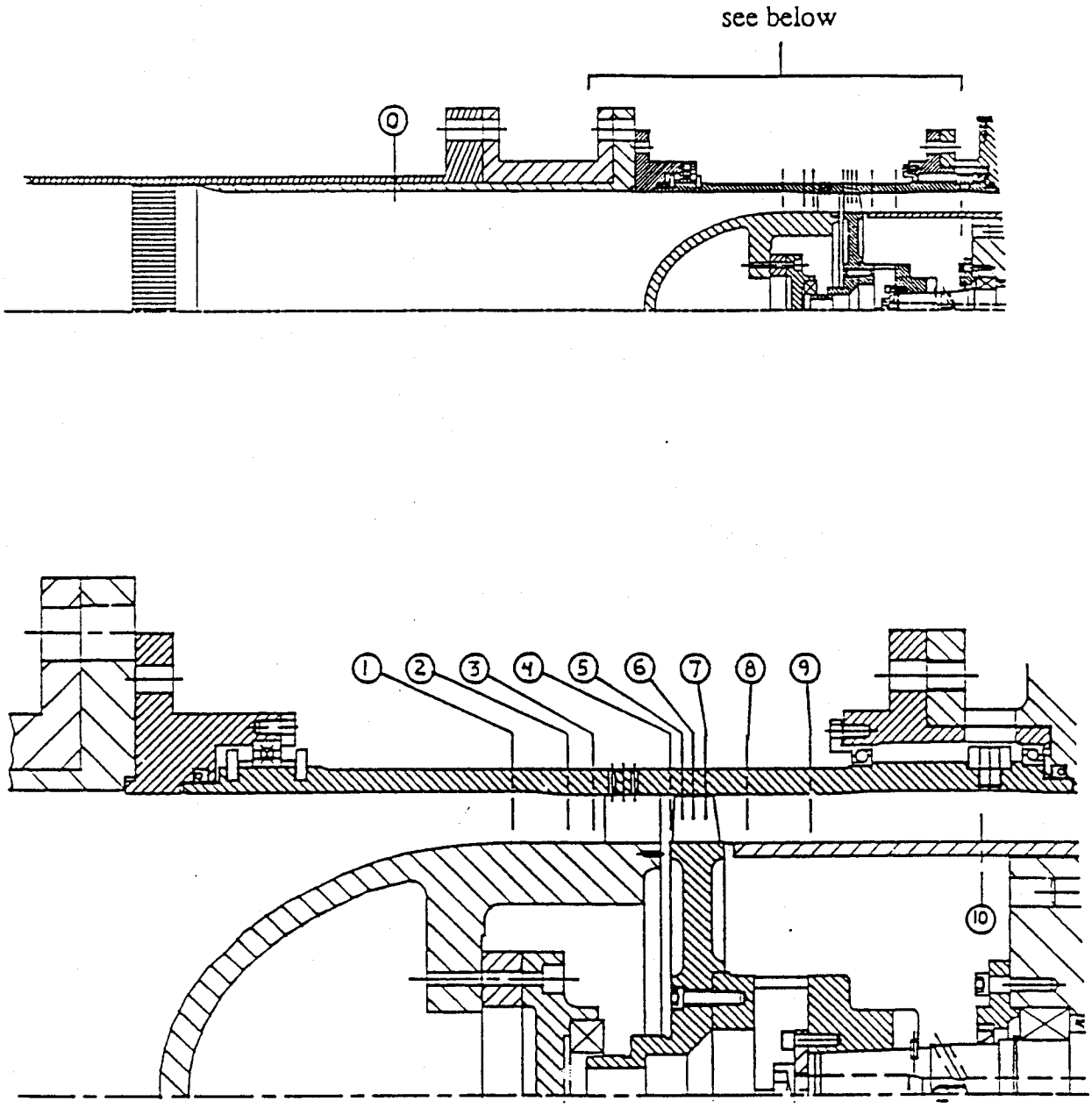

Fig. 2.14 Axial instrumentation station locations

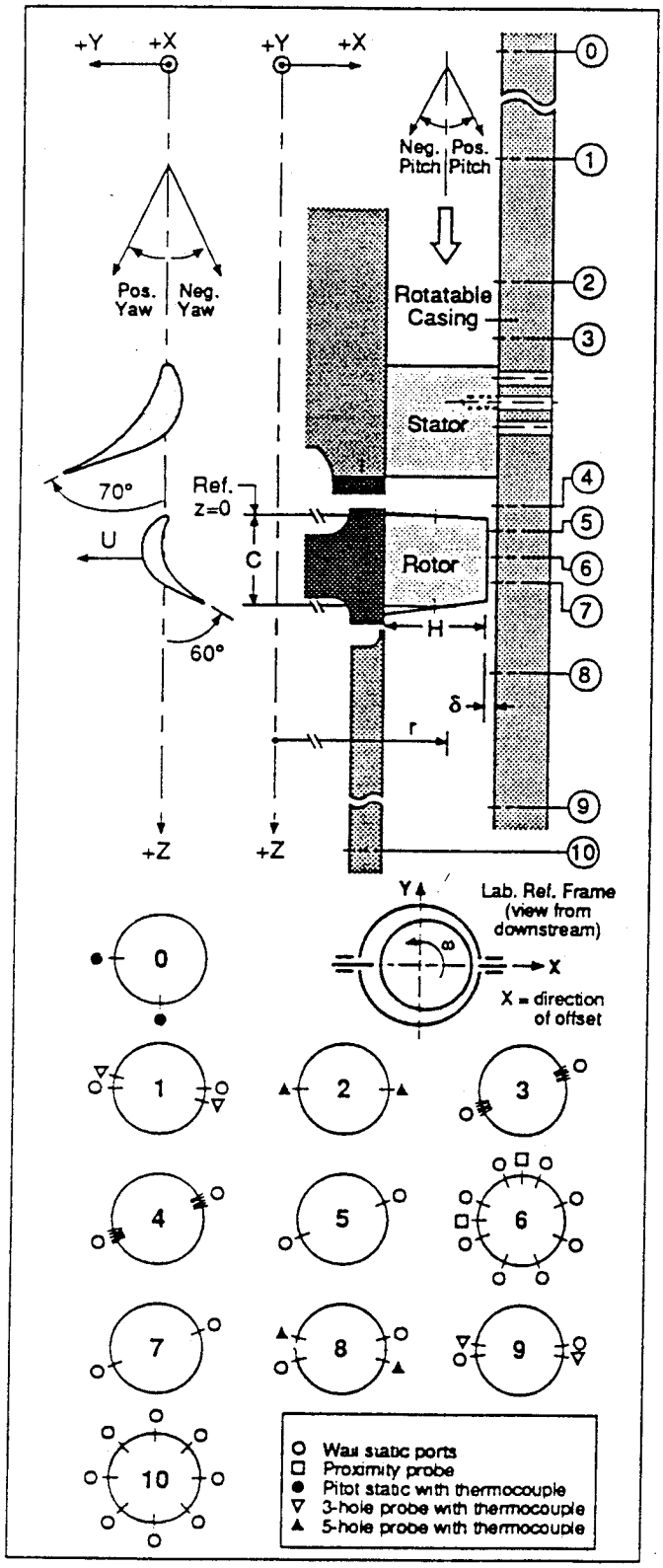

Fig. 2.14b Type of instrument used at each station

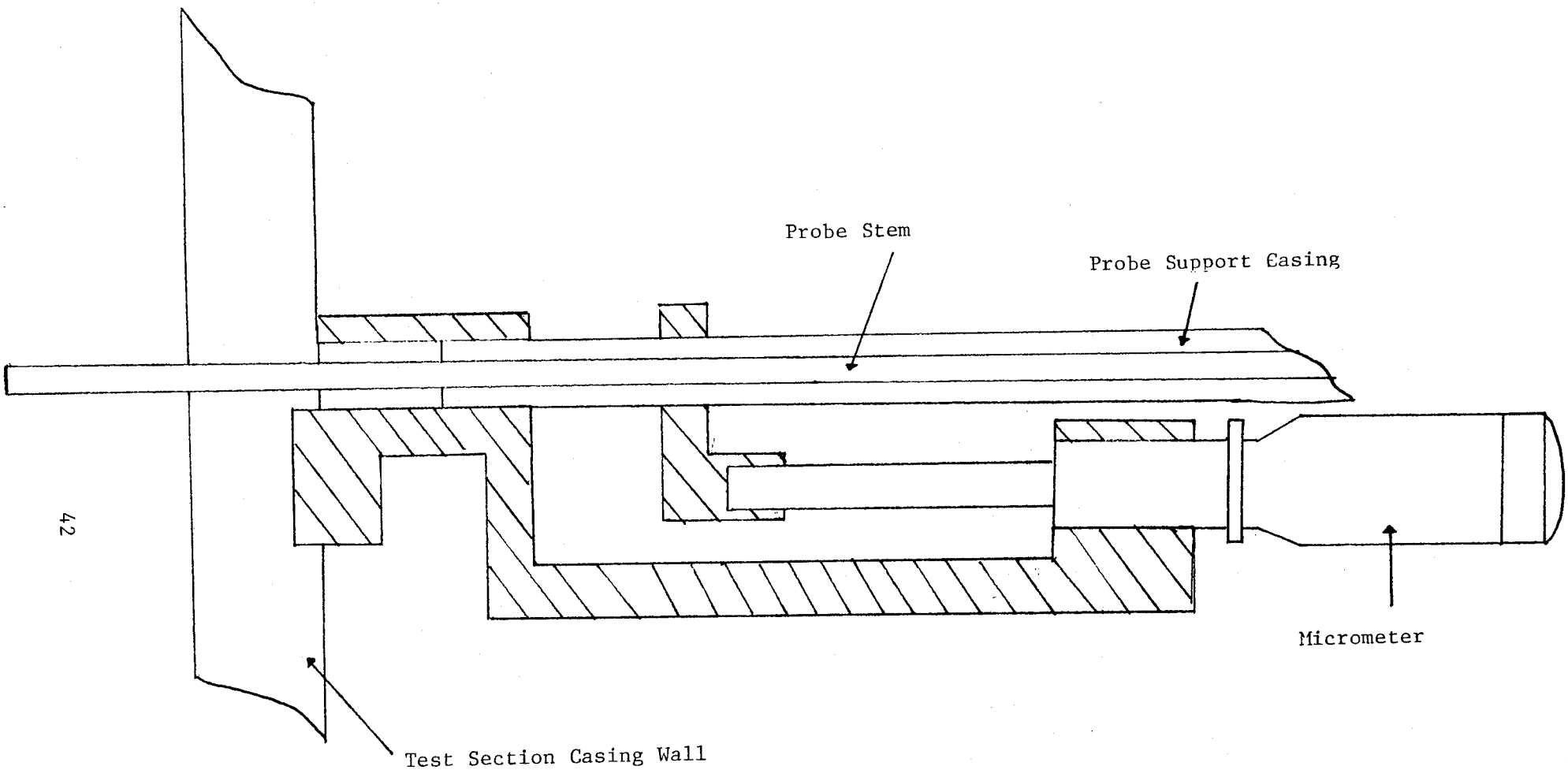

Figure 2.15 Probe Holder/Traverser

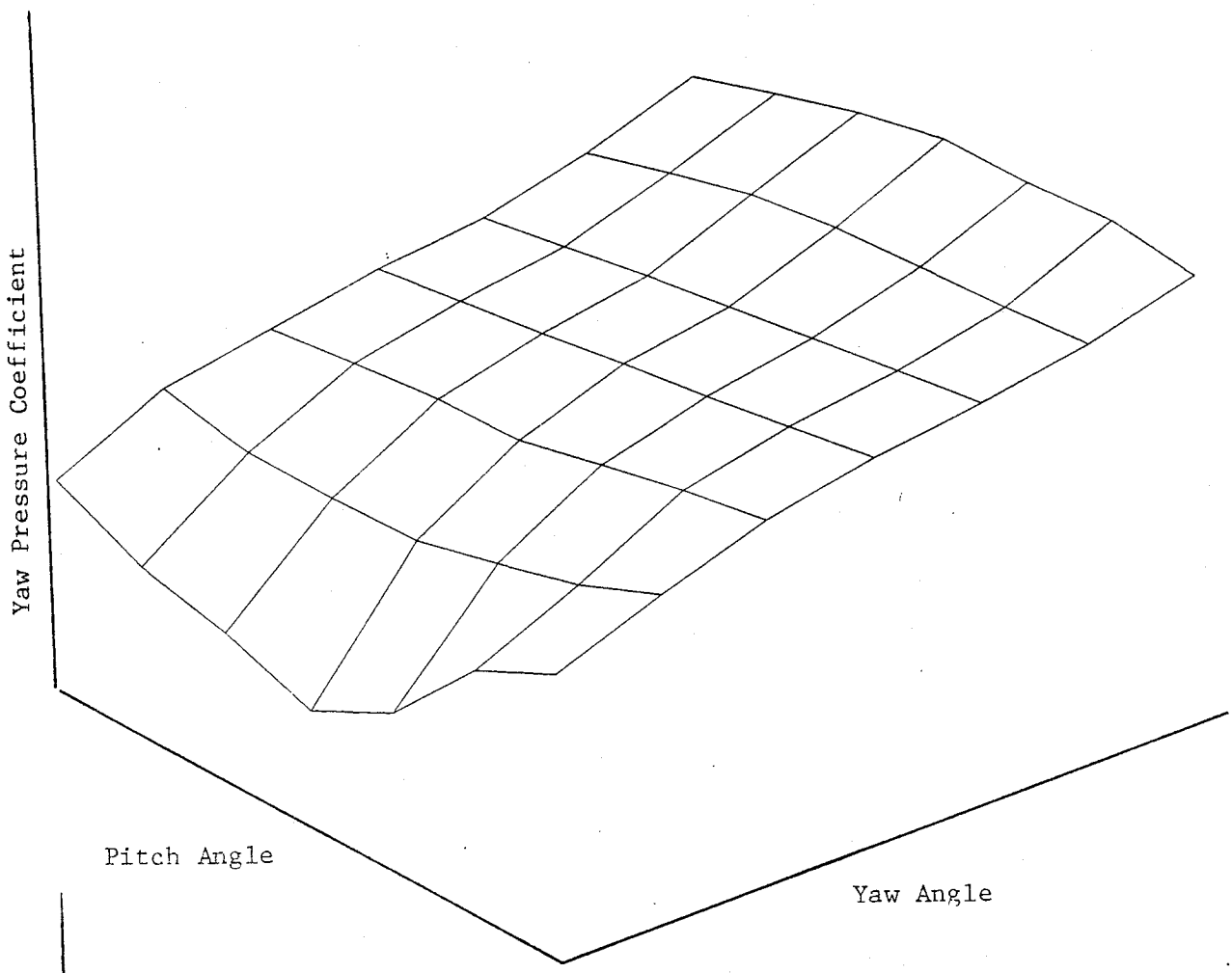

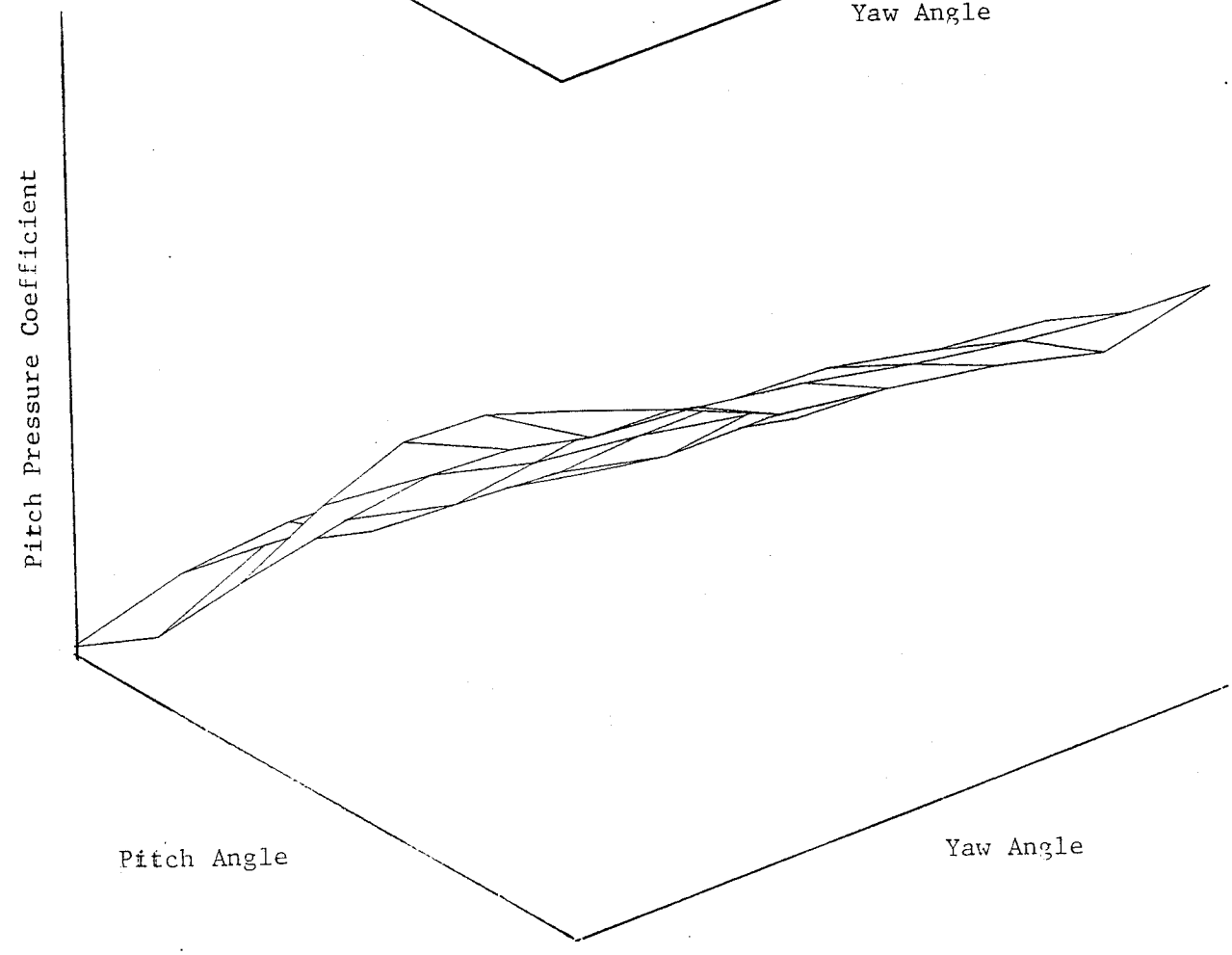

Figure A2 5-Hole Probe Calibration Data

problem, because the tip-induced flow underturning is very small in the inner half of the passage. The three-hole probes, on the other hand, can scan all but the bottom 6 mm of the passage.

The normal mode of usage of these probes is to align them to the flow by zeroing the pressure differences between side holes. This would be cumbersome in our experiment, and we opted instead for placing each probe at an angle near the middle of the expected flow angles, and recording the side-to-side and upper-lower hole pressure differentials. This required a separate calibration experiment, which was performed in the Wright Brothers Wind Tunnel. The three-hole probes were calibrated in the yaw range of ±30°. The five-hole probes were calibrated in ±10°, except for one, which was also calibrated to ±30°. The calibration data are included in Appendix 2A for reference. Occasionally, the data from a five-hole probe calibrated to ±10° exceeded this range. In such cases, the one ±30° calibration curve was used instead.

The 16 pressure lines from the multi-blade probes were also routed to the Scanivalve. The arrangement of the full set of static tap and probe pressure lines is detailed in Ref. [4]. Frequent recalibration of the pressure transducers was made with respect to a model 398 Baratron precision transducer.

The manner in which the data from these instruments was analyzed is best described in connection with the data themselves (Sections 4.3 and 5.2).

2.3.3 Other Instrumentation

Induction proximeter probes (Ref. [4]) were used to sense the passage of each individual blade tip for clocking purposes. These also provided rotor displacement information during dynamic tests. For static tests, calibrated shims were used, as noted before. These were verified against measurements made with the rotor stopped by means of a micrometer depth gauge inserted through holes in the casing.

Turbine torque is sensed by means of strain gauge bridges at two locations on the shaft, one above and one below the bearing set. The upper location has the advantage of being free from bearing friction uncertainties, but, because of the stiffness of the upper shaft section, its sensitivity has proven insufficient. The lower sensor, located on the thinner middle shaft, has adequate sensitivity, but it measures turbine torque minus bearing friction. Bearing friction tare can be removed by running the turbine in vacuum using the DC generator as a motor. Any reading on the lower torque gauge is then due to the bearings. This procedure suffers from the defect that the actual running conditions on the lower bearing set include the full axial thrust (approximately 2000 N ≅ 440 lb) under which the frictional force may be different than with no axial load. Calibration at full load and running conditions was not feasible. Instead, we have performed static calibration tests under axial loads (weights) up to 310 lb, with the result that axial load effects are negligible in this range (less than 0.1%). The procedure is therefore to correct the torque calibration data only for the vacuum friction effects. The results are given in Appendix 2B.

The instruments and calibrations used for flow and other status data can be found in Ref. [4].

2.4 Instrumentation and Data Acquisition (LSTF)

The major data from the Labyrinth Seals Test Facility were the time-dependent gland pressure data from the four Kulite transducers. These, as well as their calibration and reference arrangements, were fully discussed in Ref. [4]. Also discussed were the proximeters, flow and pressure sensors, and speed and frequency counters.

The only important addition since January 1990 was the hot wire anemometry instrumentation used to directly measure the gland exit swirl velocity. This was a single-wire arrangement. The wire (0.005 mm thick and 1.6 mm long) was placed 1

Appendix2A

This appendix describes the calibration procedure for the 3 and 5-hole-probes. Each 3 hole probe was calibrated at zero pitch angle for yaw angle values from -25 to +25 degrees in 5 degree increments. Figure A1 shows the nondimentsional pressure coefficients for yaw anle, total pressure, and static pressure vs yaw angle for a typicla 3-hole probe. For 5-hole probes the nondimentsional pressure coefficients for pitch angle, yaw angle, total pressure, and static pressure were taken for a combination of yaw-pitch angles. Both the pitch and yaw angles were varied from -10 to +10 degress in 5 degree increments. Finally, one 5-hole probe was chosen for calibration over a wider range, and was calibrated for pitch and yaw anlges from -30 to +30 degrees in 10 degree increments. The data can be seen in Figure A2.

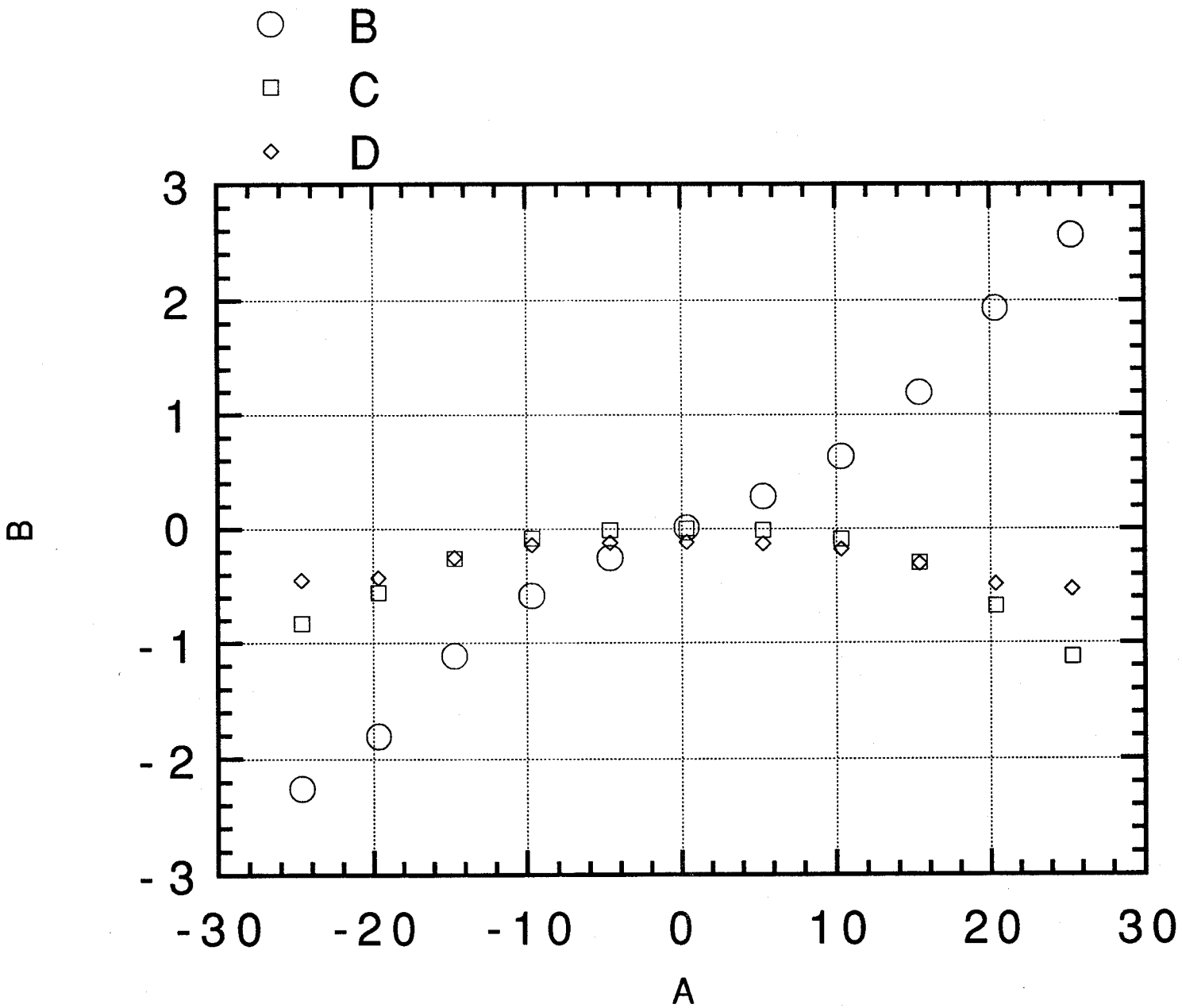

Figure A1 Calibration Data for a 3-hole probe

Appendix B

This appendix contains lower torque bridge calibration data. Torque bridge was calibrated by hanging equal weights at diametrically opposed locations about the shaft. The loading values were 1.2, 41.2, 81.2, 121.2, 161.2, 193.2, and 225.2 in-lbf. These loadings were repeated under various thrust loads. Figure B1 shows torque calibration data under thrust loads of 0, 78, 105, 167, 220, 269, 309 lbf. There is no measurable difference in the slope. Then the shaft was spun in vacuum at various speeds to evaluate the effects of bearing friction on the torque reading. As seen in B2, no correlation with speed exists

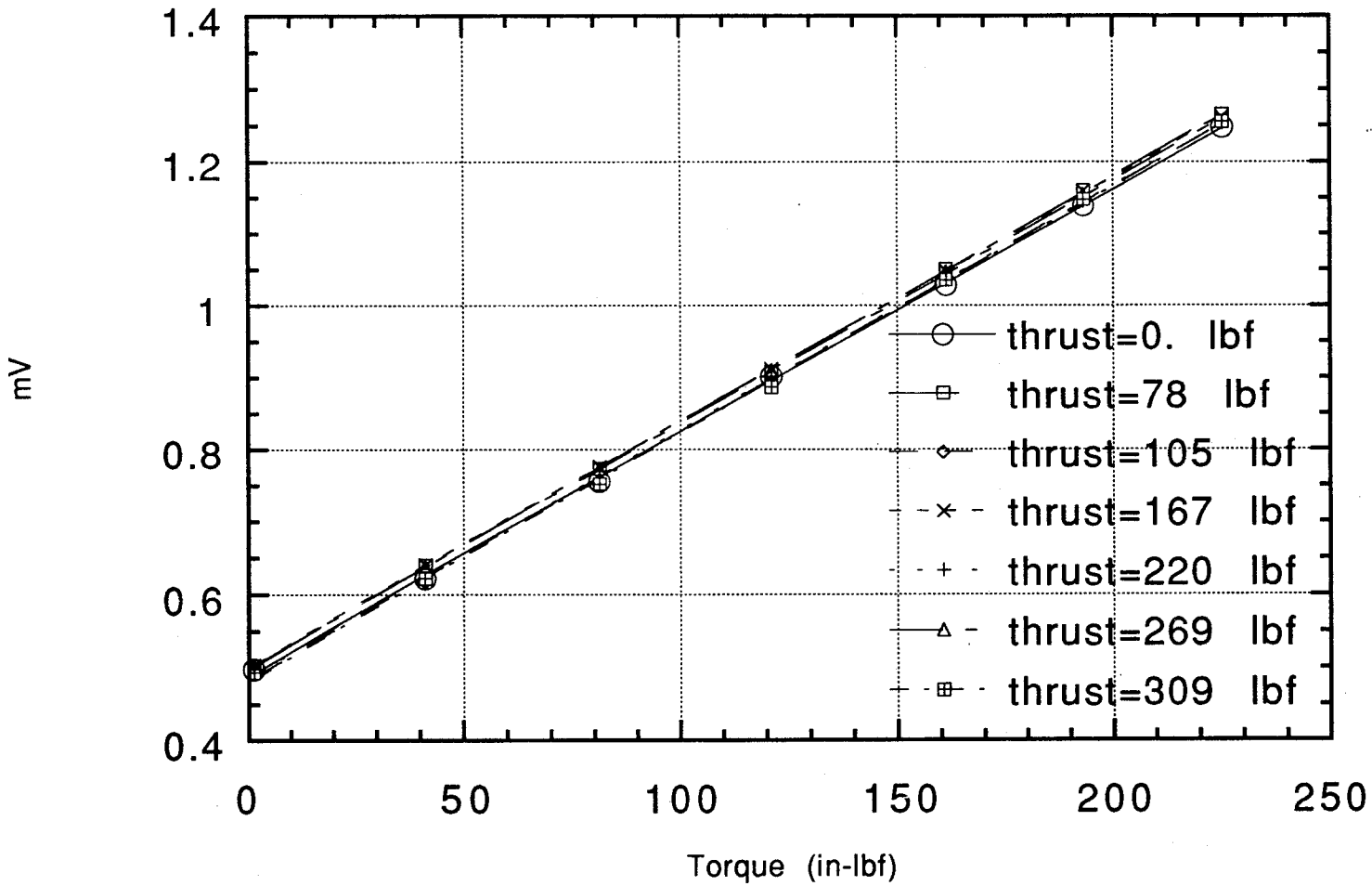

Figure B1 Calibration Data for Lower Torque Bridge under various thrust loads.

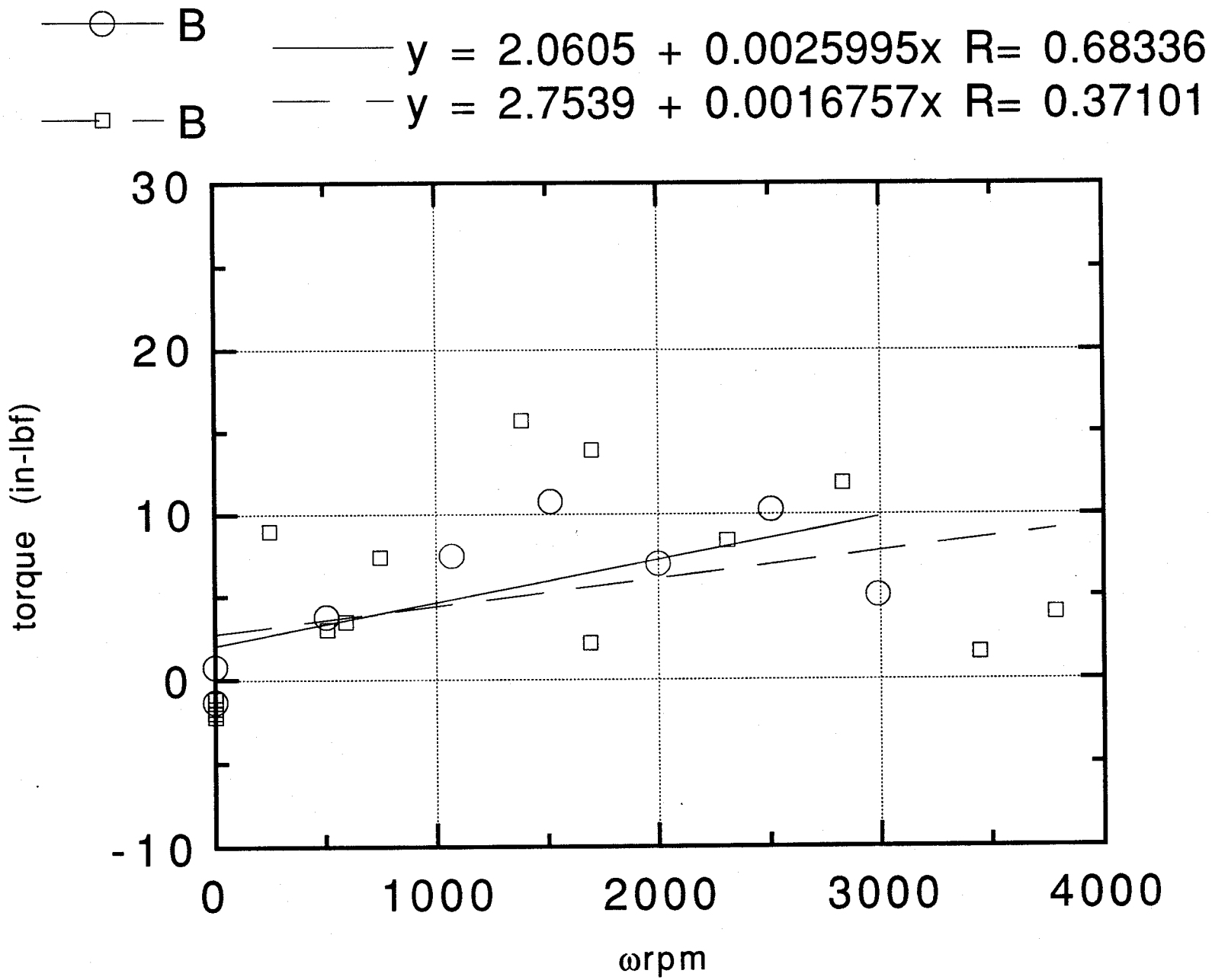

Figure B2 Friction measured by torque bridge at various speeds

mm downstream of the seal discharge, and could traverse radially across the width of the discharge jet, as well as rotate inside the plane of the jet, i.e. while remaining parallel to the casing surfaces. Measurements were made at 20° intervals about the approximate maximum reading, covering ±40°, then a sine curve was fitted to the data, and the maximum was thereby located more precisely. This maximum indicated the flow direction to within 1°, as determined by calibration tests in a well-defined jet, and also in the facility at zero speed, whirl and swirl.

3.0 Parameters Investigated and Test Matrix

3.1 Alford Force Test Facility

Figure 3.1 shows the geometrical parameters that were varied in the AFTF rig. The nominal values were:

H = 22.8 mm (blade height)

c = 21.4 mm (mean axial chord, not varied)

d = 10.6 mm (d/c = 0.50)

d′ = 8.2 mm (d′/c = 0.38)

t_m = 0.68 mm (t_m/H = 0.030)

e = ±0.46 mm (e/H = ±2.0%, eccentricity)

No shroud

In terms of operating parameters, the nominal conditions were:

m = 4.48 kg/sec

$\bar{P}$ = 2 atm (mean loop pressure, Freon 12)

$\bar{T} \cong$ 295 K

ω = 3440 RPM (spin rate)

Ω = 0 (shaking or whirl rate)

The variations on these parameters for which data were obtained are summarized in Table 3.1.

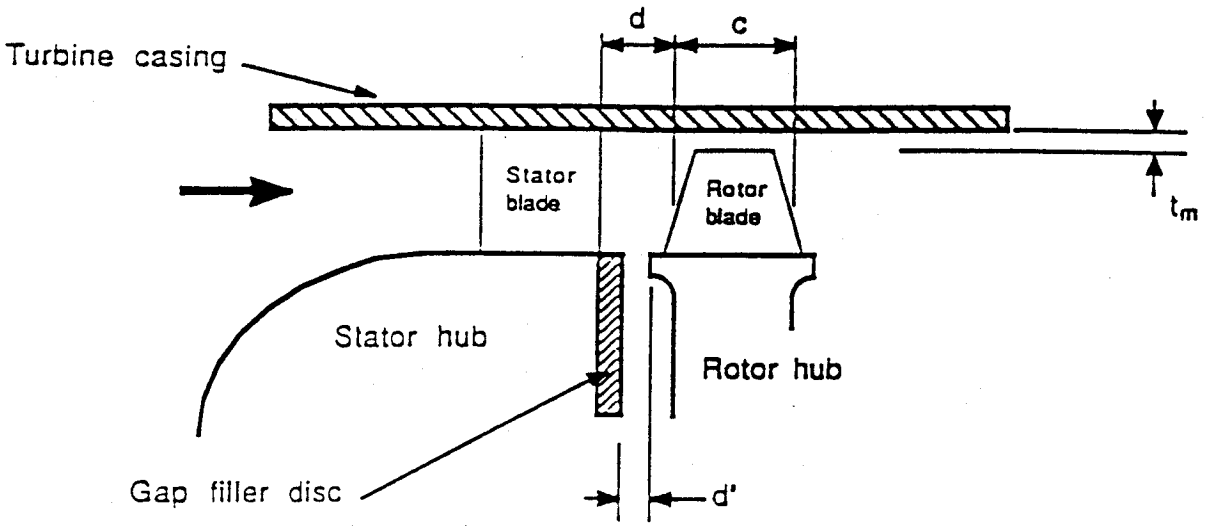

Fig. 3.1: Schematic showing major dimensions of interest for the test turbine

TABLE 3.1

Conf. #	t_m/H %	d/c %	d'/c %	Shroud (Y/N)	$\dot{m}/\dot{m}_{DES}$ %	ω/ω_{DES} %	e/t_m Range, %	Ω/ω Range, %	$\bar{P}$ (atm)	Forces (Y/N)	Flow Map (Y/N)
1	3.0	50	38	N	50	100	-67/+67	0	1	Y	N
					100	70			2	Y	Y
					100	100			2	Y	Y
					100	110	(e=±0.46mm)		2	Y	Y
					100	70		40/80	2	Y	N
					100	100		40/60	2	Y	N
					100	110		40/55	2	Y	N
2	3.0	26	15	N	100	70	-67/+67	0	2	Y	N
						100				Y	Y
						110				Y	N
3	3.0	26	1.3	N	100	70	-67/+67	0	2	Y	N
						100				Y	N
						110				Y	N
4	1.87 (t_m=0.43mm)	26	15	N	100	70	-59/+59	0	2	Y	N
						100	(e=±0.25mm)			Y	Y
						110				Y	N
5	1.87	26	1.3	N	100	70	-59/+59	0	2	Y	N
						100				Y	Y
						110				Y	N
6	4.5	26	1.3	Y	100	70	-59/+59	0	2	Y	N
						100				Y	Y
						110				Y	N

For the nominal geometry (called Configuration 1), the operating parameters were varied over a fairly wide range: mass flow and mean pressure were simultaneously reduced by 50%, speed was varied from 70% to 110% of nominal, the eccentricity was statically varied between -2.0% and +2.0% of chord (i.e., ±67% of mean tip gap), and tests were run in air instead of Freon 12. For each of these conditions (except the air and the low $\bar{P}$ tests), both force and flow mapping data were acquired. In addition, tests were done under dynamic (shaking along one axis) conditions, with shaking frequency in the range of 40% to about 80% of spin rate. In these dynamic tests, only force measurements were attempted.

Configuration 1 featured, as noted, fairly large axial gap values (this was intentionally done to minimize the risk of rubbing, since the final axial gap is the most uncertain dimension during assembly). Also, the Shuttle HPFTP turbine has $d/c \cong 0.36$, not far from our values. The first variation (Configuration 2) consisted of mounting the stator 5.6 mm closer to the rotor, using the lower set of stator blade mounting screw holes. This reduced both d and d′ (Fig. 3.1) simultaneously. A full set of turbine speed variations, and in each case, of static eccentricity variations, was then executed. Force data were taken in each case, while flow mapping was done at zero and (+/-) maximum eccentricity, but only at nominal turbine speed.

The third variation (Configuration 3) involved insertion of a ring between the stator and rotor hubs, such as to reduce d′ to as nearly zero as practicable, while leaving d unchanged. The same set of speed and static eccentricity conditions as in Configuration 2 was then repeated. Force data were obtained in all cases, but flow mapping data were inadvertently lost due to a bad connection (which was only noticed after the configuration had been changed by enlarging the blades, see below).

For Configuration 4, the turbine blade tips were chromium-plated (by approximately 15/1000 of an inch, or 0.38 mm), and then ground back to a net addition of 10/1000 of an inch (0.25 mm). This left a mean blade-tip gap of 0.43 mm, or 1.87%

of blade height. The axial gaps were as in Configuration 2 (axial insert ring removed).

Because of the loss of flow data for Configuration 3, it was not possible to assess the effect on flow details of reducing the hub gap alone (although this assessment was still possible in terms of net forces). For this reason, Configuration 5 was added to the original test plans. This configuration differs from Configuration 4 only in the re-insertion of the axial ring to reduce d′ to a minimum. The full set of force data were acquired, plus complete flow maps at the nominal turbine speeds.

Throughout the preceding set of configurations, the turbine remained unshrouded, thus faithfully reflecting the conditions on the Shuttle HPFTP (first stage) turbine. There is also interest in the radial forces on shrouded turbines, similar to those used in the HPOTP. Rather than attempting again a good 1:1 match to that turbine (which would have entailed substantial re-design of the rig), it was decided, in consultation with cognizant NASA personnel, to modify the same turbine used in the previous tests by the addition of a shroud band, fitted with suitable sealing strips. This is our Configuration 6 (Table 3.1). The detailed geometry of the shroud and seal will be discussed in Section 6. The tests once again included force data and flow mapping for design and off-design conditions. In addition, gland pressure data were also acquired (both low frequency, as in the other configurations, and also real time, for comparison to LSTF data).

The above test matrix encompasses all of the parameters that were identified as potentially significant in our preliminary investigations (Reports for Phases I and II, Refs. [3] and [4]). The major shortfall with respect to the test plans that were formulated at the end of Phase II occurred in the area of dynamic offset testing. As indicated, this was only done for Configuration 1, with results which, as will be discussed in Section 8, were not satisfactory. This was in spite of a strong effort in this area, which consumed a disproportionate fraction of our time and resources. A consequence of this disproportionate attention to the dynamics part of the test plan was the need to

reduce somewhat the number of variations of each of the other parameters, from the originally planned three to, in most cases, only two. The results indicate that the parametric sensitivities are not large and the trends are consistently identified, despite the limited number of variations.

3.2 Labyrinth Seals Test Facility

The general geometry of the labyrinth seals used in this investigation is shown in Fig. 3.2. Five different configurations were built and tested. These are detailed in Table 3.2.

Builds 1 and 2 are geometrically very similar, Build 2 being an improved version of Build 1. Both are "short" seals, with the ratio (l tan 6°)/δ*, which characterizes the spreading of the jet from the first gap in relation to the width of the second gap, being only 1.44. The land surface is smooth, and knife edges are sharp.

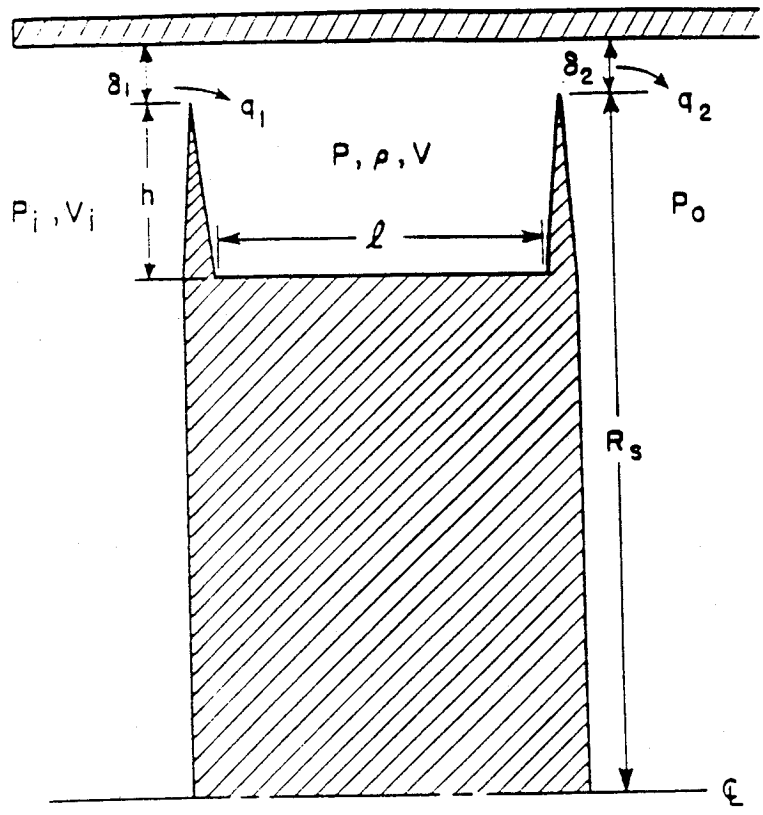

Fig. 3.2 Cross-section of seal; geometry and flow variables are given

TABLE 3.2
SEAL AND LAND GEOMETRY FOR THE 5 DIFFERENT BUILDS

Build	Seal Dimensions (Rotor) cm in.						Land Dimensions (Stator) cm in.				
	Material	R_s	l	h_1	d	α_s	Material	ϕ_s	h_2	l_s	δ_1^*
#1	4140 steel	15.16 6 5.971	1.016 0.400	0.508 0.200	0 0	20°	1117 steel	15.240 6.000	0 0	0 0	0.073 7 0.029
#2	4140 steel	15.16 6 5.971	1.016 0.400	0.508 0.200	0 0	20°	1117 steel	15.245 6.002	0 0	0 0	0.078 7 0.031
#3	304 SS	15.17 7 5.975	1.727 0.680	0.508 0.200	0.043 0.017	17°	1117 steel	15.245 6.002	0 0	0 0	0.068 6 0.027
#4	304 SS	15.17 7 5.975	1.727 0.680	0.508 0.200	0.043 0.017	17°	304 SS Hastelloy X	15.245 6.002	0.483 0.190	1.905 0.750	0.068 6 0.027
#5	4140 steel	15.16 6 5.970	1.016 0.400	0.508 0.200	0 0	17°	304 SS Hastelloy X	15.245 6.002	0.483 0.190	1.905 0.750	0.078 7 0.031

R_s = seal mean radius
l = distance between knife edges (seal length)
h_1 = seal depth
d = knife edge width at tip
α_s = knife edges, included angle
ϕ_s = casing (land) diameter
h_2 = honeycomb width
l_s = length of honeycomb section
δ_1^* = mean seal gap

Build 3 is a longer seal (l tan 6°/δ^* = 2.65) with the knife edges slightly flattened. The land is still smooth.

($\hat{r}$-mils) $\hat{\epsilon} = \frac{\hat{r}}{\hat{c}}$	VANE ANGLE	PRESSURE RATIO π_s	SPIN SPEEDS ω (Hz.)	WHIRL SPEEDS Ω (Hz.)
(7.3) 0.2517	0°*plate*	1.00	0	±7.57, ±14.12, ±20.10 ±26.18, ±32.29, ±40.53
(7.3) 0.2517	0°plate	1.21	0	±7.11, ±14.72, ±21.99 ±25.87, ±33.85, ±40.03
(7.3) 0.2517	0°plate	1.32	0	±8.08, ±14.98, ±21.76 ±26.87, ±33.73, ±40.98
(7.3) 0.2517	0°plate	1.44	0	±7.08, ±14.73, ±21.95 ±26.98, ±33.93, ±40.05
(7.3) 0.2517	0°plate	1.68	0	±7.64, ±14.98, ±21.79 ±26.61, ±33.03, ±40.94
(7.3) 0.2517	0°*plate*	1.32	+20.11, +27.50, +32.97 +45.00, +57.02	±7.53, ±14.29, ±20.03 ±26.94, ±32.24, ±40.49
(7.3) 0.2517	0°plate	1.32	-20.87, -27.07, -33.05 -44.91, -57.03,	±8.00, ±14.52, ±20.11 ±26.21, ±32.07,±40.45
(7.3) 0.2517	0°*plate*	1.44	+20.48, +28.20, +32.05 +44.36, +57.11	±8.59, ±14.20, ±19.59 ±26.18, ±32.22, ±40.43
(7.3) 0.2517	0°plate	1.44	-20.07, -27.33, -33.83 -44.06, -57.41,	±7.04, ±13.87, ±20.88 ±26.48, ±32.37, ±40.65
(7.3) 0.2517	45°	1.00	0	±8.48, ±15.02, ±20.58 ±26.07, ±32.42, ±40.90
(7.3) 0.2517	45°	1.21	0	±7.34, ±14.81, ±20.75 ±26.03, ±32.21, ±39.04
(7.3) 0.2517	45°	1.32	0	±7.76, ±14.71, ±21.84 ±26.48, ±32.44, ±39.69
(7.3) 0.2517	45°	1.44	0	±7.29, ±14.48, ±20.29 ±26.19, ±32.34, ±42.19
(7.3) 0.2517	45°	1.68	0	±7.26, ±14.21, ±20.25 ±27.87, ±32.24, ±39.03
(7.3) 0.2517	45°	1.32	+20.34, +27.54, +32.87 +44.87, +57.87	±7.05, ±14.98, ±20.35 ±26.97, ±32.34, ±40.08
(7.3) 0.2517	45°	1.32	-21.03, -27.07, -33.35 -44.47, -56.34,	±6.99, ±14.23, ±20.87 ±26.38, ±32.42, ±40.15
(7.3) 0.2517	45°	1.46	+20.34, +28.09, +32.65 +44.96, +57.87	±7.07, ±13.95, ±21.24 ±26.88, ±32.98, ±40.94
(7.3) 0.2517	45°	1.46	-20.47, -27.35, -33.75 -43.96, -57.49,	±7.18, ±14.47, ±20.37 ±26.58, ±32.37, ±39.89

TABLE 3.3: Test matrix for build #1. For geometry see Table 3.2. All combinations on a given row of the matrix were tested. $\hat{r}$ = seal offset.

($\hat{r}$-mils) $\hat{\epsilon} = \frac{\epsilon}{r_c}$	VANE ANGLE	PRESSURE RATIO π_s	SPIN SPEEDS ω (Hz.)	WHIRL SPEEDS Ω (Hz.)
(7.3) 0.2355	0°*plate*	1.47, 1.54, 1.61 1.68, 1.75, 1.89	0	±7.06, ±14.22, ±21.07 ±26.18, ±32.45, ±40.98
(7.3) 0.2355	0°*plate*	1.61	21.34, 43.90, 65.01	±7.06, ±14.22, ±21.07 ±26.18, ±32.45, ±40.98
(7.3) 0.2355	0°*plate*	1.61	-22.44, -43.43, -64.93	±7.06, ±14.22, ±21.07 ±26.18, ±32.45, ±40.98
(7.3) 0.2355	0°*plate*	1.75	22.57, 44.53, 65.73	±7.06, ±14.22, ±21.07 ±26.18, ±32.45, ±40.98
(7.3) 0.2355	0°*plate*	1.75	-21.67, -43.53, -65.20	±7.06, ±14.22, ±21.07 ±26.18, ±32.45, ±40.98
(7.3) 0.2355	15°*plate*	1.47, 1.54, 1.61 1.68, 1.75, 1.89	0	±7.06, ±14.22, ±21.07 ±26.18, ±32.45, ±40.98
(7.3) 0.2355	15°*plate*	1.61	22.14, 43.71, 65.98	±7.06, ±14.22, ±21.07 ±26.18, ±32.45, ±40.98
(7.3) 0.2355	15°*plate*	1.61	-22.23, -42.45, -65.33	±7.06, ±14.22, ±21.07 ±26.18, ±32.45, ±40.98
(7.3) 0.2355	15°*plate*	1.75	22.03, 44.97, 67.23	±7.06, ±14.22, ±21.07 ±26.18, ±32.45, ±40.98
(7.3) 0.2355	15°*plate*	1.75	-21.06, -41.13, -65.29	±7.06, ±14.22, ±21.07 ±26.18, ±32.45, ±40.98
(7.3) 0.2355	30°	1.47, 1.54, 1.61 1.68, 1.75, 1.89	0	±7.06, ±14.22, ±21.07 ±26.18, ±32.45, ±40.98
(7.3) 0.2355	30°	1.61	21.54, 44.18, 67.36	±7.06, ±14.22, ±21.07 ±26.18, ±32.45, ±40.98
(7.3) 0.2355	30°	1.61	-22.03, -43.93, -65.13	±7.06, ±14.22, ±21.07 ±26.18, ±32.45, ±40.98
(7.3) 0.2355	60°	1.47, 1.54, 1.61 1.68, 1.75, 1.89	0	±7.06, ±14.22, ±21.07 ±26.18, ±32.45, ±40.98
(7.3) 0.2355	60°	1.61	21.48, 43.50, 64.91	±7.06, ±14.22, ±21.07 ±26.18, ±32.45, ±40.98
(7.3) 0.2355	60°	1.61	-22.38, -43.00, -64.49	±7.06, ±14.22, ±21.07 ±26.18, ±32.45, ±40.98
(7.3) 0.2355	60°	1.75	21.03, 44.93, 65.35	±7.06, ±14.22, ±21.07 ±26.18, ±32.45, ±40.98
(7.3) 0.2355	60°	1.75	-21.67, -43.53, -65.20	±7.06, ±14.22, ±21.07 ±26.18, ±32.45, ±40.98
(7.3) 0.2355	0°plate	1.47, 1.61 1.75	0	±7.52, ±20.87 ±33.17, ±48.15
(7.3) 0.2355	15°plate	1.47, 1.61 1.75	0	±7.52, ±20.87 ±33.17, ±48.15
(7.3) 0.2355	30°	1.47, 1.61 1.75	0	±7.52, ±20.87 ±33.17, ±48.15
(7.3) 0.2355	60°	1.47, 1.61 1.75	0	±7.52, ±20.87 ±33.17, ±48.15

Table 3.4 Test Matxix for build #2.

($\hat{r}$-mils) $\hat{\epsilon} = \frac{\epsilon}{\delta^*}$	VANE ANGLE	PRESSURE RATIO π_s	SPIN SPEEDS ω (Hz.)	WHIRL SPEEDS Ω (Hz.)
(1.0) 0.0370	0°plate	1.27, 1.38, 1.46 1.65, 1.83	0	±7.52, ±20.87 ±33.17, ±48.15
(1.0) 0.0370	15°plate	1.25, 1.39, 1.42 1.65, 1.84	0	±7.52, ±20.87 ±33.17, ±48.15
(1.0) 0.0370	30°	1.27, 1.38, 1.44 1.66, 1.82	0	±7.52, ±20.87 ±33.17, ±48.15
(1.0) 0.0370	60°	1.25, 1.40, 1.46 1.66, 1.85	0	±7.52, ±20.87 ±33.17, ±48.15
(3.8) 0.1407	0°plate	1.13, 1.21, 1.27 1.38, 1.48, 1.65	0	±7.52, ±20.87 ±33.17, ±48.15
(3.8) 0.1407	0°plate	1.73, 1.79, 1.94 2.07, 2.29, 2.40	0	±7.52, ±20.87 ±33.17, ±48.15
(3.8) 0.1470	0°plate	1.48	±44.87, ±66.52	±7.52, ±20.87 ±33.17, ±48.15
(3.8) 0.1470	15°plate	1.24, 1.40, 1.55 1.64, 1.81	0	±7.52, ±20.87 ±33.17, ±48.15
(3.8) 0.1407	15°plate	1.55	±44.87, ±66.52	±7.52, ±20.87 ±33.17, ±48.15
(3.8) 0.1470	30°	1.23, 1.38, 1.55 1.66, 1.76	0	±7.52, ±20.87 ±33.17, ±48.15
(3.8) 0.1470	30°	1.55	±44.87, ±66.52	±7.52, ±20.87 ±33.17, ±48.15
(3.8) 0.1407	60°	1.11, 1.19, 1.23 1.38, 1.55, 1.66	0	±7.52, ±20.87 ±33.17, ±48.15
(3.8) 0.1407	60°	1.79, 1.88, 2.02 2.21, 2.30, 2.38	0	±7.52, ±20.87 ±33.17, ±48.15
(3.8) 0.1407	60°	1.54	±44.87, ±66.52	±7.52, ±20.87 ±33.17, ±48.15
(7.3) 0.2704	0°plate	1.20, 1.38, 1.58 1.67, 1.88	0	±7.52, ±20.87 ±33.17, ±48.15
(7.3) 0.2704	15°plate	1.21, 1.38, 1.55 1.67, 1.93	0	±7.52, ±20.87 ±33.17, ±48.15
(10.7) 0.3963	0°plate	1.23, 1.39, 1.52 1.65, 1.79	0	±7.52, ±20.87 ±33.17, ±48.15
(10.7) 0.3963	60°	1.25, 1.40, 1.46 1.66, 1.85	0	±7.52, ±20.87 ±33.17, ±48.15
(13.1) 0.4852	0°plate	1.27, 1.38, 1.46 1.65, 1.83	0	±7.52, ±20.87 ±33.17, ±48.15
(13.1) 0.4852	15°plate	1.25, 1.39, 1.42 1.65, 1.84	0	±7.52, ±20.87 ±33.17, ±48.15
(13.1) 0.4851	30°	1.27, 1.38, 1.44 1.66, 1.82	0	±7.52, ±20.87 ±33.17, ±48.15
(13.1) 0.4851	60°	1.25, 1.40, 1.46 1.66, 1.85	0	±7.52, ±20.87 ±33.17, ±48.15

Table 3.5 Test Matxix for build #3.

($\hat{r}$-mils) $\hat{\epsilon} = \frac{r}{R}$	VANE ANGLE	PRESSURE RATIO π_s	SPIN SPEEDS ω (Hz.)	WHIRL SPEEDS Ω (Hz.)
(3.8) 0.1407	0°plate	1.08, 1.19, 1.28 1.43, 1.58, 1.68	0	±7.52, ±20.87 ±33.17, ±48.15
(3.8) 0.1407	0°plate	1.83, 1.96, 2.02 2.11, 2.21, 2.31	0	±7.52, ±20.87 ±33.17, ±48.15
(3.8) 0.1407	0°plate	1.58	±20.80, ±44.87, ±66.52 ±85.37, ±105.03	±7.52, ±20.87 ±33.17, ±48.15
(3.8) 0.1407	15°plate	1.25, 1.40, 1.58 1.65, 1.80	0	±7.52, ±20.87 ±33.17, ±48.15
(3.8) 0.1407	15°plate	1.58	±44.87, ±66.52	±7.52, ±20.87 ±33.17, ±48.15
(3.8) 0.1407	30°	1.25, 1.42, 1.59 1.68, 1.81	0	±7.52, ±20.87 ±33.17, ±48.15
(3.8) 0.1407	30°	1.59	±20.80, ±44.87 ±66.52, ±85.37	±7.52, ±20.87 ±33.17, ±48.15
(3.8) 0.1407	60°	1.24, 1.41, 1.56 1.67, 1.83	0	±7.52, ±20.87, ±33.17 ±48.15, ±57.37
(3.8) 0.1407	60°	1.56	±44.87, ±66.52	±7.52, ±20.87 ±33.17, ±48.15,

Table 3.6 Test Matxix for build #4.

($\hat{r}$-mils) $\hat{\epsilon} = \frac{r}{R}$	VANE ANGLE	PRESSURE RATIO π_s	SPIN SPEEDS ω (Hz.)	WHIRL SPEEDS Ω (Hz.)
(3.8) 0.1407	0°plate	1.21, 1.32 1.44	0	±7.52, ±20.87 ±33.17, ±48.15
(3.8) 0.1407	0°plate	1.32	±44.87, ±66.52	±7.52, ±20.87 ±33.17, ±48.15
(3.8) 0.1407	15°plate	1.22, 1.30 1.46	0	±7.52, ±20.87 ±33.17, ±48.15
(3.8) 0.1407	15°plate	1.30	±44.87, ±66.52	±7.52, ±20.87 ±33.17, ±48.15

Table 3.7 Test Matxix for build #5.

Builds 4 and 5 feature a honeycomb land surface with a depth of 4.83 mm and a cell diameter of 0.8 mm. The seal is "long" in Build 4, and "short" in Build 5, being the same as those of Builds 3 and 2 respectively.

The parameters varied for each of these basic configurations, and are given in Tables 3.3 through 3.7. The seal pressure ratio was in the range from 1.11 to 2.38, which means that most of the tests were in the unchoked regime. The exit pressure was in all cases atmospheric. The rotor spin rate varied from 0 to ±65 Hz (3990 rpm), positive being defined as the inlet swirl direction. The circular whirl amplitude was kept constant over many runs, with variations (mainly in Build 3) to check linearity. The whirling speed varied from ±7 Hz (420 rpm) to ±48.15 Hz (2890 rpm). The nominal inlet swirl was 0°, 15°, 30°, 45° (Build 1 only), and 60°.

4.0 Experimental Results for the Basic Configuration

The basic configuration (Configuration 1 in Table 3.1) was investigated first and in somewhat more detail than the others. For this reason, this section will be devoted to a presentation of the Configuration 1 data in greater detail than will be the case for the subsequent configurations. On the other hand, the quality of the data was in some respects less good for this than for later cases, because of the cumulative experience gained during the course of the investigation. Therefore, some of the points will be better illustrated by particular pieces of data from later configurations (Sec. 5).

Section 4 is organized as follows: first, the basic performance of the (centered) turbine will be discussed. Next, the radial forces (direct and cross-force) for the eccentric turbine (static offsets only) will be shown, as derived from dynamometer data. Following this, the results of the flow mapping upstream and downstream of the turbine will be shown, and will be processed to obtain independent measures of the radial forces. Finally, the total radial forces (velocity triangles plus pressure nonuniformity) will be compared to those measured directly by the dynamometer.

4.1 Turbine Performance Map

Performance measurements were made to map the turbine. The mass flow was determined by a Venturi flowmeter. The inlet total pressure and temperature were measured by a total-static pitot tube with an attached thermocouple. The pressure drop was measured by directional probes placed at the mean radius both upstream and downstream of the turbine stage. The rotation rate was measured by an optical encoder.

Figures 4.1 and 4.2 show the dimensional and non-dimensional plot of pressure ratio versus mass flow for the unshrouded turbine at four different rotational speeds. Figure 4.3 shows the pressure ratio and the total-to-static efficiency versus mass flow at the design operating speed (3440 rpm) and shows that the efficiency peaks around 4.4 kg/s which is close to the design mass flow rate.

4.2 Dynamometer Force Data for the Basic Configuration

Forces were measured directly using the dynamometer, with a variety of shim combinations to obtain turbine offsets of up to 18 mil = 0.45 mm (gap = 27 mil = 0.68 mm). This was done at the nominal turbine speed of ω_D = 3440 rpm, plus at 0.7 ω_D and 1.1 ω_D. Considerable effort was devoted to improving the procedures to ensure repeatability of data. This involved several re-runs of each condition. The experience gained in this process proved valuable in expediting the process for the subsequent configurations.

The static forces obtained (F_x along the offset, positive if de-stabilizing; F_y perpendicular to offset, positive if leading to forward whirl) are displayed in physical units in Figs. 4.4, 4.5, and 4.6. Three data points are shown for each eccentricity, and the repeatability is obviously excellent (the individual data points can barely be distinguished). Linearity is good, especially for F_y, even though the offset was 67% of the mean gap. The correlation coefficient to a linear fit is from 0.995 to 0.999.

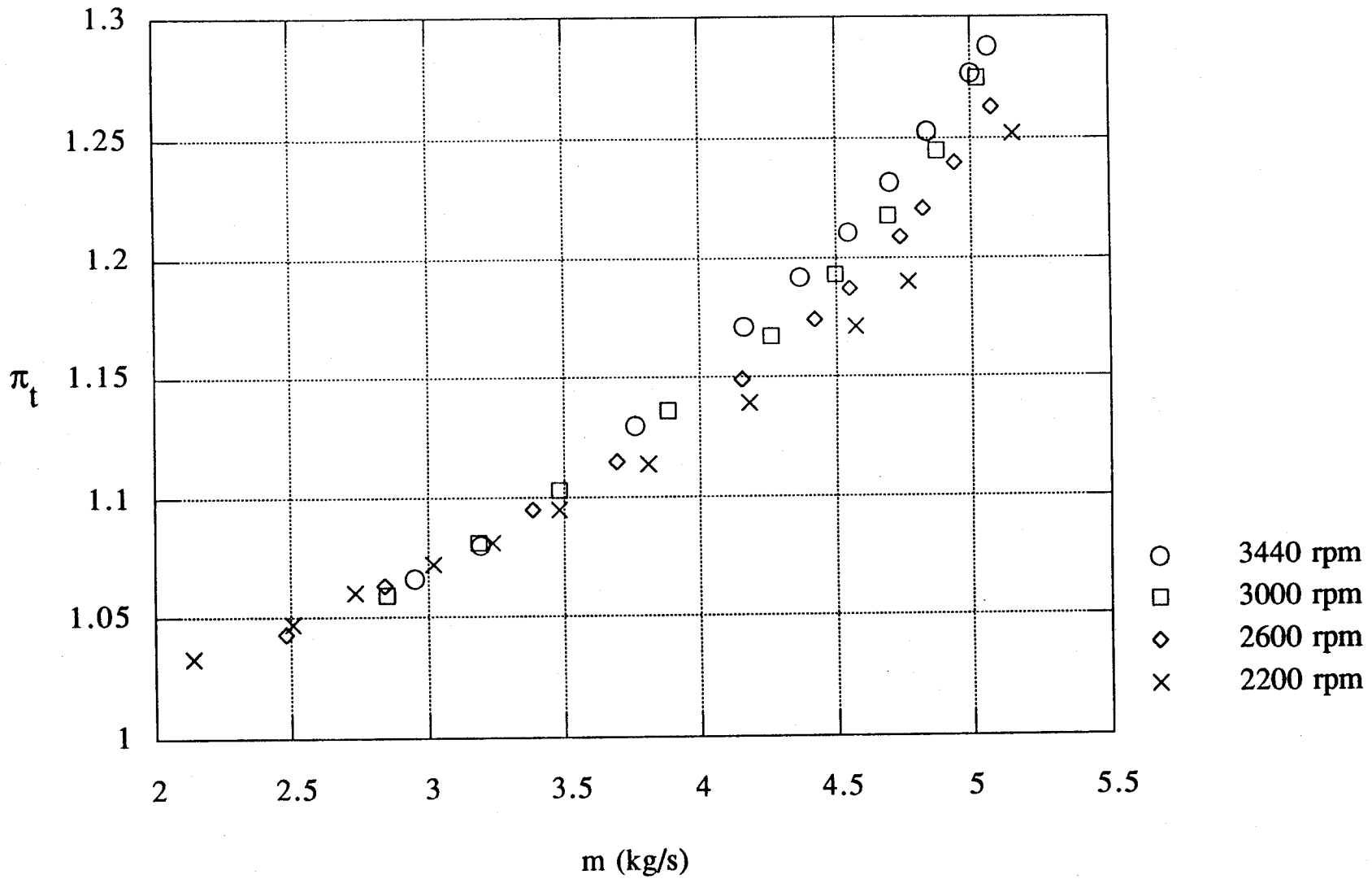

Fig. 4.1: Turbine pressure ratio vs. mass flow and speed

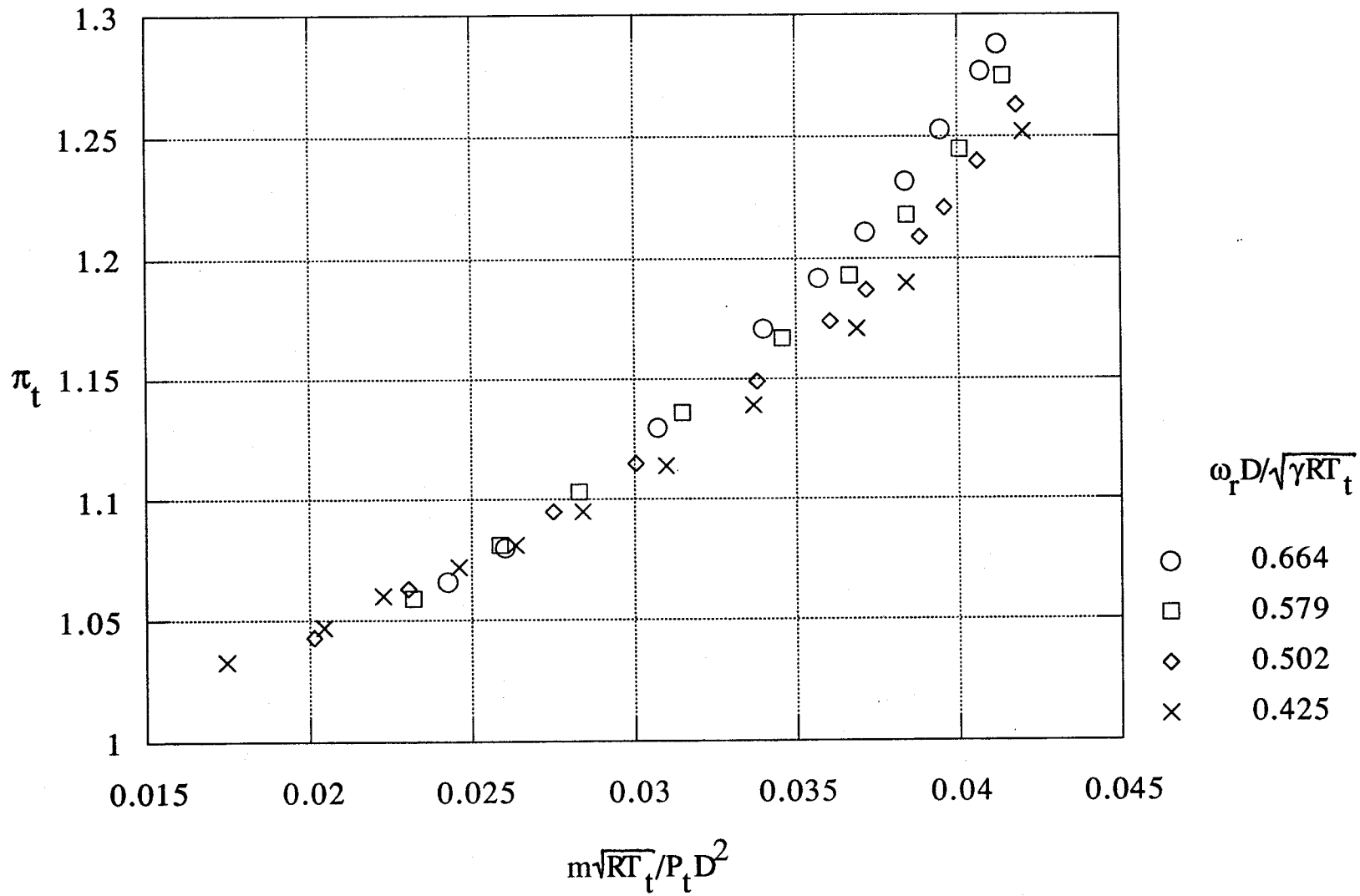

Fig. 4.2: Non-domensional turbine map

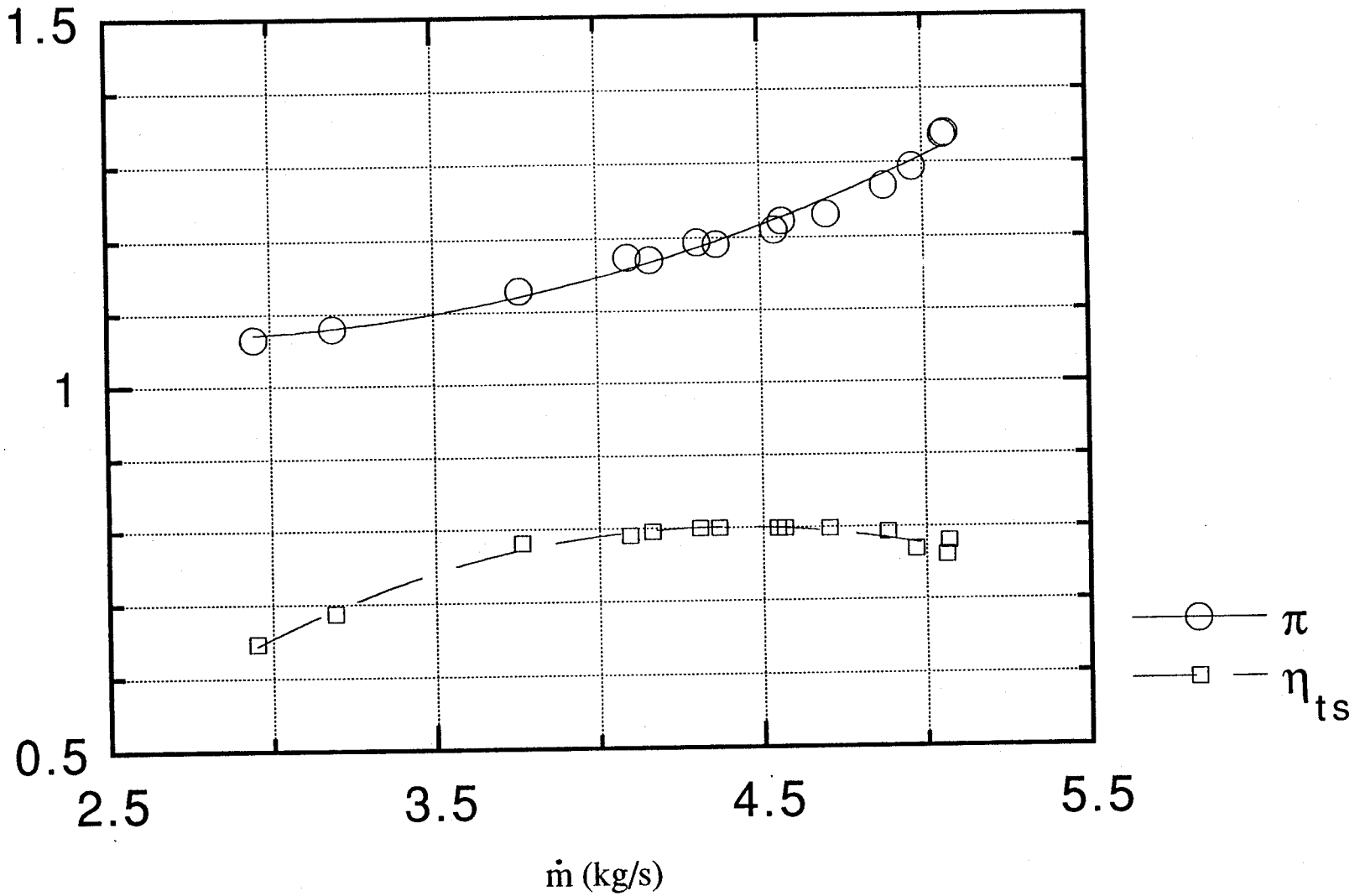

Fig. 4.3: Pressure ratio and total-to-static efficiency at design speed

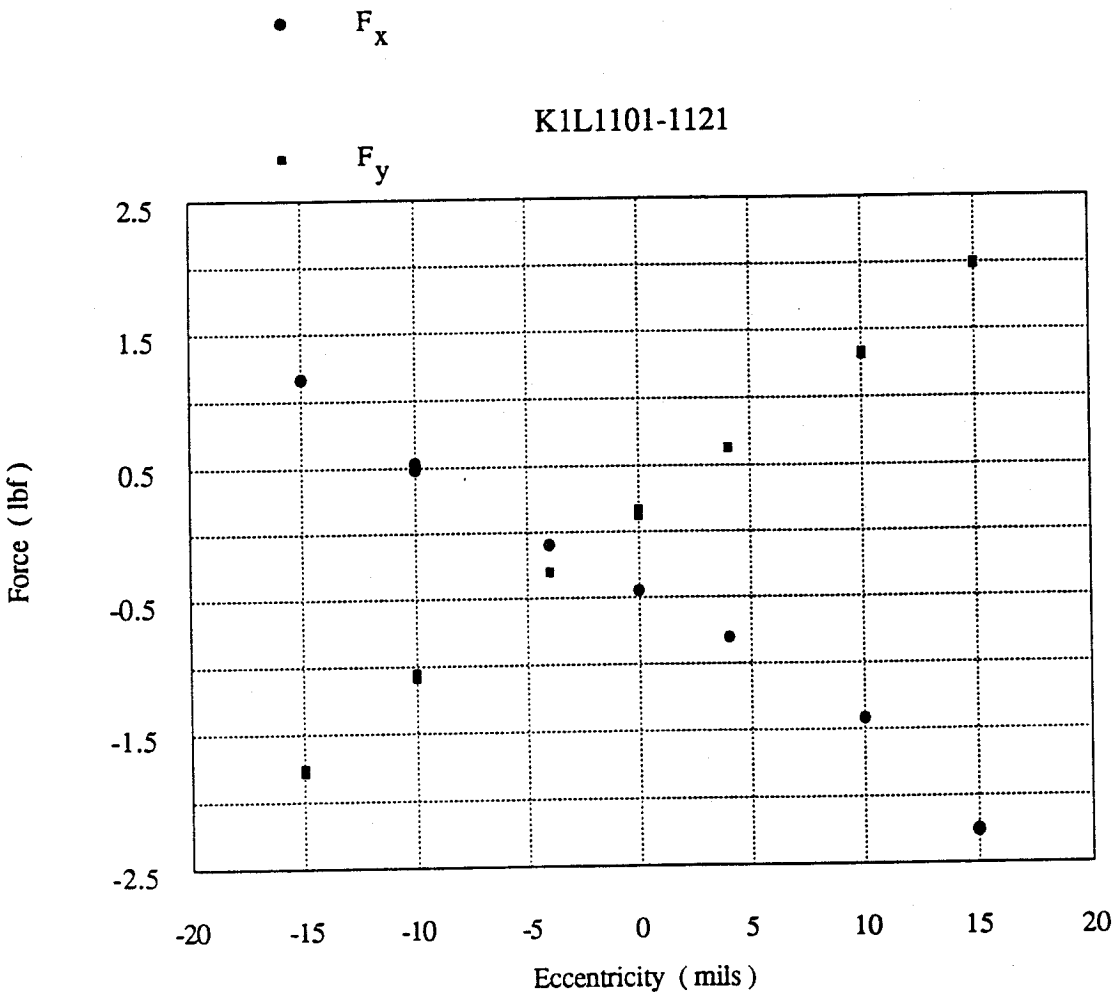

Figure 4.4 Static direct and cross-force for Configuration 1, $\bar{P}$ = 2 atm, w/w_d = 0.7

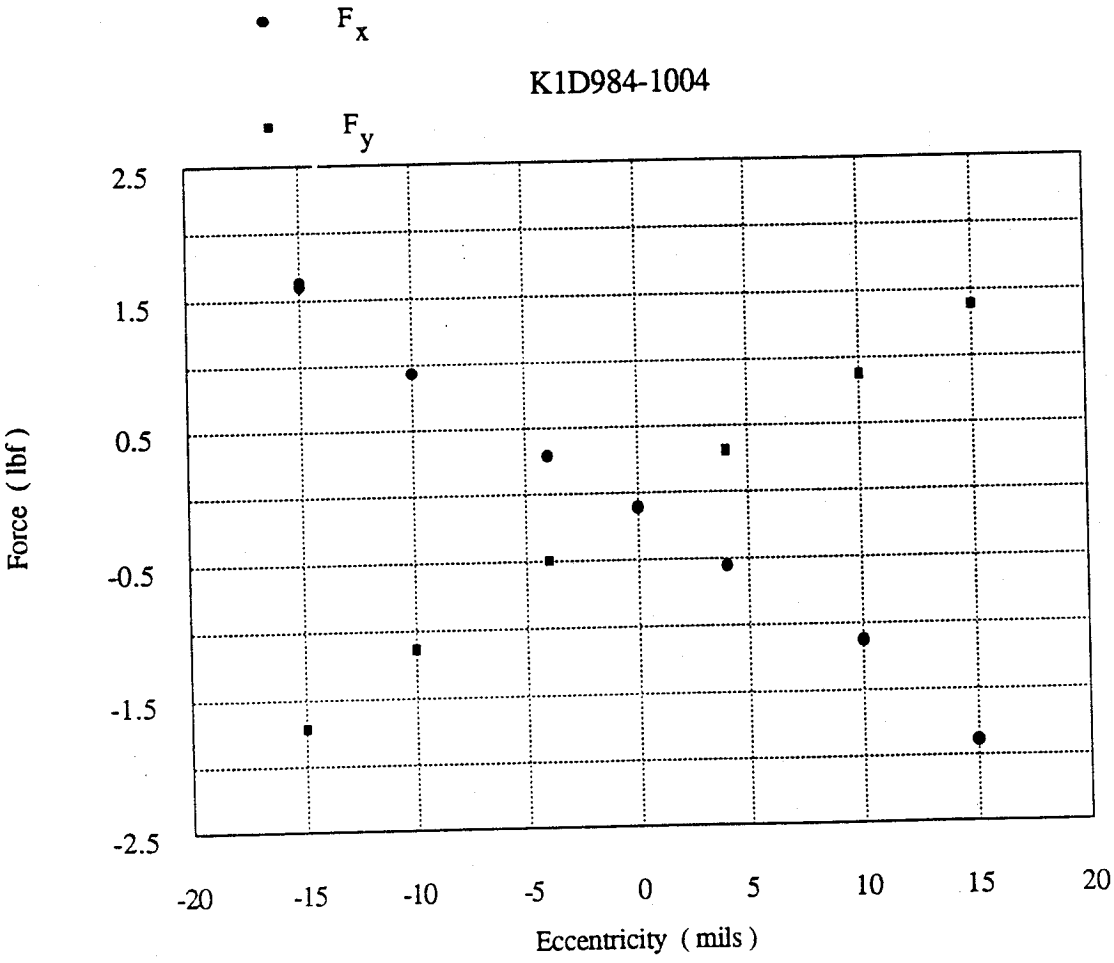

Figure 4.5 Static direct and cross-force Configuration 1
$\bar{P}$ = 2 atm, w/w_d = 1.0

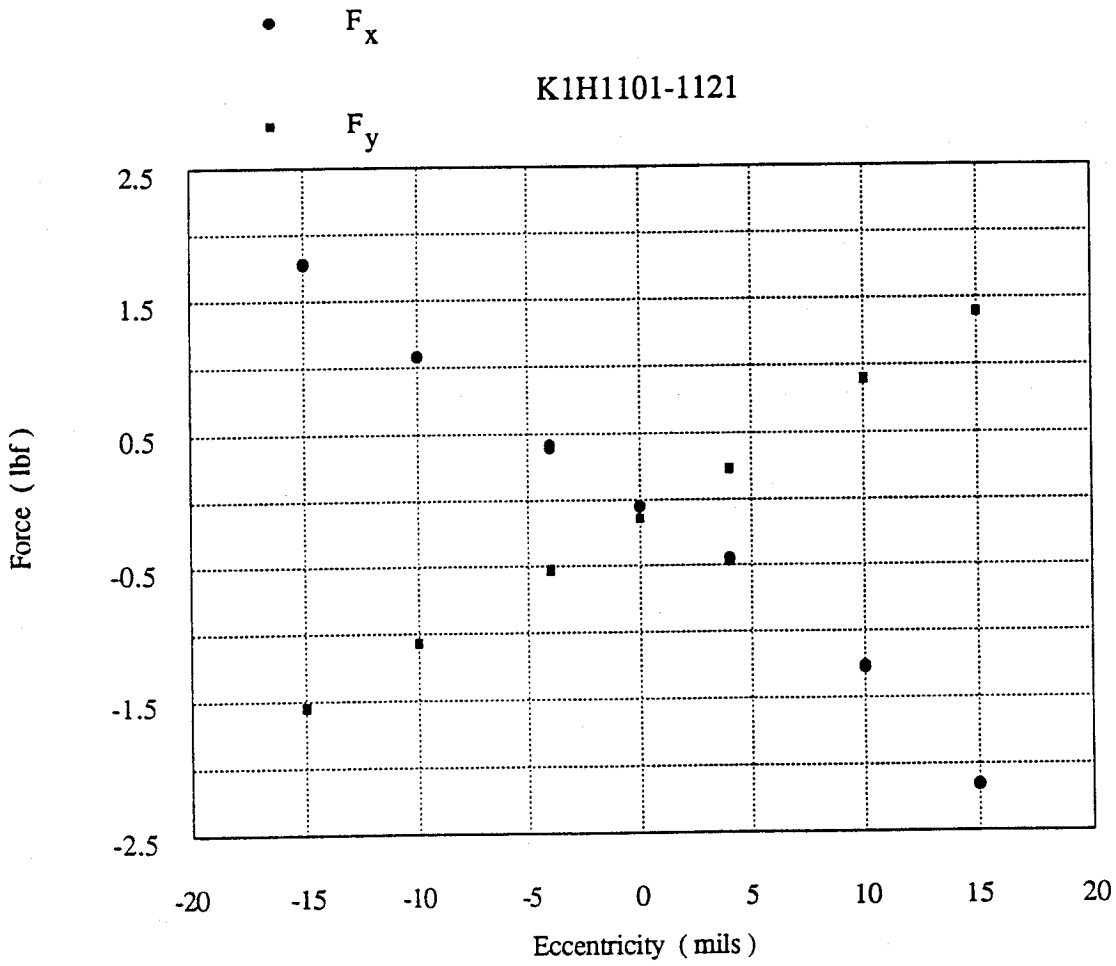

Figure 4.6 Static direct and cross-force for Configuration 1
$\overline{P}$ = 2 atm, w/w_d = 1.1

These data were reduced to mean stiffness data (F_x/e, F_y/e), and then to coefficient form. The definition of the direct and cross-force coefficients, here denoted α_x and α_y, is as suggested by the simple argument leading to Eq. (1.1), namely

$$\alpha_x = \frac{2F_x R}{Q\,(e/H)} \tag{4.1}$$

$$\alpha_y = \frac{2F_y R}{Q\,(e/H)} \tag{4.2}$$

where R is the mean radius, Q is the measured torque, e is the turbine eccentricity, and H is the blade height. The results are given in Table 4.1.

TABLE 4.1
FORCE COEFFICIENTS FROM DYNAMOMETER-DERIVED FORCES IN CONFIGURATION 1

ω/ω_{DESIGN}	α_x	α_y
0.7	-2.12	2.43
1.0	-2.81	2.57
1.1	-3.42	2.66

The basic independence of these coefficients from turbine power level was verified by repeating the nominal speed tests at a loop pressure $\overline{P}$ = 1 atm, with the flow rate reduced accordingly. To within experimental accuracy, the measured forces (both F_x and F_y) were one-half those in the 2 atm tests, and hence the coefficients were the same. The turbine torque was still adequate to overcome frictional losses, but operation was generally less steady (in part because the blower was forced to near its stall limit).

The observed independence of α_x, α_y from pressure is not over a sufficiently broad range of Reynolds numbers that any conclusions can be obtained about the effect of that parameter, particularly since in both cases we were well above the range of 10^5 - 2×10^5 (based on chord and stator leaving velocity) at which transition effects

are noticeable. The sensitivity of our force sensors is probably insufficient to obtain reliable data for runs in air (at 1/5 the freon density).

4.3 Survey of Flow Data

The nature and location of the various flow sensors used is summarized in Fig. 4.7. The 3-hole probes at stations 1 and 9, and the 5-hole probes at stations 2 and 8 can be radially traversed (the latter only over the outer 25% of the passage height, due to interference with the hub). All of the sensors shown, except for those at stations 0 and 10, are carried by the rotatable casing, and can be azimuthally traversed over ±90°. Thus, two diametrically opposed probes can provide full circumferential coverage (with some overlap). In sections with multiple wall tap holes, such as stations 3, 4, and 6, this capability provides redundancy and cross-checking of the data.

Since the main interest of the survey centers on azimuthal variations due to the turbine offset rather than absolute values, most of the data to be presented have been processed by subtracting the corresponding values measured with the turbine centered. Particularly for the probe data, this procedure has the advantage of removing residual probe alignment errors, which are difficult to eliminate otherwise. An example of this is shown in the tangential velocity surveys shown in Fig. 4.8. Because of the use of two individually aligned probes, each covering half of the perimeter, there are apparent discontinuities at $\theta = 90°$ and $\theta = 270°$, which are the overlapping points. Figure 4.9 shows data taken in the same experiment, with the same probe alignment, but with the turbine centered. The same discontinuities are also apparent. Subtracting the two sets of data, as in Fig. 4.10, produces a smooth transition. This procedure is, of course, not available when absolute values are required, such as if the net torque were to be calculated from the flow deflections in Fig. 4.8. On the other hand, if only the cross-force and direct force due to the non-

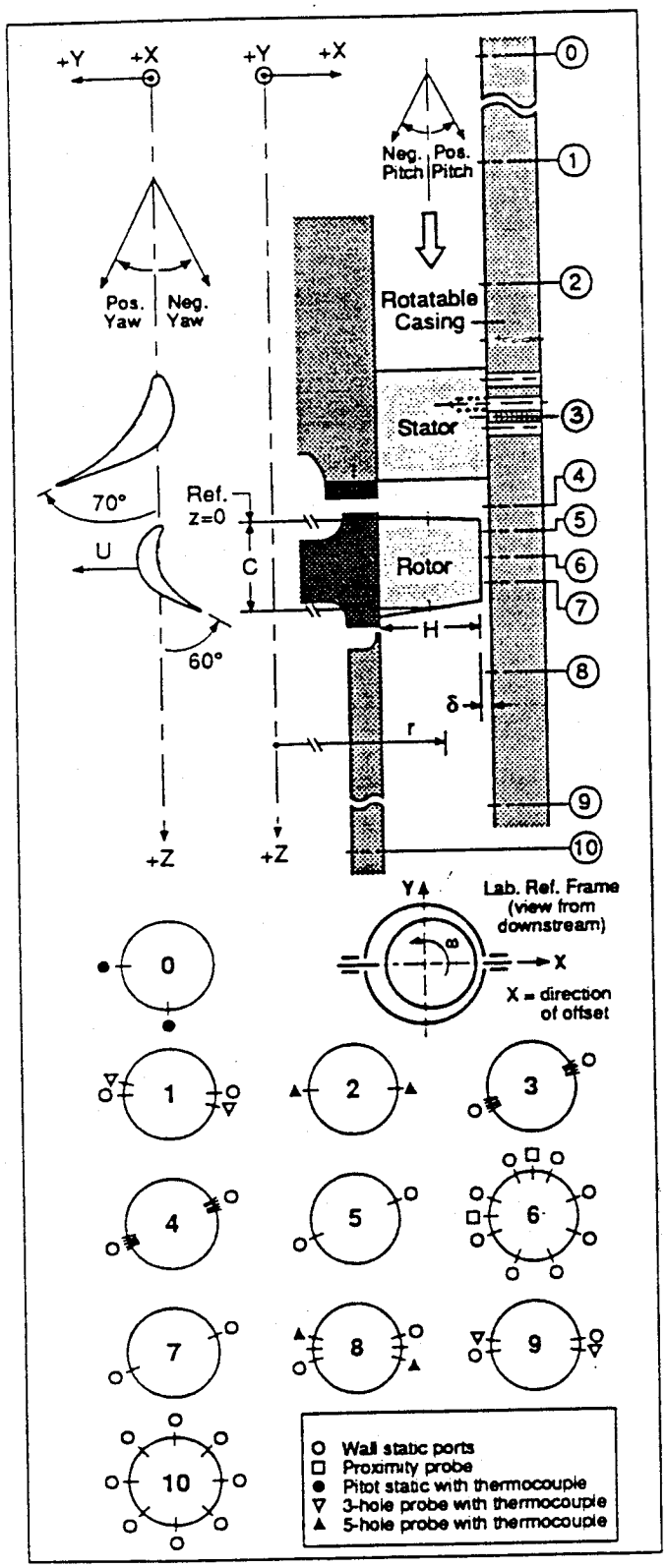
+Y
+X
+Y
+X
Neg. Pitch
Pos. Pitch
Pos. Yaw
Neg. Yaw
Rotatable Casing
Stator
Rotor
70°
Ref. z=0
C
U
60°
H
δ
r
+Z
+Z
0
1
2
3
4
5
6
7
8
9
10
Y
Lab. Ref. Frame (view from downstream)
ω
X
X = direction of offset
Wall static ports
Proximity probe
Pitot static with thermocouple
3-hole probe with thermocouple
5-hole probe with thermocouple

Figure 4.7

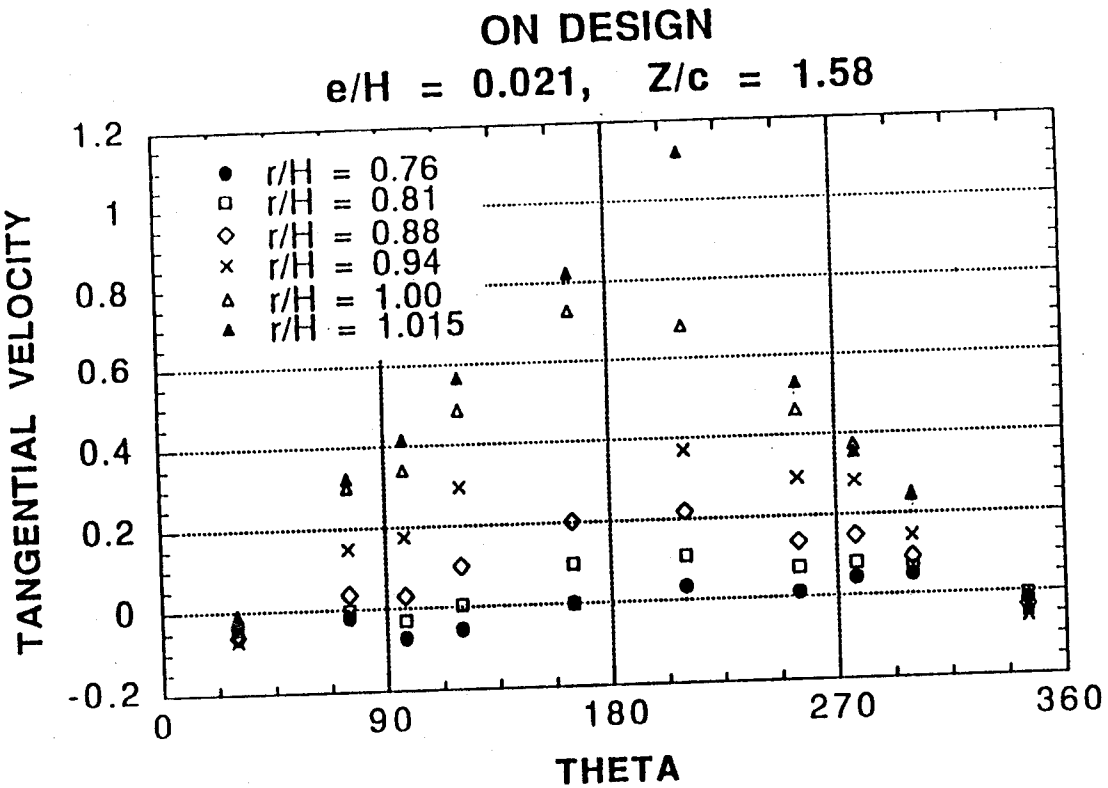

Figure 4.8 Uncorrected data at station 8 for eccentric turbine. Notice discontinuities at $\Theta = 90^{\circ}$ and 270°

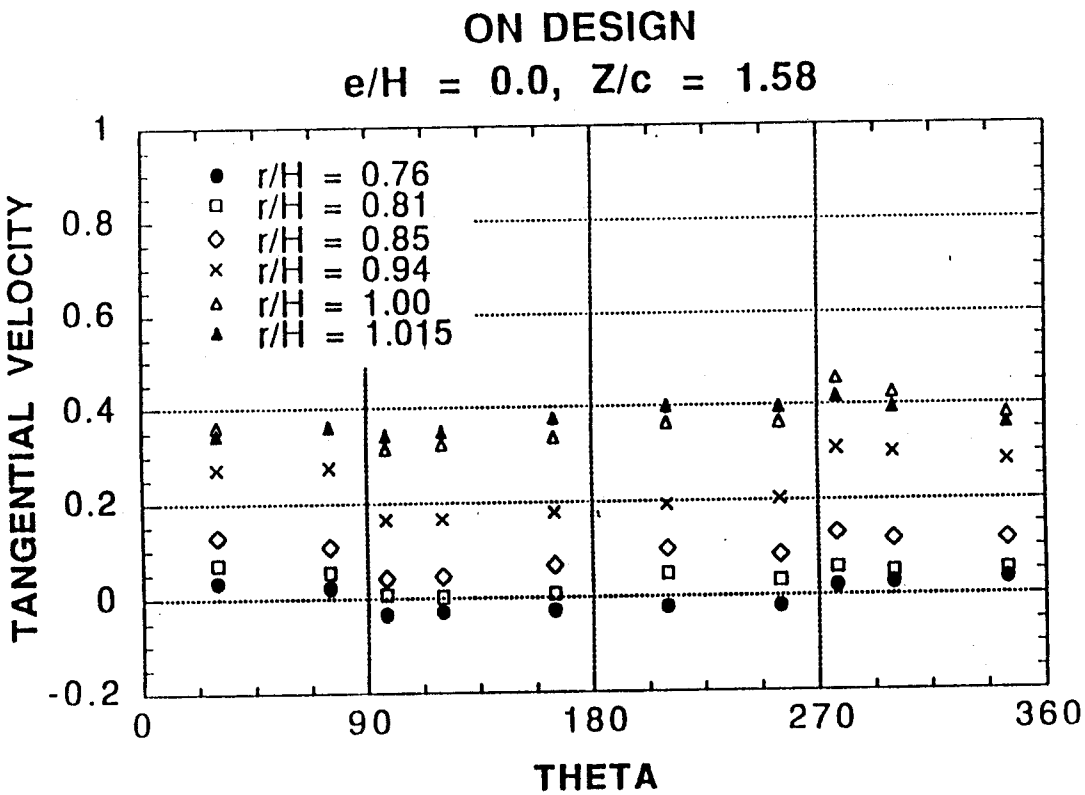

Figure 4.9 Uncorrected data at station 8 for the centered turbine

uniformities are desired, elimination of the mean value introduces no error.

For reference, in what follows, $\theta = 0°$ corresponds to minimum tip gap, $\theta = 180°$ to maximum tip gap. The flow survey data to be discussed in the following sections refer to Configuration 1, nominal speed (3440 rpm), with an eccentricity of 0.45 mm (e/H = 0.019). The mean loop pressure is 2 atm.

4.3.1 Upstream Survey

Generally speaking, the upstream data indicated uniform flow properties down to the level of accuracy of the data. This may still miss some small non-uniformity due to upstream redistribution, as will be discussed below.

Figure 4.11 shows a total pressure nonuniformity survey at station 1, some two blade chords upstream of the stator. The measured P_t is, as expected, tangentially uniform down to about ±0.2%. The expected P_t defect in the boundary layer has been suppressed largely by the centered turbine subtraction. The static pressure survey taken by the same 3-hole probe shows the same level of azimuthal uniformity.

Figure 4.12 shows the axial velocity survey. Again, the boundary layer radial dependence has been largely suppressed by the subtraction. There is a hint of a redistribution of flow, with perhaps 1-2% axial velocity excess at 180° (maximum tip gap). This is what theory (Sec. 9) would indicate, but the effect is too small to be unambiguously resolved. Similar comments apply to the tangential velocity survey shown in Fig. 4.13. Here we can see a slight positive maximum of v_t (i.e. in the direction against rotation) at the 90° location, and a minimum at 270°. These would be consistent with azimuthal flow migration towards the wide gap region (at 180°) and hence with both theory and the axial velocity indications of Fig. 4.12. Once again, the effect is in the 1-2% range, and not well resolved.

The surveys at station 2 (one chord ahead of the stator) were hampered in this test by clogging of one of the two 5-hole probes at that location. The slight indication

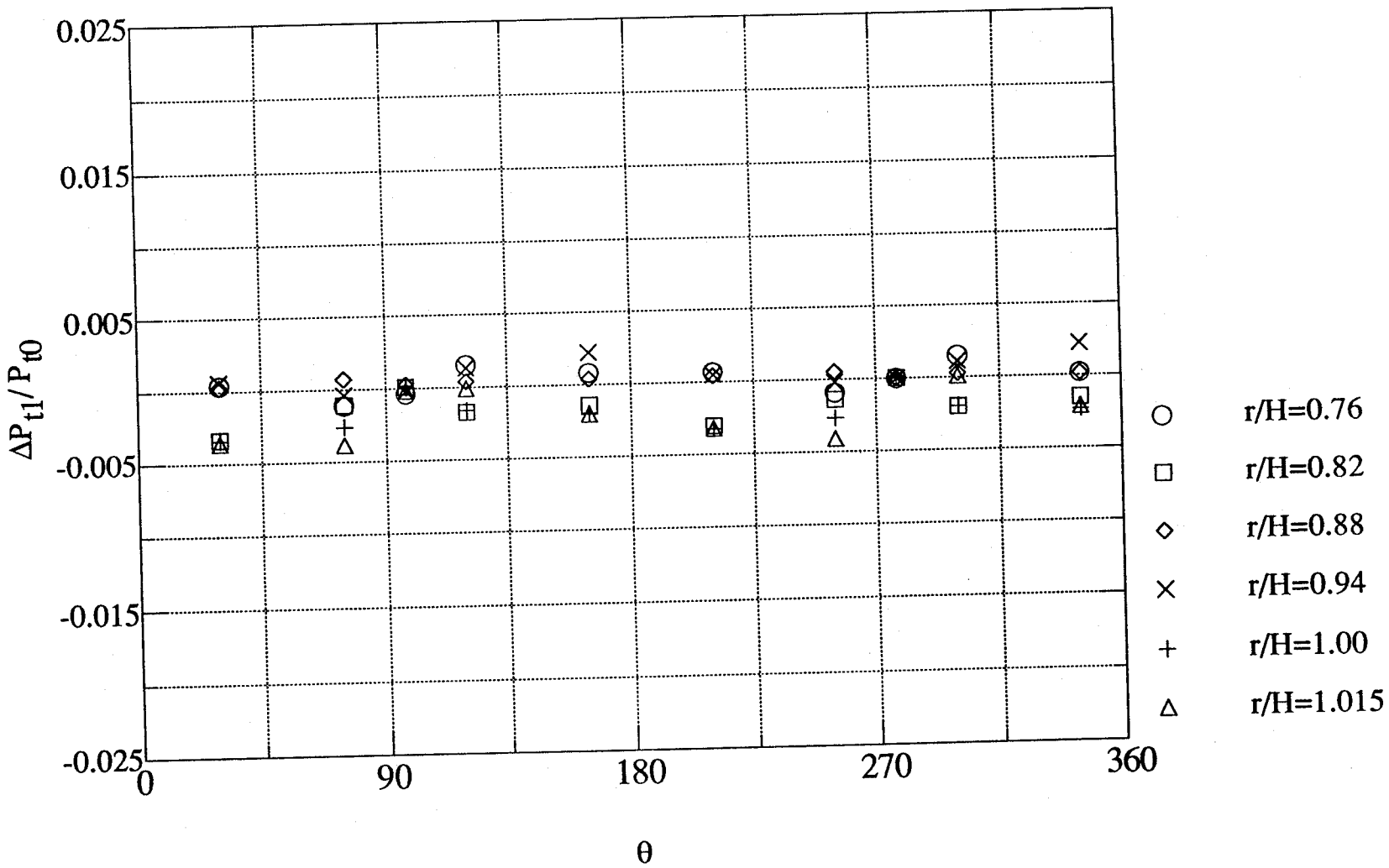

Figure 4.11 Total pressure at Station 1. Eccentric turbine, e/H = 0.019

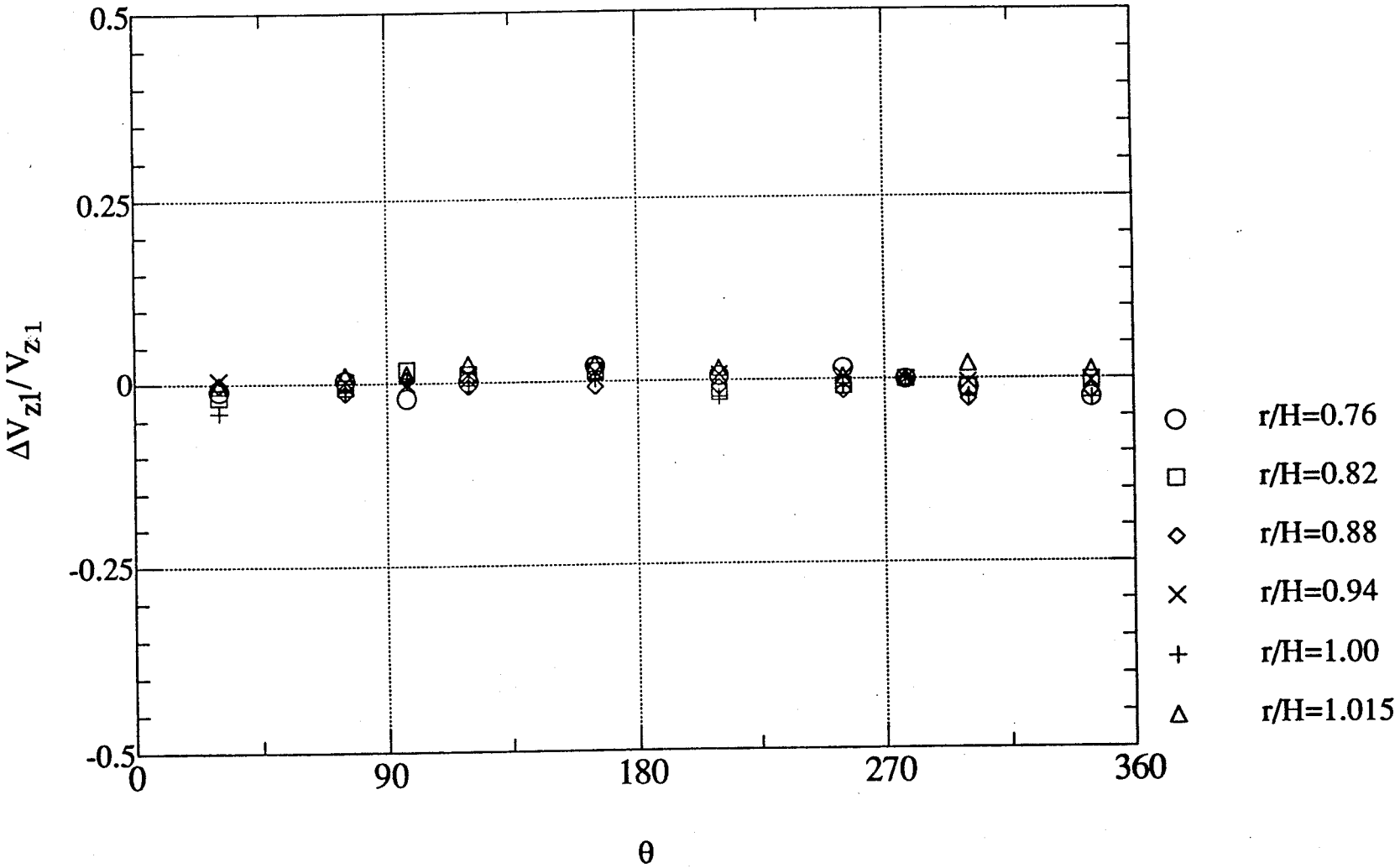

Figure 4.12 Upstream axial velocity non-uniformity, e/H=0.019

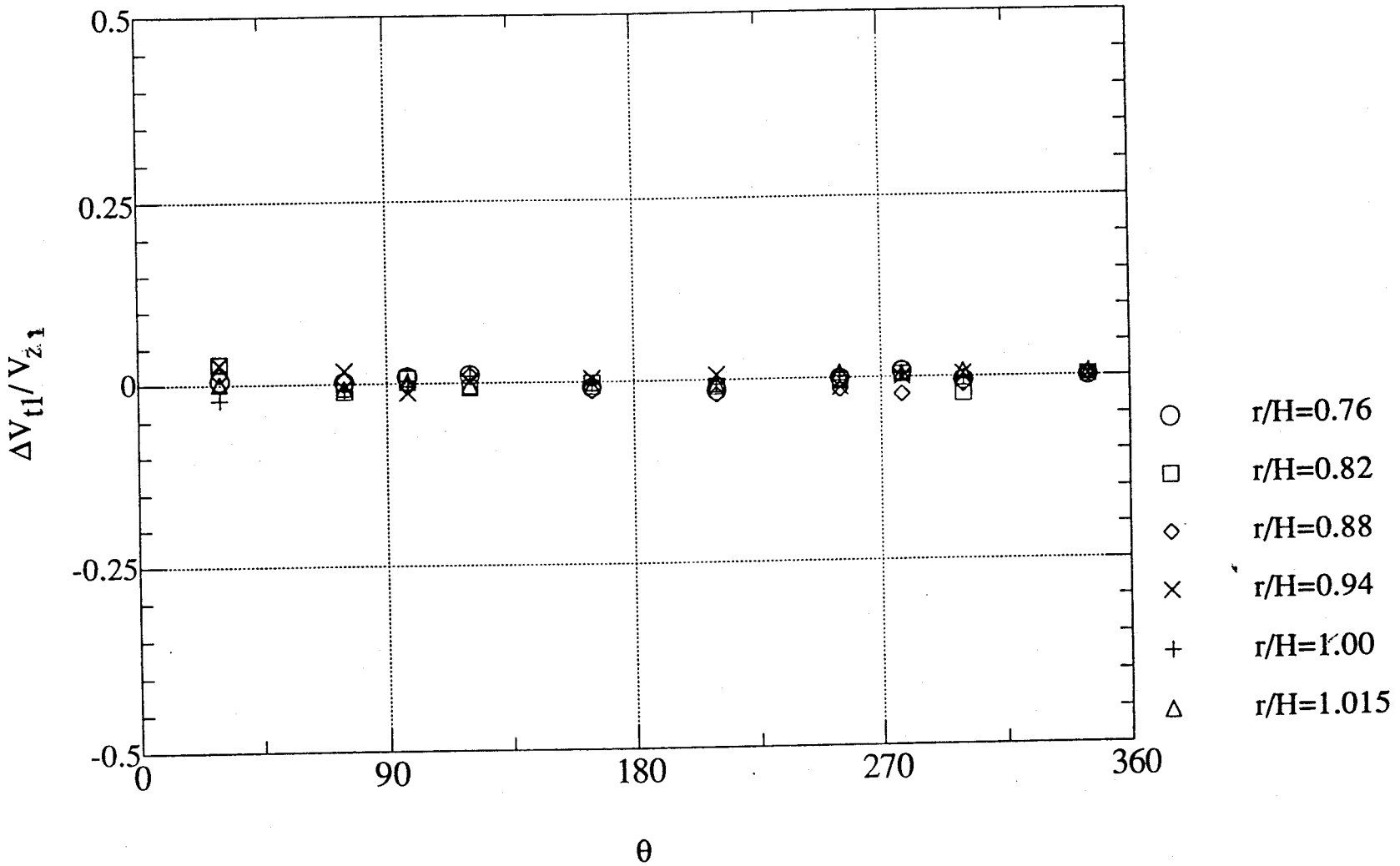

Figure 4.13 Unstream tangential velocity non-uniformitv. e/H = 0.019

of a v_t minimum at 270°, which is barely visible in Fig. 4.13 for station 1, appears to be confirmed at this station (Fig. 4.14).

The radial velocity data at station 2 are shown in Fig. 4.15. Very small if any variations are noticeable. Perhaps one can detect a 1-2% positive radial velocity in the 180° region, again consistent with migration towards the wider gap.

Finally, Figs. 4.16 and 4.17 show the pressure distribution from wall taps in the middle of the stator blade passages. These were not subtracted (Fig. 4.16 is for the eccentric turbine, Fig. 4.17 for the centered turbine). The scatter corresponds to the multiple taps and also to the measurements taken at different times during the process of radially translating the 3- and 5-hole probes (H is when the probes are almost withdrawn completely, C to full insertion spanning the passage). Even though these probes are some distance up and downstream of the station being measured, some sort of disturbance seems to be induced, in view of the systematic trend visible in Fig. 4.16. Equally possible is a slight time drift of the pressures, since Fig. 4.17 shows no correlation to probe depth. In any case, the azimuthal pattern is still very slight, with only a hint of a depression in the 180° region in Fig. 4.16.

4.3.2 Pressure Survey in the Rotor Region

Immediately past the stator, the picture changes radically as far as tangential variations. Figure 4.18 shows the collection of wall tap pressures at station 4, between stator and rotor. Aside from the scatter, which is similar to that seen at station 3, there is now an unmistakable nonuniformity, with a minimum located some 30° ahead of the 180° location (maximum gap). The amplitude and phase of this nonuniformity are the same for each individual pressure tap on the rotatable casing, and shifts between taps appears to be due to residual influences of the blading of the stator. For comparison, the centered-turbine pattern is shown in Fig. 4.19. The amplitude of this pressure nonuniformity appears to be about 0.0027 P_{t_0}, or 0.22 $(\rho c_{x_0}^2/2)$, or 0.028 ρU^2.

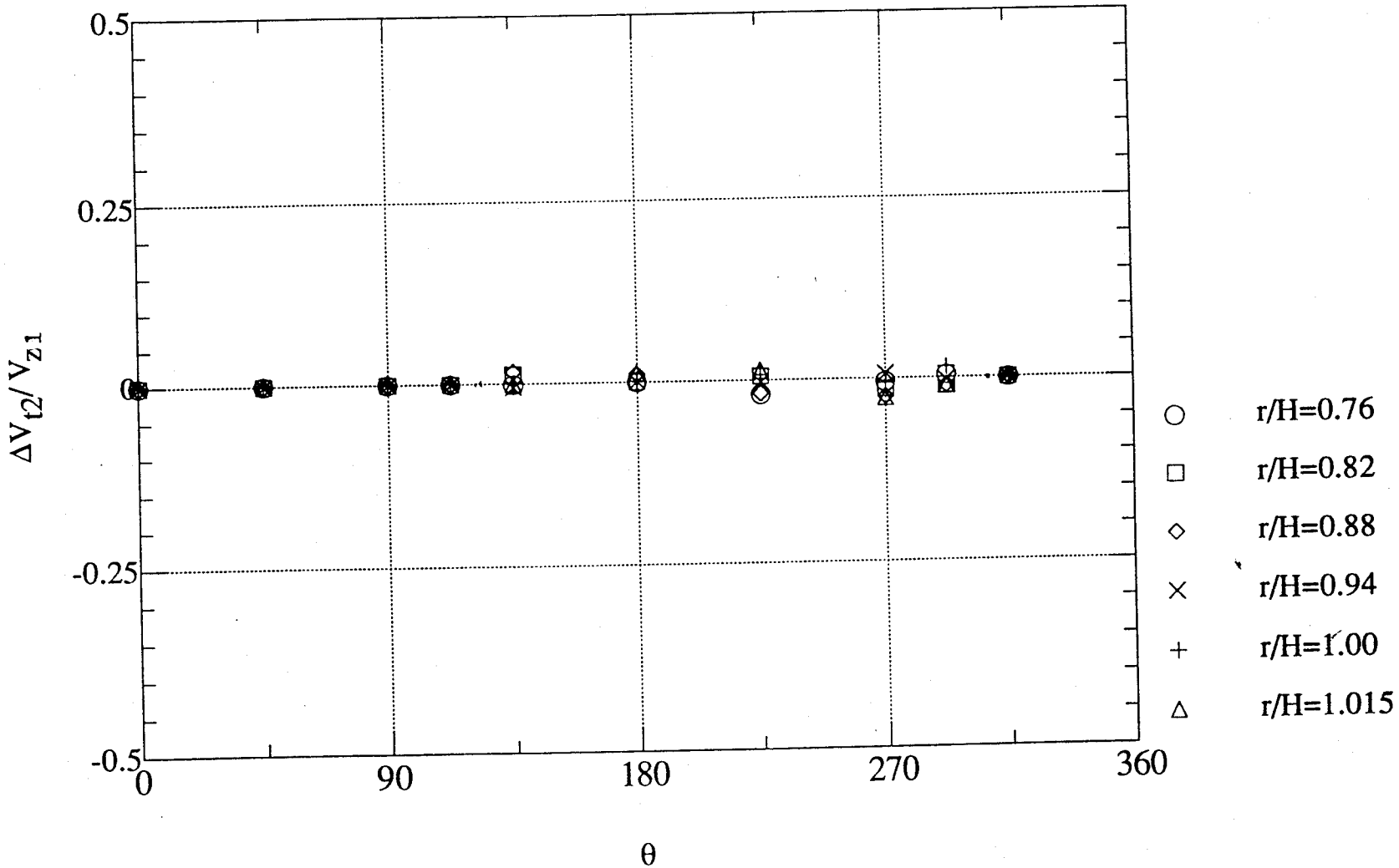

Figure 4.14 Tangential velocity non-uniformity at Station 2. e/H = 0.019

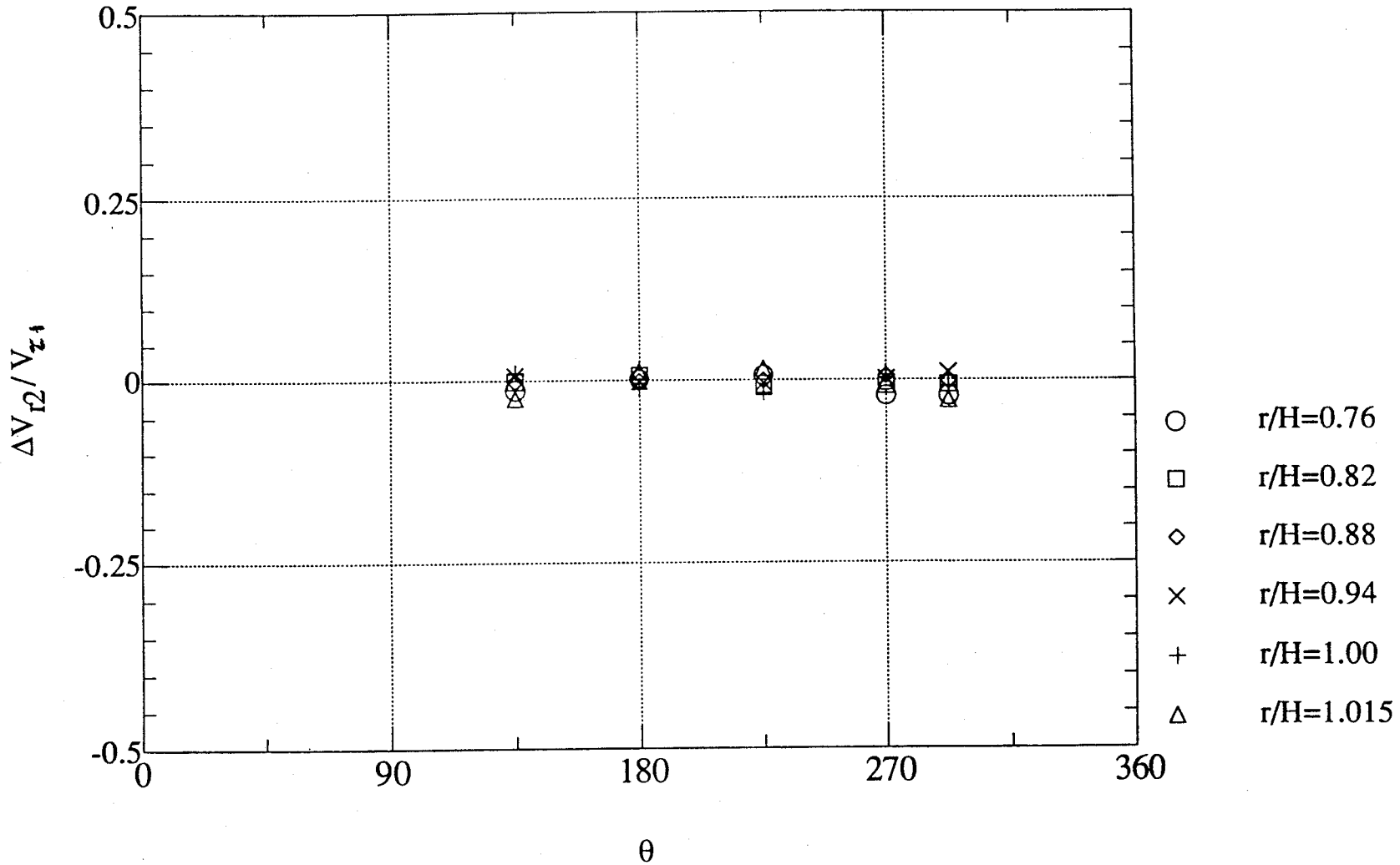

Figure 4.15 Radial velocity variation at Station 2. e/H = 0.019

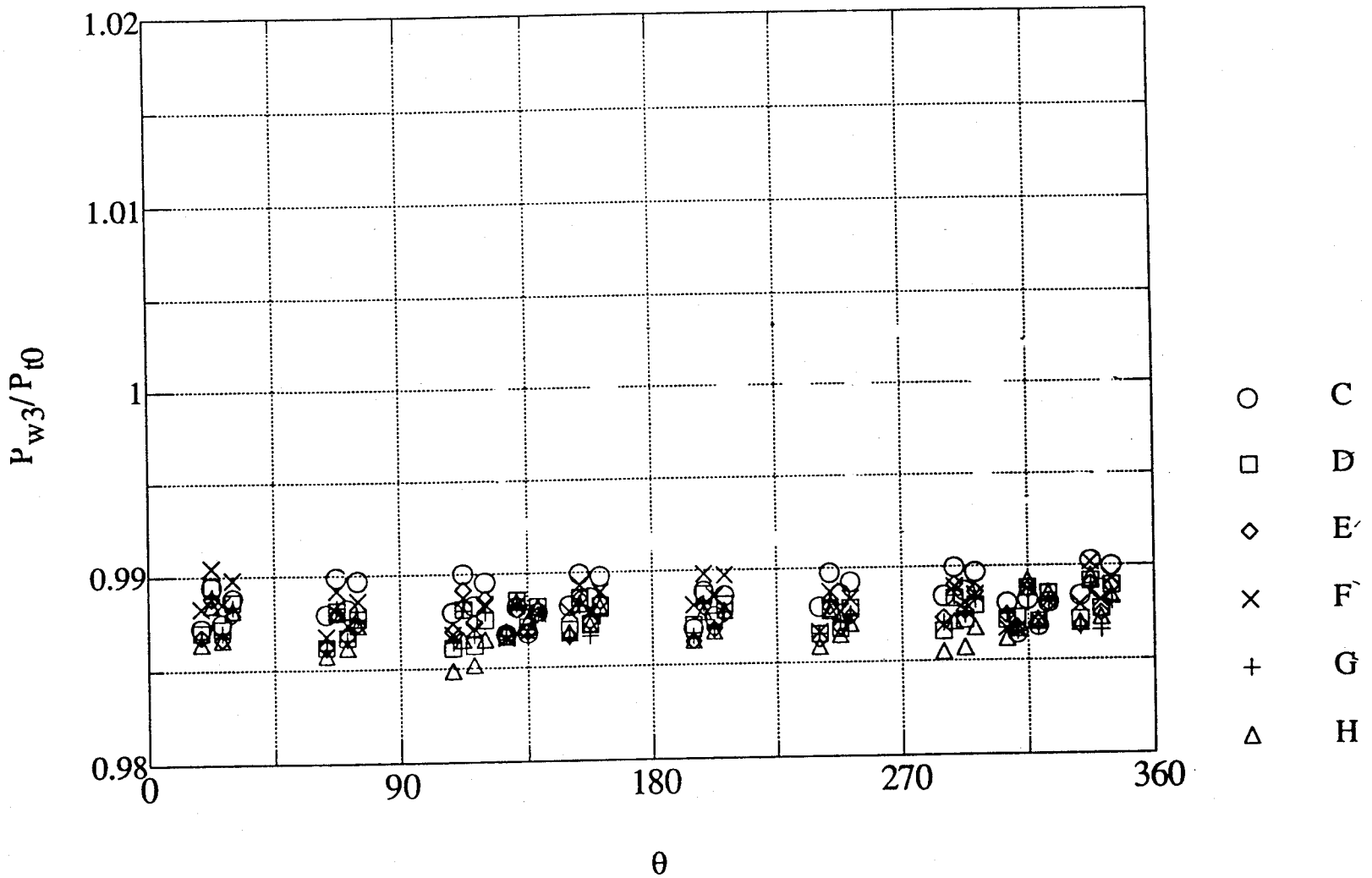

Figure 4.16 Wall tap pressure in stator passages. e/H = 0.019

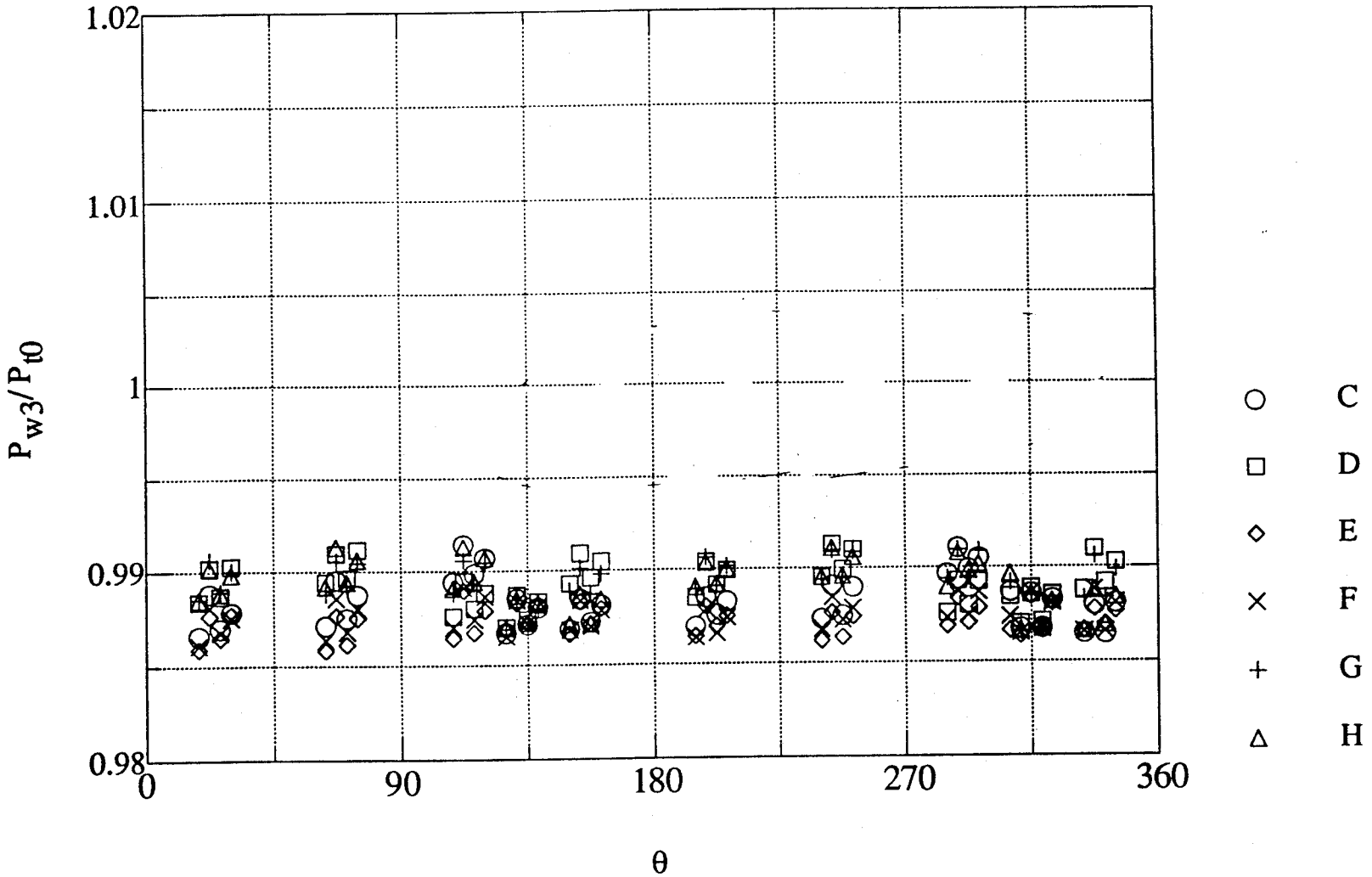

Figure 4.17 Wall tap pressure in stator passages. e/H = 0.0

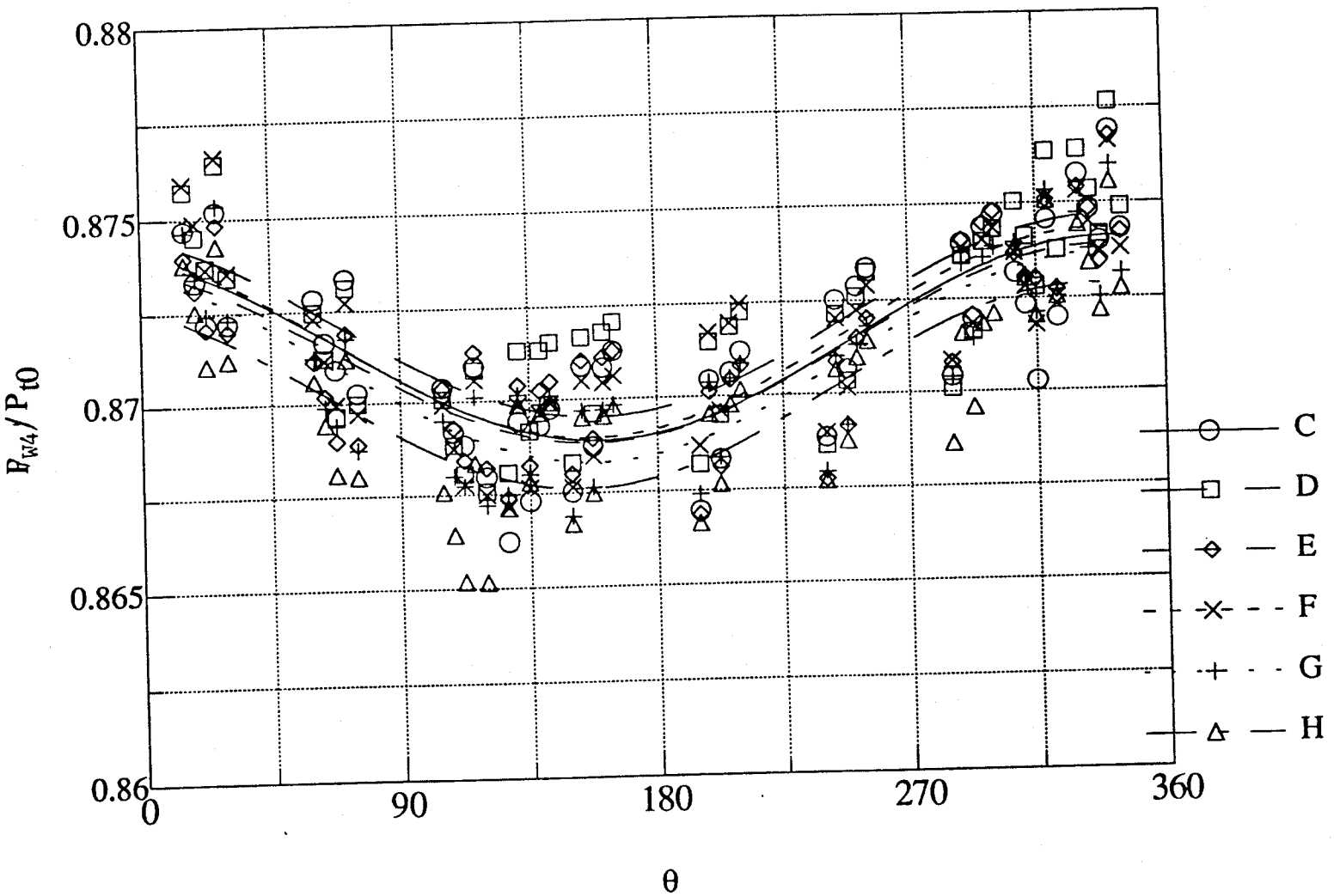

Figure 4.18 Wall tap pressure between stator and rotor. e/H = 0.019

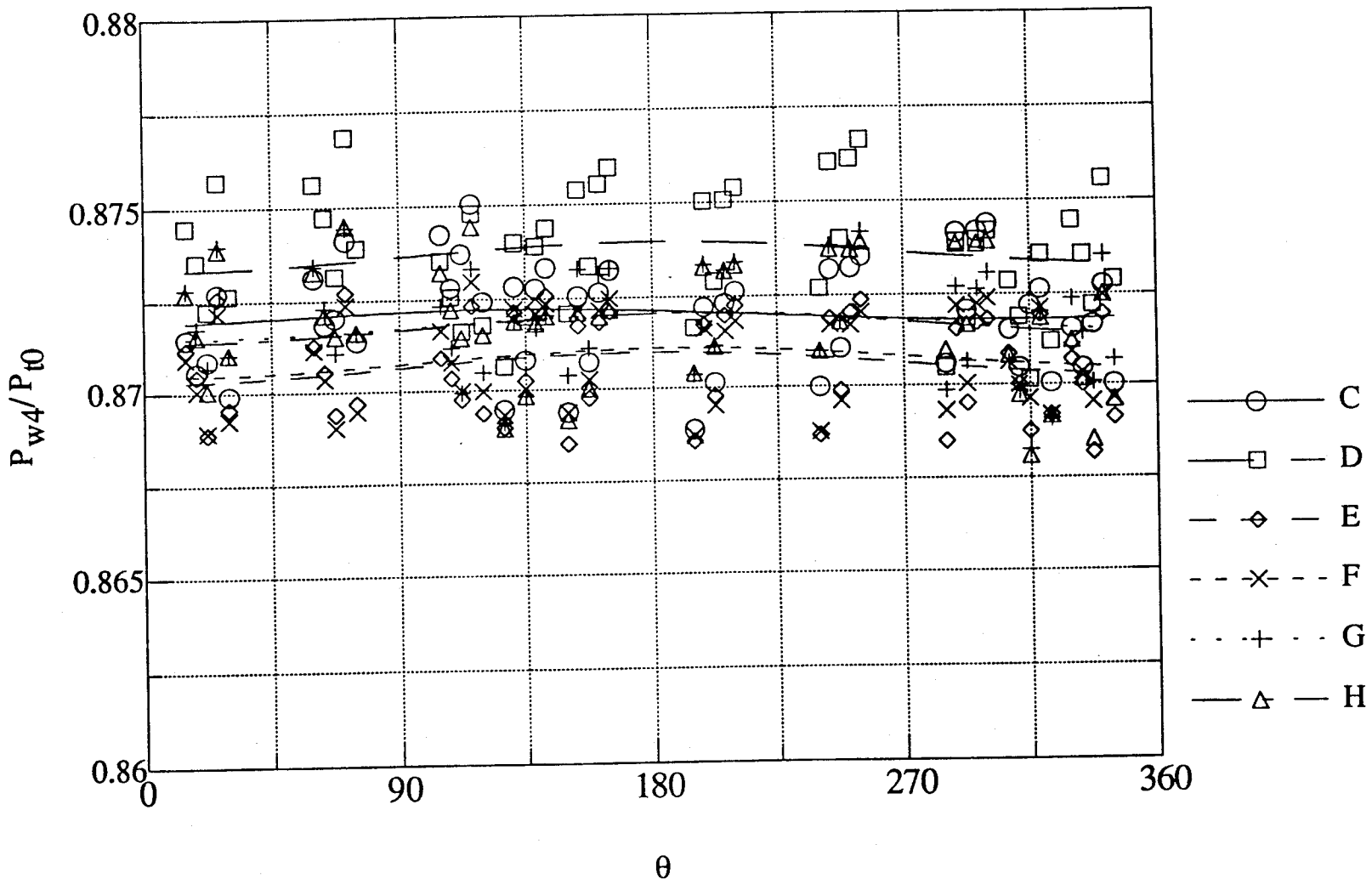

Figure 4.19 Wall tap pressure between stator and rotor. e/H = 0.0

The same pattern is visible at station 5 (over the rotor leading edge region) in Fig. 4.20. The amplitude has increased slightly, to 0.0031 P_{t_o}, although the precision is somewhat less, because only two taps are used in that section. Even more clear is the set of data for station 6 (rotor mid-chord), as shown in Fig. 4.21, where 8 taps are used. The amplitude is now 0.0042 P_{t_o}. Further downstream, nearly over the rotor trailing edge (station 7) the amplitude, although a bit uncertain, appears to have increased further to 0.0055 P_{t_o} (Fig. 4.22).

The theoretical treatment in Sec. 9.3, where the flow is allowed to redistribute as it approaches the stage, does predict this kind of pressure pattern, at least qualitatively. In essence, the flow migrates tangentially (over a length scale of order R) towards the wider gap, by a relative amount of the same order as the relative gap or a fraction of it. This amounts in our case to perhaps ±0.5% variations of the axial flow entering the stator which, as noted, may be there but are difficult to measure. However, as the flow expands in the stator, these differences get magnified by 1/cos α_2 (α_2 = stator trailing edge angle) and, from Bernoulli's equation, they translate to pressure variations which are strongly amplified. If P_1 = constant is the upstream pressure, P_2 is the pressure after the stator (with fluctuations P_2') and c_{x_o} is the axial velocity, we can write

$$\frac{P_0 - P_2}{\rho} = \frac{1}{2} c_{x_o}^2 \tan^2 \alpha_2 \tag{4.3}$$

and, in terms of the perturbations,

$$\frac{P_2'}{\rho c_{x_o}^2} = - \frac{c_{x_o}'}{c_{x_o}} \tan^2 \alpha_2 \tag{4.4}$$

In our case, $\tan^2\alpha_2 = 7.55$, and so even fluctuations of less than 1% in c_{x_o} translate into several percent in $P^2/\rho c_{x_o}^2$.

More quantitatively, we show in Fig. 4.23 the results of the model modification explained in Sec. 9.3.8 (radially uniform stator flow) for the parameters of our

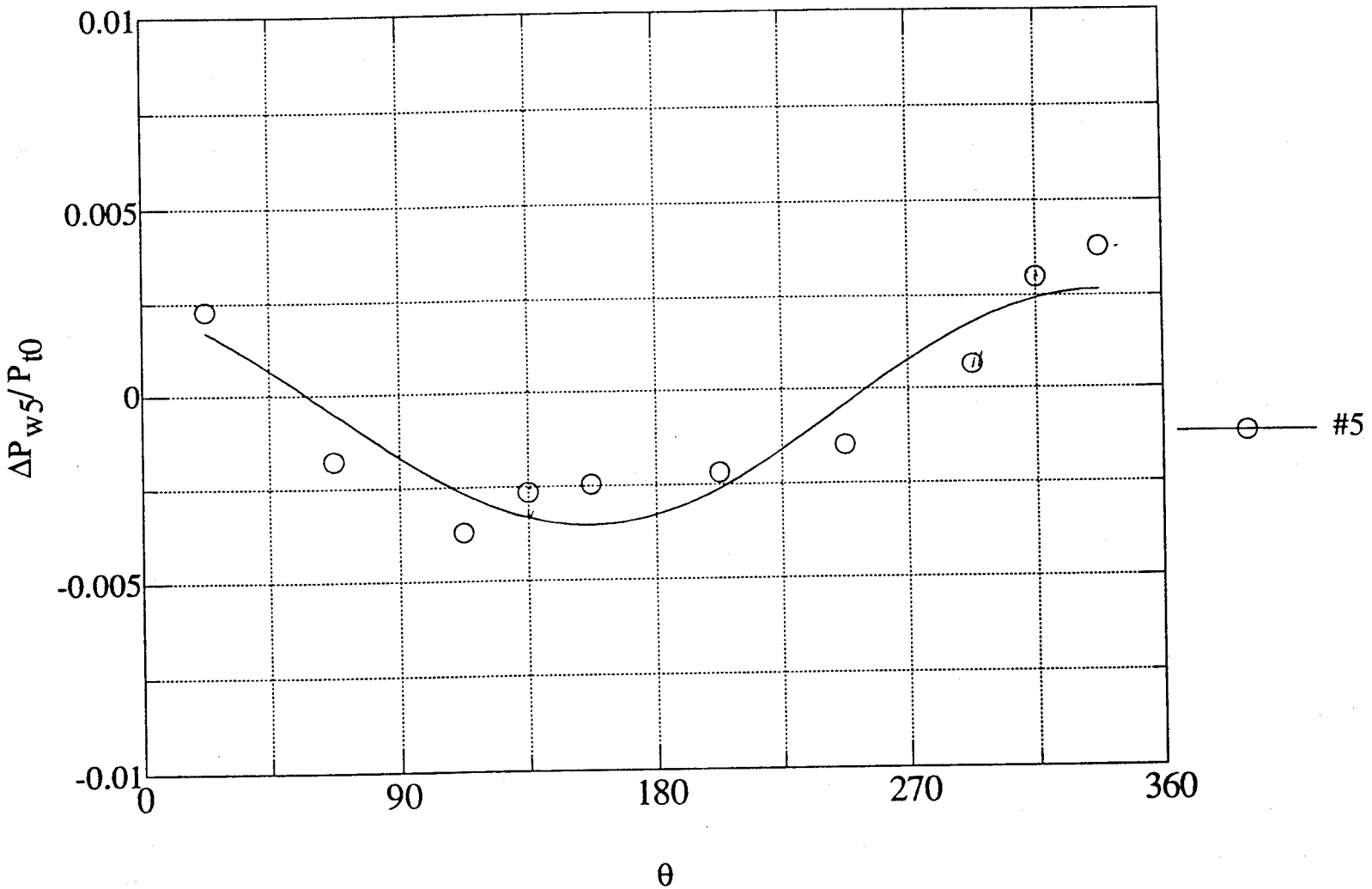

Figure 4.20 Wall tap pressure over rotor leading edge. e/H = 0.019

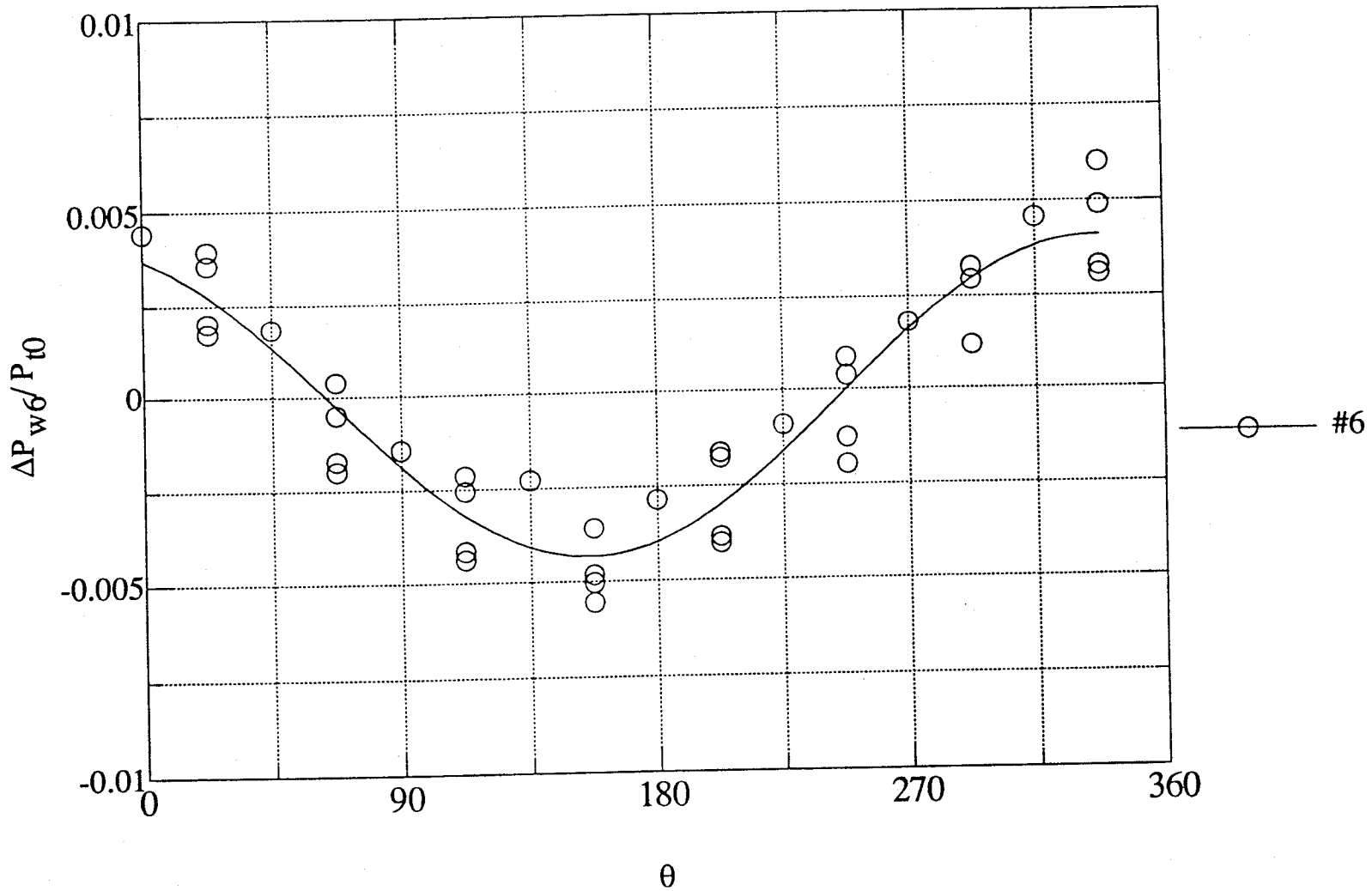

Figure 4.21 Wall tap pressure at mid-chord. e/H = 0.019

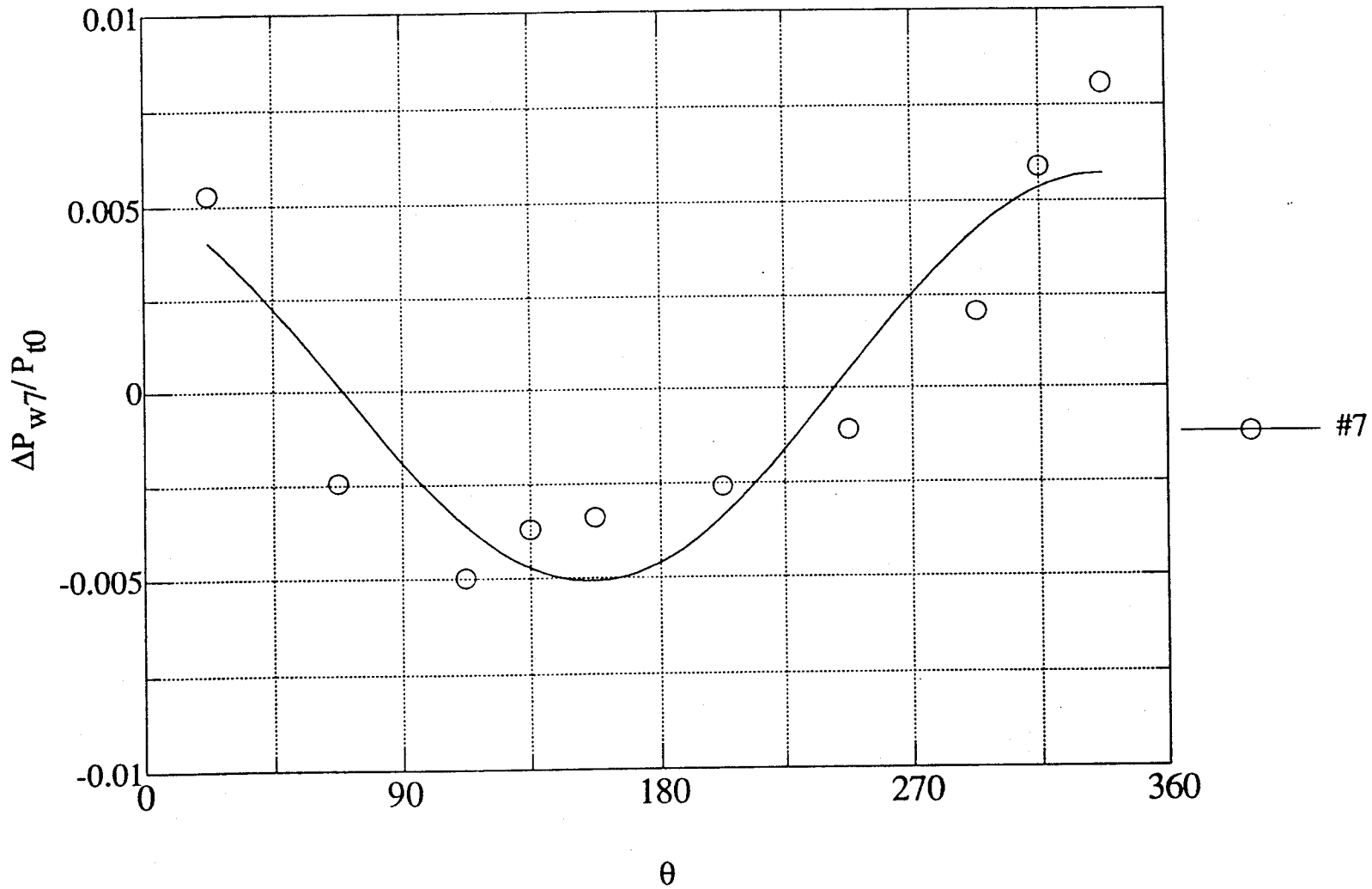

Figure 4.22 Wall tap pressure near the trailing edge. e/H = 0.019

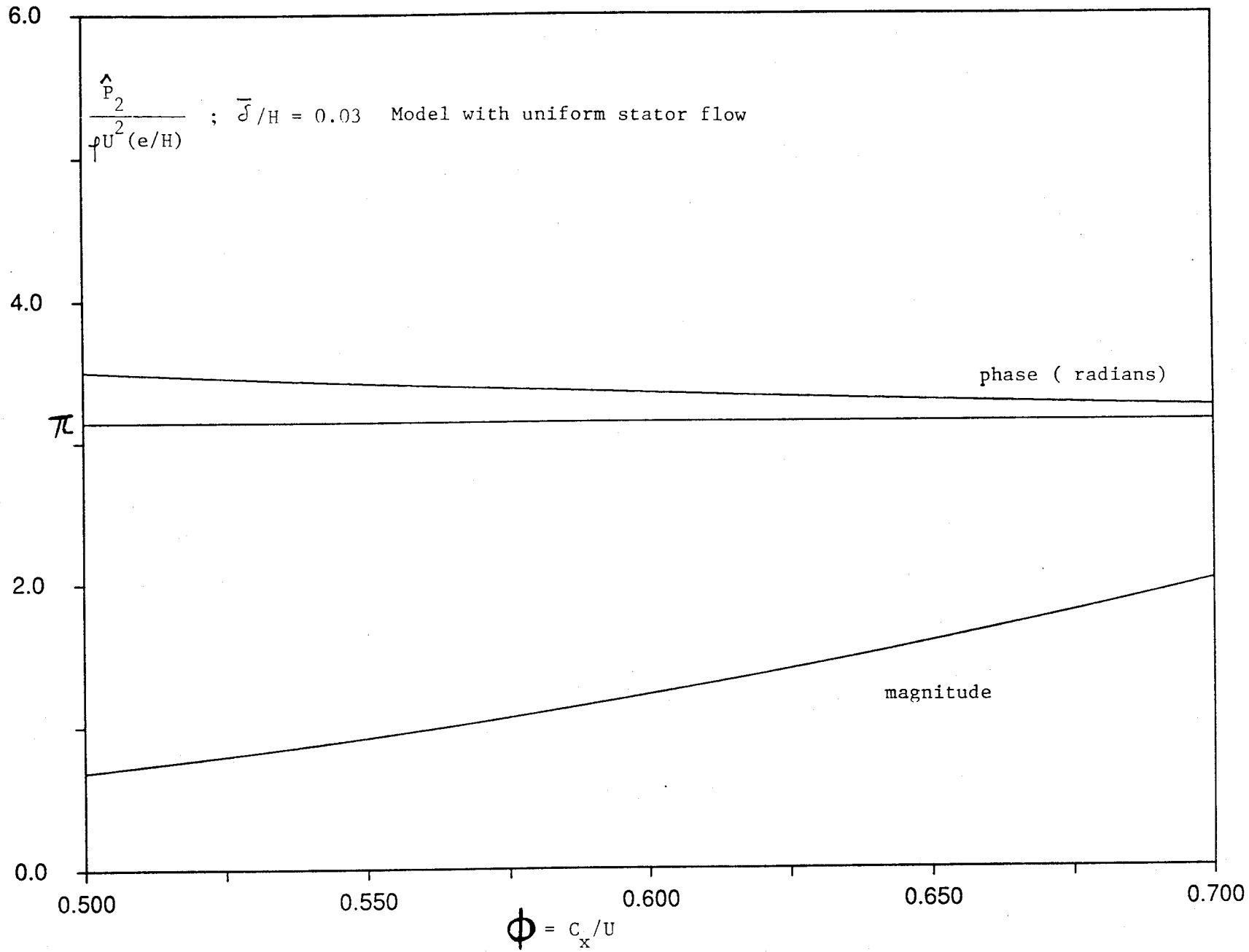

Figure 4.23 Theoretical pressure fluctuation at stator exit

experiments. Plotted is the amplitude and phase angle (with respect to the maximum gap location) of the fluctuation of $P_2/[\rho U^2(e/H)]$, where U is the wheel speed, H the blade height and e the rotor offset. At the nominal condition, $\phi = 0.58$, the magnitude is about 1.15, and so we predict

$$\frac{P_2'}{\rho U^2} = 1.15 \times 0.019 = 0.022$$

As noted, the experimental value at stator exit (station 4) is $P_2'/\rho U^2 = 0.028$. Further downstream over the rotor, this increases, for reasons which are not entirely clear but, as we will see shortly, the amplitude reverts to its value at station 4 when we move downstream of the rotor. Part of the increased nonuniformity over the rotor blades may be due to radially localized near-tip effects, such as the rolled-up tip vortex. Another part is simply due to continued flow expansion although, due to the low reaction, this is a weak effect in our case. Yet another possibility is non-linear pressure averaging, introducing a bias in the measurement when the very large fluctuations due to individual blade passage are averaged by the measuring system. This latter possibility was explicitly investigated by using locally a fast-response Kulite probe. It was found that the averaging was, in fact, correct.

The phase shift of some 20-30° which is visible in all the experimental pressure patterns is such as to introduce a pressure force component in the forward-whirling direction. It will be seen later that this is a significant effect, accounting for 30% to 40% of the total measured Alford force. More directly, these pressure forces are almost entirely responsible for the restoring direct forces F_x measured, and here this phase shift plays only a minor role (as the cosine of the shift).

The theory does not predict the correct sign for the phase shift. This is most likely because it ignores the net pattern rotation due to the finite axial length of the stator and rotor. This is an unfortunate consequence of the "actuator disk" idealization, but it should be correctable with some additional work by, for example, splitting the

"disk" into two, one for stator and one for rotor, with realistic axial spacing between them. Thus, it seems well established that the theory is correct at predicting azimuthal flow redistributions, although their magnitude over the rotor blading is underpredicted, and the small phase shift is predicted with the wrong sign.

Additional evidence about this redistribution is presented in the next sub-section.

4.3.3 Static Pressures Downstream of the Rotor

Figure 4.24 shows the azimuthal pressure pattern at station 8, about 1 chord downstream of the rotor exit. It is interesting to notice the persistence of the nonuniformity, with little change in relative phase, and its return to the same amplitude as in station 4 (between stator and rotor). At station 9 (about 3 chords downstream of the rotor), the amplitude is somewhat reduced, to about 0.0023 P_{t_0} (Fig. 4.25), probably because this downstream distance is becoming comparable with the characteristic distance (R) for azimuthal flow redistribution (Sec. 9).

These results prove that, at least the part of this pressure pattern visible at stations 4 and 8, is not a local blade-tip effect, but one with a much broader length scale, of order R. Further corroboration can be seen in radial static pressure surveys taken with the multi-hole probes at these stations. The extraction of P_{static} from the readings of these probes, which are not aligned to the local flow, is more prone to error than that from simple wall taps, but the patterns still emerge clearly. Figure 4.26 shows the case of station 8, and Fig. 4.27 that of station 9. Although there is scatter, it is clear that, at least down to the surveyed depth of r/H = 0.76 (where tip effects are substantially damped), the static pressure still preserves the same azimuthal distribution as at the wall. This is to be expected from the large-scale nature of the flow redistribution responsible for these variations. This is an important point, because it gives credence to our procedure (explained later) of calculating pressure forces by projecting on the turbine hub the pressures measured on the casing.

One other point should be mentioned here which appears to have no direct bearing on our research, but is puzzling in its own right. For the centered turbine (and also for the offset turbine, in an average sense), the wall static pressure shows a sudden drop between stations 7 and 8, namely, between the level on the turbine and that downstream. This is illustrated clearly in Figs. 4.28 and 4.29, for a case with the

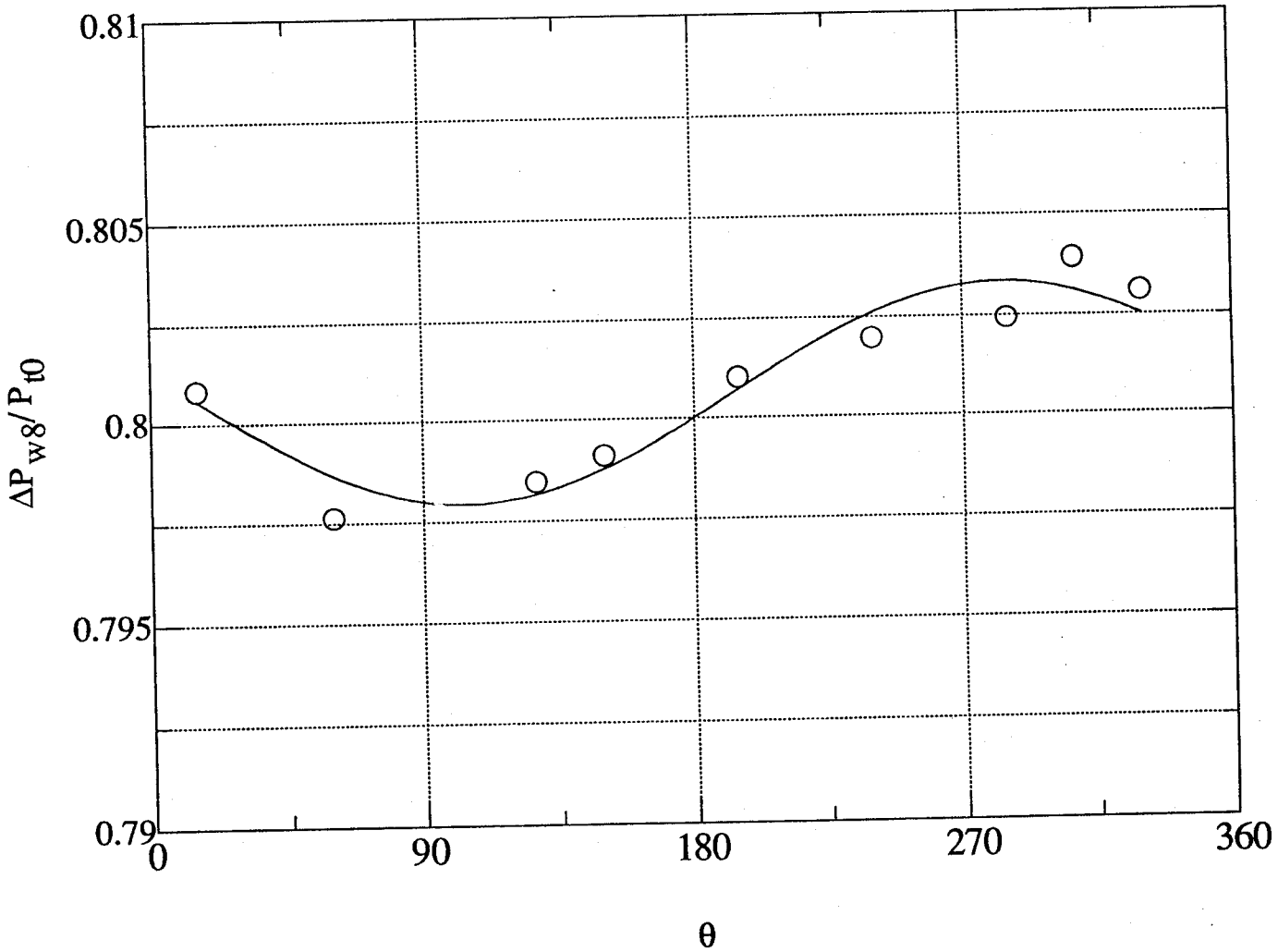

Figre 4.24 Wall tap pressure downstream of rotor e/H = 0,019

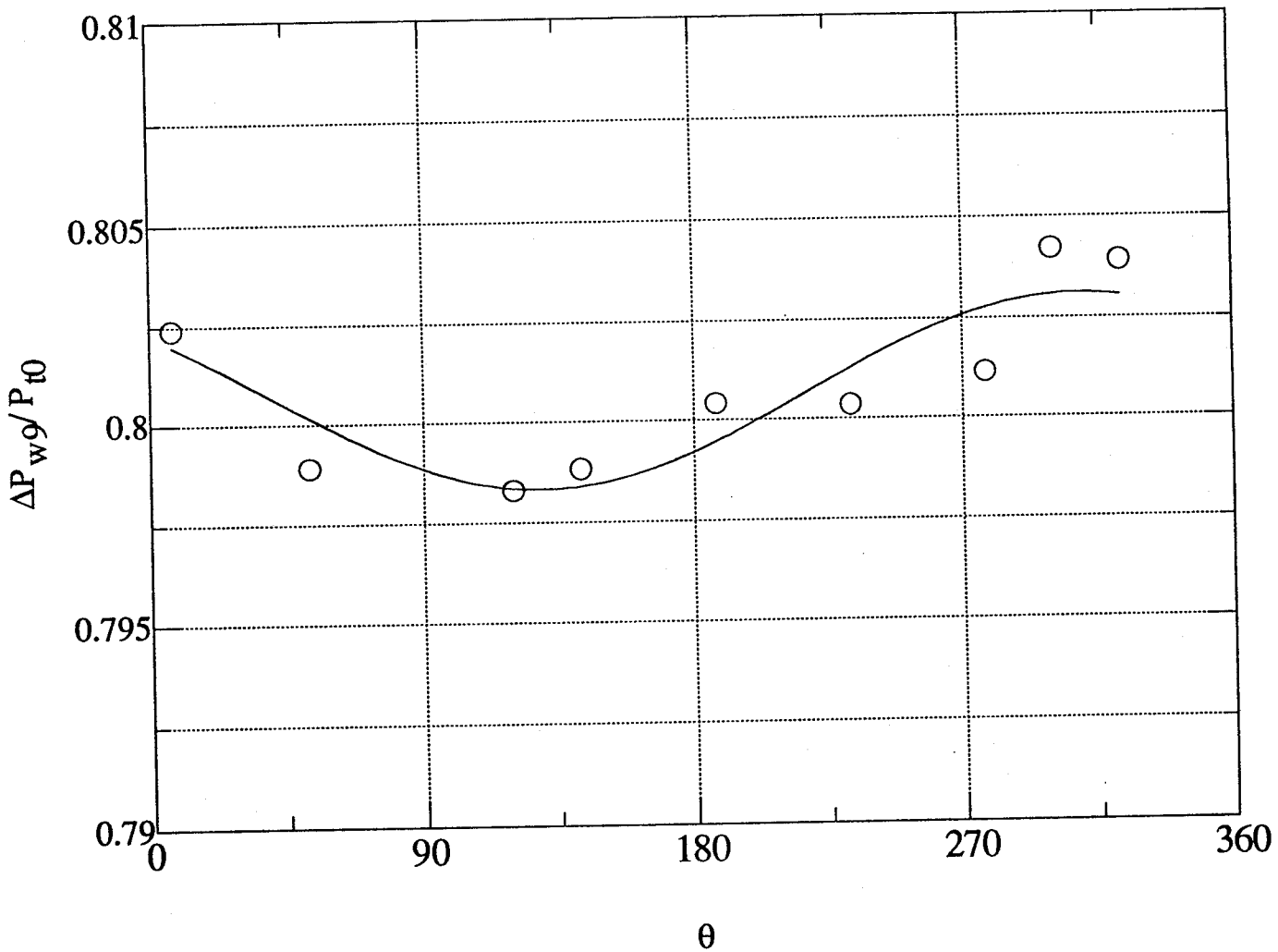

Figure 4.25 Wall tap pressure 3 chords downstream of rotor e/H = 0.019

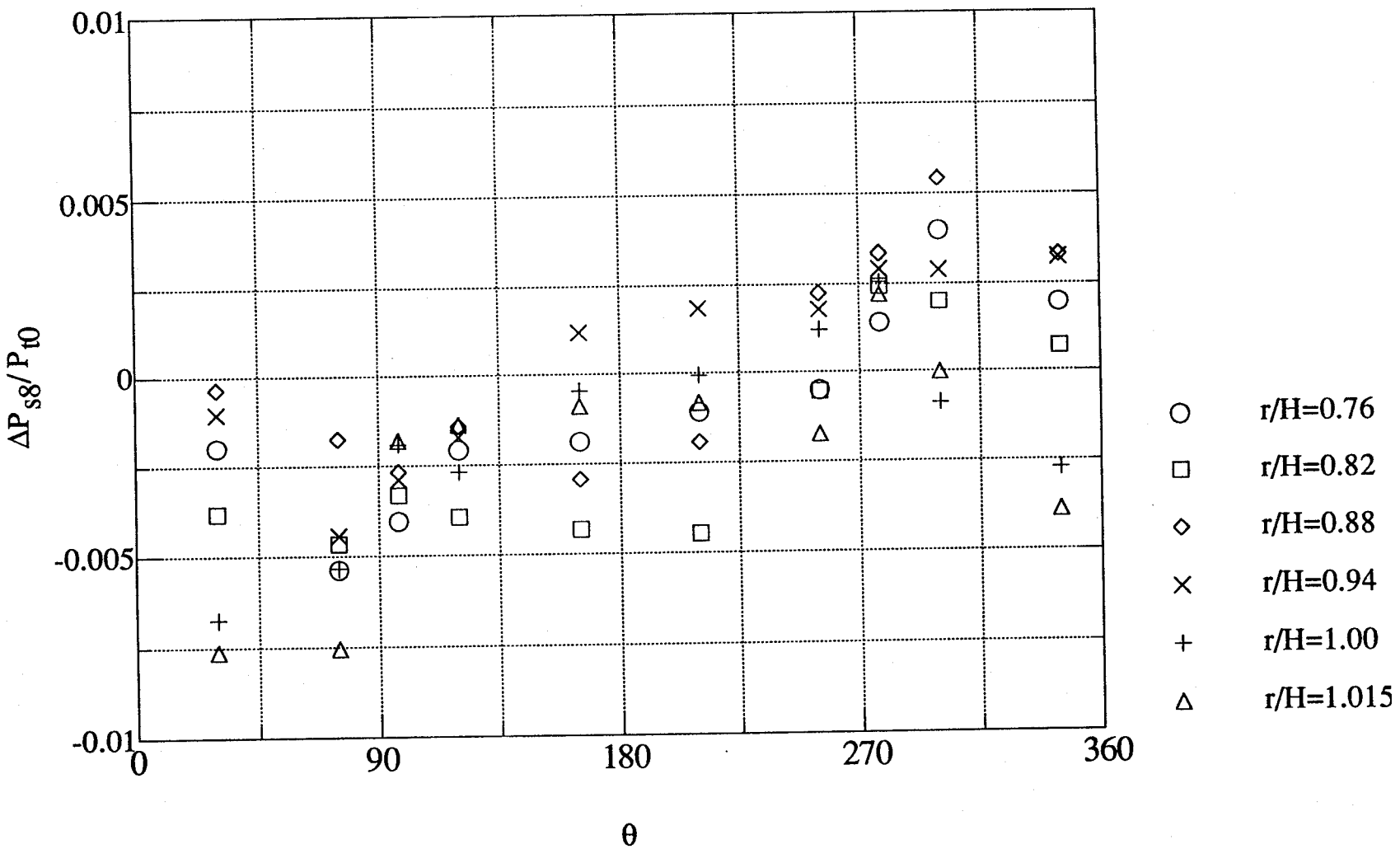

Figure 4.26 A radial and tangential survery of static pressure at Station 8

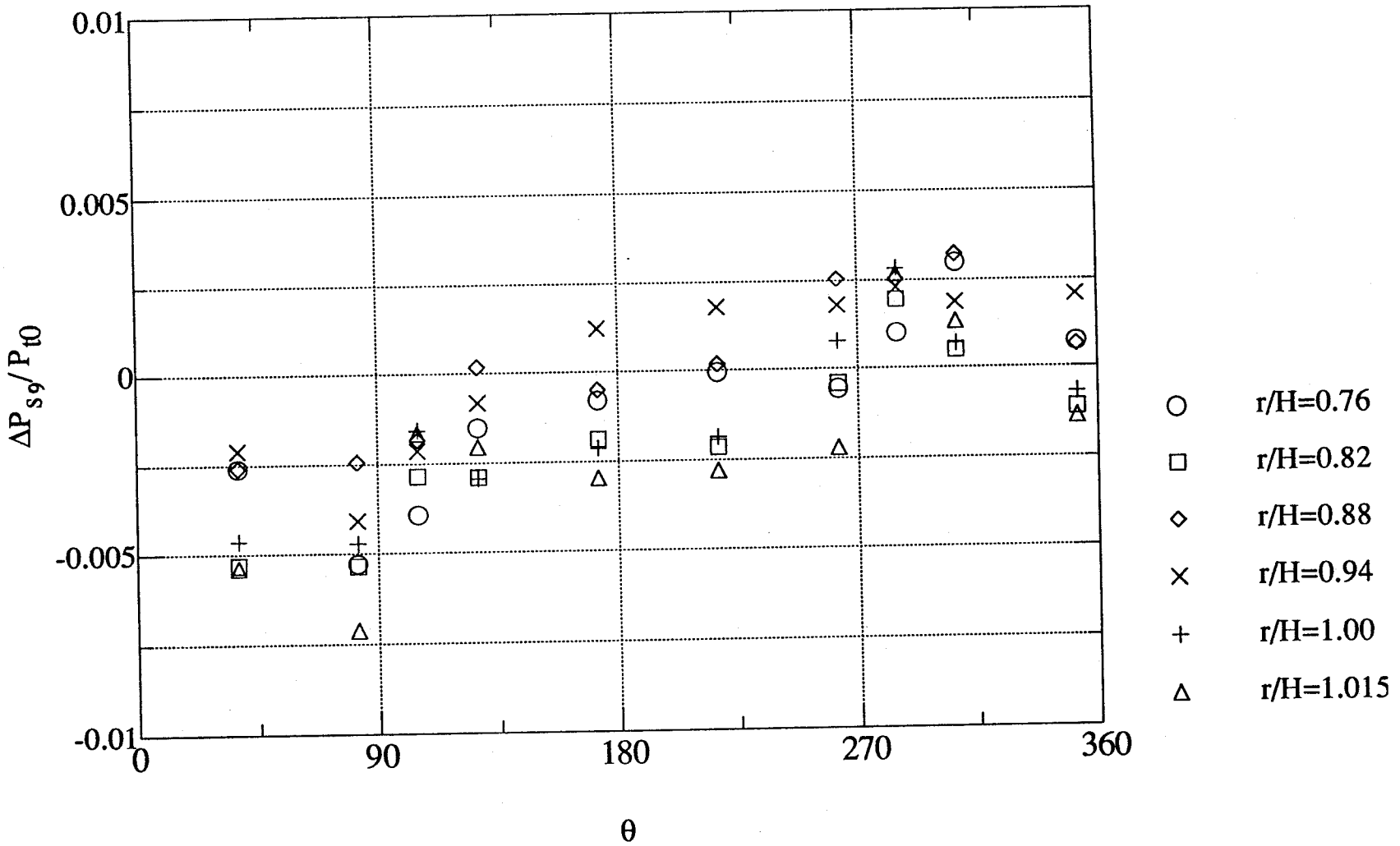

Figure 4.27 A radial and tangential survey of static pressure at Station 9

turbine centered. With reference to the upstream total pressure, the taps over the turbine show a regular pressure decrease to about 0.855 at station 7 (Fig. 4.28). At stations 8 and 9 (Fig. 4.29), this has dropped to 0.805. The design of the casing and of the hub is perfectly smooth, with constant height and no obstructions, and there appears to be no satisfactory explanation for a drop of that magnitude (comparable to $\frac{1}{2}\rho U^2$). It was suspected that perhaps the slow-responding pressure sensing system had a nonlinear response to the rapid pressure fluctuations caused by blades passing over the taps, such as to cause an averaging bias. This has been mentioned in the turbomachinery literature [10b] as a danger to guard against when performing measurements near rotating components. To test this hypothesis, we installed a flush-mounted 5 psi Kulite transducer, with very high frequency response, on one of the station 6 plug holes (used normally for the proximeters). The reference was to one of the downstream points (station 10). A typical time-resolved pressure trace from this transducer is shown in Fig. 4.30. Each blade passage produces a characteristic rapid pressure fluctuation, but the time average of these pressures corresponds very closely to the difference of those read directly by the other wall taps at station 6 and the reference at station 10. In fact, the time average $\overline{P}_6 - P_{10}$ is about 2.3 psi, slightly more than the 2.1 psi read by the wall taps. The effect seems to be real, but we have no explanation for it.

4.3.4 Velocity Components Downstream of the Rotor

The 5-hole probes at station 8 were used to measure all three velocity components in the outer 1/4 span region there. Figure 4.31 shows the somewhat unexpected results for the radial component. The flow is seen to be differentially moving radially away from the tip in the region with the wider gap, and towards the tip in the region with the smaller gap. The radial velocity is, of course, very small very close to the wall, and also as the core is approached, and, in fact, a trend can be seen

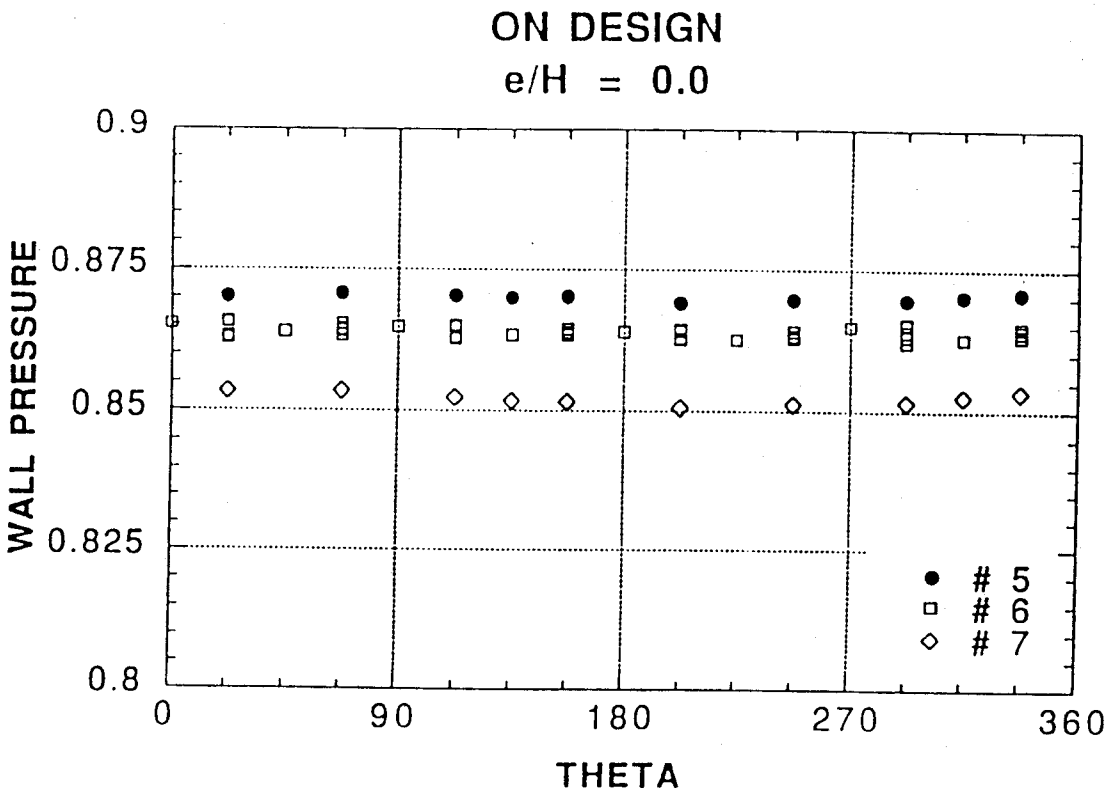

Figure 4.28 Pressure levels on the wall taps over the centered turbine

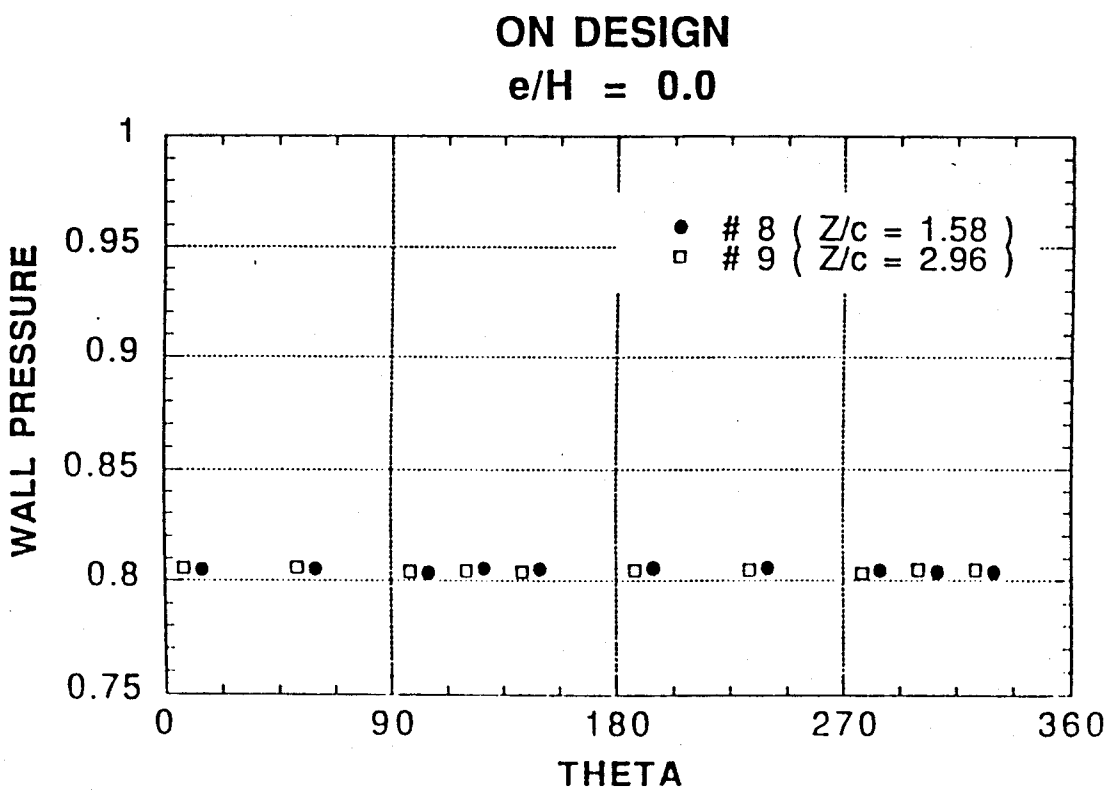

Figure 4.29 Pressure levels on the taps downstream of the turbine

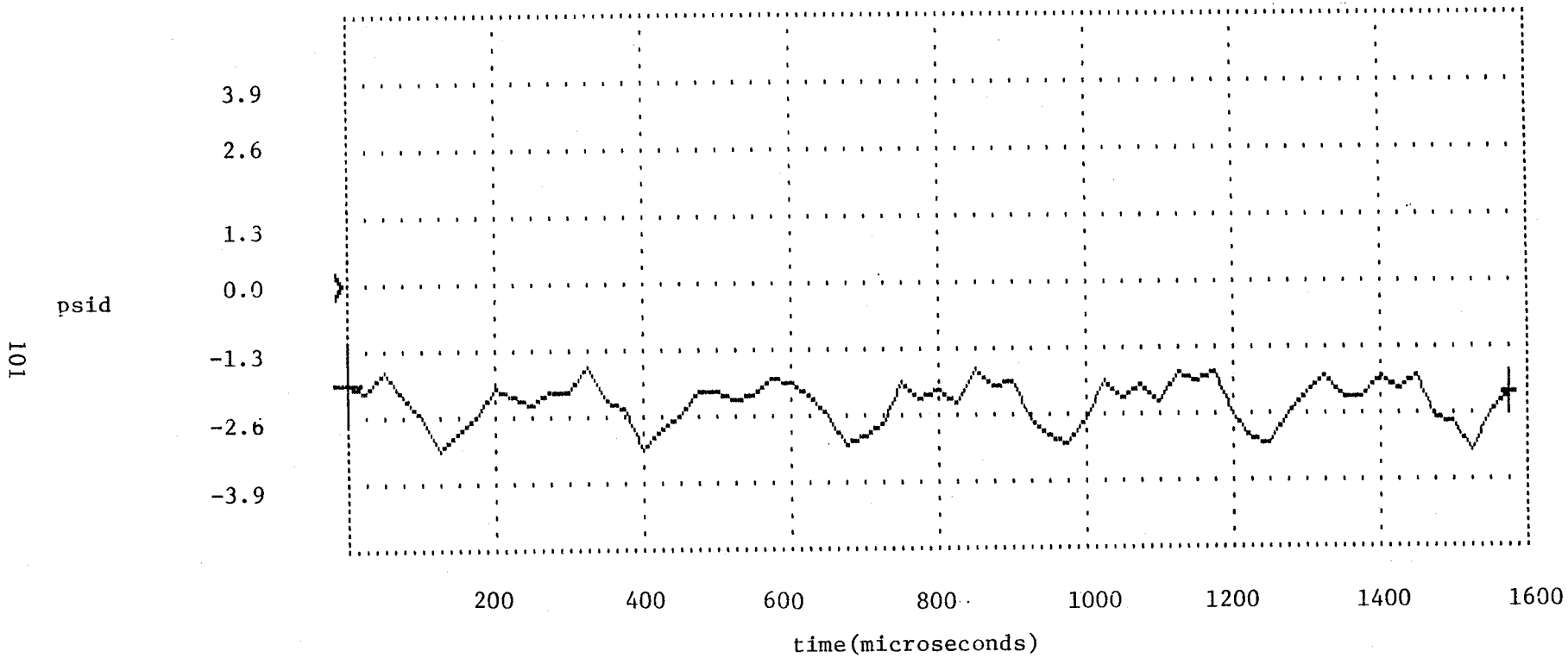

Figure 4.30 Time resolved trace of $P_{10} - P_6$

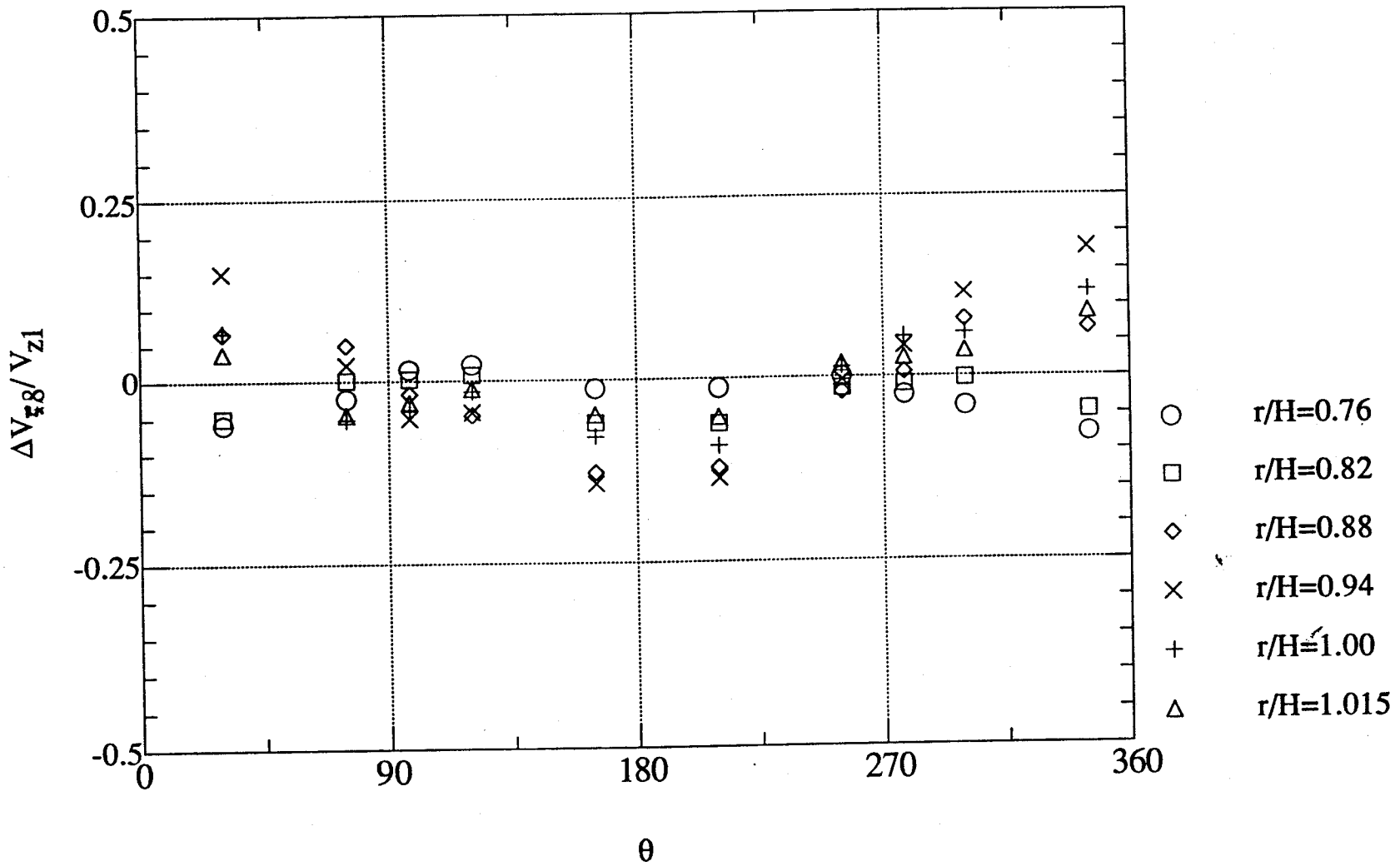

Figure 4.31 Radial velocity 1 chord downstream of rotor

to reverse the radial velocities in the r/H = 0.82, 0.76 curves, i.e. the flow now moves away from the narrow gap. These trends are not understood at present.

Also surprising is the axial velocity survey shown in Fig. 4.32. The nonuniformity is largely confined to the tip region, and is seen to indicate lower axial velocities near the 180° area, where the fluid is coming from the wider gap. This is consistent with the radial migration pattern from Fig. 4.31, and, like it, is not explainable by our theoretical work.

The most important data for interpretation of the cross-forces are the tangential velocities after the turbine because, through the use of the Euler turbine equation, they can be converted to local driving forces, and then integrated to yield direct and cross-forces. Figure 4.33 shows these velocities (after subtracting the centered turbine values) for station 8. The positive values seen near 180° indicate underturning there by the rotor blades, clearly because of the flow leaking through the wider gap. This underturning is seen to be nearly uniform in the first 5% or so near the casing wall, and then it decreases to near zero by the time r/H = 0.76. Since our measurements are time-averaged, this appears to represent a steady shear pattern where the flow continuously changes its orientation as we traverse in the radial direction. In reality, there is a discrete blade-to-blade pattern, of which our data represent the average only. This pattern is quite complex, typically involving a collection of rolled-up tip vortices arising one from each blade-tip gap (see Sec. 9.3). Because of this, there is a question as to whether our probes are averaging linearly these wide velocity fluctuations, and whether the calibrations (validated typically for orientations under ±30° from the flow direction) remain valid over the range of fluctuations. Lacking much more elaborate calibration and checking procedures, these questions must remain unanswered here. As a tentative argument in favor of the procedure used, we can assume that the instantaneous angular fluctuations will not exceed twice their mean value, in which case the majority of the data points are within calibration range. The

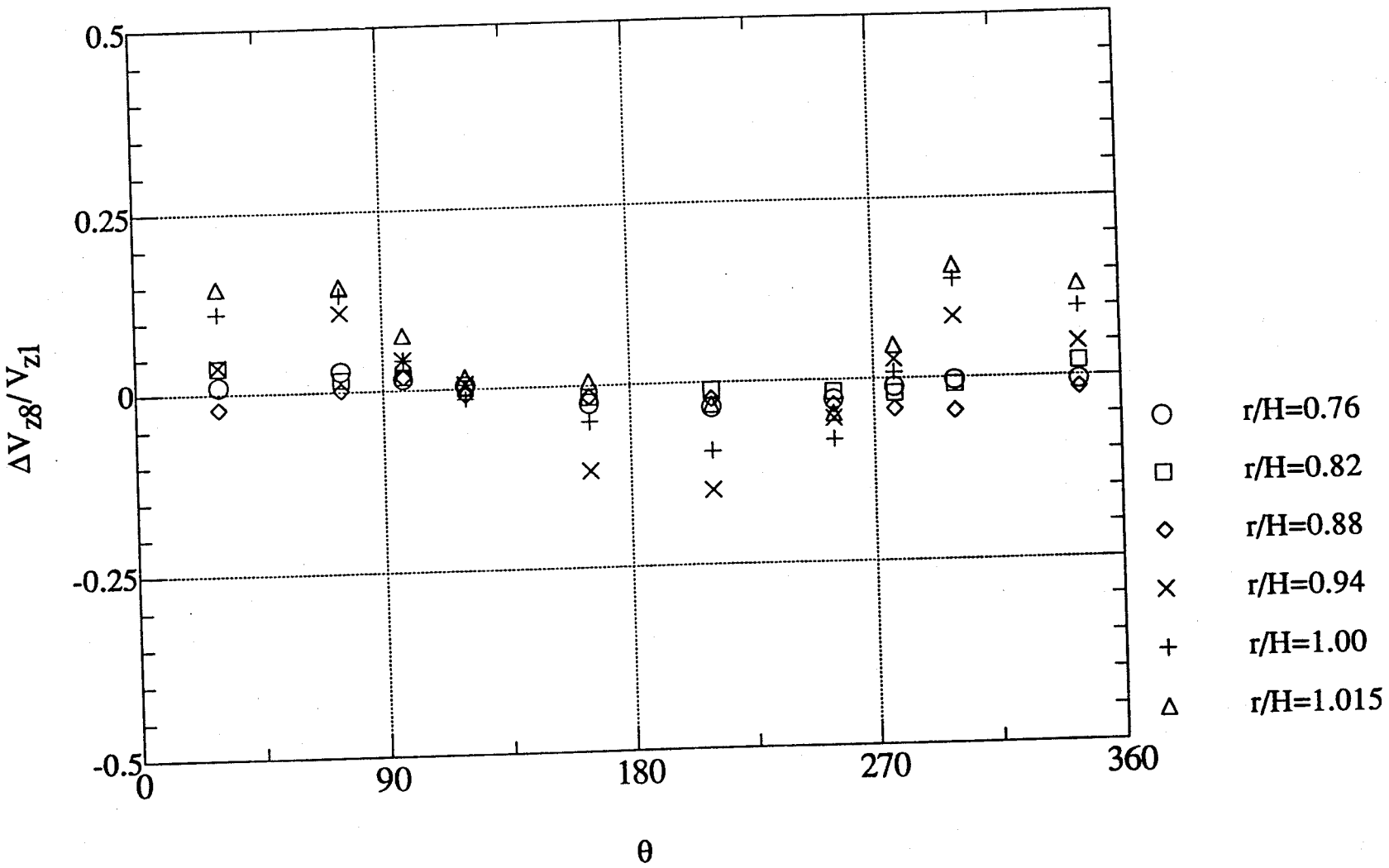

Figure 4.32 Axial velocities 1 chord downstream of rotor

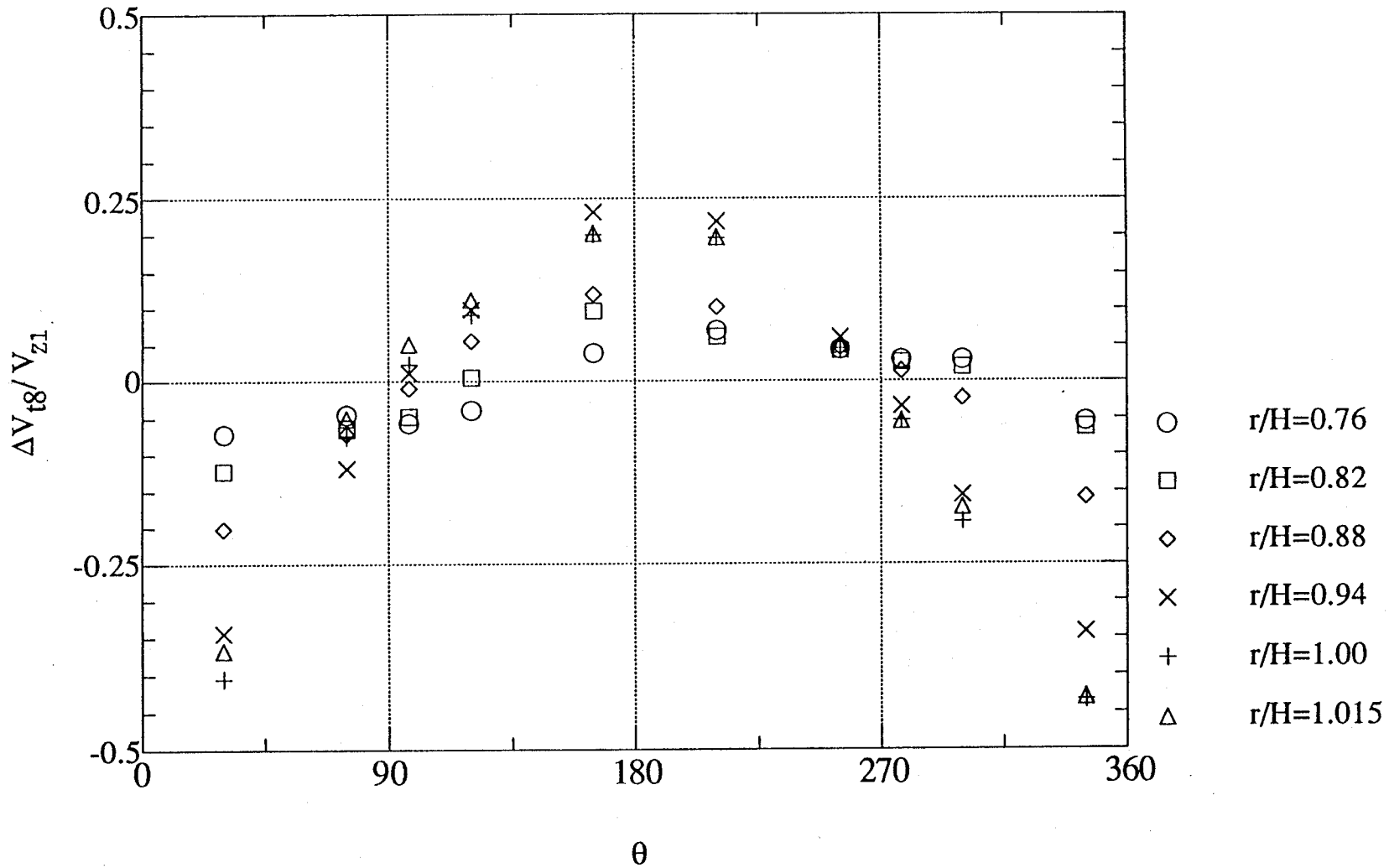

Figure 4.33 Tangential flow velocities at station 8

linear averaging properties of at least the wall taps were commented on before.

The same tangential velocity survey, but this time at station 9 (3 chords downstream of the rotor), is shown in Fig. 4.34. The underturning pattern is now seen to have penetrated deeper, and is actually maximum at the last surveyed depth (r/H = 0.76). It is unfortunate that no deeper points were surveyed in this case because the thickness of the underturned region cannot be discerned from the data. At the same time, the amplitude of these tangential velocity variations has decreased compared to station 8, as is to be expected from angular momentum conservation.

4.3.5 Estimation of Alford Forces From Fluid Data

There are two main sources of radial force on the turbine from the flow properties we have surveyed: (a) a non-uniformity in flow turning by the rotor blades, which will create non-uniform work extraction around the perimeter; and (b) a non-uniformity in static pressure around the perimeter, which will directly integrate to a radial force.

The force exerted by the blades per unit perimeter is given by Euler's turbine equation:

$$f_y(\theta) = \int_0^H \rho v_x \left(v_{\theta_2} - v_{\theta_3}\right) dz \qquad (4.5)$$

where v_{θ_2} and v_{θ_3} are the tangential velocities before and after the rotor, and ρv_x is the mass flux. All the quantities inside the integral depend on θ, but the variations of v_{θ_2} are only minor, and those of v_x (Fig. 4.32) are restricted to a very narrow radial zone and can be shown to contribute little to the integral. Thus, mainly the variations of v_{θ_3} (Figs. 4.33 and 4.34) matter. The integrand for Eq. (4.5) at station 8 is shown in Fig. 4.35, and its radial integral (the force f_y per unit length) in Fig. 4.36.

This force can generally be represented as a Fourier series in θ, of which only the first harmonic contributes to the radial forces. Assuming a truncated Fourier series

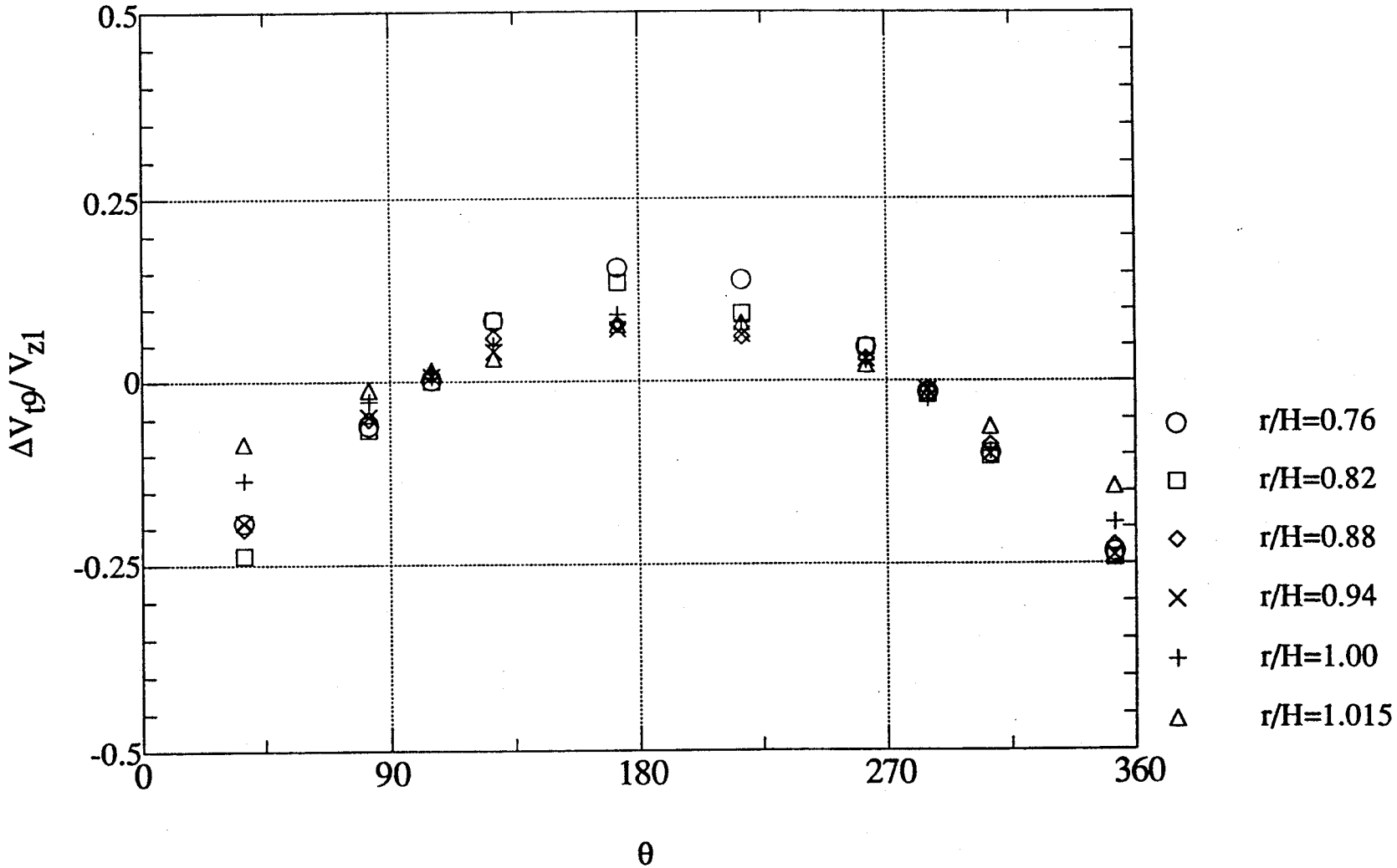

Figure 4.34 Tangential flow velocities at Station 9

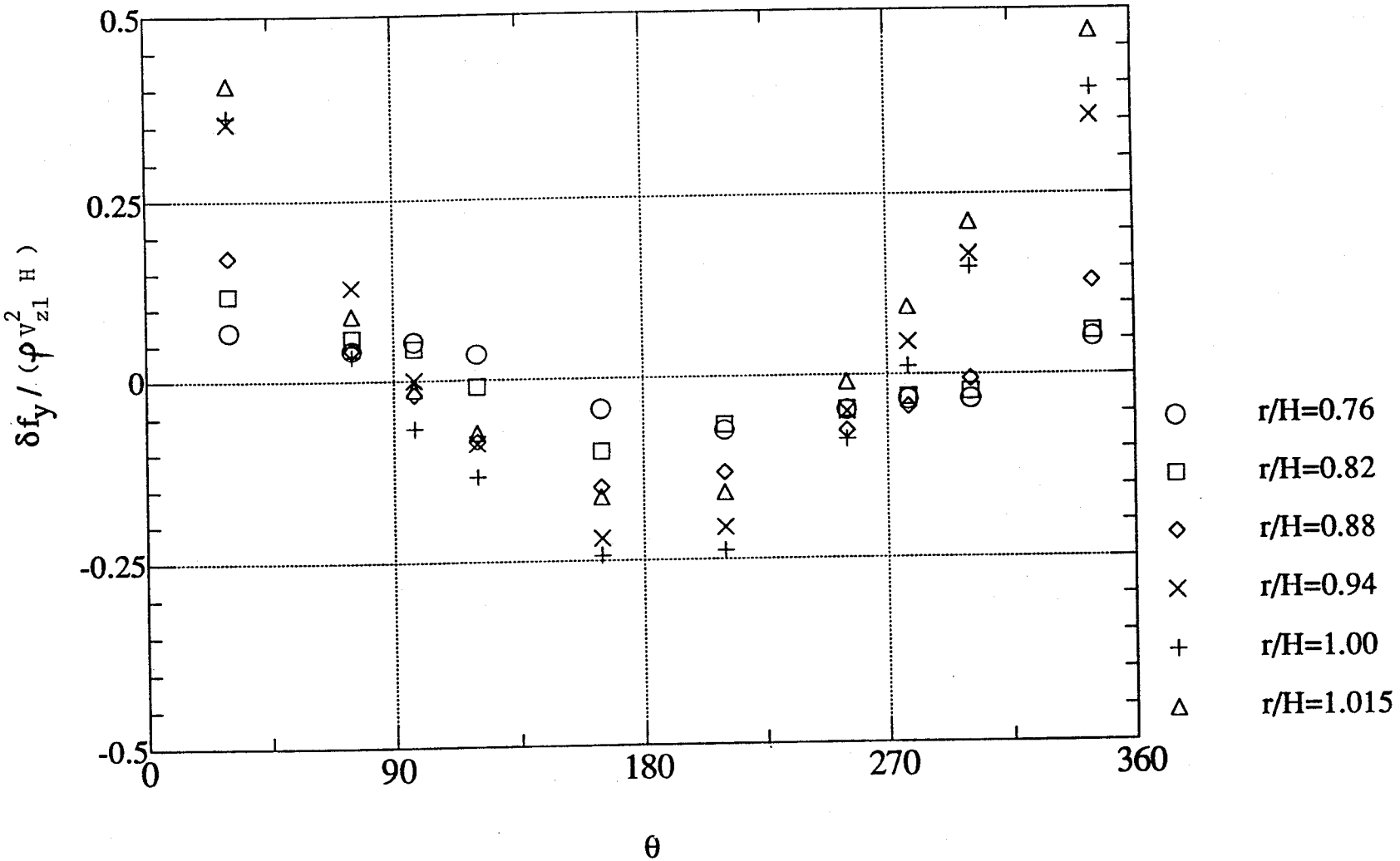

Figure 4.35 Tangential turbine force per unit frontal area (from tangential velocity data at Station 8) e/H = 0.019 Average values suppressed.

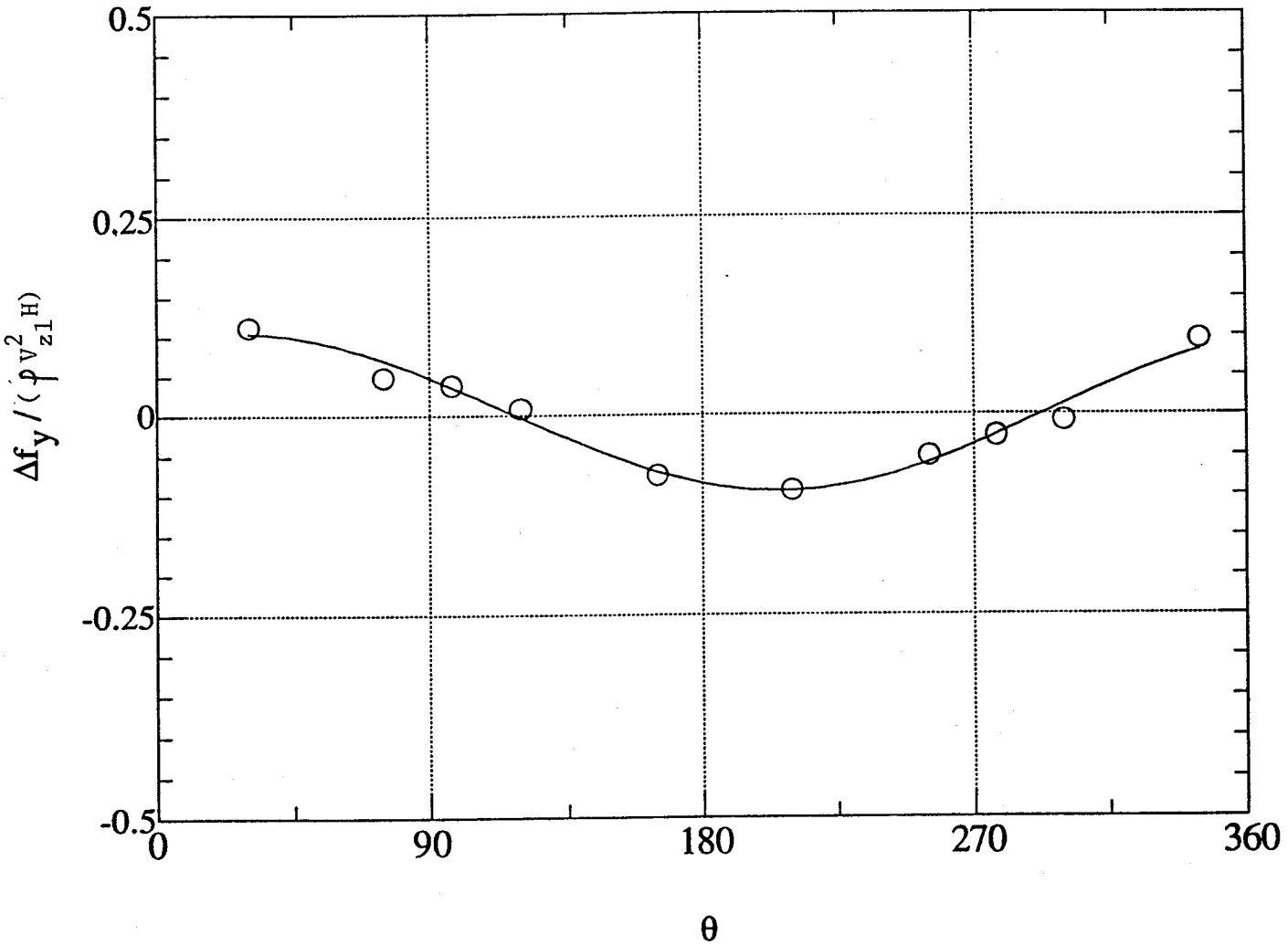

Figure 4.36 Tangential turbine force per unit length. Average value suppressed.

representation

$$f_y(\theta) \cong \bar{f}_y + \Delta f_y \cos(\theta - \phi_f) \tag{4.6}$$

and defining the forces F_x along the displacement of the rotor (negative if restoring), and F_y perpendicular to the displacement (positive if feeding into forward whirl), we have

$$F_x = - \int_0^{2\pi} f_y \sin\theta \, R d\theta = - \pi R \, \Delta f_y \sin\phi_f \tag{4.7}$$

$$F_x = - \int_0^{2\pi} f_y \sin\theta \, R d\theta = - \pi R \, \Delta f_y \cos\phi_f \tag{4.8}$$

The torque can also be, in principle, obtained from the f_y distribution as

$$Q = 2\pi R \, \bar{f}_y \tag{4.9}$$

but, as explained in Sec. 4.3, this introduces probe alignment errors which are not present in Δf_y. Nevertheless, this can be used as an approximate check of the measurements. In the present case, we measured $\bar{f}_y$ = 373 N/m, and Eq. (4.9) gives an estimate Q = 39.0 Nm, which is close to the torque measured directly by the shaft gauge (Q = 39.9 Nm). Incidentally, an independent check is provided by the total temperature measurements upstream and downstream of the turbine (24.0°C, 19.0°C), which yield 39.2 Nm. This degree of agreement with the ΔT_t data is, however, somewhat misleading, because the uncertainty in the thermocouple readings is perhaps as high as ±0.25°C. In other cases, we have indeed obtained much worse agreements.

The pressure contribution to the forces Fx, Fy is obtained here by simply applying the pressures measured on wall taps at station 6 on the turbine hub. Assuming this pressure is of the form

$$P(\theta) = \bar{P} + \Delta P \cos(\theta - \phi_P) \tag{4.10}$$

we then obtain

$$F_x = -\int_0^{2\pi} P \cos\theta \, RW \, d\theta = -\pi RW \, (\Delta P) \cos\phi_P \tag{4.11}$$

$$F_y = -\int_0^{2\pi} P \sin\theta \, RW \, d\theta = -\pi RW \, (\Delta P) \sin\phi_P \tag{4.12}$$

where $W \cong 2.4$ cm. is the axial width of the rotor hub. As noted in Sec. 4.3.2, there are good reasons to believe that at least the degree of tangential nonuniformity seen at stations 4 and 8 does penetrate throughout the annulus. There is some question, however, about the excess between the nonuniformity amplitudes at stations 6 vs. 4 (0.0042 P_{t_0} at station 6, 0.0027 P_{t_0} at 4), because there is no direct way of measuring the near-hub static pressure. Thus, our procedure may, in the worst case, overestimate pressure forces by about 50%.

The forces F_x and F_y will be reported in the non-dimensional form of α_x, α_y, as in Eqs. (4.1) and (4.2). The results are shown in Table 4.2, where the dynamometer-measured α_x and α_y (Sec. 4.2) are also shown for comparison.

TABLE 4.2
FORCE COEFFICIENTS OBTAINED FROM FLUID DATA VS. DYNAMOMETER DATA: CONFIGURATION 1, DESIGN CONDITION

$(\alpha_x)_{\text{Work Defect}}$	$(\alpha_x)_{\text{Pressure}}$	$\alpha_{xWD} + \alpha_{xP}$	$(\alpha_x)_{\text{Dynamometer}}$
-0.72	-2.52	-3.24	-2.81
$(\alpha_y)_{\text{Work Defect}}$	$(\alpha_y)_{\text{Pressure}}$	$\alpha_{yWD} + \alpha_{yP}$	$(\alpha_y)_{\text{Dynamometer}}$
1.52	1.18	2.70	2.57

There is reasonable agreement between fluid-derived and dynamometer-derived forces. The split between work defect contributions (from the nonuniform underturning of the flow) and pressure contributions is interesting. Pressure effects dominate the

direct forces -2.52/-3.24 = 78%, while work defect (the classical Alford effect) is the larger contribution to cross-forces (1.52/2.70 = 56%). However, there are significant contributions of the work defect to direct force, and even more so of the pressure nonuniformity to the cross-forces. To our knowledge, these effects were not so far known.

4.3.6 Fluid Effects at Off-Design Conditions

In configuration 1, we also surveyed the flow field for off-design conditions (70% and 110% speed, at nominal flow). This was not done for the remaining configurations.

Qualitatively speaking, the same features were found as at $\omega = \omega_{DESIGN}$. The flow angles at rotor exit were considerably different, of course, and some iteration was required to bring the probes within approximate alignment at each station and each depth. We only give here the final integrated force conditions, with their work defect and pressure parts indicated (Tables 4.3 and 4.4).

TABLE 4.3
FORCE COEFFICIENTS FROM FLUID EFFECTS AND FROM DYNAMOMETER
ω/ω_D = 0.7

$(\alpha_x)_{Work\ Defect}$	$(\alpha_x)_{Pressure}$	$\alpha_{xWD} + \alpha_{xP}$	$(\alpha_x)_{Dynamometer}$
-0.46	-2.30	-2.76	-2.12
$(\alpha_y)_{Work\ Defect}$	$(\alpha_y)_{Pressure}$	$\alpha_{yWD} + \alpha_{yP}$	$(\alpha_y)_{Dynamometer}$
1.20	0.72	1.92	2.43

TABLE 4.4
FORCE COEFFICIENTS FROM FLUID EFFECTS AND FROM DYNAMOMETER $\omega/\omega_D = 1.1$

$(\alpha_x)_{Work\ Defect}$	$(\alpha_x)_{Pressure}$	$\alpha_{xWD} + \alpha_{xP}$	$(\alpha_x)_{Dynamometer}$
-0.94	-3.46	-4.40	-3.42
$(\alpha_y)_{Work\ Defect}$	$(\alpha_y)_{Pressure}$	$\alpha_{yWD} + \alpha_{yP}$	$(\alpha_y)_{Dynamometer}$
2.98	1.44	4.42	2.66

5.0 Effects of Varying Geometrical Parameters (Unshrouded Turbine)

This section presents the static force and flow data for Configurations 2, 3, 4, and 5 (Table 3.1):

Configuration 2 differs from Conf. 1 in that the stator was moved closer to the rotor. This decreased both d and d′ (Fig. 3.1) to d/c = 0.26, d′/c = 0.15.

Configuration 3 kept the same blade-to-blade distance (d/c = 0.26), but further reduced the hub gap (d′/c = 0.013).

Configuration 4 returned to the same d′/c as Conf. 2 but reduced the blade tip gap to $\overline{\delta}/H = 0.0187$.

Configuration 5 also used $\overline{\delta}/H = 0.0187$, this time with the narrow hub gap, d′/c = 0.013.

From the above, it is clear that we can obtain information on the effect of varying d′/c alone if we compare results from Configurations 2 and 3, and also from comparing Configurations 4 and 5. We can also obtain information on the effect of varying the tip gap $\overline{\delta}/H$ alone by comparing Configurations 2 and 4, and also by comparing Configurations 3 and 5. Finally, comparison of Configurations 1 and 2 gives information on the effect of varying d and d′ together. Separating out the effect of d alone depends on using the sensitivity data to d′ from the pairs 2-3 and 4-5.

5.1 Dynamometer Force Data

The complete set of direct and cross-force static measurements for Configurations 2-5 is given in physical units (lbf vs. mils) in Figs. 5.1 through 5.12.

In these figures, the abscissa is the turbine offset e_x, as determined by the thickness of the metal shims inserted on one or the other side of the traversing mechanism. The ordinates are the forces F_x (along the offset) and F_y (perpendicular to the offset). These are derived from the dynamometer bridge signals, as explained in Sec. 2.3.1. For most conditions, three measurements were made at each eccentricity

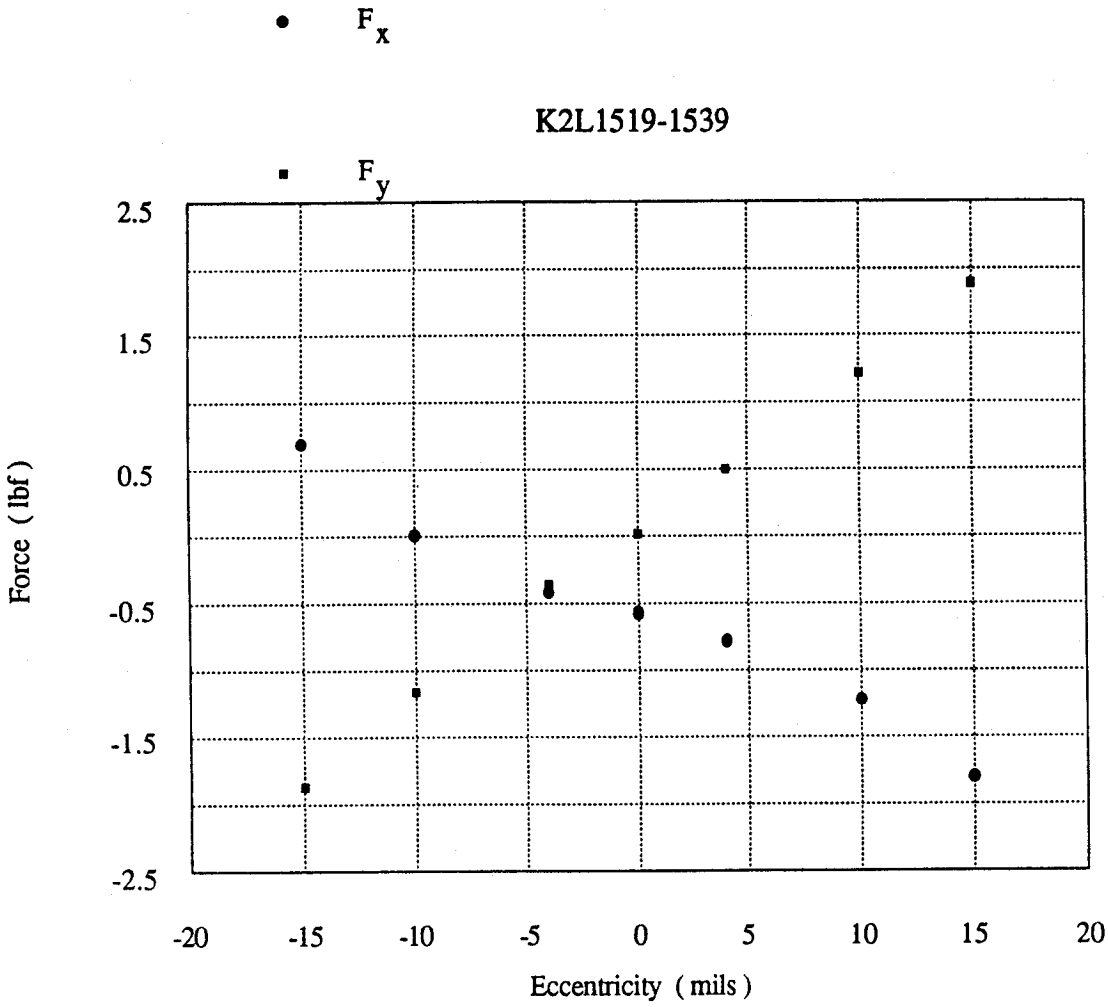

Fig. 5.1: Dynamometer-measured forces. Conf. 2, $\omega/\omega_D = 0.7$

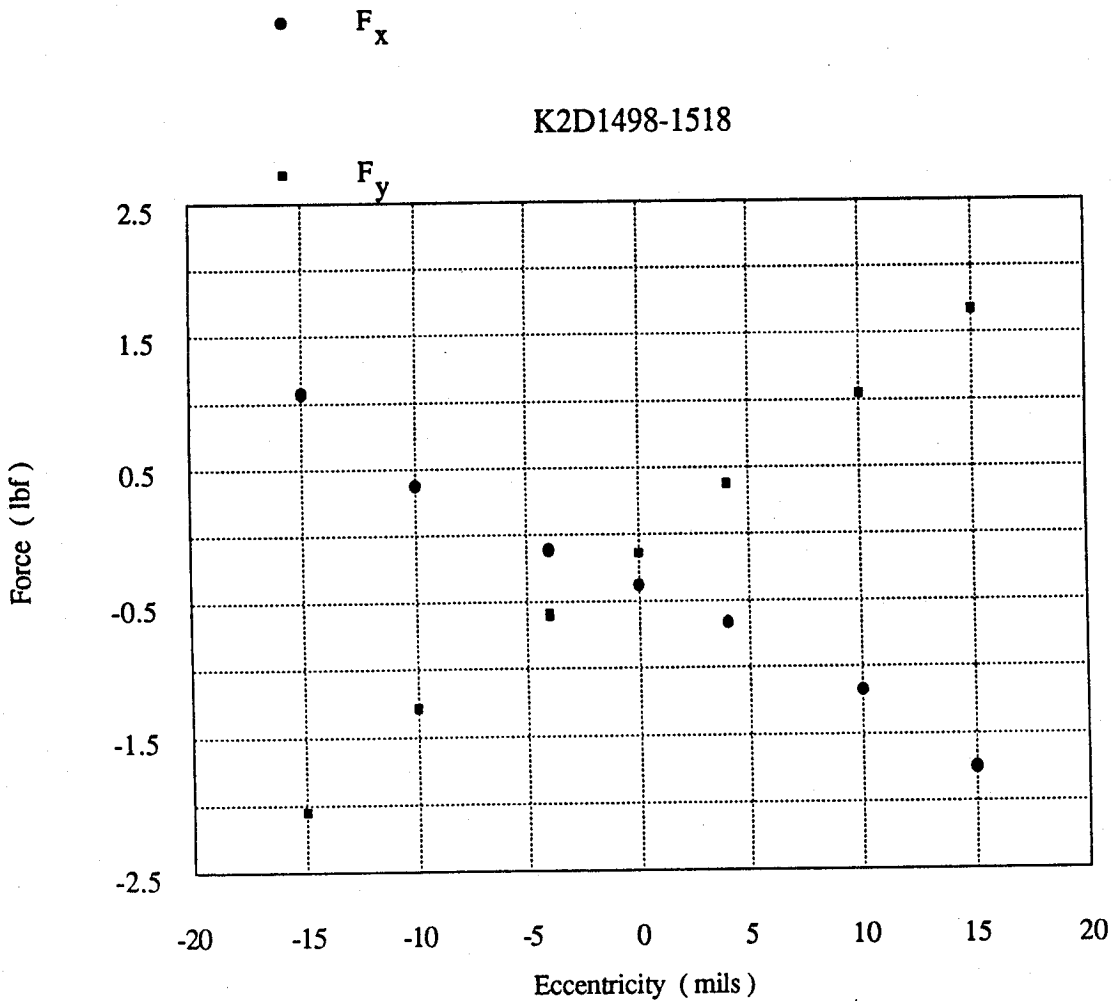

Fig. 5.2: Dynamometer-measured forces. Conf. 2, $\omega = \omega_D$

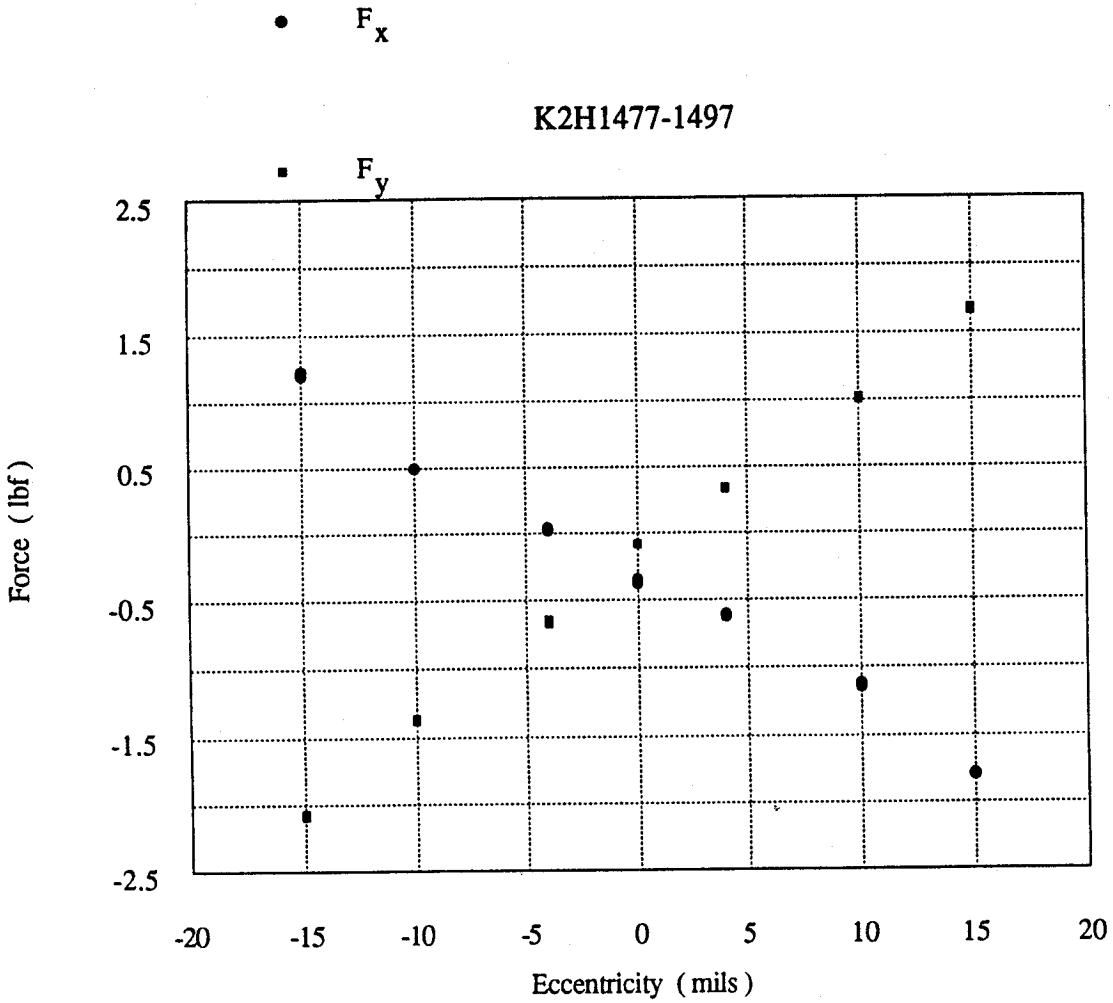

Fig. 5.3: Dynamometer-measured forces. Conf. 2, $\omega/\omega_D = 1.1$

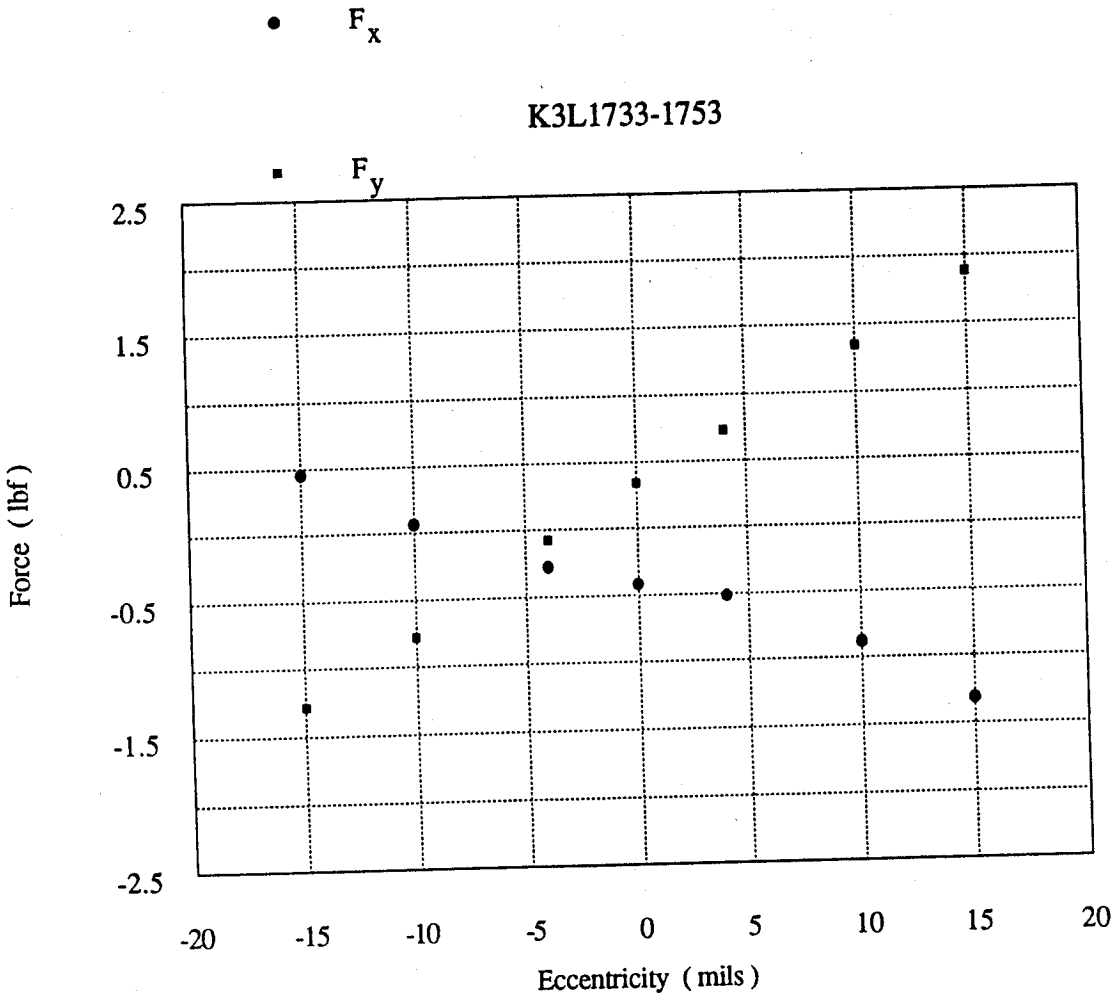

Fig. 5.4: Dynamometer-measured forces. Conf. 3, $\omega/\omega_D = 0.7$

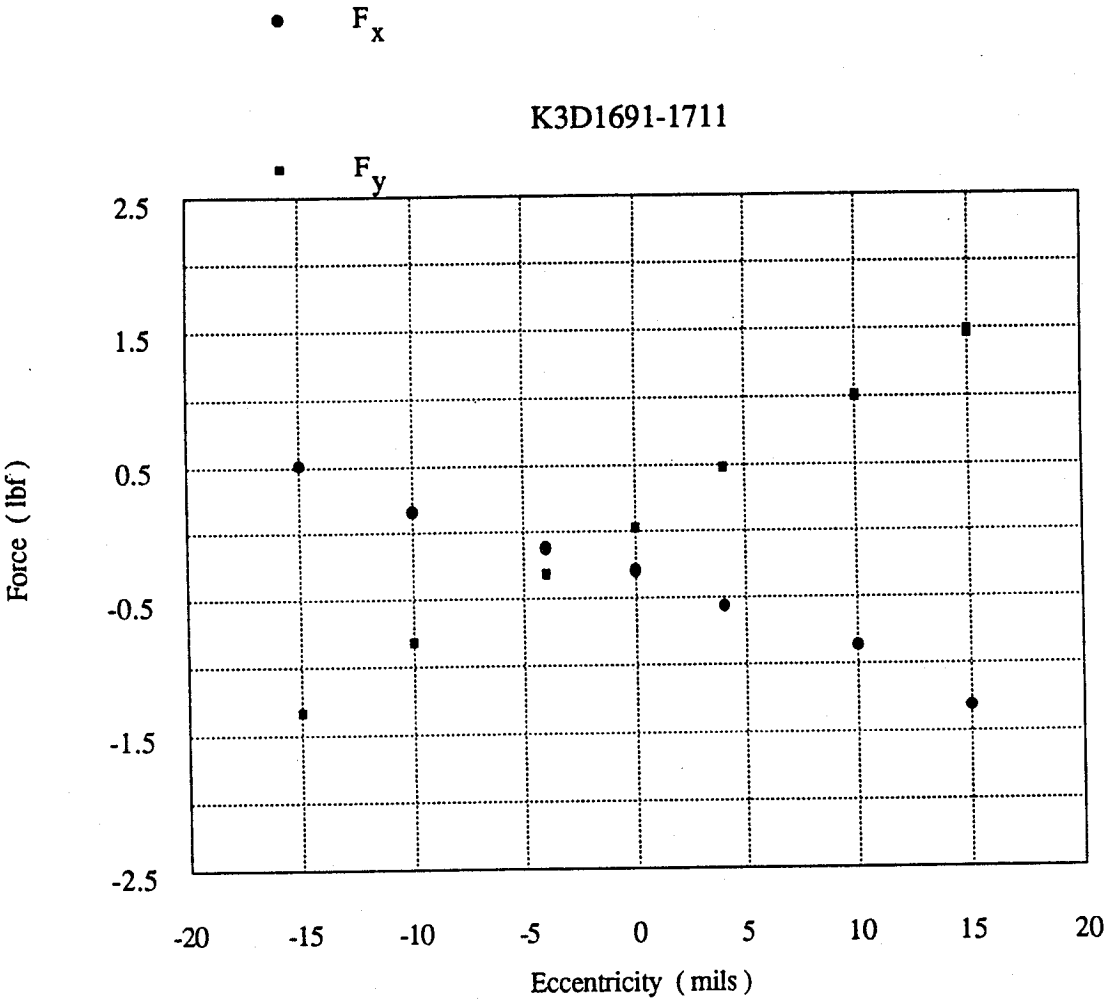

Fig. 5.5: Dynamometer-measured forces. Conf. 3, $\omega = \omega_D$

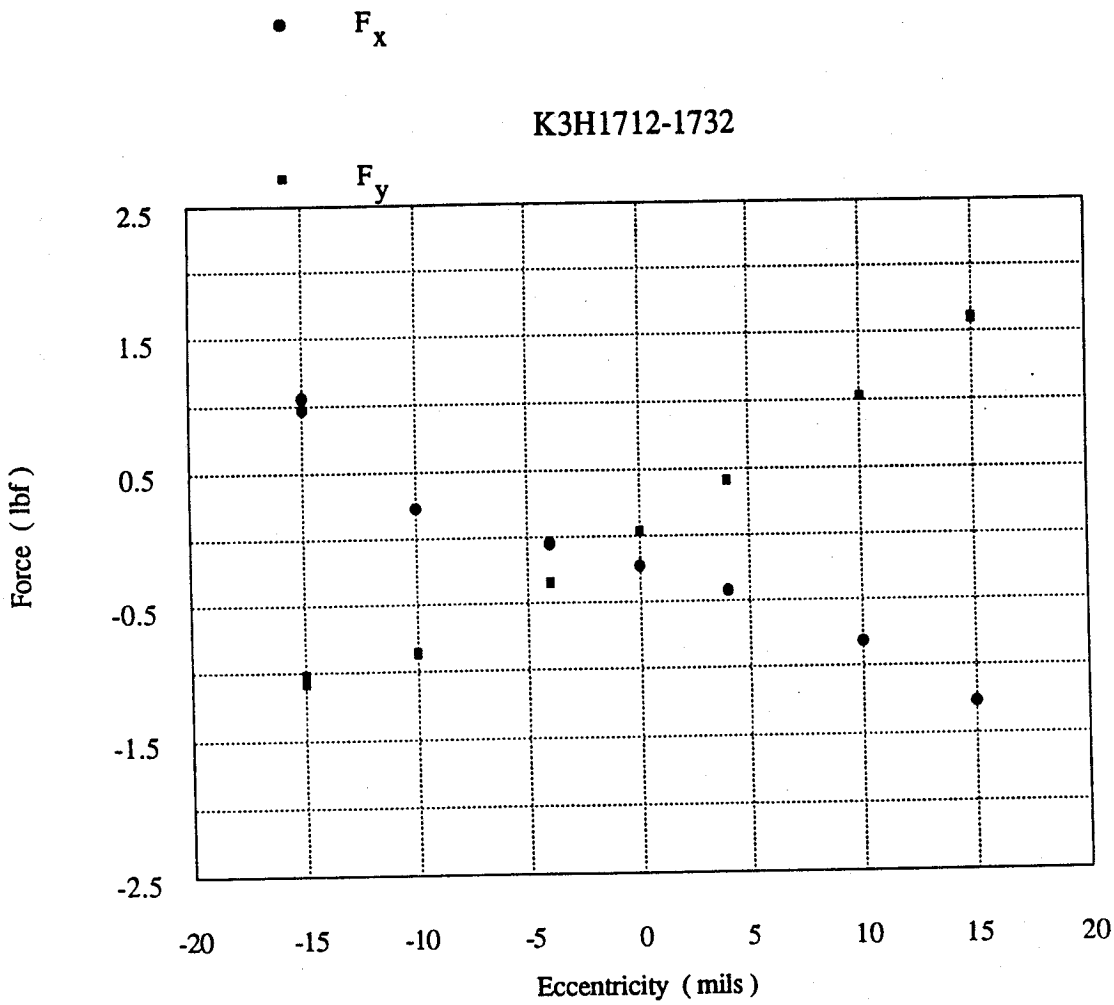

Fig. 5.6: Dynamometer-measured forces. Conf. 3, $\omega/\omega_D = 1.1$

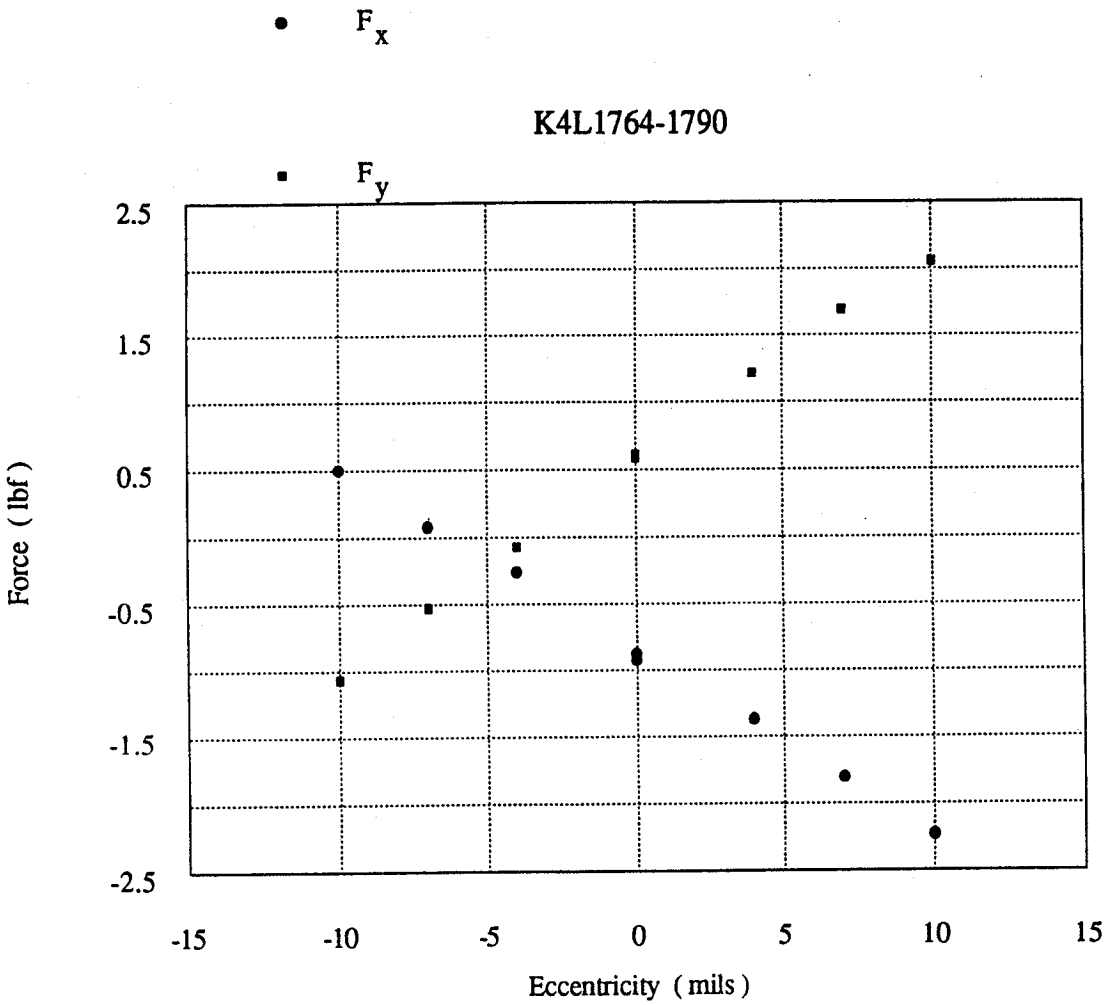

Fig. 5.7: Dynamometer-measured forces. Conf. 4, $\omega/\omega_D = 0.7$

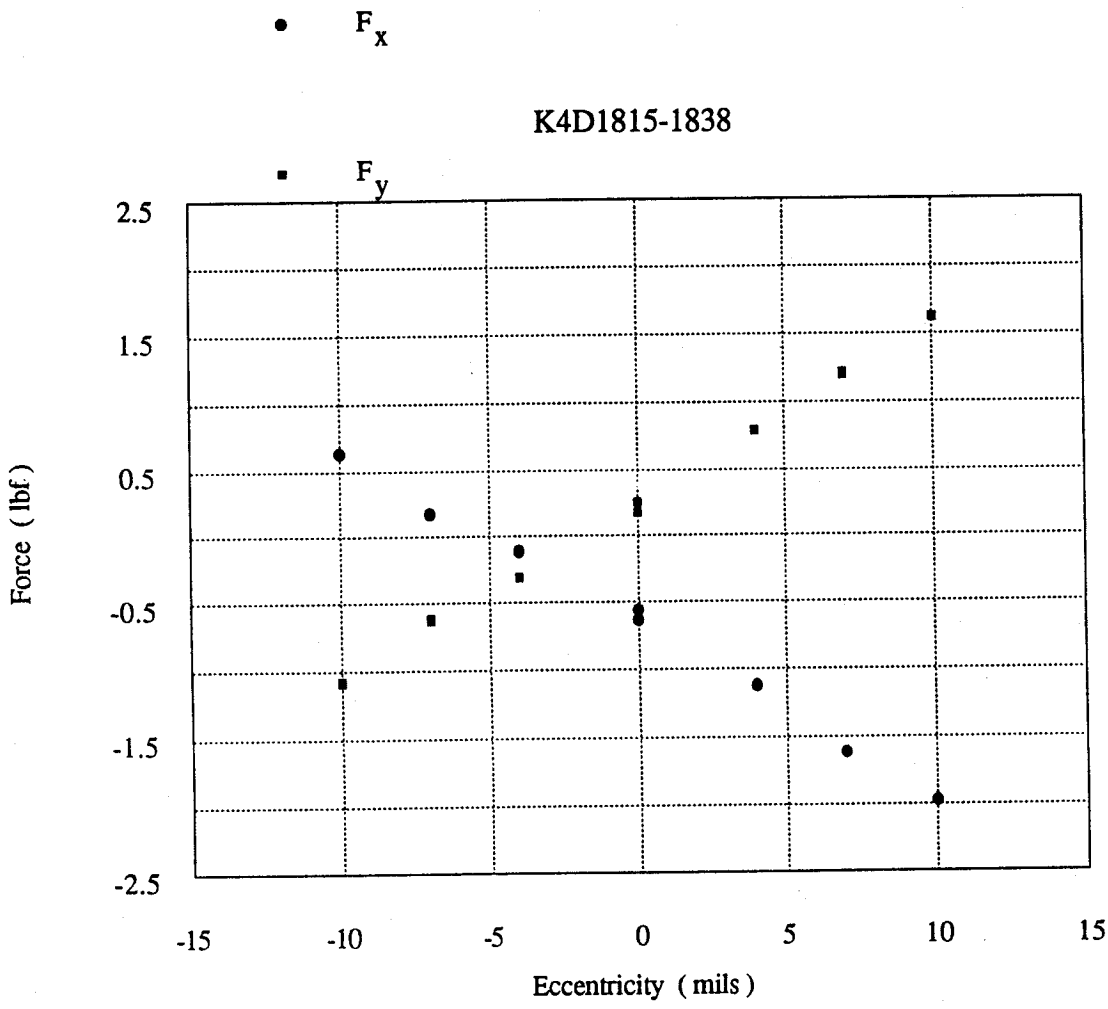

Fig. 5.8: Dynamometer-measured forces. Conf. 4, $\omega = \omega_D$

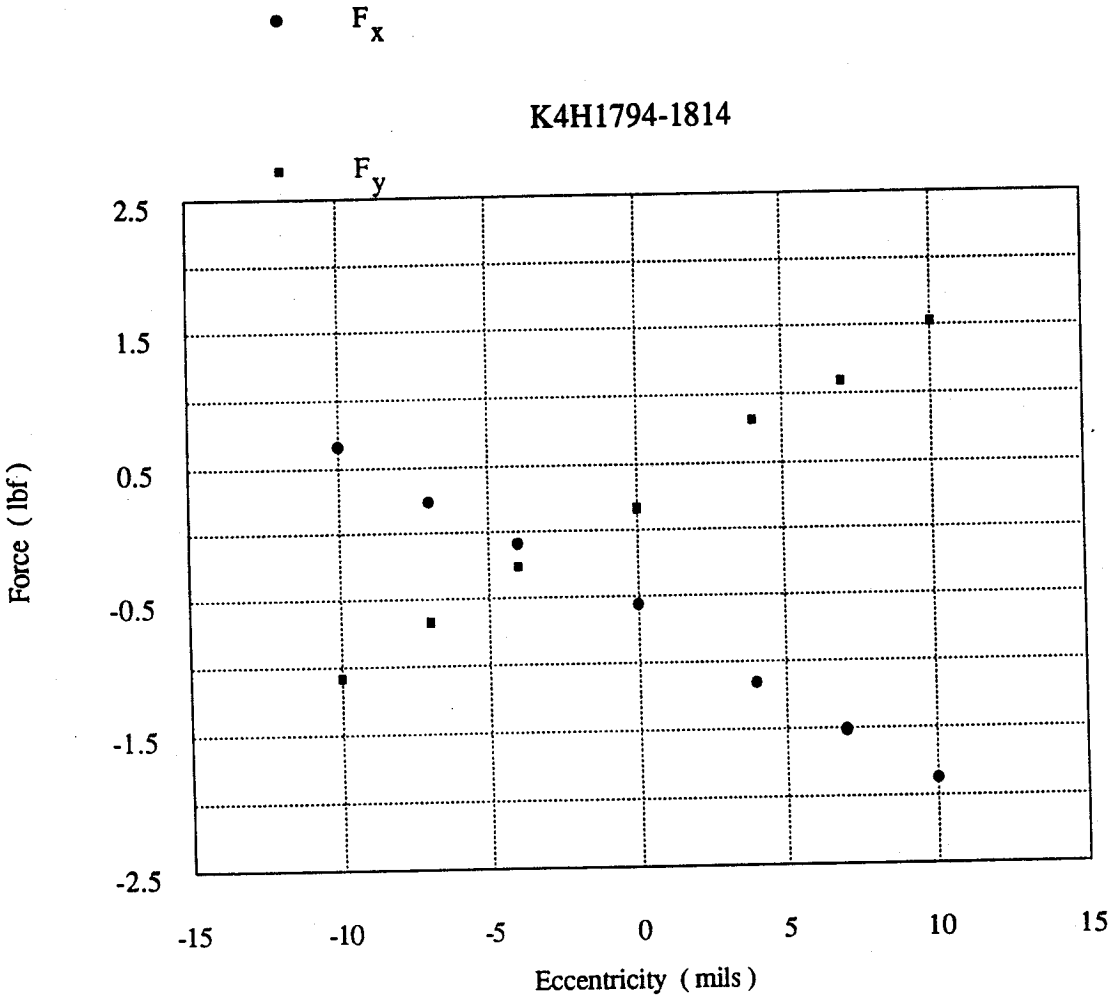

Fig. 5.9: Dynamometer-measured forces. Conf. 4, $\omega/\omega_D = 1.1$

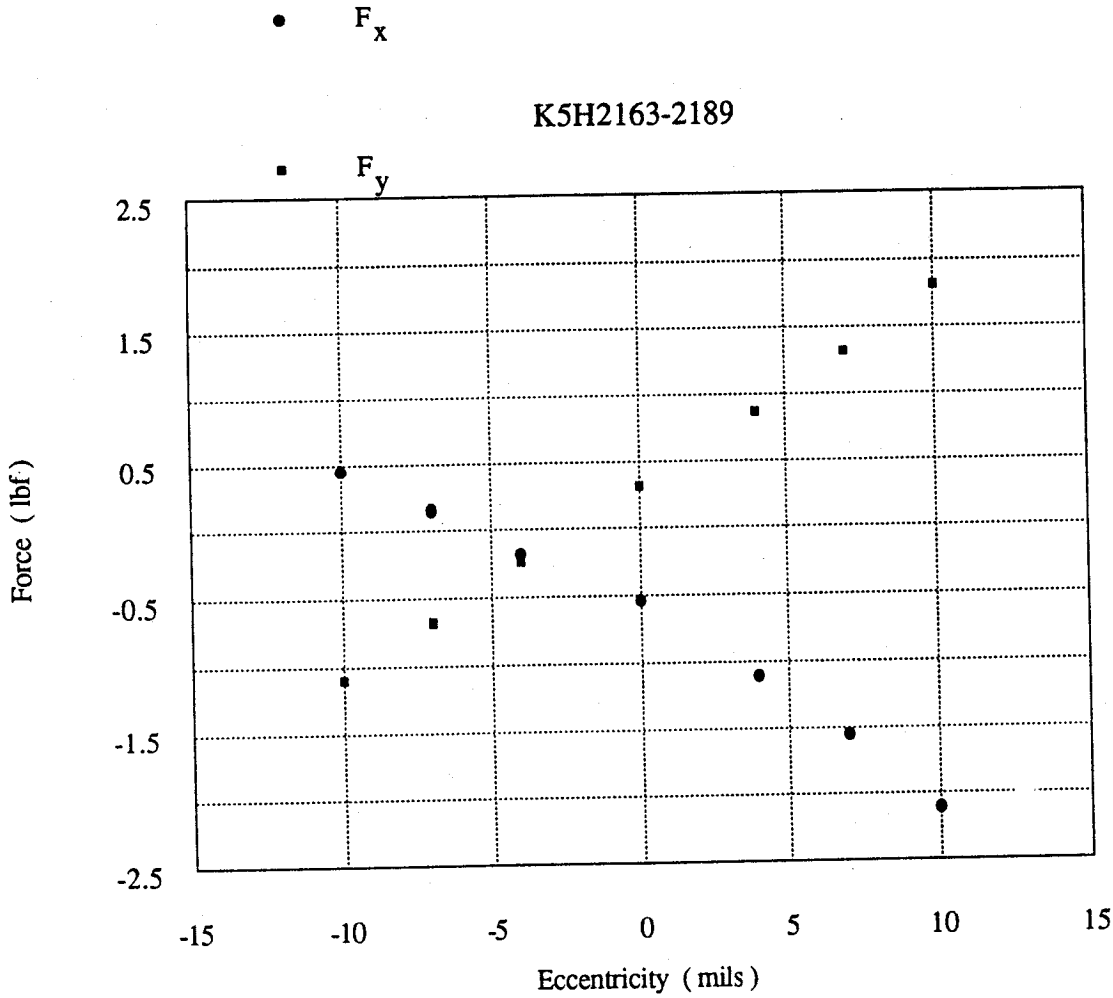

Fig. 5.10: Dynamometer-measured forces. Conf. 5, $\omega/\omega_D = 0.7$

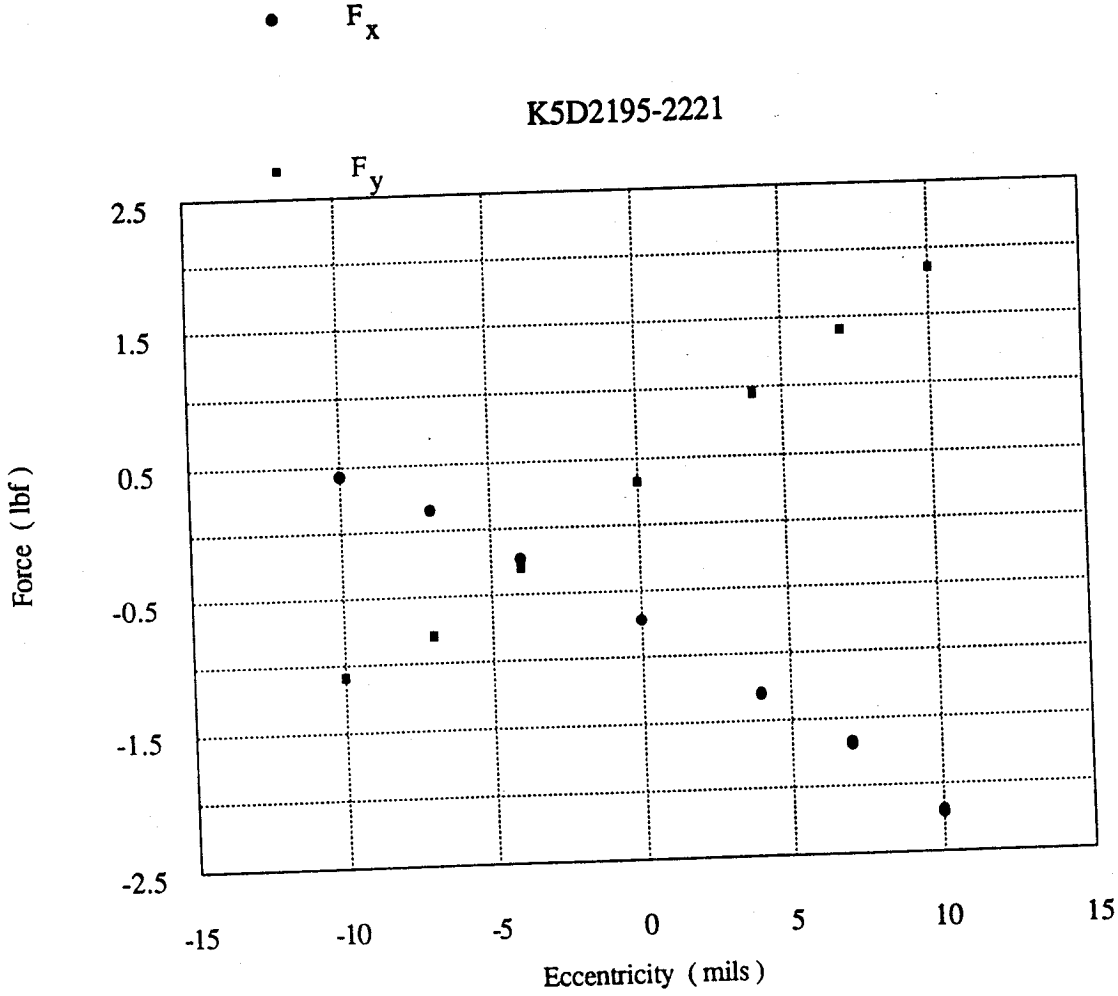

Fig. 5.11: Dynamometer-measured forces. Conf. 5, $\omega = \omega_D$

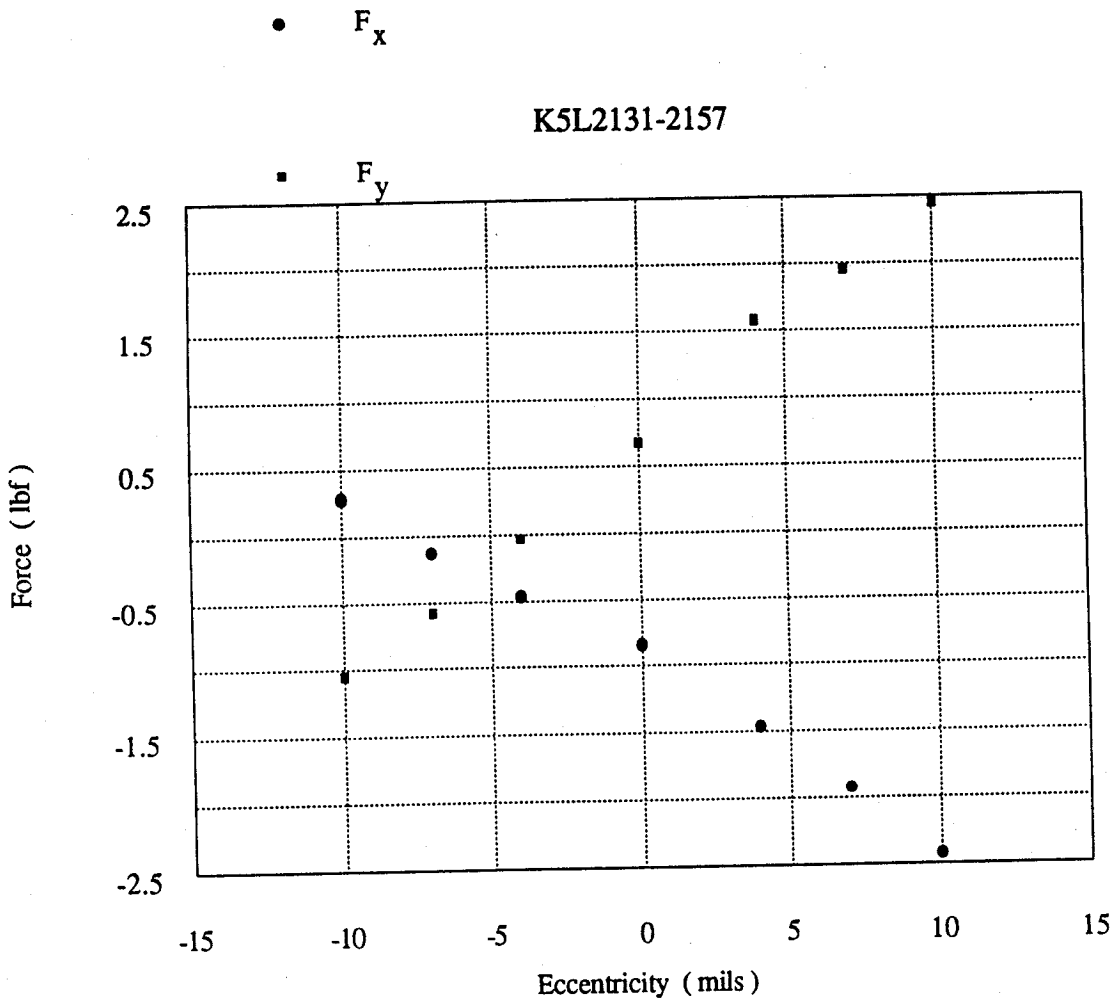

Fig. 5.12: Dynamometer-measured forces. Conf. 5, $\omega/\omega_D = 1.1$

setting, and all three points are shown in the graphs. For each of the geometrical configurations, data are shown for the design speed, $\omega = \omega_D = 3440$ rpm, as well as for a low speed case (L), with $\omega = 0.7\ \omega_D$ and a high speed case (H), with $\omega = 1.1\ \omega_D$ (all at the nominal mass flow rate).

The very small data scatter is apparent from the graphs. In terms of determining the curve slopes (i.e. the direct stiffness K_{xx} and the cross-stiffness K_{xy}) the scatter effect can be estimated to be under 1% for K_{xy} and ±5% for K_{xx}, which does show some consistent non-linearity. The origin is seen to be due shifted to some uncertainty on the location of the centered position and to some lack of roundedness of the casing. The latter effect is probably responsible for the fact that, at the eccentricity at which the best fit line to the cross-forces crosses through zero, the best-fit line to the direct forces is consistently between -0.3 and -0.5 lbf. As noted before, the linearity is better for the cross-forces. This may be related to the fact that the direct forces are mainly due to the pressure nonuniformity around the turbine periphery, while the cross-forces are mainly due to uneven work extraction by the blading.

The best fit lines were used to calculate the direct and cross-force Alford force coefficients

$$\alpha_{x,y} = \frac{2F_{x,y}R}{Q(e_x/H)} \tag{5.1}$$

where R = 0.129 m = 5.08 in. is the mean turbine radius, Q is the torque, measured by the torque gauge in the intermediate shaft (see Table 5.1), and H = 22.8 mm = 0.897 in. is the nominal blade height. The results are shown in Table 5.2, where the corresponding values for Configuration 1 (from Sec. 4) are also included.

Several trends are noticeable from these data. The first is a general increase of both $|\alpha_x|$ and α_y with turbine speed or, equivalently, a decrease as the flow coefficient $\phi = c_x/(\omega R)$ increases. In ratio form, this is shown in Fig. 5.13. For reference, the theoretical curve obtained from the 2-D theory explained in Sec. 9.2 is also shown. The theory exhibits the same trend, including the acceleration of the dependence towards the lower ϕ values.

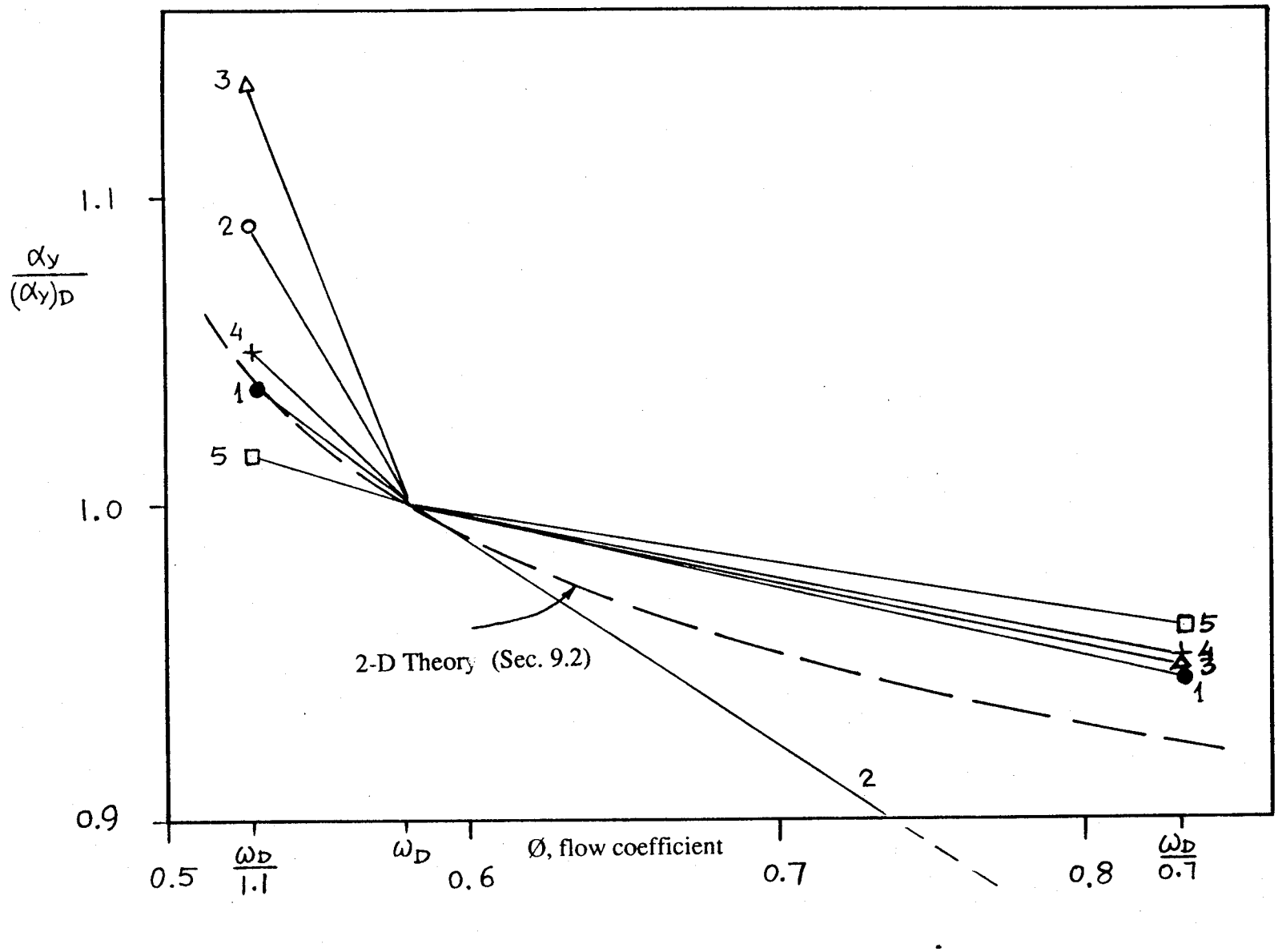

Fig. 5.13 Effect of flow coefficient on cross force coefficient

TABLE 5.1
TORQUE MEASURED AT THE VARIOUS CONDITIONS
ω_D = 3440 RPM

Configuration	Speed (ω)	Torque Q (Nm)
1	0.7 ω_D	47.3
	1.0 ω_D	39.9
	1.1 ω_D	37.3
2	0.7 ω_D	50.2
	1.0 ω_D	42.2
	1.1 ω_D	39.2
3	0.7 ω_D	49.2
	1.0 ω_D	41.1
	1.1 ω_D	38.4
4	0.7 ω_D	48.6
	1.0 ω_D	39.1
	1.1 ω_D	35.3
5	0.7 ω_D	48.5
	1.0 ω_D	40.0
	1.1 ω_D	37.0

TABLE 5.2
ALFORD COEFFICIENTS FROM DYNAMOMETER DATA

Configuration #	α_x	α_y
1L	-2.12	2.43
1	-2.81	2.57
1H	-3.42	3.66
2L	-1.54	2.49
2	-2.14	2.96
2H	-2.46	3.23
3L	-1.47	2.87
3	-1.87	3.02
3H	-2.04	3.43
4L	-2.93	3.38
4	-3.42	3.55
4H	-3.65	3.72
5L	-2.82	3.83
5	-3.47	3.98
5H	-3.50	4.04

A second trend, apparent from comparison of Configurations 2 and 4 and Configurations 3 and 5, is an increase of both $|\alpha_x|$ and α_y when the blade tip gap is reduced. With only two values of $\bar{\delta}/H$ tested, it is not possible to ascertain whether the trend is linear or it accelerates at small $\bar{\delta}/H$. The indications from the theory of Sec. 9, which also shows this trend, is that it should be a fairly linear effect, although the theory underestimates its magnitude substantially. Table 5 3 shows the differences between α_y with the narrower gap (1.87% of height) and with the wider gap (3% of height), both for the wide axial hub gap (Configurations 2 and 4) and with the narrow axial hub gap (Configurations 3 and 5). Assuming linearity, we obtain the approximate result

$$\frac{\partial \alpha_y}{\partial(\delta/H)} \cong \begin{cases} -\ 0.57\%\ \text{per}\ 1\%\ \dfrac{\bar{\delta}}{H} & \text{(wide axial gap)} \\ -\ 0.74\ \text{per}1\%\ \dfrac{\bar{\delta}}{H} & \text{(narrow axial gap)} \end{cases} \tag{5.2}$$

The effect on $-\alpha_x$ is of similar magnitude. Some of the difference between sensitivities for narrow and wide axial gaps can be distributed to the fact that the mean coefficients are themselves larger in configurations with the narrower axial gap (see below).

TABLE 5.3
EFFECT OF VARYING BLADE TIP GAP ON CROSS-FORCE COEFFICIENT, FOR TWO DIFFERENT AXIAL HUB GAPS

	Low ω	ω_D	High ω	Avg.
$(\alpha_y)_4 - (\alpha_y)_2$	0.88	0.59	0.49	0.65
$(\alpha_y)_5 - (\alpha_y)_3$	0.96	0.96	0.61	0.84

The third effect that can be extracted from the results in Table 5.2 is an increase of both $|\alpha_x|$ and α_y, when the axial hub gap d′ is decreased. This is visible both by comparing Configurations 2 and 3, and by comparing Configurations 4 and 5. Once again, the issue of linearity of these effects cannot be resolved with the available data. It is interesting, however, to make the assumption of linearity in order to separate the effects of varying d and d′ (Fig. 3.1). This is, in principle, possible because, as noted, Configurations 2 and 3 differ only in d′, while Configuration 1 differs from 2 and 3 in both d and d′. If we postulate a linear variation of α_y, of the form

$$\alpha_y = A + B\left(\frac{d}{c}\right) + C\left(\frac{d'}{c}\right) \tag{5.3}$$

and use the data for configurations 1,2 and 3 in Table 5.2, the following results are obtained (all for $\left(\frac{\overline{\delta}}{H} = 0.03\right)$:

At $\omega = \omega_{DES}$: $\alpha_y = 3.343 - 1.209\frac{d}{c} - 0.438\frac{d'}{c}$ (5.4a)

At $\omega = 0.7\ \omega_{DES}$: $\alpha_y = 2.280 + 2.423\frac{d}{c} - 2.781\frac{d'}{c}$ (5.4b)

At $\omega = 1.1\ \omega_{DES}$: $\alpha_y = 3.707 - 1.001\frac{d}{c} - 1.438\frac{d'}{c}$ (5.4c)

The sensitivity to inter-blade (stator-rotor) spacing is uncertain in sign, although if the α_y for Configuration 2 at 0.7 ω_{DES} were raised to be the same fraction of α_y (ω_D) as for the other configurations (see Fig. 5.13), the sign of this sensitivity (the coefficient of $\frac{d}{c}$ in Eqs. (5.4) would then be negative throughout. On the other hand, the coefficient of $\frac{d'}{c}$, i.e. the sensitivity to axial hub gap is negative in all cases, averaging approximately - 1.55 over the speeds tested.

For the cases with the smaller radial clearance (configurations 4 and 5) only the coefficient of ($\frac{d'}{c}$) can be extracted, since d/c was not varied in these cases. From the values in Table 5.2 we obtain for this coefficient -3.32, -3.13 and - 2.32 at 0.7 ω_D, ω_D and 1.1 ω_D, respectively. These values are larger than those for the larger radial clearance, but they are roughly comparable, and of the same sign.

We have not so far been able to identify positively the origin of these trends. Earlier experiements by K. Urlicks [5] indicated an <u>opposite</u> effect, namely, an increase of α_y with axial clearance. This is illustrated in Fig. 5.14. The effect of radial clearance (s" in the figure) is also illustrated in Fig. 5.14, and this does agree with our own findings (increased α_y at narrower radial clearances).

The theoretical indications regarding the effect of axial clearance are ambiguous, and no complete theory exists of this effect. On the one hand, it is shown in Sec. 9.3.8 that the work defect, or classical Alford mechanism for cross-force production, is weakened by the tangential flow redistribution induced by the upstream effects of the rotor eccentricity, and that opening up the axial gap which connects the stator-rotor space to the hub volume should, in turn, reduce this redistribution, and therefore should <u>increase</u> the Alford forces. This would agree with Urlicks' data, but conflicts with ours. On the other hand, as Sec. 9.3.8 also implies, the reduction of the upstream redistribution when the axial gap increases is itself due to a corresponding reduction of the pressure non-uniformity just ahead of the rotor. Since this pressure nonuniformity does contribute a net forward-whirling force component, opening up the

axial clearance can be expected to reduce the pressure contribution to α_y (a similar effect is documented in Secs. 6 and 7 in connection with labyrinth seals). Thus , the net effect must depend on which of the α_y components (blade work nonuniformity or pressure nonuniformity) is more sensitive to axial clearance. Additional analysis of our flow data and further theoretical work (as part of the doctoral dissertations of Seung Jin and Soomyung Yoo) is expected to clarify the situation.

5.2 Flow Data in Configurations 2-5

No flow survey was obtained in Configuration 3. For the others (Confs. 2, 4, and 5), only the nominal speed was surveyed. In Configuration 2, with the wide tip gap ($\overline{\delta}$ = 27 mil = 0.68 mm), the surveys were done at the centered turbine position and at an eccentricity e =18 mil = 0.45 mm (e/H = 0.019). After the tip gap was reduced to 17 mil (0.43 mm), namely, for Configurations 4 and 5, the surveys were done at the centered position and at e = 10 mil = 0.25 mm (e/H = 0.011).

5.2.1 Forces From Flow Data

The most important results were the final, integrated direct and cross-forces obtained according to the procedures explained in Sec. 4.3.5. They are here reported in coefficient form in Table 5.4.

TABLE 5.4
DIRECT AND CROSS-FORCE COEFFICIENTS FROM WORK DEFECT NONUNIFORMITY, $(\ )_{WD}$, AND PRESSURE NONUNIFORMITY $(\ )_P$

Configuration	$(\alpha_x)_{WD}$	$(\alpha_x)_P$	$\alpha_{xWD} + \alpha_{xP}$	$(\alpha_y)_{WD}$	$(\alpha_y)_P$	$\alpha_{yWD} + \alpha_{yP}$
2	-0.46	-2.28	-2.74	1.68	0.98	2.66
4	-0.88	-5.00	-5.88	3.16	1.56	4.72
5	-0.50	-4.20	-4.70	2.46	2.08	4.54

The table separates the contribution from nonuniform work extraction and from nonuniform rotor area pressures. The overall α_x and α_y so calculated are compared to those measured by the dynamometer (from Table 5.2) in Table 5.5.

TABLE 5.5
COMPARISON OF FLOW-DERIVED AND DYNAMOMETER-DERIVED FORCE COEFFICIENTS

Configuration	$(\alpha_x)_{FLOW}$	$(\alpha_x)_{DYN.}$	$(\alpha_y)_{FLOW}$	$(\alpha_y)_{DYN.}$
2	-2.74	-2.61	2.66	2.96
4	-5.88	-3.36	4.72	3.55
5	-4.70	-3.47	4.54	3.98

The overall coefficients from flow data compare reasonalby well with those measured directly, although the flow-derived coefficients for Configurations 4 and 5 are too high by about 30%. This very large value of α_x and α_y in Confs. 4 and 5 is seen in Table 5.4 to arise both from high work defect forces and high pressure forces. The reasons for this are not understood. From the dynamometer data, these configurations (which have the smaller tip gap), do show higher force levels than those in the larger gap cases (Confs. 1, 2, and 3), but the difference from fluid forces appears exaggerated.

This substantial effect of the smaller tip gap is, in any case, not understood at present. It appears to suggest a stronger sensitivity of blade work loss to tip gap when the gap is very small. This would seem to imply some new effect, quite possibly a strong role of viscous forces in the gap flow dynamics. We are currently working on a theoretical model of such effects. One hint that viscous effects, which have to date been generally ignored based on cascade scaling laws, such as that given by Rains [11], may be prominent in turbines is the data of Graham [12] in a moving wall

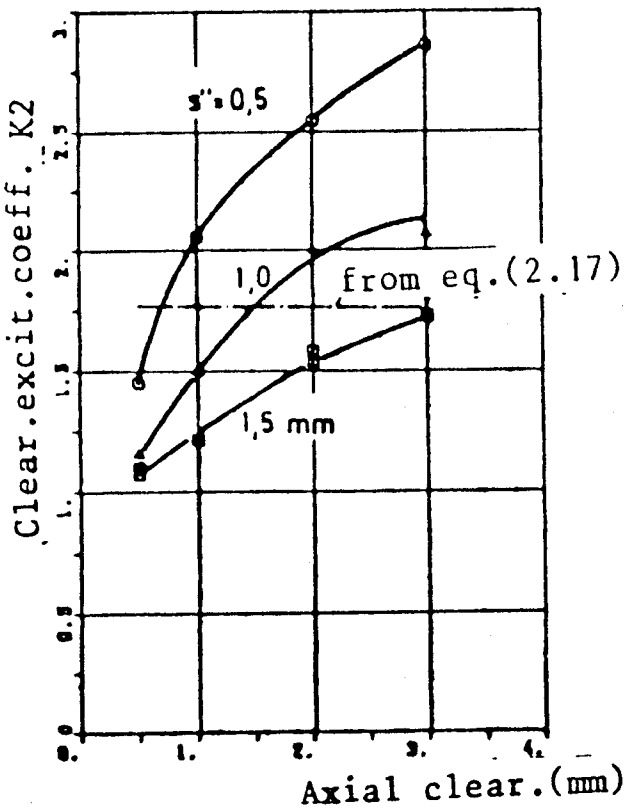

Rotor without shroud-band

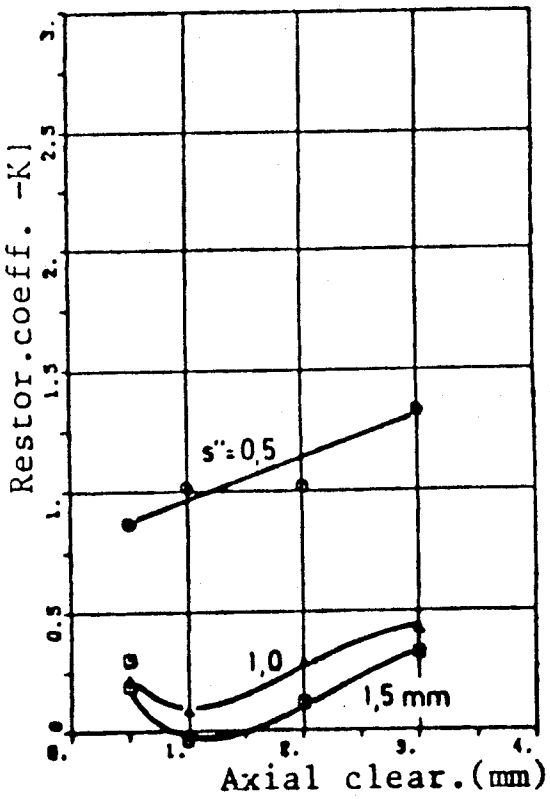

Rotor without shroud-band

Fig. 5.14: "Excitation coefficient", $K_2 = \alpha_y/2$, and "Restoring coefficient", $K_1 = \alpha_x/2$, from K. Urlichs [5], showing effects of tip gap (s″) and axial hub clearance

cascade. These experiments showed that the viscous drag of the moving endwall, which in a turbine opposes the pressure-driven gap flow, can easily modify or suppress the leakage jet and its roll-up into a vortex.

Incidentally, this effect was also noticed by K. Urlichs [5], as shown in Fig. 5.14, reproduced from his work. Note also the increase in α_y (= 2 K_2) with axial clearance, in disagreement with our results of Sec. 5.1.

5.2.2 Selected Flow Survey Results

Rather than including all of the large data base collected in these surveys, we will select for presentation a few items that illustrate specific effects.

By and large, the trends are as discussed in more detail in Sec. 4.3.

Figures 5.15 and 5.16 illustrate clearly the nature of the mean flow behind the turbine in the near-tip region. Here the raw tangential velocities are shown (centered and eccentric cases, not subtracted). In the centered position (Fig. 5.15), we can see at all azimuths the substantial flow underturning that occurs in the outer 10-20% of the blade. At the r/H = 0.76 depth, the flow has returned more or less to axial, as corresponds to the design condition for our turbine. In the eccentric case (Fig. 5.16), the underturning is actually very slight in the side of the turbine with the small gap (about 27 - 18 = 9 mil = 0.23 mm), while it is even greater than before near the wider gap (about 27 + 18 = 45 mil = 1.12 mm). It is this asymmetry that produces the work-defect forces F_y.

The origin of the large pressure forces in the configurations with small tip is illustrated in Fig. 5.17 (from Conf. 4). This shows even higher pressure fluctuation amplitude than Fig. 4.21, for Conf. 1, even though the relative eccentricity here is only 0.011, vs. 0.019 in Conf. 1. Similarly, the fluctuation of force per unit length shown for Conf. 4 in Fig. 5.18 is comparable to that shown in Fig. 4.36 for Conf. 1, with the higher eccentricity.

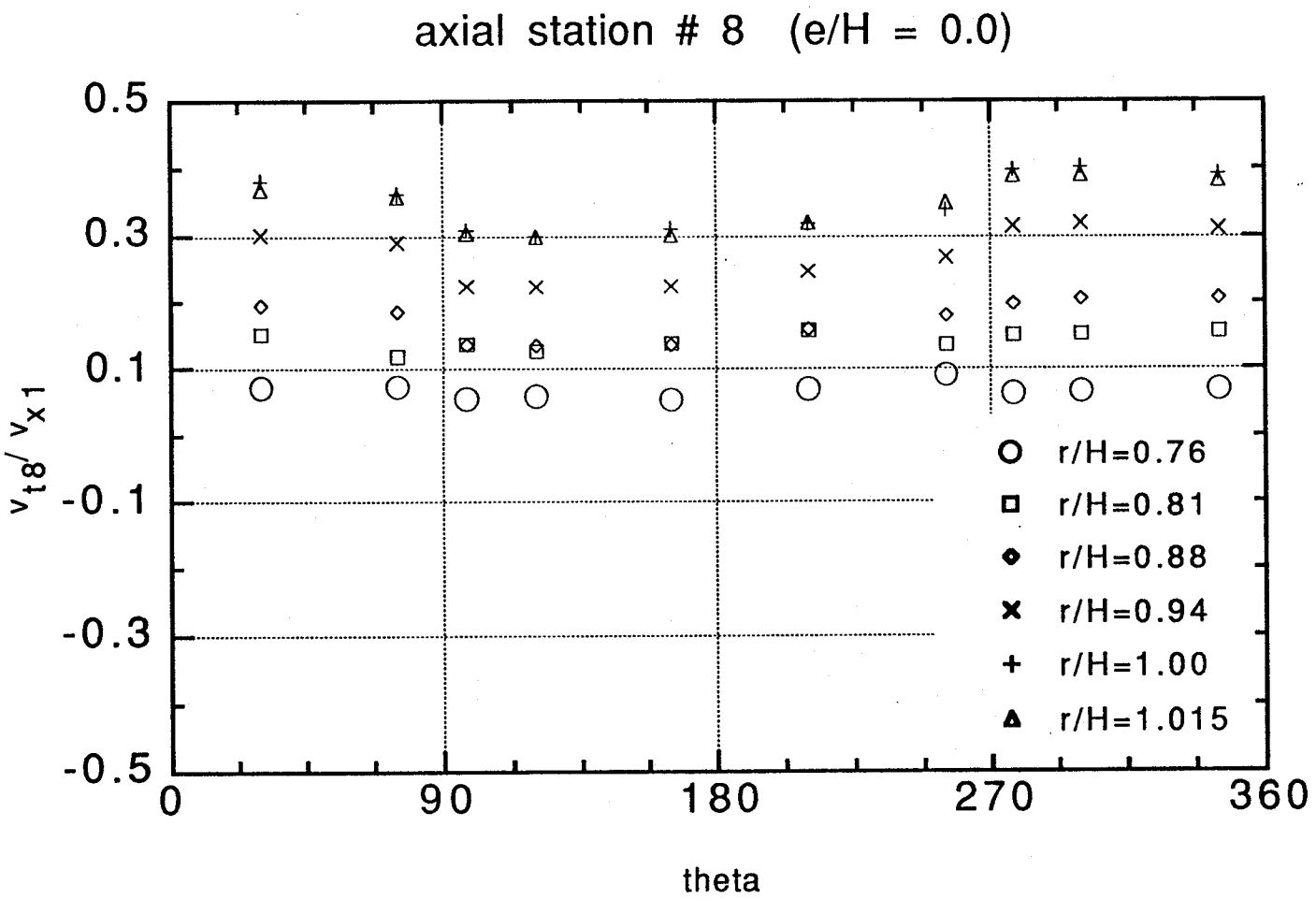

Fig. 5.15: Tangential velocities downstream of centered rotor (Conf. 2)

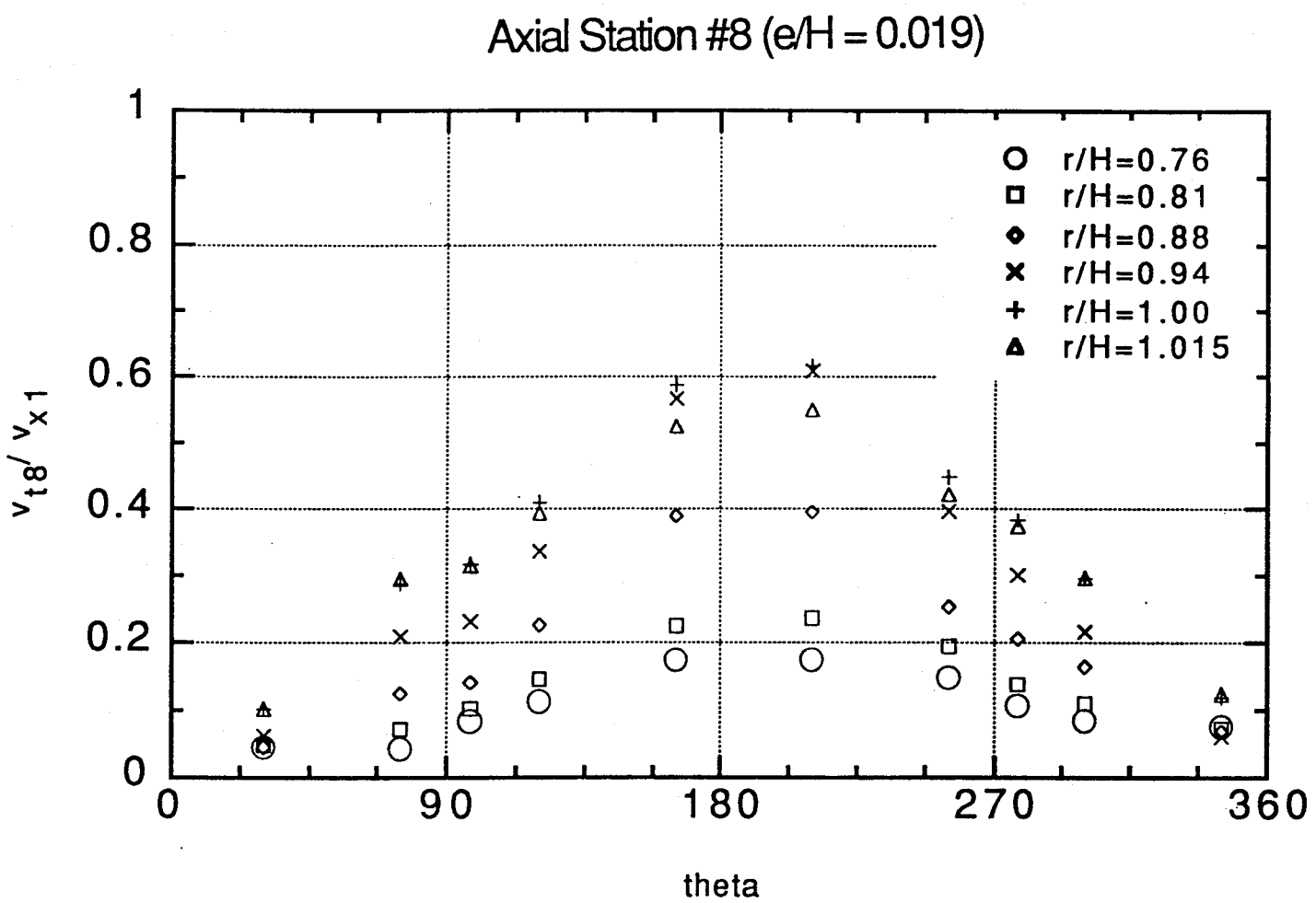

Fig. 5.16: Tangential velocities (centered values not subtracted) behind eccentric rotor, e/H = 0.011 (Conf. 2)

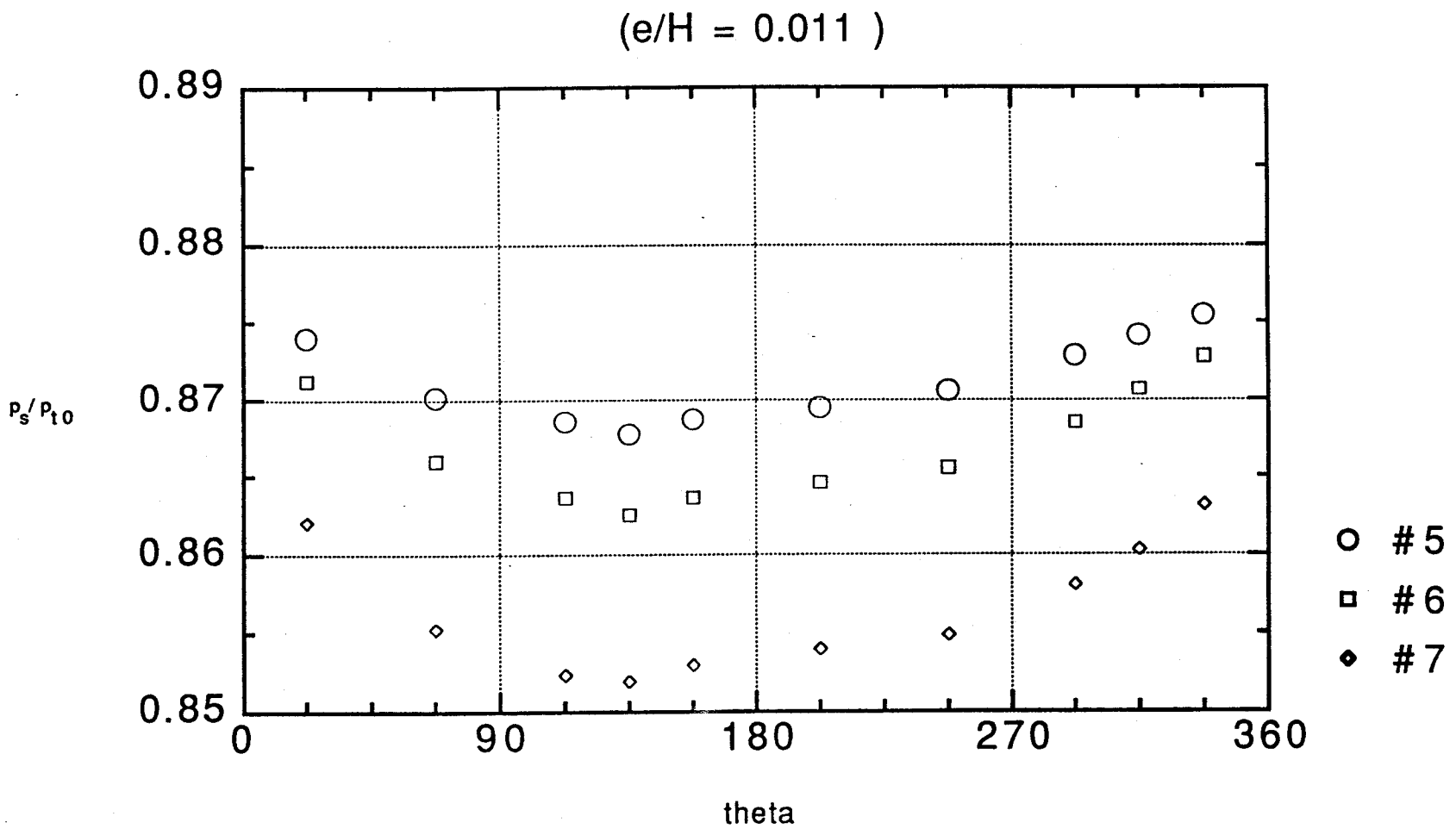

Fig. 5.17: Wall tap pressures over the rotor (Conf. 4)

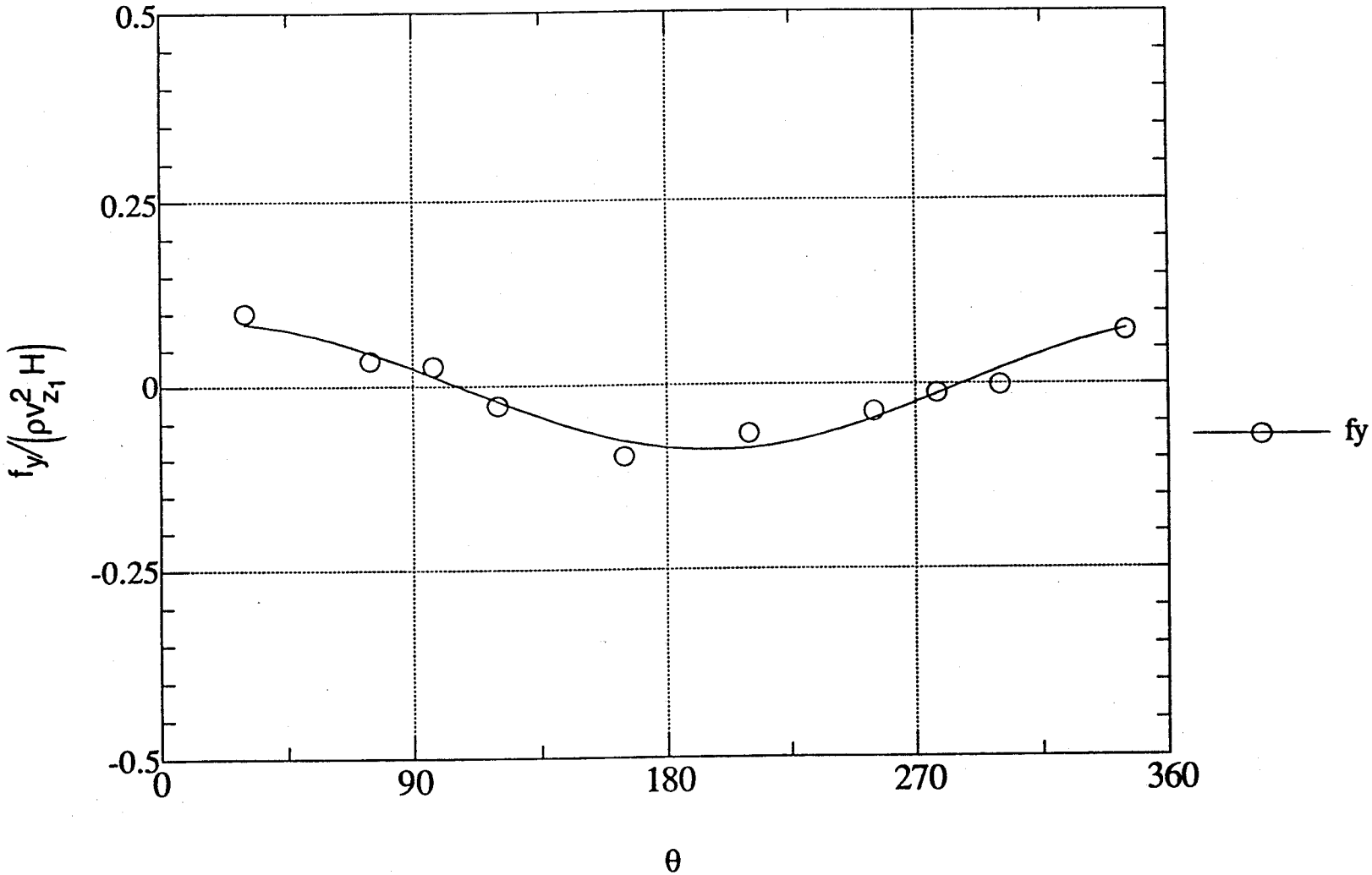

Fig. 5.18: Tangential force per unit length, e/H = 0.011 (Conf. 4)

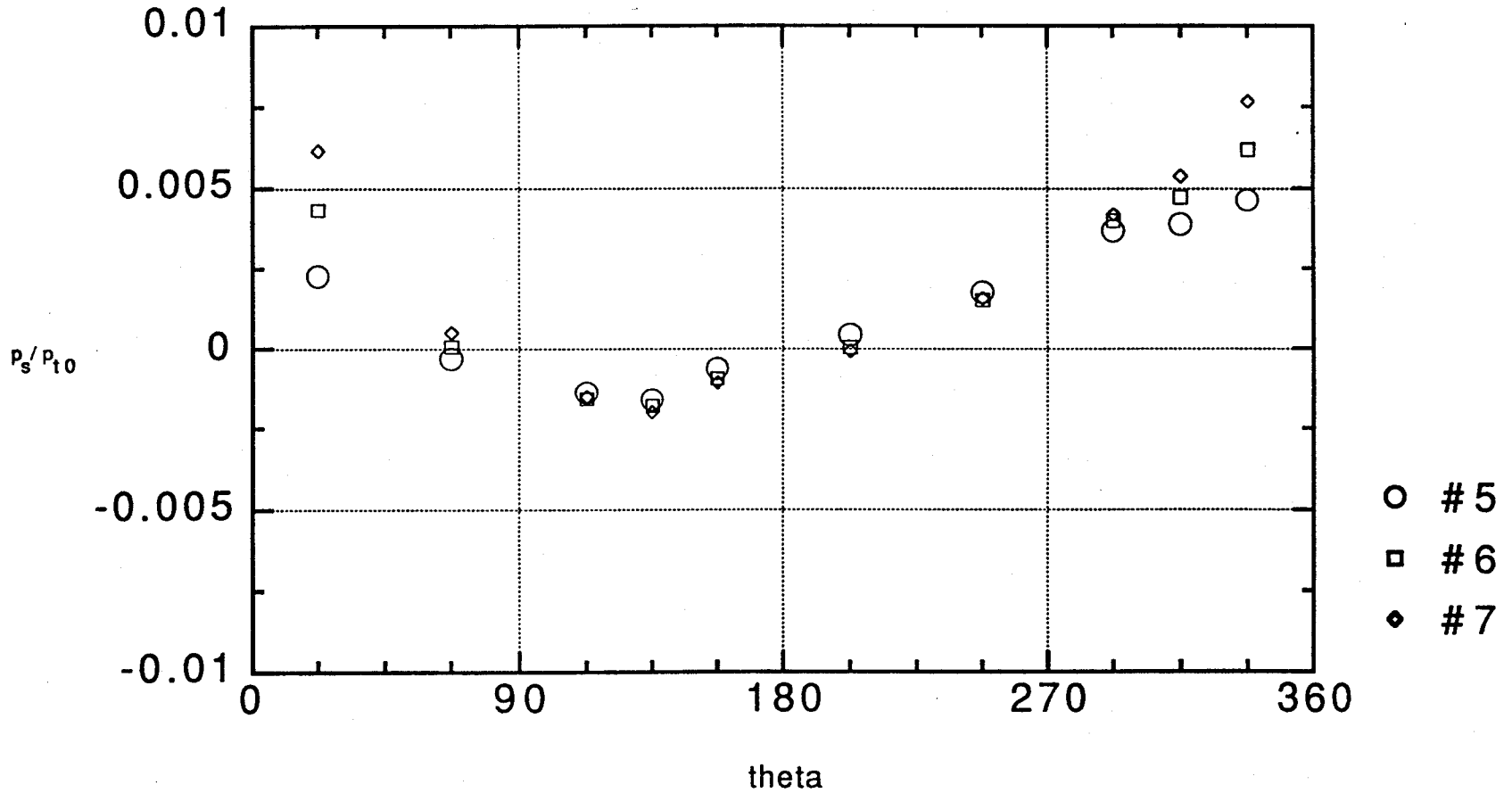

Fig. 5.19: Wall tap pressure (minus average value) for stations over rotor (Conf. 5)

By suppressing the concentric contribution to the wall pressure distributions at stations 5, 6, and 7, over the rotor, Fig. 5.19 (Conf. 5) brings out an interesting observation. We noted in Sec. 4.3.3 that the amplitude of the wall pressure nonuniformity increased steadily between stations 5 and 7, i.e. from leading to trailing edge. Figure 5.19 shows that the increase is entirely concentrated in the narrow tip gap region, where the wall pressure shows a strong peak. There is no corresponding minimum in the wide gap region and, in fact, the nonuniformity pattern outside the 60-90° nearest the narrow gap is exactly repeated in the three axial stations. This again highlights a qualitatively different behavior when the tip gap is narrow. According to Fig. 5.19, the difference appears fairly suddenly some 45° from the minimum gap. At this point, the local gap width is $17\text{-}10\cos\theta \cong 12$ mil. Perhaps this is the gap width where, for the present configuration and flow parameters, the viscous effects of the counter-moving casing become strong. This area needs to be researched much more carefully.

6. Forces in a Shrouded Turbine

6.1 Background

Many Turbine designs feature a tip shroud band with two or more labyrinth seal strips. There are two motivations for this design: (a) to reduce tip losses by cutting down on the leakage flow, and, (b) to add stiffness to the blading. From the point of view of the Alford force, one would expect the shroud and its seal to minimize or eliminate them altogether, precisely because of the tip loss reduction. It is known, however, that labyrinth seals with strong inlet swirl are themselves prone to developing cross-forces, because the swirling flow in the seal cavity tends to skew the cavity pressure pattern. Also, it was recently found (see Sec. 7.3) that the nonuniformity in pressure that exists upstream and downstream of the seal is responsible for increased levels of the cross force. Urlichs (Ref 5) actually found cross force coefficients 20 - 40% higher when he added a shroud with various types of seals to his turbine. He explained the increase on the basis of his measurements of the azimuthally nonuniform cavity pressure. Our Configuration 6 was developed to study these effects, taking advantage of the parallel work on labyrinth seals reported elsewhere in this document. (Sec. 7)

6.2 Implementation

After completing our tests on the five configurations using the unshrouded turbine (configurations 1 through 5), we modified it by removing the outer 30% of each blade and inserting a full shroud band fitted with two sealing bands. Since the casing was left smooth and hence the seal is not recessed, the turbine is not expected to be as efficient as before. On the other hand, this configuration is very similar to the configuration present in the labyrinth seal tests (Sec. 7 of this report), which allows for cross comparisons.

The entire shroud band is shown in Figure 6.1 and a cross section view is shown in figure 6.2. The sealing band angles and tip thicknesses are similar to those used in our seals rig. The ratio (l tan 6°)/δ is approximately 2.0, where l is the distance between knife edges and δ is the nominal gap. The value 2.0 is in the range of those used in the seals rig. The seal length is such as to cover exactly the blade tip axial chord.

The band was designed with a 2/1000 inch interference and was then shrunk-fit over the blades. The blades were previously cut and ground to the required height in order to accommodate the shroud. The tensile stress developed in the shroud due to the shrink-fit is 2×10^{11} N/m^2, well within the strength of stainless steel. It was also verified by calculation that the additional bending stress due to the slight straightening tendency of the band between blades is negligibly small. This is because of the large number of blades, which makes the bowing between blades very slight. Centrifugal effects can at most add the equivalent of 0.5/1000 inch to the band radius. Therefore, even if centrifugal growth of the rest of the disk is ignored, the fit should remain tight. No significant differential thermal effects are expected.

The configuration of the axial gaps is the same as for Configurations 3 and 5, namely, d'=1.3% and d=26%. The seal tip gap is also as in configuration 3, i.e., δ/H=0.03. The flow reaches the seal region directly from the stator exit, leaving the stator with an angle to the axial direction of $\alpha_2 = 70°$, and the tangential velocity at the seal inlet is $(c_x)_{rotor} \tan 70°$. Notice that, because of contraction, $(c_x)_{stator} < (c_x)_{rotor}$. In addition, the presence of the unrecessed seal acts as an obstacle to the flow and further reduces c_x near the outer casing. Thus, some care must be exercised in estimating the tangential velocity at the seal inlet (see sec. 6.5).

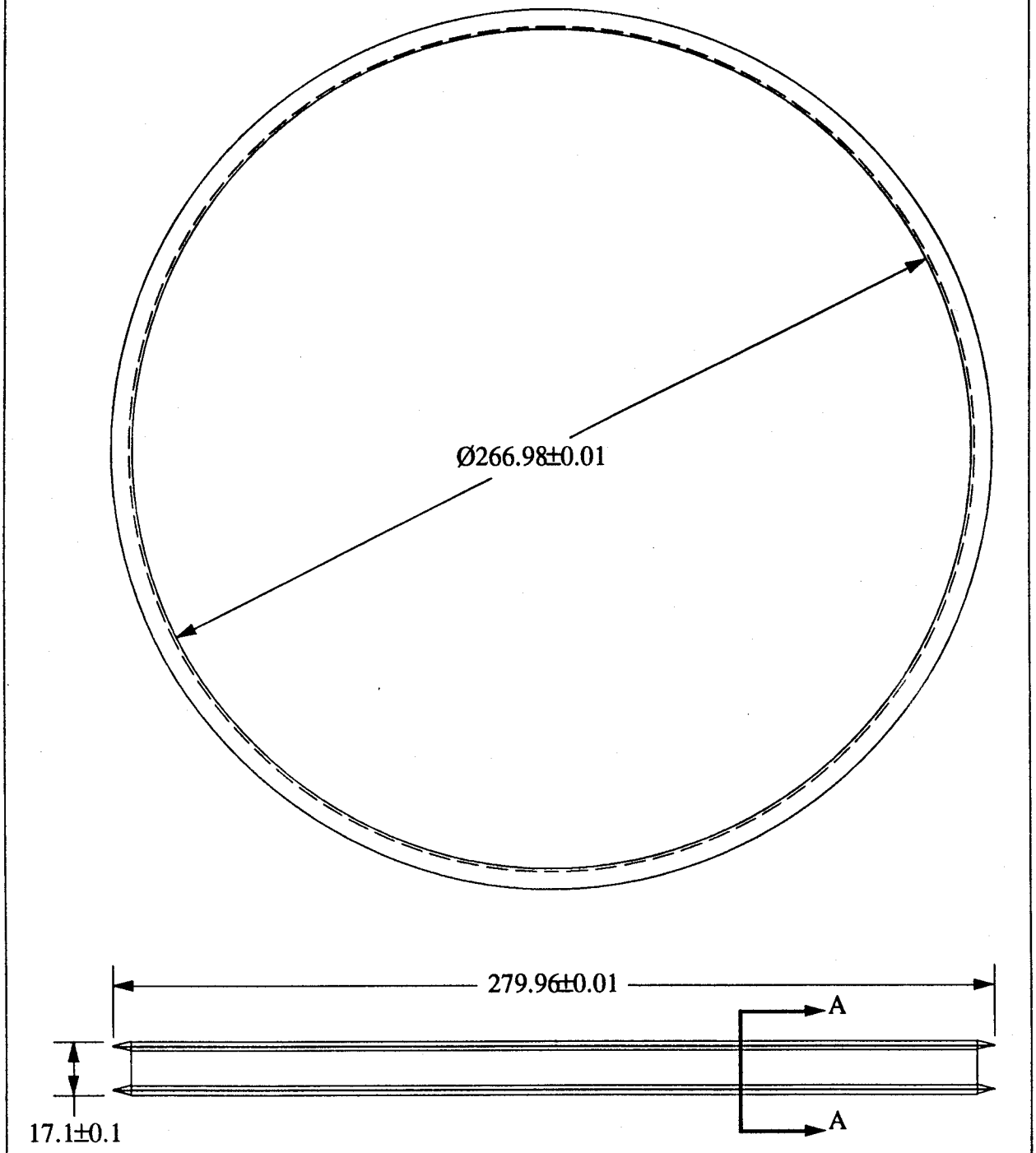

Figure 6.1: Machine drawing of shroud.

Figure 6.1: Shroud
Material: Stainless Steel
Scale: 1 to 4
Dimensions: millimeters

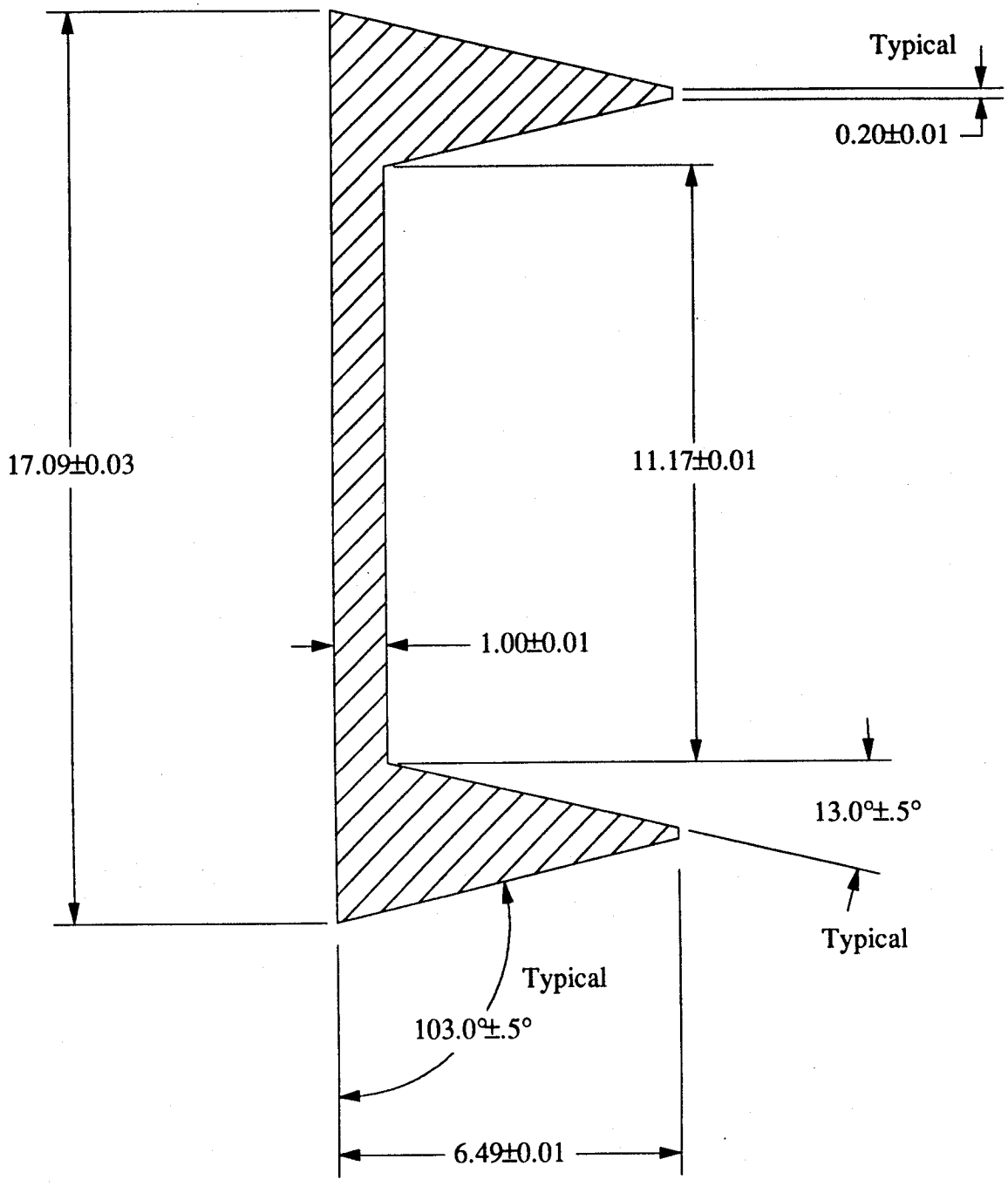

Figure 6.2 Section A-A of shroud.

Figure 6.2: Section A-A
Material: Stainless Steel
Scale: 1 to 8
Dimensions: millimeters

6.3 Turbine Performance, Operating Points

Because of the reduced blade height, down from 23.9mm to 16.3mm, if the wheel speed and the average pressure remain the same as in the unshrouded turbine we expect the flow rate for best efficiency to be reduced by approximately the same factor, to 4.48x(16.3/23.9) = 3.06 kg/s. A series of tests were conducted to verify this and to select the nominal conditions for the Alford force tests. The optimal result is shown in Figure 6.3. Figure 6.3 is a graph of efficiency vs. the mass flow rate for the speed of 3440 RPM, which was determined to be the speed where the optimal efficiency lies. The efficiency was determined from measurements of torque, pressure

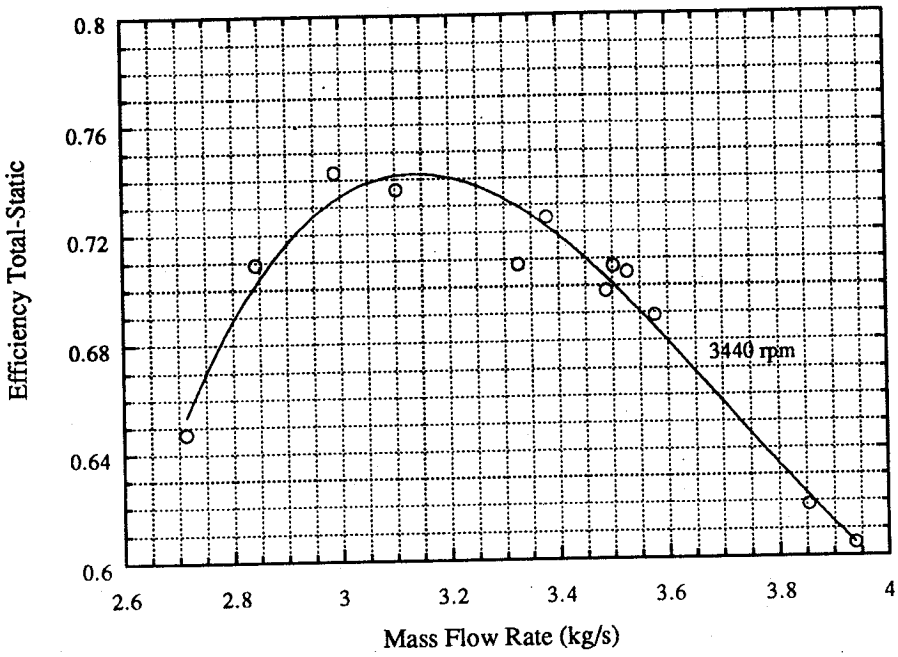

Figure 6.3: Total-to-Static efficiency vs. mass flow rate at optimal speed of 3440 rpm.

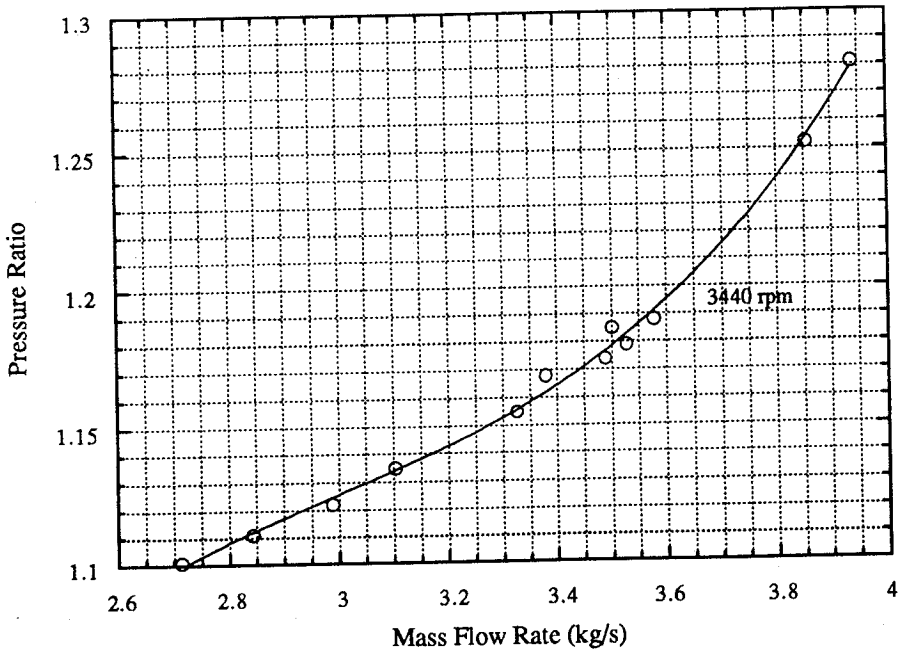

Figure 6.4: Pressure ratio vs. mass flow rate at Optimal speed of 3440 rpm.

drop and speed. It can be seen from Figure 6.3 that the flow rate which yields the highest efficiency is $\dot{m}$=3.15 kg/s. These tests were conducted at 2.2 atm mean pressure and they yielded results close to the simple estimate presented previously. It was decided, in analogy to the other configurations, to conduct static Alford force measurements at the pressure of 2.2 atm, at the flow rate of 3.15 kg/s and at $\omega=0.7\omega_D$, $\omega=1.0\omega_D$, and at $\omega=1.1\omega_D$. The efficiency levels are similar to those for the unshrouded turbine. The pressure ratios for 3440 RPM are shown in Figure 6.4 and are somewhat lower in this shrouded turbine, due to smaller flow acceleration in the stator.

6.4 Force Measurements

The first test series, conducted at 2.2 atm. pressure and 3.2 kg/s, gave (with our initial data reduction procedures) anomalous force results with a strong asymmetry in the force-aft direction. A new test series was then conducted at reduced pressure (p = 1.24 atm) and mass flow ($\dot{m}$ = 1.70 kg/s). Once again the forces obtained were not repeatable and had excessive scatter. Two addition test series were then undertaken. Therefore, at total of four test series, two taken at 2.2 atm and two taken at 1.24 atm were completed. Each test series was conducted such that three force readings were taken at each of the 6 eccentric locations (+15, +10, +4, -4, -10, -15 mils) and the concentric location and at each of the three speeds, $\omega=0.7\omega_D$, $\omega=1.0\omega_D$, and at $\omega=1.1\omega_D$. All the data that were taken had excessive scatter.

The source of this problem was recently found to lie in the triggering of the data acquisition system. Since the raw data were all available this problem was correctable through software and the four test series mentioned above were once again reduced to yield very repeatable results. These data are plotted in the following twelve figures each corresponding to a particular test at a particular speed. Each figure shows the direct and cross force (lbf) vs. the eccentricity (mils) and the corresponding least squares linear curve fits. The linear fits presented in Figures 6.5

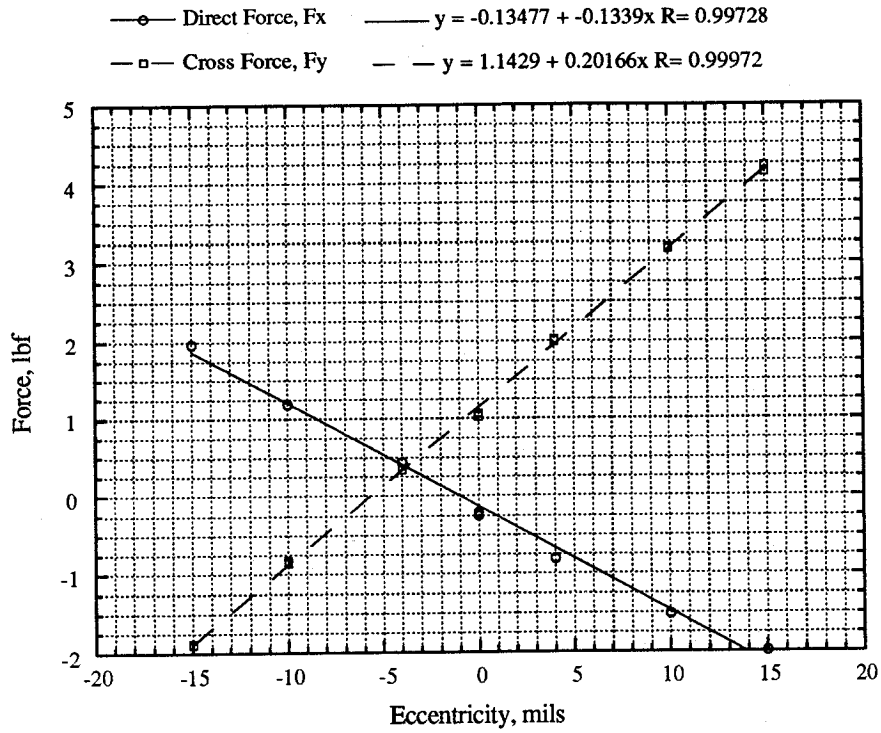

Figure 6.5: Test Series 1, P_0=2.21 atm. Off-design Speed of 2408 rpm (ω=0.7ω_D).

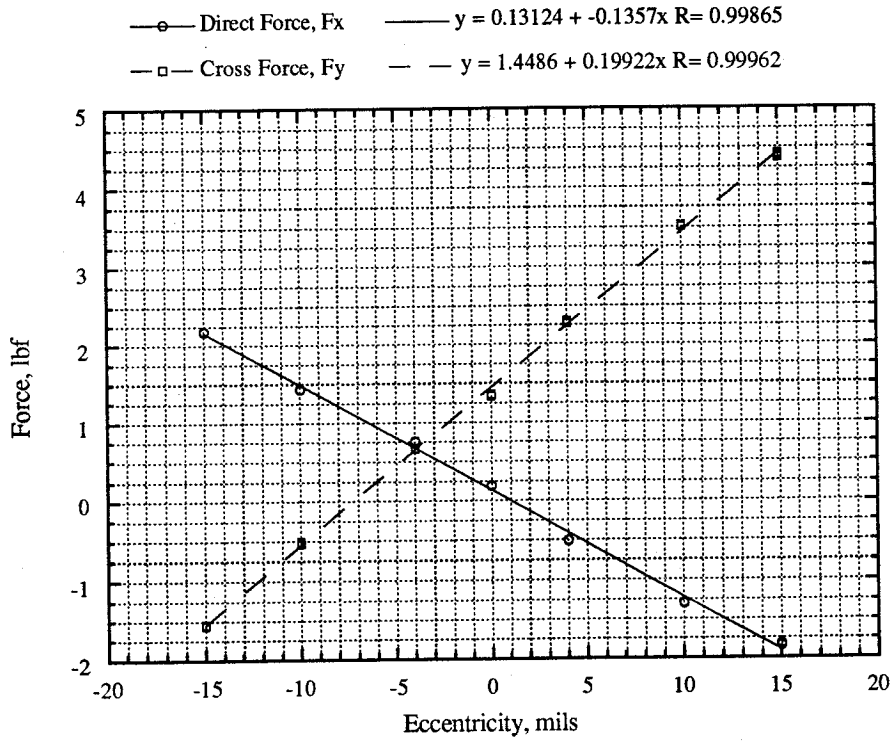

Figure 6.6: Test Series 3, P_0=2.21 atm. Off-design Speed of 2408 rpm (ω=0.7ω_D).

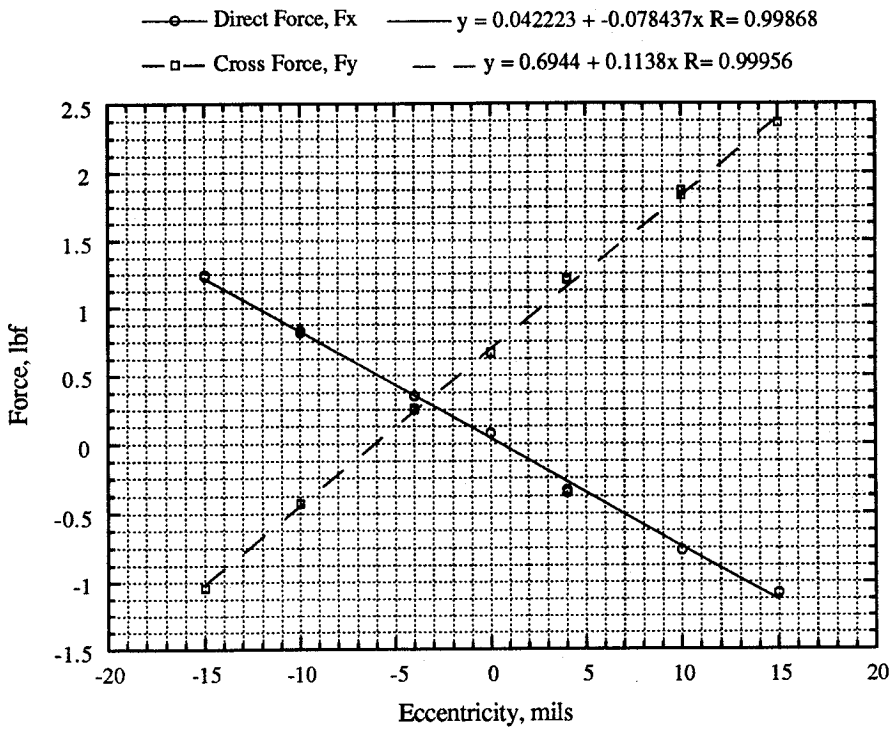

Figure 6.7: Test Series 2, P_0=1.25 atm. Off-design Speed of 2408 rpm (ω=0.7ω_D).

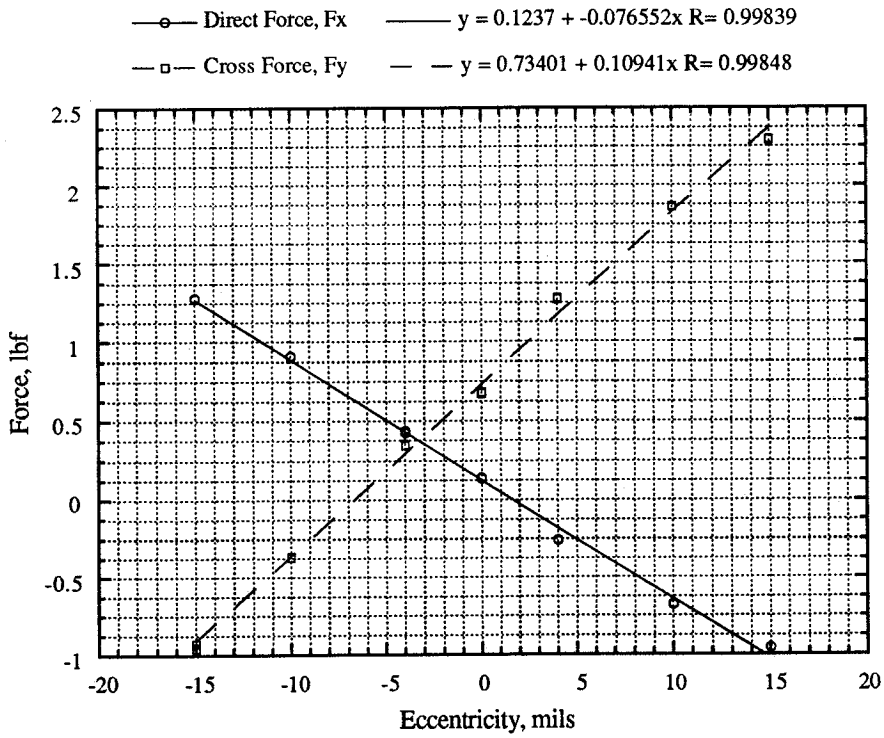

Figure 6.8: Test Series 4, P_0=1.24 atm. Off-design Speed of 2408 rpm (ω=0.7ω_D).

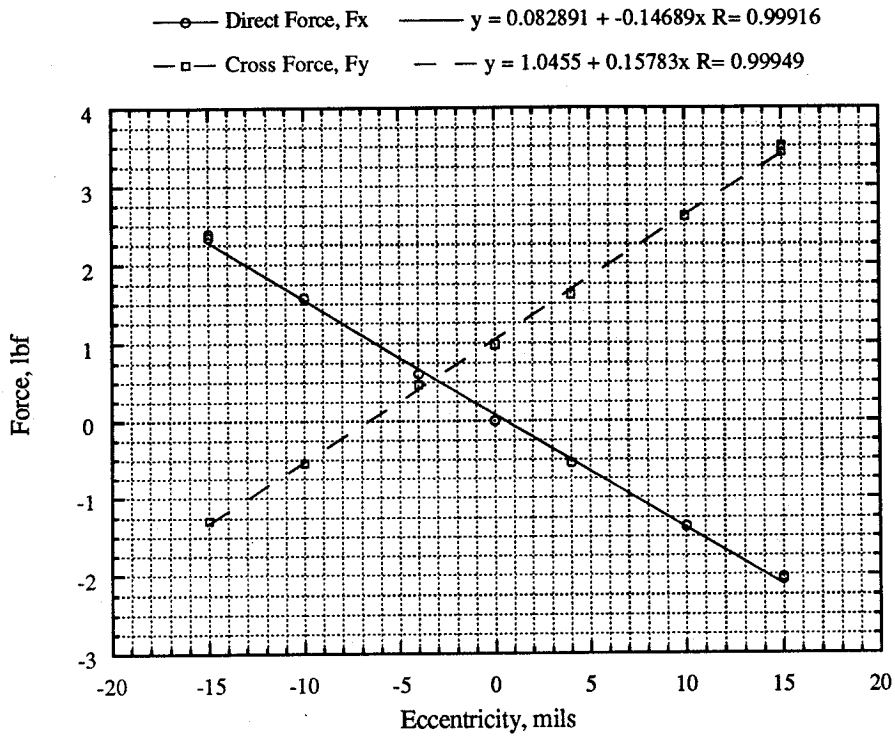

Figure 6.9: Test Series 1, P_0=2.21 atm. Design Speed of 3440 rpm ($\omega=\omega_D$).

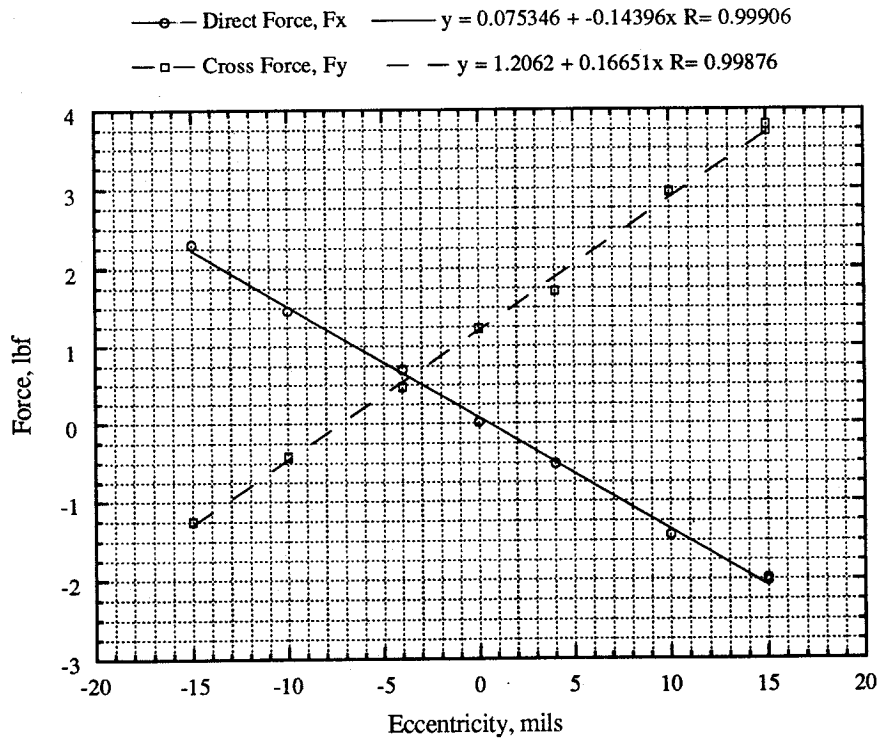

Figure 6.10: Test Series 3, P_0=2.21 atm. Design Speed of 3440 rpm ($\omega=\omega_D$).

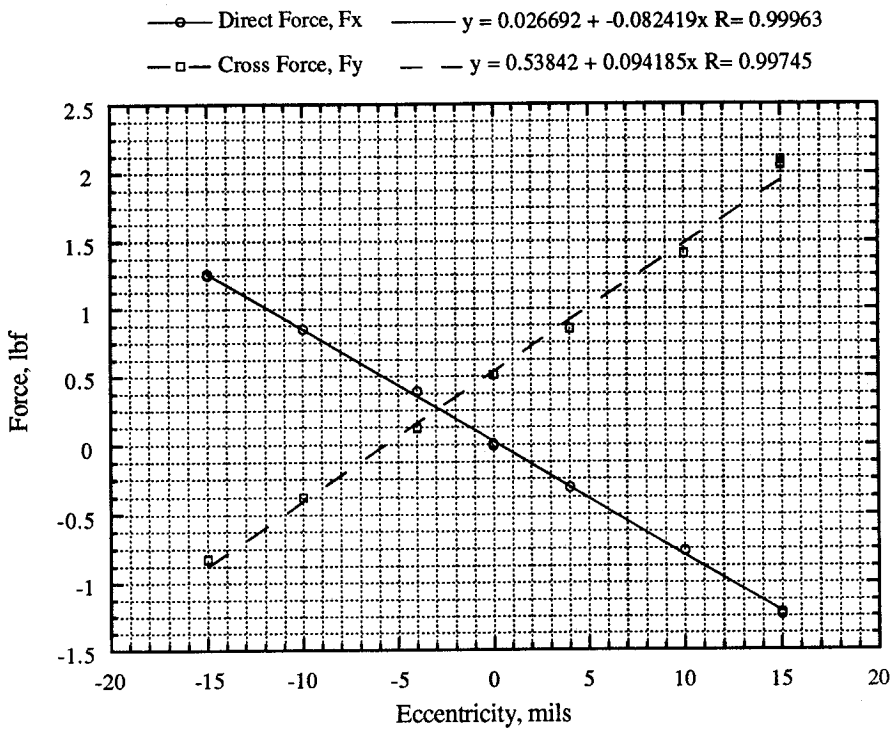

Figure 6.11: Test Series 2, P_0=1.24 atm. Design Speed of 3440 rpm ($\omega=\omega_D$).

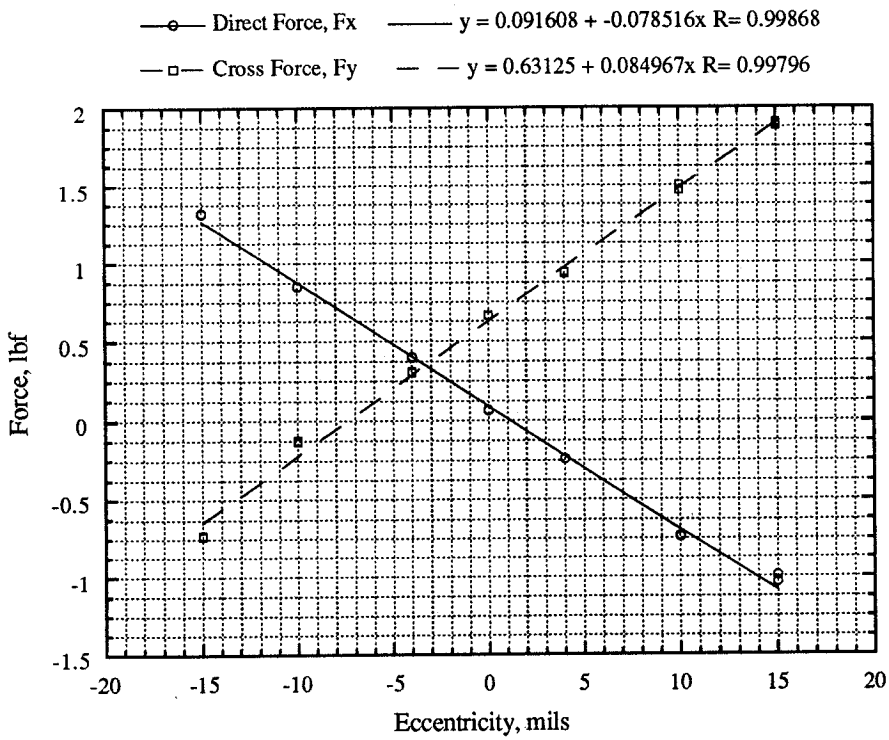

Figure 6.12: Test Series 4, P_0=1.24 atm. Design Speed of 3440 rpm ($\omega=\omega_D$).

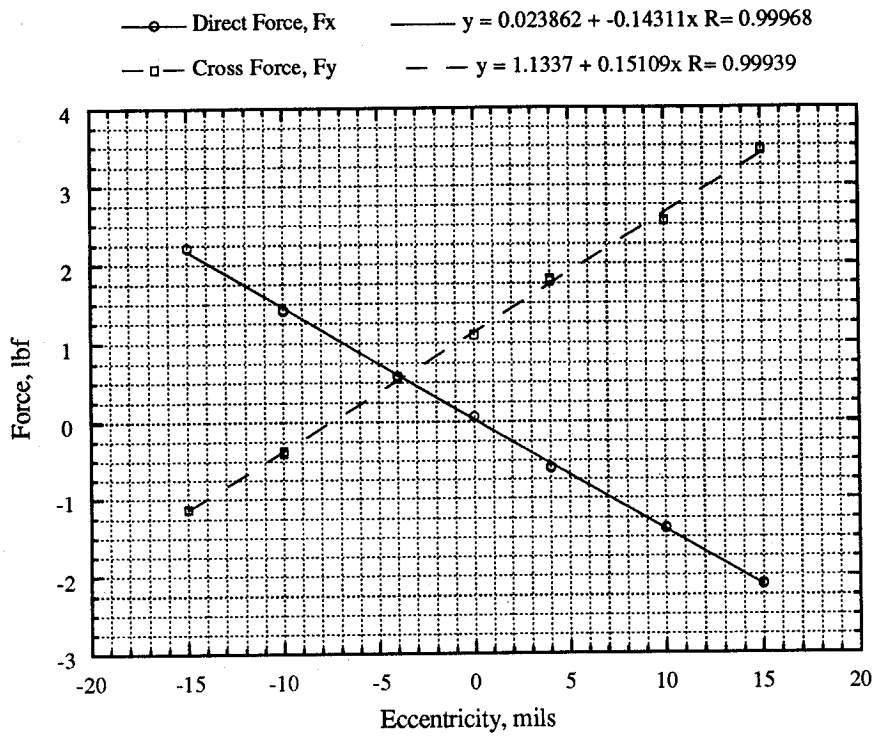

Figure 6.13: Test Series 1, P_0=2.21 atm. Off-Design Speed of 3784 rpm (ω=1.1ω_D).

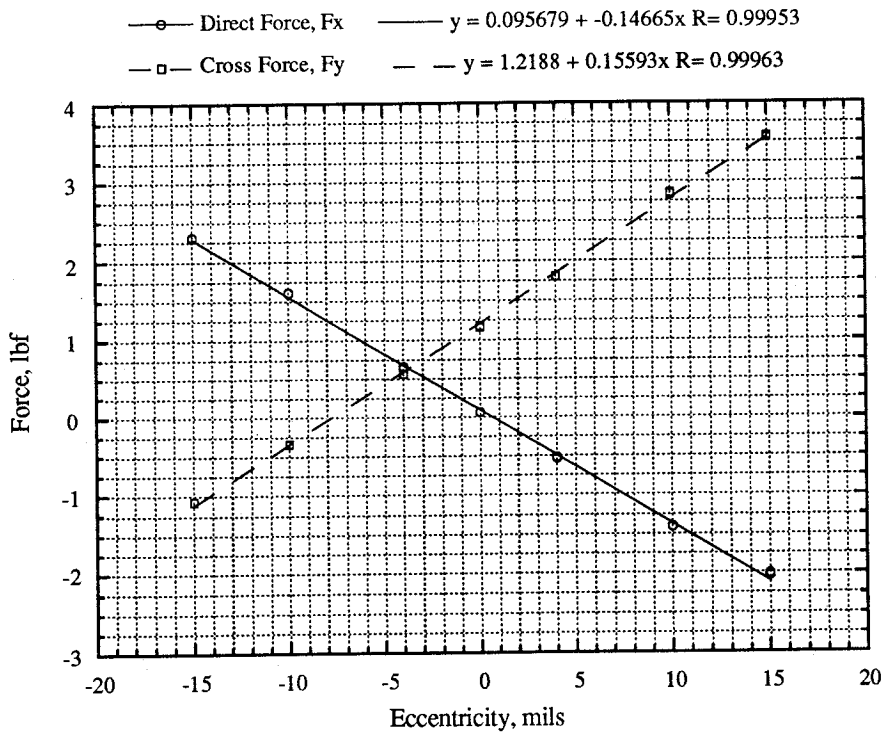

Figure 6.14: Test Series 3, P_0=2.21 atm. Off-Design Speed of 3784 rpm (ω=1.1ω_D).

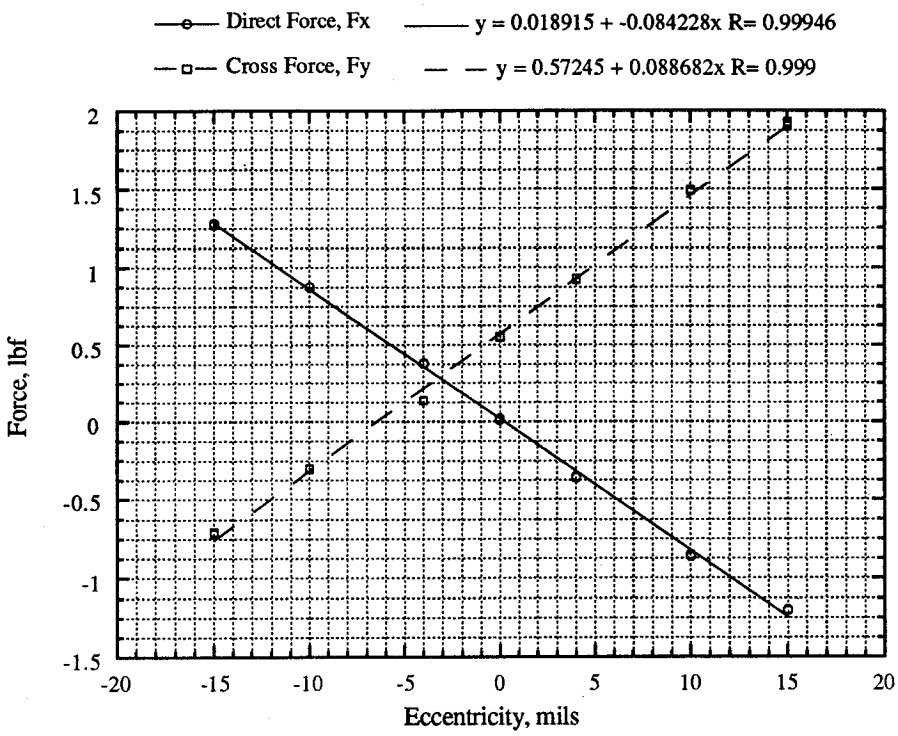

Figure 6.15: Test Series 2, P_0=1.24 atm. Off-Design Speed of 3784 rpm (ω=1.1ω_D).

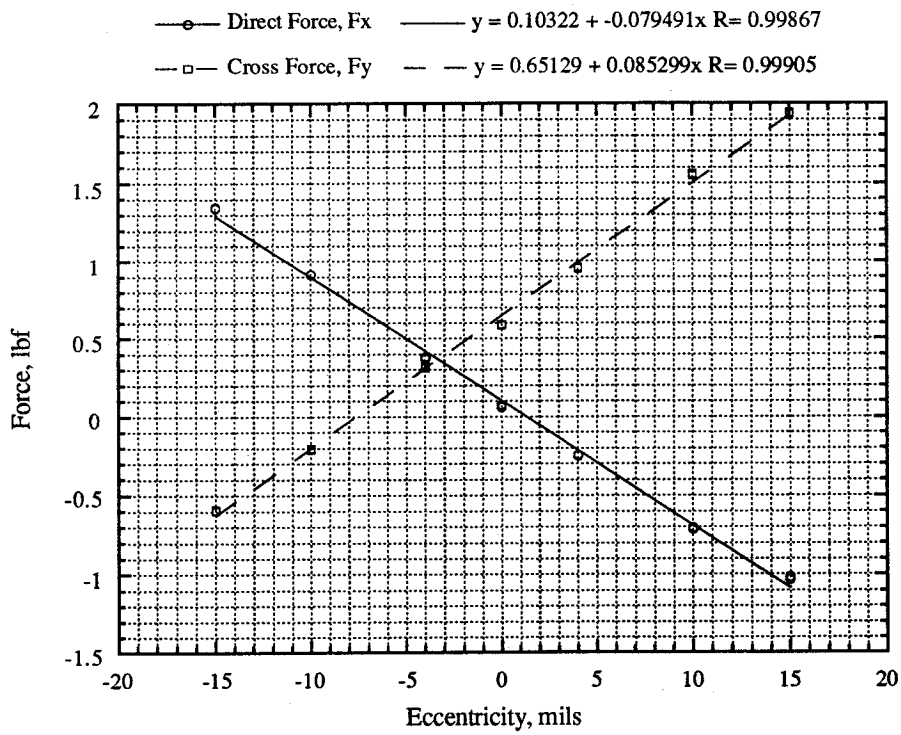

Figure 6.16: Test Series 4, P_0=1.24 atm. Off-Design Speed of 3784 rpm (ω=1.1ω_D).

through 6.16 were used together with the measured torque values shown in Table 6.1, the blade height of
H=16.3 mm and the mean radius of R_m=125mm to calculate the force coefficients α_x and α_y. Note, that in this case, with the shroud, the mean radius is taken from the hub to the tip of the
blade, not to the tip of the knife edge on the shroud. The Alford coefficients, α_x and α_y, for each test series and speed are listed in Table 6.2. An average of each row is given at the bottom of the table. These Alford coefficients are roughly 50% larger than those obtained in the unshrouded case (for comparison see Table 5.1). For convenience, Table 6.3 was created which lists all the least squares linear curve fits obtained from Figures 6.5 through 6.16, with each of them adjusted as if the measurements obtained were taken at 2.21 atm. For comparison with the results of Sec. 7, Table 6.4 takes the non-adjusted linear curve fits from Figures 6.5 through 6.16 and creates the stiffness coefficients. The stiffness coefficients are given by the following equation:

$$K_{xx,xy} = \frac{\left(\frac{F_{x,y}}{e}\right)\delta^*}{lR_m(p_i - p_o)}$$

Where $\frac{F_{x,y}}{e}$ is the slope of the line, δ^* is the nominal gap, l is the length of the land, R_m is the mean radius and $(p_i - p_o)$ is the pressure difference across the rotor. These values can be compared to those obtained from the seals rig, except that here $K_{xx} < 0$ is a restoring force, whereas in Sec. 7.5.2 the opposite convention was used. Note also, that these contain both, seal and blade (work loss) effects.

TABLE 6.1: Test Conditions and Measured Torque

Test Series	ω/ω_D	P_0(atm)	$\dot{m}$(kg/s)	Q(N m)
1	0.7	2.21	3.22	23.68
1	1.0	2.21	3.20	18.84
1	1.1	2.21	3.22	17.32
2	0.7	1.25	1.75	13.87
2	1.0	1.24	1.70	9.76
2	1.1	1.24	1.78	9.99
3	0.7	2.21	3.16	23.36
3	1.0	2.21	3.19	18.27
3	1.1	2.21	3.14	16.89
4	0.7	1.24	1.74	13.77
4	1.0	1.24	1.75	10.69
4	1.1	1.24	1.75	9.79

TABLE 6.2: Alford Coefficients for the Shrouded Turbine

Test Series	α_x ω/ω_D=0.7	α_y ω/ω_D=0.7	α_x ω/ω_D=1.0	α_y ω/ω_D=1.0	α_x ω/ω_D=1.1	α_y ω/ω_D=1.1
1	-4.05	6.10	-5.58	6.00	-5.92	6.25
2	-4.05	5.88	-6.05	6.91	-6.04	6.36
3	-4.16	6.11	-5.64	6.53	-6.22	6.61
4	-3.98	5.69	-5.26	5.69	-5.82	6.25
Average	-4.06	5.94	-5.63	6.28	-6.00	6.37

TABLE 6.3: Slopes of Linear Curve Fits for all Test Series in lbf/mil. Adjusted to 2.21 atm.

Test Series	$Slope_x$ ω/ω_D=0.7	$Slope_y$ ω/ω_D=0.7	$Slope_x$ ω/ω_D=1.0	$Slope_y$ ω/ω_D=1.0	$Slope_x$ ω/ω_D=1.1	$Slope_y$ ω/ω_D=1.1
1	-0.134	0.202	-0.147	0.158	-0.143	0.151
2	-0.139	0.201	-0.147	0.168	-0.150	0.158
3	-0.136	0.199	-0.144	0.167	-0.147	0.156
4	-0.136	0.195	-0.140	0.151	-0.142	0.152
Average	-0.136	0.199	-0.144	0.161	-0.145	0.154

TABLE 6.4: Stiffness Coefficients for the Shrouded Turbine

Test Series	K_{xx} ω/ω_D=0.7	K_{xy} ω/ω_D=0.7	K_{xx} ω/ω_D=1.0	K_{xy} ω/ω_D=1.0	K_{xx} ω/ω_D=1.1	K_{xy} ω/ω_D=1.1
1	-0.440	0.662	-0.437	0.470	-0.401	0.424
2	-0.448	0.649	-0.412	0.471	-0.479	0.504
3	-0.410	0.602	-0.435	0.504	-0.435	0.462
4	-0.469	0.670	-0.436	0.472	-0.434	0.466
Average	-0.441	0.646	-0.430	0.479	-0.437	0.464

6.5 Comparison to Theory

These data can be compared to theoretical predictions based on a combination of seal pressure forces (Sec. 7) and blade work losses associated with tip leakage (Sec. 9).

The seal forces model, as explained in Ref. 9 and modified to account for the variation of carryover factor with flow (Sec. 7) and for the pressure perturbations upstream and downstream of the seal can be easily applied here. Aside from the seal geometry (length, depth, gap, wetted perimeter on rotor and stator, and spin and whirl rate), the most important input parameters are the inlet and exit pressures along with their perturbations, and the inlet tangential flow velocity along with its perturbation. The inlet seal pressure is basically the pressure after the stator. However, a modification is made to account for the stagnation of the axial momentum component against the first sealing strip, i.e., adding to the static pressure P_2 the dynamic head $\frac{1}{2}\rho_2 u_2^2$. Since the tangential component $\frac{1}{2}\rho_2(u_{x2}\tan\alpha_2)^2$ is preserved, the correction is relatively small. It is, however, noticeable because the rotor pressure drop in this low reaction turbine is itself small. The axial velocity u_{x2} used here has been determined theoretically taking into account the blockage caused by the shroud band. First, as mentioned above, the axial velocity component, u_{x2}, of the fluid exiting the stator stagnates at the sealing strip, however, the tangential component, $u_{x2}\tan\alpha_2$, is preserved and has the same value as at the exit of the stator. The axial velocity component at the exit of the stator has to be determined in order to calculate this tangential velocity component. The axial velocity is first found as if there is no blockage and then the blockage is taken into account. In order to model this blockage it is found that the flow in the cross plane is decoupled from the axial flow. This allows one to model the flow within the test section as a flow within a two-dimensional channel with a step change in channel height. Upstream the channel has a height of H_S (representing the height of the stator blades) and downstream the channel has a height of H_r (representing the height of the rotor blades). The change in height is accomplished through a step (representing the blockage by the seal). At the corner of the step is a sink (representing the leakage through the seal). Through a conformal mapping technique (Schwarz-Christoffel transformation) this problem can be easily solved for the ratio of the axial velocity with blockage to the axial velocity without blockage. For the geometry found in this test facility the ratio is found to be 0.7039.

The model is linear in the offset, so the stiffnesses are the natural outputs. These are reduced to coefficient form using the same normalization as used for the measured data. The averaged measured values given in Table 6.2 and the predicted theoretical values given in Table 6.5 differ from 3.3% to 7.0% for α_x. Comparison of α_y requires accounting for the blade work loss, as will be shown below.

TABLE 6.5: Force Coefficients From Labyrinth Seal Theory

ω/ω_D	α_x	α_y
0.7	-3.83	3.59
1.0	-5.26	4.52
1.1	-5.81	4.87

It is interesting to understand how the direct force, Fx, comes about. In the simple form of seal theory, as is explained in Sec. 7, in which the inlet and outlet seal effective gaps are identical (as are the geometrical gaps in our seal) one would predict nearly zero direct force. It is only the allowance introduced for variations of the carryover coefficient that introduce direct forces of the correct order of magnitude, as shown in Table 6.5.

Regarding the cross-force Fy, the usual Alford mechanism must be still active, although in reduced form, in this shrouded turbine. Indeed, as long as a fraction of the surviving flows can escape through the seal gap without doing work, the Alford mechanism remains in place. Once again, this can be explained by the fact that there will be less work lost in the regions where the gap is reduced by the offset, and vice versa.

The simplest version of the theory of Sec. 9 is applicable in this case. In this theory (Sec. 9.2) the fluid which escapes through the gap at the blade tips is taken to do no work at all. This is inappropriate for unshrouded blades, and is corrected in

Sec. 9.3, but it fits exactly the condition in a turbine with labyrinth seals on the shrouded band. The only modification is the inclusion of a factor $\frac{1}{\sqrt{2}}$ in the final α_y result, to account for the fact that the flow rate through a 2-strip seal is $\frac{1}{\sqrt{2}}$ of that through a single gap with the same pressure differential.

The results of applying this scheme to our cases are shown in Table 6.6. Notice that this simple form of the work loss theory predicts zero direct force, therefore, α_x remains fully attributed to seal pressure forces. The discrepancy between theory and Fy force measurements is now larger (9% to 27%), but still reasonable.

TABLE 6.6: Work Loss Contributions and Total Force Coefficients, Compared to Data

ω/ω_D	$(\alpha_x)_{seal}$	$(\alpha_x)_{data}$	$(\alpha_y)_{seal}$	$(\alpha_y)_{work\ loss}$	$(\alpha_y)_{seal+w.l.}$	$(\alpha_y)_{data}$
0.7	-3.83	-4.06	3.59	0.76	4.35	5.94
1.0	-5.26	-5.63	4.52	0.85	5.37	6.28
1.1	-5.81	-6.00	4.87	0.92	5.79	6.37

6.6 Flow Measurements

The same flow survey as discussed in Sections. 4 and 5 was carried out for the shrouded turbine. This was done at the full 2.21 atm. mean loop pressure, and at the nominal 3440 RPM speed, with the flow rate at 3.15 kg/s.

With the shroud in place, the pressure tap holes at station 4 are before the seal. One notices a perturbation in pressure at station 4 and this may be viewed in Figure 6.17. The magnitude and phase of this perturbation was used as an input into the seals theory. These perturbations increase the cross force and have a large effect on the final theoretical result. The pressure tap holes at station 5 are approximately over

the first seal knife edge, which is at a location where static pressures are rapidly changing. This makes their interpretation difficult. The pattern is still very similar to those observed for the unshrouded cases as Figure 6.18 shows.

Stations 6 and 7 are both inside the labyrinth gland, 6 being near its center and 7 near its exit. The corresponding wall pressures are shown in Figures 6.19 and 6.20. These show identical nonuniformity patterns, which validates the procedure used in the labyrinth seals rig, where one fast-response transducer was used to obtain the gland pressure at each of four locations around the perimeter. Compared to the distributions seen in these locations with no shroud, we notice a large increase in amplitude, by about a factor of two, and also a phase shift away from the region of maximum gap and towards the 90° location. This shift has the effect of further increasing the contribution of these pressure forces to the forward-whirling cross force component F_Y. The magnitude and phase of the perturbation in pressure at the exit of the seal was used as an input into the seals theory to calculate the direct and cross forces. As in the case of the perturbation in pressure at the inlet to the seal, the perturbation in pressure at the exit has a large effect on increasing the cross force. The total forces due to the gland pressure distribution can be calculated using equations 4.11 and 4.12. The width W used here is 14.2 mm, which is the knife-to-knife distance, and the radius is R = 125 mm, which corresponds to the end of the blades (start of the shroud band).

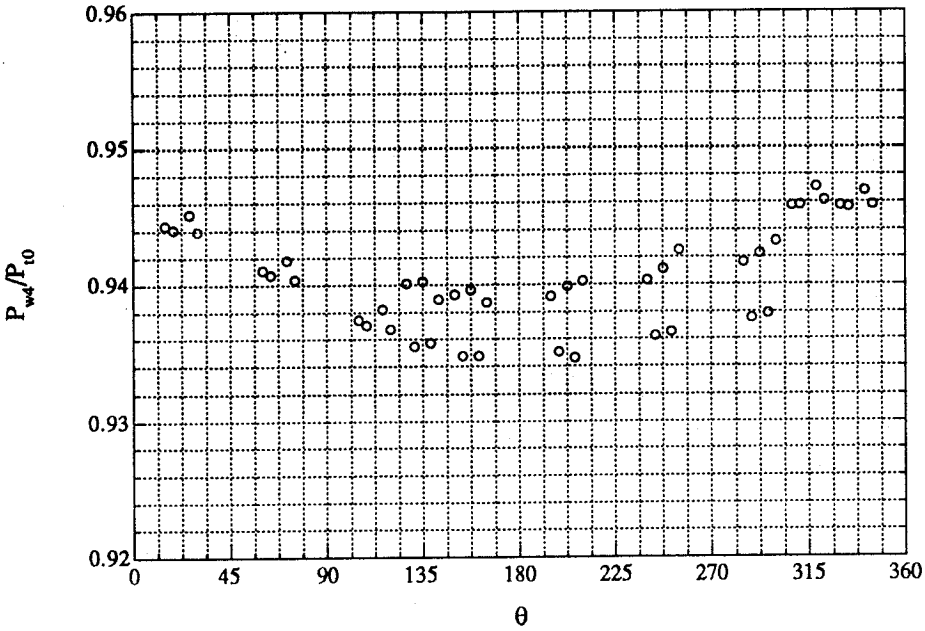

Figure 6.17:Wall Tap Pressure Distribution at Station 4, Between Stator and Rotor.

P=2.21 atm, Eccentricity = 18 mils = 0.46 mm.

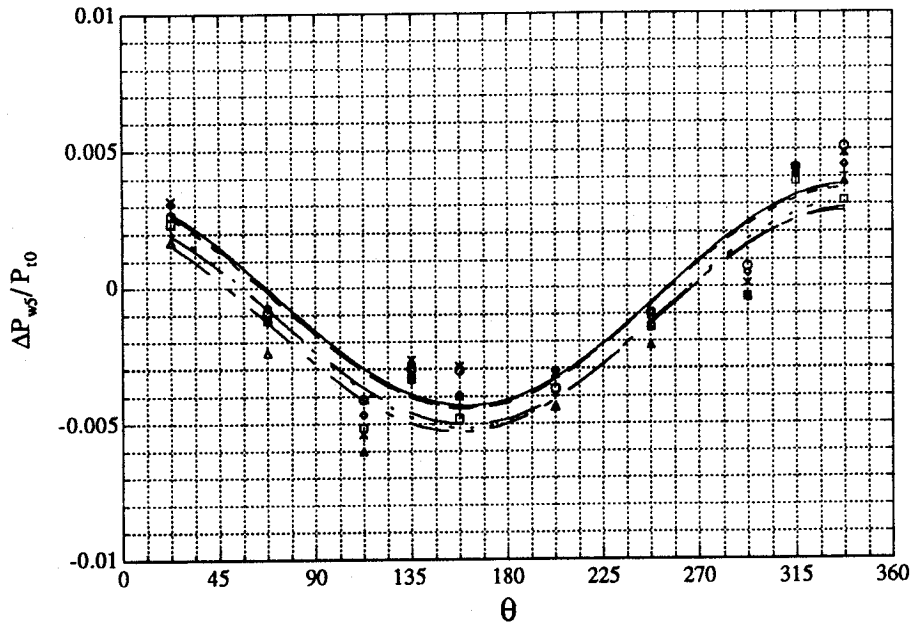

Figure 6.18:Wall Tap Pressure at Station 5 Over the First Seal Dam. P=2.21 atm, Eccentricity = 18 mils = 0.46 mm.

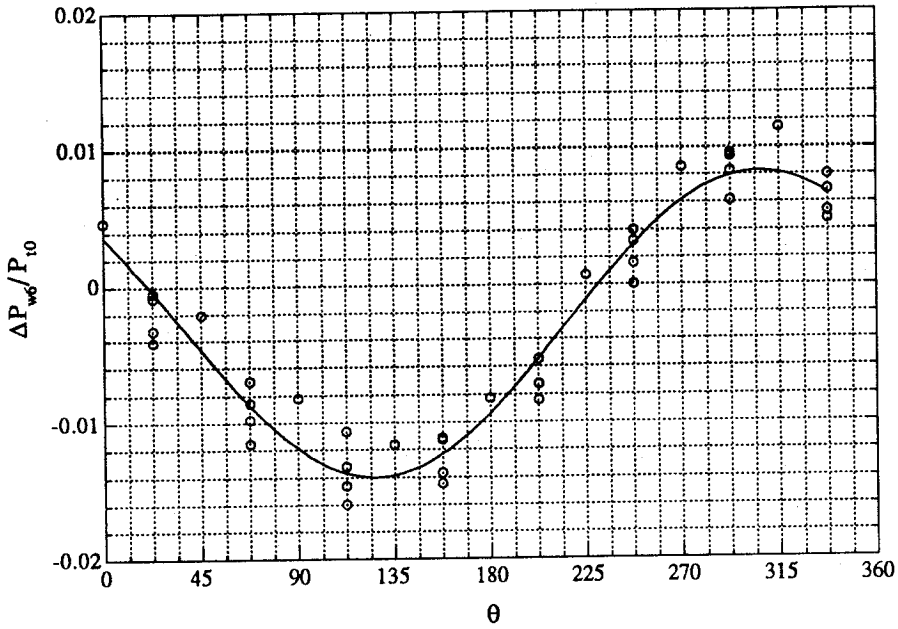

Figure 6.19:Wall Tap Pressure Distribution in the Center of the Shroud Labyrinth Seal.Station 6, P=2.21 atm, Eccentricity = 18 mils = 0.46 mm.

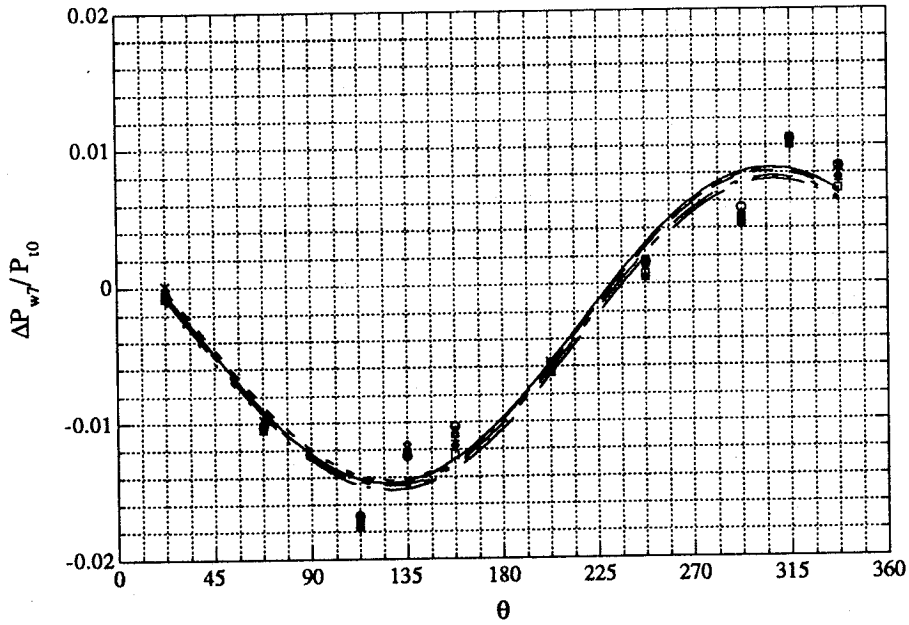

Figure 6.20:Wall Tap Pressure Distribution Near the Exit of the Shroud Seal. The Symbols refer to probe depths at various radial locations. Station 7, P=2.21 atm, Eccentricity = 18 mils = 0.46 mm.

We find:

$F_x = -8.77N$

$F_y = 11.64N$

For non-dimensionalization (Equations 4.1 & 4.2), the torque is Q = 16.8 N-m and the eccentricity e = 18 mil = 0.46 mm. This gives the coefficients:

$\alpha_x = -4.07$

$\alpha_y = 5.39$

These can be compared to the directly measured values (Table 6.4) of α_x =-5.63 and α_y = 6.28, and to the values predicted by the seals theory (α_x =-5.26 and α_y = 4.52). The agreement with measurements is reasonable, but it must be remembered that the work defect contribution should be subtracted from the directly measured values before comparison. Table 6.7 compare these six Alford force coefficients. Note that the work defect contribution has been subtracted from the dynamometer results.

Table 6.7: Comparison of Alford Force Coefficients at 2.21 atm and Design Speed.

Method	α_x	α_y
Dynamometer minus Alford Component	-5.63	5.43
Pressure	-4.07	5.39
Theory	-5.26	4.52

When this is done, the cross-force, as determined from theory appears to be underestimated by about 16%, and the cross-force, as determined from the wall tap pressures, is in good agreement with the dynamometer cross-force. The direct-force agreement is reasonable.

The flow angle survey at station 8 was not successful, and will have to be repeated in the near future. This was due to the fact that one of the tow 3-hole probes

used was not properly aligned to the prevailing mean flow angles, and so it was out of calibration range most of the time. The survey at station 9, further downstream, did give valid results, and is shown in Figure 6.21. Here we used a 5-hole probe, which cannot be inserted past the r/H = 0.76 depth, and so the last four depths shown are all at this location, and should be coincident. The lack of coincidence gives a measure of the data scatter. The first three depths (nearest the tip) are in the direct wake of the seal, but since this station is three chord lengths downstream of the rotor, the wake is probably sufficiently diffused by then. The underturning shown in Figure 6.21 is, in fact, greater than that seen in the unshrouded cases (Sections 4 & 5)

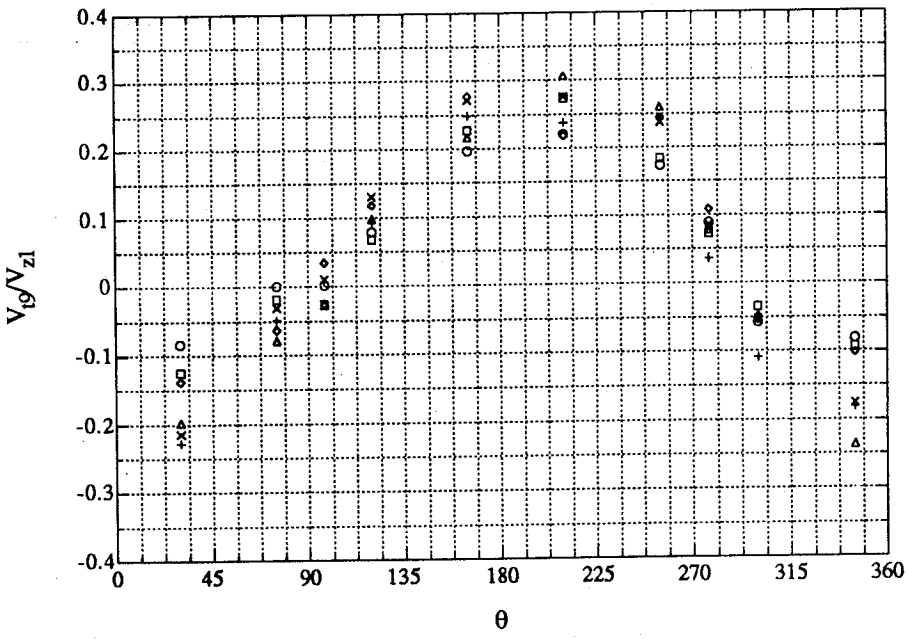

Figure 6.21:Tangential velocities at Station 9. The circle, square, diamond and X data points are all nearest the core at r/H=0.76.

7.0 Labyrinth Seals: Static and Dynamic Forces

7.1 Foreword

Our work on labyrinth seal cross-forces has been both experimental and theoretical. The initial theoretical development [9], [4] produced a linearized model of the flow in a one-cavity seal, following Iwatsubo's approach [14]. This was used to aid the design of the test facility and the planning of the test program. Our principal goal was the clarification of the mechanisms involved in the generation of the forces and, particularly, of the damping components.

The test facility (LSTF), which was briefly described in Secs. 2.2 and 2.4, was then used to generate an extensive data base, according to the test matrix explained in Sec. 3.2, in which we independently varied inlet flow angle, rotor whirl speed, rotor spin rate, pressure ratio and mean eccentricity for four different one-cavity seals. These were all of the straight-through type, with teeth on rotor. Two were short (l = 1.02 cm) and two others were longer (l = 1.73 cm), and each was tested with smooth and honeycomb land surfaces.

When the test data were correlated to the theory, it was found that the predicted cross-forces were systematically smaller than those measured by factors between 2 and 3, although the trends were all correctly predicted. Several consistency checks ruled out most potential sources for the discrepancy. Thus, although the theory uses relatively crude estimates of the frictional fluid forces, generous allowances for error there merely shifted the calculated results by ±20%. Similarly, the carryover effects, and their variation with gap width, introduce significant uncertainty in the direct forces, but, again, only ±20% on the cross-forces. This will be further discussed below.

At the same time, the results of experiments in the Alford turbine test facility, with a shroud seal (Sec. 6), showed the presence of pressure nonuniformities ahead of the seal, an effect not included in our theory (or, to our knowledge, in any other existing theory). It was thus suspected that this may have been the source of the discrepancy,

and an extended theory was developed, which accounts for nonuniformities in the pre-seal inlet cavity. The results of this development confirm the importance of these effects, and explain many other peculiarities of the data. It is seen that the axial gap in the face seal separating this inlet cavity from the hub volume has a strong influence on the seal forces and, in the limit when uninhibited communication exists between inlet cavity and hub volume, the uniform-inlet results are recovered, while in the opposite limit, with no radial leakage allowed, the predicted forces consistently exceed measurements. Since this effect was unexpected, no tight control was exercised in the tests over this important parameter. However, using our best estimates of the face seal gap for the various tests, there is substantial agreement between data and theory on cross-forces, and several other parameters, such as cross-damping and effective inertia, which the original theory completely missed, are correctly calculated. The realization that the prediction of seal cross-forces requires careful evaluation of the inlet nonuniformities is likely to have significant engineering implications.

Because of the close interplay between theoretical arguments and experimental data, we present first a summary of the theory (a complete account can be found in Ref. [10]), followed by selected detailed data for one configuration and reduced data for all cases. We conclude with data vs. theory comparisons and a general discussion.

7.2 Summary of the Theory for Uniform Inlet

We consider here the situation depicted in Fig. 7.1, which shows the main notation and geometrical parameters. For now, the inlet and exit conditions are assumed uniform (i.e., P_i, P_o, V_i are constant). The shaft executes circular whirl of speed Ω and amplitude r, such that the first and second radial gaps vary according to

$$\delta_1 = \delta_1^* - r\cos(\theta - \Omega t) \tag{7.1a}$$

$$\delta_2 = \delta_2^* - r\cos(\theta - \Omega t) \tag{7.1b}$$

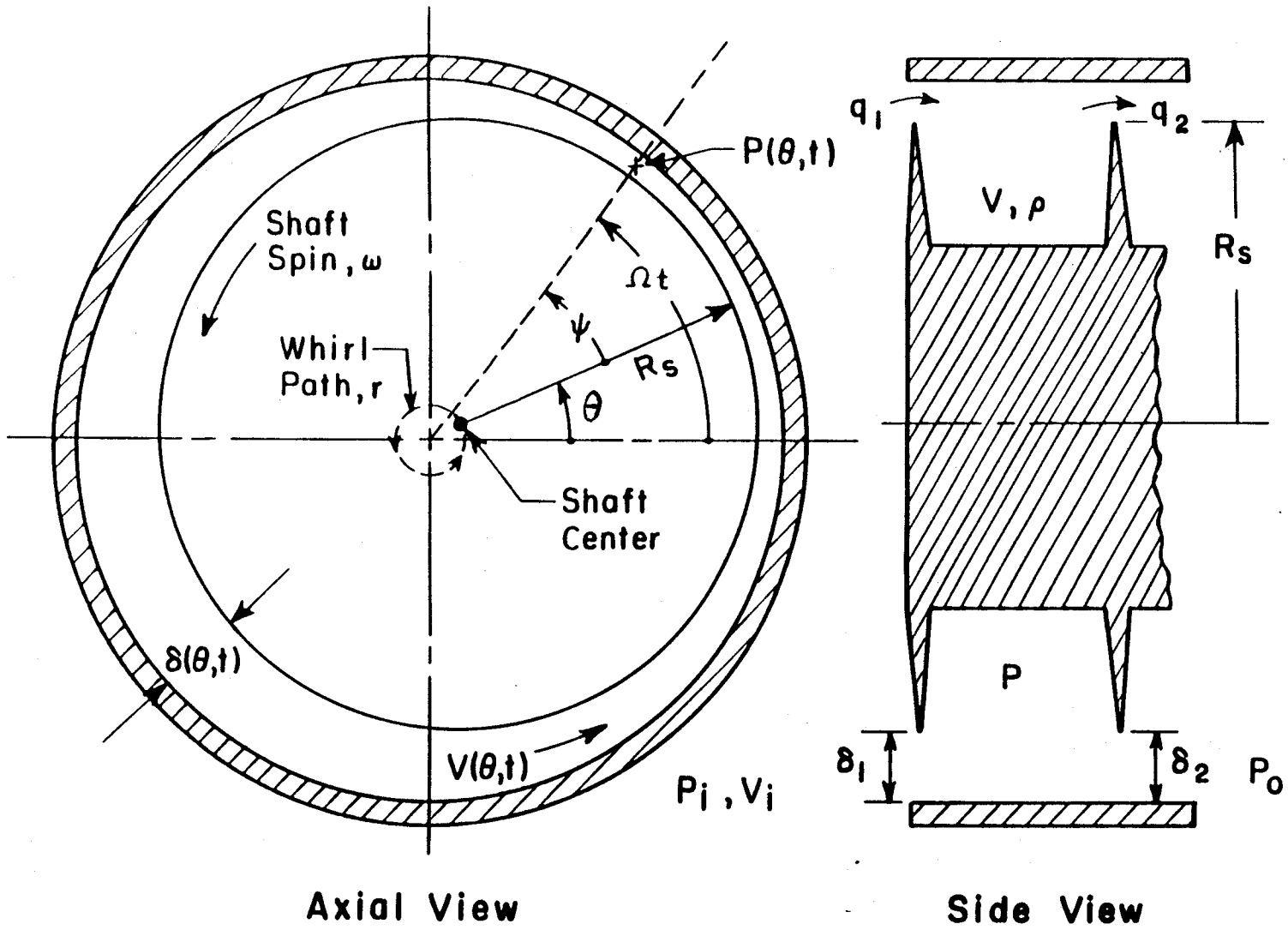

Figure 7.1: Kinematic quantities associated with a labyrinth seal. The the shaft is spinning at an angular frequency ω, while simultaneously under going a circular precession of amplitude $\hat{r}$ and frequency Ω.

The mean temperature T of the gas is assumed constant, but fluctuations are assumed isentropic. The equations of conservation of mass and of tangential momentum in the seal cavity are

$$\frac{\partial(\rho f)}{\partial t} + \frac{1}{R_s}\frac{\partial}{\partial \theta}(\rho f V) + q_2 - q_1 = 0 \tag{7.2}$$

$$\rho f\left(\frac{\partial V}{\partial t} + \frac{V}{R_s}\frac{\partial V}{\partial \theta}\right) - q_1(V_i - V) + \frac{f}{R_s}\frac{\partial P}{\partial \theta} + \tau_s l - \tau_r (l + 2h) = 0 \tag{7.3}$$

where $f = l\,(h + \delta)$ is the cavity cross-sectional area (Fig. 7.1), V is the tangential velocity in the gland, q_1 and q_2 are the inflow and outflow rates per unit length, and τ_s, τ_r are the frictional stresses on stator and rotor gland surfaces, respectively. The leakage rates are calculated, using a mean-density formulation, as

$$q_1 = \delta_1 \mu_1 \sqrt{\frac{P_i^2 - P^2}{R_a T}} \tag{7.4a}$$

$$q_2 = \delta_2 \mu_2 \sqrt{\frac{P^2 - P_o^2}{R_a T}} \tag{7.4b}$$

where R_a is the gas constant. The gap flow coefficients, μ_1, μ_2, are each the product of a contraction coefficient $C_c = 0.65$, times a carryover coefficient, β, which accounts for non-zero axial momentum of the incoming flow. This is not important in the first gap (in our design, the turning vane or turning hole discharge jets impinge below the seal gap), but it is for the second gap in a straight-through design, particularly if the seal is relatively short. We correlate this effect, following Vermes [15], as

$$\beta = \frac{1}{(1-a)^{1/2}} \quad , \qquad a = \frac{8.52}{\frac{l_e}{\delta_2} + 7.23} \tag{7.5}$$

where l_e is the effective seal pitch, accounting for the mean swirl angle of the flow. It is important to note that β, and hence μ_2, depends on δ_2. Thus, at the location of minimum clearance δ_2, μ_2 is also minimum, and vice versa. This introduces the same effect as if the second gap δ_2 were smaller than δ_1, namely, flow entering through δ_1 at

the narrowest gap location tends to be dammed by the relative "closing" of the second clearance. This will be further discussed later, as it has major implications in generating the direct force component.

Equations (7.2) and (7.3) are solved by linearization about a steady, centered condition. The zeroth order yields expressions [10] for the mean gland pressure, P^*, the mean leakage rate through both gaps, q^*, and the mean tangential velocity V^* in the gland. This differs from V_i, the inlet tangential velocity, only by the relatively small effects of friction against the stationary and rotating parts of the gland. These differences are important, however, as one of the two main mechanisms for cross-force generation, as will be seen shortly.

In the perturbation part, we ignore transient effects and look for steady whirling, such that the conditions would appear stationary if viewed from the whirling frame. Then, if $\phi = \theta - \Omega t$ is the angle measured from the instantaneous location of the narrowest gap, we have

$$\frac{\partial}{\partial t} = -\Omega \frac{\partial}{\partial \phi} \quad , \quad \frac{\partial}{\partial \theta} = \frac{\partial}{\partial \phi} \tag{7.6}$$

The pressure and tangential velocity are linearized as

$$P = P^* (1 + \xi) \quad , \quad V = V^* (1 + \eta) \tag{7.7}$$

and q_1, q_2 are expressed as

$$q_1 = q^* \left[1 - \frac{P^{*2}}{P_i^2 - P^{*2}} \xi - \frac{r}{\delta_1^*} \cos \phi \right] \tag{7.8a}$$

$$q_2 = q^* \left[1 + \frac{P^{*2}}{P^{*2} - P_o^2} \xi - \frac{r}{\delta_2^*} \cos \phi + \frac{\beta'}{\beta^*} \right] \tag{7.8b}$$

Here, the terms in ξ and in $r \cos\phi$ arise from variations in pressure and clearance, respectively, while β' in Eq. (7.8b) arises from the carryover variations, i.e., $\beta' = \left(\frac{\partial \beta}{\partial a}\right)\left(\frac{\partial a}{\partial \delta_2}\right)\delta_2'$ and $\delta_2' = - r \cos\phi$. Defining

$$\kappa = \left[\frac{\partial(C_c\beta)}{\partial\delta_2}\right]_{\delta_2^*} \tag{7.9}$$

we can write the term β'/β^* as $-\left(\kappa/\mu_2^*\right) r\cos\phi$.

The complete perturbation analysis is detailed in Ref. [10]. Here, however, we wish to focus on the essential points and disregard secondary effects. To that end, returning to Eqs. (7.2) and (7.3), we will neglect the following effects:

a) In Eq. (7.2), density variations are unimportant. The ratio of the two parts of the perturbation $(\rho f)'$ is, in order of magnitude, $\frac{\rho' f}{\rho f'} \cong \gamma \frac{\xi}{r/h}$. The solution to be obtained shortly will show this to be small.

b) In Eq. (7.3), both the inertia and the friction force perturbations are unimportant. For the inertia, compare its perturbation $\rho f\,(V/R_s)\,V'$ to one of the terms in the perturbation of $q_1\,(V_i - V)$, namely, qV'. The ratio is $\frac{l}{\delta}\frac{h}{R_s}\frac{V}{V_x}$, where $V_x = (q/\rho\delta)$ is the axial velocity in the seal gap. The geometrical group $lh/\delta R_s$ is ~1 typically, while the mean swirl V/V_x is usually small. This may require re-evaluation at very high inlet swirls. As to the friction, its variations are of order $\rho V C_f\, l\, V'$, and the ratio of this to, again, qV' is $C_f \frac{l}{\delta}\frac{V}{V_x}$. Here, although l/δ is large, the small factors C_f and V/V_x make the product small.

c) When substituting q_1 into Eq. (7.3), the pressure part of the perturbation $-\frac{P^{*2}}{P_i^2 - P^{*2}}\xi$ is small compared to the gap variation term $-(r/\delta_1^*)\cos\phi$. This is again because of the smallness of $\xi/(r/\delta_1^*)$.

With these simplifications, the first order perturbations of Eqs. (7.2) and (7.3) are

$$\rho^* lh\left(-\Omega + \frac{V^*}{R_s}\right)\frac{r}{h}\sin\phi + \rho V^*\frac{l}{R_s}\frac{h}{d\phi}\frac{d\eta}{d\phi} + q^*\left(\frac{P^{*2}}{P^{*2} - P_o^2} + \frac{P^{*2}}{P_i^2 - P^{*2}}\right)\xi$$
$$+ q^*\left(\frac{1}{\delta_1^*} - \frac{1}{\delta_2^*} - \frac{\kappa}{\mu_2^*}\right) r\cos\phi \cong 0 \tag{7.9}$$

and

$$q^*\left(\frac{r}{\delta_1^*}\cos\phi\right)(V_i - V^*) + q^*V^*\eta + \frac{lh}{R_s}P^*\frac{d\xi}{d\phi} \cong 0 \tag{7.10}$$

The velocity perturbation η can now be isolated from Eq. (7.10) and substituted into (7.9), to obtain a second-order equation for ξ. Expressing the solution in the form $\xi = A\cos\phi + B\sin\phi$, we obtain

$$A = \frac{K - \left(1 - \frac{1}{\alpha}\right)}{1 + (\alpha\beta^*)^2 + \left(\frac{L}{D\,\mu_1^*}\right)^2}\Delta^2\varepsilon \tag{7.10}$$

$$B = -\frac{\sigma\frac{L}{D}[\Gamma + (1-W)\,D]}{1 + (\alpha\beta^*)^2 + \left(\frac{L}{D\,\mu_1^*}\right)^2}\Delta^2\varepsilon \tag{7.11}$$

The following dimensionless groups appear here (in addition to those already defined):

$$\alpha = \frac{\delta_2^*}{\delta_1^*}\ , \qquad L = \frac{l}{R_s}\ , \qquad D = \frac{\delta_1^*}{h}\ , \qquad \varepsilon = \frac{r}{\delta_1^*} \tag{7.12}$$

$$\sigma = \frac{\rho^* V^* \delta_1^*}{q^*} \cong \frac{V^*}{V_x}\ , \qquad W = \frac{\Omega R_s}{V^*} \tag{7.13}$$

$$\Delta = \frac{q^*}{\mu_1\delta_1^*\rho^*\sqrt{R_aT}} = \sqrt{\left(\frac{P_i}{P^*}\right)^2 - 1} \cong \sqrt{\frac{1}{2}\frac{\Delta P}{P^*}} \tag{7.14}$$

$$\Gamma = \frac{V_i}{V^*} - 1 \tag{7.15}$$

$$K = \frac{\kappa\delta_1^*}{\mu_2^*} \tag{7.16}$$

As Eq. (7.13) shows, σ is approximately the mean swirl angle in the gland and W is a measure of the whirling velocity. From Eq. (7.14), the last expression for Δ (valid when $\Delta P = P_i - P_o << P_o$) shows that $2\Delta^2 \cong \Delta P/P^*$ is a measure of the driving pressure differential. Finally, Γ (7.15) describes the friction-induced "flow twist", or change in

swirl velocity.

The significance of A and B is that they are proportional to the direct and cross-force on the seal, respectively. Projecting in the direction of the seal offset, we calculate the "direct" or "normal" force

$$F_N = -\int_0^{2\pi} P \cos\phi \; d\phi \; R_s l = -A \; \pi R_s l \; P^* \tag{7.17}$$

where a negative F_N would indicate a restoring force. Projecting now perpendicular to the offset, in the direction that would promote forward whirl, we obtain the "cross-force", or "tangential force"

$$F_T = -\int_0^{2\pi} P \sin\phi \; d\phi \; R_s l = -B \; \pi R_s l \; P^* \tag{7.18}$$

so that negative B values would drive forward whirl.

We are now in a position to discuss the force generation mechanisms. Starting with the normal forces, we see from Eq. (7.10) that they arise from the differences between δ_2^* and δ_1^* (this is represented by $1 - (1/\alpha)$ in the numerator), as well as by the sensitivity of carryover to gap (the K term). In our experiments, $\delta_2^* = \delta_1^*$, and so only the latter term survives. This is a modification of the "convergent seal" mechanism first discussed by Alford [1]. The inlet swirl, σ, does not influence F_N. Since K is a positive quantity, restoring direct forces are expected.

The more important cross-forces are given by Eq. (7.11). We first notice the proportionality to inlet swirl, σ, and the negative sign, at least at small whirl W. This indicates forward-whirling excitation. There are two distinct contributions to the cross-force, indicated by the terms Γ and (1-W)D in the numerator of (7.11). The first of these is related to the flow "twist", i.e., the change in tangential velocity from inlet to gland. Being a velocity difference, this twist is the same when viewed from the static or from the whirling frame, and so its effect is independent of whirl W. It thus contributes only to cross-stiffness, but not to its damping. A physical interpretation of this effect is as

follows: Assuming $V_i > V^*$, the fluid entering the seal gland brings with it extra tangential momentum, which energizes the motion within the gland. On average, this just compensates for frictional losses; however, more fluid enters the wide-gap region than its opposite and, as a result, there is a positive $dP/d\theta$ pressure gradient induced near the wide gap, and a negative $dP/d\theta$ near the narrow gap. Hence, a pressure maximum develops 90° past the wide gap in the swirl direction, and this originates the cross-force. Because of this description, we can call this the "ejector pump" effect.

The other component, proportional to (1-W)D, can be described as a modified mass-storage effect. While the ejector pump effect can be understood with reference to the momentum balance only, the mass storage effect arises, naturally, from the continuity equation, in particular, from an approximate balance between the first term in Eq. (7.9) and the $\sin\phi$ part of the third term. In other words, the fluid circulating in the cavity sees the flow area f changing at a rate $\left(-\Omega + \frac{V^*}{R_s}\right)$ lh $\sin\phi$. This can be accommodated either by changes V_η^* in the tangential velocity (the second term in Eq. (7.9)) or by local imbalances in the inlet-outlet gap flows (the third term). If the latter effect is predominant (as it is in most of our experiments), the pressure nonuniformity $P^*\xi$ required to unbalance these gap flows is what creates this cross-force component. From the description, it can be seen that the effect is dependent upon whirl velocity Ω, and, in particular, when $\Omega = V^*/R_s$ (W = 1), it disappears. At this point, the fluid tangential motion just follows the travelling gap width wave, and the fluid sees no area change. At any whirl speed greater than this, the force contribution is stabilizing.

One important consequence of this mechanism for generation of damping (Ω-dependence of F_T) is the possibility of deducing C_{xx}, the relevant damping coefficient, from purely static offset measurements. The coefficient C_{xx} would be proportional to the factor which multiplies (1-W) in Eq. (7.11), and would therefore be isolated from cross-force measurements at zero whirl if the Γ part of the equation were either zero or separately known. The first route can be implemented by spinning the rotor to the

speed at which $V^* = V_i$, which can be verified by exit swirl measurements such as those reported here. Alternatively, V^* can be measured and the Γ term contribution calculated, although this involves some uncertainty in the friction coefficients required. The accuracy of these procedures was verified from our data (Sec. 7.5).

7.3 The Effect of Nonuniform Inlet Conditions

The theory of the previous section is appropriate to cases where a large plenum volume ahead of the seal ensures pressure uniformity there. This assumption is routinely made in existing theories [13], [14]. When the inlet plenum is small, however, its pressure can be strongly influenced by the pressure nonuniformities in the seal cavity. In turn, for our design, the plenum pressure nonuniformity leads to inlet swirl variations because, for example, the swirl vane assembly will deliver higher velocity (both axial and tangential) to plenum regions where the pressure is lower. These plenum nonuniformities, particularly that in swirl velocity, can, in their turn, have significant impacts on those in the main seal cavity, and hence on the seal forces. In addition, for a practical application, there will be new shaft force components arising from these pressure variations outside the seal. These effects need to be all taken into account for design purposes, and also in interpreting experimental data. We next present an extension of the model to this end. In addition to its value in improving cavity pressure predictions, this extension permits calculation of the true seal inlet swirl, as distinct from the swirl vane angle. Figure 7.2 shows a cross-section of the LSTF test section. The swirl vanes which are located l_i upstream from the first knife have a radial gap of δ_v and deliver air into the first cavity with an effective swirl angle of α_v. This is the metal angle minus some small turning deviation. This cavity is h_i deep and is sealed from a large volume by an axial fact labyrinth seal with gap δ_c. Since there is no net flow into this center cavity, the pressure here is uniform and the same as in the swirl cavity, namely P_i^*. The continuity equation for the swirl chamber, which

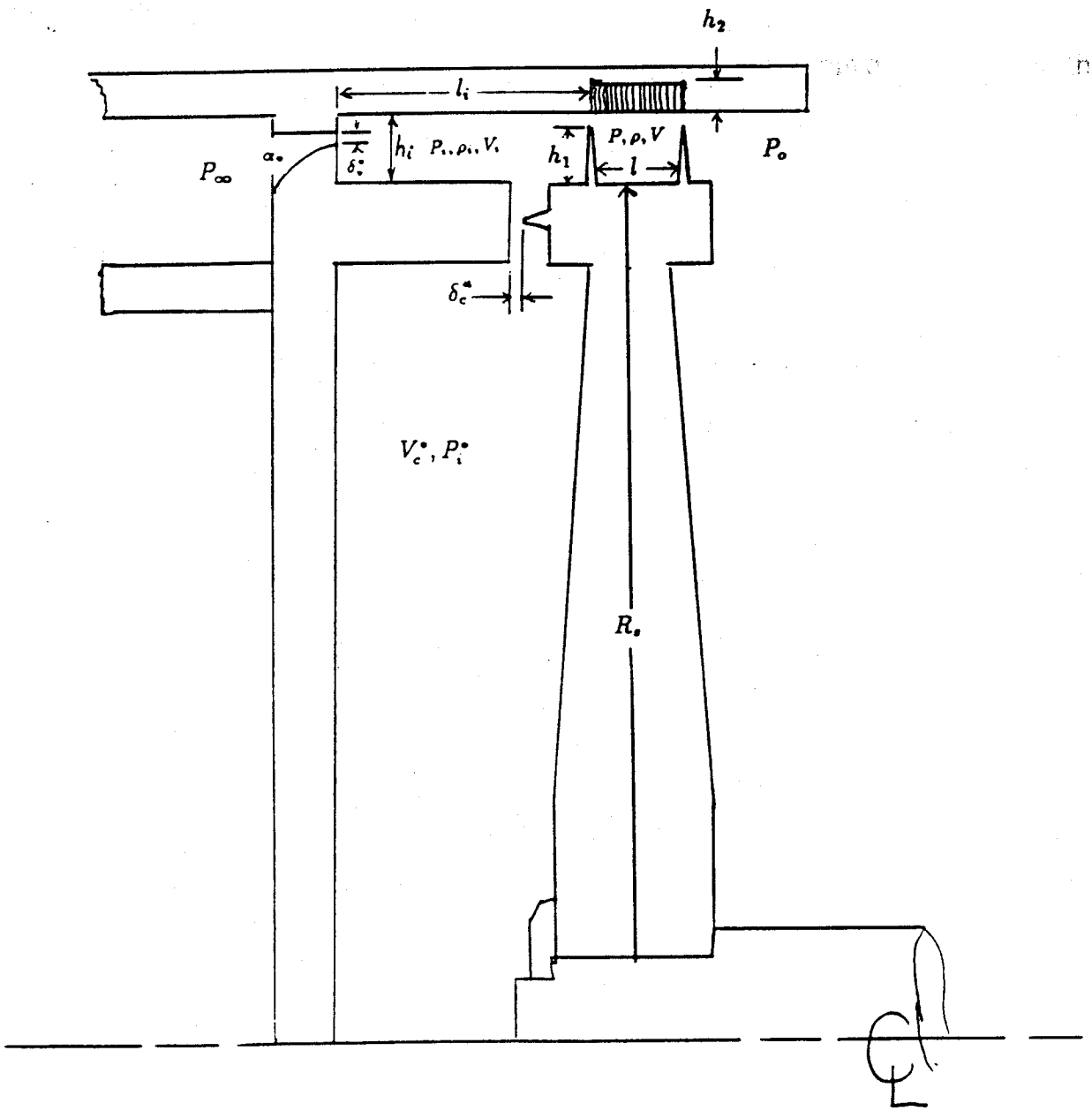

Figure 7.2: Schematic of the test section, showing the pre-seal cavity

is analogous to Eq. (7.2) is

$$\frac{\partial[\rho l_i h_i]}{\partial t} + \frac{1}{R_s}\frac{\partial}{\partial \theta}[\rho l_i h_i V_i] + q_1 - q_v + q_{c,out} - q_{c,in} = 0 \tag{7.19}$$

where V_i is no longer constant, q_v is the flow rate per unit length issuing from the swirl vanes, and the q_c's are the flows in and out of the center cavity respectively. Incompressible relations are sufficient for treating these flows since the transfer velocities are very low. These flows can be written as

$$q_c = \mu_c \delta_c \sqrt{2\rho_i^* (p_i - p_i^*)} \tag{7.20}$$

This relation is fundamentally different from those for q_v, q_1 and q_2 in that there is no flow to or from the center volume when the seal is centered in the casing because $P_i = P_i^*$. This basic nonlinearity is very important and must be dealt with appropriately in the analysis. Likewise, the momentum equation in this cavity is

$$\frac{\partial[\rho l_i h_i V_i]}{\partial t} + \frac{1}{R_s}\frac{\partial[\rho l_i h_i V_i^2]}{\partial \theta} + q_1 V_i - q_v V_v + q_{c,out} V_i - q_{c,in} V_c + \tau_s(2l_i + h_i) - \tau_r h_i + \frac{l_i h_i}{R_s}\frac{\partial P_i}{\partial \theta} = 0 \tag{7.21}$$

V_c is the swirl velocity inside the center volume. In this cavity, the cross-sectional area, $l_i h_i$, and the vane gap, δ_v, are constant. However, the inlet swirl component of velocity, V_v, is not. The angle of the fluid leaving the vanes, α_v, is constant. Therefore, a drop in the pressure at one location in this cavity will induce a greater mass influx and hence a higher swirl velocity at that location.

The original equations for the seal gland (Eqs. (7.2) and (7.3) are still valid within the constraints of the model, but the perturbation inflow conditions η_i, ξ_i must be allowed to be nonzero, thus coupling the seal gland to the upstream cavity.

The same solution procedure used for the single gland seal can be used when there is no flow into the center cavity. However, as previously stated, the nature of the oscillating flow between the two upstream volumes is quite different from the others.

These terms introduce essential nonlinearities into the governing equations of the upstream cavity.

The physical reason for this difficulty is clear enough. When the two volumes are nominally at the same pressure, a small positive perturbation in the swirl cavity pressure $\widetilde{P}_i$ may drive a large leakage perturbation flow, depending on the gap ratio δ_v^*/δ_1^* and the perturbation amplitude, into the center volume relative to the two other perturbation flows $\widetilde{q}_v$ and $\widetilde{q}_1$. In mathematical terms, the other perturbation flows are of first order in ε_1 and hence ξ, while $q_c \sim O(\xi^{1/2})$.

The method for creating a solution will proceed along the same general lines as before. The steady solution for both chambers is found and then first harmonic perturbations are substituted into the governing equations. All terms except the center cavity leakage flow are treated as before. The new terms will be averaged to obtain their first Fourier component for a harmonic balance. The addition of these terms creates a nonlinear algebraic system for the perturbation amplitudes.

The zeroth order velocity, pressure and density in the swirl cavity will be denoted by V_i^*, P_i^* and ρ_i^* respectively. The pressure and velocity in the swirl cavity are expressed by the following harmonic perturbation expressions:

$$P_i = P_i^*\left(1 + \hat{\xi}_i e^{i(\theta-\Omega t)}\right) \quad , \qquad V_i = V_i^*\left(1 + \hat{\eta}_i e^{i(\theta-\Omega t)}\right) \tag{7.22}$$

where real parts are understood for the perturbation terms.

The perturbation expressions for $\hat{\xi}_i$, $\hat{\eta}_i$, $\hat{\xi}$, and $\hat{\eta}$ are substituted into the continuity and momentum equations for both the upstream swirl cavity and the seal gland. The nondimensional perturbation leakage flow into the center cavity is

$$\frac{q_c}{q^*} = \frac{\mu_c^*\delta_c^*}{\mu_1^*\delta_1^*}\sqrt{\frac{2P_i^*}{P_i^* - P^*}}\left[\mathrm{Re}\left\{\hat{\xi}_i e^{i\phi}\right\}\right]^{1/2} \qquad \phi = \theta - \Omega t \tag{7.23}$$

The first harmonic component of this function will be extracted by averaging over one period. The first harmonic is

$$C_1 = \frac{1}{\pi}\int_{-\pi}^{\pi} \left[\mathrm{Re}\left\{|\hat{\xi}_i| e^{i\phi}\right\}\right]^{1/2} \mathrm{sgn}(\xi_i)\, e^{-i\phi}\, d\phi \tag{7.24}$$

After some manipulation, this reduces to

$$C_1 = \frac{4\sqrt{|\hat{\xi}_i|}}{\pi}\int_0^{\pi/2} \cos^{3/2}\phi dP \text{ si} = \frac{4\sqrt{|\hat{\xi}_i|}}{\pi} 2^{1/2} B\left(\frac{5}{4}, \frac{5}{4}\right) \tag{7.25}$$

where B is the beta function. From this, the first harmonic of $q_{c,out} - q_{c,in}$ is found to be

$$\frac{q_c'}{q^*} = 1.57377 \frac{\mu_c^* \delta_c^*}{\mu_1^* \delta_1^*}\left[\frac{P_i^*}{P_i^* - P^*}\right]^{1/2} |\hat{\xi}_i|^{-1/2} \hat{\xi}_i\, e^{i(\theta - \Omega t)} \tag{7.26}$$

Similarly, the first harmonic of $q_{c,out}V_i - q_{c,in}V_c$ is

$$1.57377 \frac{\mu_c^* \delta_c^*}{\mu_1^* \delta_1^*}\left[\frac{P_i^*}{P_i^* - P^*}\right]^{1/2} |\hat{\xi}_i|^{-1/2} \frac{1}{2}\left(V_c^* + V_i^*\right) \hat{\xi}_i\, e^{i(\theta - \Omega t)} \tag{7.27}$$

Other than these nonlinear terms, additional terms arise coupling the two cavities' momentum and mass conservation equations, but these are fairly straightforward, and can be found detailed in Ref. [10]. Altogether then, we now need to solve a set of four coupled equations for $\hat{\xi}_i$, $\hat{\eta}_i$, $\hat{\xi}$, and $\hat{\eta}$, where the first two contain the nonlinearities given by Eqs. (7.26) and (7.27). With zero axial gap ($\delta_c^* = 0$), the system is still linear, although fully coupled, and can be solved easily. When δ_c^* is nonzero, an iteration is required, starting with the $\delta_c^* = 0$ solution. If those terms in the mass and momentum equations for the seal which contain $\hat{\xi}_i$ or $\hat{\eta}_i$ are artificially suppressed, one recovers the uncoupled, or single-cavity, analysis that was described in Sec. 7.2. A consistency check is provided by solving the fully coupled set, but artificially increasing the depth h_i of the pre-seal chamber. This again produces, in the limit, the uncoupled results.

7.4 Discussion of Theoretical Results

We give here some selected results pertaining to the configuration of Build #3. For the single-cavity, uncoupled case, we use:

$R_s = 0.1524$ m $l = 0.01727$ m $h_1 = 0.00508$ m

$\delta_1^* = \delta_2^* = 0.6858$ mm $\quad P_i = 1.585 \times 10^5$ Pa $\quad P_o = 1.0133 \times 10^5$ Pa

$V_i = 33.41$ m/sec $\quad T = 295$ K $\quad \hat{r} = 0.09525$ mm

The flow coefficients are $\mu_1 = 0.65$ (first gap) and, from Eq. (7.5), $\mu_2^* = 0.76$. The zeroth order solution provides the mean seal properties:

$P^* = 1.2861 \times 10^5$ Pa $\quad q^* = 0.1419$ Kg/m/sec $\quad V^* = 32.03$ m/sec

which then allow calculation of the following nondimensional parameters:

$\alpha = 1 \quad \beta^* = 1.16 \quad D = 0.1350 \quad H = 0.0333 \quad L = 0.1133$

$\Delta = 0.720 \quad \sigma = 0.245 \quad \Gamma = 0.04 \quad \varepsilon_1 = 0.1390$

As a baseline case, we will use K = 0, thus ignoring the carryover variation effect discussed in Sec. 7.2. We also baseline the case with zero spin $\omega = 0$. The factor K, as calculated from Eqs. (7.16) and (7.9), is 0.1385. The nondimensional forces are defined by

$$\widetilde{F}_N = \frac{F_N}{R_s \, l \, P^*} \quad , \quad \widetilde{F}_T = \frac{F_T}{R_s \, l \, P^*} \tag{7.28}$$

The calculations were made with the full uncoupled model, as given in Ref. [10], and the main trends should be as in the simplified discussion of Sec. 7.2.

Figures 7.3 and 7.4 show the effects of carryover variations, from K = 0 to about twice the theoretical value. Also shown are the effects of whirl rate $W = \Omega R_s / V^*$. In Fig. 7.3 we verify the basic independence of F_N from whirl (very small C_{xy}), as well as the fact that when K = 0, the normal force is essentially zero. Nonzero values of K introduce restoring normal forces. Figure 7.4 shows the damping effect of whirl on the cross-force. $\widetilde{F}_T$ crosses zero at W slightly above 1, as suggested by the simplified Eq. (7.11), which would give a crossing at $W = 1 + \Gamma/D = 1.296$. The figure also shows a relatively small, but noticeable, increase of F_T with the carryover factor K. This was missed by Eq. (7.11), and would amount to about 28% at all whirl speeds for the theoretical K value.

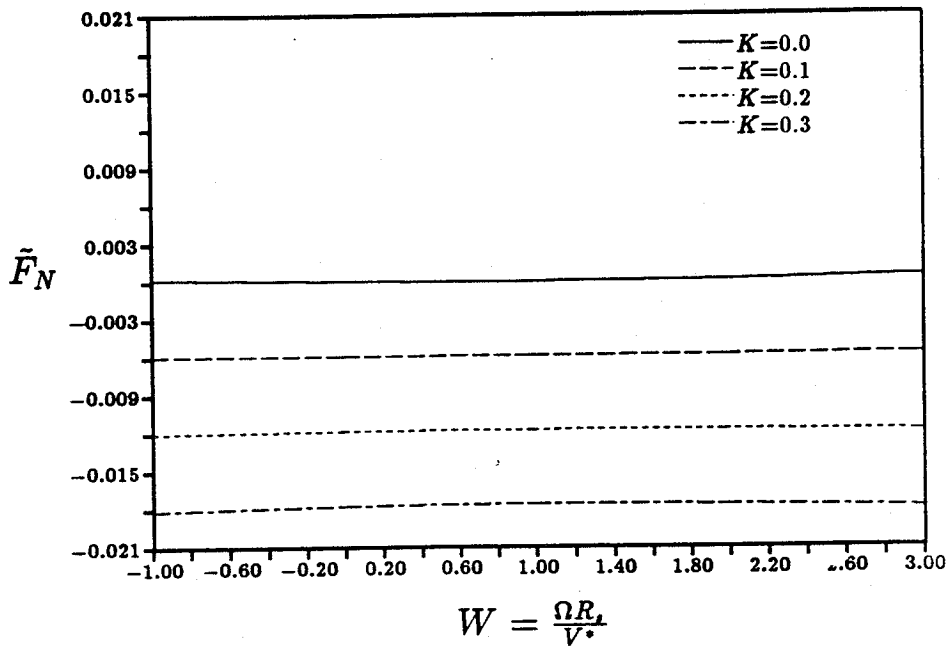

Figure 7.3: Nondimensional direct force, $\tilde{F_N}$, vs. the nondimensional whirling frequency, $W = \frac{\Omega R_s}{V^*}$, for K=0.0, 0.1, 0.2, 0.3. All other parameters are the same as in the baseline case.

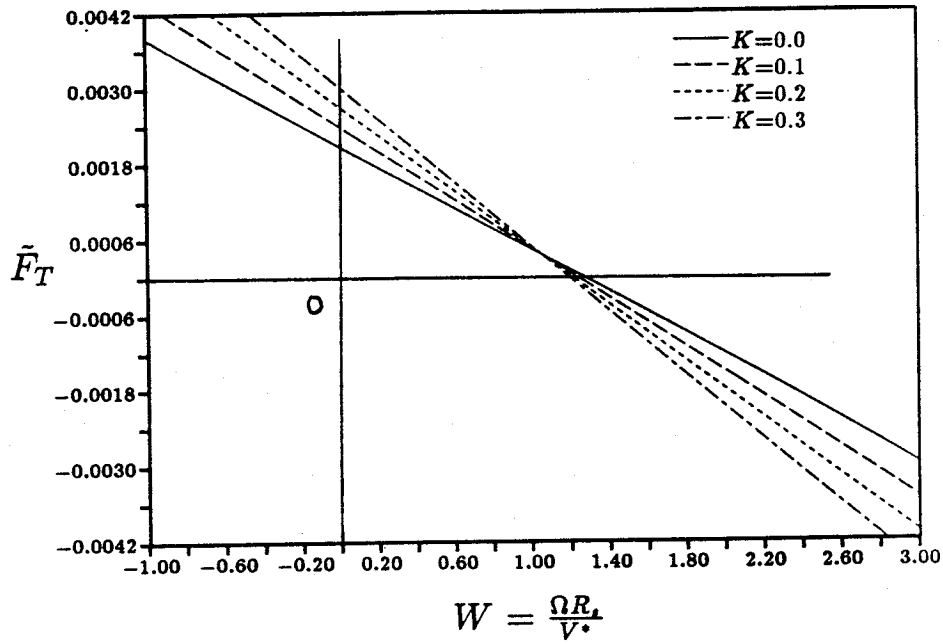

Figure 7.4: Nondimensional cross force, $\tilde{F_T}$, vs. the nondimensional whirling frequency, $W = \frac{\Omega R_s}{V^*}$, for K=0.0, 0.1, 0.2, 0.3. All other parameters are the same as in the baseline case.

Figures 7.5 and 7.6 show the effect of various levels of inlet swirl, up to $\sigma \cong V^*/V_x = 0.9$. The effect on F_T is essentially a proportionality, as the simplified formulation in Sec. 7.2 showed. The effects on F_N are more complicated. The simplified model indicated no effect, but Fig. 7.5 shows a coupling of the effects of swirl and whirl speed, producing curvature (effective mass) and asymmetry (cross-damping, C_{xy}).

The effect of spin is contained in two nondimensional parameters, namely $S = \omega R_s/V^*$ and $\Gamma = V_i/V^* - 1$. This is because the gland tangential velocity V^* depends on the state of motion of the surfaces in contact with the seal fluid. If S alone is varied, the effects on both F_T and F_N are relatively minor (Ref. [10]). If Γ alone is varying, we obtain the results shown in Figs. 7.7 and 7.8. The effect on the cross-force F_T (Fig. 7.8) is basically an increase at all whirl speeds, as predicted by the simplified Eq. (7.11). The effect on F_N (not captured by Eq. (7.10)) is a tilting of the curves, which indicates a slight damping effect (C_{xy}). Experiments (Sec. 7.5) will confirm this trend, but also show that its magnitude is grossly underpredicted. This has not been explained, and it is fortunate that F_N plays only a secondary role in rotor-dynamic problems. By contrast, the trends in F_T are confirmed quantitatively by the data. This illustrates one common theme found in our sensitivity studies: the important force component, F_T, is relatively insensitive to model parameter variations (except σ, W, and geometry), while the direct force F_N responds strongly to such variations, including K, frictional forces, and inlet nonuniformities. One view of this situation is that predicting F_N accurately will be in each case a difficult task, while one can hope to achieve this for both the static and the damping components of F_T. From a different perspective, it would seem that careful measurements of F_N can serve as sensitive and critical tests of future theoretical refinements.

Other sensitivities to various parameters are shown in Ref. [10], including those to driving pressure difference $P_i - P_o$ (practically a linear scaling), friction coefficients used, and geometrical modifications. Regarding the latter, it is of interest to notice that

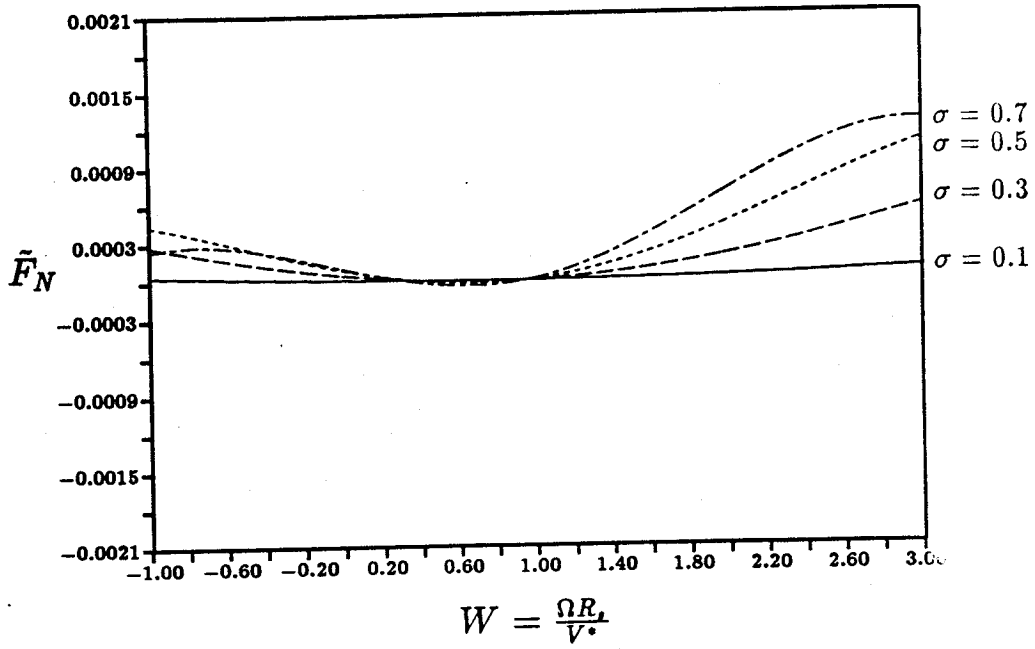

Figure 7.5: Nondimensional direct force, $\tilde{F_N}$, vs. the nondimensional whirling frequency, $W = \frac{\Omega R_s}{V^*}$, for σ=0.1, 0.3, 0.5, 0.7. All other parameters are the same as in the baseline case.

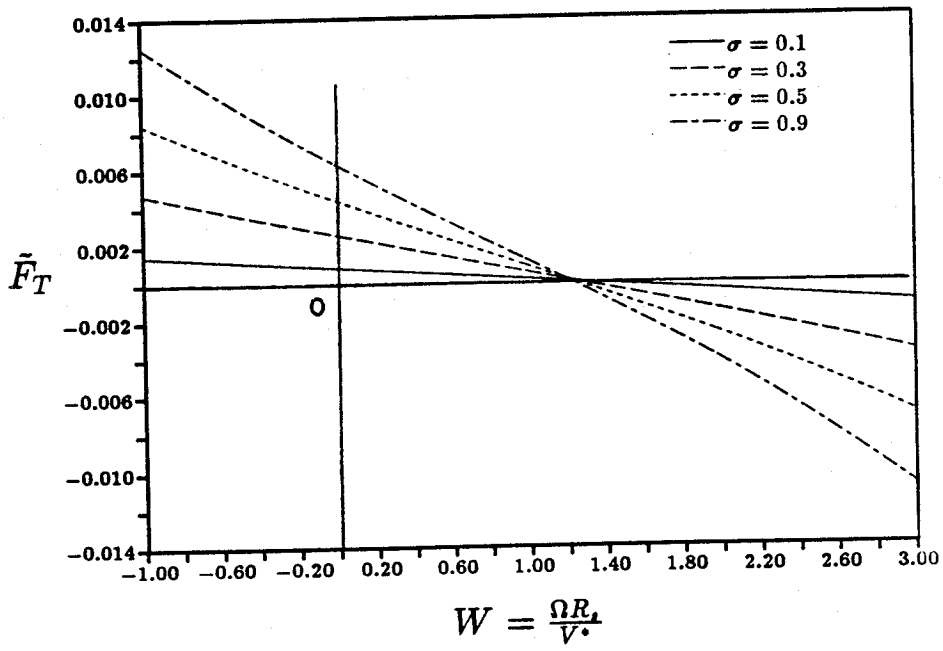

Figure 7.6: Nondimensional cross force, $\tilde{F_T}$, vs. whirling frequency, $W = \frac{\Omega R_s}{V^*}$ for σ=0.1, 0.3, 0.5, 0.7. All other parameters are the same as in the baseline.

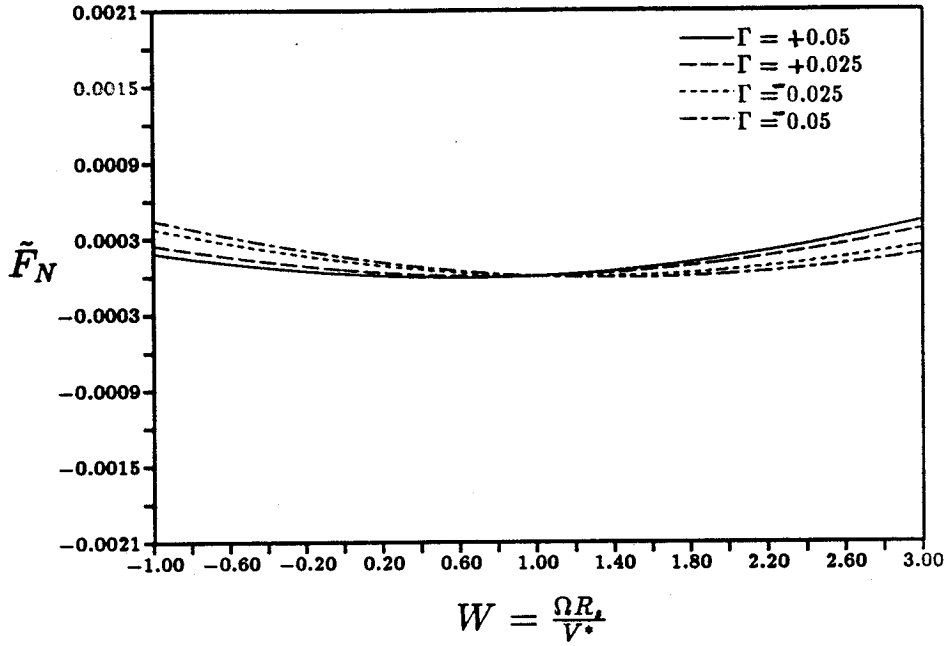

Figure 7.7: Nondimensional direct force, $\tilde{F_N}$, vs. the nondimensional whirling frequency, $W = \frac{\Omega R_s}{V^*}$, for Γ=-0.05, -0.025, 0.025, 0.05. All other parameters are the same as in the baseline case.

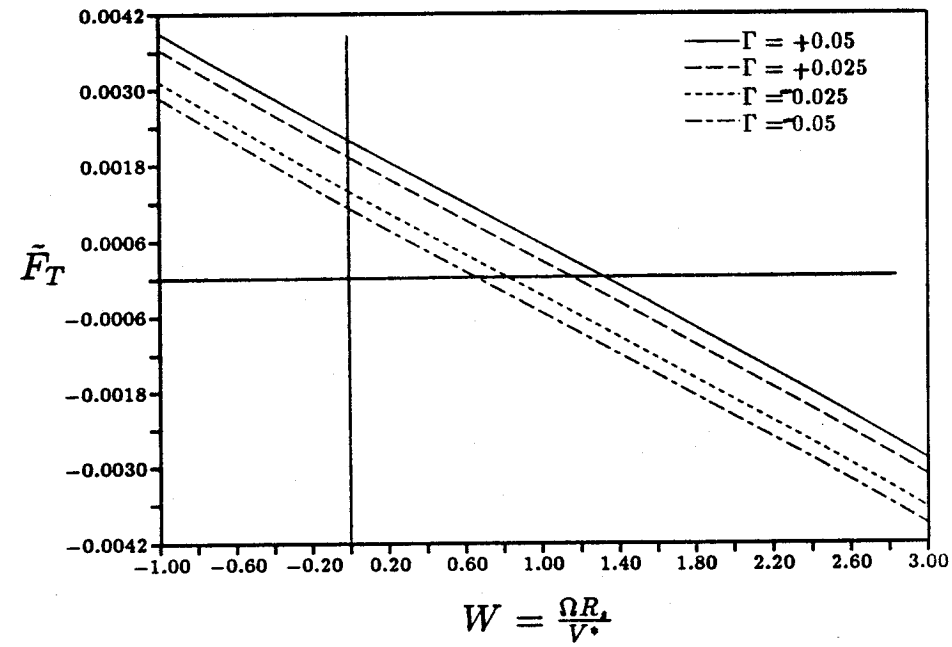

Figure 7.8: Nondimensional cross force, $\tilde{F_T}$, vs. the nondimensional whirling frequency, $W = \frac{\Omega R_s}{V^*}$, for Γ=-0.05, -0.025, 0.025, 0.05. All other parameters are the same as in the baseline case.

the simplified Eq. (7.11) indicates that the cross-force component due to mass storage effects (the main part in our baseline case) scales roughly as the group $\frac{g}{1+g^2}$, where $g = \frac{2\mu_1 D}{L} = \frac{2\mu_1 \delta_1^* R_s}{l_i h_i}$. This shows that the cross-forces will be largest at g = 1, and will be smaller for either deeper or shallower cavities than this. In our baseline case, g ≅ 1.44.

The upstream cavity can have a large effect on the rotordynamic forces. The parameters that characterize the influence are:

1. The ratio of the swirl cavity area to the seal gland area, $l_i h_i / l h_1$.
2. The relative size of the axial sealing gap, δ_c^* / δ_1^*.
3. The swirl velocity inside the center cavity, V_c. This is strongly influenced by rotation of the seal disk.
4. The whirl eccentricity, $\hat{r}/\delta_1^*$. This is a purely non-linear effect. For the linear system, all of the forces are directly proportional to the whirl eccentricity.

Each of these effects will now be considered separately.

According to the model, if there is no leakage into the center cavity, the effect of the upstream coupling always acts to increase the magnitude of both the cross-stiffness and direct damping and in the same proportions. Figure 7.9 shows the ratio of the direct damping from the coupled model, with $\delta_c^* = 0$, to that of the uncoupled one for various swirl chamber to seal area ratios. As the swirl cavity area approaches zero, the predicted force augmentation does not vanish but approaches a value of 1.62. This residual effect in the absence of the first cavity is due to the condition imposed at the swirl vanes. In the simple model, V_i is constant. If, instead, the vanes are close coupled, a reduction in the gland pressure will bring in more flow and hence will induce a higher swirl component locally. The maximum increase in the cross-stiffness and direct damping over the uncoupled model is about 4.42 and occurs at an area ratio, $l_i h_i / l h_1$, of 1.35. Evan at an area ratio of 10, the forces are increased by a factor of

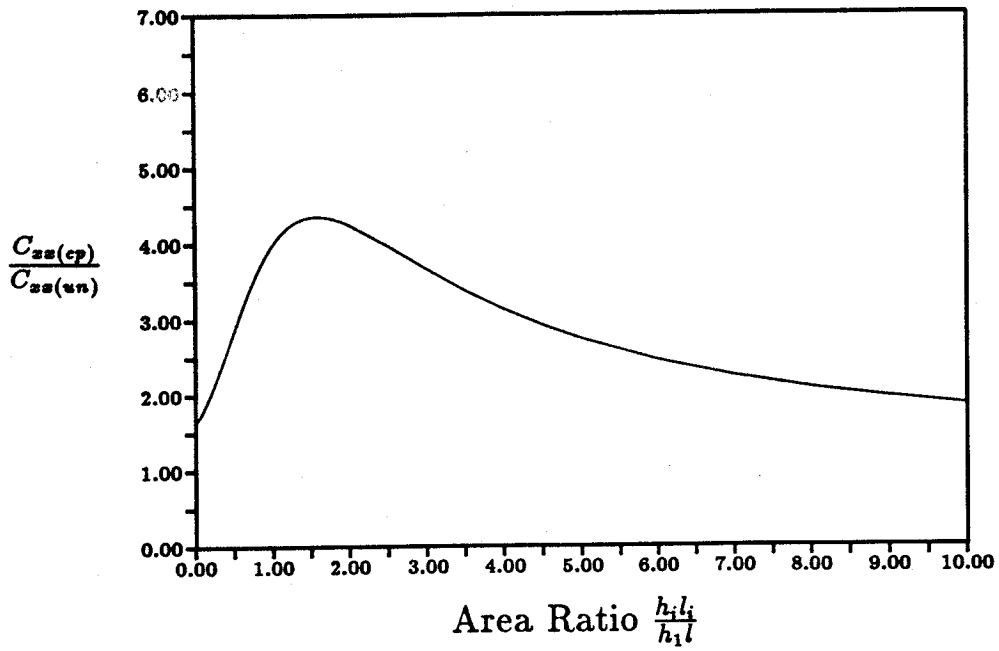

Figure 7.9: Ratio of direct damping with upstream coupling to that with no coupling vs. swirl cavity to seal gland area ratio. The maximum occurs ≈ 1.35 and the damping ratio comes to within 1% at a area ratio of 75.

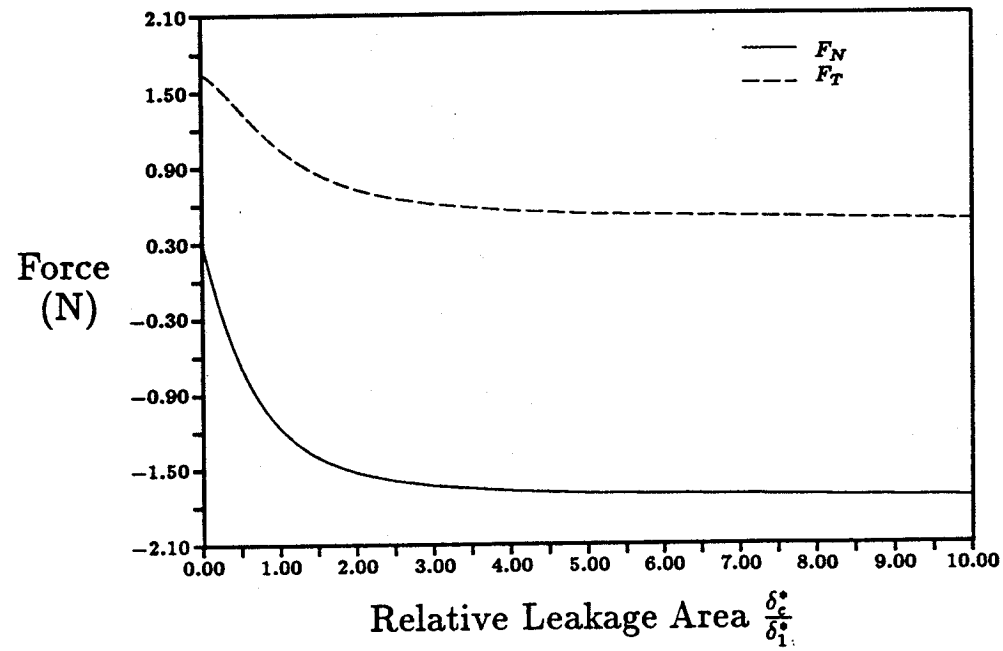

Figure 7.10: Predicted direct and cross force at $\Omega = 0$ from the fully coupled model vs. the relative axial clearance ratio, $\frac{\delta_c^*}{\delta_1^*}$. The geometry is the same as for build #3. π_s=1.4, $\alpha_v = 15°$, $\epsilon_1 = 0.1407$ and $\omega = 0$.

two. The force predicted by the coupled model asymptotically approaches the uncoupled one as $l_i h_i / l h_1 \rightarrow \infty$. The two match within 1% for an area ratio of 80. Well before this value, the assumptions of the model probably break down. In particular, significant variations in the perturbation quantities are likely to occur in the axial direction within the swirl cavity.

The presence of the axial clearance between the swirl cavity and the large center volume permits for a "venting" that reduces the magnitude of $\hat{\xi}_i$. This effect tends to mitigate the large augmentation of the forces that the upstream cavity may induce. Figure 7.10 shows the direct and cross-force vs. the relative leakage area, δ_c^*/δ_1^*. It is assumed that $V_c^* = V_i^*$ for simplicity. As δ_c goes from $0 \rightarrow \infty$, both force components go from the fully coupled value to those predicted by the uncoupled model. However, this does not occur when $V_c \neq V_i^*$. The forces are very sensitive to small changes in the axial gap when it is less than δ_1. However, when $\delta_c^*/\delta_1^* > 1$, there is a greatly reduced sensitivity to small changes in axial gap.

The model predicts that the swirl velocity inside the center volume can have a major impact on the seal pressure perturbations. For cases where there is no seal rotation, it is probably safe to say that $V_c^* = 0$. This is because the tangential momentum fed into the seal is of perturbation order and the shear stresses acting to retard the flow are O(1). For cases with seal rotation, it would be difficult to estimate the swirl velocity inside the center cavity. Figure 7.11 shows the effect that changes in the center cavity swirl velocity have on the forces.

In the absence of the leakage flow nonlinearity, the theory predicts that the forces should scale with whirl eccentricity and hence the rotordynamic coefficients, K_{ij}, C_{ij}, and M_{ij}, should be independent of the whirl amplitude. In the coupled model, the nonlinearity of the venting rate (Eqs. (7.26), (7.27)) changes this, and the stiffnesses are now functions of the offset amplitude. Figure 7.12 shows K_{xx} and K_{xy} vs. the relative eccentricity $\hat{r}/\delta_1^*$. The behavior of C_{xx} is the same as for K_{xy}. The direct force

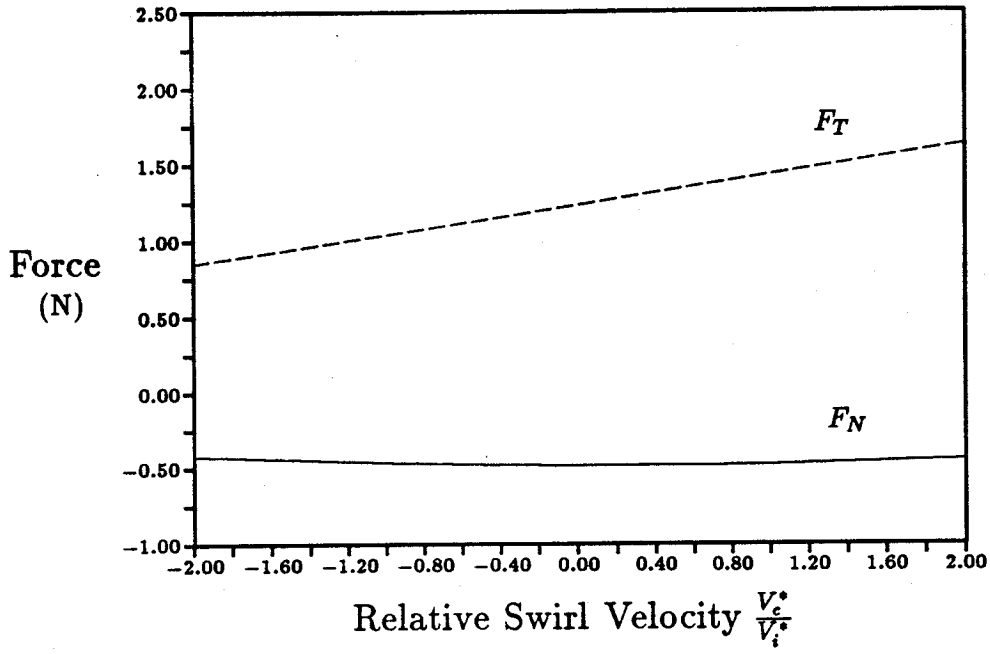

Figure 7.11: Direct and cross force predicted by the coupled model vs. center cavity swirl velocity. This is for the geometry of build #3, π_s=1.4, $\alpha_v = 15^o$, $\frac{\delta_c^*}{\delta_1^*} = 0.3702$ and $\omega = 0$.

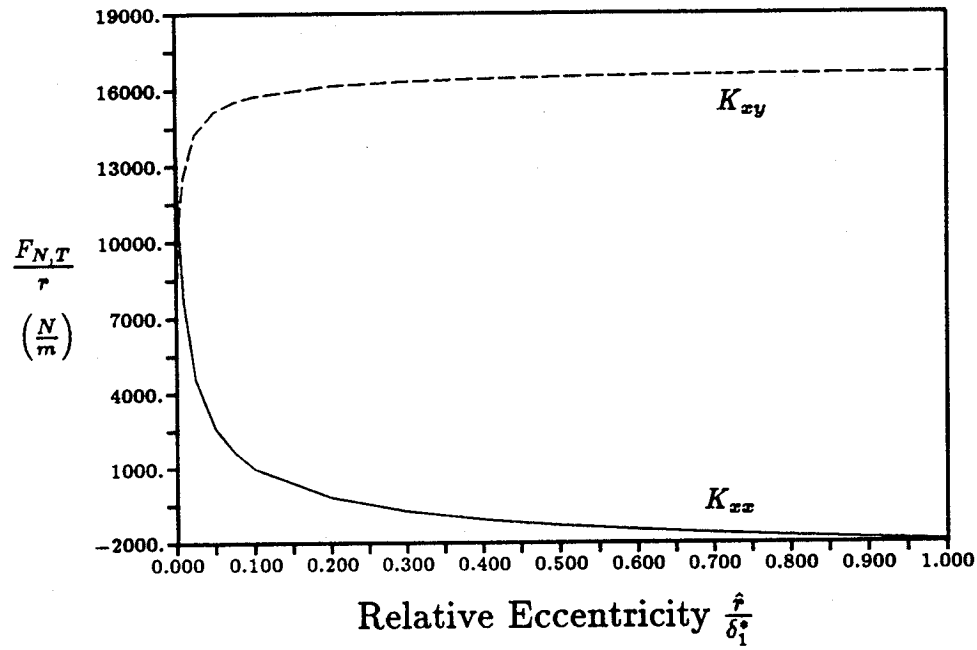

Figure 7.12: Effect of relative whirl amplitude, $\frac{\hat{r}}{\delta_1^*}$ on the direct and cross stiffnesses as predicted by the fully coupled model. Build #3 geometry π_s=1.4, $\alpha_v = 15^o$, $\omega = 0$ and $\frac{\delta_C^*}{\delta_1^*}$ = 0.1852.

is much more sensitive to the whirl amplitude than is the cross-force. At large whirl amplitudes, the predicted forces approach those obtained for $\delta_c^* = 0$ (i.e. the fully coupled case). However, as $\hat{r} \rightarrow 0$, the center leakage flow is able to "kill" the swirl cavity pressure perturbation at a faster rate than $1/\hat{r}$. This effectively decouples the whirling seal from the upstream cavity, and one recovers the results of the uncoupled model as $\hat{r} \rightarrow 0$.

7.5 Experimental Results

7.5.1 Survey of Selected Detailed Data

Builds 3 and 4 were selected for discussion of data in some detail. These are both "long" seals (l = 1.7 cm), Build 3 with smooth land, and Build 4 with a honeycomb land. The complete data set for Builds 2 through 5 (Build 1 was superseded by Build 2) is contained in Ref. [10]. This includes additional Builds 3 and 4 data not shown here. A more generalized data presentation, with less detail, will follow in Sec. 7.5.2.

The general format for this section will be dimensional plots of normal and tangential forces (in Newtons) vs. whirl frequency (rad/sec), with several other parameters being varied. The forces are themselves the result of integrations on the measured pressure nonuniformity patterns, as discussed in Sec. 2.2 and Ref. [4].

In the absence of inlet swirl, the theory of Sec. 7.2 showed that the cross-force F_T must be zero. This is true at $\Omega = 0$ (no whirl), but once whirl is introduced the damping component does produce cross-force. With reference to Eq. (7.11), the product σW is non-zero when V*, and hence σ, to go zero, because V* appears in the denominator of $W = \Omega R_s/V^*$. Experimentally, this is shown in Fig. 7.14. The force F_T is indeed zero at $\Omega = 0$, but it is seen to vary linearly with whirl. The increase with seal pressure ratio is also apparent. Since discharge was to atmosphere, increasing pressure ratio directly increases the driving pressure difference $P_i - P_o$.

In contrast to the strong dependence of F_T on inlet swirl and whirl rate, we saw

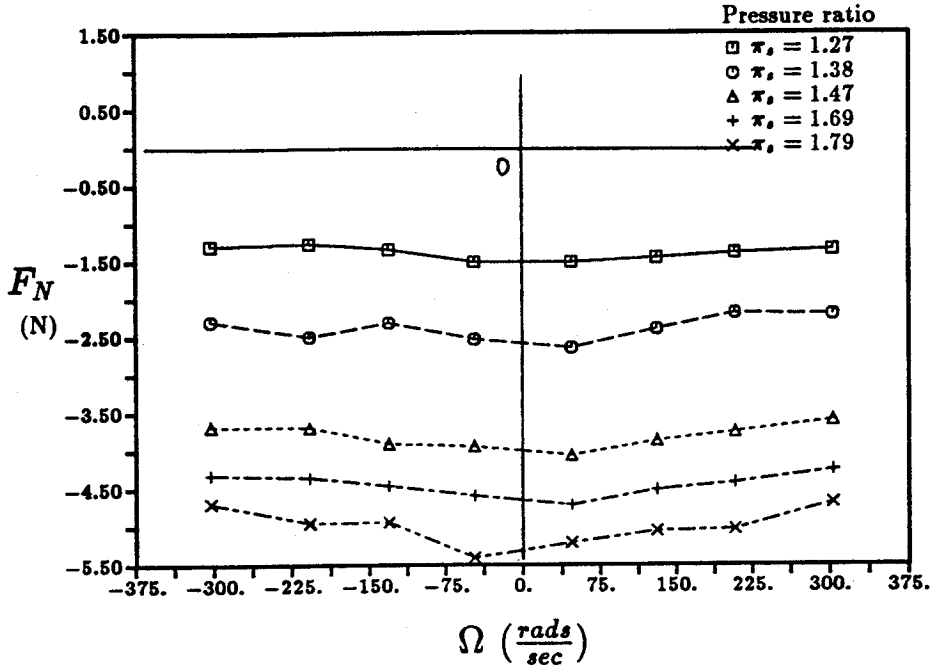

Figure 7.13: Experimentally obtained direct force, F_N, vs. the whirl frequency, for five different inlet pressures, π_s =1.27, 1.38, 1.47 1.69 and 1.79. These data are from build #3 with 0° inlet swirl and $\omega = 0$.

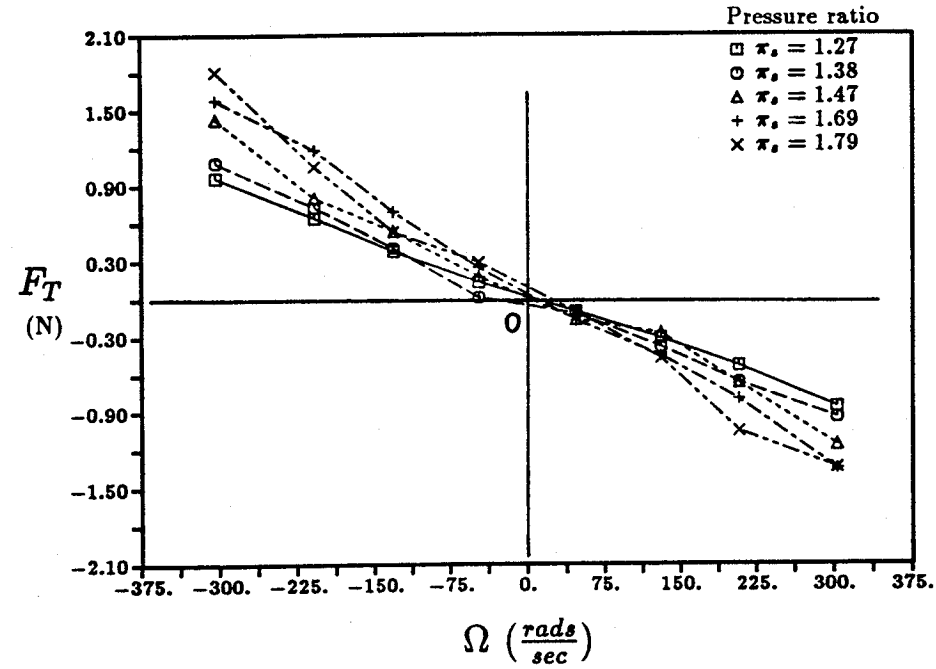

Figure 7.14: Experimentally obtained cross force, F_T, vs. the whirl frequency, for five different inlet pressures, π_s =1.27, 1.38, 1.47, 1.69 and 1.79. These data are from build #3 with 0° swirl and $\omega = 0$.

in Sec. 7.2 that the direct force (due mainly to the carryover variation effect) should be basically independent of both, and should be negative. The data in Fig. 7.13 confirm this. Even with no inlet swirl, the restoring force is present, and it does not vary appreciably with Ω. It also scales with pressure differential, i.e. with π_s - 1.

Figures 7.15 and 7.16 show the effects of spin still at zero inlet swirl. There is some evidence of a slight increase in the cross-force F_T with spin in the negative direction (which should promote the flow twist represented by $\Gamma = V_i/V^* - 1$), but the effect is small, as indicated by theory when the inlet swirl is zero. By contrast, the effect on the direct force F_N is much stronger than predicted by theory (Sec. 7.2), illustrating the general sensitivity of direct forces to various parametric variations.

For a small, but nonzero, amount of inlet swirl (produced by the 15° holes), Fig. 7.18 shows the appearance of a cross-stiffness, i.e. a cross-force at zero whirl speed. The direct forces (Fig. 7.17) are now slightly sensitive to whirl and smaller than without swirl.

The effect of spin at this inlet swirl is shown in Figs. 7.19 and 7.20. Once again, the direct force F_N (Fig. 7.19) shows the introduction of substantial damping of this force (sensitivity to whirl) when spin is present. The effect of friction-induced flow twist is now clearly visible in the cross-forces (Fig. 7.20). This can be compared to the theoretical results shown in Fig. 7.8. Clearly, spinning in a direction contrary to the inlet swirl increases the cross-stiffness without affecting the damping (sensitivity to whirl). The opposite happens when the spin is in the same sense as the inlet swirl, and the sensitivity to spin is actually greater in this direction.

Similar results, but at a higher inlet swirl angle, are shown in Figs. 7.21 and 7.22. The general level of the cross-forces is now higher, and so is also the sensitivity to spin, which appears to be symmetric in this case.

A great deal of effort went into characterizing the effect that honeycomb lands have on the rotordynamic forces. The complete theoretical model [10] includes an

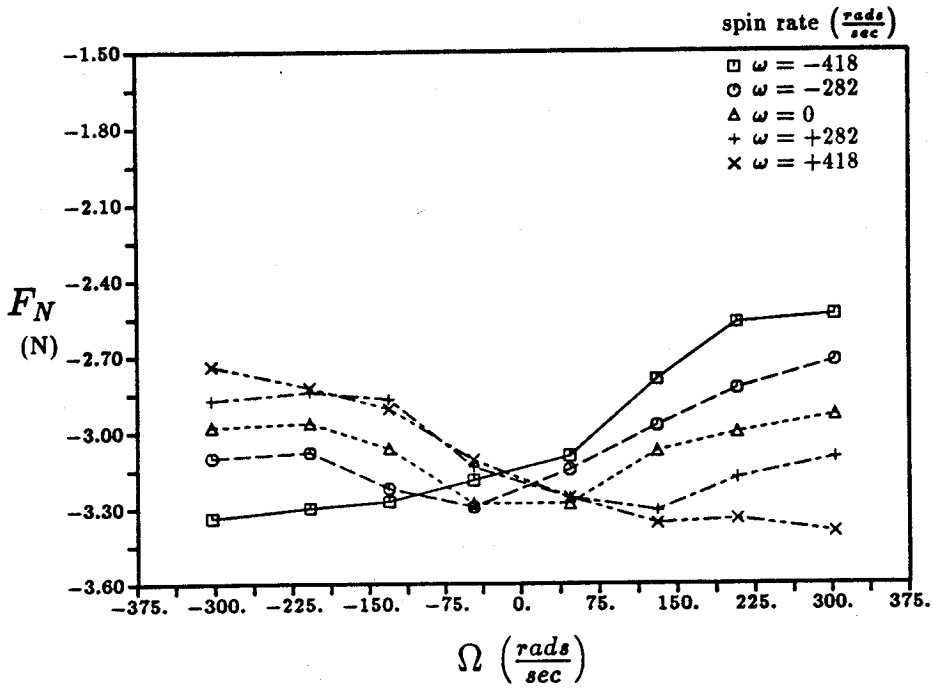

Figure 7.15: Experimentally obtained direct force, F_N, vs. the whirl frequency for five different spin rates, $\pi_s = 1.47$. These data are from build #3 with 0° inlet swirl.

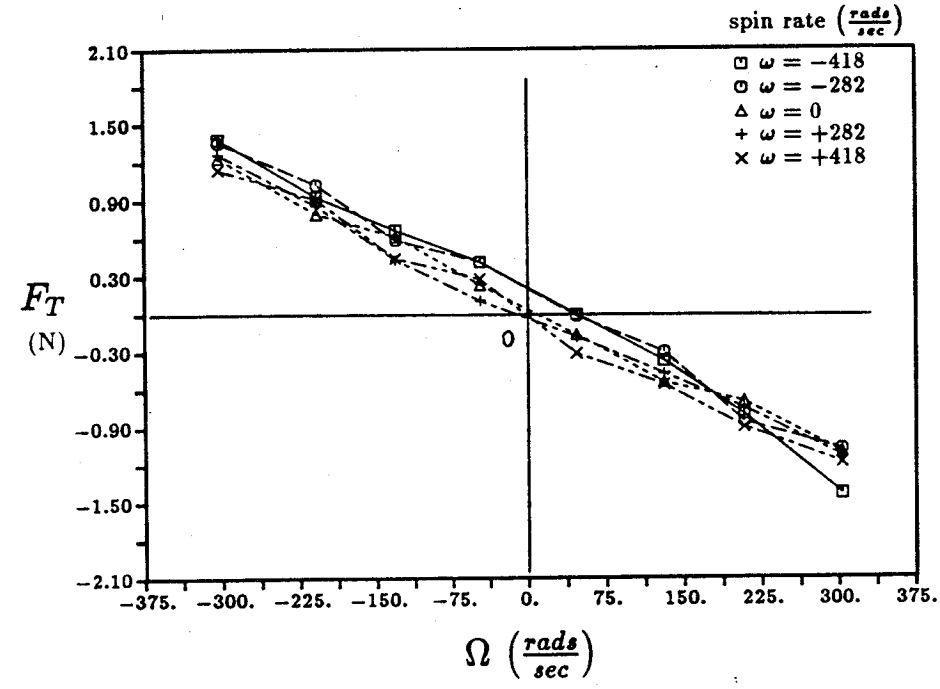

Figure 7.16: Experimentally obtained cross force, F_T, vs. the whirl frequency, for five different spin rates, $\pi_s = 1.47$. These data are from build #3 with 0° inlet swirl.

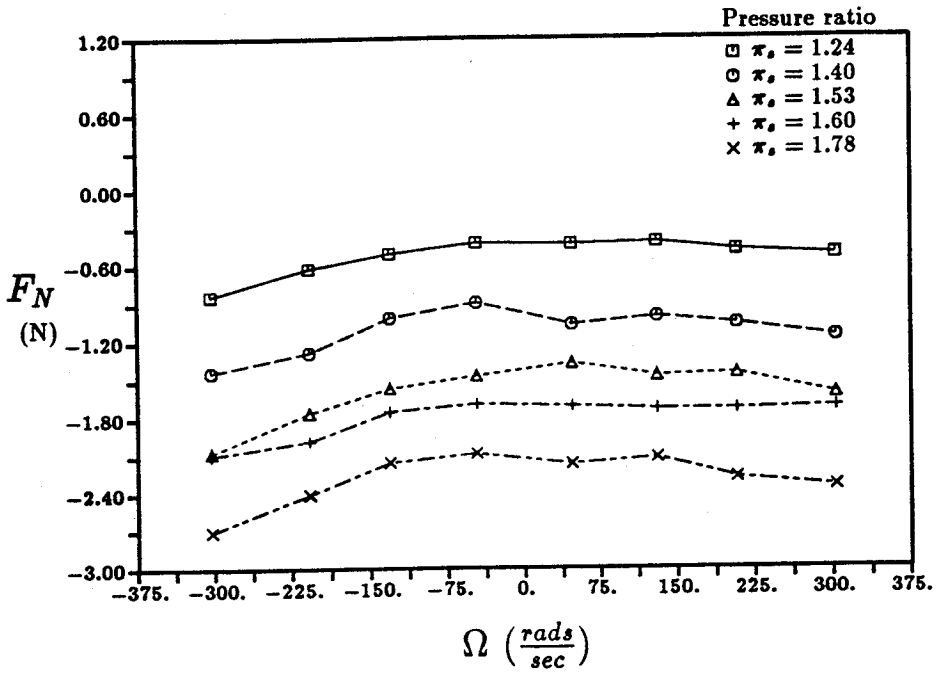

Figure 7.17: Experimentally obtained direct force, F_N, vs. the whirl frequency for five different pressure ratios. These data are from build #3 with 8.6° inlet swirl and $\omega = 0$.

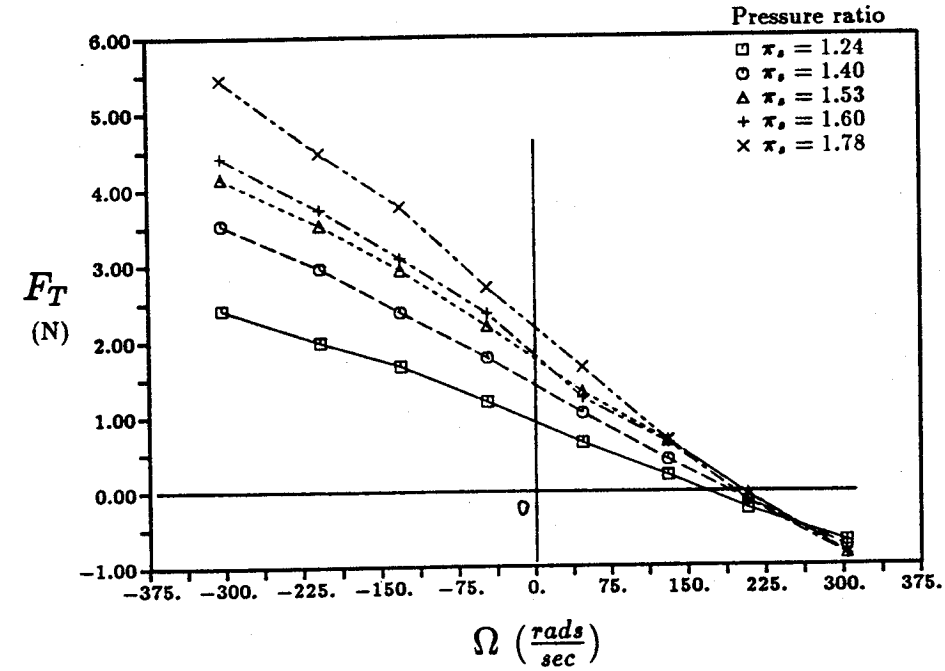

Figure 7.18: Experimentally obtained cross force, F_T, vs. the whirl frequency, for five different pressure ratios. These data are from build #3 with 8.6° inlet swirl and $\omega = 0$.

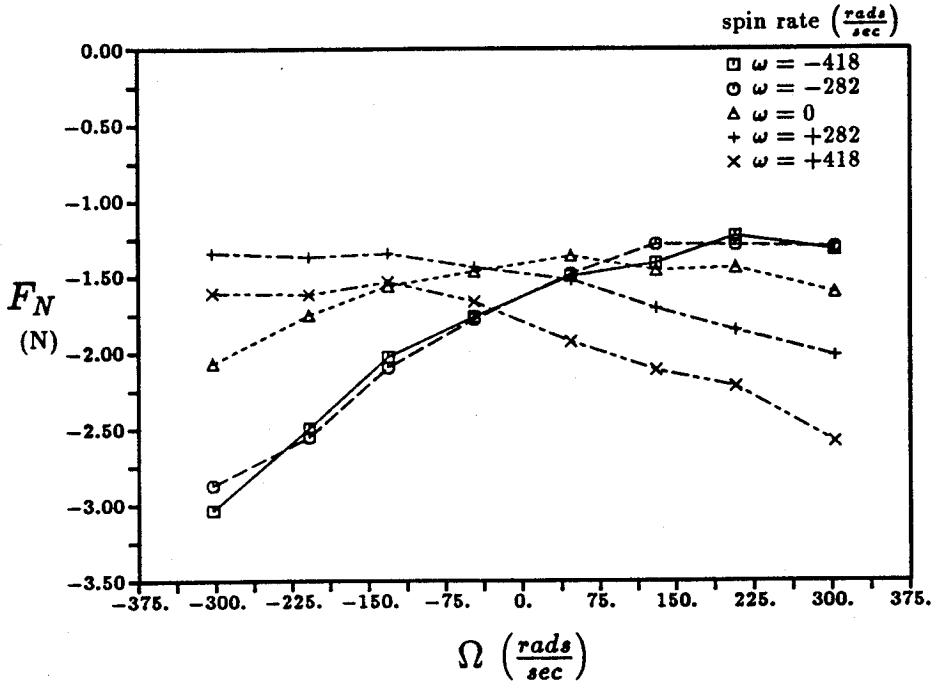

Figure 7.19: Experimentally obtained direct force, F_N, vs. the whirl frequency for five different spin rates, $\pi_s = 1.53$. These data are from build #3 with 8.6° inlet swirl.

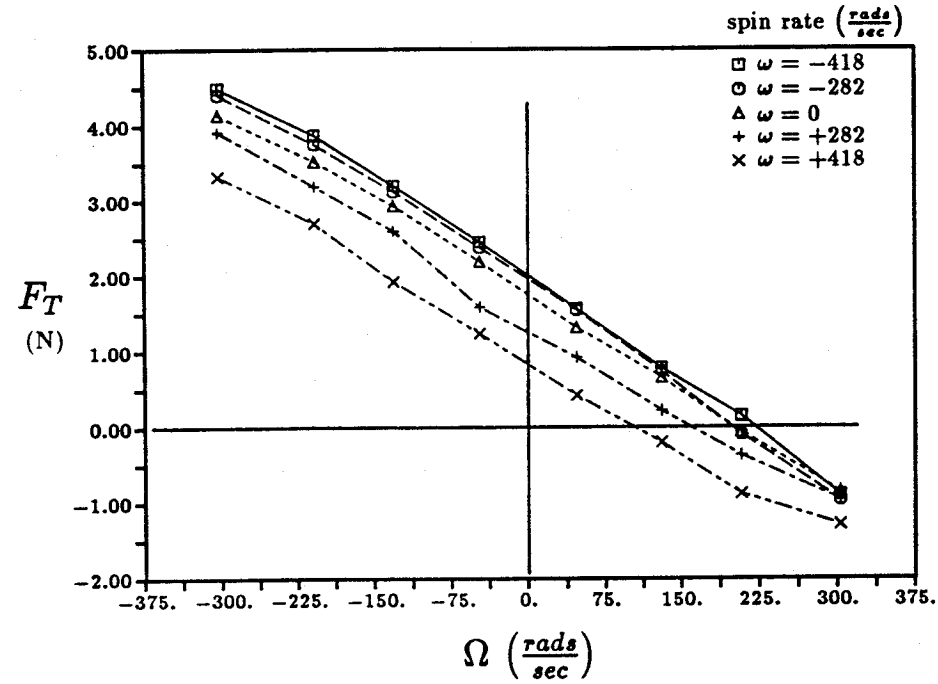

Figure 7.20: Experimentally obtained cross force, F_T, vs. the whirl frequency, for five different spin rates, $\pi_s = 1.47$. These data are from build #3 with 8.6° inlet swirl.

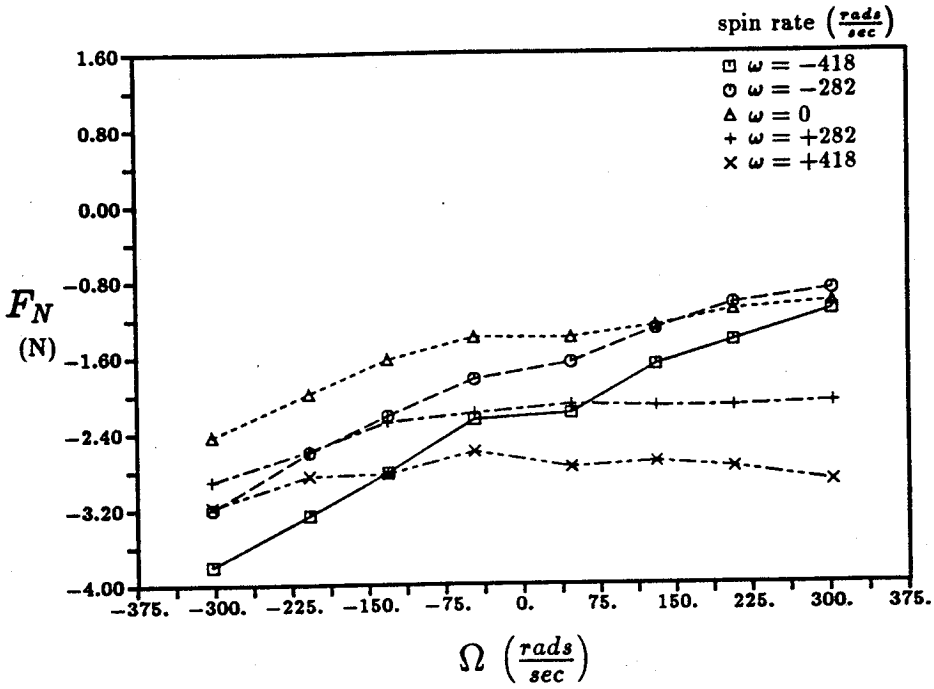

Figure 7.21: Experimentally obtained direct force, F_N, vs. the whirl frequency for five different spin rates, $\pi_s = 1.55$. These data are from build #3 with 21.4° inlet swirl.

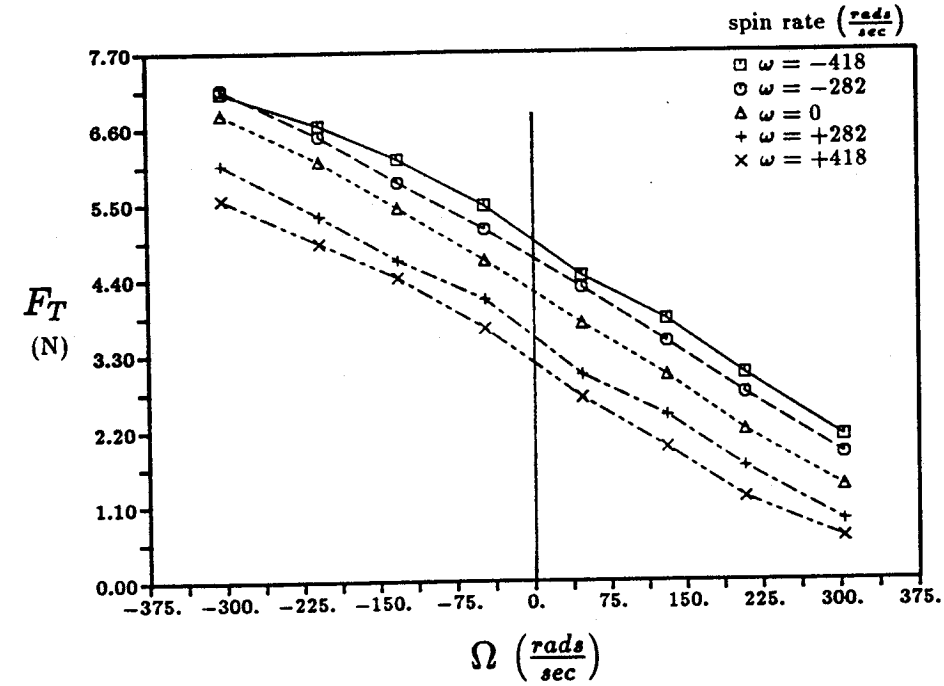

Figure 7.22: Experimentally obtained cross force, F_T, vs. the whirl frequency, for five different spin rates, $\pi_s = 1.55$. These data are from build #3 with 21.4° inlet swirl.

unsteady mass storage term due to the volume of the honeycomb cells, and it predicted a 3% reduction in cross-force at the highest frequency when the honeycomb depth was five times that of the gland seal. On the other hand, the data (with honeycomb depth close to the gland depth) indicated reductions in the 10-30% range. This effect was strongest for the longer seal (Build 5), but even for the short (1 cm) seal, comparison of Builds 2 and 5 shows a cross-force decrease of about 10%. This difference is, however, of the same order as the overall scatter in the data, so that, although the effect seems systematic, the level of confidence is not high.

Two possible explanations exist for the cross-force reduction: (a) The honeycomb acts as a swirl brake. This would have to occur preferentially ahead of the gland, where the area covered with the honeycomb is very small. On the other hand, this action would be of importance for multi-cavity seals. (b) The honeycomb breaks up the jet from the first seal gap, and reduces or destroys the carryover (or at least its sensitivity to gap width). According to the predictions of the model, totally eliminating the carryover sensitivity K would reduce the cross-force by about 17% in Build 3. This is of the order measured, suggesting a nearly total cancellation of the carryover. Some support for this interpretation comes from the measured discharge coefficient of the second seal gap, which was 0.85 for the smooth land (Build 3), but only 0.75 with honeycomb (Build 5).

In contrast with these small changes in the cross-force, the direct force was dramatically altered by the honeycomb land, to the point of reversing its sign. Once again, this points at a disruption of the jet carryover, which is the only major source of direct forces in our case. However, the sign reversal cannot be easily explained in these terms. Given the strong sensitivity of direct forces to the assumed face seal clearance in the pre-seal plenum, it is possible that part of the changes may be due to differences in this clearance between assemblies (this effect was not suspected, and no precise control was kept of the axial clearance).

Figures 7.23 and 7.24 illustrate the above discussion. These are for Build 4 (honeycomb) with zero inlet swirl and no spin, and should be compared to Figs. 7.13 and 7.14 where the land was smooth. The reversal (but with relatively small magnitudes) of F_N is most noticeable. Also visible is the ~25% reduction of F_T at comparable pressure ratios.

The behavior of the cross-forces in Build 4 vs. inlet swirl and vs. spin is comparable to that described for Build 3 (see the extensive data plots in Ref. [10]).

The effects of honeycomb land on the shorter seal (Builds 2 and 5) are less strong than on the long seal, again pointing at an effect in the first gap jet. We illustrate this here with a comparison between both components of force measured on Build 2 (smooth land) and in Build 5 (honeycomb), in both cases at zero inlet swirl and zero spin. Figures 7.25 and 7.26 show the results for the smooth land, and Figs. 7.27 and 7.28 for the honeycomb land. In this case (after accounting for the different clearances, $\hat{r}$), the direct force and the cross-force are cut by about 10% only by the honeycomb.

7.5.2 Non-Dimensional Data and Comparisons to Theory

For more compact presentation, the force data were reduced to the form of stiffness and damping coefficients. Since the F_N data showed significant curvature when plotted vs. whirl, a direct effective mass coefficient was also extracted. This was not necessary for the cross-forces, where the curves were linear:

$$\frac{F_N}{\hat{r}} = -K_{xx} - C_{xy}\Omega + M_{xx}\Omega^2 \tag{7.29}$$

$$\frac{F_T}{\hat{r}} = K_{xy} - C_{xx}\Omega \tag{7.30}$$

Both stiffnesses are nondimensionalized as

$$K_{ij}^{**} = \frac{K_{ij}\delta_1^*}{l\, R_s (P_i - P_o)} \tag{7.31}$$

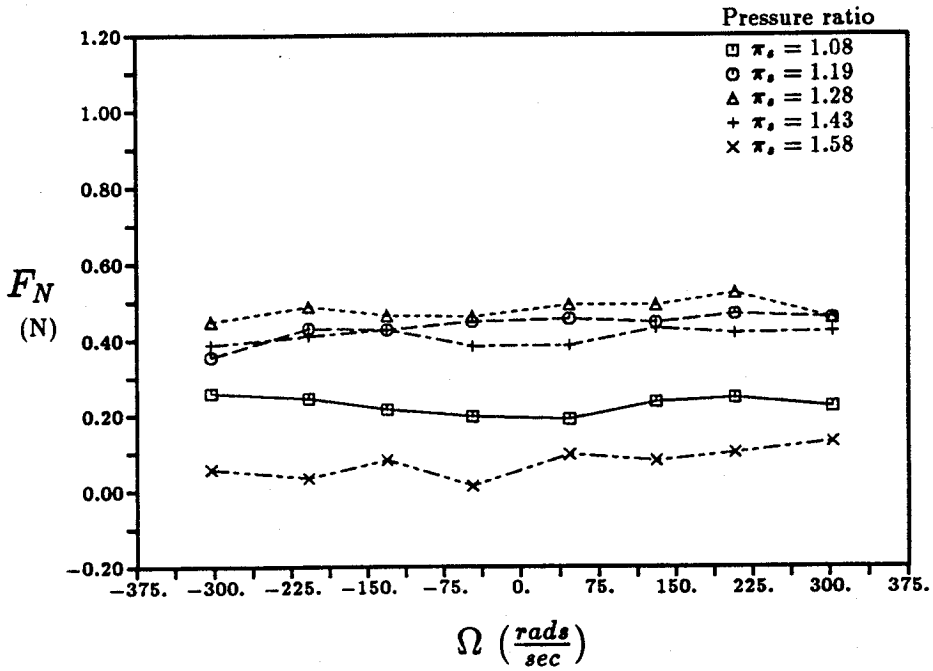

Figure 7.23: Experimentally obtained direct force, F_N, vs. the whirl frequency for five different pressure ratios. These data are from build #4 with 0° inlet swirl and $\omega = 0$.

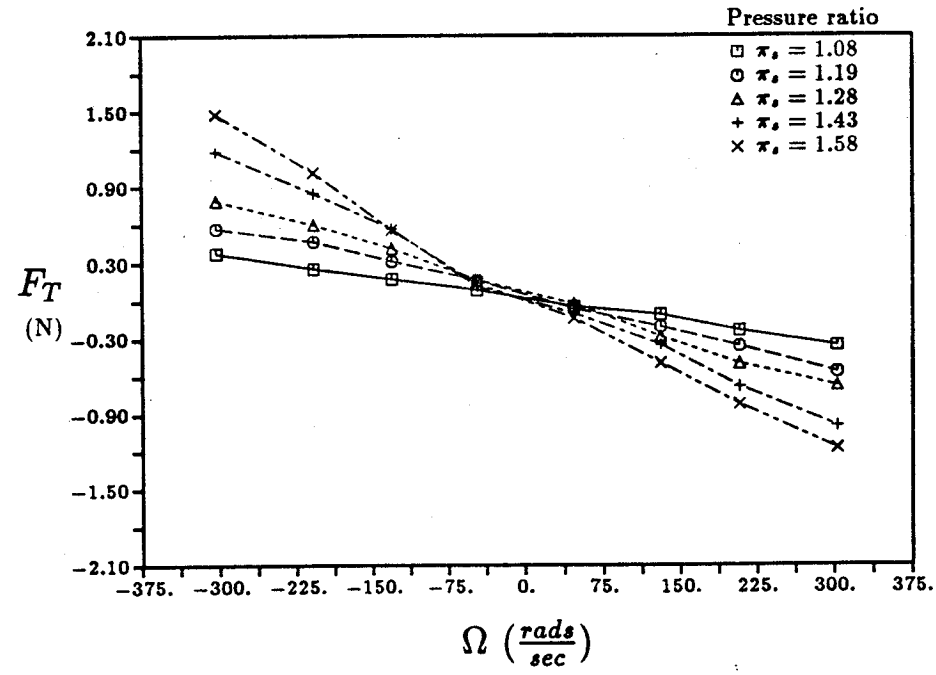

Figure 7.24: Experimentally obtained cross force, F_T, vs. the whirl frequency, for five different pressure ratios. These data are from build #4 with 0° inlet swirl and $\omega = 0$.

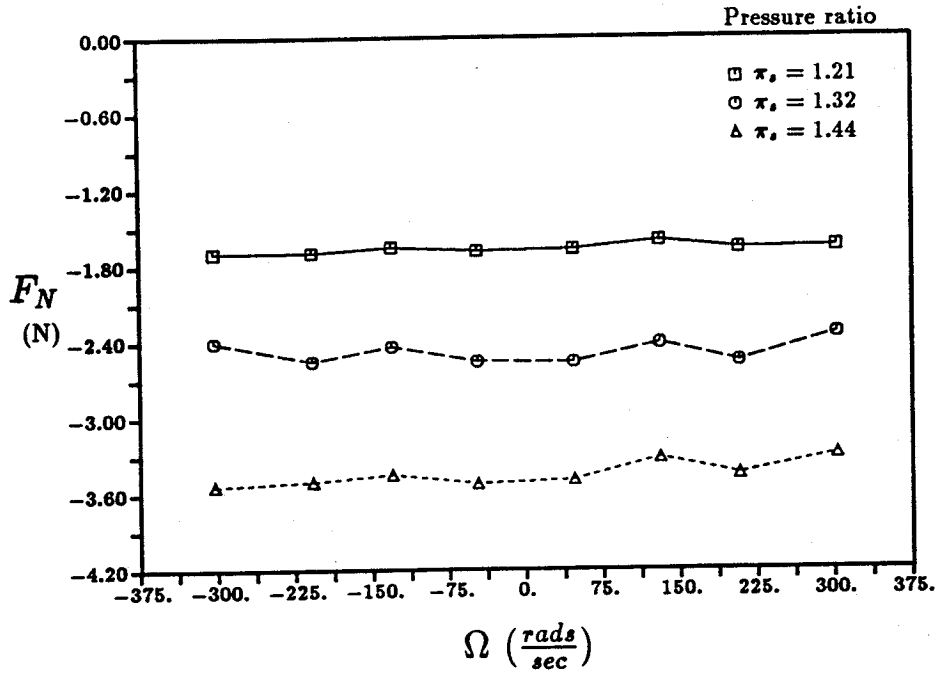

Figure 7.25: Experimentally obtained direct force, F_N, vs. the whirl frequency, Ω, for three different inlet pressures, π_s =1.21, 1.34 and 1.44. These data are from the second build with 0° inlet swirl and $\omega = 0$. $\hat{r}$ = 7.3 mil.

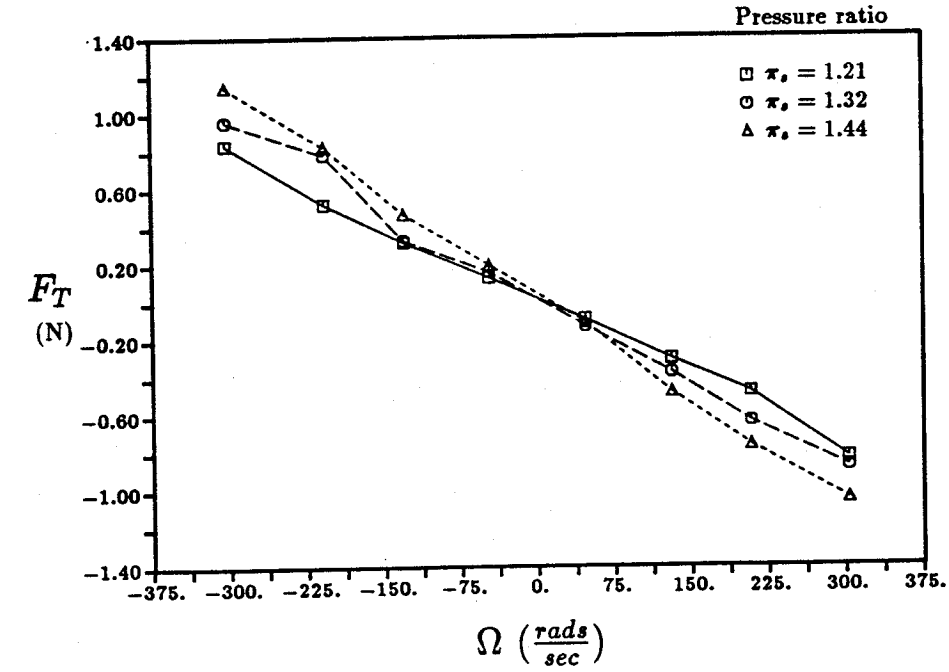

Figure 7.26: Experimentally obtained cross force, F_T, vs. the whirl frequency, Ω, for three different inlet pressures, π_s =1.21, 1.34 and 1.44. These data are from the second build with 0° inlet swirl and $\omega = 0$. $\hat{r}$ = 7.3 mil

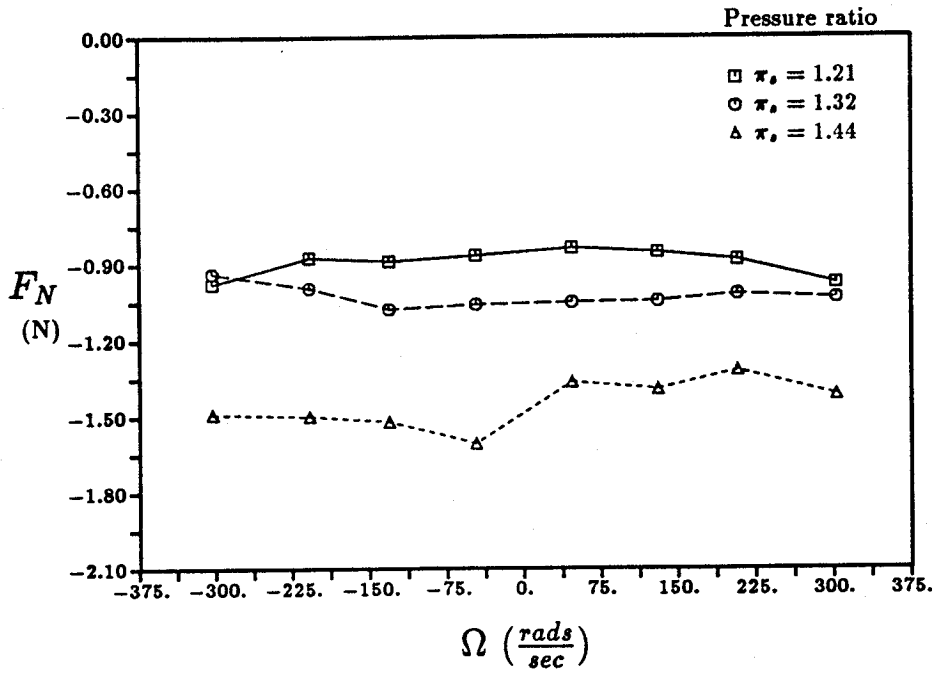

Figure 7.27: Experimentally obtained direct force, F_N, vs. the whirl frequency for three different pressure ratios. These data are from build #5 with 0° inlet swirl and $\omega = 0$. $\hat{r}$ = 3.8 mill

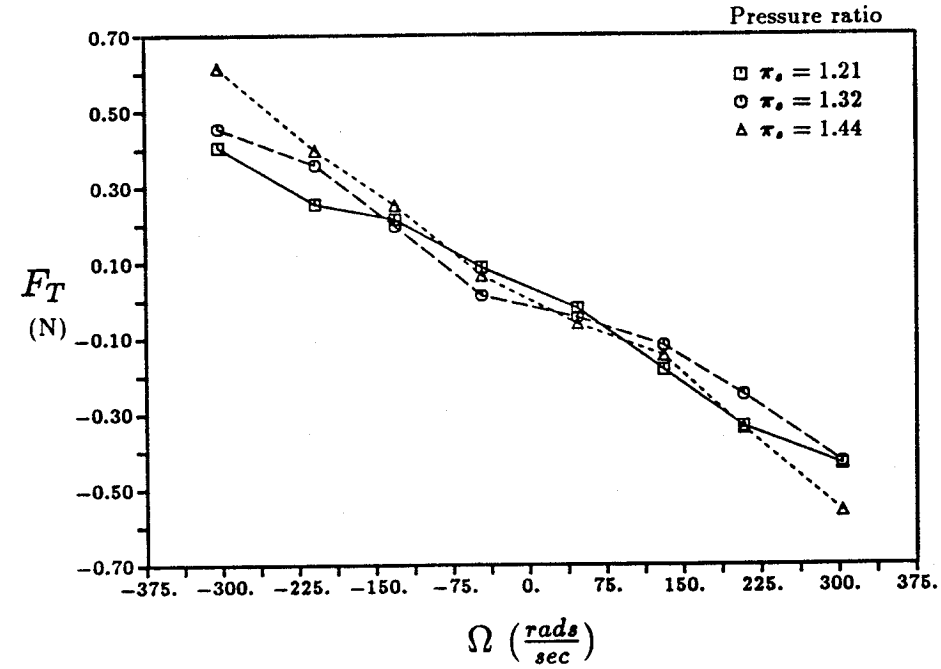

Figure 7.28 : Experimentally obtained cross force, F_T, vs. the whirl frequency, for three different pressure ratios. These data are from build #5 with 0° inlet swirl and $\omega = 0$. $\hat{r}$ = 3.8 mills

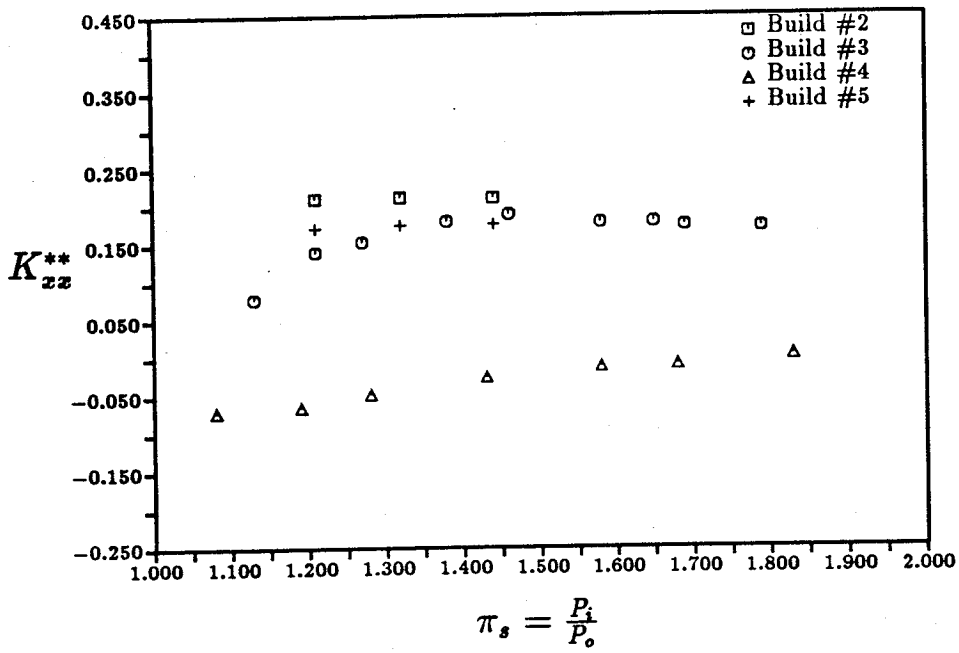

Figure 7.29: The effect of pressure ratio on the nondimensional direct stiffness coefficient, K^{**}_{xx}, for builds #2(narrow rotor-smooth land) , #3(wide rotor-smooth land), #4(wide rotor - honeycomb land) and #5(narrow rotor - honeycomb land). The inlet swirl for all cases is 0° and ϵ_1=0.1407.

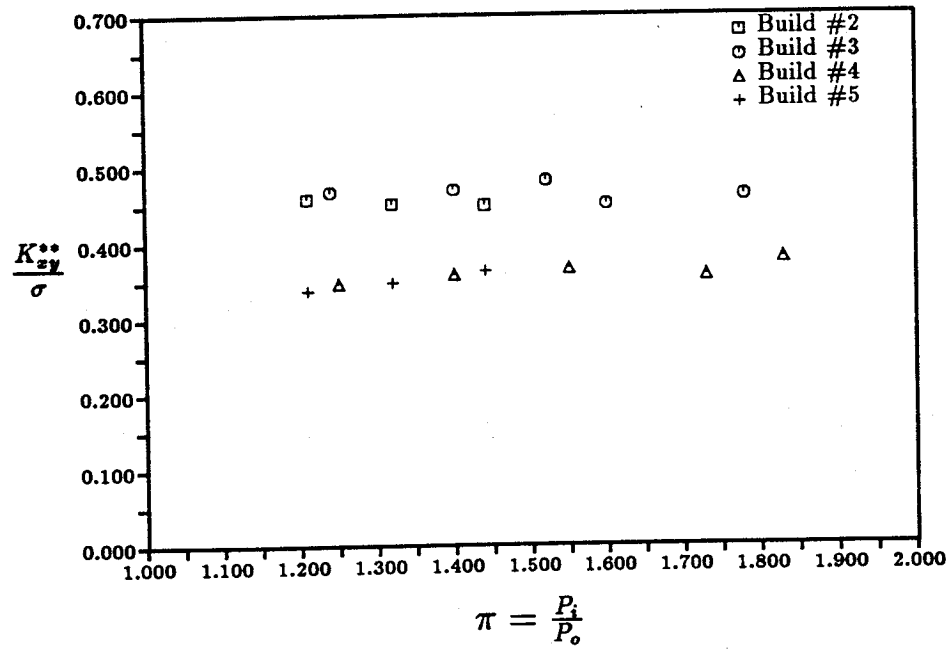

Figure 7.30: The effect of pressure ratio on the nondimensional cross stiffness coefficient, $\frac{K^{**}_{xy}}{\sigma}$ for build #2, #3, #4 and #5. All were taken with the 15° swirl orifice plate and ϵ_1=0.1407.

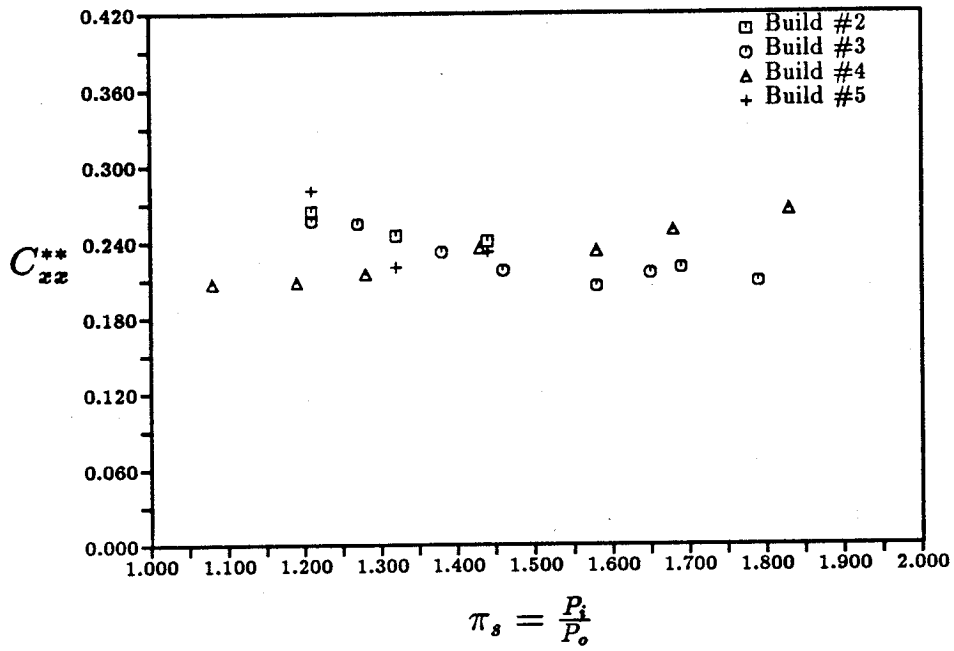

Figure 7.31: The effect of pressure ratio on the direct damping coefficient, C^{**}_{xx}, for builds #2(narrow rotor-smooth land) , #3(wide rotor-smooth land), #4(wide rotor - honeycomb land) and #5(narrow rotor - honeycomb land). The inlet swirl for all cases is 0° and ϵ_1=0.1407.

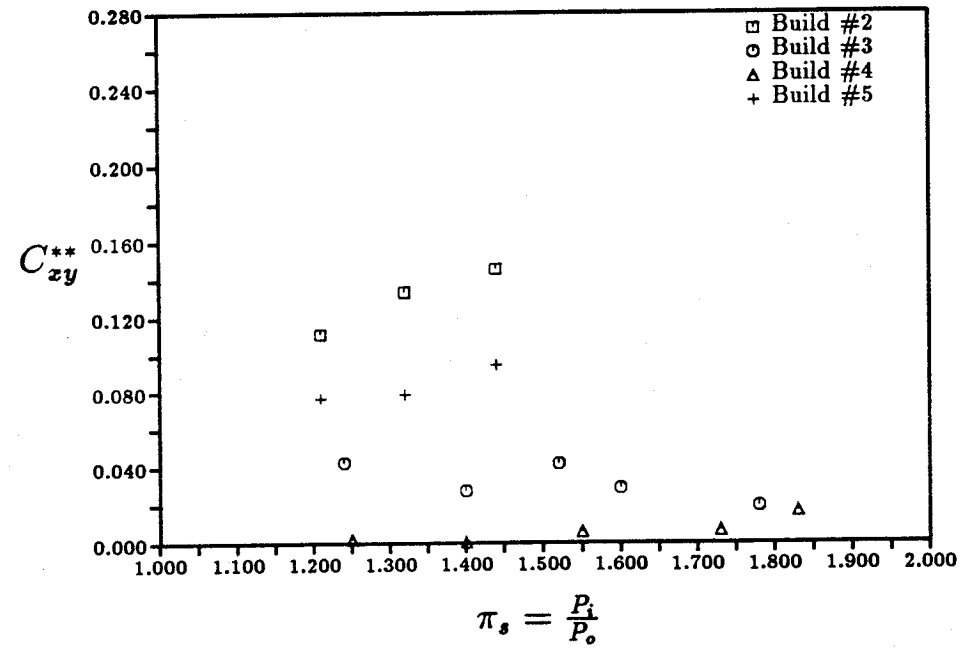

Figure 7.32: The effect of pressure ratio on the nondimensional cross damping coefficient, C^{**}_{xy} for build #2, #3, #4 and #5. All were taken with the 15° swirl orifice plate and ϵ_1=0.1407.

and the damping constants are nondimensionalized as

$$C_{ij}^{**} = \frac{C_{ij}\,\delta_1^*}{l\,R_s^2\,\sqrt{\rho_i\,(P_i - P_o)}} \tag{7.32}$$

The appropriateness of the P_i - P_o scalings is shown by Figs. 7.29 through 7.32, which present all these coefficients vs. pressure ratio for one particular hole plate angle case (15°). Only C_{xy}, which is of minor rotordynamic importance, is not well correlated. For the cross-stiffness K_{xy}, further collapsing was achieved by normalizing with the inlet swirl parameter σ, which was different for the different points plotted.

Similar degree of correlation was obtained for other vane or hole plate angles. However, the mechanical process of changing the rings carrying these vanes or holes appears to have allowed small, but significant, modifications in the uncontrolled axial seal gap δ_c (separating the pre-seal cavity from the hub volume). As a result, the degree of correlation among the various angle sets for each seal configuration is less satisfactory. This is shown in Fig. 7.34, where K_{xy}^{**} results for all vane angles and for all configurations are shown together. The groups of 3-4 data points appearing in clusters correspond to one particular ring insert, and the differences among points in any one cluster are due to changes in seal pressure ratio. In Fig. 7.34, each cluster of points for any one insert shows the expected proportionality with inlet swirl σ, but the coefficient does vary from cluster to cluster. Averaging over all the data, an approximate composite correlation gives

$$K_{xy}^{**} = 0.36\,\sigma \tag{7.33}$$

The lines drawn in Fig. 7.34 are the theoretical results for a range of assumed axial face seal gaps. This range extends from $\delta_c^* = \infty$ (the uncoupled case, where upstream nonuniformities vanish) to $\delta_c^* = 0$ (the fully coupled two-cavity limit). The nominal design value of $\delta_c^* = 10$ mils is shown, as well as several other δ_c^* values. The data points do cluster about the $\delta_c^* = 10$ mil line (which, in fact, agrees with Eq.

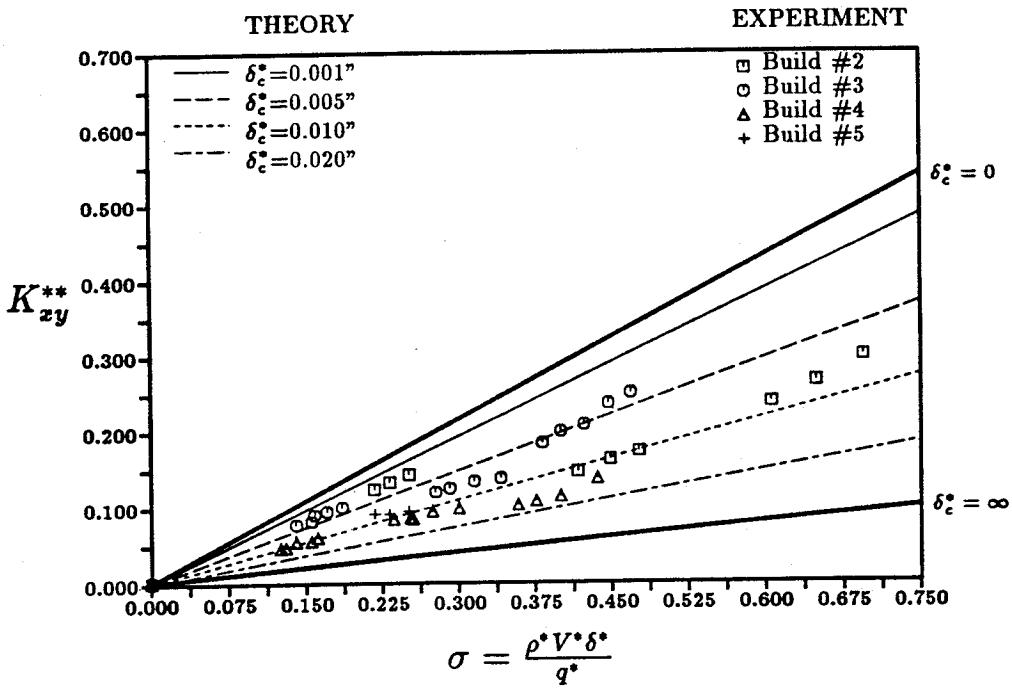

Figure 7.34: K_{xy}^{**} vs. σ for the experimental data and theory. The axial gap, δ_c^*, is used as a parameter. All experimental values fall between the theory with $0.004''(0.0001m) < \delta_c^* < 0.017(0.0004m)$.The top thick line is for full coupling (ie. no leakage). The bottom one is for uniform inlet conditions (ie. no coupling). The calculations are for build #3 geometry.

(7.33)) but, as noted, there are significant deviations.

Similar, but greater, scattering between assemblies is seen in the normal forces, Fig. 7.35 presents the normalized K_{xx}^{**} coefficients for all builds and all vane angles. As noted before, K_{xx} shows greater sensitivity to several parameters. For example, the data for Build 4 show a great deal of variation with seal pressure ratio within a particular assembly. This seems to be a reflection of varying carryover, exacerbated here by interference from the honeycomb land. The range of theoretical K_{xx}^{**} results obtained with various δ_c^* values is shown in Fig. 7.36. Here, the honeycomb land results exceed even the fully coupled limit, while the smooth land results fall near the uncoupled theoretical line. However, as noted, the difference here is most likely due to carryover effects rather than to δ_c^* variations.

The important damping coefficient, C_{xx}^{**}, correlates to about the same extent as K_{xy}^{**}, and is also predictable to a comparable extent from theory. Figure 7.37 shows the C_{xx}^{**} data for all builds. As discussed in Sec. 7.2, one important consequence of our elucidation of the mechanism for producing whirl-dependent cross-forces is the possibility of extracting C_{xx} from only static cross-force data. This is shown in Table 7.1, where the dynamically measured C_{xx}^{**} and the C_{xx}^{**} deduced from $\Omega = 0$ data are compared for all builds. The static method produces C_{xx}^{**} values which are 13-28% too high, an excellent agreement level considering the many separate measurements that went into the statically derived C_{xx}^{**}.

We close by commenting briefly on the application of our new understanding of upstream nonuniformity effects to the data of Benckert and Wachter (Ref. 28). This set of static data on various seal configurations has long been used as a benchmark for various theoretical efforts. Several researchers have reported agreement to within ±20% with their multi-cavity seal data (Refs. 29, 30, 31), but no model has been able to match their 2- and 3-cavity seal data. Benckert and Wachter report pressure nonuniformity levels in the first chamber of their seals which are 2-3 times higher than

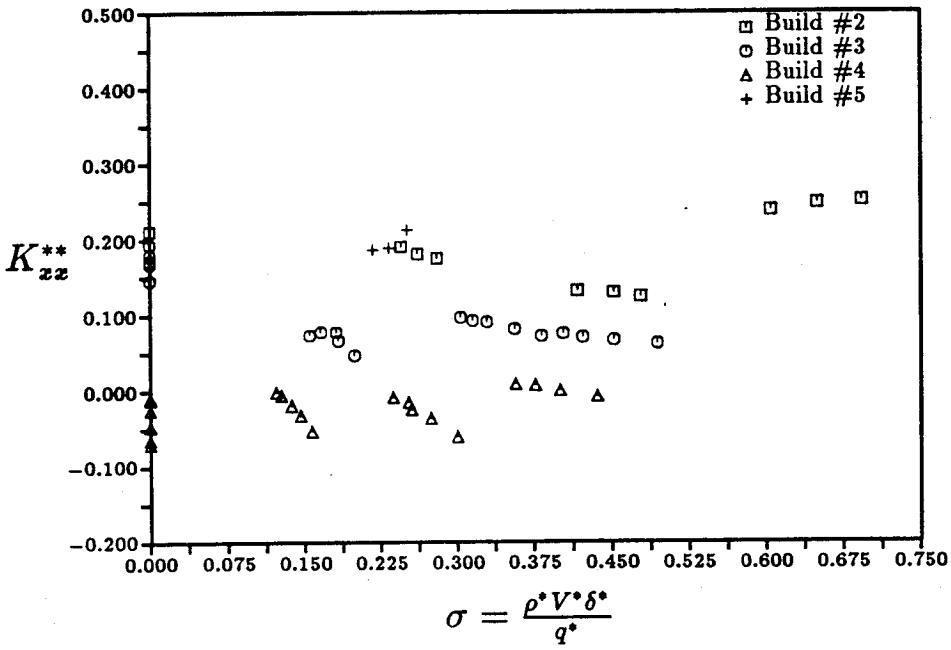

Figure 7.35: The effect of inlet swirl on the direct stiffness coefficient, K_{xx}^{**}, for builds #2(narrow rotor-smooth land) , #3(wide rotor-smooth land), #4(wide rotor - honeycomb land) and #5(narrow rotor - honeycomb land). ϵ_1=0.1407.

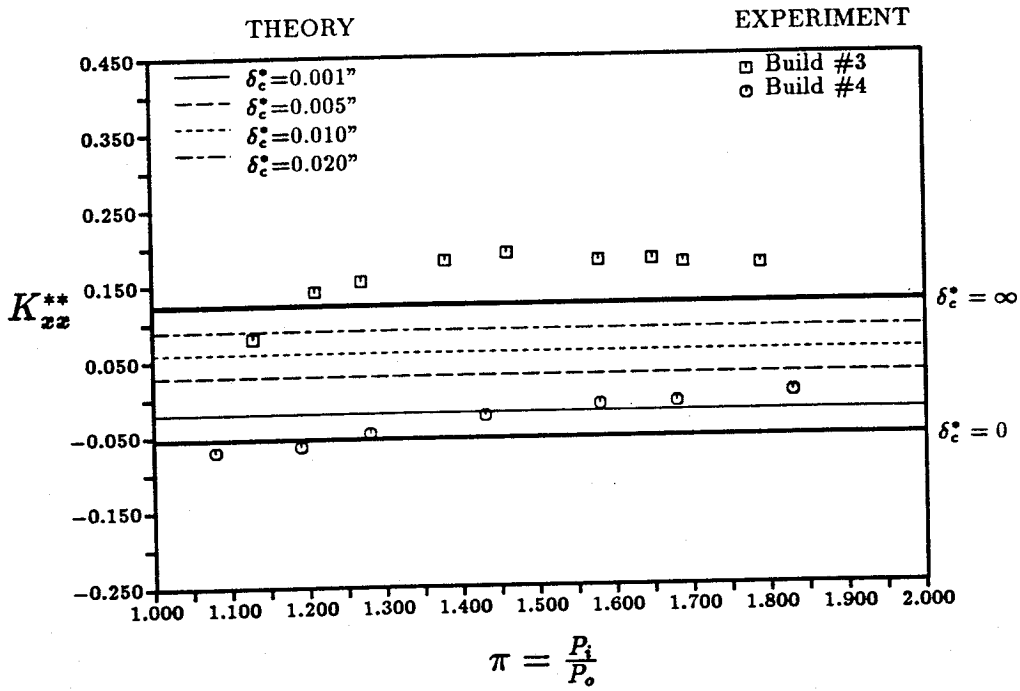

Figure 7.36: K_{xx}^{**} vs π, for the experimental data and theory for builds 3 (smooth land) and 4 (honeycomb land). $\alpha_v = 15^o$, $\omega = 0$ and $\epsilon_1 = 0.1407$. δ_c^* is used as a parameter.

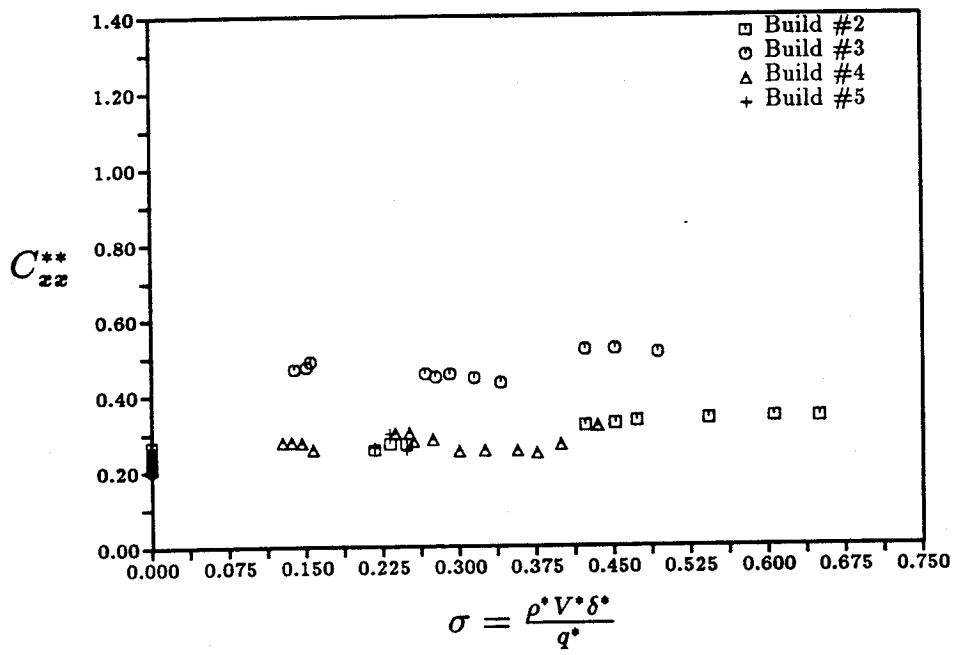

Figure 7.37: The effect of inlet swirl on the direct damping coefficient, C_{xx}^{**}, for builds #2(narrow rotor-smooth land) , #3(wide rotor-smooth land), #4(wide rotor - honeycomb land) and #5(narrow rotor - honeycomb land). ϵ_1=0.1407.

BUILD#	$\frac{\partial K_{xy}^{**}}{\partial \sigma}$	$\frac{F_T(\Omega_d)}{\hat{r}}$	$\frac{F_{TT}(\Omega_d)}{\hat{r}}$	C_{xx}^{**}	From Static Correlation $C_{xx}\left(\frac{Ns}{m}\right)$	Measured Directly $C_{xx}\left(\frac{Ns}{m}\right)$
2	0.372	7763	953	0.289	22.70	19.95
3	0.416	27821	3162	0.371	82.19	75.80
4	0.283	20001	3162	0.247	56.13	48.54
5	0.338	7053	953	0.231	20.33	15.81
Composite	0.357					
Data of Benckert	0.357 0.423 0.265					

Table 7.1 The first column shows the cross-stiffness correlation for all builds and for the static data of Benckert [28] The next two columns show the total cross force and frictional component evaluated at $\Omega_d = 300\left(\frac{rads}{sec}\right)$ and design pressure ratio. The next column is the measured nondimensional direct damping coefficient. The final two columns give the damping calculated from the cross-stiffness coefficient and the average value that was directly measured.

CONFIG.	$F_T(meas.)$	$F_T(\delta_c^* = 0)$	$F_T(\delta_c^* = \infty)$	Matched δ_c^*
1	10.21(N)	16.28(N)	4.99(N)	0.008"
2	8.28(N)	16.15(N)	4.25(N)	0.011"
3	11.91(N)	15.51(N)	4.09(N)	0.010"

Table 7.2 Comparison of the data of Benckert and Wachter [28] to the coupled model predictions. All cases are for standard conditions. P_i = 1.58 (bar), P_o = 1 (bar) and α_v = 28.4°. The first column shows the experimental value. The second column gives the value predicted with full coupling, that is no leakage flow. The third column has the predictions for constant upstream boundary conditions. The last column gives the value of the axial space needed for the model to match the experimentally obtained value.

the models predict. For the remaining chambers, the agreement to theory is much better.

All the models used constant upstream boundary conditions. However, the test section in the apparatus of Benckert and Wachter is quite similar to ours, in that swirl vanes feed a swirl cavity which is nominally sealed by an axial clearance from a large central cavity, and so the suspicion arises that undetected upstream nonuniformities must have played an important role in their case as well. No information was reported on the axial clearance used, but we can compare data for three of their configurations with the theoretical limits of $\delta_c^* = \infty$ (the implicit assumption of previous models) and $\delta_c^* = 0$ (our fully-coupled limit). The results (Table 7.2) show that the measured cross-forces on the first seal cavity are much more closely predicted by the $\delta_c^* = 0$ limit than by the usual uncoupled models.

7.6 Summary and Conclusions

A large body of fluid force data was obtained for several 1-cavity labyrinth seals under realistic controlled whirl conditions. The combined use of experiment and theory allowed clarification of several mechanisms and effects of importance for rotordynamic applications:

- Seal cross-forces are proportional to inlet swirl and to driving pressure difference. Direct forces are largely insensitive to inlet swirl.
- Direct forces in throughflow labyrinths with equal inlet and exit clearances are mainly due to variations with clearance of the carryover coefficient for the exit gap.
- There are two main mechanisms producing cross-forces: one is an inviscid mass storage effect, which is proportional to the cavity fluid tangential velocity with respect to the whirling frame; the other mechanism is friction-related, and is proportional to the decrease in tangential velocity between inlet and cavity. In addition, carryover variations add ~20% to the cross-forces.

- The first of these mechanisms leads directly to a linear decrease of cross-force with whirl speed, and is almost exclusively responsible for the direct damping coefficient C_{xx}. The second and third mechanisms affects K_{xy} but not C_{xx}.
- Because of the above, C_{xx} can be extracted from purely static seal force test data, with no need for actual whirling.
- Honeycomb lands appear to interfere with carryover, and hence strongly affect direct forces. Their influence on cross-forces is limited due to the limited contribution of carryover to these forces.
- We have identified a very important influence of the nonuniformities existing upstream of the seal on the seal forces. This nonuniformity is coupled to those in the seal cavity, and its magnitude depends additionally on the leakage allowed between the pre-swirl cavity and uniform regions, such as the hub volume.
- For the relative size of our pre-swirl cavity, the above effects lead to variations by factors of 3-4 in the labyrinth seal forces. It is clear that designers must account for such effects in assessing the rotordynamic effects of seals. The analysis will have to be dependent on the pre-seal configuration of each application.

8.0 Dynamic Alford Force Investigation

8.1 Background

As discussed in Sec. 1, considerable effort was devoted to modifying the apparatus and data gathering techniques in order to investigate the possible effects of non-static turbine offsets. A literature review on the subject revealed no prior data on dynamic Alford forces on unshrouded turbines. For turbines with a shroud band and a tip labyrinth seal, Wohlrab [6] did present some data, but only for effective whirl to spin rate ratios Ω/ω in the range 0.1-0.15. Most incidences of unstable whirl have been observed at about $\Omega/\omega \cong 0.5$ (Ref. [16]), primarily because modern turbines tend to operate at about twice their first transverse mode frequency. Wohlrab was able to detect a decrease of cross-force F_y by about 15% in his Ω/ω range, although the exact conditions were not documented. In any case, this was almost certainly attributable to the well known damping properties of the labyrinth seal (see our Sec. 7), and has no direct relevance to unshrouded turbines.

The theoretical background is also quite deficient. Our simplified X-Y actuator disk theory [17] predicted a 10-20% decrease of F_y for $\Omega/\omega = 0.5$.

The more refined theory explained in Sec. 9.3 of this report indicates larger damping for our turbine, but only if the upstream flow redistribution is fully allowed for. It is argued in Sec. 9.3.8 that the finite axial gaps between stator and rotor (both between blades and between hubs) must have the effect of reducing this redistribution substantially, and hence of also reducing the dynamic effects on Alford forces. The reason for this connection between XY redistribution and dynamic effects is simply the fact that the reduced frequency $\Omega R/c_x$, appropriate to the redistribution length scale R, is of order unity, whereas the reduced frequency $\Omega H/c_x$, appropriate to the radial migration effects in the absence of tangential redistribution, is only of order 0.2. Thus, if the upstream flow does not reorganize on the R-scale, the flow through the stage will respond essentially quasi-statically to whirling frequencies, and no dynamic effects will

appear.

The importance of improving our understanding of the dynamic Alford effects is obvious. It could, in fact, happen that whatever K_{xy} stiffness may exist under static conditions would be negated by the dynamic damping. The dynamic effects of this damping are somewhat non-intuitive, due to the circular whirling trajectory. Consider a mass M with axial symmetry, restrained centrally by an elastic stiffness K_o and with ordinary damping C_o. In addition, suppose the fluid forces are of the general form

$$F_x = K_{xx}\, e_x - K_{xy}\, e_y + C_{xx}\, \dot{e}_x - C_{xy}\, \dot{e}_y \tag{8.1}$$

$$F_y = K_{xy}\, e_x + K_{xx}\, e_y + C_{xy}\, \dot{e}_x + C_{yy}\, \dot{e}_y \tag{8.2}$$

Here K_{xx} and C_{xx} would be positive if they destabilize the motion (this is negative stiffness and damping in the ordinary sense, but the sign is chosen to conform to our experimental Alford force convention). Also, K_{xy} would be positive for whirling in the sense $X \rightarrow Y$. The normal C_o damping simply reduces C_{xx}.

We can solve the shaft equations of motion using the structural stiffness K_o and C_o, plus Eqs. (8.1) and (8.2) by assuming a complex displacement vector $z = e_x + ie_y = \hat{z}\, e^{i\Omega t}$, as suggested by the circular symmetry. The imaginary part of Ω will indicate damping (if positive) or growth (if negative). It is found that, provided $|K_{ij}| << K_o$ and $\Omega |C_{ij}| << K_o$,

$$\frac{\Omega}{\sqrt{K_o/M}} \cong \pm 1 \pm \frac{1}{2} k_{xx} + \zeta_{xy} + i\left(\pm \frac{1}{2} k_{xy} - \zeta_{xx}\right) \tag{8.3}$$

where

$$k_{ij} = \frac{K_{ij}}{K_o} \quad , \quad \zeta_{ij} = \frac{C_{ij}}{2\sqrt{K_o M}} \tag{8.4}$$

Two things can be noticed about Eq. (8.3). First, one of the two roots will be unstable due to the $i\, \frac{1}{2}\, k_{xy}$ term. This is the expected effect of the Alford cross-force. Second, damping is pro-vided by $-\zeta_{xx}$ (i.e., by $-C_{xx}$), and not by $-C_{xy}$, as would appear intuitively to be the case. The cross-force damping C_{xy} simply changes slightly the

whirl frequency, as does the direct stiffness K_{xx}.

8.2 Implementation

The kinematics of our test facility allows for dynamic turbine offset along one axis (called here the OX axis). At the same time, the instrumentation allows for real time monitoring of all components of force on the turbine during this motion. The forces are first sensed in the rotating frame, but can be projected to fixed axes, so that, in principle, records of both $F_x(t)$ and $F_y(t)$ (at right angles to the offset motion) can be obtained versus time. According to the discussion above, the task at hand is the extraction of C_{xx} from these records. With reference to Eq. (8.1), since $e_y \equiv 0$, and assuming $e_x = e \cos \Omega t$, we obtain

$$\begin{aligned} F_x &= e\left(K_{xx}\cos \Omega t - \Omega C_{xx} \sin \Omega t\right) \\ &= e\sqrt{K_{xx}^2 + (\Omega C_{xx})^2}\cos\left[\Omega t + \tan^{-1}\left(\frac{\Omega C_{xx}}{K_{xx}}\right)\right] \end{aligned} \tag{8.5}$$

Equation (8.5) indicates two possible routes for obtaining C_{xx}: (a) through a force magnitude increase for a given displacement amplitude, and (b) through a phase shift $\tan^{-1}(\Omega C_{xx}/K_{xx})$ between force $F_x(t)$ and displacement $e_x(t)$. The latter should be more sensitive, particularly at relatively small values of the damping force $\Omega C_{xx}e$ compared to the stiffness force $K_{xx}e$. A similar procedure can also be used for determining C_{xy} from $F_y(t)$.

Whereas for static tests both F_x and F_y are obtained from the dynamometer data with about equal precision, the situation is more complex in the dynamic case because of inertia forces. If the mass of the turbine is M_t (about 7.2 kg in our case), the dynamometer senses an inertia force $F_x = -M_t \ddot{e}_x$ as well as the aerodynamic forces. In terms of $e_x = e \cos \Omega t$, the total F_x signal will then be

$$F_x = e\left[\left(M_t\Omega^2 + K_{xx}\right)\cos \Omega t - \Omega C_{xx} \sin \Omega t\right] \tag{8.6}$$

In order of magnitude, $K_{xx} \cong$ -1 lb/10 mil = -1.75×10^4 N/m, whereas, at $\Omega = @\ \omega_{DES.}$,

$M_t \Omega^2 \cong 7.2 \times (180)^2 = 2.33 \times 10^5$ N/m. If we assume, as a probable upper bound, that the damping from

$-C_{xx}$ eliminates fully the static K_{xy} effect, we see from Eqs. (8.3) and (8.4) that $|\Omega C_{xx}| = |K_{xx}|$. In that case, the phase angle of $F_x(t)$ with respect to $e_x(t)$ will be

$$\phi = \tan^{-1} \frac{\Omega C_{xx}}{M_t \Omega^2 + K_{xx}} = \tan^{-1} \frac{1.75 \times 10^4}{2.33 \times 10^5 - 1.75 \times 10^4} = 4.6°$$

This indicates that, in order to resolve damping coefficients capable of changing the net (dynamic) Alford effect by ±20%, we need to resolve relative phase angles to about ±1°. This is a significant experimental challenge, which we have not successfully met so far. In what follows, we will discuss the rig modifications that were introduced to this end and the limited data set that was obtained, and will give an assessment of the feasibility of quantitatively resolving the issue in a future effort.

8.3 Apparatus

The linear dynamic offsets of the turbine were forced by a matched pair of inertial shakers (VIBCO, Model 4P-700, element No. 11 in Fig. 2.3). Each of them features a rotor with an adjustable imbalance. Using a synchronized counterrotating pair, as shown in Fig. 2.3, produces inertial forces along one axis, in our case along the axis of the rods supporting the turbine shaft. The effective linear force produced, depending on eccentricity setting and speed, ranges up to 700 lbf (each) at 1800 rpm. The mass to be shaken (turbine and shaft, bearing assembly, shakers, mounting plate) can be estimated at about 150 kg, and assuming $\Omega \leq @ \omega_{DES.} \cong 180$ rad/sec and $e \leq$ 0.4 mm = 1.6 mil, we need a maximum force of $M\Omega^2 e \cong 440$ lbf, well within the shaker ratings.

The matched pair is normally used, according to the manufacturer, without any hardware synchronization, because the rotors tend to "lock" in sympathy in response to the structure's vibration. However, when this mode of operation was attempted in

our rig, it was found that no synchronization occurred. Instead, there was a slight speed difference (the shakers have induction motors, which can have slightly different slips), so that the unbalanced forces were in a gradually shifting relation to each other, and resulted in periods of very strong and periods of very weak vibration. This behavior is probably related to the large dry friction of the rod linear bearings (about 60 lbf), which is a result of their very close packing for high precision. At speeds low enough that the shaker force was below this dry friction, no vibration was happening (the structure, as a whole, is very rigid), and self-synchronization was not occurring. Given the nearly random direction and strength of the forces from the unsynchronized pair, it was not thought prudent to increase the speed to the point where friction would be overcome and locking would occur. Instead, a timing belt arrangement was built into the back end of the shakers (Fig. 8.1), and this proved satisfactory throughout the operations.

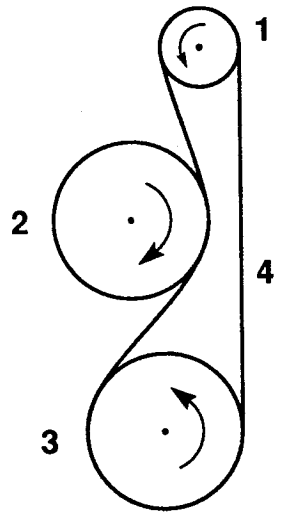

Fig. 8.1: Shaker synchronizer
1. Idler
2. Shaker
3. Shaker
4. Timing Belt

The shakers operate with no connection to any external base, and so they

provide no absolute position anchoring, and a centering device is required. This took the form of a spring whose neutral position is at the centered turbine location. The initial version of this spring is seen in Fig. 2.3 as a flexible plate mounted between the shaker assembly and the main plate, and supporting the shaker assembly from below. This initial design proved inadequate and failed in tests. The final design and relevant considerations are reviewed next.

The spring must (a) be strong enough to provide centering within about 1/1000" against the 60 lbf (266 N) of linear bearing dry friction, (b) allow a linear motion amplitude of about ±12/1000" (3×10^{-4} m), and (c) have resonances outside of the desired shaking frequency range of 17-30 Hz (38 to 50% of design turbine speed). In addition, it must be dimensioned to fit in the available 1 inch space between the main mounting plate and the shaker assembly vertical mounting plate, and it must not buckle under the weight of the shaker assembly.

If the design is for a soft spring, with natural frequency below 17 Hz, the dead band due to the dry friction is too large. For example, for a natural frequency ω_o = 10 Hz, the spring stiffness would be $150 \times (10 \times 2\pi)^2 = 5.9 \times 10^5$ N/m, and the dead band would be Δe = 266 N/5.9×10^5 N/m = 4.5×10^{-4} m = 18.0/1000 inch, clearly too large. In fact, if we wish to reduce this dead band to 1/1000", the design stiffness must be $18 \times 5.9 \times 10^5 = 1.06 \times 10^7$ N/m, which yields a natural frequency $\omega_o = 10\sqrt{18}$ = 42.5 Hz. This is then high enough above the intended shaking frequencies. Thus, the "hard spring" design can indeed satisfy both, centering precision and resonance avoidance requirements. The requirement to allow a 12 mil deflection proves difficult to meet, however. The first design, with a single flexible plate acting as a beam-column, is shown in Fig. 8.2.

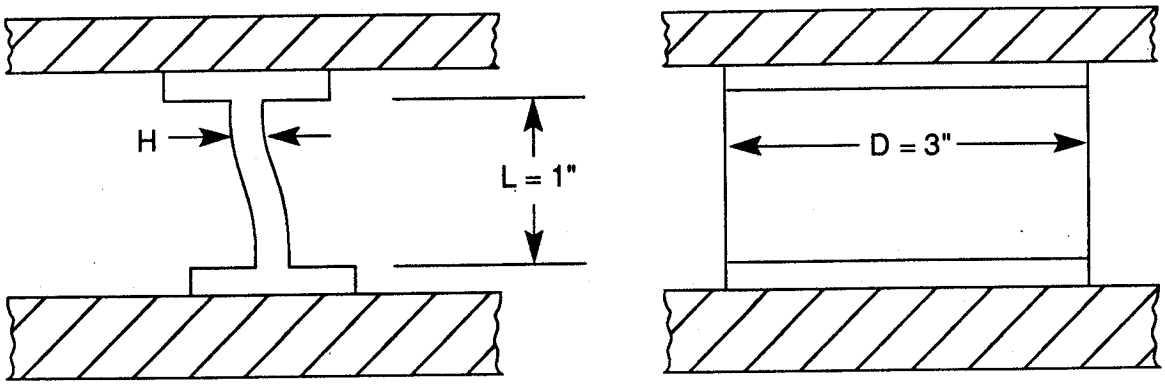

Fig. 8.2: First spring design

Using the equation $K = 12\ EI/L^2$, where $I = H^3D/12$, and with the modulus E for steel, the required thickness H for $K = 1.06 \times 10^7$ N/m is 2.24 mm. This relatively large thickness leads to large maximum stresses in the flexure. For a deflection $\delta = 0.3$ mm = 12 mil, $\sigma_{MAX} = 3EH\delta/L^2 = 6.25 \times 10^8$ N/m^2, which is above the strength of ordinary spring steel.

This difficulty, which was not initially recognized, led to a redesign using a multiplicity of thinner plates, as shown in Fig. 8.3. Using N such plates, each with stiffness K_1, the total stiffness is $K = NK_1$, and since $K \sim H^3$, for the same total K, the individual thickness H_1 is $H_1 = H/N^{1/3}$, and stress is reduced in the same proportion. With N = 40, the individual thickness and stress are

$H_1 = 2.24$ mm / $N^{1/3} = 0.65$ mm

$\sigma_1 = 6.25 \times 10^8 / N^{1/3} = 1.83 \times 10^8$ N/m2

which is now acceptable. It can be verified that other stresses (column loading, shear) are comparatively small, and that the buckling load is much higher than expected vertical loads.

The design in Fig. 8.3 consists of a stack of 40 steel plates, held in place by three tie rods which clamp a split frame. Each plate is separated from its neighbors by 25 mil spacers, to minimize rubbing during deflections. For additional safety, the number of plates was later raised to 50. This design proved satisfactory.

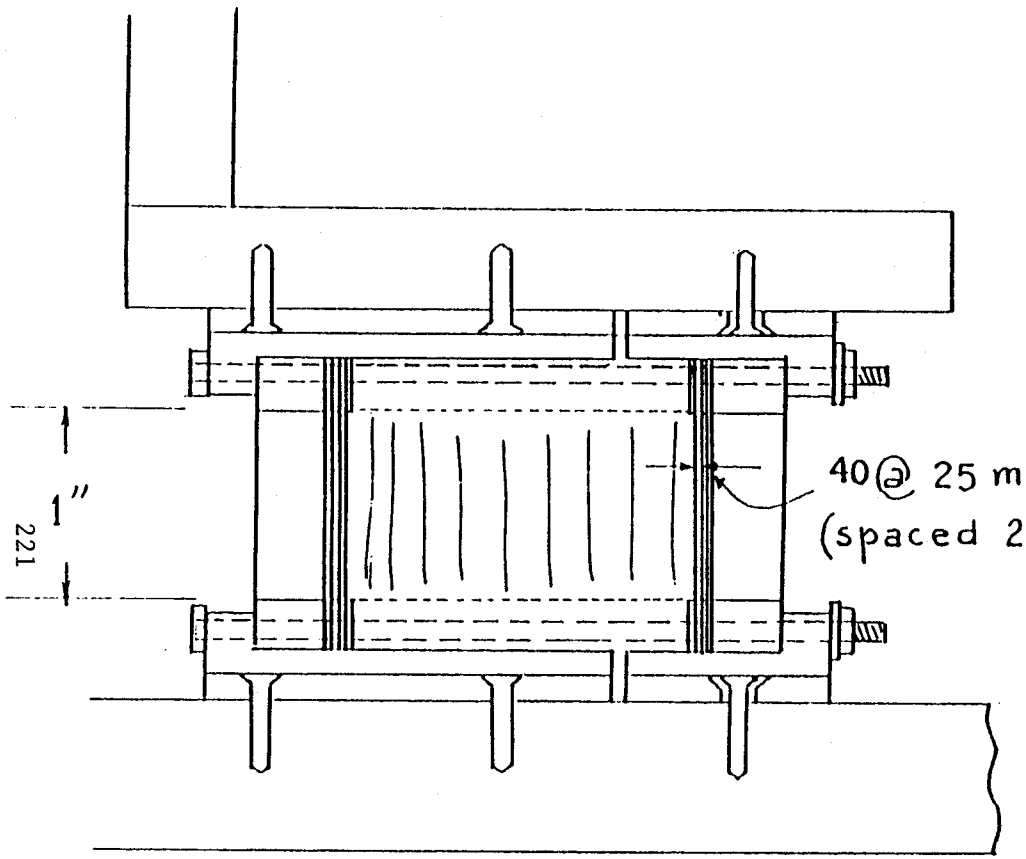

Figure 8.3a Side View

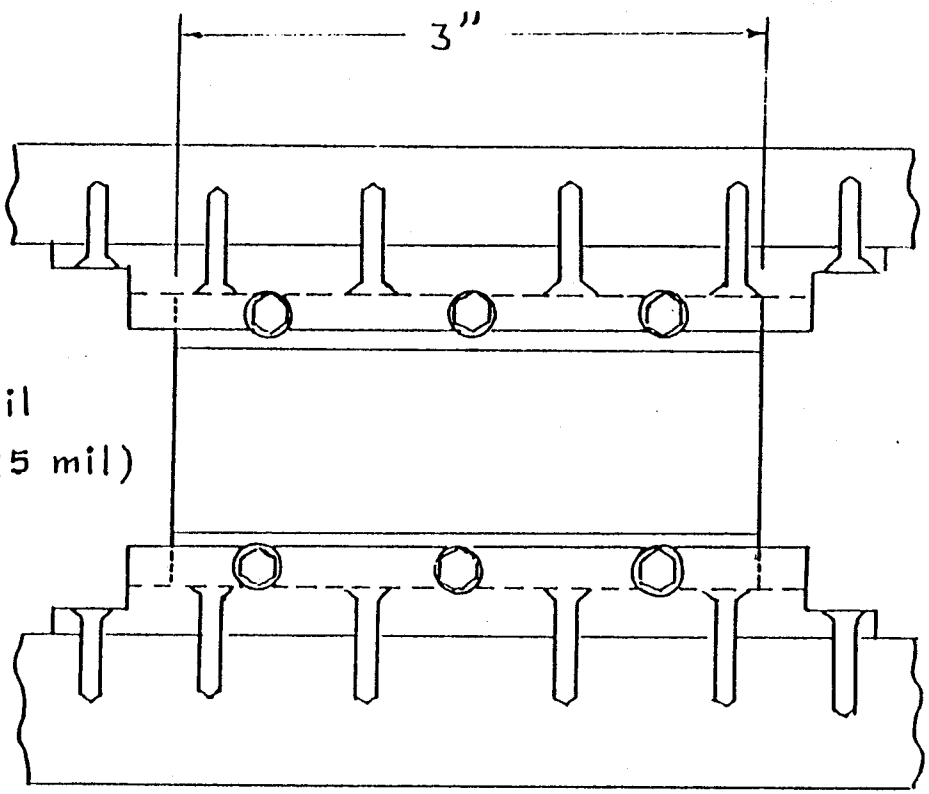

Figure 8.3b Front View

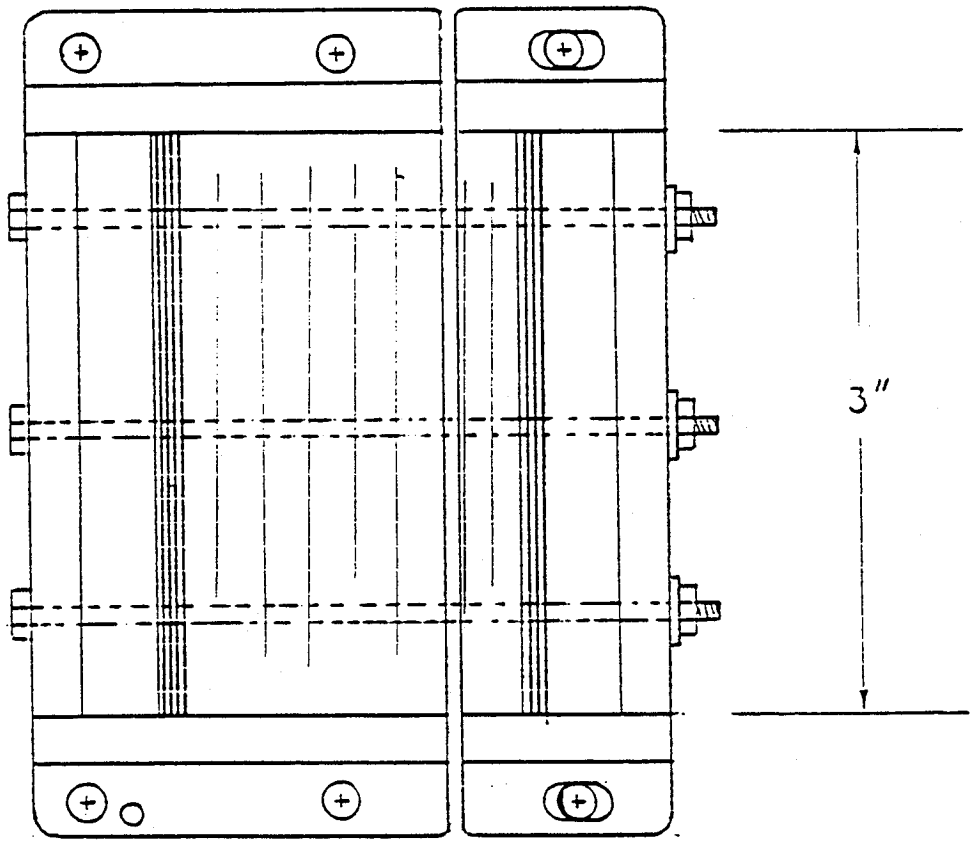

Figure 8.3c Elevation View

8.4 Measured Displacements and Forces

In view of the large contribution of inertia to the F_x force component, a preliminary investigation was made of the magnitude and phase of these forces, as well as of the linear shaking amplitude under various conditions. An effort was also made to model the shaker dynamics, as affected by bearing dry friction.

The shaker was operated in vacuum, at $\bar{P}$ = 1 atm and at $\bar{P}$ = 2 atm, with the turbine running at its nominal speed in all cases, and at its nominal flow rates in the last two. The turbine was motor-driven in vacuum. The procedures used to take data under dynamic conditions were as follows:

(a) Set and stabilize the turbine running conditions, in the centered position.

(b) Set the shaker amplitude, and bring its frequency to the desired value. Observe the proximeter output in an oscilloscope to verify proper operation.

(c) Use an external clock signal to determine the data sampling times (approximately 72 per cycle). Sample all dynamometer channels, plus proximeter.

(d) Correct for the small variations in shaker speed (±1%) by dividing the record into cycles and interpolating the data to a fixed number of points per cycle.

(e) Average over a large number (~100) of cycles (phase-locked filtering).

(f) Extract the first harmonic of each signal (magnitude and phase with respect to the shaker linear motion).

The amplitudes and phases of e_x (zero phase by definition), F_x and F_y are listed in Tables 8.1, 8.2, and 8.3. The phase angle is defined by, for instance, $F_x = \hat{F}_x \sin(\Omega t - \theta_x)$. The run number is also listed, for reference.

The values given in the tables are averages for each run. A sample of the instantaneous e_x data (in raw form) is shown in Figs. 8.4 and 8.5. Considerable modulation is observed, for reasons that were not sufficiently investigated, and this produces uncertainty of up to ±20% in e_x. As Fig. 8.5 shows, the individual displacement cycles were reasonably sinusoidal, indicating that dry friction, although

present, was not large enough to create stopping periods at peak displacement.

The magnitude of F_X is largely determined by inertia forces, as discussed in Sec. 8.2. This is verified in Table 8.4, where we collect the mean values of the measured $\widehat{F}_X$ values, together with the values calculated from $F_X = M_t \Omega^2 e_X$, with M_t = 7.2 Kg and using the measured Ω and e_X. The agreement is reasonably good, and the scatter appears to be mainly random. The ratio $\widehat{F}_X/e_X$ is slightly lower for conditions with flow. This reflects the negative sign of the fluid K_{XX} coefficient,

TABLE 8.1
DYNAMIC FORCES IN VACUUM

Run #	e (mil)	Ω/ω_D	$\widehat{F}_X$ (lbf)	θ_X (°)	$\widehat{F}_Y$ (lbf)	θ_Y (°)
1143	0	0	0.0226	---	-0.0132	---
1145	0	0	0.0311	---	-0.0253	---
1152	0	0	0.2922	---	-0.0928	---
1146	6	0.4	6.952	26.43	0.863	11.26
1157	6	0.4	4.855	20.54	0.522	-10.28
1151	8	0.45	9.977	19.08	0.426	14.84
1160	8	0.45	6.355	22.74	0.466	-69.84
1163	11	0.5	15.595	22.08	0.684	13.94

TABLE 8.2
DYNAMIC FORCES AT $\bar{P}$ = 1 atm

Run #	e (mil)	Ω/ω_D	$\hat{F}_x$ (lbf)	θ_x (°)	$\hat{F}_y$ (lbf)	θ_y (°)
1125	0	0	0.332	---	-0.316	---
1126	0	0	0.280	---	-0.212	---
1127	0	0	0.231	---	-0.168	---
1134	8	0.4	7.334	17.21	0.317	48.79
1131	11	0.45	11.279	7.00	0.625	-52.18
1133	11	0.45	11.263	7.10	0.628	-47.06
1138	11	0.45	10.889	+8.83	0.553	-51.90
1139	11	0.45	10.871	9.21	0.536	-54.89
1128	12	0.5	17.81	38.3	0.613	68.45
1129	12	0.5	17.98	20.53	0.185	-77.28

TABLE 8.3
DYNAMIC FORCES AT $\bar{P}$ = 2 atm

Run #	e (mil)	Ω/ω_D	$\hat{F}_x$ (lbf)	θ_x (°)	$\hat{F}_y$ (lbf)	θ_y (°)
1164	0	0	0.117	---	-0.546	---
1165	0	0	0.302	---	-0.289	---
1166	0	0	0.252	---	-0.505	---
1173	6	0.4	4.829	12.37	0.411	3.17
1174	6	0.4	4.850	11.96	0.391	2.17
1175	6	0.4	5.015	12.23	0.395	9.71
1179	6	0.4	6.236	12.00	0.350	1.01
1180	6	0.4	6.416	12.52	0.362	0.91
1171	10	0.45	10.377	12.80	0.843	-25.68
1176	10	0.45	10.54	12.70	0.866	-30.92
1169	12.2	0.5	16.100	2.90	1.259	49.33

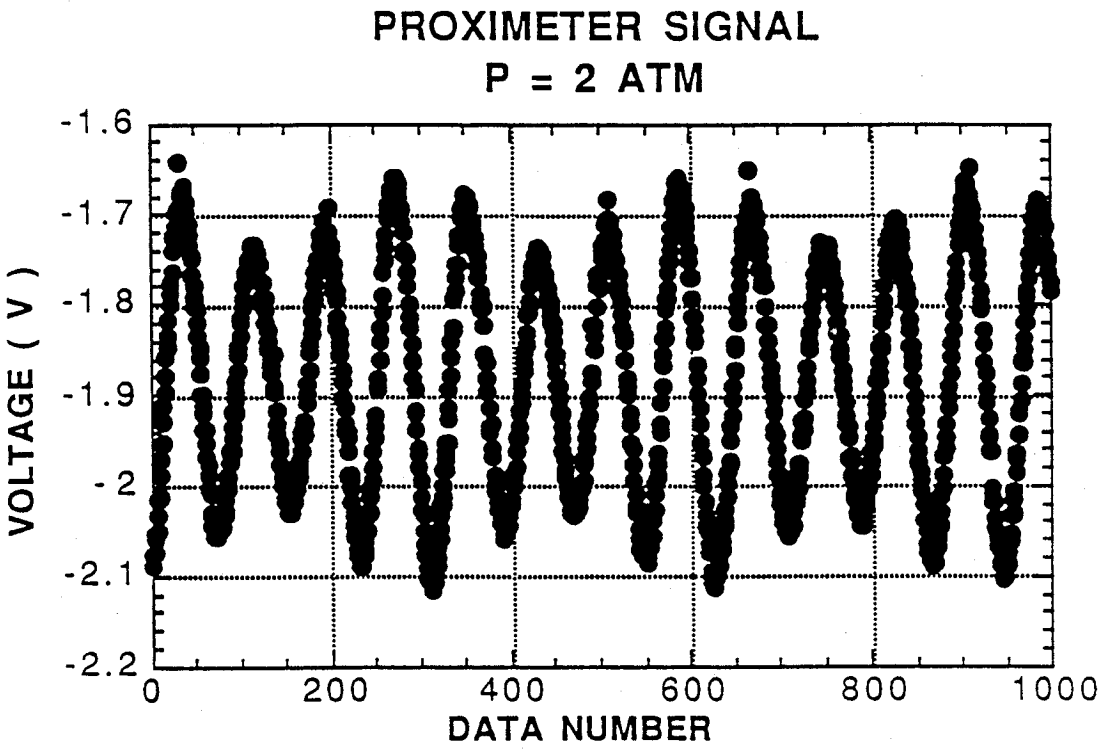

Figure 8.4 Proximeter signal over a number of shaker cycles

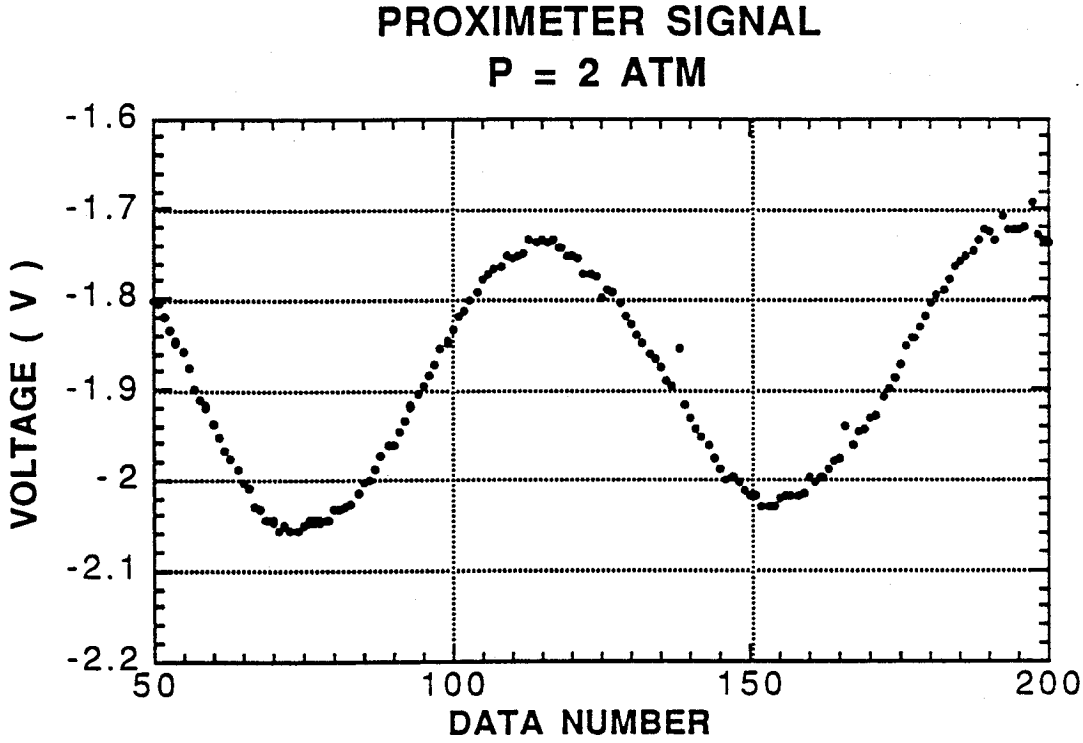

Figure 8.5 Proximeter signal over two consecutive cycles

which, as noted in Sec. 8.2, should lower $\hat{F}_x$ at $\Omega = @\ \omega_{DES}$, P = 2 atm, by approximately

$K_{xx}/M_t\,\Omega_t \sim 0.07$. This is indeed of the order shown in Table 8.4 for Ω = 1720 rpm, P = 2 atm.

TABLE 8.4
MEASURED AND CALCULATED (INERTIAL) F_x AMPLITUDES

P (atm)	Ω (rpm)	e (mil)	$\hat{F}_x$ (lb) (meas., avg.)	$\hat{F}_x$ (lb) (calc.)	
0	---	0	0.12	0	
0	1376	6	5.90	5.13	$\bar{\varepsilon}$ = -0.33 lb
0	1548	8	8.17	8.65	σ = 0.65 lb
0	1720	11	15.60	14.69	
1	---	0	0.28	0	
1	1376	8	7.33	6.84	$\bar{\varepsilon}$ = -0.46 lb
1	1548	11	11.08	11.90	σ = 1.06 lb
1	1720	12	17.90	16.02	
2	---	0	0.19	0	
2	1376	6	5.47	5.13	$\bar{\varepsilon}$ = 0 lb
2	1548	10	10.46	10.82	σ = 0.28 lb
2	1720	12.2	16.10	16.29	

The phase angles θ_x and θ_y are more erratic. Particularly for $\bar{P}$ = 2 atm, most of the θ_x values are within one degree, but unexplained jumps can be seen occasionally. This seems to be mostly due to the difficulty in completely filtering out the high frequency turbine ringing forces, as well as occasional noise in the proximeter data.

The high frequency effects are illustrated in Fig. 8.6, which is an ensemble-averaged record of the in-line force measured over slightly over one shaking cycle (72 samples/cycle). The conditions were P = 2 atm, $\Omega = 0.45\ \omega_D = 1548$ rpm, nominal flow rate. One can discern a first harmonic force, with an amplitude of 12-15 lbf (maximum at points #15 and #80, minimum at point #55). However, this first harmonic, which is used to extract the F_X data in Tables 8.1-8.3, is masked by a very prominent superimposed signal at about 6/cycle (i.e., at about 9300 rpm). This extra force has a modulated amplitude, peaking at about the same point as the first harmonic (with peak value of over 20 lbf), and decreasing to a minimum amplitude of 6-7 lbf at mid-cycle. The frequency of this signal is close to the lower branch of the pair into which turbine rotation splits the first transverse mode, i.e. $\omega_0 - \omega \approx 12{,}700 - 3440 = 9260$ rpm (Ref. [4]). An approximate analysis of this effect is given later (Sec. 8.6).

8.5 Dynamic Model of Shaken Turbine

The presence of dry friction in the linear shaker bearings introduces nonlinearity into the dynamics, and can be the source of the observed excitation of the higher modes. The first consideration should be the modeling of the displacement x(t) of the turbine shaft, assuming it to be stiff enough to allow neglect of the higher modes. Because of the sudden changes of sign of the dry friction at points of zero $\dot{x}(t)$, discontinuities appear in the higher derivatives of x(t), which give x(t) a full spectrum of higher harmonics. It is these higher harmonics that can then excite the shaft modes, and this can be subsequently analyzed.

Let x be the absolute linear displacement of the turbine and its bearing assembly (of mass M), and x_S the absolute displacement of the unbalanced effective shaker mass M_S. The synchronized pair arrangement produces a relative harmonic motion

$$x_S - x = e_S \sin \Omega t \tag{8.7}$$

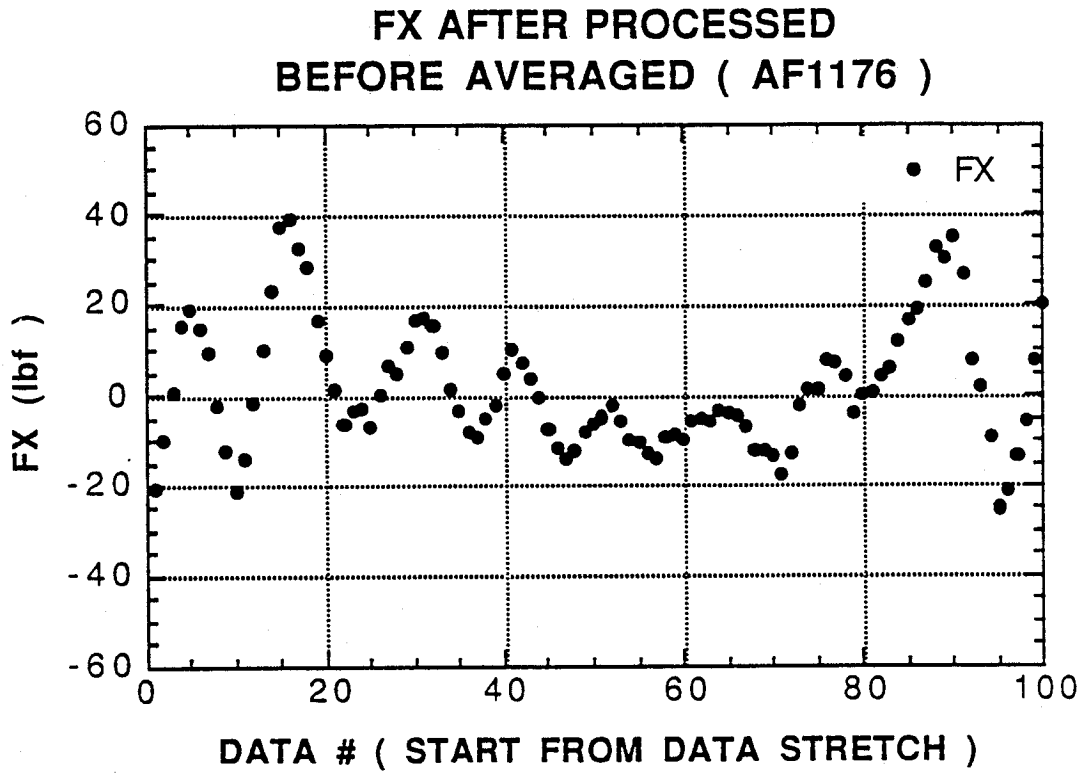

Figure 8.6 Direct-axis dynamics force over a little more than one cycle, after ensemble-averaging.
$\overline{P}$ = 2 atm, Ω/ω = 0.45

Because of this, the force along 0X which the mass M_s exerts on the mass M must be

$$F_s = -M_s \ddot{x}_s = -M_s \left(\ddot{x} - e_s \Omega^2 \sin \Omega t\right) \tag{8.8}$$

The dry friction force from the linear bearings is taken to be independent of speed:

$$\text{Friction force} = \begin{cases} -F_f & \text{when } \dot{x} > 0 \\ +F_f & \text{when } \dot{x} < 0 \end{cases} \tag{8.9}$$

In addition, the spring support adds a force -Kx. The equation of motion of the mass M is then

$$M\ddot{x} = -Kx - M_s \left(\ddot{x} - e_s \Omega^2 \sin \Omega t\right) - F_f \, sg(\dot{x}) \tag{8.10}$$

where $sg(\dot{x})$ is ±1 depending on the sign of $\dot{x}$. Reorganizing, and calling $M_T = M + M_s$,

$$M_T \ddot{x} + Kx = M_s e_s \Omega^2 \sin \Omega t - F_f \, sg(\dot{x}) \tag{8.11}$$

This nonlinear dynamic problem was analyzed by Den Hartog Ref. [32] who identified steady-state regimes with none, two or more than two stops per cycle, and gave analytical descriptions of the first two of these regimes. We have performed numerical integrations of Eq. (8.11), in the dimensionless form

$$\frac{d^2\xi}{d\tau^2} + \frac{\xi}{\nu^2} = \sin \tau - \frac{\rho_o \, sg(\dot{\xi})}{\nu^2} \tag{8.12}$$

where

$$\xi = \frac{M_T}{M_s e_s} x \tag{8.13}$$

$$\tau = \Omega t \tag{8.14}$$

$$\nu = \frac{\Omega}{\omega_o} \; ; \; \omega_o = \sqrt{\frac{K}{M_T}} \tag{8.15}$$

$$\rho_o = \frac{F_f}{M_s e_s \omega_o^2} \tag{8.16}$$

Using $M_s e_s$ = 0.082 Kgm, M_T = 150 Kg, ω_o = 285 rad/sec (2724 rpm), and F_f = 60 lbf = 266 N, we calculate ρ_o = 0.04. The calculated amplitudes $\hat{\xi}$ proved to be fairly

insensitive to the precise value of ρ_o up to about 0.08. For $\rho_o = 0.04$, the wave pattern $\zeta(\tau)$ shows no stops for $\tau \geq 0.48$ ($\Omega \geq 1300$ rpm), and two stops below this forcing frequency. Some amplitude values are listed (in both dimensionless and dimensional form) in Table 8.5.

TABLE 8.5
SHAKING AMPLITUDES VERSUS SHAKING FREQUENCY, CALCULATED FOR $\rho_o = 0.04$

ν	0.404	0.441	0.514	0.587	0.624
Ω (rpm)	(1100)	(1200)	(1400)	(1600)	(1700)
$\hat{\xi}$	0.186	0.238	0.359	0.526	0.637
$\hat{x}$ (mil)	(4.00)	(5.12)	(7.42)	(11.32)	(13.72)

These calculated amplitudes are compared to the data of Table 8.4 in Fig. 8.7. Aside from the obvious scatter, it is to be noted that, at least for the 1 atm case, the data showed no motion for $\Omega \leq 1100$ rpm, while the calculations would indicate zero motion (non-starting due to dry friction) only for $\Omega \leq 520$ rpm. Reproducing this threshold behavior would have required F_f levels much higher than were measured directly. Thus, the simple dry friction model is not completely satisfactory.

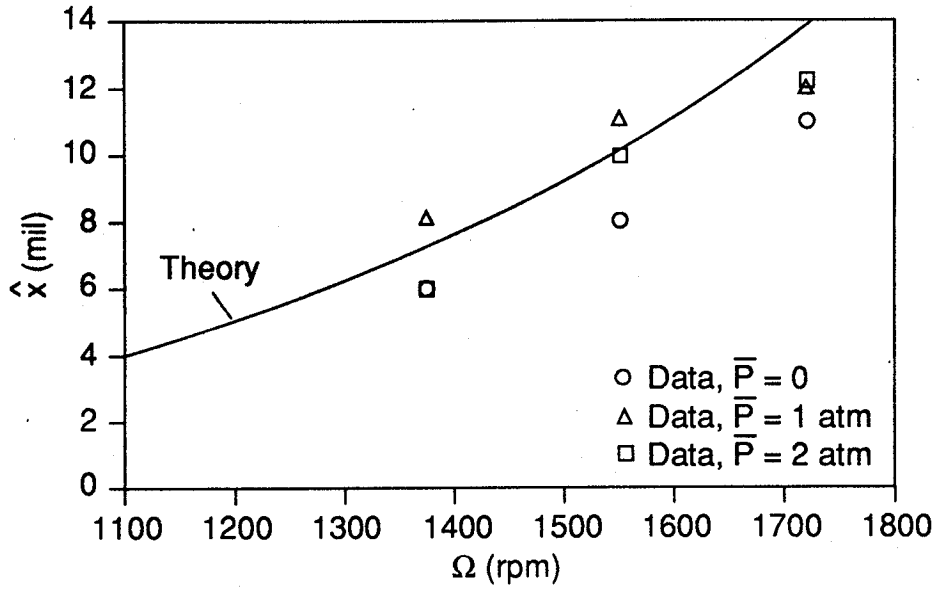

Fig. 8.7: Theoretical vs. experimental amplitudes

8.6 Excitation of Higher Modes

It was mentioned before that high frequency ringing such as observed in Fig. 8.6 seriously interferes with precise measurements of F_x. If the motion x(t) of the turbine shaft is known, the inertial excitation force $-M_t \ddot{x}$ acting on the turbine mass M_t can be calculated, and the resulting high frequency vibrations can be analyzed. More precisely, M_t here must represent the effective mass of a higher mode (of natural frequency ω_t) under the given inertial excitation. If x_t represents the relative displacement of this effective vibrating mass, then

$$\ddot{x}_t + \omega_t^2 x_t = -\ddot{x} \tag{8.17}$$

where x(t) is the solution to Eq. (8.11).

For the present purposes, a Fourier representation of x(t) is most appropriate. This approach was also indicated by Den Hartog [32], and uses the fact that, as long as there are no stops, the friction force is a square-wave function with a simple Fourier expansion:

$$F_f \, sg(\dot{x}) = \frac{4F_f}{\pi} \sum_{n=1,3,\ldots} \frac{\sin n\Omega(t - t_1)}{n} \tag{8.18}$$

where t_1 is the time at which x peaks, to be found presently.

Using this representation in Eq. (8.11), we easily calculate

$$x = \frac{M_s e_s}{M_T} \frac{\Omega^2}{\omega_0^2 - \Omega^2} \sin \Omega t - \frac{4F_f}{\pi M_T} \sum_{n=1,3,\ldots}^{\infty} \frac{\sin n\Omega(t - t_1)}{\omega_0^2 - n^2\Omega^2} \tag{8.19}$$

The time t_1 now follows from $\dot{x}(t_1) = 0$:

$$\cos \Omega t_1 = \frac{4}{\pi} \frac{(\omega_0^2 \Omega^2) F_f}{M_s e_s \Omega} \sum_{n=1,3,\ldots}^{\infty} \frac{1}{\omega_0^2 - n^2\Omega^2} \tag{8.20}$$

At first sight, Eqs. (8.19) and (8.20) show singularities at $\Omega = \omega_0/3$, $\omega_0/5$, ... (in addition to $\Omega = \omega_0$, the normal resonance). However, at these low frequencies, it can be verified that stops do occur and the expansion (8.18) is invalid (this distinction is not

explicitly made in Ref. [32]). Direct numerical simulations, in fact, show finite limit cycles for all F_f at these subharmonic frequencies. In our experiments, $\omega_o \approx 2720$ rpm, and $\Omega \geq 1100$ rpm, which is high enough to ensure oscillations with no stops, for which Eqs. (8.19) and (8.20) are valid.

Using Eq. (8.19) in the right-hand side of (8.17), we can calculate $x_t(t)$ and, of more direct interest, the force $F_t = -M_t \ddot{x}_t$ which the oscillating shaft assembly would sense as a reaction to the vibrations. We find

$$F_t = M_t \frac{M_s e_s}{M_T} \frac{\Omega^4 \sin \Omega t}{(\omega_o^2 - \Omega^2)(\omega_t^2 - \Omega^2)} - \frac{4}{\pi} F_f \frac{M_t \Omega^4}{M_T} \sum_{n=1,3,\ldots}^{\infty} \frac{n^3 \sin n\Omega(t - t_1)}{(\omega_o^2 - n^2\Omega^2)(\omega_t^2 - n\Omega^2)} \quad (8.21)$$

Here, in addition to the apparent resonances at $\Omega = \omega_o/3$, $\omega_o/5$, etc., we notice the real resonances at $\Omega = \omega_t/3$, $\omega_t/5$, etc. (plus $\Omega = \omega_o$, $\Omega = \omega_t$). These are not ruled out by the non-stopping restriction in our operating range. Since, for our conditions, ω_t = 9300 rpm, we should have resonances at 9300/9 = 1033 rpm, 9300/7 = 1329 rpm, 9300/5 = 1860 rpm (plus others at ω_o, $\omega_t/3$, etc., which are outside our range). These are, as Eq. (8.21) shows, directly attributable to the "jerkiness" in the dry friction force.

It is interesting to see the behavior midway between resonances, say when Ω is $\omega_t/n+1$
(n = 3,5,7,...). For n >> 1, if only the two neighboring resonances are retained as being dominant, we can show that the force varies as

$$F_{el}(t) \cong \frac{4}{\pi} \frac{M_t}{M_T} F_f \cos\Omega(t - t_1) \sin \omega_t(t - t_1) \quad (8.22)$$

Here, we see a high frequency oscillation, at $(n+1)\Omega$ (halfway between the $n\Omega$ and $(n+2)\Omega$ resonances), modulated in amplitude at the basic frequency Ω. This is the behavior seen in Fig. 8.6. We noticed that in that case $\omega_t \cong 9300$ rpm, and so $\omega_t/5$ = 1860 rpm, $\omega_t/7$ = 1330 rpm, with the mean value being 1595 rpm, not far from the shaking frequency of 1550 rpm. The figure shows clearly the $\omega_t/6$ oscillation with once-per-cycle modulation. Using M_t = 7.2 Kg, M_T = 150 Kg, and F_f = 266 N, the peak

value of Eq. (8.22) is 16.3 N ≅ 3.7 lbf. This is only about 1/4 of the value seen in Fig. 8.6. This indicates that the mode which is being excited is one in which the linear motion of the turbine itself is about 4 times that of the center of mass of the vibrating structure. This is quite plausible because, as was shown in our approximate modal analysis in Ref. [4], the first transverse mode involves a combination of rod deflections and dynamometer deflections, with the rods being the most flexible element. Thus, when the center of mass of the shaft assembly is pushed back and forth by the shaker, and vibrations are excited due to the dry friction, the pivot point for these vibrations is likely to be much closer to the center of mass of the structure than it is to the turbine. Clearly, however, a more detailed modal analysis is needed to firm up this conclusion.

The vibration amplitude (or the vibratory force amplitude) at one of the resonances ($\omega_t/5$ or $\omega_t/7$, for instance) should be limited only by unmodeled viscous damping, and can be shown to be $(F_t)_{RES.} = \frac{2}{N\pi}\frac{M_t}{M_T}\frac{F_f}{\zeta}$ where N = 3,5,7,... and ζ is the ordinary viscous damping factor. The physical origin of this damping should include any C_{xx} factor due to dynamic Alford force effects, and we could in principle try to exploit this fact to extract such forces. However, operating at resonance might damage the rig and, in addition, at these higher frequencies, the aerodynamic phenomena responsible for introducing damping would probably be different from those of interest at fractions of the turbine speed.

8.7 Alternative Methods for Dynamic Force Measurements

In view of the severe difficulties encountered in our attempts to extract dynamic Alford forces from linear shaking tests, we have considered several possibilities for future work in this important area. These are listed here, with some preliminary discussion of each. Further details will then be discussed for the more attractive options:

(a) **To measure θ_x accurately with present apparatus.** As noted, this is

possible, but difficult. Extensive testing and improved data reduction methods would be necessary to characterize and filter out the various sources of noise.

(b) **To modify the apparatus for reduced friction.** This would substantially improve the measurement accuracy. Unfortunately, the linear bearings were originally packed very tightly for precision. The supporting rods were cold-rammed through the linear bearings and into the casing of the turbine bearing assembly. Any attempt at repacking would entail cutting these rods, and very extensive reconstruction work.

(c) **To extract damping data from ringing amplitudes.** This would require near-resonant operation and, as discussed, might yield misleading information in any case.

(d) **To replace linear shaking by circular whirling.** This cannot be done in general without complete re-design of the turbine support. However, if attention is restricted to the special case $\Omega = \omega$ (whirling at spin speed), all that is required is to mount the turbine eccentrically on the centered shaft. The overriding advantage of this procedure is that the force of interest is now on the Y axis, and is in principle a constant. This decouples it from the centrifugal (inertial) force along OX. More will be said below about this option.

(e) **To use wall-mounted transducers to measure real-time pressures during shaking.** This is fairly simple to implement, but will only yield the part of the dynamic cross-forces due to pressure non-uniformity (about 40% for unshrouded turbines, 75% for the shrouded case).

(f) **To replace the traversing directional probes by traversing hot wires.** These can, in principle, measure flow angles in real time and, following an extension of the procedure of Sec. 4.3.5, yield the blade part of the dynamic cross-forces. This should be done in conjunction with option (e) above, to obtain a complete picture of the real-time fluid forces.

Procedures (e) and (f) are indirect, but since we have shown good correlation between directly measured and fluid-derived forces for the static case, there is a good basis for extracting at least trends versus frequency in this manner.

Of these, option (d) (eccentrically mounted turbine) is the simplest procedure, and deserves some more scrutiny. It would yield the desired component of force (perpendicular to displacement) only at one whirl frequency, $\Omega = \omega$, but this one whirl speed is conveniently located above the expected range (Ω ~ @ ω), so that dynamic effects which may be only modest at $\omega/2$ will now be amplified and easier to measure.

The essential points in favor of the eccentrically mounted turbine method are two:

(a) **No linear shaking is involved.** From our discussion and partial data, it is clear that the difficulties associated with linear bearing friction are to be avoided if at all possible. In the method under consideration, the shaft bearings would be statically set at their centered position, and locked there. The whirling turbine motion is created by mounting the turbine eccentrically on the shaft. This gives true circular whirl, not shaking along an axis.

(b) **The force to be measured is now F_y, which appears in the dynamometer axis perpendicular to the offset.** The existence of damping would manifest itself as a change in the magnitude of this F_y when compared to a static measurement. This is very different from the linear shaking case, where we need to extract the phase of F_x (where the main inertia forces occur) in order to measure damping of the F_y forces.

Because of the absence of linear shaking, we don't expect a high level of noise in the form of high frequency ringing or other dry friction effects. The inertia of the turbine, which dominates the F_x component, is now (a) not along the axis of interest, and (b) steady. Thus, the relevant data, those sensed by the gauges for the Y axis, should be fairly clean.

An additional reason to expect clean signals in the dynamometer Y axis is that, with the turbine shaft statically fixed at its centered position, the disturbances due to the slight misalignment of the intermediate shaft segment do not arise. These disturbances have been there even in our static offset testing, and have been dealt with (as explained in Sec. 2.3.1) through careful phase-locked filtering. However, we think they are the cause of the residual ±5% or so error in our static force data.

The inertia $M_t \omega^2 e_x$ (where e_x is the offset) of the turbine will produce some centrifugal deflection. The lowest estimate for the stiffness here comes from the observed ringing frequency of ω_t = 9300 rpm and the mass M_t (in reality some additional mass must be involved). This gives $K = M_t \omega_t^2$ and the deflection δ can then be found from

$$M_{turb.}\omega^2 e_x \cong M_{turb.}\omega_n^2 \delta$$

$$\delta = \left(\frac{\omega}{\omega_n}\right)^2 e_x = \left(\frac{3440}{9300}\right)^2 e_x = 0.14\, e_x$$

This being an upper-bound estimate, it shows that centrifugal deflection is not a real problem, although one would need to monitor the actual tip gap in operation using the proximeters.

In terms of data acquisition, since the output is now a DC signal, synchronization ceases to be a driving concern (which it very much is for linear shaking, or even static offsets). All that is required is control of sensor drift and some form of zero suppression to boost the sensitivity. These do not appear to be serious problems.

The quality of the data can be improved by repeating the whirling test at various turbine speeds, in each case keeping the ratio (mass flow/speed) constant. This ensures both equal operating point parameters, such as flow coefficient and pressure ratio, and also equal reduced whirl frequencies ($\Omega H/C_X$). The forces themselves should scale with flow rate, but the Alford coefficient should remain the same. It is to

be observed in this connection that this set of different speed tests does not serve to span the whirl frequency gap between zero and running speed, because it still corresponds in each case to the latter.

Turning now to the possible experimental program, the approach's validity can be verified fairly easily if attention is first focused on the shrouded turbine. All that is required is a new set of mounting holes for the turbine as it mates with the dynamometer, and a slight re-machining of the lip on the mounting surface, to allow for a 10-15 mil offset. The forces under static deflection have already been measured, and could be repeated for verification by still using the current mounting holes. The next step would be to change to the new (eccentric) mounting position, center the shaft, and attempt to measure the (DC) F_y component, as discussed. As verification that whatever difference may be found between the two measurements originates from the dynamic effects, we can monitor the seal cavity pressure distributions using one or more Kulites (as we have already done for other purposes). Since we have verified that most of the cross-force in the shrouded turbine arises in fact from the seal pressure distribution, we should be able to detect almost the same variance between static and dynamic pressure nonuniformities as between static and dynamic dynamometer data.

After verification of the method as described, additional work (including an unshrouded turbine) could proceed along two optional paths:

(a) To limit measurements to the eccentric turbine ($\Omega = \omega$) case, including supporting Kulite data on wall pressure distributions in real time. This would provide complete data on a single, but important, whirl frequency and answer the fundamental question of whether dynamic effects are or are not important in unshrouded turbines.

(b) To include fluid surveys with hot wire anemometers placed at the downstream locations where the 3- and 5-hole probes were for the static tests. This can be

done over the whole range of linear shaking frequencies and, as we did in the static case, the flow angles measured can be used to calculate the Alford forces, this time at various Ω frequencies. We showed (Sec. 8.2) that, with linear shaking, the Alford damping must be obtained from F_x data, most likely from their phase angle. This was very difficult using the dynamometer, because of the intrusion of the large F_x component from turbine inertia. On the other hand, if the F_x measurement is from flow angles, there is no such problem and the phase to be measured is of the order of $\tan^{-1}(\Omega C_{xx}/K_{xx})$, which is large if C_{xx} is significant. Also, obviously, the ringing and irregularities introduced by linear bearing friction have no effect on these data.

8.8 Recapitulation

Due to the much higher level of difficulty involved, this was the least successful segment of our work, and the original goals of measuring the dynamic, as well as the static, Alford forces was not met. A good start was made, however:

- The test facility was modified to produce dynamic linear offsets in the frequency range of 0.3 to 0.5 of nominal spin rate.
- Data acquisition procedures were developed to continuously monitor all forces and displacements.
- Data reduction procedures were developed to filter out low frequency noise by phase-locked averaging.
- A first order interpretation of data obtained at various facility pressures and at various shaking frequencies was made. In particular, the nature and origin of the observed high frequency noise was clarified as deriving from the dry friction present in the linear bearings.

Several alternative avenues were preliminarily investigated to obtain the important information on dynamic Alford forces. Of these, the method based on

eccentric placing of the turbine on a concentric shaft was found most attractive. Other feasible options involved real-time acquisition of fluid data and extraction for forces from them.

9.0 Theoretical Investigation

9.1 Overview

Despite the fact that the emphasis of this program was clearly on the acquisition of experimental data, it was recognized from the beginning that these data could never cover more than a small fraction of the practical turbine configurations, and that a rational basis was needed to extend the results to potential future designs. This was the motivation for our theoretical work.

The general area of turbine blade tip gap flows and their effects constitutes a large subset of turbine aerodynamics, and has been approached theoretically in a variety of ways. In particular, if the aim is the clarification of the very complex flow patterns in the tip region, the rapid advances made recently in computational fluid mechanics, including 3-D viscous flows, make this the most promising avenue of research. However, our particular interest is in the perturbations introduced by the non-symmetric placement of an offset turbine. These effects are relatively small in the context of the strong localized flow features associated with tip leakage (leakage jets, leakage vortices, local separation, etc.), and a straightforward 3-D turbine calculation attempting to capture them all would need to cover the whole stage, plus commensurate distances upstream and downstream, and would also need to be quite detailed and precise. While this may be a desirable topic for future work, a simpler and more focused approach was sought for our purposes.

A possible ordering principle that can be used to sort out the various phenomena associated with the Alford force problem is the disparity of the scales involved. The most detailed level involves the scale of the gap itself. This includes the discharge jet, the development of thin boundary layers on the hub and blade tip, the local separation bubble at the gap inlet, on the sharp corner of the blade tip, etc. At the next lower level of detail are a variety of blade-scale effects due to the tip gap: radial migration of approaching flow towards the gap, formation of a vortical rolled-up structure on the downstream side, flow under-turning over the outer 20-30% of the blade span, etc. Finally, on an even broader and less detailed scale, namely, the scale of the turbine radius, we can discern most clearly the specific effects of the turbine offset: azimuthal variations of efficiency and work per blade, azimuthal pressure non-uniformity, and azimuthal redistribution of flow.

These three scales, δ, H, and R, are typically in ratios of the order $\delta/H \sim 0.01$, $H/R \sim 0.1$-0.3, and the smallness of these ratios can be exploited analytically to simplify the formulation. In essence, the gap-scale flows are set up by conditions of pressure, etc., which occur very near the tip itself, when measured on the scale of H. Thus, they can be understood separately with minimal reference to blade-scale effects (and even less to radius scale effects) except insofar as these broader scales set up the boundary conditions for the gap flow. Similarly, the radial redistribution and other blade-scale effects are driven by "local" values of quantities which are variable in the azimuthal direction, and can be analyzed as if there were no such variation. They are, at the same time, influenced by the details of the near-tip (gap scale) phenomena, referred to above. Finally, the azimuthal variations "see" the effects on the smaller scales mainly as connecting conditions between upstream and downstream flows, with an inherent asymmetry introduced by the turbine offset.

These distinctions acquire an even sharper meaning when we examine time-dependent offsets due to vibration or whirling of the turbine shaft: the unsteady effects are then entirely associated with the largest scale, R. This is because the reduced frequency $\Omega R/c_x$ can be of order unity (Ω, the whirl speed, is not far from ω, the spin rate, and $\omega R/c_x = 1/\phi \sim 1$-3, where ϕ is the flow coefficient). On the other hand, the reduced frequencies $\Omega H/c_x$, $\Omega\delta/c_x$ formed with the other scales are smaller by H/R and δ/R, respectively, which makes the flow *quasi-static* on these scales – it can be described as if it were steady flow, only using the instantaneous values of the gap, pressure ratio, etc.

We have explicitly made use of these multiple-scale considerations in setting up a hierarchy of interconnected analytical models. These will be briefly described here, and a detailed account of each will follow (in some cases, by reference to earlier work).

1) **On the gap scale**, three different, progressively more refined models have been developed:
   a) Zero work done by the leakage flow. This is incorporated into the simpler form of the blade-scale model below (2a).
   b) Partial tip work, derived by examination of the vortex roll-up dynamics. This enters the

more refined version (2b) of the blade-scale model.

c) Viscous effects on gap flow. These can be important for very small tip gaps and thick turbine blades, particularly due to wall motion against the pressure gradient. This work has yet to be connected explicitly to the other models.

2) **On the blade scale,** the effects of a constant tip gap have been analyzed by:

a) A meridional plane actuator disc model with a gap through which escapes non-working fluid.

b) A variation of (2a) in which the model (1b) is incorporated to allow for the partial turning of the gap flow.

These two models allow predictions of the loss of work due to the gap, the efficiency loss, the size and flow velocity vector in the gap flow, etc. These can then be used in the radius-scale model (3b) (below).

3) **On the radius scale,** two distinct models were developed, one early in the program, one much later:

a) A very simple radial plane (constant radius) 2-D actuator disc model, with radially averaged properties. The disc connecting conditions reflected the variability of the gap through an empirical coefficient, $\beta = \partial\eta/\partial(e/H)$. Perfect trailing edge guidance was assumed on both, stator and turbine.

b) A refined radial plane actuator disc model which uses as the connecting conditions the results of the blade scale models above, thus incorporating consistently the smaller scale effects, with no recourse to empiricism.

Both these radial scale models account for unsteady gap variations.

As noted, the work on the viscous effects has not reached the point where it can be incorporated into the more global analysis. For this reason, it will be discussed separately at the end of the theory section. The simplified radial plane 2-D model (3a) was fully discussed in Ref. [3], and will not be repeated here, as it has been superseded by the more complete model (3b). We will next give a detailed account of models (2a) and (2b), which include (1a) and (1b) respectively.

This will lead to the large scale synthesis of model (3a).

The account that follows is largely taken from our previous writing in Ref. [3].

9.2 Blade-Scale Effects of Tip Leakage

9.2.1 Introduction

The effects of the finite gap at the tip of the blades of various kinds of turbomachinery has long been a topic of study, both theoretical and experimental, motivated largely by its strong impact on stage performance. An additional motivation arises, in our case, from the role of blade-tip losses in the generation of de-stabilizing cross forces on turbine disks. The mechanism for these forces, as first proposed by Alford [1] and Thomas [2], is depicted in Fig. 9.1. It is an empirical observation that the efficiency of a turbine decreases more or less linearly with the ratio of tip gap to blade height:

$$\eta = \eta_o - \beta \frac{\delta}{H} \tag{9.1}$$

where β is a numerical factor of order 1-2. Alford assumed that the same fractional reduction would also affect the force f per unit tangential length:

$$\frac{f}{f_{IDEAL}} = \frac{f_o}{f_{IDEAL}} - \beta \frac{\delta}{H} \tag{9.2}$$

It will be clear in what follows that the fractional loss of force f (or work) is in general different from that of efficiency, and may actually have variation trends which are opposite. For now, we follow Alford's argument. If a turbine disk with mean gap $\bar{\delta}$ is offset by e_x in the transverse Ox direction, then, measuring azimuth θ from the point where the gap is maximum,

$$\delta(\theta) = \bar{\delta} + e_x \cos\theta \tag{9.3}$$

We can now project all forces in the OY direction, (perpendicular to the offset), to obtain $f_y = f \cos\theta$ per unit length, for a total cross-force

$$F_y = \int_0^{2\pi} f_y R \, d\theta \ .$$

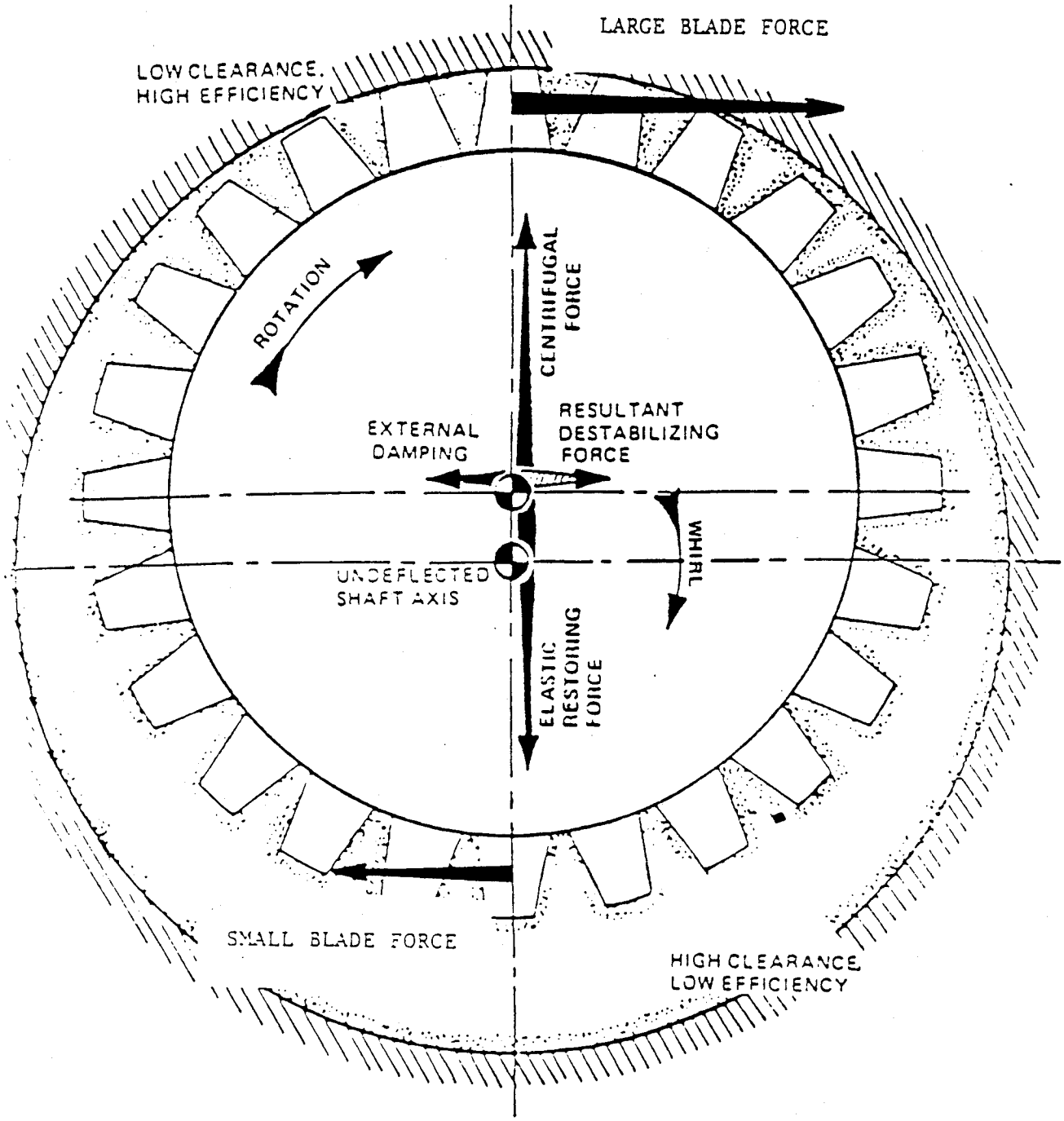

Fig. 9.1: Contribution to whirl from turbine tip clearance effects

Using Eqs. (9.2) and (9.3),

$$F_y = \beta \frac{e_x}{H} f_{IDEAL} \pi R$$

or, noting that the ideal torque is $Q_{IDEAL} = 2\pi R^2 f_{IDEAL}$,

$$F_y = \frac{\beta}{2} \left(\frac{Q_{IDEAL}}{R}\right) \left(\frac{e_x}{H}\right) \tag{9.4}$$

This force is only opposed by inertia and damping forces, since the structural restoring reactions to e_x would normally act along OX. The result, if damping is insufficient, is a divergent whirling motion. Equation (9.4) shows the importance of the loss factor β (Eq. (9.1)) (or, more correctly, the work loss factor, to be introduced later) for prediction of the stability properties of a rotor.

The extensive data base on tip-loss factors has been correlated by many authors on the basis of various levels of analysis. A good review of these efforts was presented by Waterman [18], from whose paper we have borrowed Fig. 9.2. Waterman selected 10 well documented turbine test cases and five tip-loss prediction schemes, and obtained results which are statistically summarized in Table 9.1, also taken from Ref. [18]. (Results based on Lakshminarayana's method were omitted because of their systematic overpredictions). Given that β averages roughly 1.5, the variances in the first column of Table 9.1 indicate a fairly unsatisfactory state of affairs regarding predictive capabilities. Perhaps at the root of this situation is the lack of a clear model of how the losses arise. Generally speaking, the various approaches used have fallen into three categories:

(a) Models based on calculation of the pressure-driven tip gap flow rate, plus the assumption that some portion of the kinetic energy of the flow is lost. Various corrections are used for viscous and other effects. The models of Rains [11] and Vavra [19] are in this category.

(b) Models based on adaptations of wing theory to predict the "induced drag" produced by the trailing vorticity escaping at each blade tip. A key difficulty is the prediction of tip lift retention, which determines the strength of such vortices. Examples are Lakshminarayana

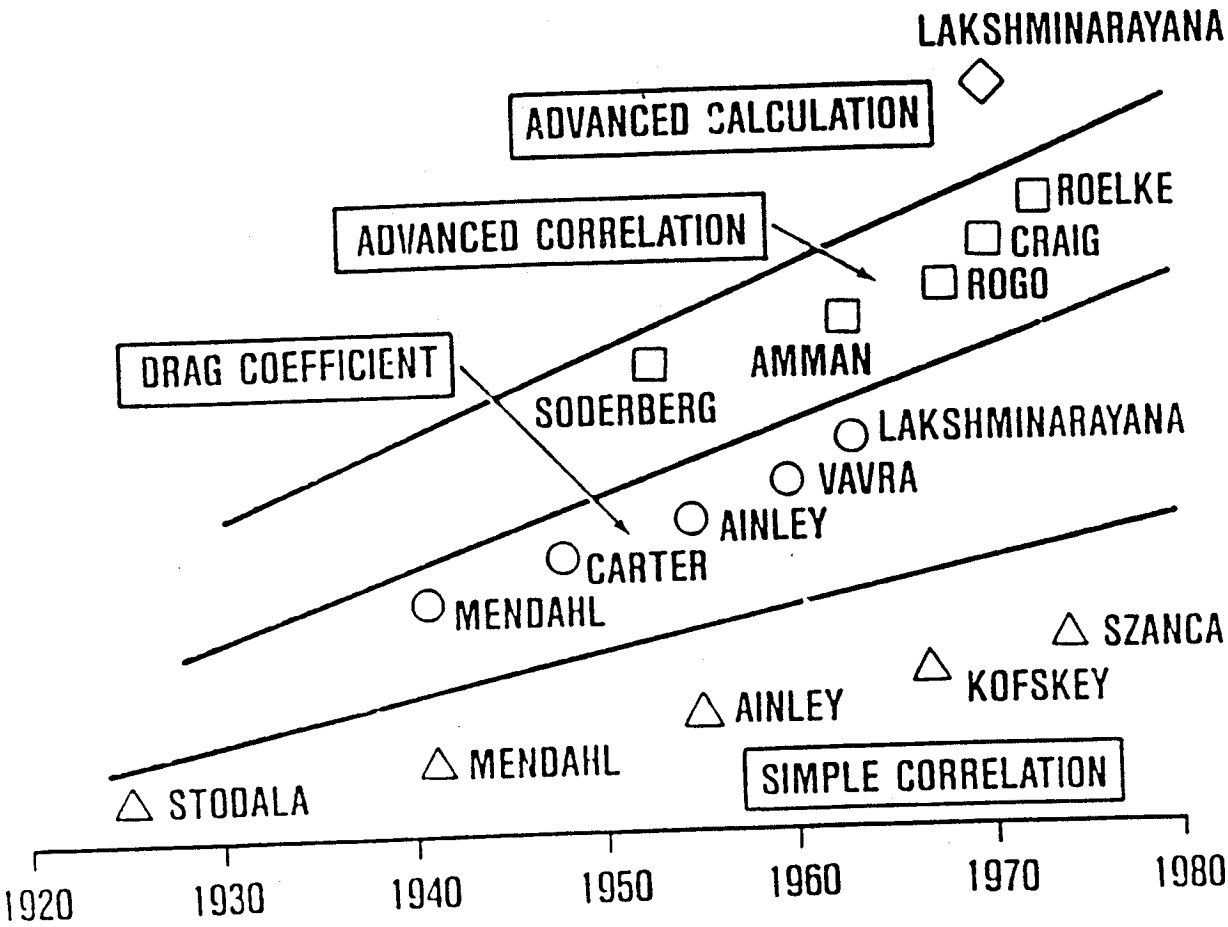

Fig. 9.2: Various levels of blade-tip loss theory (from Waterman, Ref. 18)

TABLE 9.1

MEAN SQUARED ERROR AND MEAN ERROR MAGNITUDE FOR VARIOUS TIP LOSS CORRELATIONS (FROM REF. 18)

	$\frac{1}{N}\sum\left(\frac{\Delta\eta}{\Delta\tau/h}\Big\vert_{PRED} - \frac{\Delta\eta}{\Delta\tau/h}\Big\vert_{EXP}\right)^2$	$\frac{1}{N}\sum\left(\frac{\Delta\eta}{\Delta\tau/h}\Big\vert_{PRED} - \frac{\Delta\eta}{\Delta\tau/h}\Big\vert_{EXP}\right)$
Kofskey	0.227	-0.093
Ainley	1.186	-0.074
Soderberg	0.638	0.500
Roelke	0.192	0.235

[20], [21] and Lewis and Yeung [22].

(c) More recently, detailed two- and three-dimensional numerical computations of flow in a passage, including gap effects, have become possible [23], [24]. While these give important insight as to many details of the flow pattern, they still lack the precision required to calculate the small deficits which add up to the losses. This is not unlike the situation regarding a much better explored problem, i.e., drag predictions on a 2-D airfoil.

The models in Group (a) above are basically correct as to gap flow predictions, and can be regarded as a satisfactory first order description of near-gap effects, at least for thin blades, where viscous effects can often be neglected. On the other hand, they ignore the concomitant small changes to the flow over the rest of the blade when a small gap is present. We will show later that it is these changes that are responsible for most of the blade force losses.

The models of Group (b), with their emphasis on induced drag, come closer to capturing the essence of the phenomenon. Indeed, the flow disturbances at the blades induced by trailing vortices can be one way of describing the blade-scale effects of tip leakage. What has been lacking is a globally consistent model of the strength and distribution of these vortices. Thus, Lakshminarayana [20] used an array of straight-line trailing vortices of uniform strength, equal to an empirically determined fraction of the blade lift. Ad-hoc corrections for vortex roll-up [21] improve the details of blade pressure distributions with little positive impact on loss prediction.

In this work, we emphasize the global nature of the blade-tip problem by using an actuator disk model for the stage. Details of the near-blade flow are in this way simplified by being relegated to the role of algebraic connecting conditions between the upstream and downstream flows. On the other hand, the spanwise rearrangement of the flow pattern due to preferential migration towards the gap region can be correctly captured, provided one recognizes the discontinuous nature of the downstream velocity distribution (i.e., the presence of a shear layer along the tip streamsurface). This shear layer is, of course, the result of azimuthally smearing the individual "trailing vertices" of the blades. With some reasonable mathematical approximations, results can be obtained from this model which agree with data to an equal or greater extent than

existing correlations. Perhaps more importantly, these results are easily enough related to the basic nature of the problem that generalization is possible to include effects such as non-uniform gap distributions (our principal goal) or non-uniform inlet flow. Improvements can also be introduced on the details of the flow on the gap scale to account for partial tip loading, as will be discussed.

9.2.2. Formulation

For maximum simplicity, our initial model will make the following assumptions, some of which will be later relaxed:

(a) Incompressible, inviscid flow

(b) Two-dimensional geometry

(c) Uniformity along the tangential (y) direction

(d) Fluid passing through the rotor blade-tip gap does no work.

(e) Stage collapsed in the axial direction to a single plane, and smeared in the azimuthal direction.

The "actuator disk" which represents the stage consists of a full-span stator and a partial-span rotor (Fig. 9.3), both occupying the x = 0 plane. Since there are no variations with y, the azimuthal momentum equation reads

$$c_x \frac{\partial c_y}{\partial x} + c_z \frac{\partial c_y}{\partial z} = 0 \tag{9.5a}$$

or, introducing the vector $\vec{c}_\perp = \vec{i}c_x + \vec{k}c_z$ to represent the meridional velocity projection,

$$\vec{c}_\perp . \nabla c_y = 0 \tag{9.5b}$$

showing that c_y is simply convected by $\vec{c}_\perp$. Similarly, the vorticity equation reduces in this case to

$$\vec{c}_\perp . \nabla \omega_y = 0 \tag{9.6}$$

where

$$\omega_y = \frac{\partial c_x}{\partial z} - \frac{\partial c_z}{\partial x} \tag{9.7}$$

and the Bernoulli equation reduces to

$$\vec{c}_\perp . \nabla B_\perp = 0 \tag{9.8}$$

where

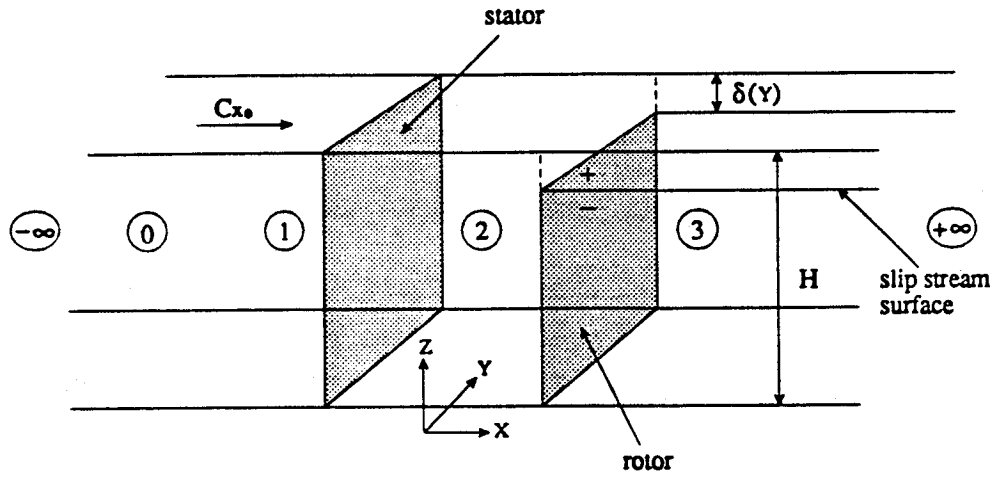

Fig. 9.3: Channel flow with constant blade-tip clearance

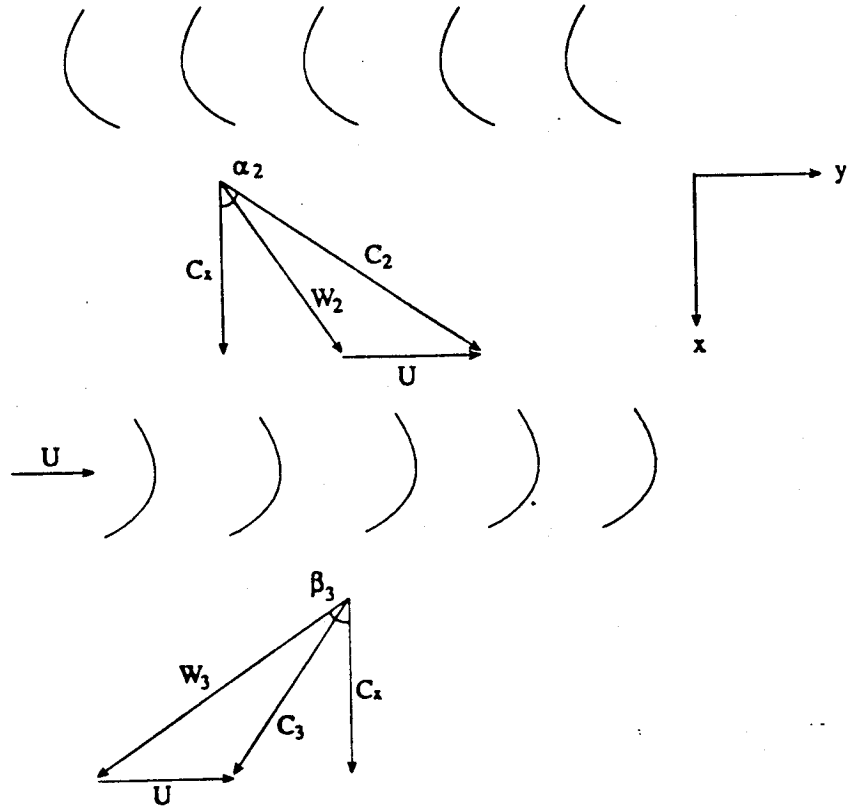

Fig. 9.4: Velocity triangles

$$B_\perp = \frac{P}{\rho} + \frac{1}{2} c_\perp^2 \tag{9.9}$$

Continuity is satisfied by introducing the stream function $\Psi(x,z)$ for the meridional flow:

$$c_x = \frac{\partial \Psi}{\partial z} \; ; \; c_z = -\frac{\partial \Psi}{\partial x} \tag{9.10a,b}$$

and then Eqs. (9.5b), (9.6) and (9.8) reduce to

$$c_y = c_y(\Psi) \tag{9.11}$$

$$\omega_y = \omega_y(\Psi) \tag{9.12}$$

$$B_\perp = B_\perp(\Psi) \tag{9.13}$$

Using in Eq. (9.12), the definitions in Eqs. (9.7) and (9.10) produce the equation which governs $\Psi(x,z)$:

$$\nabla^2 \Psi = \omega_y(\Psi) \tag{9.14}$$

where, in this case,

$$\nabla^2 = \nabla_\perp^2 = \frac{\partial^2}{\partial x^2} + \frac{\partial^2}{\partial z^2}.$$

Notice that the meridional flow (c_x, c_z) is decoupled from c_y, and can be solved for first. The component c_y, as well as

$$\omega_x = -\frac{\partial c_y}{\partial z}, \quad \omega_z = \frac{\partial c_y}{\partial x},$$

can be found *a posteriori.*

Upstream of the stage ($x < 0$), we assume the flow is irrotational ($\omega_y = 0$), and Ψ simply obeys Laplace's equation. Uneven work extraction as the flow goes through the stage gives rise to non-zero vorticity ω_y downstream of the disk, and the value of ω_y is carried unchanged on each streamline from here on.

The vorticity ω_y and the meridional Bernoulli constant, $B_\perp$ are related to each other in a simple way. Starting from the Lamb form of the meridional momentum equation,

$$\nabla B_\perp + \omega_y \vec{k} \times \vec{c}_\perp = 0 \qquad \left(\vec{k} = \frac{\vec{\omega_y}}{\omega_y}\right)$$

and taking the cross-product with $\vec{c}_\perp$,

$$\omega_y = -\frac{1}{c_\perp^2} \vec{c}_\perp \times \nabla B_\perp \tag{9.15}$$

Remembering that, $B_\perp = B_\perp(\Psi)$, we have

$$\nabla B_\perp = \left(\frac{dB}{d\Psi}\right) \nabla\Psi ,$$

and

$$(\vec{c}_\perp \times \nabla B_\perp)_y = \left(\frac{dB}{d\Psi}\right) (\vec{c}_\perp \times \nabla\Psi)_y .$$

From the definition of Ψ (Eq. (9.10)), $(\vec{c}_\perp \times \nabla\Psi)_y = -c_\perp^2$, so that

$$\omega_y = \frac{dB_\perp}{d\Psi} \tag{9.16}$$

This relationship opens the way for a connection between the downstream ω_y and the non-uniformity of extracted work at the disk. Let subscripts 1 and 3 denote stations just upstream and just downstream of the stage (Fig. 3). Then, because of continuity,

$$c_{x_3} = c_{x_1} \tag{9.17}$$

and, since we assume spanwise uniform blading, which can exert no forces on the flow in the z-direction,

$$c_{z_3} = c_{z_1} \tag{9.18}$$

Because of Eqs. (9.17), (9.18) and the definition (9.9),

$$B_{\perp_1} - B_{\perp_3} = \frac{P_1 - P_3}{\rho} \tag{9.19}$$

Now, upstream of the stage, the absence of vorticity implies $\left(dB_{\perp_1}/d\Psi\right) = 0$ and so, from (9.16),

$$\omega_y = \frac{dB_{\perp_3}}{d\Psi} = -\frac{d(B_{\perp_1} - B_{\perp_3})}{d\Psi} = -\frac{d}{d\Psi}\left(\frac{P_1 - P_3}{\rho}\right) \tag{9.20}$$

which gives the vorticity ω_y when the distribution of (isentropic) static enthalpy extraction $(P_1-P_3)/\rho$ is known.

The geometry of the stage blading is shown in Fig. 9.4. Euler's equation gives for the stagnation enthalpy decrease across the stage

$$- \Delta h_t = U[c_x \tan \alpha_2 - (U - c_x \tan \beta_3)] \tag{9.21}$$

where U is the wheel speed. Adding to this the kinetic energy increase

$$\Delta \text{ (K.E.)} = \frac{1}{2} c_{y_3}^2 = \frac{1}{2} (U - c_x \tan \beta_3)^2 \tag{9.22}$$

we obtain, for any streamline which crosses the disk in the region covered by the blades (not the gap)

$$\left(\frac{P_1 - P_3}{\rho}\right)_{BL} = U c_x \tan \alpha_2 - \frac{1}{2}(U^2 - c_x^2 \tan^2 \beta_3) \tag{9.23}$$

Exactly how much work is extracted from those streamlines which at some point cross the blade-tip gap is a relatively complicated question to answer, and to which we will return in Sections 9.2.8 and 9.2.9. For now, we will make the simplest possible approximation, namely, that no work is extracted. This implies for such streamlines

$$\left(\frac{P_1 - P_3}{\rho}\right)_{GAP} = \frac{P_1 - P_2}{\rho} = \frac{1}{2} c_x^2 \tan^2 \alpha_2 \tag{9.24}$$

In Eqs. (9.23) and (9.24), the axial velocity c_x at the disk is to be regarded as a function of z, in anticipation of redistribution of the flow in response to the presence of the gap. When using Eq. (9.20), therefore, we will put

$$\frac{d}{d\Psi} = \frac{\partial}{\partial c_x}\left(\frac{\partial c_x}{\partial z}\frac{\partial z}{\partial \Psi}\right)_{x=0} = \left(\frac{1}{c_x}\frac{\partial c_x}{\partial z}\right)_{x=0}\frac{\partial}{\partial c_x}$$

and so the ω_y vorticity can be calculated from Eqs. (9.23,) and (9.24) as

$$\text{BLADES:} \quad \omega_y = -\left[\frac{U}{(c_x)_{x=0}} \tan \alpha_2 + \tan^2 \beta_3\right]\left(\frac{\partial c_x}{\partial z}\right)_{x=0} \tag{9.25a}$$

$$\text{GAP:} \quad \omega_y = -\tan^2 \alpha_2 \left(\frac{\partial c_x}{\partial z}\right)_{x=0} \tag{9.25b}$$

Since there is a discontinuity in the connecting conditions for flow through the gap versus flow through the blade passages, we can also expect a discontinuity, in the form of a shear layer,

on the downstream portion of the streamline which passes through the blade tips. Denoting by superscripts (+) and (-) the regions on the gap and blade side of this layer, respectively, its strength (at least for the y-component) will be

$$Q = \int_{-}^{+} \omega_y \, d\Psi = B^{+}_{\perp_3} - B^{-}_{\perp_3} \tag{9.26}$$

With the help of Eqs. (9.19), (9.23) and (9.24), and the fact that no discontinuity exists in $B_{\perp_1}$ we obtain

$$Q = U c_{\bar{x}} \tan \alpha_2 - \frac{1}{2}\left(U^2 - c_{\bar{x}}^2 \tan^2 \beta_3\right) - \frac{1}{2} c_{\bar{x}}^{+2} \tan^2 \alpha_2 \tag{9.27}$$

Recapitulating, the equation for Ψ is

$$\text{UPSTREAM:} \qquad \nabla^2 \Psi = 0 \tag{9.28a}$$

$$\text{DOWNSTREAM:} \quad \begin{Bmatrix} \text{GAP} \\ \text{BLADES} \end{Bmatrix}$$

$$\nabla^2 \psi = \begin{Bmatrix} -\tan^2 \alpha_2 \\ -\left[\dfrac{U}{(c_x)_{x=0}} \tan \alpha_2 + \tan^2 \beta_3\right] \end{Bmatrix} \left(\frac{\partial c_x}{\partial z}\right)_{x=0} + Q\,\delta(\Psi - \Psi_{TIP}) \tag{9.28b}$$

where $\delta(\Psi - \Psi_{TIP})$ is Dirac's delta function.

The boundary conditions are:

$$\Psi(x,0) = 0 \quad ; \quad \Psi(x, H) = c_{x_o} H$$

$$\Psi(-\infty, z) = c_{x_o} z \quad ; \quad \frac{\partial \Psi}{\partial x}(+\infty, z) = 0$$

$$\Psi(0^-, z) = \Psi(0^+, z) \quad ; \quad \frac{\partial \Psi}{\partial x}(0^-, z) = \frac{\partial \Psi}{\partial x}(0^+, z) \tag{9.29}$$

9.2.3. Inverse Coordinates and Linearization

Given the convective nature of several key quantities, the stream function Ψ is a natural independent variable for our problem. This will be particularly helpful for numerical solution,

since the discontinuity at $\Psi = \Psi_{TIP}$ can then be explicitly retained with no numerical smearing. We therefore change independent variables from (x,z) to (x,Ψ), and regard z as the new dependent quantity; the function z(x,Ψ), of course, represents the shape of the streamlines. Using subscripts on z to denote differentiation, the velocity components are then

$$c_x = \frac{1}{z_\Psi} \quad , \quad c_z = \frac{z_x}{z_\Psi} \tag{9.30 a,b}$$

and also

$$\left(\frac{\partial c_x}{\partial z}\right)_{x=0} = -\left(\frac{z_{\Psi\Psi}}{z_\Psi^3}\right)_{x=0} \tag{9.31}$$

and the Laplacian operator becomes

$$\nabla^2\Psi = \frac{1}{z_\Psi^3}\left[-z_\Psi^2 z_{xx} + 2 z_x z_\Psi z_{x\Psi} - \left(1 + z_x^2\right) z_{\Psi\Psi}\right] \tag{9.32}$$

The governing equation $\nabla^2\Psi = \omega_y(\Psi)$, which in its original form was nonlinear by virtue of the dependence of ω_y on Ψ, is now non-linear only because of the derivative products on its left-hand side. Whereas linearization in the original coordinates would imply regarding ω_y as a small quantity, linearization in inverse coordinates can fully retain ω_y, and implies only neglecting certain products of velocity disturbances on the LHS of the equation. Thus, although the results will be later verified by numerical solution of the full non-linear equation, we begin our investigation by linearizing z(x,Ψ) about the uniform flow condition:

$$z = \frac{\Psi}{c_{x_0}} + \tilde{z} \tag{9.33}$$

where c_{x_0} is the velocity far upstream of the disk, and $\tilde{z} << z$.

For the velocity components this implies, to first order,

$$c_x \cong c_{x_0} - c_{x_0}^2 \tilde{z}_\Psi$$

$$c_z \cong c_{x_0} \tilde{z}_x \tag{9.34a,b}$$

The governing equation (Eq. (9.28)) reduces, to first order, to:

$$\text{UPSTREAM:} \quad \frac{1}{c_{x_0}^2}\tilde{z}_{xx} + \tilde{z}_{\Psi\Psi} = 0 \tag{9.35}$$

DOWNSTREAM $\left\{ \begin{matrix} \text{GAP} \\ \text{BLADES} \end{matrix} \right\}$:

$$\frac{1}{c_{x_0}^2}\tilde{z}_{xx} + \tilde{z}_{\Psi\Psi} = -\begin{Bmatrix} \tan^2\alpha_2 \\ \dfrac{U}{(c_x)_{x=0}}\tan\alpha_2 + \tan^2\beta_3 \end{Bmatrix}(\tilde{z}_{\Psi\Psi})_{x=0} - \frac{Q}{c_{x_0}^3}\delta(\Psi-\Psi_{TIP}) \tag{9.36}$$

and the boundary conditions are now

$$\tilde{z}(x,0) = \tilde{z}(x, c_{x_0} H) = 0 \tag{9.37a}$$

$$\tilde{z}(-\infty,\Psi) = \tilde{z}_x(+\infty,\Psi) = 0 \tag{9.37b}$$

$$\tilde{z}(0^-, \Psi) = \tilde{z}(0^+,\Psi) \tag{9.37c}$$

$$\tilde{z}_x(0^-, \Psi) = \tilde{z}_x(0^+,\Psi) \tag{9.37d}$$

The shear layer strength Q in Eq. (9.36) remains as defined by Eq. (9.27), where c_x^+ and c_x are to be found as part of the solution.

9.2.4. The Nature of the Throughflow Distribution at the Disk

Although there is some interest in the flow distributions elsewhere, the main results to the obtained depend on how the flow is distributed at the disk itself. We will show in this section that, in the present linearized approximation, the distribution consists of two constant, but different axial velocity levels; one for flow crossing the gap, and one for flow through the bladed region.

One part of the proof relies on a general property of linearized actuator disk flow; the disturbance at the disk is half as strong as it is far downstream. This property is best known from elementary propeller theory, where it holds (with no need for linearization) by virtue of the constancy of the background pressure. For linearized, confined flows, it is proven, for example, in Horlock's monograph [25].

Since Horlock's analysis is in direct coordinates, the statement must be qualified by saying that the disturbance doubles between disk and downstream stations at the same z coordinate. In our analysis i.e., with (x,Ψ) as coordinates, the disturbances double along a given streamline. A

proof is given in Appendix 9A. The "disturbance" can be either $\tilde{z}(\Psi)$, the displacement of a streamline, or the shear, $\partial c_x/\partial z$. Using the latter form, then,

$$\left(\frac{\partial c_x}{\partial z}\right)_{x=\infty} = 2\left(\frac{\partial c_x}{\partial z}\right)_{x=0} \tag{9.38}$$

On the other hand, the shear $(\partial c_x/\partial z)_{x=\infty}$ far downstream equals the corresponding vorticity $(\omega_y)_{x=\infty}$, which is given, for example, by the right-hand side of Eq. (9.36), times - $c_{x_o}^3$. Excluding the concentrated vorticity Q at $\Psi = \Psi_{TIP}$, and using Eq. (9.31), this takes the form

$$\left(\frac{\partial c_x}{\partial z}\right)_{x=\infty} = \omega_y(\Psi) = F(\Psi)\left(\frac{\partial c_x}{\partial z}\right)_{x=0} \tag{9.39}$$

where

$$F(\Psi) \equiv -\left\{ \begin{array}{c} \tan^2 \alpha_2 \\ \\ \dfrac{U}{(c_x)_{x=0}} \tan \alpha_2 + \tan^2 \beta_3 \end{array} \right\} \quad \left\langle\!\left\langle \begin{array}{c} \text{GAP} \\ \text{BLADES} \end{array} \right\rangle\!\right\rangle \tag{9.40}$$

Comparing Eqs. (9.38) and (9.39), we can see that, <u>both</u> shears, $(\partial c_x/\partial z)_{x=0}$ and $(\partial c_x/\partial z)_{x=\infty}$ must be zero, unless $F(\Psi) = 2$. This latter condition is ruled out by Eq. (9.40), which shows $F(\Psi) \leq 0$. Once again, this excludes the vorticity concentration at $\Psi = \Psi_{TIP}$.

We can therefore conclude that the axial velocity distribution at the disk must have the piecewise constant form shown schematically in Fig. 9.5. Since the work done by the flow is uniquely related to the disk throughflow $(c_x)_{x=0}$ (see Eqs. (9.23), (9.24)), the implication is that <u>the turbine work defect due to the presence of the gap will be distributed uniformly along the blade span</u>, in correspondence with the uniform decrease of $(c_x)_{x=0}$. This is at first sight counter-intuitive, given the strong localized effects produced by the gap flow (leakage jets, rolled-up structures, etc). Indeed, the non-linear solutions reported later (Sec 9.2.7.) show some amount of extra work defect near the tip, but the main component by far still remains distributed. This effect may be thought of as the result of the transverse pressure forces set up in the confined flow by the presence of the gap. These forces ensure that the extra flow going to from the gap jet is evenly supplied by the whole passage, and it is this small flow defect that is responsible for the work

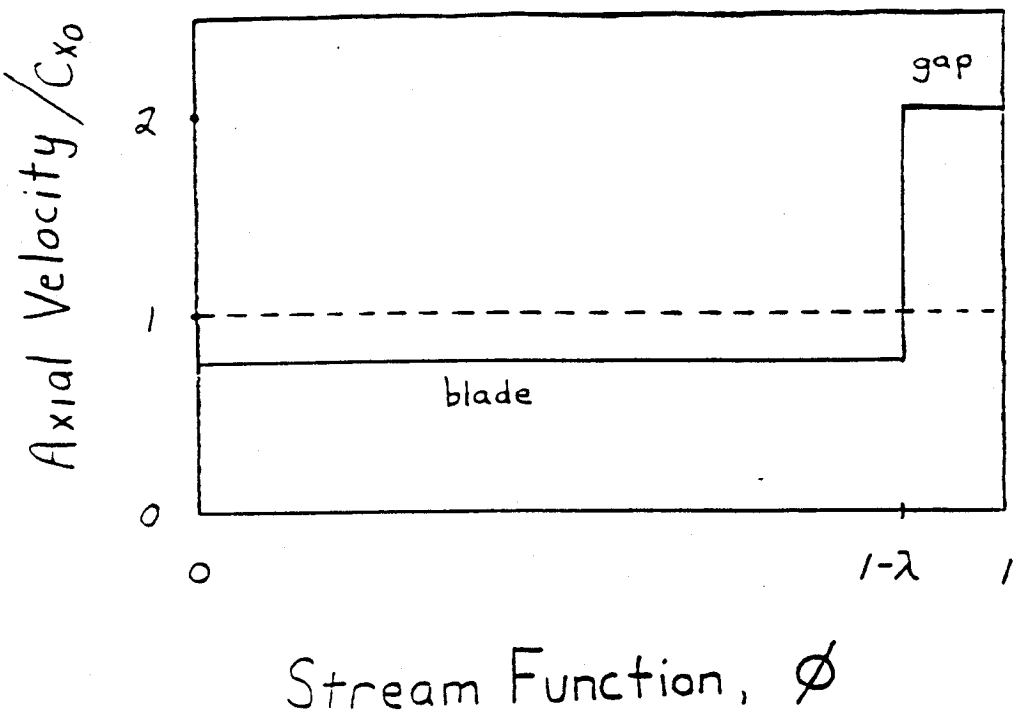

Fig. 9.5: Axial velocity distribution at disk

defect. On the other hand, it remains true that strong total pressure losses must be associated with the dissipation of the sharp discontinuities created near the tip, and this must be taken into account as well when calculating the effect of the tip gap on turbine efficiency (See Sec. 9.2.5.2).

9.2.5 Solution of the Linearized Equations

9.2.5.1 Disk Quantities

Since c_x (x=0) is piecewise constant, the distributed part of the forcing term in Eq. (9.36) disappears, leaving only the shear layer:

$$\frac{1}{c_{x_0}^2}\tilde{z}_{xx} + \tilde{z}_{\Psi\Psi} = -\frac{Q}{c_{x_0}^2}\delta(\Psi - \Psi_{TIP}) \quad (x > 0) \tag{9.41}$$

The values of the two disk velocity levels (Figs. 9.5) can be obtained as follows. First, since $(\omega_y)_\infty = -c_{x_0}^3(\tilde{Z}_{\Psi\Psi})_\infty$ (the x-derivatives vanish), then, integrating across the shear layer at $x = \infty$, and using the definition of Q (Eq. 9.26),

$$\left(\tilde{z}_\Psi^+ - \tilde{z}_\Psi^-\right)_{x=\infty} = -\frac{Q}{c_{x_0}^3} \tag{9.42}$$

where the superscripts (+) and (-) refer to the jet and blades side of the layer, respectively. At the disk, the difference of the $\tilde{z}_\Psi$ values must then be ½ as much:

$$\left(\tilde{z}_\Psi^+ - \tilde{z}_\Psi^-\right)_{x=0} = -\frac{Q}{2c_{x_0}^3} \tag{9.43}$$

Also, integrating z_Ψ from $\Psi=0$ to $\Psi = Hc_{x_0}$, and using the boundary conditions in Eq. (9.37a),

$$\lambda\left(\tilde{z}_\Psi^+\right)_{x=0} + (1-\lambda)\left(\tilde{z}_\Psi^-\right)_{x=0} = 0 \tag{9.44}$$

where λ is the fractional flow through the gap (namely, $\Psi_T = (1-\lambda)\,Hc_{x_0}$) The quantity λ is regarded as a given in our formulation, while the geometrical gap width, δ, is not.

Solving Eqs. (9.43) and (9.44) together,

$$\left(\tilde{z}_\Psi^+\right)_{x=0} = -\frac{1-\lambda}{2c_{x_0}^3}Q \tag{9.45a}$$

$$\left(\tilde{z}_\Psi\right)_{x=0} = \frac{\lambda}{2c_{x_0}^3} Q \tag{9.45b}$$

which translates into the axial velocities (see. Eq. 9.34)

$$\frac{c_x}{c_{x_0}} = \begin{cases} 1 + \dfrac{Q}{2\,c_{x_0}^2}(1-\lambda) & \text{(GAP)} \\ 1 - \dfrac{Q}{2\,c_{x_0}^2}\lambda & \text{(BLADES)} \end{cases} \tag{9.46a,b}$$

Since this gives us the velocities c_x^+ and c_x^- at the disk, we can now substitute (9.46a,b) into the definition (Eq. (9.27)) of Q, which yields a quadratic equation for Q as a function of λ.

After some rearrangement, this is

$$\frac{(1-\lambda)^2 \tan^2\alpha_2 - \lambda^2 \tan^2\beta_3}{4} q^2 + \left[2 + (1-\lambda)\tan^2\alpha_2 + \frac{\lambda}{\phi}\tan\alpha_2 + \lambda \tan^2\beta_3\right] q$$

$$- \left[\frac{2}{\phi}\tan\alpha_2 - \frac{1}{\phi^2} + \tan^2\beta_3 - \tan^2\alpha_2\right] = 0 \tag{9.47}$$

where ϕ is the flow coefficient

$$\phi \equiv \frac{Cx_0}{U} \tag{9.48}$$

and the dimensionless shear layer strength is

$$q = \frac{Q}{c_{x_0}^2} \tag{9.49}$$

The implied gap width, δ, can be easily calculated. Integrating Eq. (9.45b) from $\Psi = 0$ to $\Psi = \Psi_{TIP} = (1-\lambda)\,Hc_{x0}$

$$\frac{\tilde{Z}_{TIP}}{H} = \lambda\,(1-\lambda)\,\frac{q}{2} \tag{9.50}$$

Adding to this the undisturbed value $(1-\lambda)H$, we obtain z_{TIP}, and then $\delta = H - z_{TIP}$. The result is

$$\frac{\delta}{H} = \lambda\left[1 - (1-\lambda)\frac{q}{2}\right] \tag{9.51}$$

This can also be solved for the leakage if the gap is given:

$$\lambda = \frac{2\,(\delta/H)}{1 - \frac{q}{2} + \sqrt{\left(1 - \frac{q}{2}\right)^2 + 4\left(\frac{\delta}{H}\right)\left(\frac{q}{2}\right)}} \tag{9.52}$$

Notice that λ depends non-linearly on (δ/H), both explicitly, and through the dependence of q on λ (Eq. (9.47)). For the practical, small values of λ and (δ/H) this is not a strong non-linearity, however.

9.2.5.2 Work Defect and Efficiency Losses

The power extracted by the turbine, and hence the tip loss coefficient, can also be calculated easily. In coefficient form,

$$\psi \equiv \frac{1}{\dot{m}U^2} \int_0^{\Psi_{TIP}} (h_{t_1} - h_{t_3})\, \rho d\Psi \tag{9.53}$$

The total enthalpy drop is given by Eq. (9.21) for the bladed area (using $c_x = c_{\bar{x}}$), and is zero for the gap.

Remembering that $\rho \frac{\Psi_{TIP}}{\dot{m}} \equiv 1 - \lambda$, we obtain

$$\psi = (1 - \lambda)\left[\phi(\tan\alpha_2 + \tan\beta_3) - 1 - \lambda\phi\frac{q}{2}(\tan\alpha_2 + \tan\beta_3)\right]$$

For zero leakage, $\psi_o = \phi\,(\tan\alpha_2 + \tan\beta_3) - 1$. The relative work defect is then

$$\frac{\psi_o - \psi}{\psi_o} = \lambda\left[1 + \frac{\psi_o + 1}{\psi_o}\frac{1 - \lambda}{2}\,q\right] \tag{9.54}$$

We can now calculate a work defect coefficient w as the relative work decrease (Eq. 9.54) divided by the relative gap width, δ/H. Using Eq. (9.51),

$$w = \frac{1 + \frac{\psi_o + 1}{\psi_o}\,\frac{1 - \lambda}{2}\,q}{1 - \frac{1 - \lambda}{2}\,q} \tag{9.55}$$

This coefficient is not to be confused with the efficiency-loss coefficient β introduced earlier (Eqs. (9.1) to (9.4)). If we agree to work with the total-to-total efficiency η, its evaluation requires in addition the calculation of the total pressure $(P_t)_{MIX}$ at a hypothetical downstream

section where the shear layer has dissipated and conditions are again uniform.

At this "mixed-out" downstream station, the axial velocity must again be c_{x_o} (to conserve mass) and the tangential velocity (from y- momentum balance) must be

$$c_{y_{MIX}} = \lambda\, c_y^+ + (1 - \lambda)\, c_y^- \tag{9.56}$$

where c_y^+ and c_y^- are the tangential velocities in the fluid above and below the shear layer, respectively. Prior to mixing, both c_y^+ and c_y^- are uniform in their respective domains, because they are uniform at the disk (in our two-level approximation), and are then purely convected from there. From Fig. 9.4 we have

$$c_y^+ = c_x^+ \tan \alpha_2 \tag{9.57}$$

$$c_y^- = U - c_x^- \tan \beta_3 \tag{9.58}$$

where Eq. (9.57) reflects the assumption of zero turning of the gap flow, and (9.58) assumes perfect guidance by the rotor blades for the rest of the flow.

The total pressure in the mixed-out region is given by

$$\frac{P_{t_o} - P_{t_{MIX}}}{\rho} = \frac{P_o - P_\infty}{\rho} - \frac{1}{2} c_{y_{MIX}}^2 \tag{9.59}$$

where P_∞ is at a far downstream position, (before or after mixing in the linearized approximation), and we have taken advantage of $(c_x)_\infty = c_{x_0}$, $(c_z)_\infty = 0$. The static pressure drop can be calculated for a streamline which goes through the blades. The drop $P_1 - P_3$ <u>at the disk</u> is given in Eq. (9.23). Upstream of the disk,

$$\frac{P_o - P_1}{\rho} = \frac{1}{2}\left(c_x^2\right)_{x=o} - \frac{1}{2} c_{x_o}^2 \tag{9.60}$$

and downstream, since c_y^- remains invariant,

$$\frac{P_\infty - P_3}{\rho} = \frac{1}{2}\left(c_x^2 + c_z^2\right)_{x=o} - \frac{1}{2}\left(c_x^2\right)_\infty \tag{9.61}$$

Here c_z^2 (x = 0) is a 2nd order quantity in our linear analysis, and will be ignored. Substracting (9.60) and (9.61),

$$\frac{P_o - P_\infty}{\rho} = \frac{P_1 - P_3}{\rho} + \frac{1}{2}(c_{x_\infty})^2 - \frac{1}{2} c_{x_o}^2 \tag{9.62}$$

Combination of Eqs. (9.58), (9.61) and (9.23) therefore gives the total pressure from far upstream to the hypothetical downstream mixed-out station. This quantity is the ideal work extracted per unit volume, and the efficiency is then

$$\eta = \frac{\psi}{\left(\frac{P_{t_o} - P_{t_{MIX}}}{\rho U^2}\right)} \tag{9.63}$$

where ψ is as given by Eq. (9.54). The efficiency loss factor follows as

$$\beta = \frac{1 - \eta}{\delta/H} \tag{9.64}$$

As noted, the efficiency η is affected by the decrease of ψ due to the gap, also by that of the total pressure drop. With no gap, and everything else being ideal, we would have $\eta = 1$. Let the total pressure drop be therefore expressed as

$$\frac{P_{t_0} - P_{t_{MIX}}}{\rho U^2} = \psi_0 \left(1 - \xi \frac{\delta}{H}\right) \tag{9.65}$$

where ξ (which is a positive quantity) can be calculated following the outline explained above. Then it is easy to show that the loss factor β and the work defect factor w are related through

$$\beta = \frac{w - \xi}{1 - \xi \frac{\delta}{H}} \tag{9.66}$$

so that β is in general smaller than w. Calculated results will be shown in Section 9.2.6.

9.2.5.3 Velocity Distribution Away from Disk

The solution to Eq. (9.41) is most easily written in terms of Fourier series in Ψ, which can also represent the discontinuities occurring along the shear layer. This is the form naturally obtained by formal separation of variables. Imposing all the boundary conditions listed by Eq. (9.29), we obtain

$$\frac{\tilde{z}}{H} = \begin{cases} \sum_{n=1}^{\infty} \alpha_n e^{n\pi x/H} \sin n\pi\theta & (x < 0) \\ \sum_{n=1}^{\infty} \alpha_n \left(2 - e^{-n\pi x/H}\right) \sin n\pi\theta & (x > 0) \end{cases} \tag{9.67}$$

where

$$\theta \equiv \frac{\Psi}{Hc_{x_o}} \tag{9.68}$$

and the α_n coefficients are yet to be found. The Ψ- derivative at the disk is

$$\left(\tilde{z}_\Psi\right)_{x=o} = \frac{\pi}{c_{x_o}} \sum_{n=1}^{\infty} n\alpha_n \cos n\pi\theta \tag{9.69}$$

This must be identified with the distribution of $\tilde{z}_\Psi$ given by Eqs. (9.45), i.e. $\tilde{z}_\Psi^-$ for $0 < \theta < 1 - \lambda$ and $\tilde{z}_\Psi^+$ for $1 - \lambda < \theta < 1$. Fourier inversion then yields

$$\alpha_n = \frac{Q}{\pi^2 c_{x_o}^2} (-1)^{n+1} \frac{\sin n\pi\lambda}{n^2} \tag{9.70}$$

When these α_n's are substituted back into Eq. (9.67), the resulting infinite series are in general not summable in closed form. However, the derivatives of $\tilde{z}$, which are related to velocity perturbations (Eq 9.34), can indeed be summed. Without stopping to discuss the details (see Ref. [26]) the results take the following forms:

UPSTREAM:

$$\frac{c_x}{c_{x_o}} = 1 - \frac{Q}{2\pi c_{x_o}^2} \left\{ \tan^{-1}\left[\frac{\sin \pi(1 - \theta - \lambda)}{e^{-\pi x/H} - \cos \pi(1 - \theta - \lambda}\right] - \tan^{-1}\left[\frac{\sin \pi(1 - \theta + \lambda)}{e^{-\pi x/H} - \cos \pi(1 - \theta + \lambda}\right] \right\} \tag{9.70a}$$

$$\frac{c_z}{c_{x_o}} = \frac{Q}{4\pi c_{x_o}^2} \ln\left[\frac{1 - 2\, e^{\pi x/H} \cos \pi(1 - \theta + \lambda) + e^{2\pi x/H}}{1 - 2\, e^{\pi x/H} \cos \pi(1 - \theta - \lambda) + e^{2\pi x/H}}\right] \tag{9.70b}$$

DOWNSTREAM $\left(\begin{smallmatrix}\text{GAP} \\ \text{BLADES}\end{smallmatrix}\right)$:

$$\frac{c_x}{c_{x_o}} = 1 - \frac{Q}{2\pi c_{x_o}^2} \left\{ \begin{pmatrix} -2\pi(1-\lambda) \\ 2\pi\lambda \end{pmatrix} + \tan^{-1}\left[\frac{\sin \pi(1-\theta-\lambda)}{e^{\pi x/H} - \cos \pi(1-\theta-\lambda)}\right] + \tan^{-1}\left[\frac{\sin \pi(1-\theta+\lambda)}{e^{\pi x/H} - \cos \pi(1-\theta+\lambda)}\right] \right\} \tag{9.71a}$$

$$\frac{c_z}{c_{x_o}} = \frac{Q}{4\pi c_{x_o}^2} \ln\left[\frac{1 - 2e^{-\pi x/H}\cos\pi(1-\theta+\lambda) + e^{-2\pi x/H}}{1 - 2e^{-\pi x/H}\cos\pi(1-\theta-\lambda) + e^{-2\pi x/H}}\right] \tag{9.71b}$$

The c_x discontinuity is apparent (Eq. (9.71a)). The expressions also show clearly that the axial scale of the near-disk potential effects is H/π,which, while being probably many times the gap width δ, is still likely to be small compared to the mean radius R of the stage. This fact can be exploited in studying the effects of azimuthal variations of gap width.

Particularization of Eqs. (9.70a) and (9.71a), for x = o do yield the known two-level velocity distribution (Eq. (9.46)). On the other hand, Eqs. (9.70b) or (9.71b) give the spanwise flow velocity at the disk as

$$\left(\frac{c_z}{c_{x_o}}\right)_{x=o} = \frac{Q}{2\pi c_{x_o}^2} \ln \frac{\sin\frac{\pi}{2}(1-\theta+\lambda)}{\sin\frac{\pi}{2}(1-\theta-\lambda)} \tag{9.72}$$

which exhibits a logarithmic singularity at the tip $(\theta = 1 - \lambda)$.

The shape of the streamline which supports the shear layer is of some interest. Putting $\theta = 1-\lambda$ in Eq. (9.71b) and relating $\tilde{c}_z$ to $\tilde{z}_x$ by Eq. (9.34b) gives

$$\frac{d\tilde{z}}{dx}(\psi_{TIP}, x) = \frac{Q}{4\pi c_{x_o}^2} \ln\left[1 + 4\sin^2\pi\lambda \frac{e^{-\pi x/H}}{(1 - e^{-\pi x/H})^2}\right] \tag{9.73}$$

This is not analytically integratable, but for small λ, and provided $\frac{x}{H} >> \lambda$ (which only excludes the immediate vicinity of the gap), we can expand the logarithm in (9.73), and then integrate with the condition

$$\frac{\tilde{z}}{H}(\Psi_{TIP}, \infty) = 2\frac{\tilde{z}}{H}(\Psi_{TIP}, 0) = 2\left(\lambda - \frac{\delta}{H}\right) \tag{9.74}$$

Including the unperturbed contribution $(1-\lambda)$, this gives

$$\frac{z}{H}(\Psi_{TIP}, x) \cong 1 - \lambda + Q\left\{\lambda(1-\lambda) + \left(\frac{\sin\pi\lambda}{\pi}\right)^2\left[1 - \frac{1}{(1 - e^{-\pi x/H})^2}\right]\right\} \tag{9.75}$$

9.2.6 Some Results of the Linearized Model

9.2.6.1 Parametric Trends

This subsection gives some simple calculated results from the formulae obtained so far, in order to illustrate the trends and sensitivities involved. Further results and comparisons to data are deferred to Secs. 9.2.6.2 and 9.2.9.2.

As might be expected, the degree of reaction R (see Appendix 9.B for definitions used) is an important parameter controlling the effects of tip leakage. At very high R the turbine is lightly loaded and the effect of the gap is small. This can be seen most easily in the zero exit swirl case, when Eqs. (9.B4) and (9.B7) indicate $\psi = 2(1\text{-}R)$, so that $y \rightarrow 0$ when $R \rightarrow 1$. At the other, and more realistic end (small R), the individual turbine blades are highly loaded, but there is little net pressure drop across the rotor. Since there is then little incentive for approaching flow to migrate spanwise towards the gap region, little blade unloading is expected. Thus, the shear strength Q and the loss parameter β are expected to show maximum values at some intermediate degree of reaction, For the same reasons, the difference between the relative gap δ/H and relative leakage rate, λ, will also peak at that intermediate R.

These trends are shown in Figs. 9.6 and 9.7. Here the leakage λ was held at 0.04 and the degree of reaction R was varied over the range 0-1, while the flow coefficient ϕ was given values from 0.3 to 0.7. Zero exit swirl was assumed, and so different ϕ values imply different turbine angles β_3, while varying R amounts to varying the stator blade angle α_2. The expected peak in loss factor is seen to occur for $R \cong 0.8$, which is higher than the practical range for turbines (0 - 0.6 or so). Hence, in practice, the expected trend would be for losses to increase with degree of reaction. This trend is clearly exhibited in Waterman's data compilation [18], as indicated in Fig. 9.8 (taken from Ref. [18]). More detailed data analysis will be shown in Secs. 9.2.6.2 and 9.2.9.2. The minimum of δ/H at $R \cong 0.8$ shown in Fig. 9.7 confirms that redistribution effects are indeed strongest then, since the smallest gaps is required to pass a given leakage.

So far parametric results ("rubber engine") have been discussed. For a given turbine

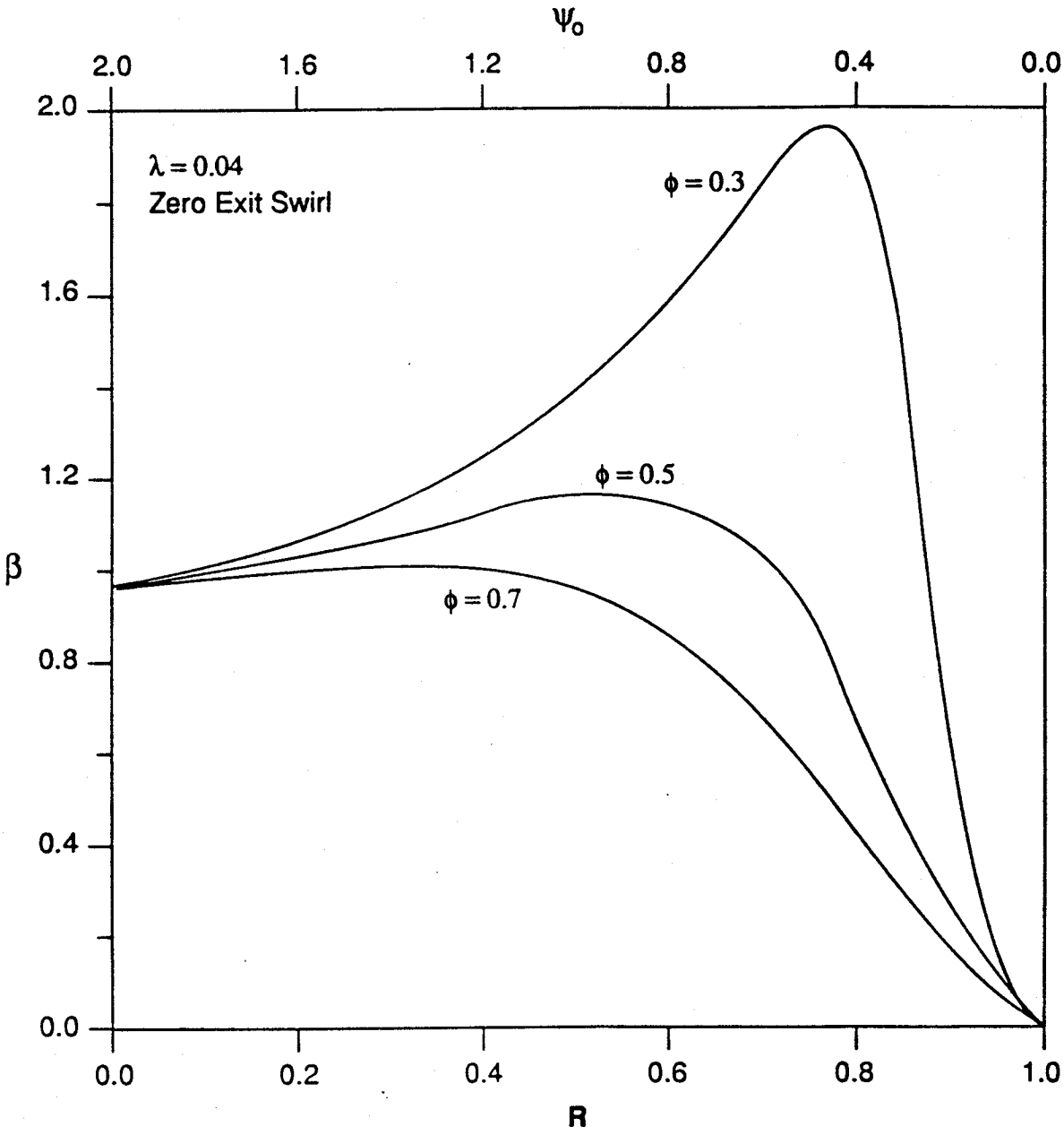

Fig. 9.6: Loss parameter variation with loading or degree of reaction for zero exit swirl (leakage fixed)

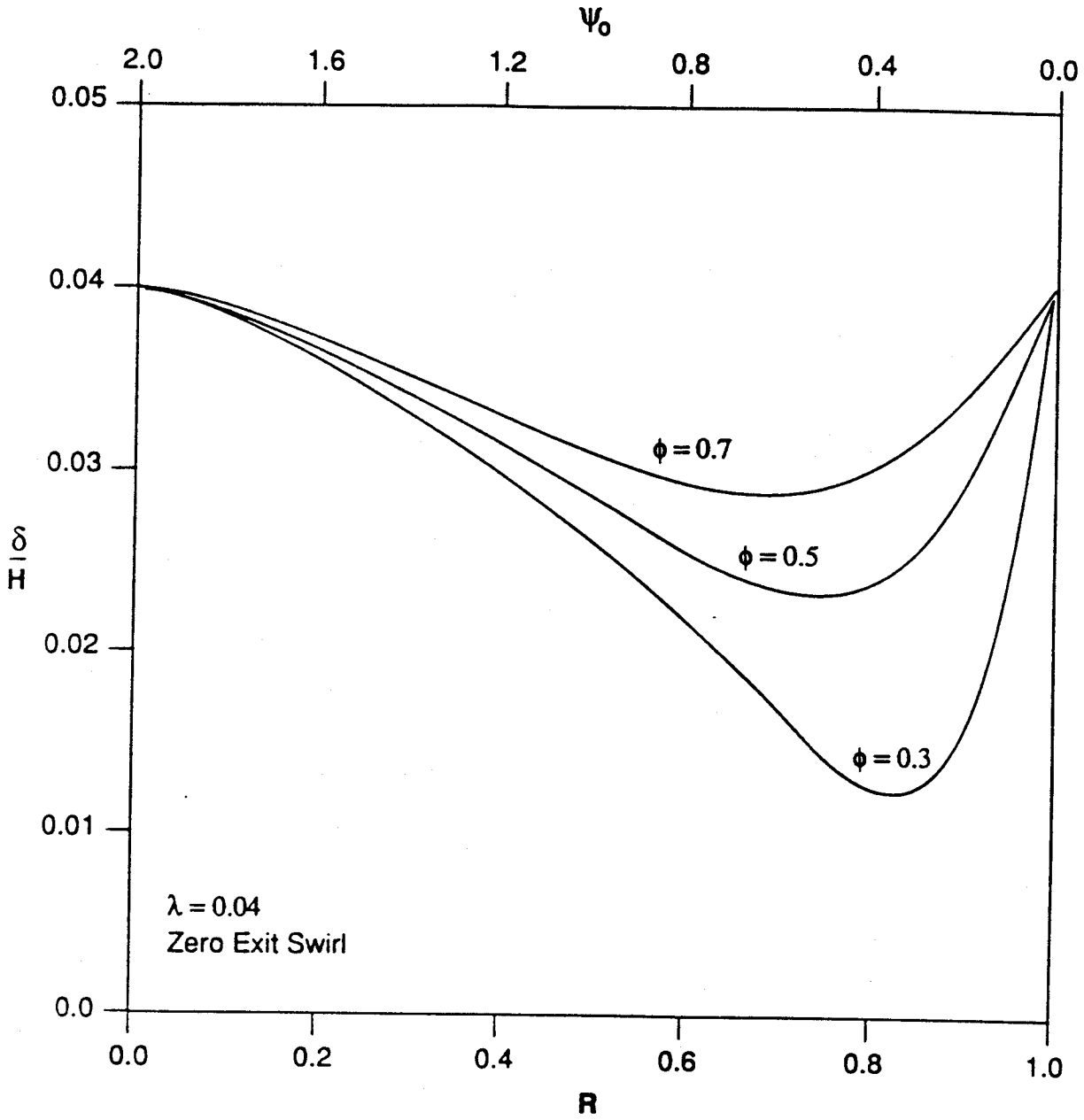

Fig. 9.7: Gap variation for conditions in Fig. 9.6

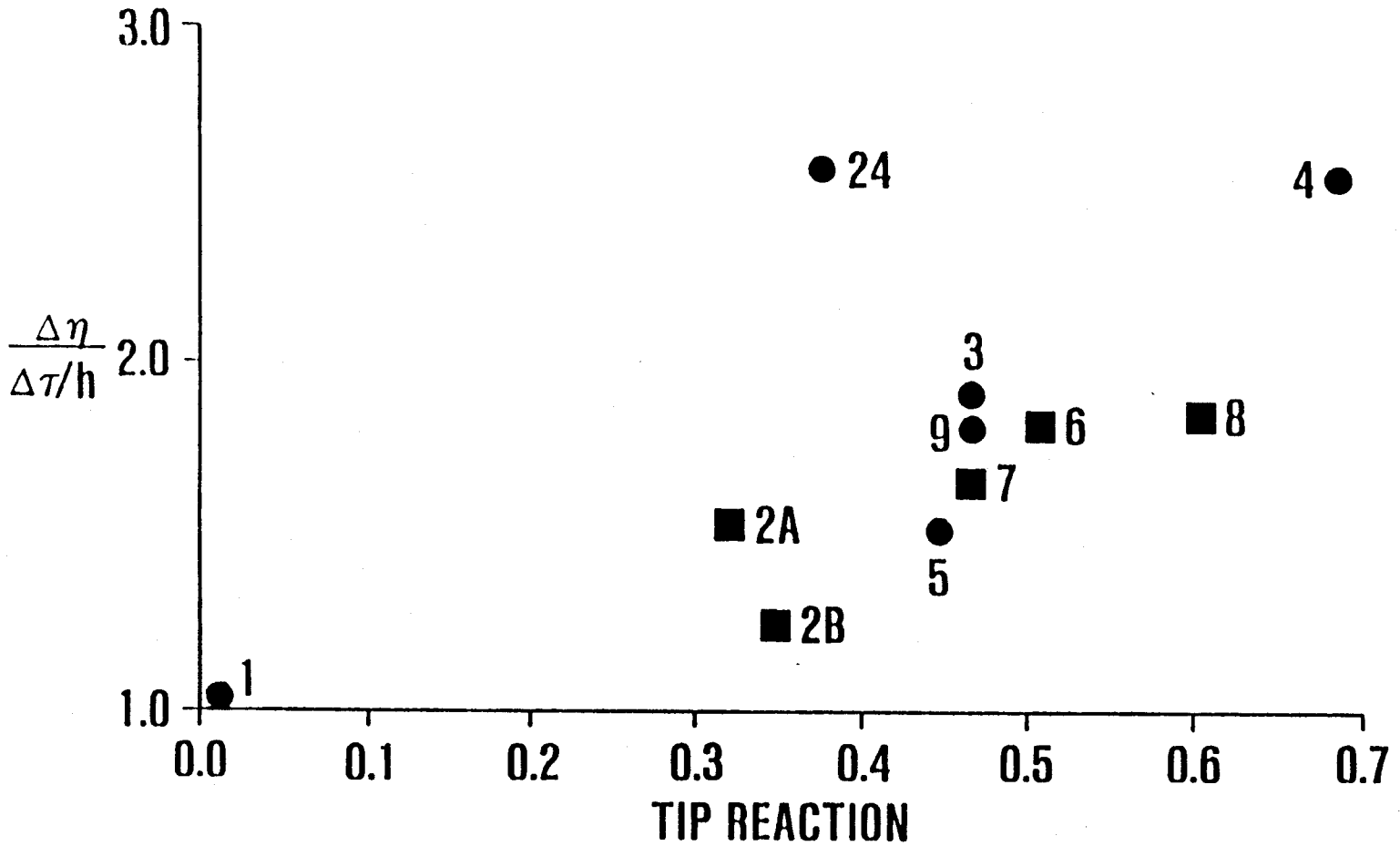

Fig. 9.8: Data collected by Ref. 3 indicate a trend of losses to increase with degree of reaction

(given α_2, β_3) some trends are shown in Figs. 9.9 and 9.10. Figure 9.9 shows the two axial velocity levels at the disk as the gap only is varied (as reflected in the leakage rate). While both velocities vary only slightly with gap, it must be remembered that for the bladed region, it is the difference $1 - \frac{c_x}{c_{x_o}}$ that controls the losses, and this difference does have a substantial variation. On the other hand, the "jet" velocity changes are not particularly significant, as one would expect, since they mostly respond to the fixed ΔP across the turbine. Of course the word "jet" must be used with caution, since only the x-component of the velocity is shown.

In Fig. 9.10 all geometrical parameters, including gap size, are fixed and the flow coefficient is varied. This allows non-zero exit swirl to occur (ranging from $c_{\bar{y}_3}/c_{x_0} \cong 0.73$ at $\phi = 0.27$ to $c_{\bar{y}_3}/c_{x_0} \cong -0.47$ at $\phi = 0.4$, with zero exit swirl at $\phi = 1/3$). As the flow varies, the degree of reaction remains approximately fixed (close to the design value of 0.5), but turbine loading ψ_0 increases with ϕ, as shown in the lower scale. As the results show, the tip leakage fraction remains at about 1.5 times the relative gap throughout. On the other hand, the loss factor β increases strongly with flow, and weakly with decreasing gap. The work loss coefficient w shows a trend with flow which is opposite to that of β, although weaker. The variation with gap remains slight.

9.2.6.2 Comparison to Literature Turbine Data

We can now compare the calculated losses to those reported in the experimental literature. We rely for this on the compilation of Ref. [18], which gives data for ten cases (nine different turbines) over a wide range of parameters. Ref. [18] reports for each case the tip values of the work coefficient Ψ_0 (two definitions), degree of reactor R, flow coefficient ϕ, and individual blade loading (lift coefficient c_L, based in inlet relative velocity and blade area, and Zweifel coefficient (tangential force coefficient based on tangential area and exit dynamic head). Also reported are the relative gap and, in some instances, other geometrical parameters. As noted in the Introduction, Ref. [18] also shows the results of several existing loss correlations or theories when applied to

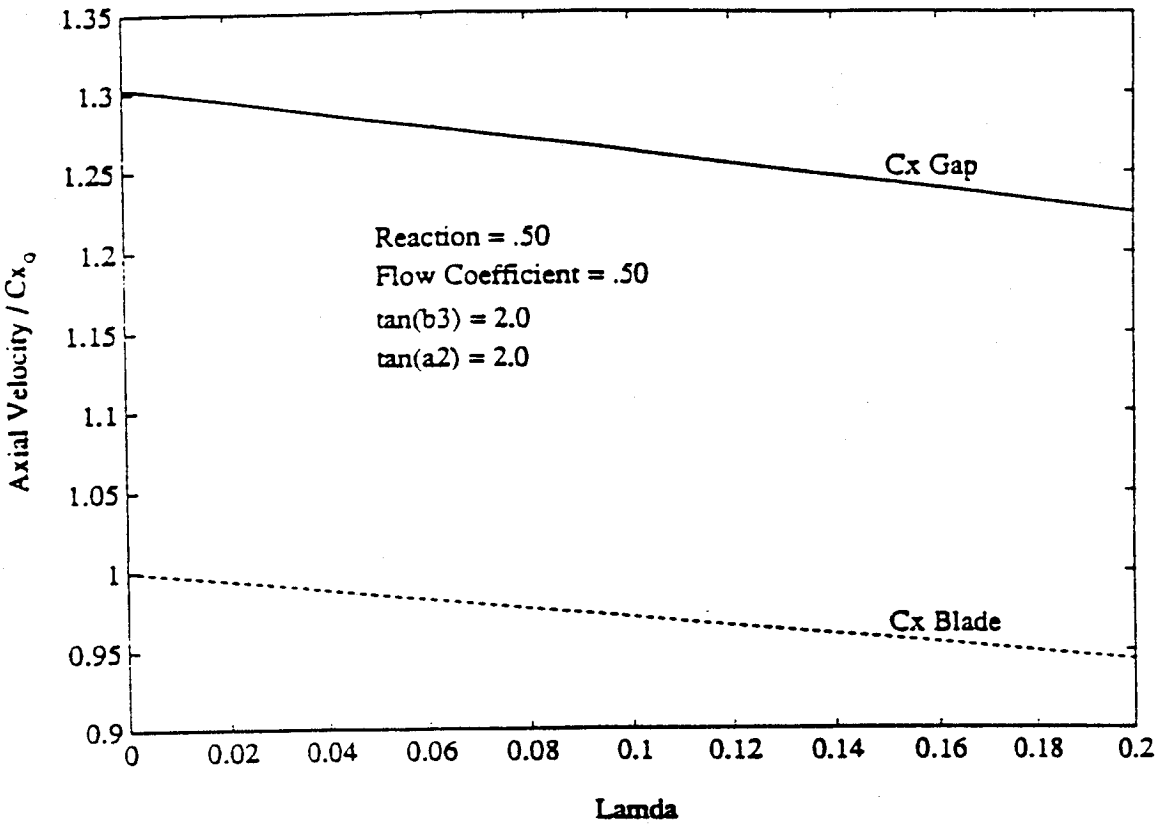

Fig. 9.9: Variation of axial velocity levels at disk with leakage

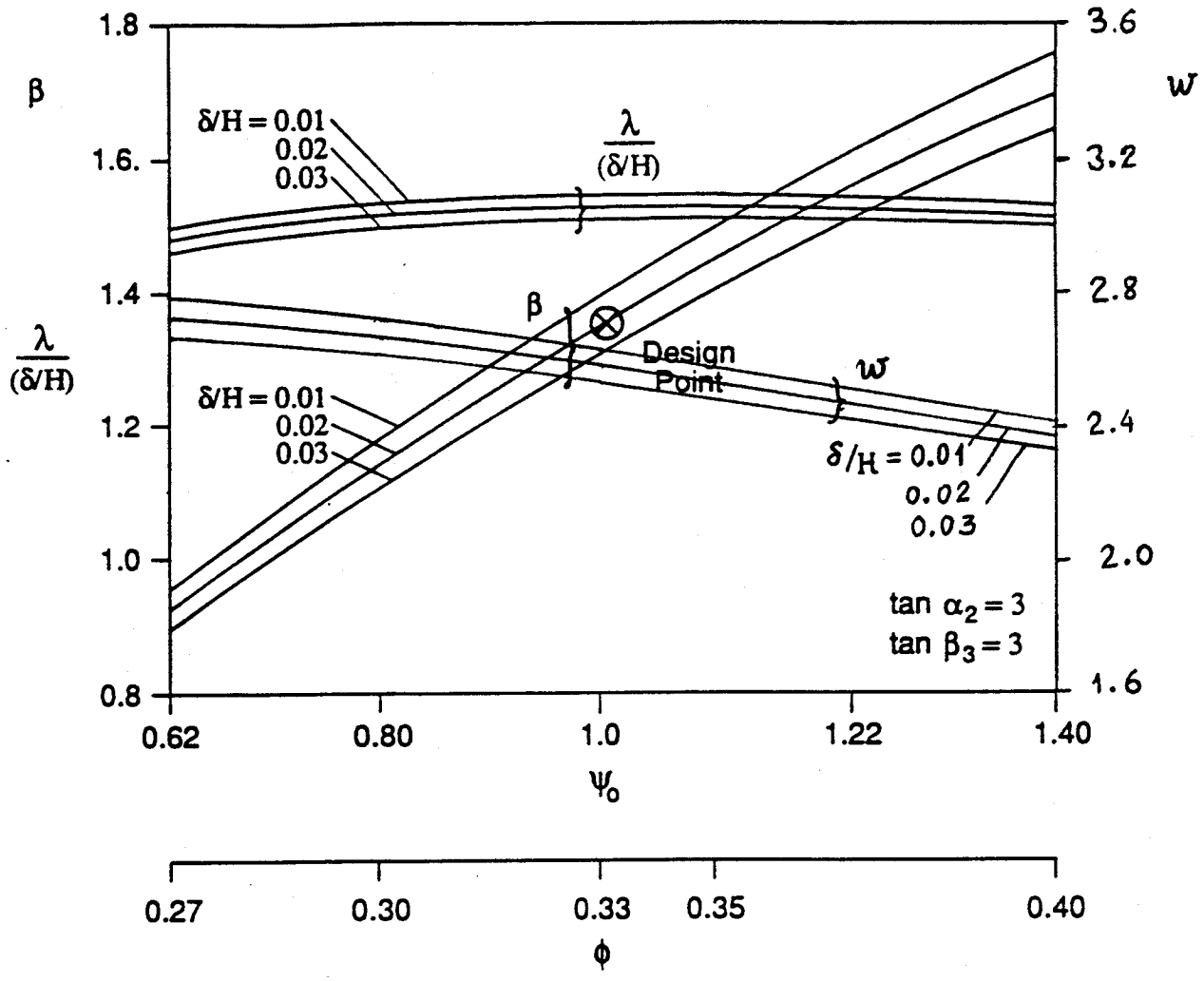

Fig. 9.10: Variation of losses and leakage rate with flow coefficient for a fixed geometry

these cases, plus the actual measured loss factor β. One potential difficulty in application is that only tip parameters are given, whereas from the nature of our theory we suspect that mean parameters might be more appropriate.

Starting from Ψ_0 (with the definition which agrees with that in our Appendix 9.B), ϕ and R, the equations in Appendix B allow calculation of the blade angles α_2, β_3. The fractional leakage, λ, is determined from the relative gap δ/H using Eq. (9.51). This involves the shear strength q, which itself depends somewhat on λ, so some iteration must be used. The remainder of the calculations is straightforward. Table 9.2 summarizes the results.

Scanning Table 9.2 we first notice a large disagreement for Case 1 (Kofskey turbine). This is an impulse rocket turbopump stage with extremely large reported tip loading ($\psi = 7.0$). As the table shows, this leads to very large exit swirl ($c_{\bar{y}}/c_{x_o} = -3.2$). No reasonable modification of the theory could be found to resolve the disagreement of the β calculated and that reported, which, as expected for a low-reaction stage, is low ($\beta = 1.02$). A calculation was made, as shown in the second-from-last row of Table 9.2, with a load Ψ_0 reduced to 2.0, which leads to near-axial exit flow, and this does predict $\beta = 0.97$, close to the measured value. This might indicate a large radial load gradient for this turbine, but this has not been investigated further.

Excluding Case 1, the mean squared error in the predicted β is

$$\overline{\varepsilon^2} = \frac{1}{N}\sum_N (\beta_{DATA} - \beta_{CALC})^2 = 0.1434$$

This compares favorably with the results of applying the correlations of Kofskey, Ainley, Soderberg and Roelke (See Table 9.1). The mean error is $\bar{\varepsilon} = \frac{1}{N}(\beta_{DATA} - \beta_{CALC}) = 0.1734$ which indicates a general under-prediction of the losses. The standard deviation is

$$\sigma = \sqrt{\varepsilon^2 - (\bar{\varepsilon})^2} = 0.337$$

9.2.7 Numerical Verification

The linearized solution has yielded important results, some of which defy our expectations. It is therefore important at this point to investigate the extent to which these results may have been

COMPARISON OF SIMPLE THEORY TO 10 TURBINE DATA SETS

CASE #	AUTHOR	ϕ	ψ_o	R	δ/H	$(\beta)_{DATA}$	$(\beta)_{CALC.}$	$(w)_{CALC.}$	$\left(\frac{C_y}{C_{x_o}}\right)_{CALC}$
1	KOFSKEY	0.79	7.0	0.02	0.05	1.02	3.032	1.020	-3.199
2A	MARSHALL -ROGO	0.50	1.48	0.32	0.035	1.51	1.156	1.541	-0.105
2B	MARSHALL -ROGO	0.44	1.25	0.35	0.035	1.23	1.068	1.663	+0.076
3	SZANCA-BEHNING-SCHUM	0.57	1.46	0.47	0.033	1.90	1.449	1.987	-0.336
4	HOLESKI-FUTRAL	0.26	0.69	0.69	0.031	2.53	1.883	5.644	+0.042
5	EWEN-HUBER -MITCHELL	0.25	1.05	0.45	0.02	1.50	1.294	2.328	0.136
6	LART	0.51	1.41	0.51	0.02	1.80	1.645	2.304	-0.416
7	YAMAMOTO	0.42	1.52	0.47	0.03	1.63	1.652	2.166	-0.528
8	PATEL	0.28	1.15	0.61	0.01	1.81	2.438	4.155	-0.648
9	HAAS-KOFSKEY	0.35	1.37	0.47	0.03	1.80	1.564	2.251	-0.408
1 (MODIFIED)	KOFSKEY (Assuming ψ_o=2)	0.79	2.0	0.02	0.05	1.02	0.973	1.019	-0.025
8 (MODIFIED)	PATEL (Assuming ψ_o=0.83)	0.28	0.83	0.61	0.01	1.81	1.823	4.234	-0.052

TABLE 9.2 Efficiency loss and work defect calculated from theory (assuming zero work done by gap fluid), compared to data. The last two lines are computed with modified work coefficients chosen for near-axial exit flow

compromised by the linearization. To this end, we need to solve by a numerical technique the complete non-liner actuator disk problem (Eqs. 9.28, 9.29). Inverse coordinates are still a convenient formulation, especially in that they fix the location of the shear layer along a coordinate line ($\Psi = \Psi_{TIP}$, $x > o$), thus avoiding the smearing inherent in any discontinuity-capturing approach that could be used in direct (x,z) coordinates. Simple finite differences on a rectangular grid can also be used effectively with such a formulation, since the main surfaces (disk, walls, shear layer) are all aligned with the coordinate lines (x,Ψ). The only disadvantage is the more complex form of the Laplacian in these coordinates (see Eq. 9.32).

The method used is a form of over-relaxation, which can be constructed starting from a minimum principle for the problem (See Ref. [26] for details). Care is taken to include the δ function on the right-hand side of Eq. (9.28) in a consistent manner. Integrating Eq. (9.28) across the shear layer, and, as before, using superscripts (+) and (-) for the gap and bladed sides, respectively, one obtains at each x

$$\left(1 + z_x^2\right)\left[\frac{1}{\left(z_\Psi^+\right)^2} - \frac{1}{\left(z_\Psi^-\right)^2}\right] = 2\,Q \tag{9.76}$$

where Q is calculated from disk velocities according to Eq. (9.27). In discretizing the connecting condition (9.76), one-sided differences are used for z_Ψ^+ and z_Ψ^- to avoid numerical "mixing" of the two streams. Most of the calculations were done on a 16 x 32 grid. As a check, one case was computed on a 24 x 48 grid, and the discrepancies (Table 9.3) were found to be below 10^{-3} in relative terms.

A series of numerical results showing the two velocity components at the disk, with the linearized theory results superimposed, are given in Figs 9.11 through 9.26. For degrees of reaction below 0.4 or above 0.90 the agreement is excellent. As expected, the worst linearization errors occur in the vicinity of $R \cong 0.8$, but even then the results of the linear theory are found to be fairly accurate. Most importantly, the prediction that the axial velocity at the disk is piecewise constant is clearly borne out by the nonlinear results. The only noticeable deviation from throughflow uniformity in the bladed region occurs very near the blade tip (on the scale of the gap

TABLE 9.3

Axial and radial velocities at x=0 for two grid sizes

	Grid 16X32	Grid 24X48
ϕ	$(C_x)_{x=0}$	$(C_x)_{x=0}$
.9750	1.36396	1.36279
.9250	.97904	.97962
.9000	.98285	.98326

ϕ	$(C_z)_{x=0}$	$(C_z)_{x=0}$
.9750	.13404	.13677
.9250	.14692	.15054
.9000	.09922	.09976

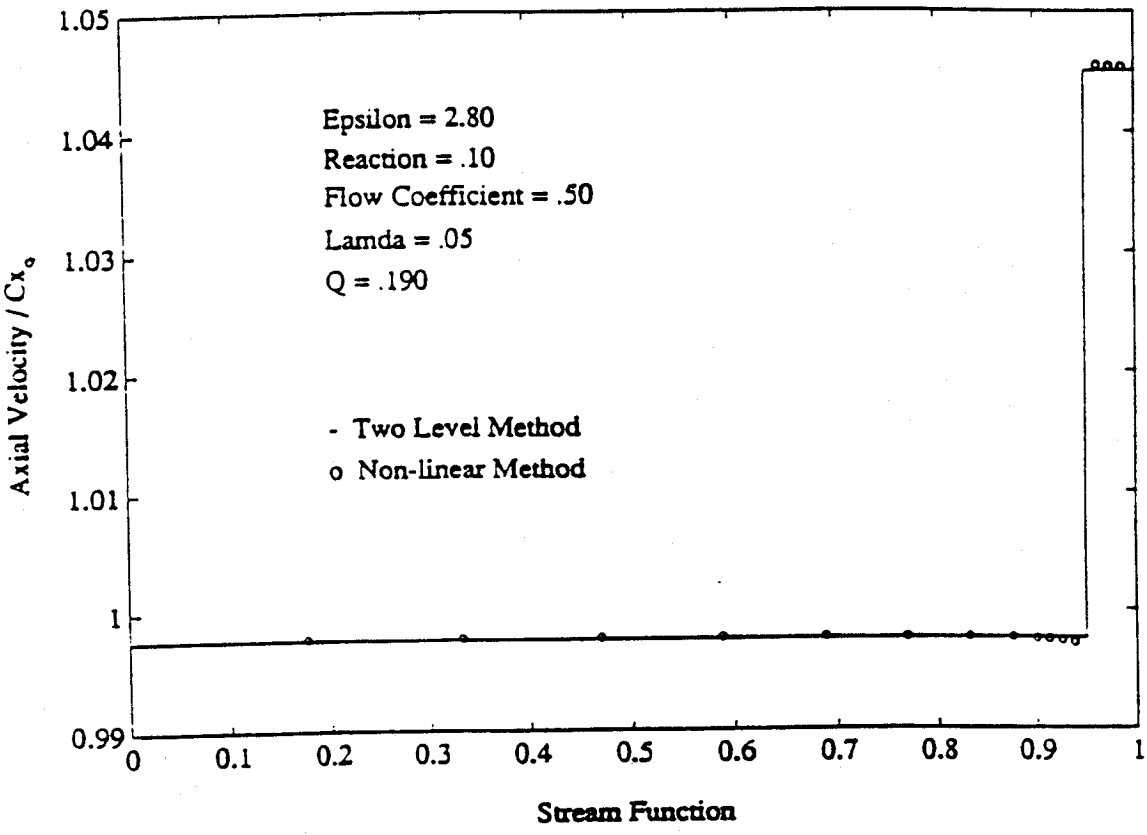

Fig. 9.11: Numerical vs. analytical axial velocity profiles at disk

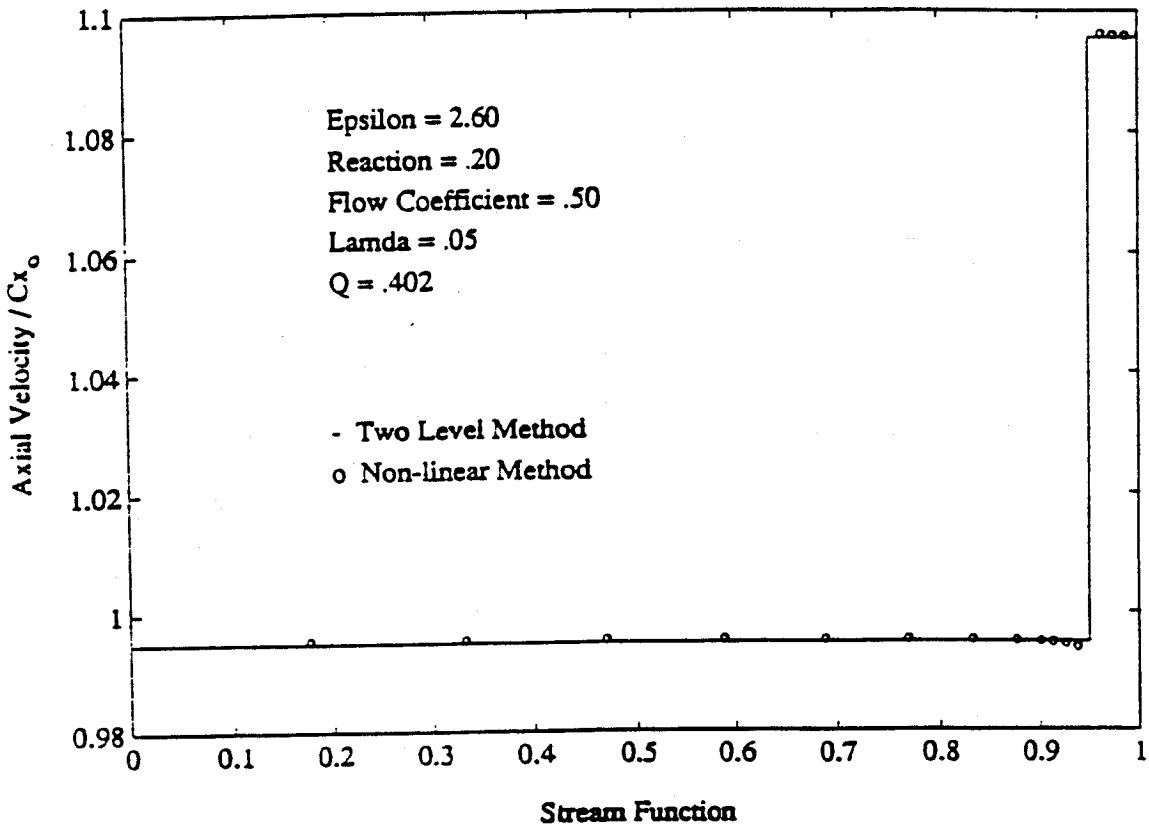

Fig. 9.12: Numerical vs. analytical axial velocity profiles at disk

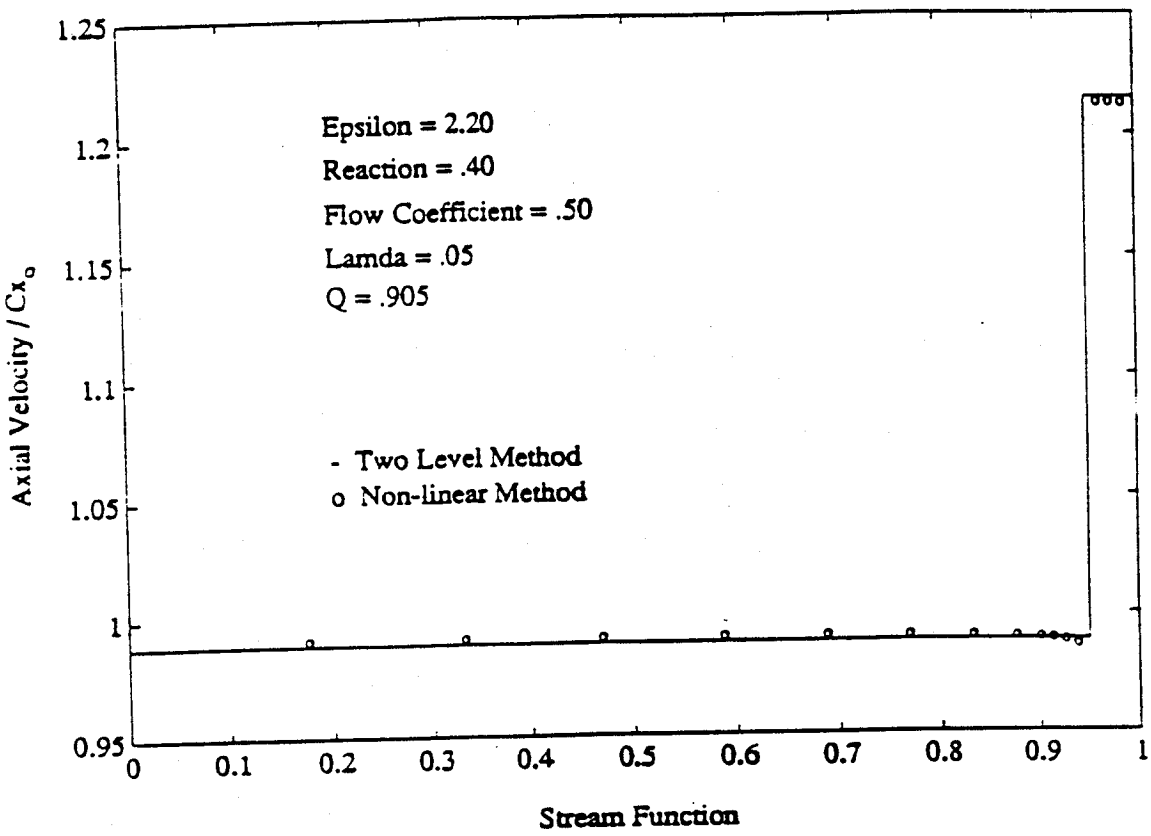

Fig. 9.13: Numerical vs. analytical axial velocity profiles at disk

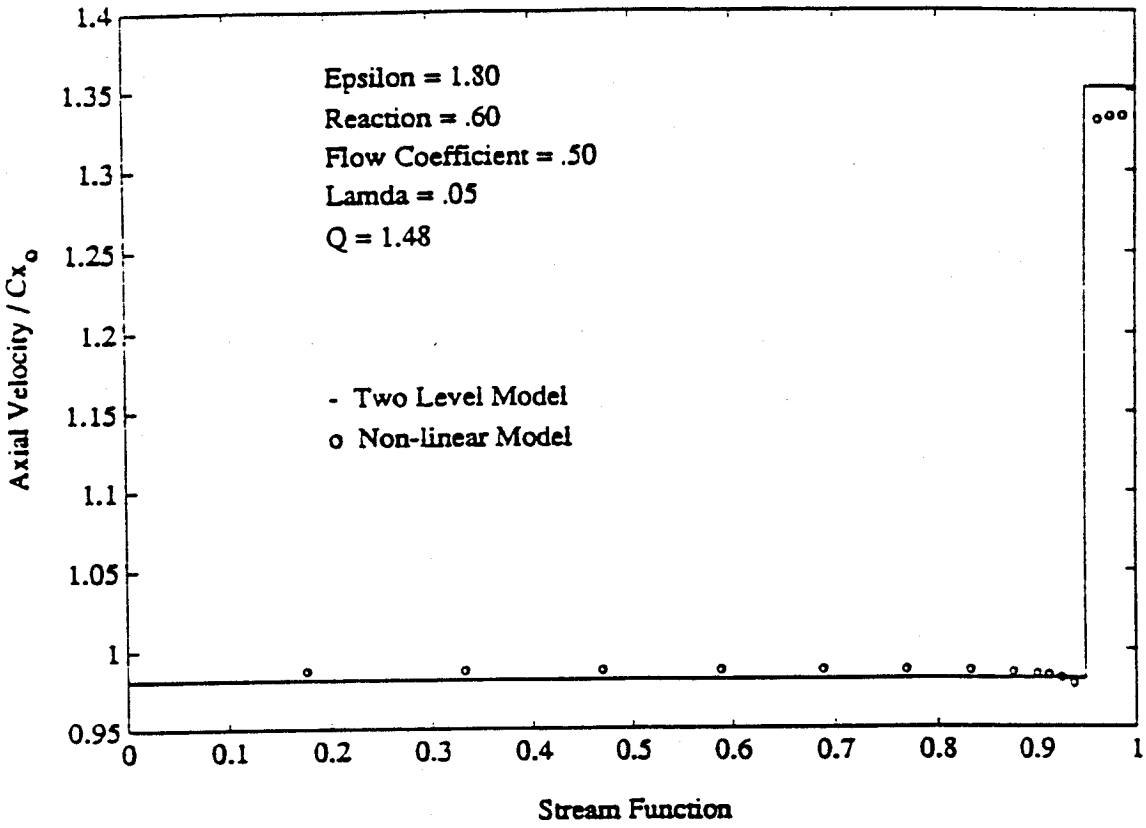

Fig. 9.14: Numerical vs. analytical axial velocity profiles at disk

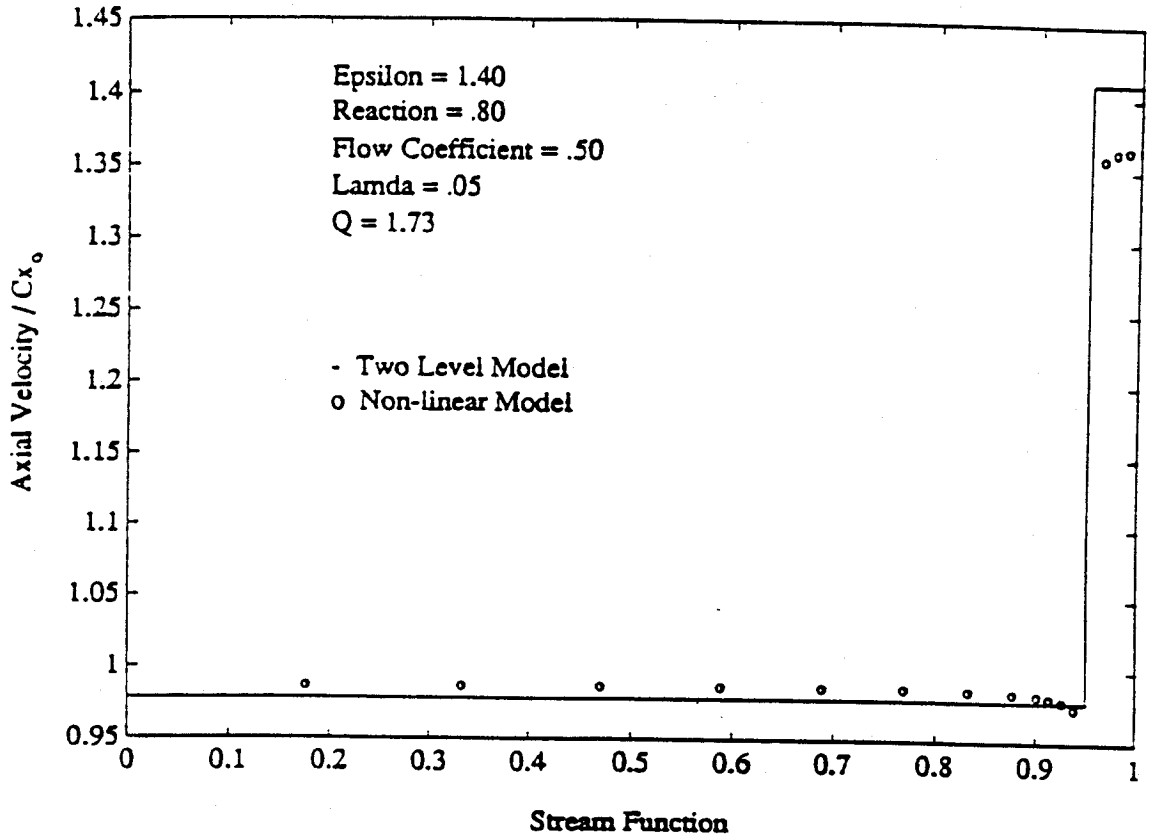

Fig. 9.15: Numerical vs. analytical axial velocity profiles at disk

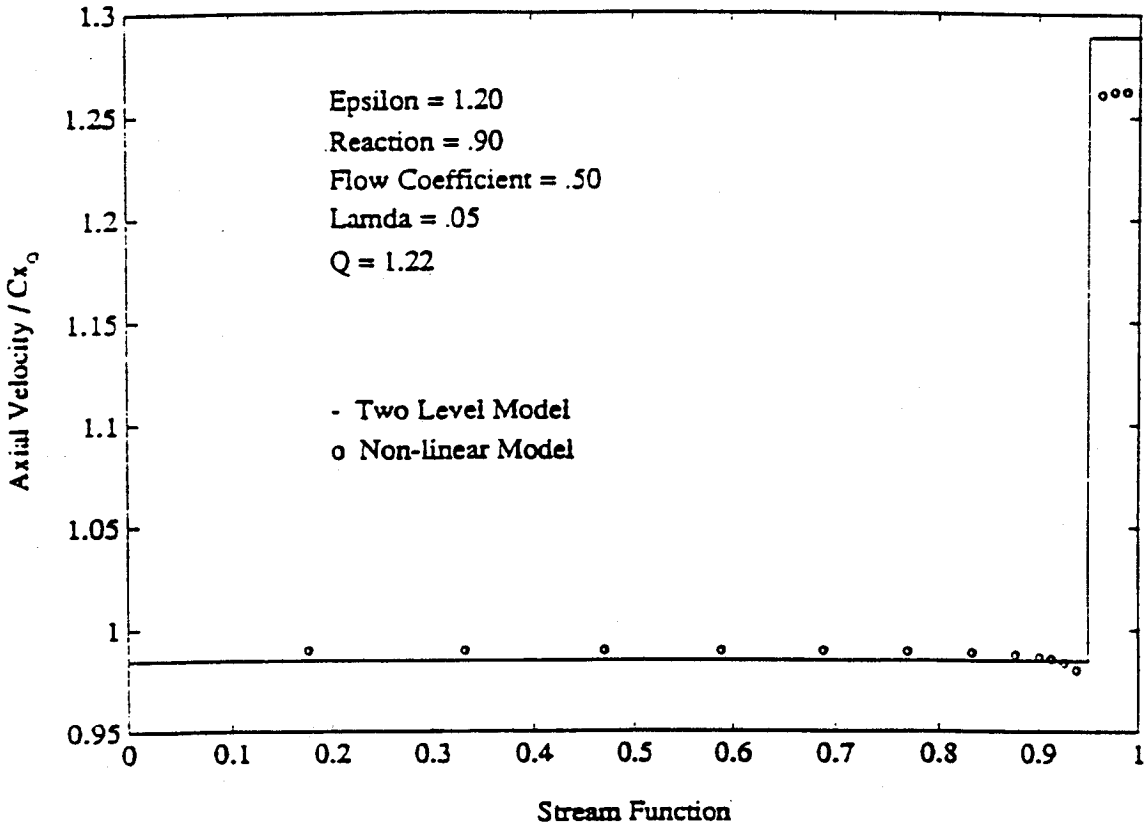

Fig. 9.16: Numerical vs. analytical axial velocity profiles at disk

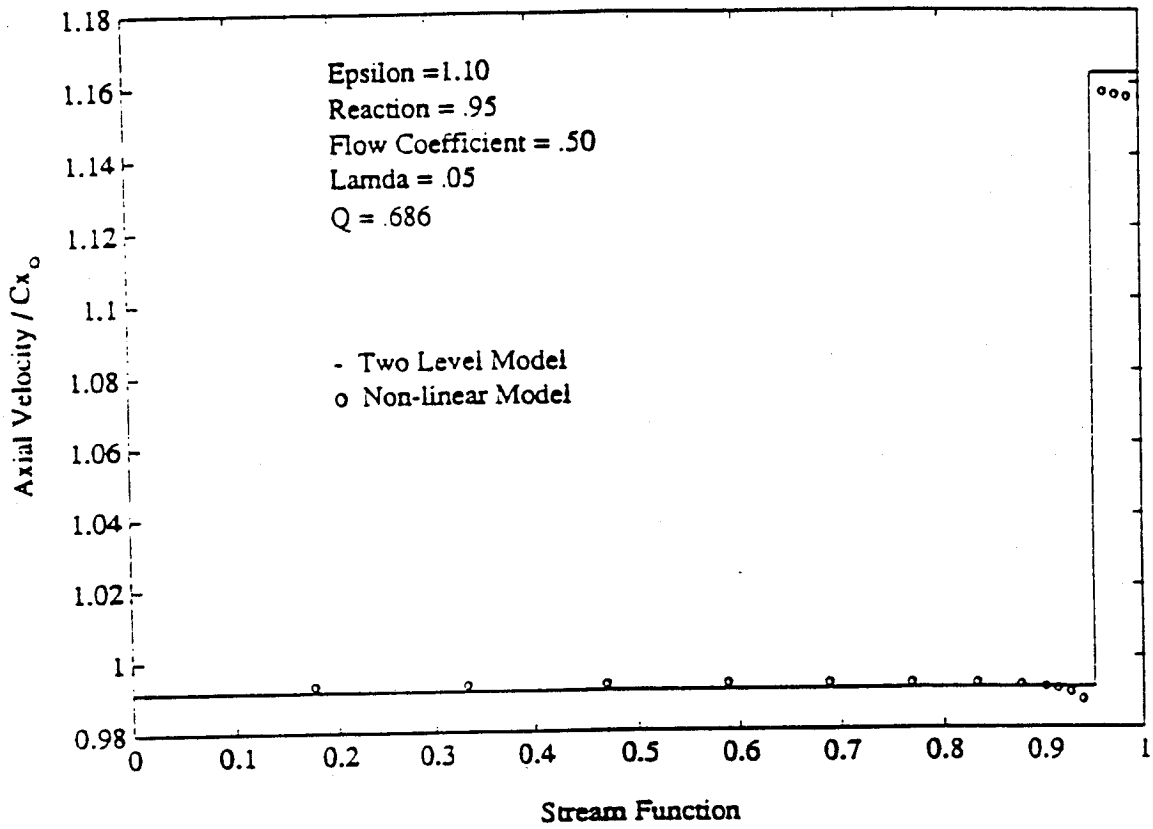

Fig. 9.17: Numerical vs. analytical axial velocity profiles at disk

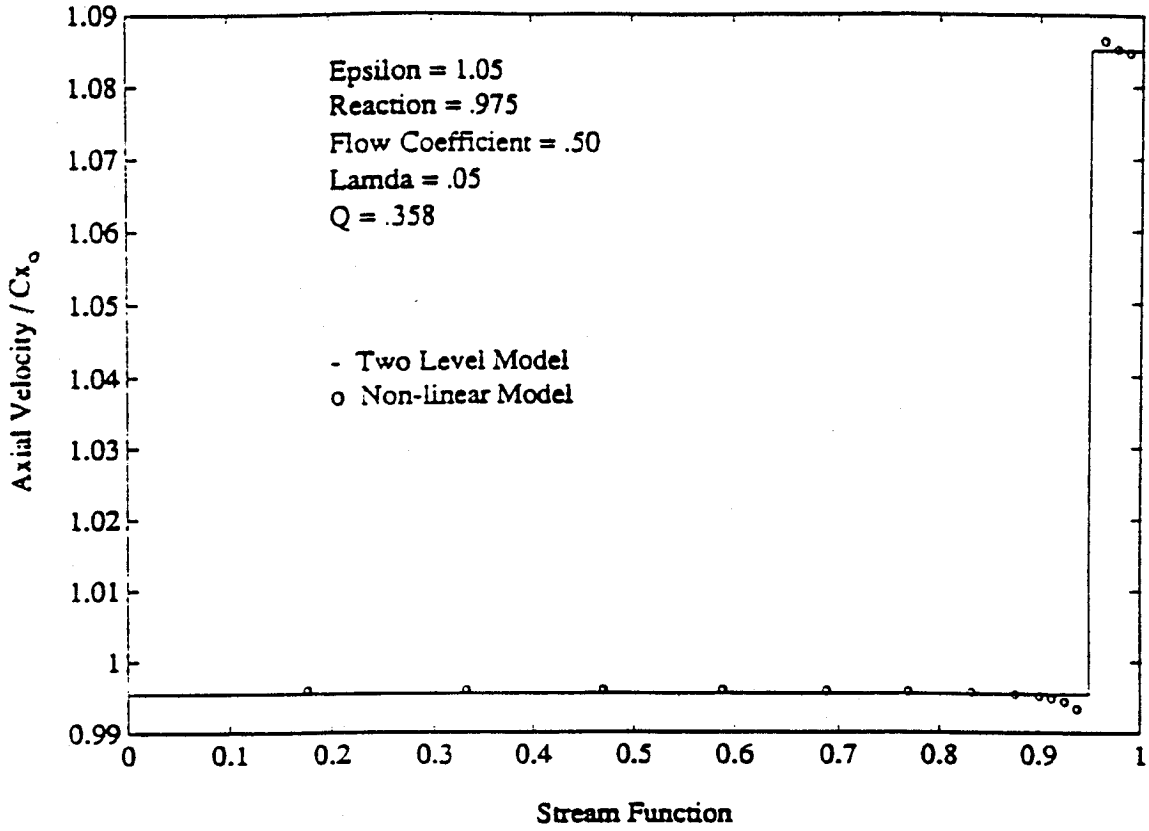

Fig. 9.18: Numerical vs. analytical axial velocity profiles at disk

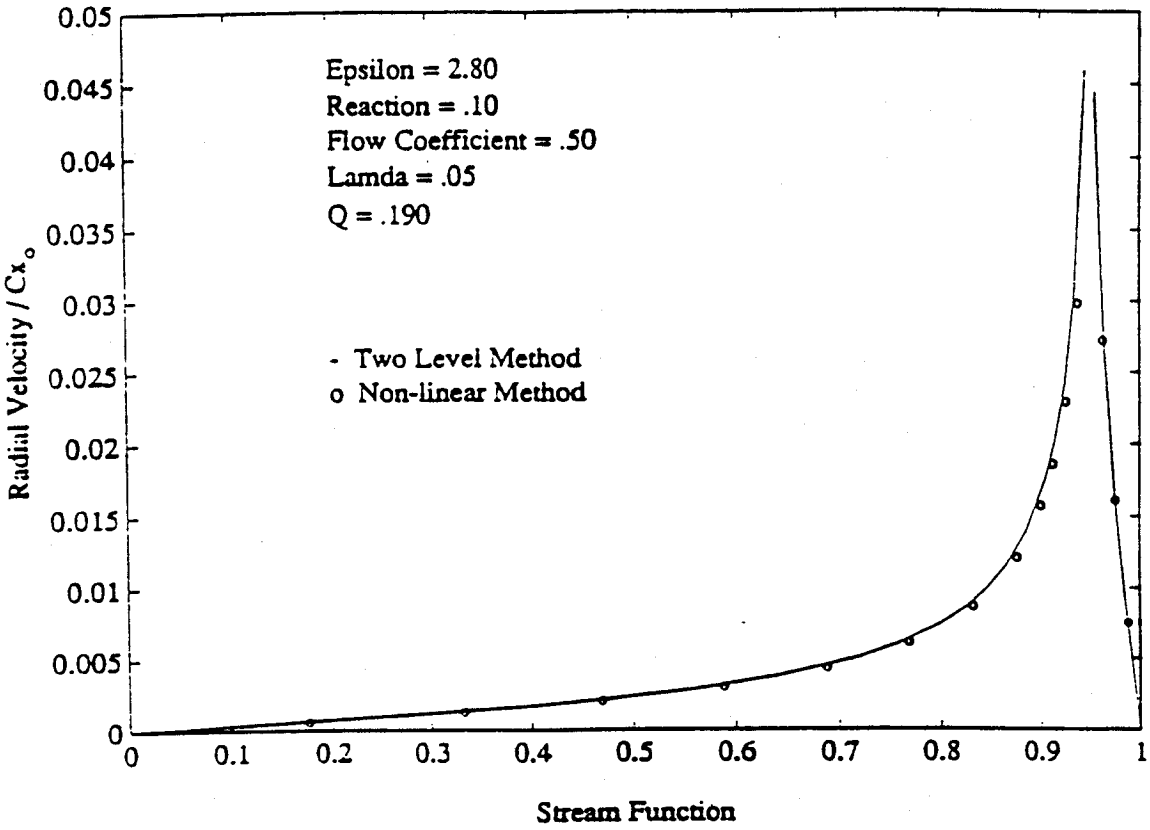

Fig. 9.19: Numerical vs. analytical spanwise velocity profiles at disk

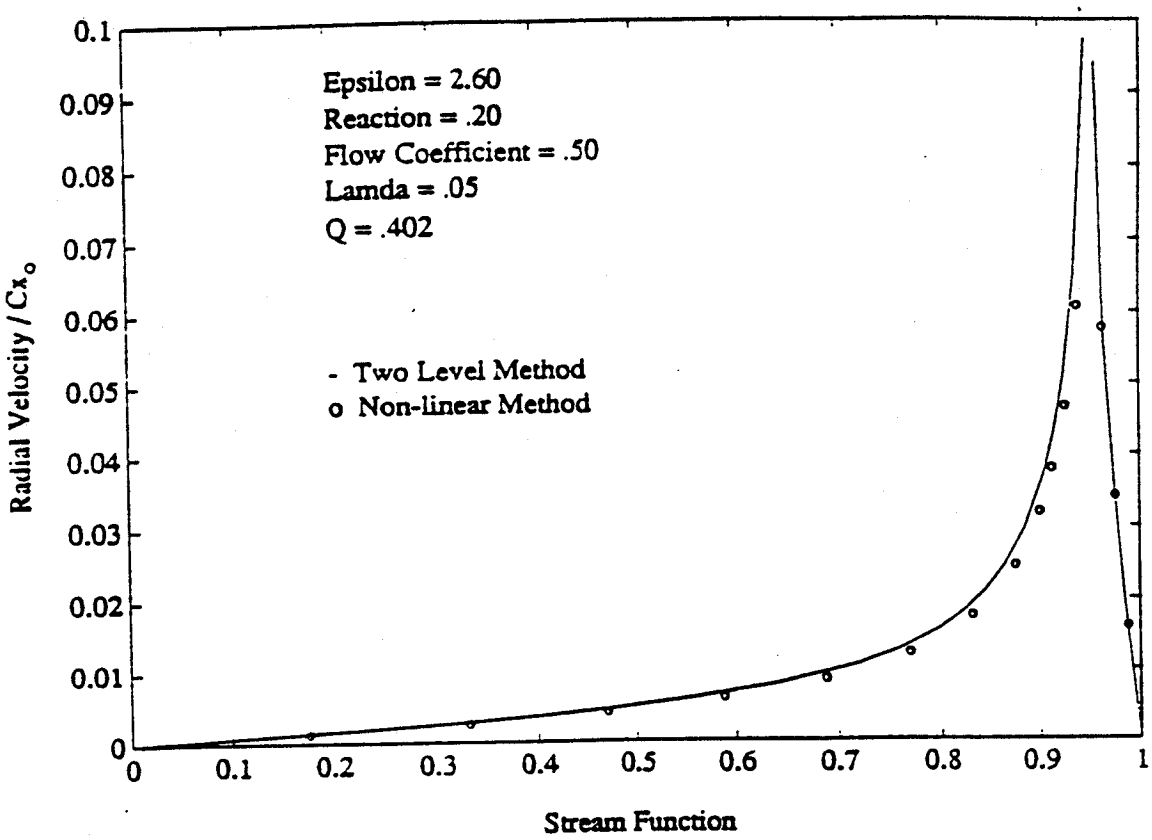

Fig. 9.20: Numerical vs. analytical spanwise velocity profiles at disk

C-4

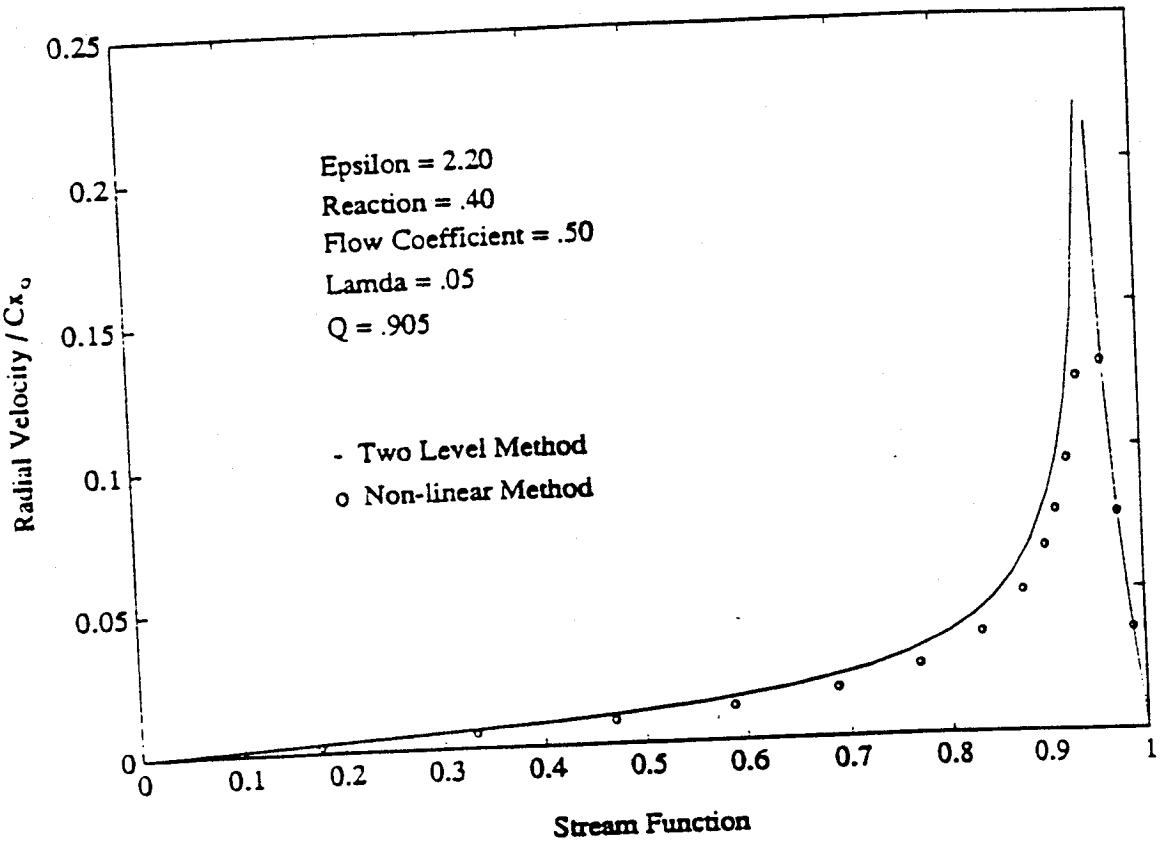

Fig. 9.21: Numerical vs. analytical spanwise velocity profiles at disk

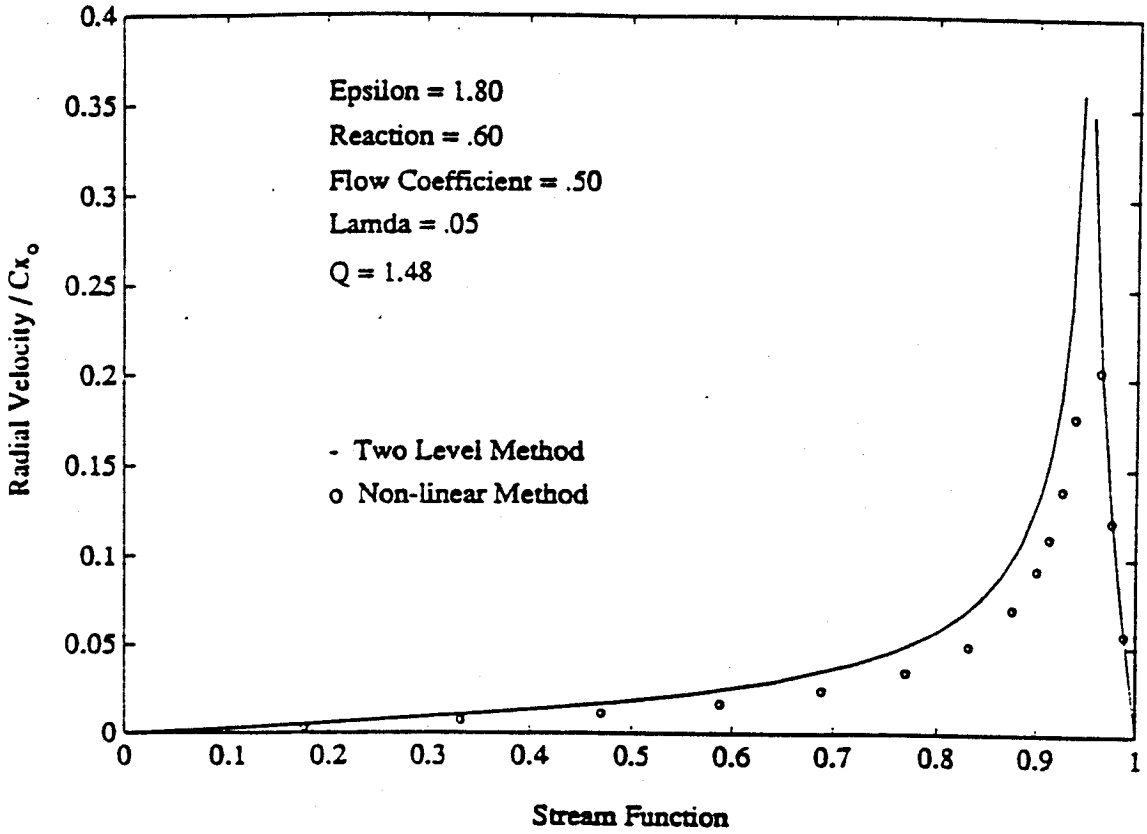

Fig. 9.22: Numerical vs. analytical spanwise velocity profiles at disk

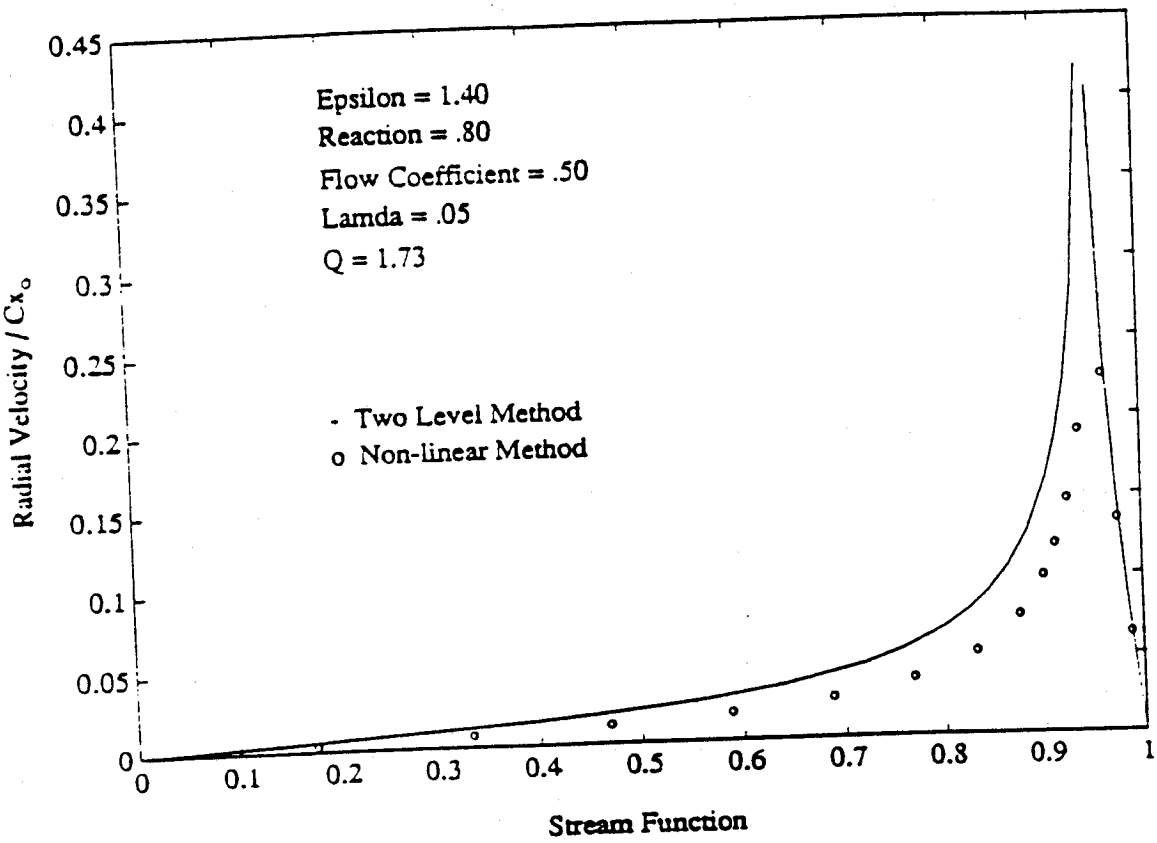

Fig. 9.23: Numerical vs. analytical spanwise velocity profiles at disk

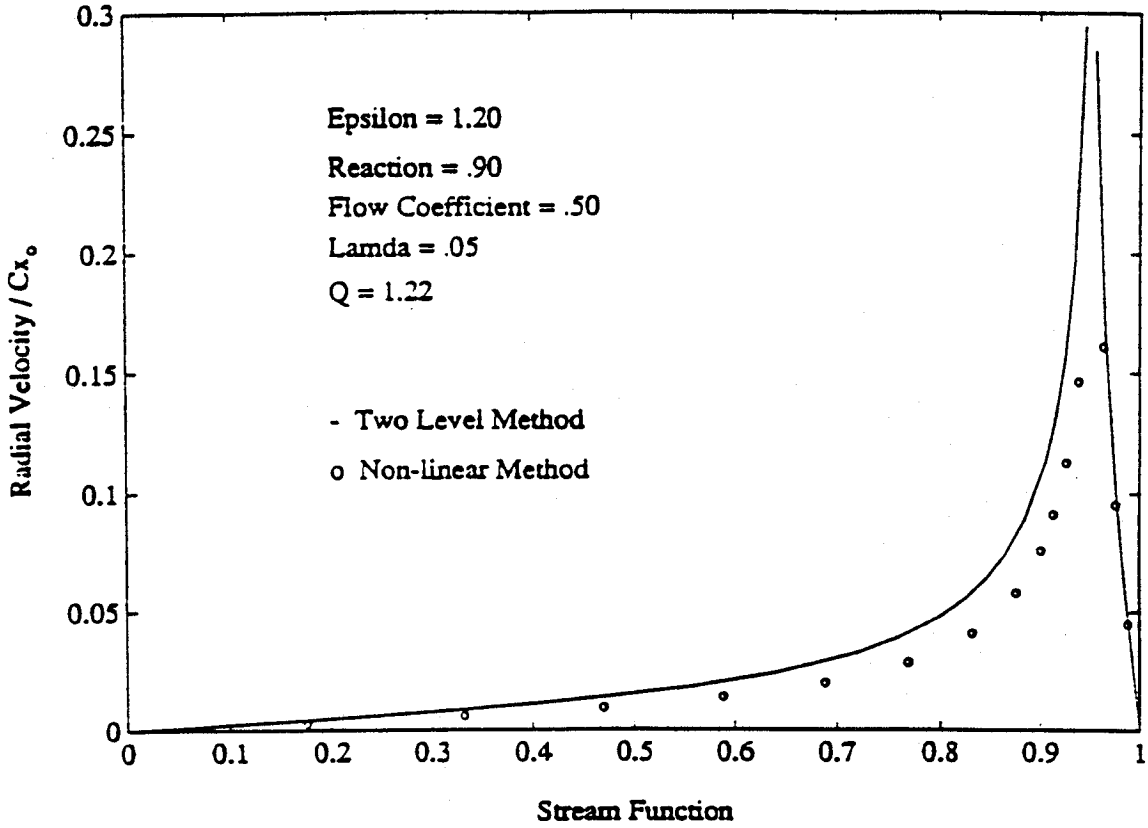

Fig. 9.24: Numerical vs. analytical spanwise velocity profiles at disk

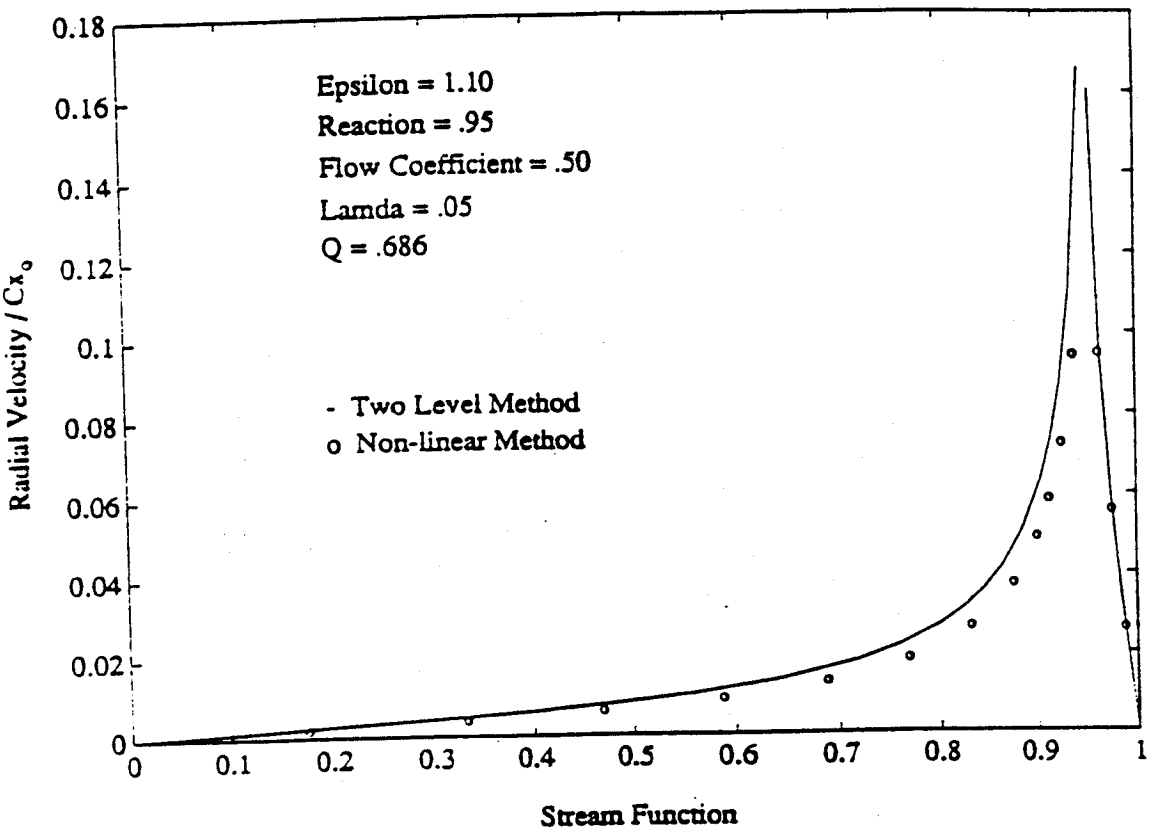

Fig. 9.25: Numerical vs. analytical spanwise velocity profiles at disk

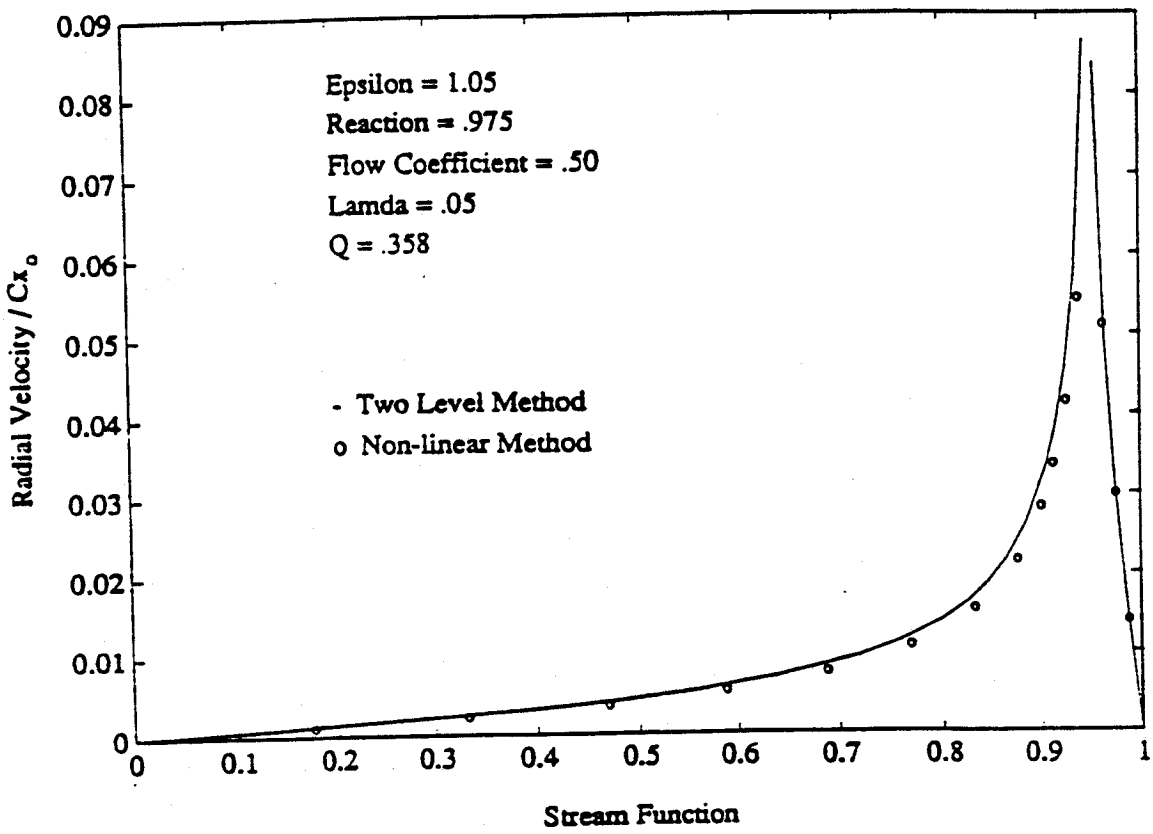

Fig. 9.26: Numerical vs. analytical spanwise velocity profiles at disk

size), and its integrated effect is in any case minimal.

9.2.8 Partial Blade-Tip Loading

9.2.8.1 Introduction

One of the basic approximations made in the theoretical treatment so far is that of zero work done by any fluid crossing the gap area. If we include under that description any streamline which passes over one blade tip, this is clearly not an accurate assumption. Fig. 9.27, for example, shows that, prior to crossing over, a streamtube is partially deflected by the blade, and hence does some push work on it. The magnitude of this work could be quantified if the flow angle for the leakage fluid leaving the passages were known, which prompts us to a more detailed examination of the flow field around the blade-tip gap region.

The blade-tip region has been theoretically treated using a variety of approaches. The simple model of Rains [11], which is most appropriate for thin, lightly loaded blades, uses ideal, pressure-driven flow concepts to derive the speed and direction of the gap "jet". Even for the case of the thicker turbine blading, ideal flow is a fairly good approximation. For example, Rains [11] gave a criterion for viscous forces to be negligible, in the form

$$A \equiv \left(\frac{\text{GAP}}{\text{THICKNESS}}\right)^2 \times \left(\frac{\text{THICKNESS}}{\text{CHORD}}\right) \times R_e\,(\text{CHORD, REL. INLET, VELOCITY}) > 125 \qquad (9.78)$$

For the experimental turbine being tested as part of our research on Alford forces, this parameter is approximately 1000, and this situation is quite common. On the other hand, the effects of chordwise pressure gradients on thick-blade tip flows, as well as that of relative wall motion are still potentially significant, and have not been treated so far (see Section 5).

The gap jet is known to interact strongly with the passage flow and to roll itself up into a concentrated vortex-like structure. Rains himself derived [11] a semi-empirical expression for the trajectory of that vortex. Lakshminarayana [20], [21] also used empirical information on the tip vortex location and strength to predict details of the blade pressure distribution, In fact, the strength of the vortex was explicitly related to a "partial blade-tip loading parameter", K, varying

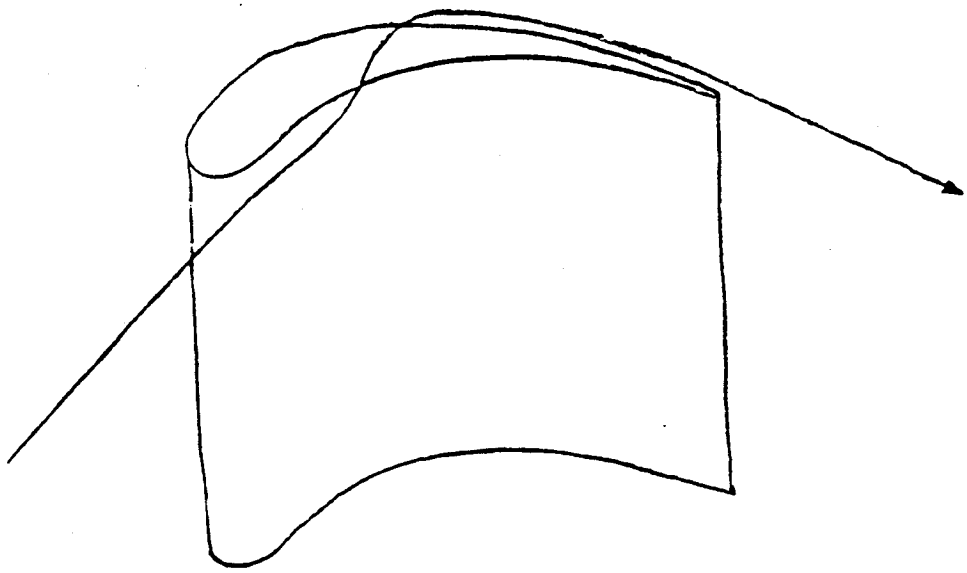

Fig. 9.27: Gap fluid does some work on the rotor

from 0 to 1, and inferred from extrapolation of surface pressure measurements near the tip to the end wall. Since there are very sharp pressure gradients in the pressure side of the blade, near the gap, this procedure is fraught with difficulties. More recently, G.T. Chen et al. [27] have used vorticity dynamics to simulate the roll-up process, and have been able to predict accurately the trajectory of the vortex.

In what follows, we will introduce an alternative viewpoint which leads to simple, but accurate expressions for the location and size of the leakage vortex. This can then be used in calculating the flow leaving angle of, and hence the work done by the leakage flow.

9.2.8.2 Collision of the Leakage Jet and the Passage Flow

Fig. 9.28 shows schematically the essential features of the leakage flow. The fluid approaches a blade (here represented as a flat plate) with a relative velocity $\vec{w}_2$, which evolves into the passage flow velocity $\vec{w}_{PASS}$ at locations not very near the tip gap. Under the action of the pressure differential across the blade, a jet of leakage flow at velocity $\vec{w}_{jet}$ escapes under the blade. This jet penetrates a certain distance into the passage, but is eventually stopped by the main flow, which separates the jet from the wall, turns it backwards, and leads to the formation of a rolled-up structure containing both, leakage and passage fluid. This "collision" of the two streams is again shown in Fig. 9.29 in plan form, and Fig. 9.30 shows a schematic of the flow structure seen in a cut such as a-a in Fig. 9.29, with leakage fluid shown dashed.

Consider the situation at points along the jet separation line, such as P in Figs. 9.29, 9.30. Ignoring frictional effects, the two streams which meet there (jet and passage flows) can both be traced back along different paths, to the inlet flow, and hence have equal total pressures and temperatures. Since they also have equal static pressures along their contact line, (and generally similar static pressures throughout the region), these two streams must have equal velocity magnitudes. If the section a-a is perpendicular to OP, we can think of point P (Fig. 9.30) as the common stagnation point of the two "colliding" flows, approaching each other with equal velocities, which are each the component of $\vec{w}_{jet}$ and $\vec{w}_{PASS}$ perpendicular to line OP. It follows that

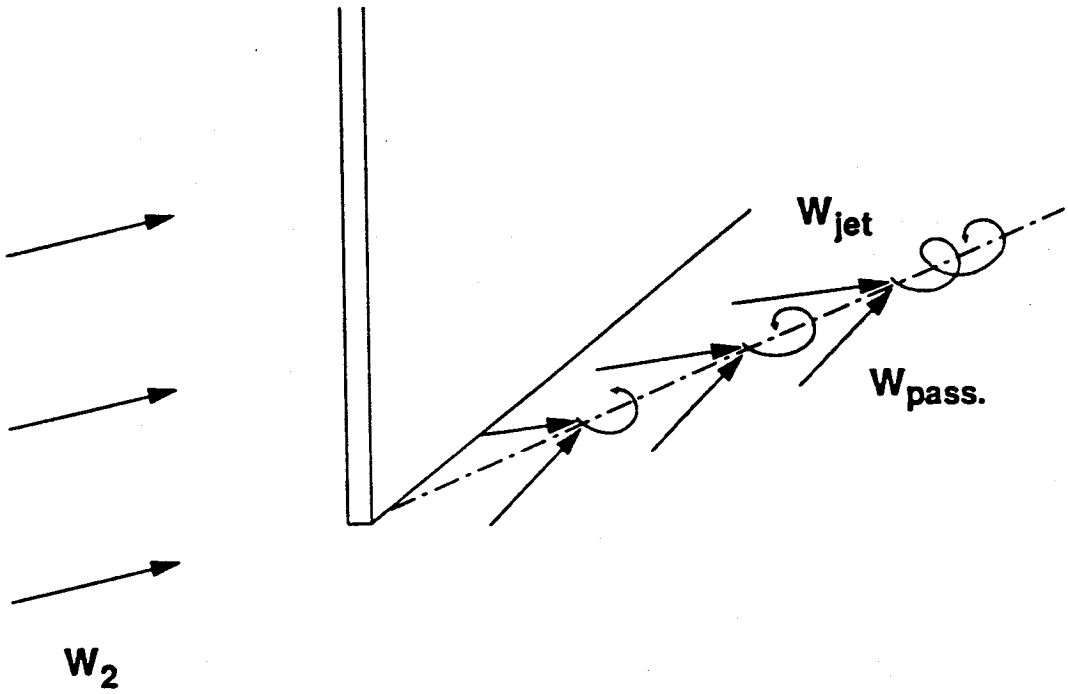

Fig. 9.28: Schematic of the colliding leakage jet and passage flows

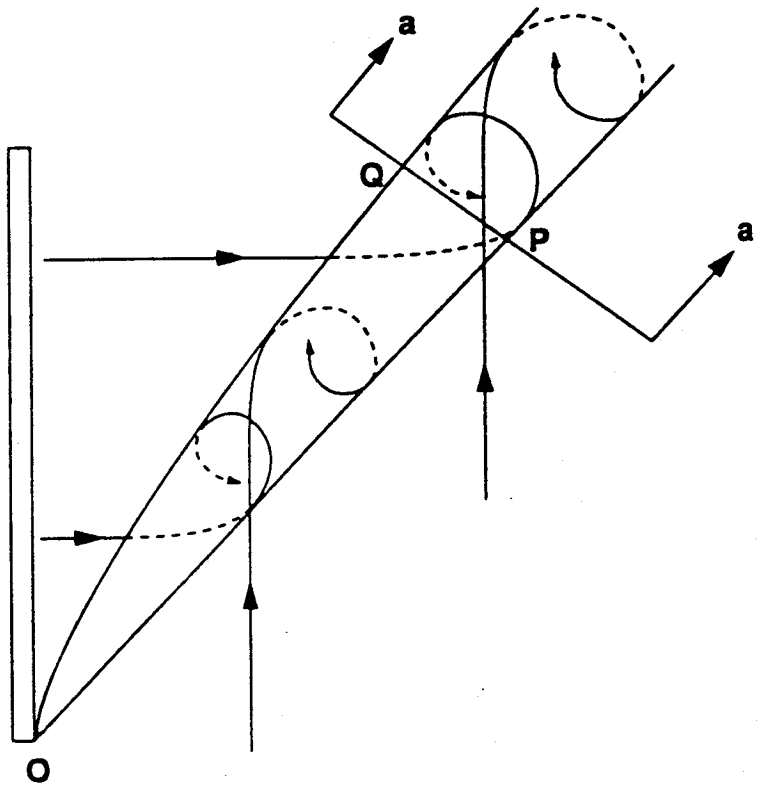

Fig. 9.29: Planform view of Fig. 9.28

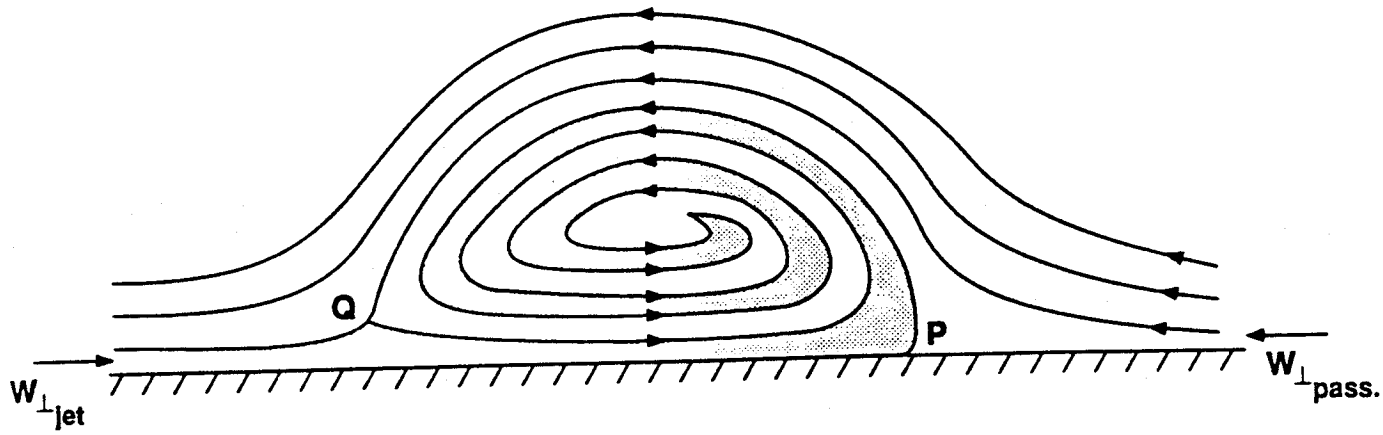

a-a View (Perpendicular to OP)

Fig. 9.30: Flow pattern in line a-a of Fig. 9.29

line OP must bisect the angle made by $\vec{w}_{jet}$ and $\vec{w}_{PASS.}$ This gives a first and important piece of information about the location of the rolled up structure, but, since this structure has a finite and increasing transverse dimension, it does not yet locate its center.

To continue our discussion, notice that the transverse momentum balance of a fluid element near point P requires that both transverse colliding flows must bring equal (and opposite) momentum fluxes to the rolled-up structure. Since the two velocities are equal, we find that equal mass flows must be entering the rolled-up structure from both fluids. In other words, the clear and dashed areas in Fig. 9.30 must occupy equal fractions of the total "vortex" cross section. Let δ_{JET} be the jet thickness, and $w_{\|}$, $w_{\perp}$ the common components along and across OP of the colliding streams. The rate of increase of the cross-section $A_{\perp}$ of the rolled structure along OP is then given by

$$w_{\|}\frac{dA_{\perp}}{ds} = 2\, w_{\perp}\, \delta_{JET} \tag{9.78}$$

or, calling $\theta = \tan^{-1}\frac{w_{\perp}}{w_{\|}}$, i.e., the angle made by the separation line OP and the blade itself,

$$\frac{dA_{\perp}}{ds} = 2\, \delta_{JET} \tan\theta \tag{9.79}$$

where s is measured along the vortex trajectory.

The precise shape of the rolled-up structure is more difficult to establish, but it seems reasonable to model it as (half) cylindrical ideal vortex in a cross-flow. Following Batchelor[14] such a vortex is describable by the stream function (Fig. 9.31)

$$\Psi = 1.298\, w_{\perp}\, R\, J_1\left(3.83\,\frac{r}{R}\right)\sin\theta_1 \tag{9.80}$$

where R is the radius of the dividing streamline, $J_1(x)$ is the Bessel's function of the 1st order (with a zero at x = 3.83) and (r, θ_1) are polar coordinates. The vorticity in this flow is distributed inside the semi-circle of radius R in proportion to Ψ:

$$\omega = \left(\frac{3.83}{R}\right)^2 \Psi \tag{9.81}$$

and is zero outside. Integration of ω gives an overall circulation

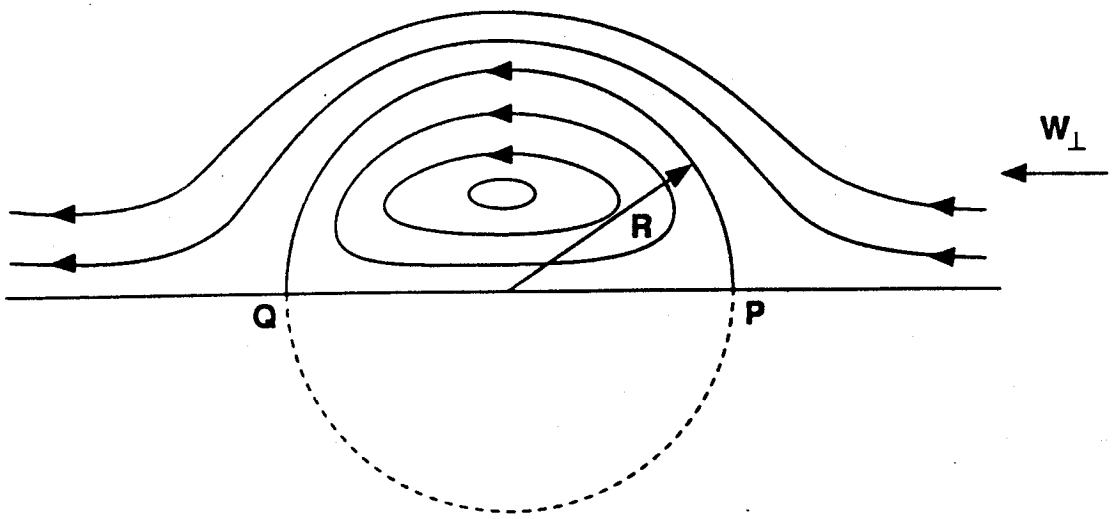

Fig. 9.31: Coordinates for model vortex

$$\Gamma = 6.83\ w_{\perp}\ R \tag{9.82}$$

whereas integration of r sin θ ω gives a center of vorticity height of

$$z_c = 0.460\ R \tag{9.83}$$

We thus make $A_{\perp} = \frac{1}{2}\pi R^2$, and measuring distance along the blade $(x_{BL} = s \cos\theta)$, we can integrate Eq. (9.79) to obtain

$$R = \sqrt{\frac{4}{\pi}\left(\frac{\tan\theta}{\cos\theta}\right)\delta_{JET}\, x_{BL}} \tag{9.84a}$$

The trajectory of the vortex center then follows (Fig. 9.32) as

$$y_c = x_{BL} \tan\theta - \frac{R}{\cos\theta} \tag{9.84b}$$

To complete the analysis, the angle θ must now be determined. From our discussion of the separation line OP, this angle was shown to be half of the angle β between the blade and the jet flow:

$$\theta = \beta/2 \tag{9.85}$$

This angle β follows from the simple local analysis first proposed by Rains [11], which applies to thin blades when viscous effects can be neglected, In Fig. 9.33, w_p and w_s are the flow velocities on the pressure and suction sides of the blade, respectively. Application of Bernoulli's equation relates these velocities to the corresponding pressures:

$$w_p = \sqrt{w_2^2 - 2\frac{P_p - P_2}{\rho}} \tag{9.86a}$$

$$w_s = \sqrt{w_2^2 + 2\frac{P_2 - P_s}{\rho}} \tag{9.86b}$$

where P_2, w_2 corresponds to inlet conditions. On the other hand, the leakage jet emerges form the gap with a velocity component perpendicular to the blade of

$$w_G = \sqrt{2\,\frac{P_p - P_s}{\rho}} \tag{9.87}$$

and its components parallel to the blade is simply w_p, since no momentum is added or lost in that

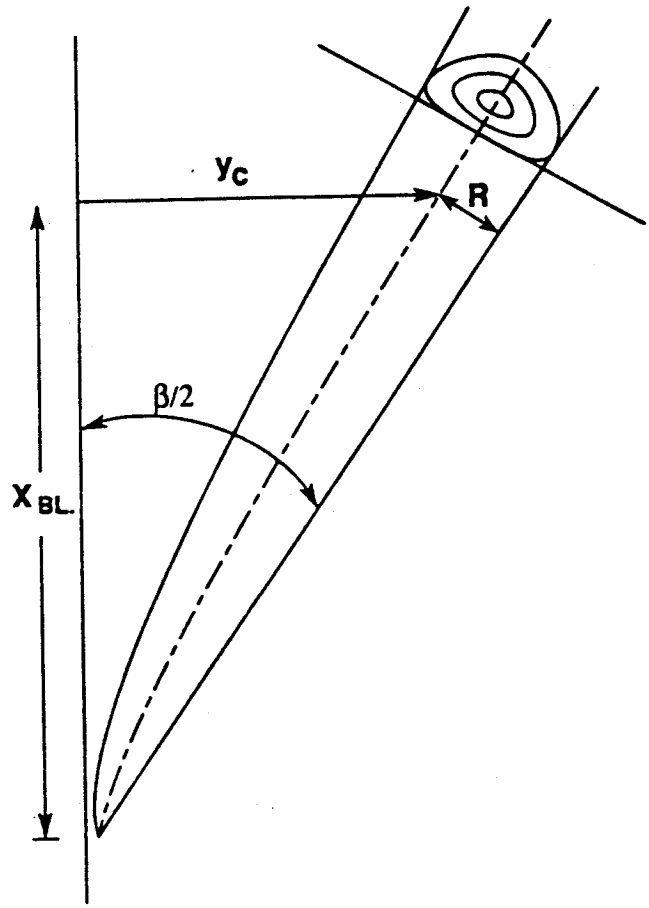

Fig. 9.32: Position and width of rolled-up leakage vortex

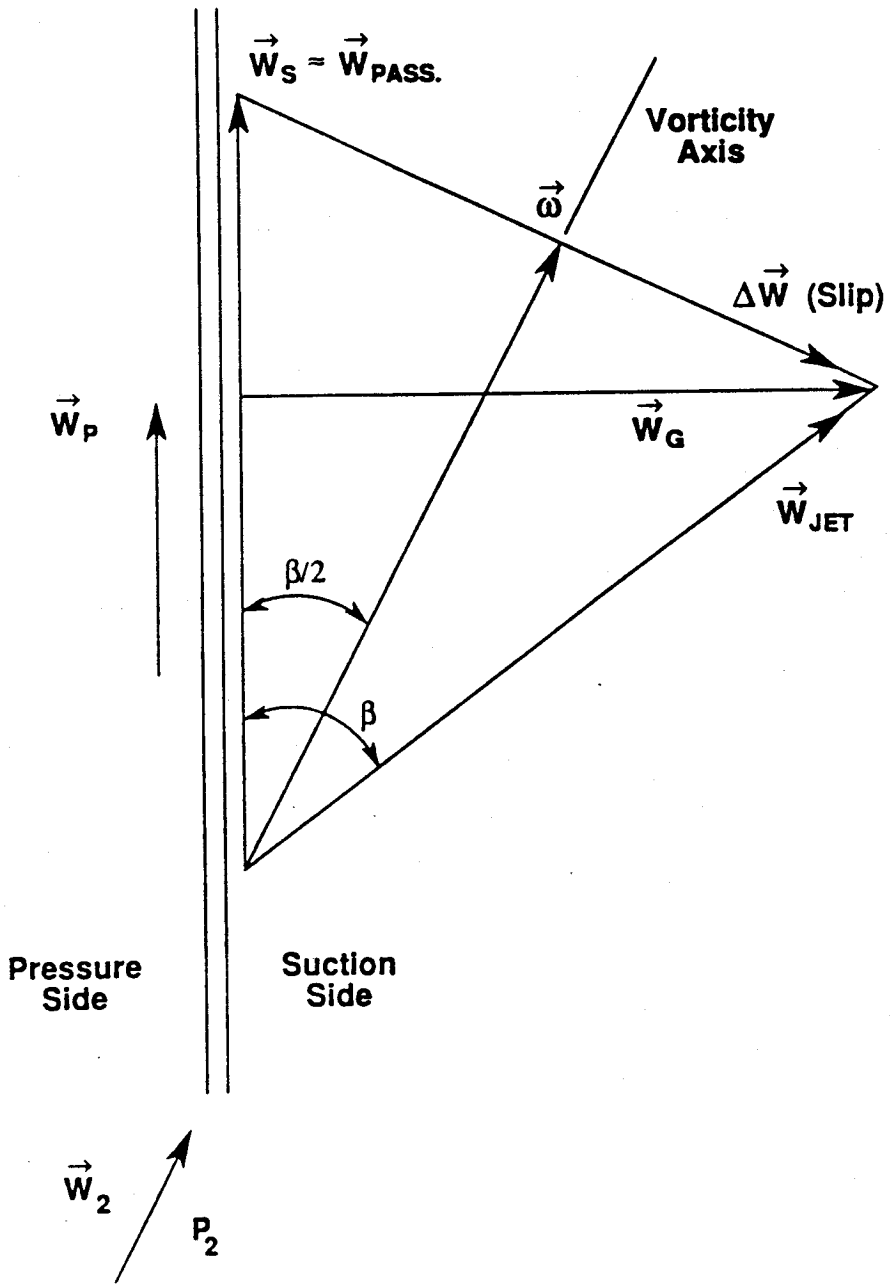

Fig. 9.33: Velocities and angles associated with roll-up

direction during passage through the gap. It can be verified that the net magnitude w_{JET} of the jet velocity is then equal to w_s, as indicated previously. We then obtain (Fig. 9.33)

$$\tan \beta = \frac{w_G}{w_p} = \sqrt{\frac{(C_p)_p - (C_p)_s}{1 - (C_p)_p}} \tag{9.88}$$

where $C_p = 2(P-P_2)/\rho\, w_2^2$ in each case. Note that $(C_p)_p - (C_p)_s$ is the local lift coefficient c'_L, referred to the relative turbine inlet velocity. Using the half-angle trigonometric formulae,

$$\tan \theta = \frac{\sqrt{(C_p)_p - (C_p)_s}}{\sqrt{1 - (C_p)_s} + \sqrt{1 - (C_p)_p}} \tag{9.89}$$

Notice that, as shown in Fig. 9.33, the vorticity vector corresponding to the shear between the jet and the adjacent passage flow is inclined at $\theta = \beta/2$ w.r.t. the blade, i.e. it is parallel to the outer edge OP of the rolled-up structure, This is also the direction of the mean flow between the two sides of the shear layer, which means that the shear vorticity is not convected at all towards the line OP. The only reason the vorticity Γ rolled up into the structure increases with downstream distance is that the growth of R gradually overlaps more and more of the shear vorticity.

Eqs. (9.84a), (9.84b) and (9.89) can now be used to calculate the vortex geometry if the suction and pressure side C_p distributions are know from experiments or calculations. A simple approximation can be obtained using the theory of lightly loaded thin wing profiles. In this approximation, $(w_p + w_s)/2 \cong w_2$, which when used in Eq. (9.86a) and (9.86b) reduces both $(C_p)_p$ and $(C_p)_s$ to functions of $c'_L = (C_p)_p - (C_p)_s$ alone. Using this in Eq. (9.89) gives finally

$$\theta = \cos^{1} \begin{cases} \sqrt{\dfrac{4}{4 + c'_L}} & \left(c'_L < 4\right) \\ \sqrt{\dfrac{c'_L}{4 + c'_L}} & \left(c'_L < 4\right) \end{cases} \tag{9.90}$$

Notice the relative insensitivity of θ to c'_L, particularly about the common value $c'_L = 4$, when θ reaches a maximum of 45°.

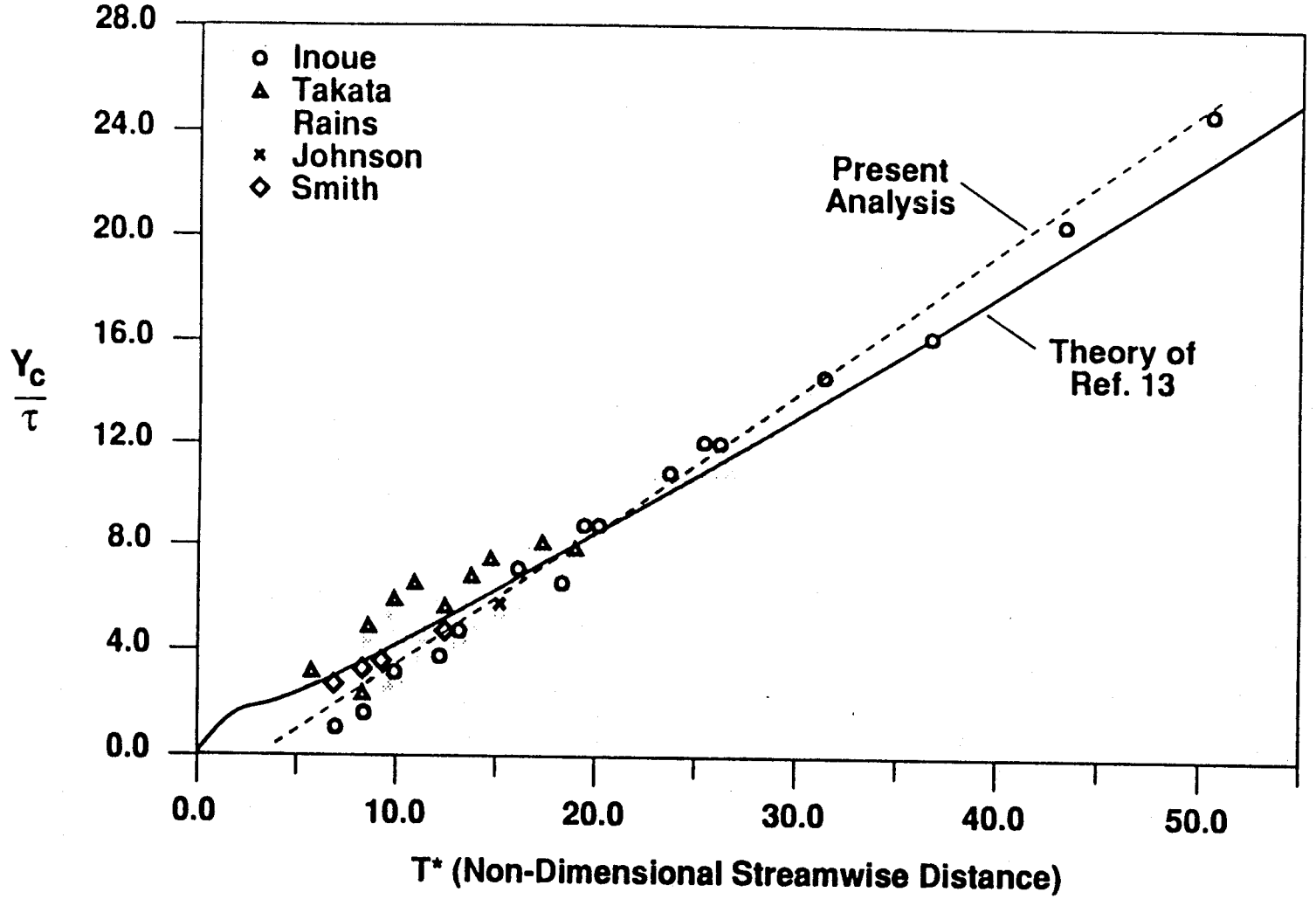

Figure 9.34 Trajectory of vortex centroid compared to data and theory of Ref. 27

9.2.8.3 Comparison to Vorticity Dynamics Model and to Data

Reference [27] has recently provided a means of correlating a variety of rolled-up vortex data using a similarity analysis. Transverse distances are normalized by gap width δ, and axial distance, or time-of-flight are characterized by a parameter

$$t^* = \frac{x}{c_x \delta} \sqrt{\frac{\Delta P}{\rho}} \tag{9.91}$$

where x and c_x are axial distance and velocity and $\Delta P = P_p - P_s$. The data from many experiments (mainly from compressor cascades) correlate well with t*. In addition, a calculational method was developed in Ref. [27] to track a series of shed tip vortices from an impulsively started plate, which represents the situation seen from a convective frame as the flow passes over a blade. The calculated results were shown to also correlate well with t* and with the data.

We use the correspondence

$$\frac{c_x}{w_2} = \cos \beta_2 \quad , \quad \frac{x}{x_{BL}} = \cos \beta_m \tag{9.92}$$

where β_2 and β_m represent the relative flow angles at the rotor inlet and on average in the rotor, respectively, to derive

$$\frac{x_{BL}}{\delta_{JET}} = \frac{\sqrt{2}}{\mu} \frac{w_2}{w_G} \frac{\cos\beta_2}{\cos \beta_m} t^* \tag{9.93}$$

where $\mu = \delta_{JET}/\delta$ is the gap discharge coefficient. Note also that $\frac{w_2}{w_G} = 1/\sqrt{c_L'}$.

For an approximate comparison, we use Rains' 4 values

$$\mu = 0.75; \quad c_L' = 1.35; \quad \frac{\cos \beta_m}{\cos \beta_2} = 1.1$$

to relate t* to our x_{BL}, and then calculate the vortex trajectory using Eqs. (9.84a), (9.84b), (9.89) and (9.90). The results are compared in Fig. 9.34 to those reported in Ref. [27]. The agreement with the data is satisfactory. Additional verification against the theory of Ref. [27] can be provided by comparing the predictions of both theories regarding the "center of vorticity" location in a cross-plant similar to that shown in Fig. 9.30. in order to be consistent with the calculations of

Ref. [27], we have included here both, the rolled-up vorticity Γ (Eq. 9.83), and a vorticity $2w_\perp$ per unit length (perpendicular to $\vec{\omega}$) of the not-yet-rolled shear layer.

In calculating the distance z_c between the center of vorticity and the wall, we took this latter contribution to be at a distance δ_{JET}, and that of the rolled-up vortex to be at $\delta_{JET} + 0.46R$ (Eq. 9.82). The results are shown in Fig. 9.35, which again shows good agreement between our method and that of Ref. [27].

9.2.9 Blade-Tip Losses Including Partial Tip Loading

9.2.9.1 Modifications of the Actuator-Disk Model

We now return to the actuator disk model, but will abandon the assumption of zero work done by the leaking fluid. Conceptually, the fluid which crosses the gap between the casing and the turbine blade is only partially underturned when compared to passage fluid. The fractional work done per unit mass of leakage fluid will turn out to be of the order of 50%. As noted, an equal amount of passage fluid will be rolled up into the leakage vortex, and will also be underturned by the same amount. In total, then, the work done per unit mass of leaking fluid is similar to that postulated in Sec. 9.2.2. But then, the work loss coefficient, w, which includes a normalization by δ/H, will be larger (only 1/2 of the underturned fluid comes from the gap itself). For similar reasons, the coefficient ξ describing the reduction of total pressure drop (Eq. (9.65) will also be larger. The efficiency loss factor, β, reflects these two counteracting effects and, as will turn out, is only slightly affected by the changes.

There are three specific modifications to be made to the theory in order to incorporate these effects:

(a) Re-defining the"leakage flow fraction", λ, to include all underturned fluid. Of this, only the fraction $\lambda/2$ is gap flow, and this is what must be related to the physical gap, δ (Eqs. (9.51) or (9.52)).

(b) Allowing a non-zero total enthalpy drop for the gap flow, and relating it to the angle θ by which the flow fraction λ underturns. This angle is supplied by a form of the theory of Sec.

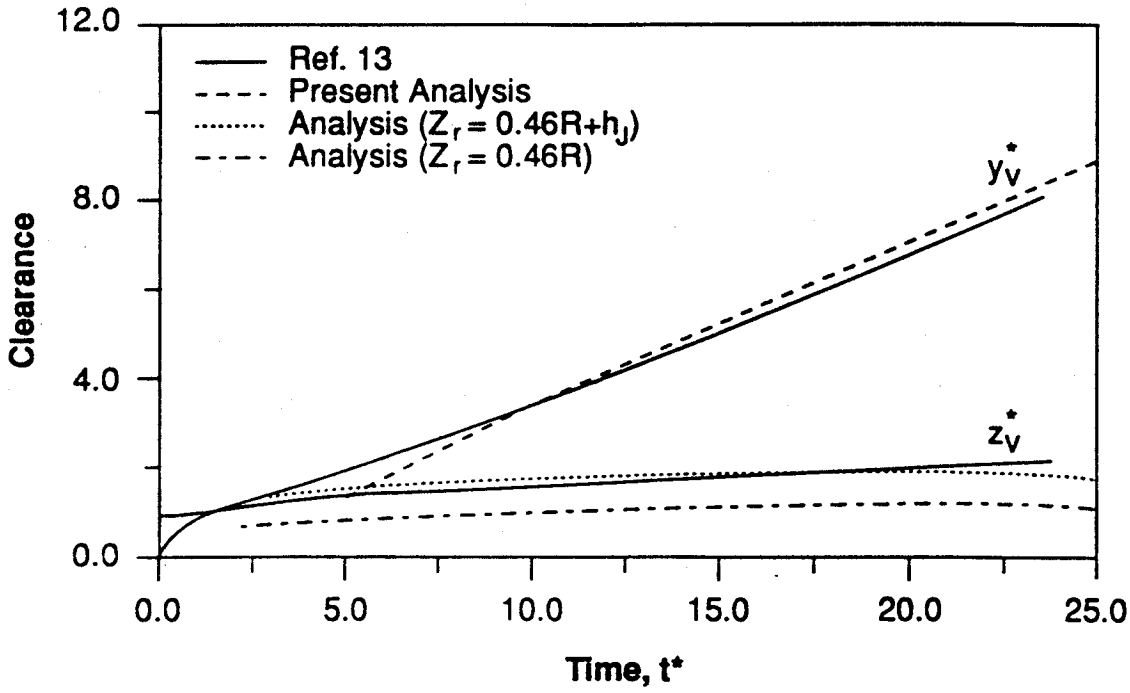

Fig. 9.35: Coordinates of vorticity centroid for tip clearance vortex

9.2.8.

(c) Recognizing that the fluid comprising λ has not undergone an isentropic work-producing process, since formation of the rolled-up vortex is intrinsically lossy.

The under-turning angle θ should be calculated as an average which includes the rolled-up flow, assumed to have its momentum directed along the centerline of the rolled-up vortex, and also the portion of the gap jet which is not yet rolled up at exit (similar to the calculation described in Sec. 9.2.8.3 for the center of vorticity). In the interest of simplicity, we will take θ to be as given by Eq. (9.85), i.e., the angle between the blade and the outer edge of the vortex (Figs. 9.32, 9.33). This will to some extent cancel the modifications due to, on one hand, the angle between this outer edge and the vortex centerline, and, on the other hand, the contribution of the un-rolled jet, which is more strongly under-turned.

Let β_m be the average angle of the rotor blades to the axial direction, which can be calculated (Fig. 9.4) as

$$\beta_m = \frac{\beta_3 - (\beta_2)_{DES.}}{2} \tag{9.94}$$

with

$$\tan(\beta_2)_{DES} = \tan\alpha_2 - \frac{1}{\phi_{DES}} = \tan\alpha_2 - \tan\beta_3 \tag{9.95}$$

The passage flow relative velocity is then (on average) $w_{PASS} = c_x/\cos\beta_m$, which has components $w_{\parallel}$ and $w_{\perp}$ parallel and perpendicular to the line OP (Figs. 9.29, 9.30) which is now taken to represent the rolled-up vortex

$$w_{\parallel} = c_x \frac{\cos\theta}{\cos\beta_m} \quad ; \quad w_{\perp} = c_x \frac{\sin\theta}{\cos\beta_m} \tag{9.96}$$

The gap flow, for its part, has components $w_{\parallel}$ and $-w_{\perp}$ in the same directions. The flow fraction λ is all assumed to leave the passage with velocity $w_{\parallel}$ along line OP, and so its relative Y-component of velocity is $w_{\parallel}\sin(\beta_m - \theta)$. In the absolute frame, then,

$$cy_3^+ = U - c_x^+ \frac{\cos\theta \sin(\beta_m - \theta)}{\cos\beta_m} \tag{9.97}$$

where we use the (+) superscript as before to denote the "gap fluid", which now, more precisely, means all of the under-turned fluid. Of course, the rest of the fluid has a $cy_3 = cy_3^-$ still given by Eq. (9.57). Also, the disk axial velocities c_x^+, c_x^- are still as given by Eqs. (9.46), although Q will now be different. Notice that Eq. (9.98) replaces the previously used non-turning assumption ($cy_3^+ = c_x \tan\alpha_2$).

Application of the Euler equation to both fluids gives the work done per unit mass by each stream:

$$W^+ = U\,(c_x^+ \tan\alpha_2 - cy_3^+) \tag{9.98}$$

$$W^- = U\,(c_x^- \tan\alpha_2 - cy_3^-) \tag{9.99}$$

and, since ideality is assumed in the bladed region, ρW^- is the same as the turbine total pressure drop in that region, i.e.

$$W^- = B_1 - B^- = B_1 - B_\perp^- - \frac{1}{2}(cy_3^-)^2 \tag{9.100}$$

In the "gap region", however, W^+ is less than the isentropic work $B_1 - B^+$ by an amount $T\Delta S$ equal the energy dissipation incurred in the mixing of the gap and passage streams. Per unit mass, this dissipation equals the kinetic energy associated with the "destroyed" component $w_\perp$ of Eq. (9.96):

$$T\Delta S = \frac{1}{2}\left(c_x^+ \frac{\sin\theta}{\cos\beta_m}\right)^2 \tag{9.101}$$

and therefore

$$W^+ = B_1 - B_\perp^+ - \frac{1}{2}(cy_3^+)^2 - \frac{1}{2}(c_x^+)^2\left(\frac{\sin\theta}{\cos\beta_m}\right)^2 \tag{9.102}$$

Subtracting Eqs. (9.100) and (9.102), and remembering that $Q = B_\perp^+ - B_\perp^-$, we obtain

$$Q = W^- - W^+ - \frac{1}{2}(c_x^+)^2\left(\frac{\sin\theta}{\cos\beta_m}\right)^2 - \frac{1}{2}(cy_3^+)^2 + \frac{1}{2}(cy_3^-)^2 \tag{9.103}$$

We can now use Eqs. (9.97) and (9.57) for the c_y's, and then Eq. (9.46) for the c_x's and, upon substitution into (9.102), we obtain the new equation for q. Rearranging this takes the form

$$\left[(1-\lambda)^2 G - \lambda^2 \tan^2\beta_3\right]\left(\frac{q}{2}\right)^2 + 2\left[2 + \frac{\tan\alpha_2}{\phi} + (1-\lambda)G + \lambda\tan^2\beta_3\right]\left(\frac{q}{2}\right) - \left(\tan^2\beta_3 - G\right) = 0 \tag{9.104}$$

where

$$G = \left(\frac{\cos\theta \sin\left(\beta_m - \theta\right)}{\cos\beta_m}\right)^2 + \left(\frac{\sin\theta}{\cos\beta_m}\right)^2 \tag{9.105}$$

which replaces Eq. (9.47).

Once q is calculated, the total turbine work per unit mass is $\lambda W^+ + (1 - \lambda) W^-$. Normalizing,

$$\psi = \psi_o - \lambda\phi\left(\tan\beta_3 - g\right)\left(1 + \frac{1-\lambda}{2} q\right) \tag{9.106}$$

where

$$g = \left(\frac{\cos\theta \sin\left(\beta_m - \theta\right)}{\cos\beta_m}\right) \tag{9.107}$$

The calculation of the total pressure drop is identical to that explained in Eqs. (9.59) - (9.62), except that, as mentioned cy_3^+ is now given by Eq. (9.97) rather than Eq. (9.57). In particular,the static pressure drop still follows from Eqs. (9.62) and (9.23), since only ideal flow through the bladed region is involved. Following calculation of $P_{t_o} - P_{t_{MIX}}$, the efficiency and the efficiency loss parameter can be found as before (Eqs. (9.63), (9.64)).

9.2.9.2 Comparison of the Theory with Partial Tip Loading to Literature Data

In order to compare the modified theory of Sec. 9.2.9.1 to the same turbine data as before (Sec. 9.2.6.2), additional data regarding individual blade loading are needed to calculate the under-turning angle θ. This information is contained in the Zweifel coefficient ZW, which is also reported by Ref. [18] in each case, This is related to the blade lift as shown in Appendix 9.B (Eq.

9.B11). The angle θ then follows from Eq. 9.90, where the overall lift coefficient c_L is used as a representative value of the local c_L'.

The results for the same set of data as was used in Sec. 9.2.6.2 are summarized in Table 9.4, where the entries are the same as in Table 9.2, except for ZW and the last column, labelled K, which is the ratio of work done per unit mass by the underturned flow to that done by the blade-guided flow:

$$K = \frac{W^+}{W^-} \tag{9.108}$$

Once again, Case 1 can only be brought into agreement with the data if the load factor is reduced to about the design value (i.e., for zero exit swirl). Case No. 4, with very high reaction, is also substantially under-predicted, which may point to an insufficient predicted underturning θ for these conditions. The rest of the cases are well predicted. Excluding Case 1, as before, the mean squared error is

$$\overline{\varepsilon^2} = 0.1162$$

and the mean error is

$$\bar{\varepsilon} = -0.1408$$

which imply a standard deviation

$$\sigma = 0.3105$$

These statistics are slightly better than those found for the zero tip loading theory (Sec. 9.2.6.2), and, although they compare favorably with those for the standard methods, they also still show some systematic over-prediction and moderate scatter. It is of interest that most of the error and scatter (other than that due to point 1) is caused by the single high-reaction data point (Case 4). If that entry were also removed, we would have $\overline{\varepsilon^2} = 0.0363$, $\bar{\varepsilon} = -0.0498$ and $\sigma = 0.184$. Perhaps more effort should be devoted to an understanding of the leakage and underturning effects for high reaction rotors. Whereas the predicted β values in Tables 9.2 and 9.4 are similar, the α values in Table 9.4 are substantially greater than those in Table 9.2, for the reasons explained above.

TABLE 9.4

CASE #	AUTHOR	ZW	ϕ	ψ_o	R	δ/H	$(\beta)_{DATA}$	$(\beta)_{CALC.}$	$(w)_{CALC.}$	$K_{CAL.}$
1	KOFSKEY	55	0.79	7.0	0.02	0.05	1.02	2.902	4.096	1.025
2A	MARSHALL -ROGO	1.02	0.50	1.48	0.32	0.035	1.51	1.443	2.563	0.346
2B	MARSHALL -ROGO	1.09	0.44	1.25	0.35	0.035	1.23	1.418	2.757	0.290
3	SZANCA-BEHNING-SCHUM	1.59	0.57	1.46	0.47	0.033	1.90	1.681	3.066	0.369
4	HOLESKI-FUTRAL	0.35	0.26	0.69	0.69	0.031	2.53	1.661	4.880	0.365
5	EWEN-HUBER -MITCHELL	0.70	0.25	1.05	0.45	0.02	1.50	1.458	3.914	0.411
6	LART	0.92	0.51	1.41	0.51	0.02	1.80	1.924	3.500	0.375
7	YAMAMOTO	0.79	0.42	1.52	0.47	0.03	1.63	1.803	3.558	0.452
8	PATEL	0.70	0.28	1.15	0.61	0.01	1.81	1.415	4.813	0.683
9	HAAS-KOFSKEY	0.80	0.35	1.37	0.47	0.03	1.80	1.640	4.714	0.468
1 (MODIFIED)	KOFSKEY (Assuming ψ_o=2)	0.55	0.79	2.0	0.02	0.05	1.02	0.926	1.614	0.473

Efficiency loss and work defect calculated from theory (including allowance for partial tip loading), compared to data. The last line is computed with modified work coefficient chosen for near-axial exit flow

9.2.10 Summary and Conclusions of Blade-Scale Theory

A theory has been developed to illuminate the effects of spanwise flow redistribution caused by the presence of a small rotor blade-tip gap. To this end, the blade-to-blade details are ignored by using an incomplete actuator disk formulation which collapses both stator and rotor to a plane, across which connecting conditions are imposed.

In the simplest version, the flow which leaks through he tip gap is assumed to do zero work. The results indicate that the flow tends to go preferentially though the gap, and that the attendant flux reduction elsewhere is very nearly uniform in the spanwise direction. The axial length scale for this flow redistribution is the blade height, and not the gap size, as might have been expected. As a consequence, the unloading of the turbine blades is uniform, and the work defect cannot be localized in the near-gap region. On the other hand, the efficiency loss is due to mixing effects downstream of the gap. In this simple model, this mixing is that between the bulk flow and the underturned and somewhat axially faster stream going through the gap.

In order to shed some more light on the details of the gap flow, a modification was made to the theory in which the underturned stream was recognized as originating partly from gap flow, partly from entrained passage flow, both leaving the passage in the form of rolled-up tip vortex. The trajectory and other details of this vortex were calculated using a simple model involving the collision of the ideal pressure-driven leakage jet with the passage fluid. This model was calibrated against both, data and the theory of G.T. Cheng et al. [27]. The modified actuator disk theory allows prediction of the fractional tip loading factor K, and introduces the effects of loading level on individual blades, which the simpler version ignores.

Both actuator disk models were then compared to a set of data involving 9 different turbines (10 operating conditions). With the exception of one anomalous case, the calculated efficiency loss factors are reasonably close to the data, showing less deviation than the loss correlations of Ainley, Soderberg, Roelke, Kofskey and Lakshminarayana. The more realistic version of the theory, which accounts for non-zero work done by the leakage fluid, predicts substantially higher work loss coefficients.

These results suggest that upstream flow redistributions which have been largely ignored so far may be of importance in understanding the basic physics of tip leakage effects. It is recognized, however, that the complete smearing out of blade-to-blade variations may be too drastic an approximation, as the neglected scales are on the same order as the axial redistribution scale which is retained. Further work is recommended to explore this issue.

9.3 Variable Gap and X-Y Flow Redistribution

9.3.1 Connection to the Constant-Gap Analysis

Throughout the analysis in Sec. 9.2, the gap δ has been kept as a constant, so that the results apply, strictly speaking, only to a centered turbine under steady conditions. However, as indicated in the Overview (Sec. 9.1), this theoretical development has wider applicability because of the disparity of length scales ($H << \pi R$) and time scales $\left(\frac{H}{c_x} << \frac{1}{\Omega}\right)$.

Consider a situation such as depicted in Fig. 9.36, where a turbine of mean radius R is executing a circular whirl of amplitude e and angular frequency Ω (positive in the direction of spin, ω). The point of maximum gap is displaced by $\Omega t + \pi$ radians from the fixed X axis, and the azimuthal location of a particular point in the gap region is specified by its distance y' (or angle $\theta = y'/R$) measured from the point of maximum gap. In the whirling coordinate frame X'Y', the flow pattern is stationary ($\partial/\partial t = 0$), but in the fixed frame we must have

$$\left(\frac{\partial}{\partial t}\right)_{\substack{\text{fixed}\\ \text{frame}}} = -\Omega R \frac{\partial}{\partial y} \tag{9.77}$$

namely, spatial variations are swept past the fixed observer, and give rise to time-dependence. For small gaps ($\delta/R << 1$), we have a cosine distribution of gap width:

$$\delta = \overline{\delta} + e \cos\frac{y'}{R} = \overline{\delta} + e \cos\left(\frac{y}{R} - \Omega t\right) \tag{9.78a}$$

or

$$\delta = \mathrm{Re}\left[\overline{\delta} + e\, e^{i(y/R - \Omega t)}\right] \tag{9.78b}$$

where $\overline{\delta}$ is the mean gap, or gap when the turbine is concentric, and the fixed-frame distance y is from the -OX axis.

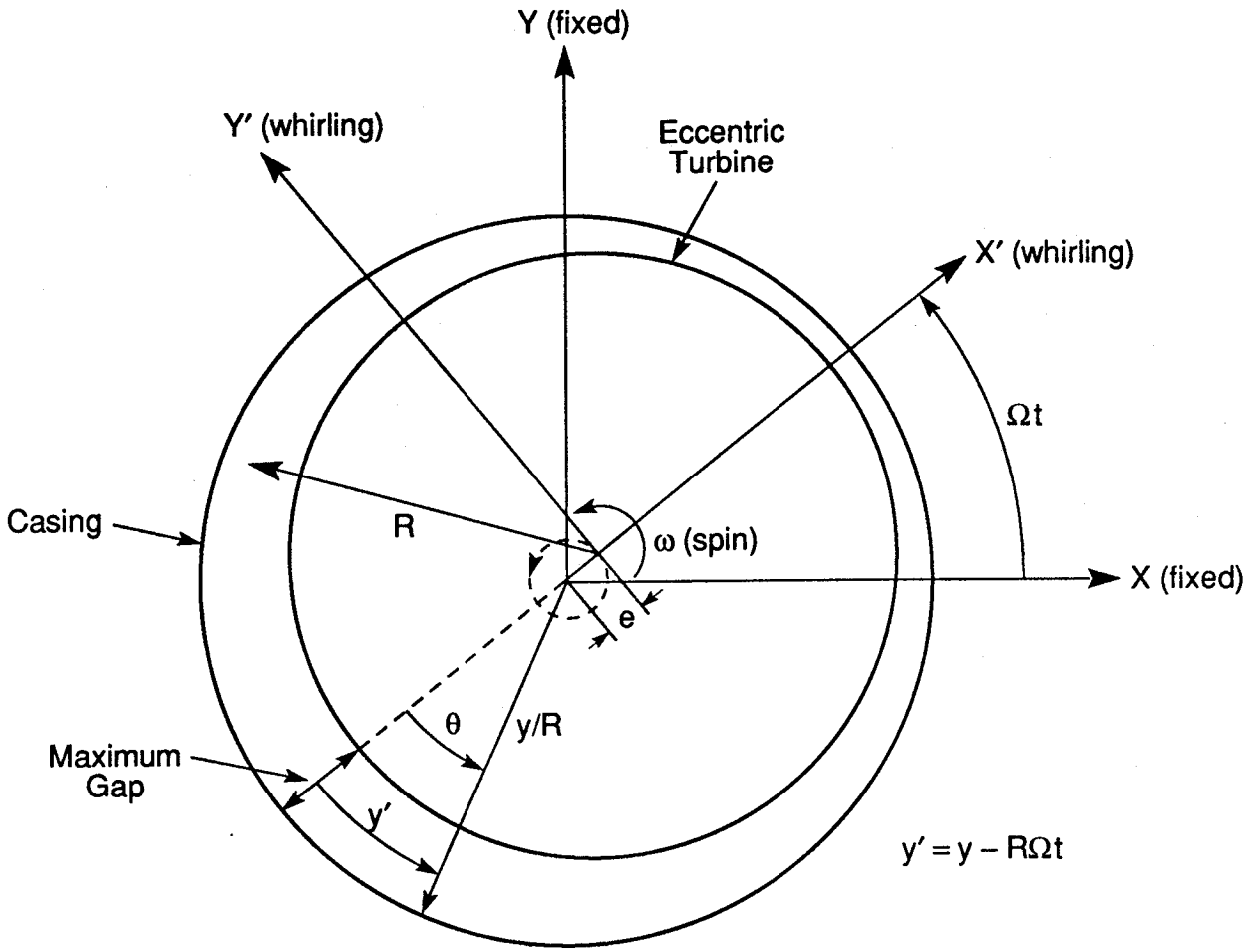

Fig. 9.36: Geometry for a whirling rotor

Because of the eccentricity, the approaching and leaving flows will be affected over distances of order R, and will respond by redistributing in the (xy) plane (where x is the axial direction, and we are reverting to a purely two-dimensional description, this time in the xy plane). Now, at distances of order R, the xz redistribution due to the gap is not present yet (or anymore, for the fluid leaving) because the flow shifts towards (or away from) the gap over distances of order H/π, as can be seen from the shape of the shearing streamline (Sec. 9.2.5.3).

This means that, to a first approximation in $H/\pi R$, the approaching flow can be taken to be independent of z up to the disk, where it has already undergone rearrangement in the y direction, and the leaving flow can be taken to have a two-layer structure with the gap jet and the blade region flow being each independent of z. On the other hand, at distances of the order of H from the stage, the y gradients and the time variations associated with whirl both have negligible effect, with radial redistribution (xz) being the dominant phenomenon. Therefore, the analysis of Sec. 9.2 is still applicable for $|x| \sim H$ even in the present, more complicated situation.

The only modification that needs to be introduced into the analysis of the xz actuator disc is the possibility of a c_{y_0} component of the velocity at upstream distances $>> H/\pi$. This may now exist because of an R-scale redistribution in the xy plane. In fact, if only the steady-state situation is of interest, even this is not necessary (in the sense that $c_{y_0} = c_{y_0}(y)$ does occur, but it does not need to be kept track of). The reason is that the stator is still assumed to be ideal and to perfectly guide the flow, so that the velocity vector entering the rotor is independent of c_{y_0}, and is fixed by c_{x_0} and the stator leaving angle alone. Bernoulli's equation (between upstream infinity (on the R-scale) and after the stator) ensures that the static pressure is also independent of c_{y_0}. Therefore, none of the flow quantities downstream of the turbine is sensitive to the tangential velocity component c_{y_0} introduced by the redistribution. In an unsteady (whirling) situation, where Bernoulli's equation contains the time derivative of the velocity potential as well, this argument is not valid, and $c_{y_0} \neq 0$ should indeed be introduced and kept consistently. Of course, in either case, c_{x_0} will also depend on y and t, because of the same R-scale redistribution, and this will directly affect the flow downstream as well.

The effect of $c_{y_0} \neq 0$ on the formulation is fairly limited. For H-scale distances, unsteadiness is ignored, and the simple form P/p + @ c^2 = const. of Bernoulli's equation applies. Likewise, c_y is still a purely convected quantity, hence equal to c_{y_0} throughout the H-scale region. Because of this, the only modification is that Eqs. (9.23) and (9.24) both have an extra term - @ $c_{y_0}^2$ on the right. This does not affect either the distributed vorticity (Eqs. (9.25a) and (9.25b)) or the concentrated shear vorticity (Eq. (9.27)). The work loss coefficient w, the leakage flow λ, etc. are then given by the same expressions derived in Sec. 9.2, using the local and instantaneous $\delta = \delta(y,t)$, $Q = Q(y,t)$, $c_{x_0} = c_{x_0}(y,t)$.

It is to be noted here that the subscript $(\,)_0$ will now denote conditions at $(-x) >> H/\pi$, but with $(-x) << R$, so that the full y-redistribution is assumed to have taken place by then. Conditions for $(-x) >> R$ will be denoted by an argument (or subscript) of $-\infty$.

To summarize, we now adopt a more "detached" viewpoint than in Sec. 9.2, so that distances of order R are of interest, and the whole xz redistribution process is "compressed" in a thin region (of order H/π). This region has transfer relationships which have been explicitly obtained in Sec. 9.2, and can now serve as a new "actuator disk" surface connecting the upstream and downstream R-scale regions. The upstream region starts with purely uniform, steady, axial flow at $x \rightarrow -\infty$, and remains ideal down to $x \rightarrow 0^-$, meaning down to x of the order of $(-H/\pi)$ in our broader length scale. The downstream region starts at $x = 0^+$, meaning at x distances of the order of $+H/\pi$, with a fully developed two-layer distribution of the type described in Sec. 9.2. This two-layer structure is modulated in y and t by the rotor eccentricity, and these modulations then propagate downstream to $x \rightarrow +\infty$ ($x >> R$). The following subsections analyze these R-scale flows.

9.3.2 The Upstream Flow

The far upstream condition is one of uniform and steady flow, and so, despite the presence of the eccentric (and unsteady) turbine, the flow remains irrotational in this region. Setting

$$\vec{c} = (c_x, c_y) = \nabla\phi \tag{9.78}$$

the continuity condition then implies

$$\nabla^2\phi = 0 \tag{9.79}$$

with boundary conditions of periodicity in 0y, plus $c_x(-\infty)$ being a given constant, and downstream conditions which match the turbine flow. For now, we assume a form for $c_x(x=0^-)$ (i.e., at $x \sim -H/\pi$) as follows:

$$c_x(0^-,y,t) = \mathrm{Re}\left[c_x(-\infty) + \hat{c}_{x_0} e^{i(y/R-\Omega t)}\right] \tag{9.80}$$

which embodies the y and t dependencies coming from the turbine tip gap (Eq. (9.78)). Here, $\hat{c}_{x_0}$ is the (complex) amplitude of the axial velocity disturbance as it approaches the disk, while $c_x(-\infty)$ is its mean value.

The solution to $\nabla^2\phi = 0$ with these conditions gives

$$c_x = c_x(-\infty) + \mathrm{Re}\left[\hat{c}_{x_0} e^{x/R + (y/R-\Omega t)}\right] \tag{9.81}$$

$$c_y = \mathrm{Re}\left[i\,\hat{c}_{x_0} e^{x/R + (y/R-\Omega t)}\right] \tag{9.82}$$

The pressure can now be calculated from either one of the components of the momentum equation. For example,

$$\frac{\partial p}{\partial x} = -\rho\left(\frac{\partial c_x}{\partial t} + c_x\frac{\partial c_x}{\partial x} + c_y\frac{\partial c_x}{\partial y}\right) \tag{9.83}$$

can be integrated with respect to x. The result is

$$P = P(-\infty) - \mathrm{Re}\left\{\rho\left[(c_x(-\infty) - i\Omega R)\,\hat{c}_{x_0} e^{i(y/R-\Omega t)} + \left|\hat{c}_{x_0}\right|^2\right] e^{x/R}\right\} \tag{9.84}$$

Notice that no linearization has been necessary so far. The downstream solution does require linearization, however, and, for consistency, we will simply drop the small $\left|\hat{c}_{x_0}\right|^2$ term in (9.84). The Re( ) (real part of) notation will also be omitted from here on.

9.3.3 The Downstream Flow

For $x \geq +H/\pi$, after the radial redistribution is completed, we have two distinct regions: (a) the region containing the flow which has crossed the bladed part of the rotor (quantities denoted by

a ($^-$) superscript); and (b) the region containing the underturned fluid (quantities denoted by a ($^+$) superscript). This latter region has a thickness $\Delta(y,t)$.

The equations of conservation of mass and momentum (x and y components) can now be written. The quasi-one-dimensional approximation is adopted for each region, i.e. we use variables which are averaged in z within Δ and H-Δ. The equations of continuity are

$$\frac{\partial \Delta}{\partial t} + \frac{\partial (c_x^+ \Delta)}{\partial x} + \frac{\partial (c_y^+ \Delta)}{\partial y} = 0 \tag{9.85}$$

$$\frac{\partial (H-\Delta)}{\partial t} + \frac{\partial \left((H-\Delta) c_x^-\right)}{\partial x} + \frac{\partial \left((H-\Delta) c_y^-\right)}{\partial y} = 0 \tag{9.86}$$

and the momentum equations are

$$\frac{\partial c_x^+}{\partial t} + c_x^+ \frac{\partial c_x^+}{\partial x} + c_y^+ \frac{\partial c_x^+}{\partial y} + \frac{1}{\rho} \frac{\partial p}{\partial x} = 0 \tag{9.87}$$

$$\frac{\partial c_y^+}{\partial t} + c_x^+ \frac{\partial c_y^+}{\partial x} + c_y^+ \frac{\partial c_y^+}{\partial y} + \frac{1}{\rho} \frac{\partial p}{\partial y} = 0 \tag{9.88}$$

$$\frac{\partial c_x^-}{\partial t} + c_x^- \frac{\partial c_x^-}{\partial x} + c_y^- \frac{\partial c_x^-}{\partial y} + \frac{1}{\rho} \frac{\partial p}{\partial x} = 0 \tag{9.89}$$

$$\frac{\partial c_y^-}{\partial t} + c_x^- \frac{\partial c_y^-}{\partial x} + c_y^- \frac{\partial c_y^-}{\partial y} + \frac{1}{\rho} \frac{\partial p}{\partial y} = 0 \tag{9.90}$$

In order to obtain analytical results, we next assume that the turbine eccentricity amplitude is small, so that Δ, c_x^+, c_y^+, c_x^-, c_y^-, and p can each be expressed as a mean value around the circumference, plus a small perturbation:

$$\Delta = \bar{\Delta} + \Delta' \quad ; \quad p = \bar{p} + p' \quad ; \quad \text{etc.} \tag{9.91}$$

Equations (9.85) through (9.90) can then be linearized. Because of the y and t periodicity forced by the turbine motion, the perturbation quantities can be expected to have variations of the form

$$\Delta' = \hat{\Delta} \exp\left[\alpha x + i\left(\frac{y}{R} - \Omega t\right)\right] \tag{9.92a}$$

$$p' = \hat{p}\exp\left[\alpha x + i\left(\frac{y}{R} - \Omega t\right)\right] \tag{9.92b}$$

etc.

where real parts are understood. The constant α is an eigenvalue to be determined.

When Eq. (9.92) is substituted into Eqs. (9.85) - (9.90), a linear, homogeneous set of equations can be obtained for the amplitudes $\hat{\Delta}$, $\hat{p}$, etc.:

$$\begin{bmatrix}
\alpha\bar{\Delta} & \frac{i}{R}\bar{\Delta} & 0 & 0 & \alpha\bar{c_x^+} + i\left(\frac{\bar{c_y^+}}{R} - \Omega\right) & 0 \\
0 & 0 & \alpha(H-\bar{\Delta}) & \frac{i}{R}(H-\bar{\Delta}) & -\alpha\bar{c_x^-} - i\left(\frac{\bar{c_y^-}}{R} - \Omega\right) & 0 \\
\alpha\bar{c_x^+} + i\left(\frac{\bar{c_y^+}}{R} - \Omega\right) & 0 & 0 & 0 & 0 & \alpha \\
0 & \alpha\bar{c_x^+} + i\left(\frac{\bar{c_y^+}}{R} - \Omega\right) & 0 & 0 & 0 & \frac{i}{R} \\
0 & 0 & \alpha\bar{c_x^-} + i\left(\frac{\bar{c_y^-}}{R} - \Omega\right) & 0 & 0 & \alpha \\
0 & 0 & 0 & \alpha\bar{c_x^-} + i\left(\frac{\bar{c_y^-}}{R} - \Omega\right) & 0 & \frac{i}{R}
\end{bmatrix}
\begin{Bmatrix}
\hat{c}_x^+ \\ \hat{c}_y^+ \\ \hat{c}_x^- \\ \hat{c}_y^- \\ \hat{\Delta} \\ \frac{\hat{p}}{\rho}
\end{Bmatrix} = 0 \tag{9.93}$$

For non-trivial solution, the determinant of the matrix in (9.93) must vanish. This gives a 6^{th} order equation for α:

$$\left[\alpha\,\bar{c_x^-} + \frac{i}{R}\left(\bar{c_y^-} - \Omega R\right)\right]\left[\alpha\,\bar{c_x^+} + \frac{i}{R}\left(\bar{c_y^+} - \Omega R\right)\right]\left(\frac{1}{R^2} - \alpha^2\right)$$

$$\times\left\{\bar{\Delta}\left[\alpha\,\bar{c_x^-} + \frac{i}{R}\left(\bar{c_y^-} - \Omega R\right)\right]^2 + (H - \bar{\Delta})\left[\alpha\,\bar{c_x^+} + \frac{i}{R}\left(\bar{c_y^+} - \Omega R\right)\right]^2\right\} = 0 \tag{9.94}$$

This equation yields 6 roots for α. When each of them is substituted in turn into the set (9.93), the corresponding mode shape (i.e., the relative values of $\hat{c}_x^+$, $\hat{c}_y^+$, etc.) can be calculated. These six downstream modes are listed below:

Mode 1:

$$\text{Eigenvalue} : \alpha_1 = -\frac{1}{R} \tag{9.95}$$

Normalized eigenfunction $\left(\text{with } \frac{\hat{p}_1}{\rho} = 1\right)$:

$$E_1 \equiv \left(\hat{c}_x^+ , \hat{c}_y^+ , \hat{c}_x^- , \hat{c}_y^- , \hat{\Delta} , \frac{\hat{p}}{\rho}\right)_1$$

$$= \left(\frac{1}{-\overline{c_x^+} + i\left(\overline{c_y^+} - \Omega R\right)} , \frac{-i}{-\overline{c_x^+} + i\left(\overline{c_y^+} - \Omega R\right)} , \frac{1}{-\overline{c_x^-} + i\left(\overline{c_y^-} - \Omega R\right)} , \frac{-i}{-\overline{c_x^-} + i\left(\overline{c_y^-} - \Omega R\right)} , 0 , 1\right) \qquad (9.96)$$

This represents potential perturbations, decaying downstream as $e^{-x/R}$.

Mode 1′:

$$\text{Eigenvalue} : \alpha_{1'} = \frac{1}{R} \qquad (9.97)$$

Since this implies exponential growth downstream, the coefficient of this mode must be made zero.

Mode 2:

$$\text{Eigenvalue} : \alpha_2 = -\frac{i}{R}\frac{\overline{c_y^-} - \Omega R}{\overline{c_x^-}} \qquad (9.98)$$

Normalized eigenfunction $\left(\text{with } \left(\hat{c}_x^-\right)_2 = \overline{c_x^-}\right)$:

$$E_2 = \left(0 , 0 , \overline{c_x^-} , \overline{c_y^-} - \Omega R , 0 , 0\right) \qquad (9.99)$$

The various perturbations in this mode vary as

$$\exp\left[\frac{i}{R}\left(y - \frac{\overline{c_y^-} - \Omega R}{\overline{c_x^-}} x - \Omega R t\right)\right] = \exp\left[\frac{i}{R}\left(y' - \frac{\overline{c_y^-}'}{\overline{c_x^-}} x\right)\right]$$

where the $(\,)'$ means quantities in the whirling frame. Thus, the mode represents <u>in that frame</u> variations in magnitude only of the vector $\vec{\overline{c_y^-}}$, which convect along $\vec{\overline{c_y^-}}$, or in other words, convection of shear disturbances and hence of vorticity ω_z and kinetic energy downstream of the blades.

Mode 3:

$$\text{Eigenvalue} : \alpha_3 = -\frac{i}{R}\frac{\overline{c_y^+} - \Omega R}{\overline{c_x^+}} \qquad (9.100)$$

Normalized eigenfunction $\left(\text{with } \left(\hat{c}_x^+\right)_3 = \overline{c_x^+}\right)$:

$$E_3 = \left(\overline{c_x^+} , \overline{c_y^+} - \Omega R , 0 , 0 , 0 , 0\right) \qquad (9.101)$$

The nature of this mode is analogous to that of Mode 2, except this time referred to the underturned tip region.

Modes 4 and 5:

Eigenvalues:

$$\alpha_{4,5} = \frac{\bar{\Delta}\,\bar{c_x}(\bar{c_y} - \Omega R) + (H-\bar{\Delta})\bar{c_x^+}(\bar{c_y^+} - \Omega R) \pm i\sqrt{\bar{\Delta}(H-\bar{\Delta})}\,\left|\bar{c_x}(\bar{c_y^+} - \Omega R) - \bar{c_x^+}(\bar{c_y^+} - \Omega R)\right|}{\bar{\Delta}\,\bar{c_x}^2 + (H-\bar{\Delta})\bar{c_x^+}^2} \tag{9.102}$$

for $\bar{\Delta} << H$, this simplifies to

$$i\,\alpha_{4,5}R \cong \frac{\bar{c_y^+} - \Omega R}{\bar{c_x^+}} \pm i\sqrt{\frac{\bar{\Delta}}{H}}\,\frac{\bar{c_x}}{\bar{c_x^+}}\left|\frac{\bar{c_y^+} - \Omega R}{\bar{c_x^+}} - \frac{\bar{c_y} - \Omega R}{\bar{c_x}}\right| \tag{9.103}$$

Normalized eigenvectors ($\bar{\Delta} << H$, and with $|\tilde{c_y}|_{4,5} = 1$):

$$E_{4,5} = \left(+ i\sqrt{\frac{H}{\bar{\Delta}}}\,s^+, \pm i\sqrt{\frac{H}{\bar{\Delta}}}, -s^+sg, sg, -\frac{H}{\bar{c_x}}\frac{1 + s^{+2}}{|s^+ - s^-|}, \bar{c_x}|s^+ - s^-|\right) \tag{9.104}$$

where

$$s^+ = \frac{\bar{c_y^+} - \Omega R}{\bar{c_x^+}},\ s^- = \frac{\bar{c_y} - \Omega R}{\bar{c_x}},\ \text{and}\ \ sg = \frac{s^+ - s^-}{|s^+ - s^-|}$$

The various perturbations in these two modes vary as

$$\exp\left[\frac{i}{R}(y' - s^+x) \pm \frac{x}{R}\sqrt{\frac{\bar{\Delta}}{H}}\,\frac{\bar{c_x}}{\bar{c_x^+}}|s^+ - s^-|\right]$$

Thus, in the whirling frame, there is mostly convection along the mean velocity $\bar{c_y^+}$ of the upper layer. In addition, one of the modes decays slowly, the other grows slowly, both in proportion to the magnitude of the difference between the tangents of the flow angles above and below the shear layer (w.r.t. axial). This can be viewed as a restricted form of a Kelvin-Helmholtz instability, where only the wavelength $2\pi R$ has been allowed, and the flows are confined between parallel walls (which limits the growth rate to the order $\sqrt{\bar{\Delta}/H}$).

It can be verified directly that, in the whirling frame where the motion is steady, Modes 1, 4, and 5 are iso-energetic (total enthalpy conserved). The same holds for Modes 2 and 3 in the $(\,)^+$ and $(\,)^-$ regions, respectively. Of course, the unsteadiness does introduce flow work when viewed from the fixed frame.

The general downstream perturbations are then a superposition of Modes 1-5:

$$\left(\hat{c}_x^+ , \hat{c}_y^+ , \hat{c}_x^- , \hat{c}_y^- , \hat{\Delta} , \frac{\hat{p}}{\rho}\right) = \sum_{i=1}^{5} K_i E_i \tag{9.105}$$

with complex constants K_i to be determined.

9.3.4 The Upstream-Downstream Connection

The results of Sec. 9.2 relate the flow quantities at $x >> H/\pi$ to those at $-x >> H/\pi$. The analysis was done for a constant gap δ (uniform and steady), but our scaling argument allows us to apply these results when $\delta = \delta(y,t)$ as well. Specifically, the following dependencies can be established:

$$\begin{aligned}
q &= q\left(\frac{\delta}{H} , \phi , \frac{c_{y_0}}{U}\right) \\
\lambda &= \lambda\left(\frac{\delta}{H} , \phi , \frac{c_{y_0}}{U}\right) \\
\frac{c_x^+}{U} &= \frac{c_x^+}{U}\left(\frac{\delta}{H} , \phi , \frac{c_{y_0}}{U}\right) \\
\frac{c_x^-}{U} &= \frac{c_x^-}{U}\left(\frac{\delta}{H} , \phi , \frac{c_{y_0}}{U}\right) \\
\frac{c_y^+}{U} &= \frac{c_y^+}{U}\left(\frac{\delta}{H} , \phi , \frac{c_{y_0}}{U}\right) \\
\frac{c_y^-}{U} &= \frac{c_y^-}{U}\left(\frac{\delta}{H} , \phi , \frac{c_{y_0}}{U}\right) \\
\frac{\Delta}{H} &= \frac{\Delta}{H}\left(\frac{\delta}{H} , \phi , \frac{c_{y_0}}{U}\right) \\
\frac{P(-\infty) - p}{\rho U^2} &= c_p\left(\frac{\delta}{H} , \phi , \frac{c_{y_0}}{U}\right)
\end{aligned} \tag{9.106}$$

where $\phi = c_{x_0}/U$ and the other symbols are as in Sec. 9.2. All the quantities on the left are

understood to be for $x >> H/\pi$, i.e. for $x \to \infty$ in the analysis of Sec. 9.2.

Consistent with the linearized approach for the downstream and upstream flows (relatively small y- and t-dependent disturbances), the functions of δ/H, ϕ, and c_{y_0}/U in (9.106) will be each evaluated as the sum of its value at $(\bar{\delta}/H, \bar{\phi}, \bar{c}_{y_0}/U)$, plus first order disturbances due to $(\delta'/H, \phi', c'_{y_0}/U)$. These disturbances can be obtained by differentiation of the functions in (9.106). In terms of the complex amplitudes (^), this takes the form,

$$\begin{bmatrix} \hat{c}_x^+ \\ \hat{c}_y^+ \\ \hat{c}_x^- \\ \hat{c}_y^- \\ \hat{\Delta} \\ \hat{p}/\rho \end{bmatrix} = \left[\frac{\hat{c}_x(x=0^-)}{U} \frac{\partial}{\partial \phi} + \frac{\hat{c}_y(x=0^-)}{U} \frac{\partial}{\partial \frac{c_{y_0}}{U}} + \left(\frac{e}{H}\right) \frac{\partial}{\partial \frac{\delta}{H}} \right] \cdot \begin{bmatrix} c_{x\infty}^+ \\ c_y^+ \\ c_{x\infty}^- \\ c_y^- \\ \Delta \\ -\frac{p_0 - p_\infty}{\rho} \end{bmatrix} \qquad (9.107)$$

The last line in (9.107) needs some clarification. The perturbation $\hat{p}$ downstream of the disk, as given by (9.107), accounts only for the pressure change between $x \sim -H$ and $x \sim H$, which is what the model of Sec. 9.2 provides. In order to obtain the full pressure non-uniformity, this must be supplemented by the perturbation of the upstream pressure, as given for instance by Eq. (9.84).

Expressions similar to (9.107) can also be written for intermediate variables such as q and λ. These are needed in the process of constructing from the theory of Sec. 9.2 the partial derivatives in (9.107). Alternatively, these partial derivatives can be calculated as finite difference ratios obtained by repeatedly exercising the computer codes which solve the equations of Sec. 9.2.

9.3.5 Solution for Upstream and Downstream Flow Constants

We can now equate the downstream amplitudes, as given by Eq. (107) (plus the $\hat{P}_0/\rho$ contribution from (9.84)) to the modal superposition expressed by (9.105). In (9.107), we also

use, from (9.81) and (9.82)

$$\frac{\hat{c}_x\left(x=0^-\right)}{U} = \frac{\hat{c}_{x_0}}{U} \tag{9.108}$$

$$\frac{\hat{c}_y\left(x=0^-\right)}{U} = i\frac{\hat{c}_{x_0}}{U} \tag{9.109}$$

The result is a system of six linear equations for K_1 through K_5, plus $\hat{c}_{x_0}$. The terms proportional to $e' = e/H$ in (9.107) are the forcing terms, which determine all the perturbation amplitudes.

In the following, we take purely axial flow at $-x >> R$, which leads to $\bar{c}_{y_0} = 0$ (but $\hat{c}_{y_0} \neq 0$) and hence the sensitivities to c_{y_0} are all zero (Appendix 9C). We also use the shorthand

$$\bar{c}_y^{+\prime} = \bar{c}_y^{+} - \Omega R \quad , \quad \bar{c}_y^{-\prime} = \bar{c}_y^{-} - \Omega R \tag{9.110}$$

The resulting system, after moving terms in $\hat{c}_{x_0}$ to the left, is

$$\frac{K_1}{-\bar{c}_x^{+} + i\,\bar{c}_y^{+\prime}} + \bar{c}_x^{+} K_3 - i\sqrt{H/\bar{\Delta}}\; s^{+}\left(K_4 - K_5\right) - \frac{\partial c_x^{+}}{\partial\phi}\frac{\hat{c}_{x_0}}{U} = \frac{\partial c_x^{+}}{\partial(\delta/H)}\frac{e}{H} \tag{9.111a}$$

$$\frac{-i\,K_1}{-\bar{c}_x^{+} + i\,\bar{c}_y^{+\prime}} + \bar{c}_y^{+\prime} K_3 + i\sqrt{H/\bar{\Delta}}\,\left(K_4 - K_5\right) - \frac{\partial c_y^{+}}{\partial\phi}\frac{\hat{c}_{x_0}}{U} = \frac{\partial c_y^{+}}{\partial(\delta/H)}\frac{e}{H} \tag{9.111b}$$

$$\frac{K_1}{-\bar{c}_x^{-} + i\,\bar{c}_y^{-\prime}} + \bar{c}_x^{-} K_2 - s^{+} sg\left(K_4 + K_5\right) - \frac{\partial c_x^{-}}{\partial\phi}\frac{\hat{c}_{x_0}}{U} = \frac{\partial c_x^{-}}{\partial(\delta/H)}\frac{e}{H} \tag{9.111c}$$

$$\frac{-i\,K_1}{-\bar{c}_x^{-} + i\,\bar{c}_y^{-\prime}} + \bar{c}_y^{-\prime} K_2 + sg\left(K_4 + K_5\right) - \frac{\partial c_y^{-}}{\partial\phi}\frac{\hat{c}_{x_0}}{U} = \frac{\partial c_y^{-}}{\partial(\delta/H)}\frac{e}{H} \tag{9.111d}$$

$$-\frac{H}{\bar{c}_x^{-}}\frac{1 + s^{+2}}{\left|s^{+} - s^{-}\right|}\left(K_4 + K_5\right) - \frac{\partial\Delta}{\partial\phi}\frac{\hat{c}_{x_0}}{U} = \frac{\partial\Delta}{\partial(\delta/H)}\frac{e}{H} \tag{9.111e}$$

$$K_1 + \bar{c}_x^{-}\left|s^{+} - s^{-}\right|\left(K_4 + K_5\right) + \frac{\partial\left(\frac{P_0 - P_\infty}{\rho}\right)}{\partial\phi}\frac{\hat{c}_{x_0}}{U} + \left(\bar{c}_{x_0} - i\Omega R\right)\hat{c}_{x_0} = -\frac{\partial\left(\frac{P_0 - P_\infty}{\rho}\right)}{\partial(\delta/H)}\frac{e}{H} \tag{9.111f}$$

Notice, in particular, the term $\left(\bar{c}_{x_0} - i\Omega R\right)\hat{c}_{x_0}$ in the last equation. This is $-\hat{P}_0/\rho$ from Eq. (9.84). In the partial derivatives $(\partial/\partial\phi)$, δ/H is understood constant, and similarly, ϕ is constant in taking $\left(\frac{\partial\phi}{\partial(\delta/H)}\right)$.

The system (9.111) can be solved for $\hat{c}_{x_0}/U$:

$$\frac{\hat{c}_{x_0}}{U} = \frac{-\frac{\partial C_p}{\partial(\delta/H)} + i\left\{\frac{\bar{c_x}}{U}\frac{\partial(\bar{c_y}/U)}{\partial(\delta/H)} - \frac{\bar{c_y}'}{U}\frac{\partial(\bar{c_x}/U)}{\partial(\delta/H)}\right\} + \left(\frac{\bar{c_x}}{U}\right)^2 \frac{|s^+ - s^-|}{1+s^{+2}}\left[|s^+ - s^-| + i(sg)(1+s^+s^-)\right]\frac{\partial(\Delta/H)}{\partial(\delta/H)}}{\frac{\partial C_p}{\partial\phi} + \phi - i\frac{\Omega R}{U} - i\frac{\bar{c_x}}{U}\frac{\partial(\bar{c_y}/U)}{\partial\phi} + i\frac{\bar{c_y}'}{U}\frac{\partial(\bar{c_x}/U)}{\partial\phi} - \left(\frac{\bar{c_x}}{U}\right)^2 \frac{|s^+ - s^-|}{1+s^{+2}}\left[|s^+ - s^-| + i(sg)(1+s^+s^-)\right]\frac{\partial(\Delta/H)}{\partial\phi}} \frac{e}{H} \tag{9.112}$$

After this, the other unknowns follow easily from (9.111a-f): $(K_4+K_5)/U$ from (9.111e), K_1/U^2 then from (9.111f), K_2 then from either (9.111c) or (9.111d), and K_3, $(K_4-K_5)/U$ from the system (9.111a), (9.111b).

Once the constants K_1-K_5 are known, the downstream velocity components, pressure and layer thickness can be calculated (Eq. (9.105)). In using Eqs. (9.111) and (9.112), it must be remembered that c_x^+, c_x^- and their perturbations and averages must refer to "$x = \infty$" on the H-scale, not to the disk itself.

9.3.6 Calculation of Radial Forces and Alford Coefficients

The work done per unit mass is $\lambda W^+ + (1-\lambda)W^-$, where W^+ and W^- are given by Eqs. (9.98) and (9.99). In the simpler theory of Secs. 9.2.1 to 9.2.7 with no work done by gap flow, $W^+ = 0$, whereas in the more general version (Sec. 9.2.8), we have $c_{y_3}^+ = U - g\,c_x^+$, with g defined in Eq. (9.107), so that $W^+ \neq 0$. Using $c_{y2} = c_x \tan\alpha_2$ for the tangential velocity after the rotor, the work per unit length is

$$f_y U = \rho c_{x_0} H\left[\lambda W^+ + (1-\lambda)W^-\right] \tag{9.113}$$

which gives for the tangential force f, per unit length,

$$f_y = \rho c_{x_0} H\left[\lambda\left(c_{y_2}^+ - c_{y_3}^+\right) + (1-\lambda)\left(c_{y_2}^- - c_{y_3}^-\right)\right] \tag{9.114}$$

This applies at each y station. The quantities c_{x_0}, λ, $c_{y_2}^+$, $c_{y_3}^+$ $c_{y_2}^-$, and $c_{y_3}^-$ all have azimuthal

variations, which lead to an azimuthally varying f_y as well. Taking logarithmic differentials, and assuming the basic form $( )' = (\hat{}) \exp\left[i\left(\frac{y - \Omega Rt}{R}\right)\right]$ for all variations,

$$\frac{\hat{f}_y}{\bar{f}_y} = \frac{\hat{c}_{x_0}}{\bar{c}_{x_0}} + \frac{\hat{\lambda}\left[\left(\bar{c}^{+}_{y_2} - \bar{c}^{+}_{y_3}\right) - \left(\bar{c}^{-}_{y_2} - \bar{c}^{-}_{y_3}\right)\right] + \bar{\lambda}\left(\hat{c}^{+}_{y_2} - \hat{c}^{+}_{y_3}\right) + (1-\bar{\lambda})\left(\hat{c}^{-}_{y_2} - \hat{c}^{-}_{y_3}\right)}{\bar{\lambda}\left(\bar{c}^{+}_{y_2} - \bar{c}^{+}_{y_3}\right) + (1-\bar{\lambda})\left(\bar{c}^{-}_{y_2} - \bar{c}^{-}_{y_3}\right)} \tag{9.115}$$

For the simpler form of the theory (K = 0), this simplifies to

$$\frac{\hat{f}_y}{\bar{f}_y} = \frac{\hat{c}_{x_0}}{\bar{c}_{x_0}} - \frac{\hat{\lambda}}{1-\bar{\lambda}} + \frac{\hat{c}^{-}_{y_2} - \hat{c}^{-}_{y_3}}{\bar{c}^{-}_{y_2} - \bar{c}^{-}_{y_3}} \tag{9.116}$$

These forces are projected onto the OX′ and OY′ directions in Fig. 9.36 (namely, along the turbine instantaneous displacement and at 90° to it). Only the perturbation part f_y' of f_y contributes to the net projected forces:

$$F_{X'} = \int_0^{2\pi R} f_y' \sin\frac{y'}{R}\, dy \tag{9.117}$$

$$F_{Y'} = -\int_0^{2\pi R} f_y' \cos\frac{y'}{R}\, dy \tag{9.118}$$

where, as before, $y' = y - \Omega Rt$. Since each perturbation quantity varies as Re [(^) exp ($i\, y'/R$)], we obtain

$$F_{X'} = -\pi R\, \mathrm{Im}\left(\hat{f}_y\right) \tag{9.119}$$

$$F_{Y'} = -\pi R\, \mathrm{Re}\left(\hat{f}_y\right) \tag{9.120}$$

where Re and Im stand for the real and imaginary parts of a complex number.

By analogy to Eq. (9.4), we define direct-force and cross-force Alford coefficients as

$$\alpha_X = \frac{2R\, F_{X'}}{Q\,(e/H)} = \frac{F_{X'}}{\pi R\, \bar{f}_y\,(e/H)} \tag{9.121}$$

$$\alpha_Y = \frac{2R\, F_{Y'}}{Q\,(e/H)} = \frac{F_{Y'}}{\pi R\, \bar{f}_y\,(e/H)} \tag{9.122}$$

so that α_Y is positive for a forward-whirling force, and α_X is positive for a de-stabilizing direct force. These can be rewritten, using (9.119) and (9.120) as

$$\alpha_x = -\mathrm{Im}\left[\frac{\hat{f}_y}{\bar{f}_y\,(e/H)}\right] \tag{9.123}$$

$$\alpha_y = -\mathrm{Re}\left[\frac{\hat{f}_y}{\bar{f}_y\,(e/H)}\right] \tag{9.124}$$

and the quantity in brackets is obtained from (9.115) or (9.116), depending on the model adopted.

There are two ways in which the R-scale azimuthal flow redistribution can affect the final results, namely the Alford coefficients α_x, α_y. First of all, in Eq. (9.115), the term $\hat{c}_{x_0}/\bar{c}_{x_0}$ is a direct contribution of that redistribution (nothing like this appears in the original Alford model, or models, based on the use of local work loss). In addition, the nonuniform perturbations of the amount of underturned flow ($\hat{\lambda}$) and of the underturning itself $\left(\hat{c}_{y_2} - \hat{c}_{y_3}\right)$ can also be affected. These terms would be present in a purely local analysis, but may be different in magnitude and phase. Of these, the direct effect of $\hat{c}_{x_0}/\bar{c}_{x_0}$ is the most important, as the calculations will show.

A gauge of the importance of redistribution is provided by comparing the α_y cross-force coefficient to the work loss coefficient w that was introduced in Secs. 9.1 and 9.2. If we simply assume that redistribution is absent $\left(\hat{c}_{x_0} = 0\right)$, and that $w \equiv \bar{w}$ is constant around the periphery, then

$$f_y = f_{y_{\mathrm{ideal}}}\left(1 - \bar{w}\,\frac{\delta}{H}\right)$$

and

$$\frac{f_y'}{\bar{f}_y} = -\,\frac{\bar{w}\,(\delta'/H)}{1 - \bar{w}\left(\bar{\delta}/H\right)}\,.$$

In terms of amplitudes,

$$\frac{\hat{f}_y}{\bar{f}_y} = -\,\frac{\bar{w}\,(e/H)}{1 - \bar{w}\left(\bar{\delta}/H\right)}\,.$$

Since $\bar{w}$ is a real number, Eqs. (9.122) and (9.124) then give

$$\alpha_x = 0 \tag{9.125}$$

$$\alpha_y = \frac{\overline{w}}{1 - \overline{w}\left(\overline{\delta}/H\right)} \cong \overline{w} \tag{9.126}$$

This is a modification of the Alford argument only in so far as w and not β (the efficiency loss) appears. This is a fairly straightforward change to make: only the nonuniformity of actual blade forces matters, not that of the isentropic reference work used to calculate efficiency. Thus, differences between α_y and $\overline{w}$, as well as non-zero α_x values, would indicate redistribution effects. Also, Eq. (9.126) would give a cross-force coefficient which is independent of Ω, whereas redistribution will introduce Ω dependencies. Numerical results will be shown in the next section.

9.3.7 Theoretical Results Including XY Redistribution

Results will first be shown for the parameters of our experimental turbine:

$\alpha_2 = 70°$, $\beta_3 = 60°$, s/b = 0.756 (solidity)

$\delta/H = 0.03$ or 0.0187

$\phi = c_{x0}/U$ from 0.3 to 1.1 (0.58 = design condition)

Starting with the "nominal" radial gap, $\delta/H = 0.03$, Figs. 9.37 to 9.43 show the most important static ($\Omega = 0$) redistribution parameters versus flow coefficient, ϕ. The quantities plotted are magnitude and phase angle of $\left(\hat{c}_{x_0}/Ue'\right)$, etc. It must be recalled that a phase of zero means the quantity is sinusoidally distributed in y/R, with its maximum value where the tip gap is maximum. A positive phase angle indicates peak value shifted from that location in the rotational sense, and vice versa.

Figure 9.37 shows the upstream axial flow velocity perturbation, $\left(\hat{c}_{x_0}/Ue'\right)$. Its magnitude varies from 0.1 to 1.2, and its phase is near zero throughout. At design ($\phi = 0.58$), $\hat{c}_{x_0}/Ue' \cong 0.343 + 0.029\,i$. Thus, the flow is increased near the maximum gap region, as was anticipated, and one can expect from this term alone a reduction in the Alford cross-force coefficient α_y (Eqs. (9.123), (9.115)) by $\mathrm{Re}\left(\hat{c}_{x_0}/\left(\overline{c}_{x_0}e'\right)\right)$, i.e. 0.343/0.58 = 0.591. This is a

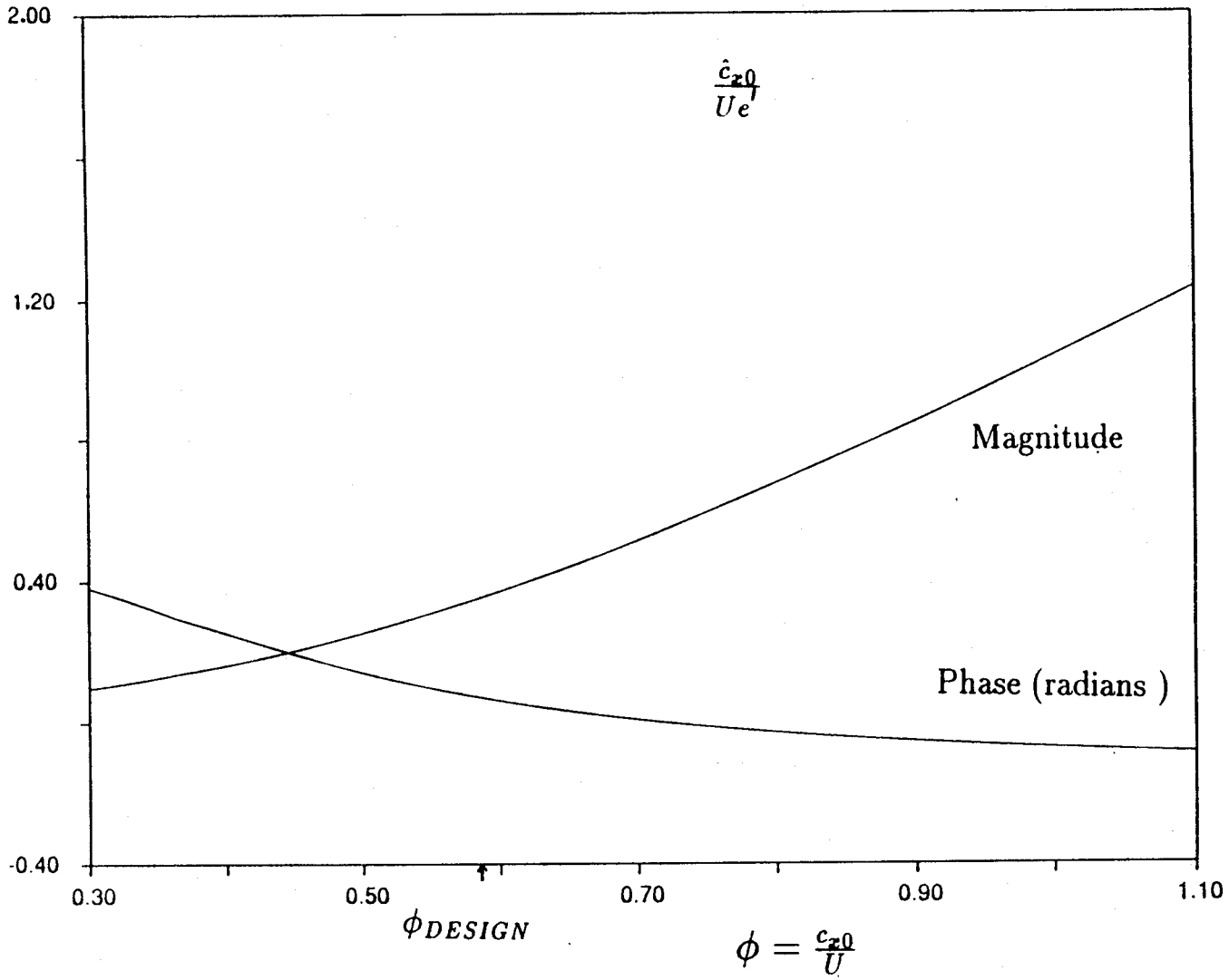

Fig 9.37 Upstream axial velocity perturbations, $\frac{\hat{c}_{x0}}{Ue'}$ $(e' = \frac{e}{H})$

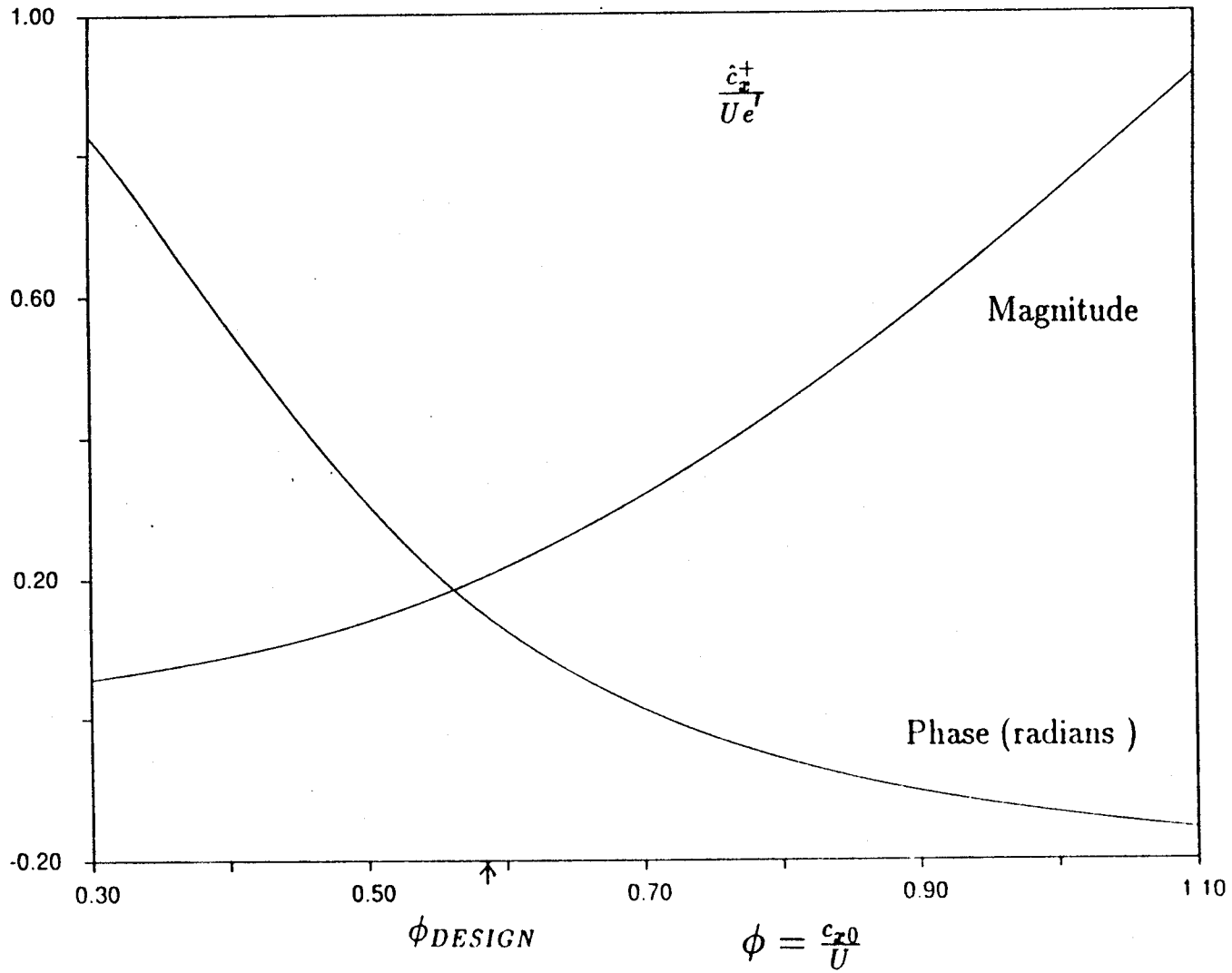

Fig 9.38 Axial velocity perturbations of the underturned flow

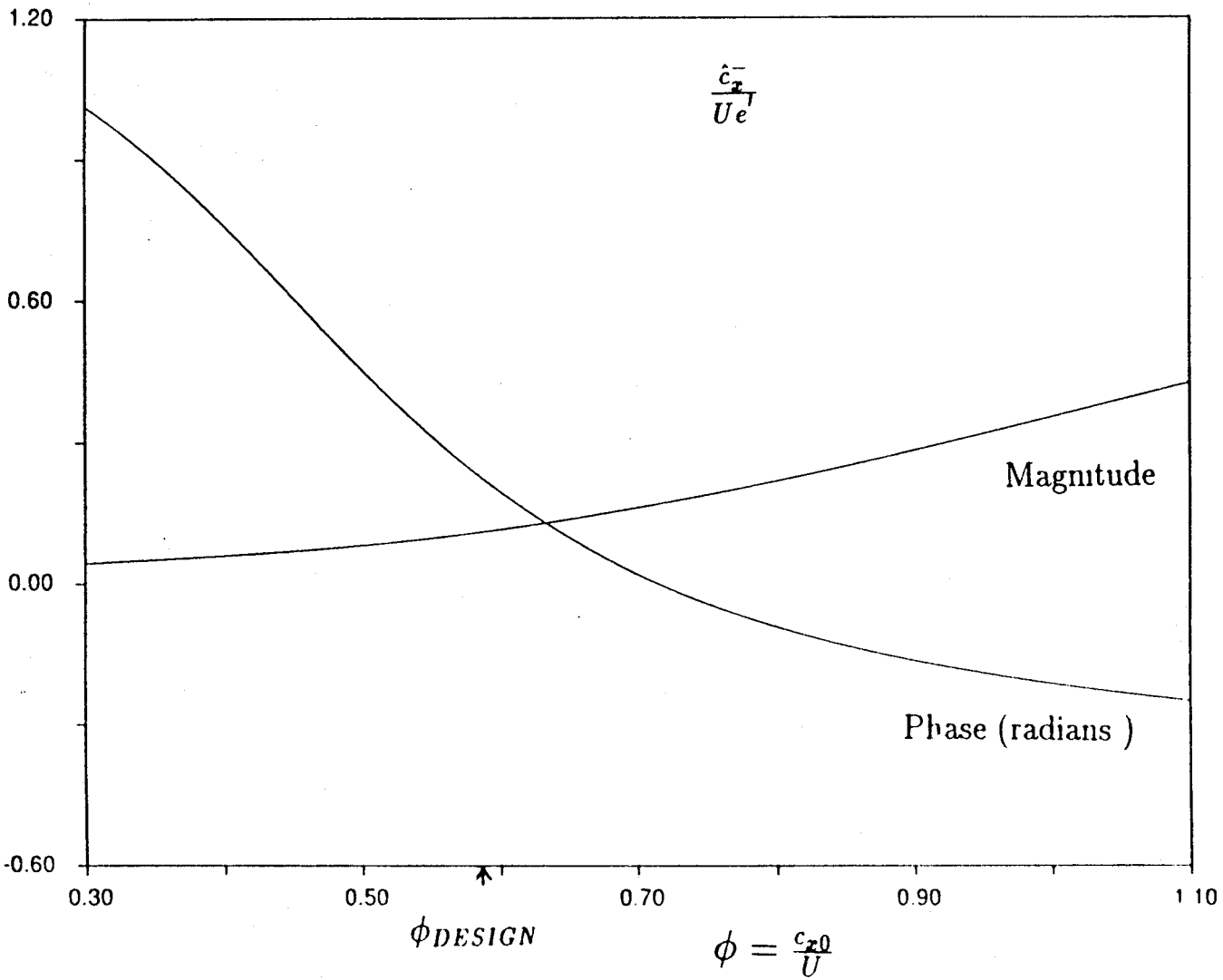

Fig 9.39 Axial velocity perturbations for the main rotor flow

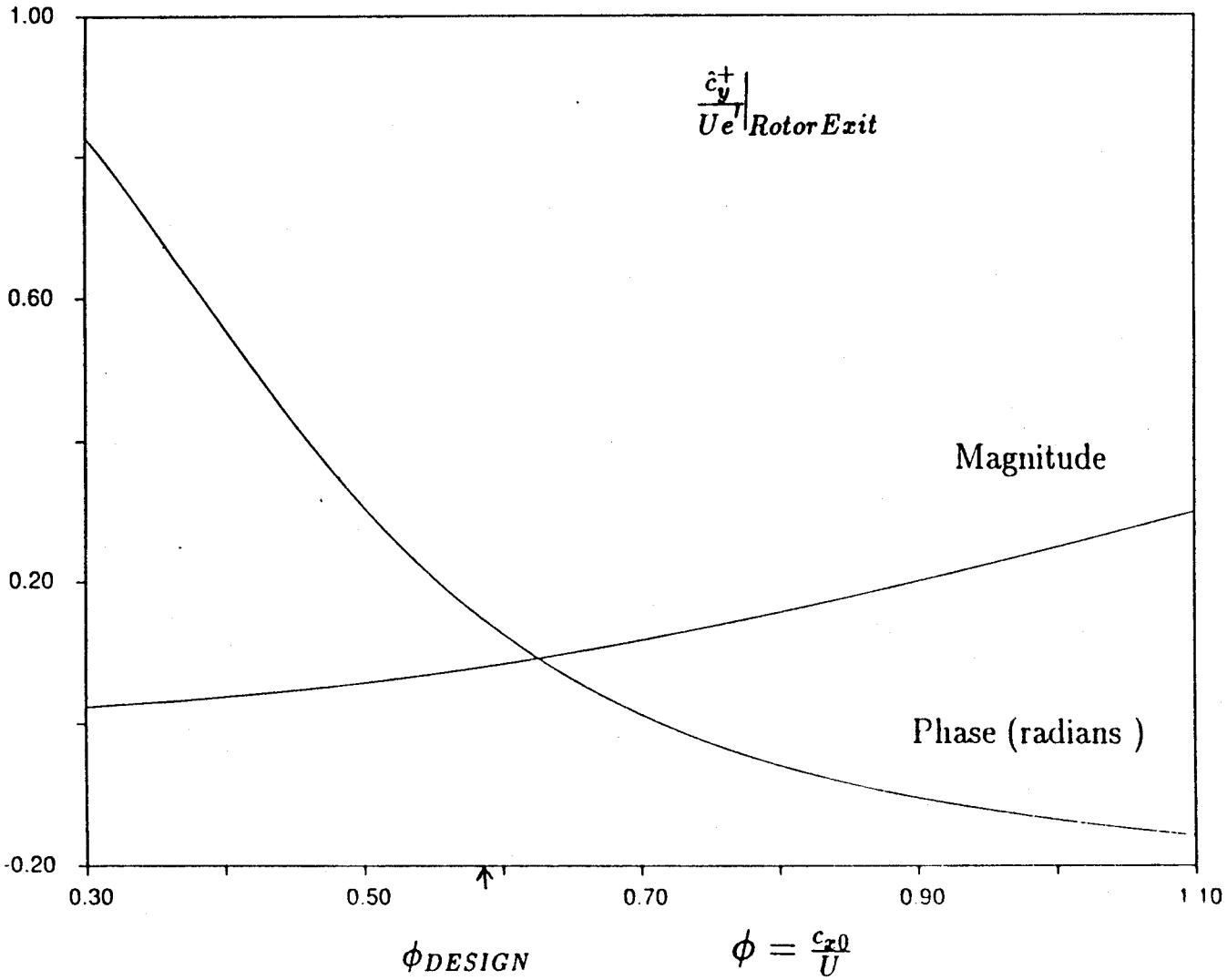

Fig 9.40 Tangential velocity perturbations for the underturned flow

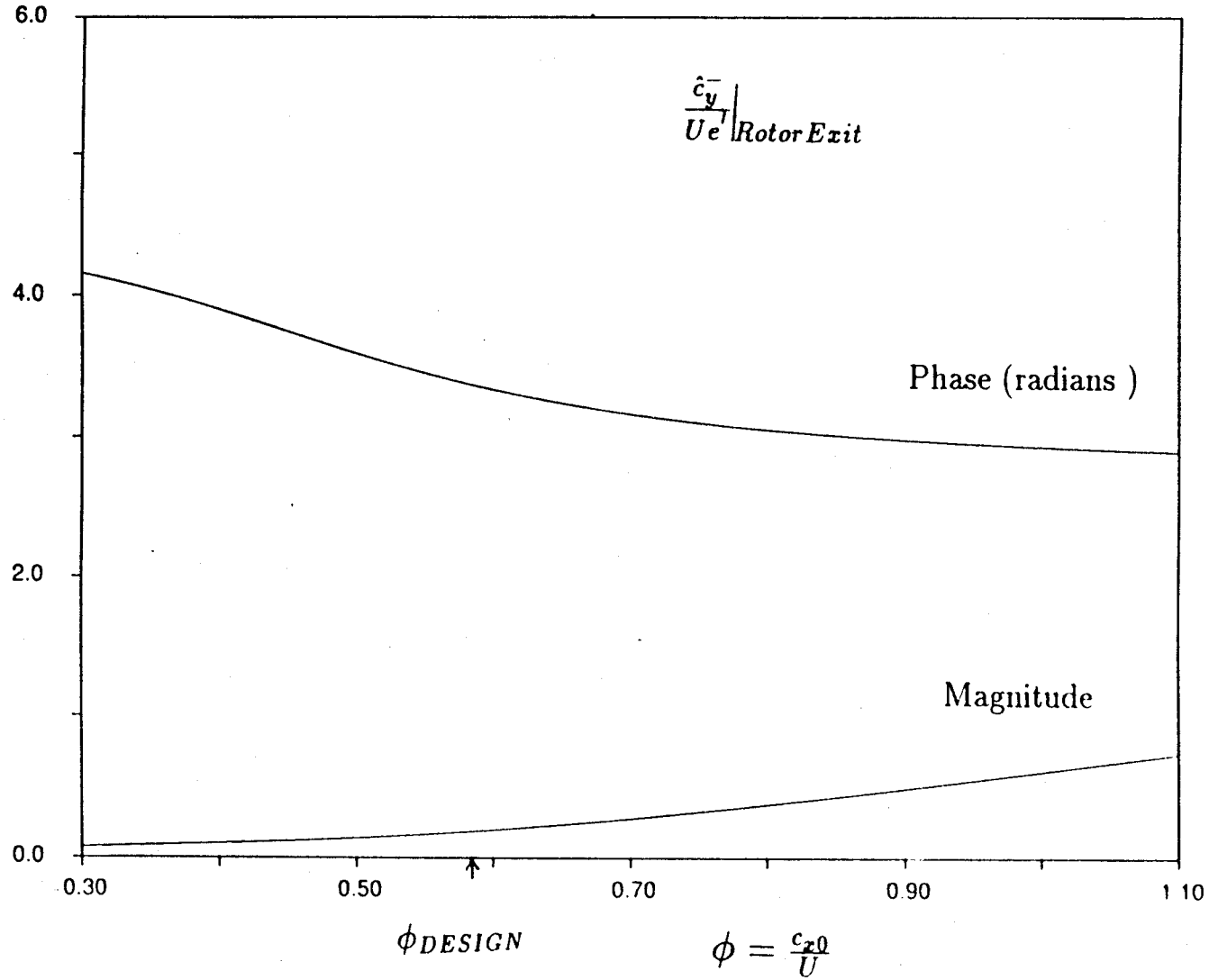

Fig 9.41 Tangential velocity perturbations for the main rotor flow

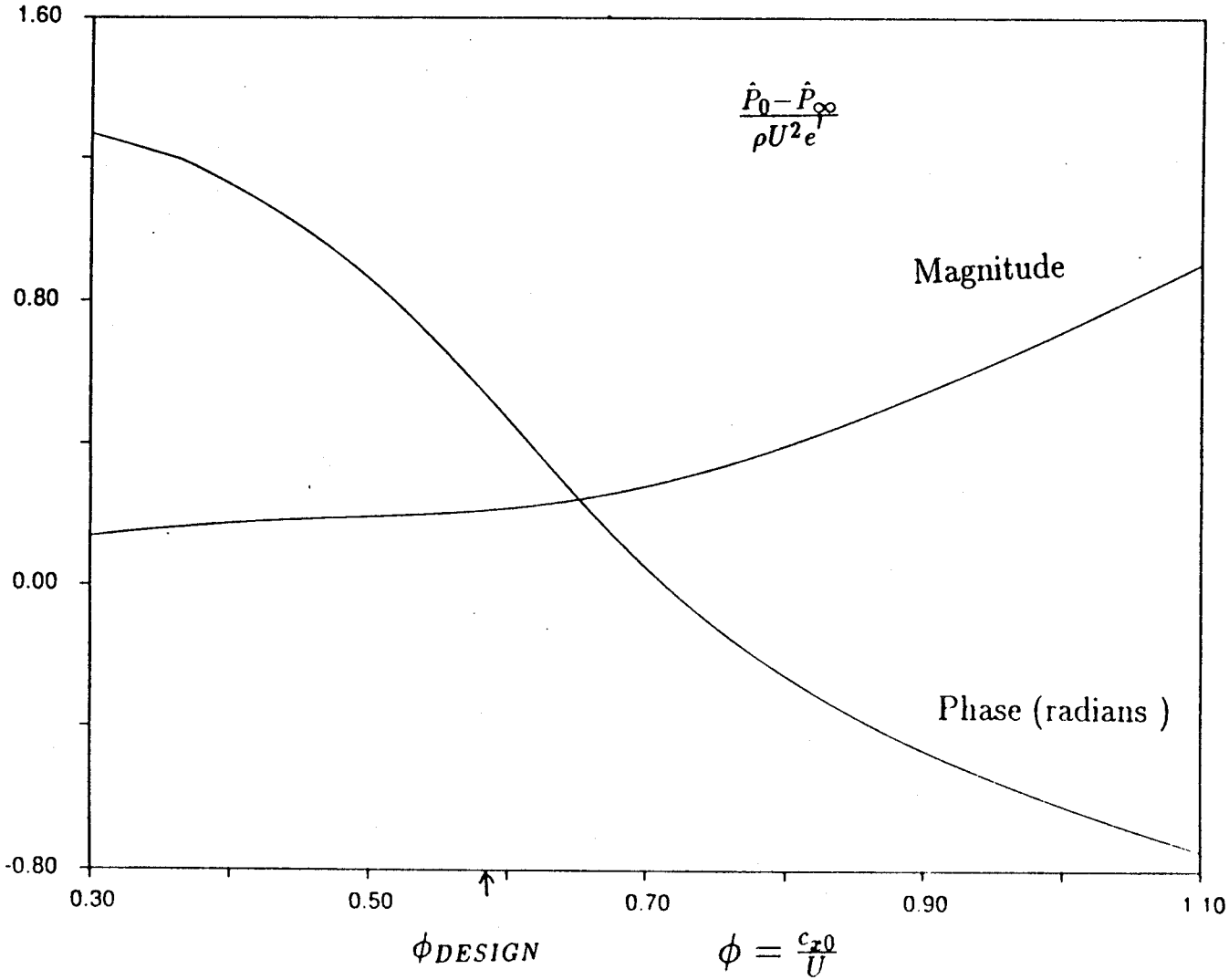

Fig 9.42 Pressure drop perturbation, $\frac{\hat{P}_0 - \hat{P}_\infty}{\rho U^2 \epsilon'}$

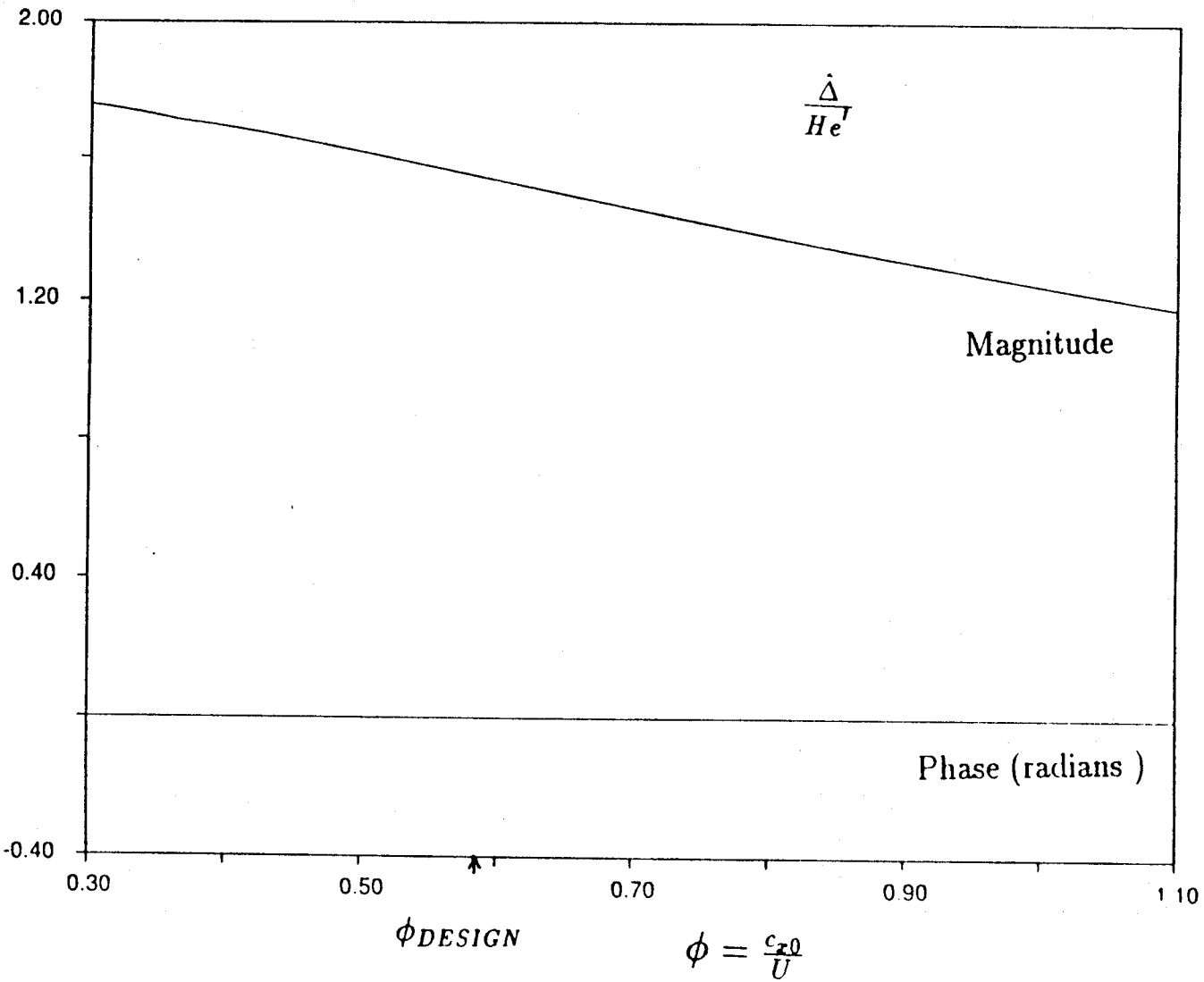

Fig 9.43 Perturbation of the underturned layer thickness, $\frac{\hat{\Delta}}{He^I}$

strong effect since, in the

2-D theory, we calculate $\alpha_y = w = 2.10$ for the same conditions.

Figures 9.38 and 9.39 show the redistribution of the gap and bladed region flows c_x^+ and c_x^-. Notice, in particular, how $\hat{c}_x^-$ is less than $\hat{c}_{x_0}$ (about 1/3 at ϕ_{design}), because about 2/3 of the extra flow $\hat{c}_{x_0}$ going to the large gap region is actually shunted to the gap itself.

The tangential velocities c_y^+ and c_y^- have perturbations shown in Figs. 9.40 and 9.41. These variations, together with those in $c_{y_2}^+$ and $c_{y_2}^-$ at the stator exit, also reduce the Alford force (Eq. (9.115)), since the higher flow through the region with wider gap also implies a larger change in tangential velocity through the rotor.

The pressure drop through the stage "P_0-P_∞" is also redistributed as shown in Fig. 9.42. Near the design point, this redistribution is relatively small, and has near zero phase angle. For a first approximation, this azimuthal variation of pressure drop could be neglected, which amounts to retaining only the first term in both numerator and denominator in Eq. (9.112) for $\hat{c}_{x_0}$. This gives $\hat{c}_{x_0}/Ue' \cong 0.292$ (exact 0.343+0.029 i). This will be exploited later.

The thickness variation $\hat{\Delta}$ of the underturned flow region is seen in Fig. 9.43 to be in phase with the gap itself. The Alford coefficients are shown in Figs. 9.44 and 9.45. Figure 9.44 shows w, the 2-D result, calculated according to Sec. 9.2 (including partial tip work), and here re-interpreted as the Alford cross-force coefficient α_y, if redistribution were ignored. The α_x would then be zero. By contrast, the results including redistribution are shown in Fig. 9.45. We see that α_y has the same trend (decreasing with ϕ) as w, but is greatly reduced (2.1 to 0.7 at design) by the relieving effects due to XY redistribution. In addition, a non-zero α_x now appears, driven by the existence of non-axial flows downstream of the turbine, which skew the passage flows somewhat. At design, α_x is stabilizing (abut -0.13).

The effect of varying the mean tip gap δ is predicted to be small, in consequence of the small degree of nonlinearity of the theory in Sec. 9.2. A representative sample is included in Fig. 9.44: reducing the gap from $\delta/H = 0.03$ to 0.0187 changes w from 2.10 to 2.13.

The unsteadiness effects are next evaluated. Figure 9.46 (a,b) shows that increasing the

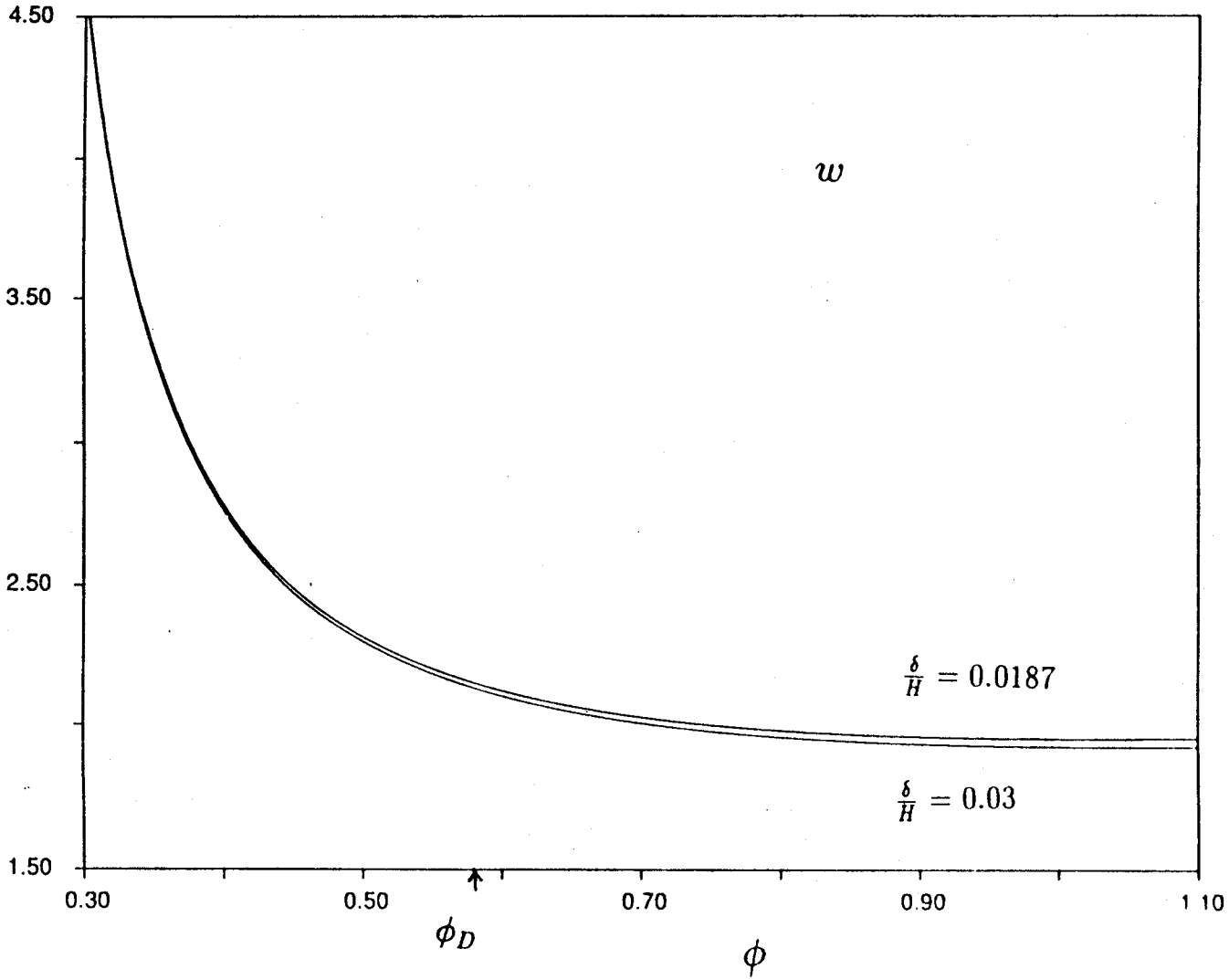

Fig 9.44 Cross-force, or work loss coefficient, w,
using the two-dimensional theory with partial tip loading.

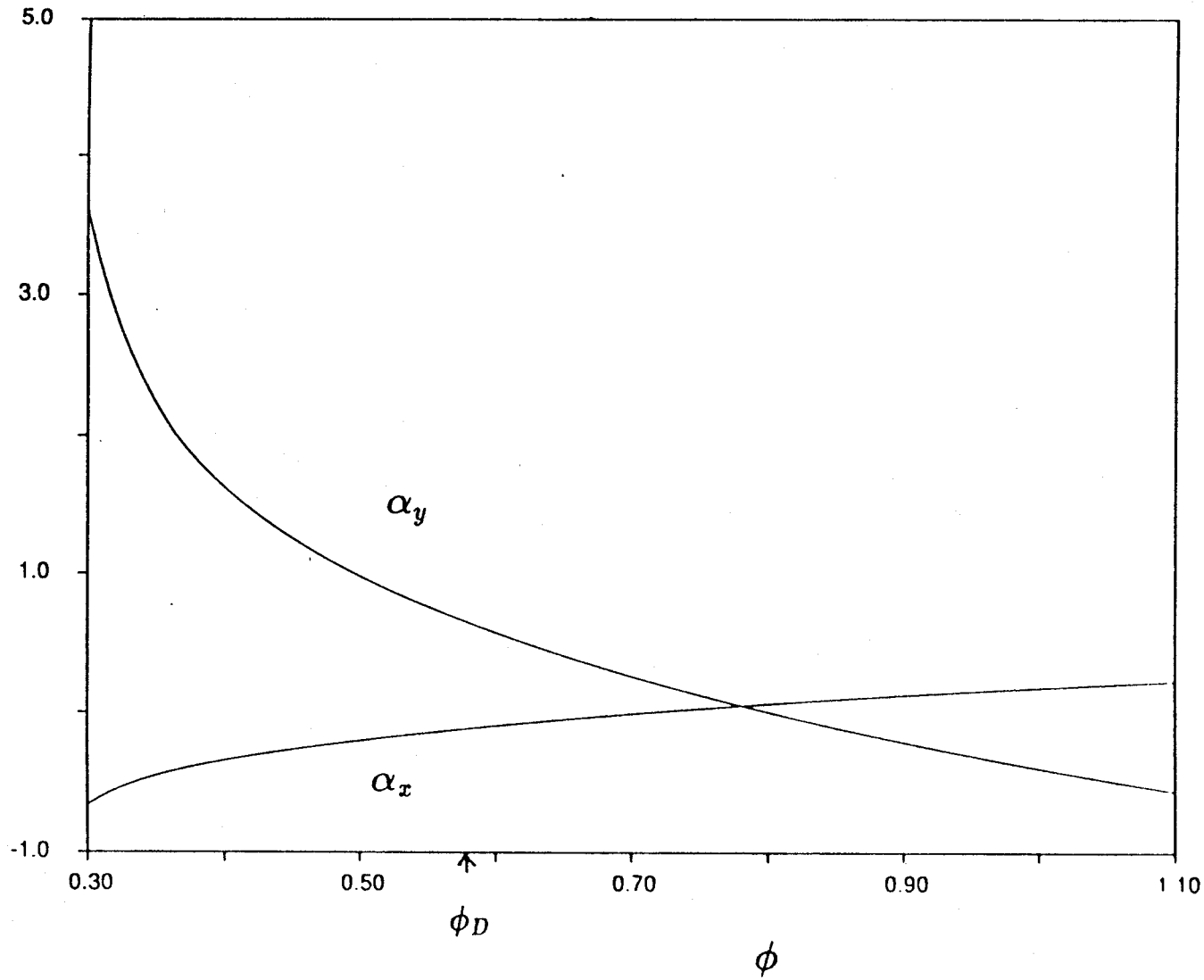

Fig 9.45 Direct and cross-force coefficients from the 3-D theory with partial tip work.

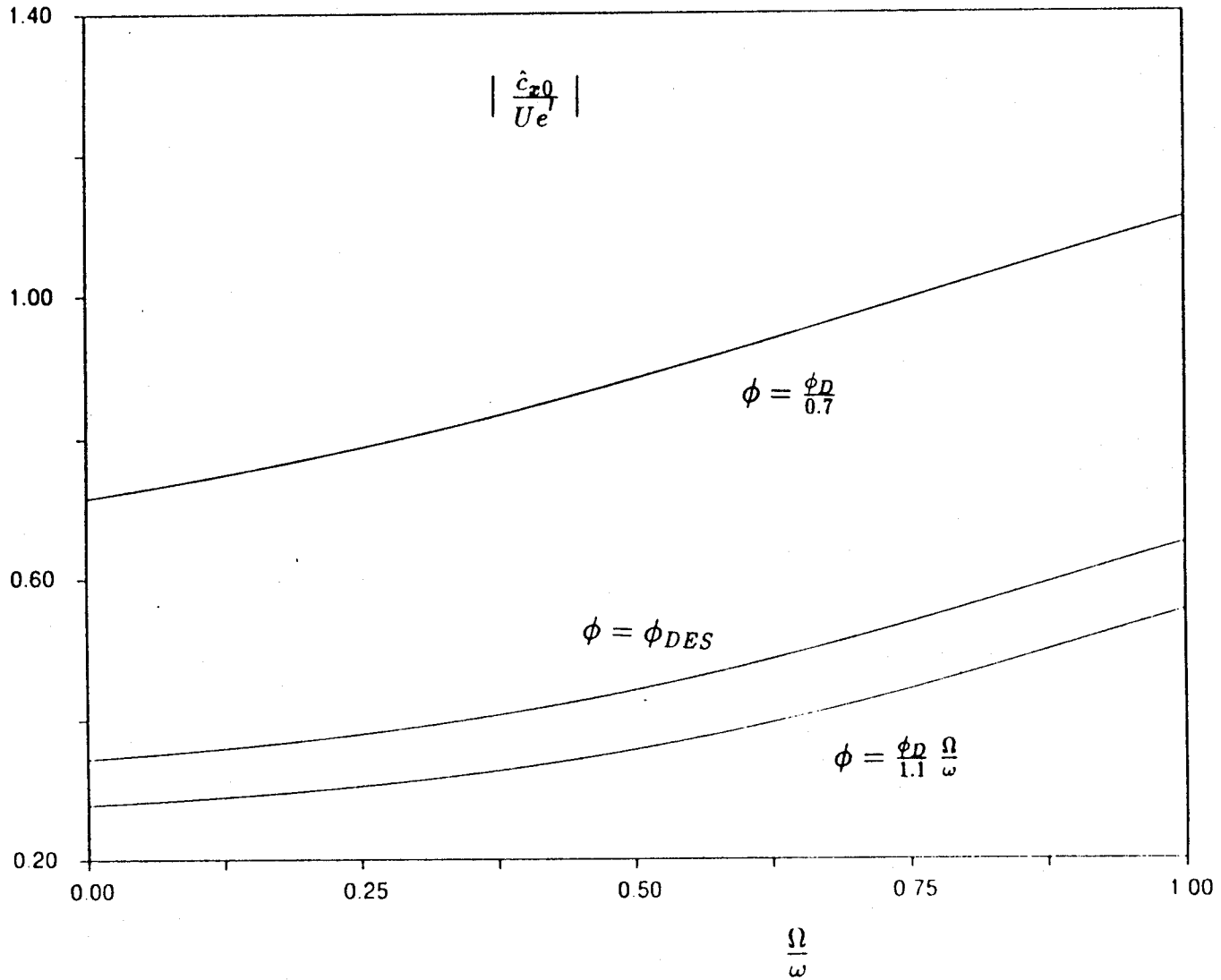

Fig 9.46a Dynamic effects on the upstream flow redistribution (magnitude). Model with partial tip work.

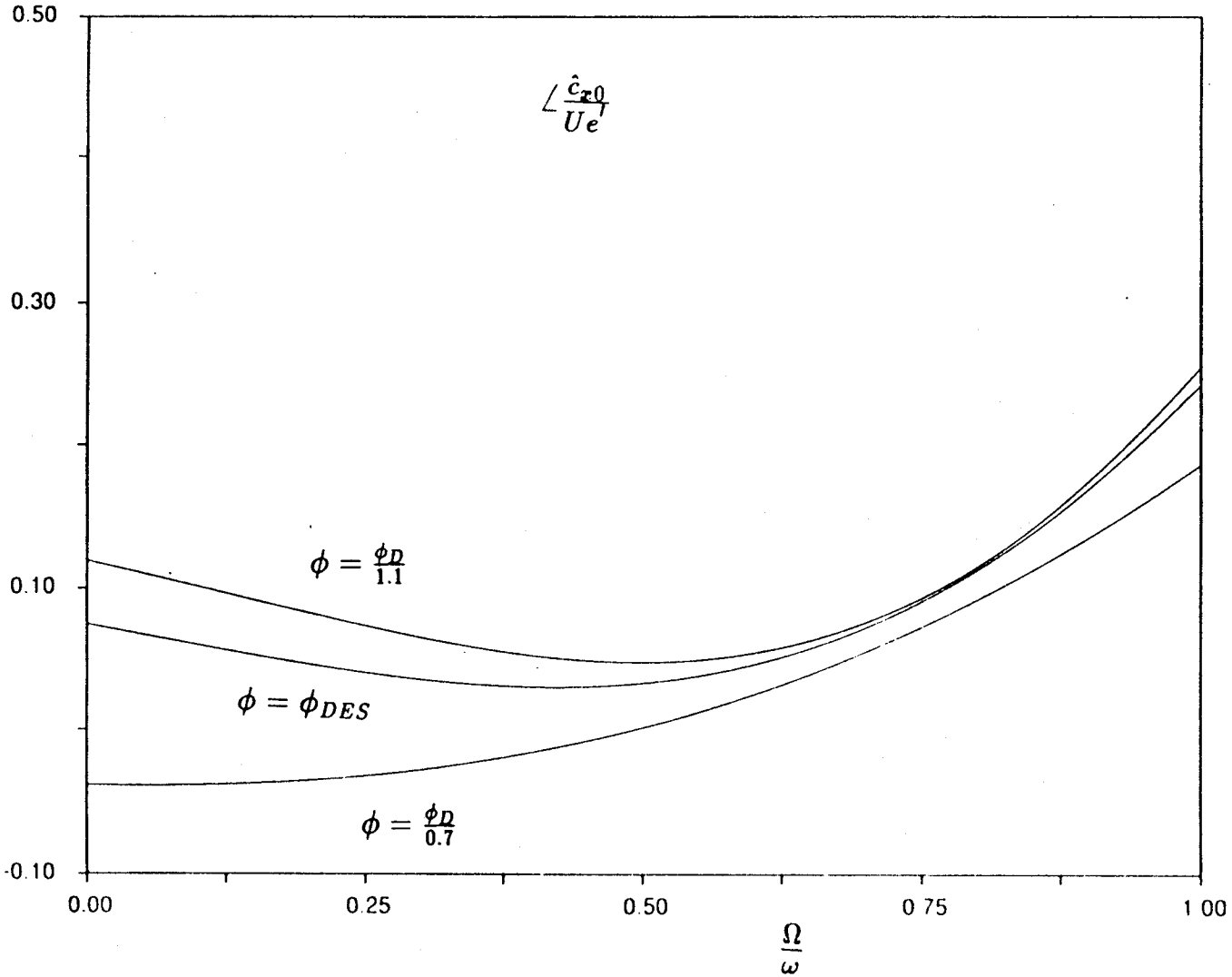

Fig 9.46b Same as 9.46a (phase)

whirl frequency Ω (normalized by spin rate, ω) has the effect of increasing the amplitude of the redistribution, with minor phase changes only. The consequence is a further decrease in α_y (Fig. 9.48), and small changes in α_x (Fig. 9.47). The decrease of α_y with Ω is, of course, equivalent to a dynamic damping of the whirl. It must be remarked here again that this strong damping is entirely due to the XY redistribution effects, and would be reduced by any effect tending to reduce that redistribution. In fact, as we will later see, our static force data support values of α_y which are closer to the $\alpha_y = w$ result of the 2-D theory than to those of the full-XY redistribution theory, which suggests that one or more such effects are at work.

Having examined variations with operating point for one turbine, we can now complete the discussion by presenting results for a variety of turbines, each of them operating at their design point. The Alford coefficient α_y is shown as contour lines in a degree of reaction (R_{DESIGN}) vs. flow coefficient (ϕ_{DESIGN}) map in Figs. 9.48-9.51. Figures 9.48 and 9.49 are for $\delta/H = 0.3$ and 0.0187, respectively, but both with validity $s/b = 1$. Figures 9.50 and 9.51 are for $s/b = 0.5$. In all cases, the most apparent trend is for increased cross-force as the degree of reaction increases. This is the same trend discussed in Sec. 9.2 for the efficiency losses. Values up to about $\alpha_y \cong 1.2$ are predicted for 50% reaction machines at flow coefficients above $\phi \cong 0.4$. Notice that these are results of the theory which allow full XY redistribution, and are therefore lower bounds.

As noted before, the effects of gap width are minor. The effect of increasing solidity, therefore, unloading individual blades, is somewhat stronger, but not dominant (see Figs. 9.48 and 9.50, for instance).

By contrast to the situation with α_y, the direct force Alford coefficient, α_x, is found to depend mainly on flow coefficient, and only secondarily on design reaction. This is illustrated in Figs. 9.52-9.55. The α_x's are all negative at these design conditions (restoring stiffness) and, like the α_y's, they depend marginally on δ/H and only weakly on solidity.

9.3.8 Effects of Axial Rotor-Stator Gap

As noted, the inclusion of XY redistribution has the effect of dramatically reducing the

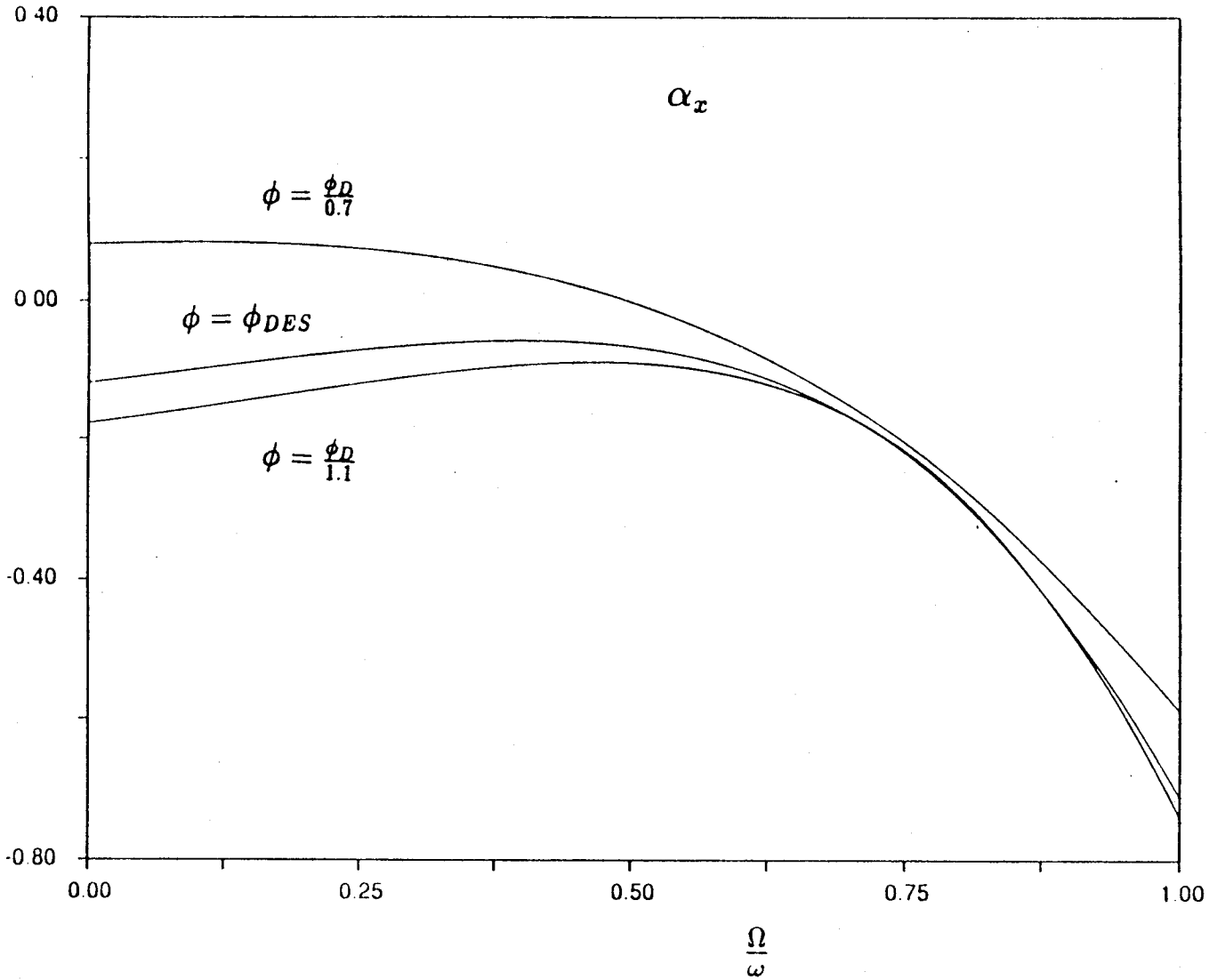

Fig 9.47a Dynamic effects on the force along the rotor displacement

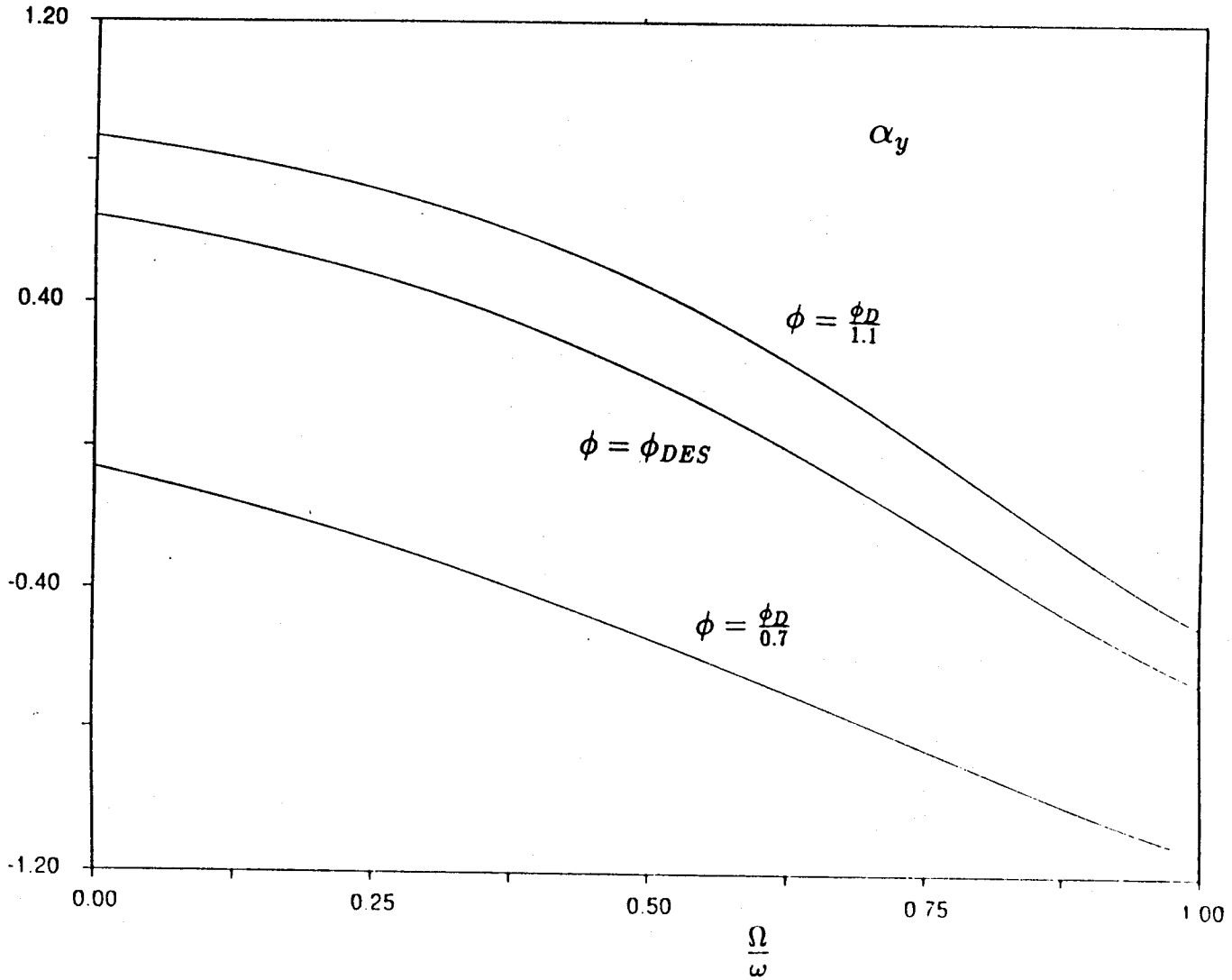

Fig 9.47b Dynamic effects on the force perpendicular to the rotor offset.

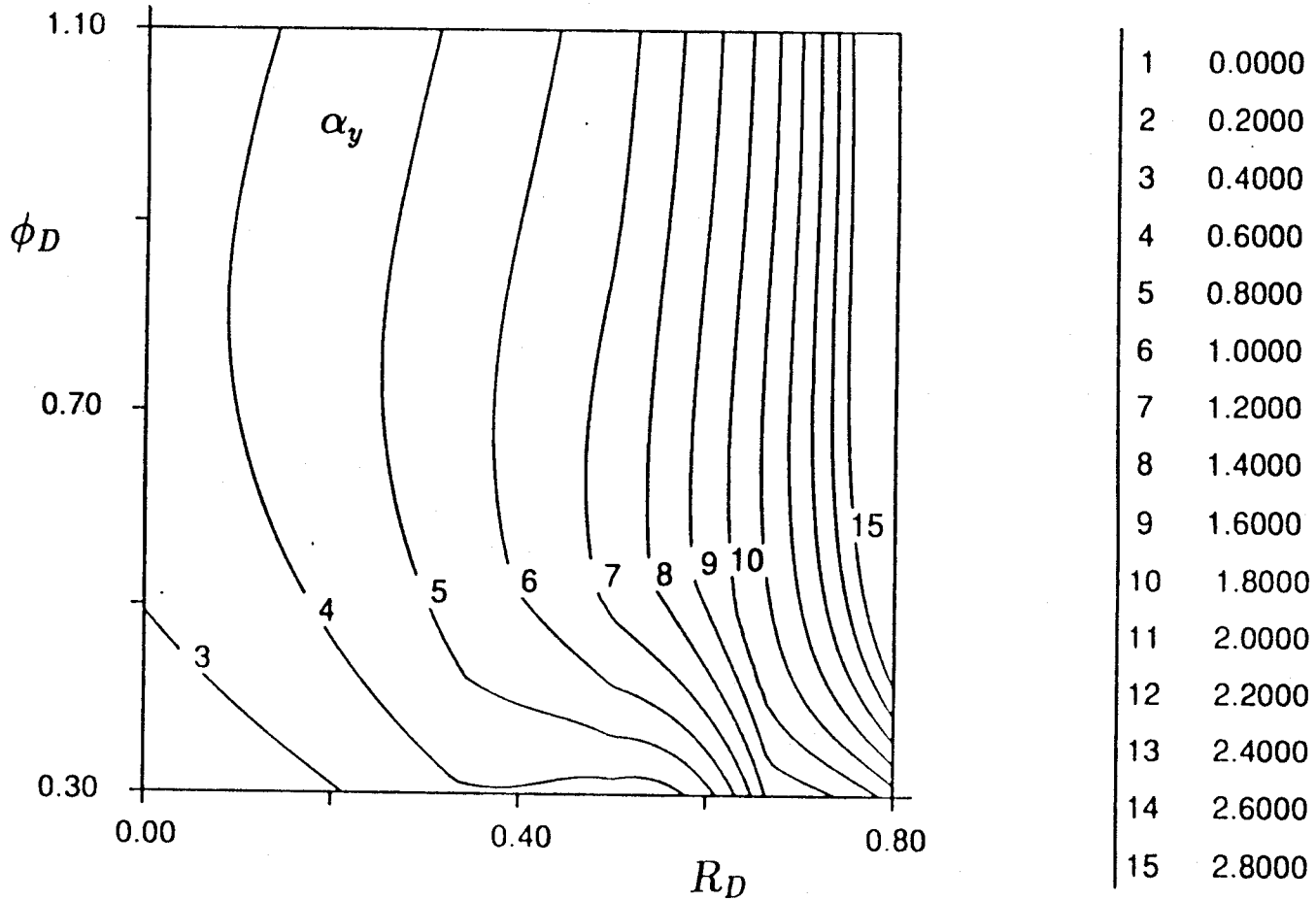

Fig 9.48 Parametric variation of the cross-force coefficient versus design degree of reaction and flow coefficient (all at zero exit swirl). Model with partial tip work.

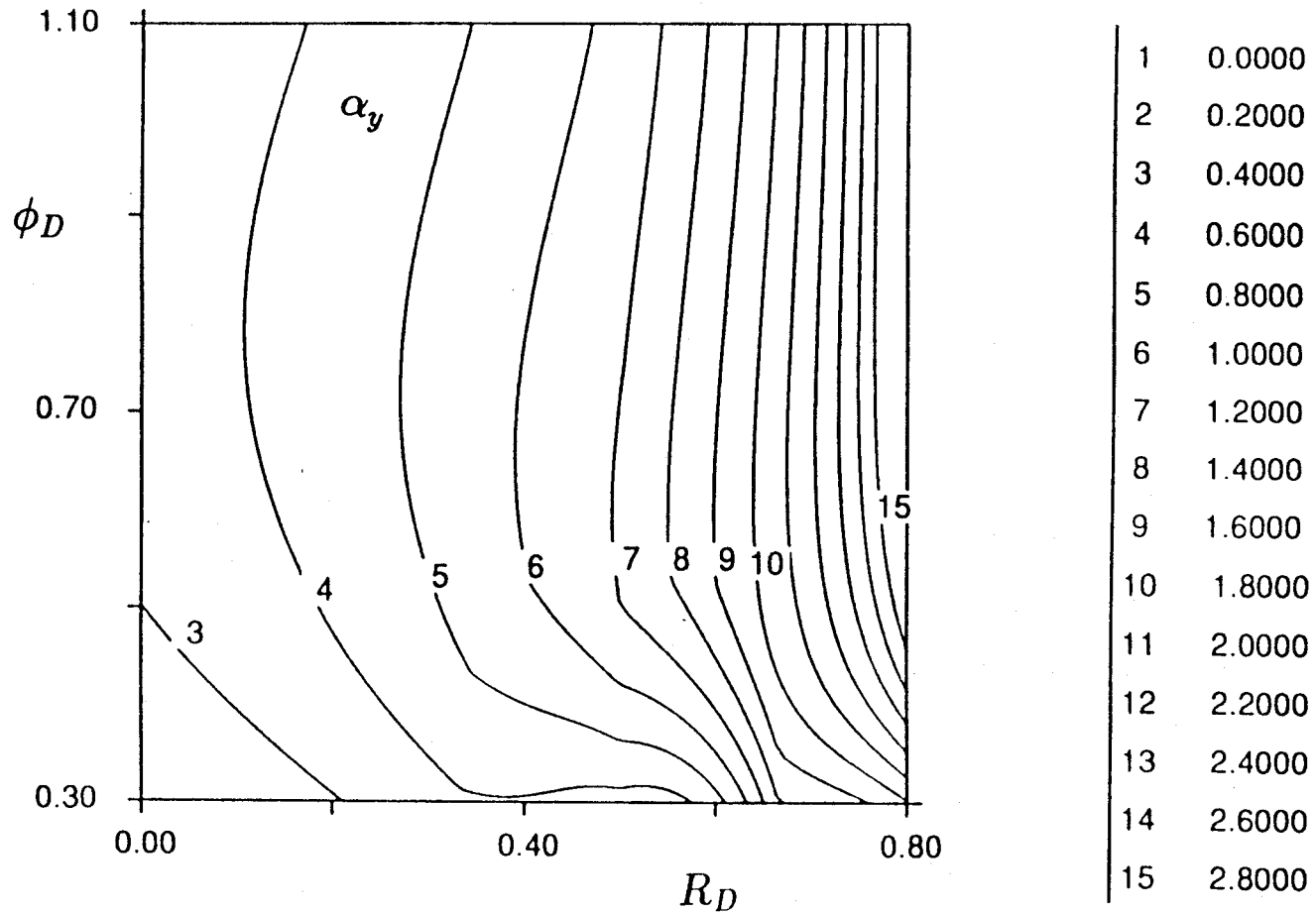

Fig 9.49 Same as 9.48, but $\frac{\overline{\delta}}{H} = 0.0187$

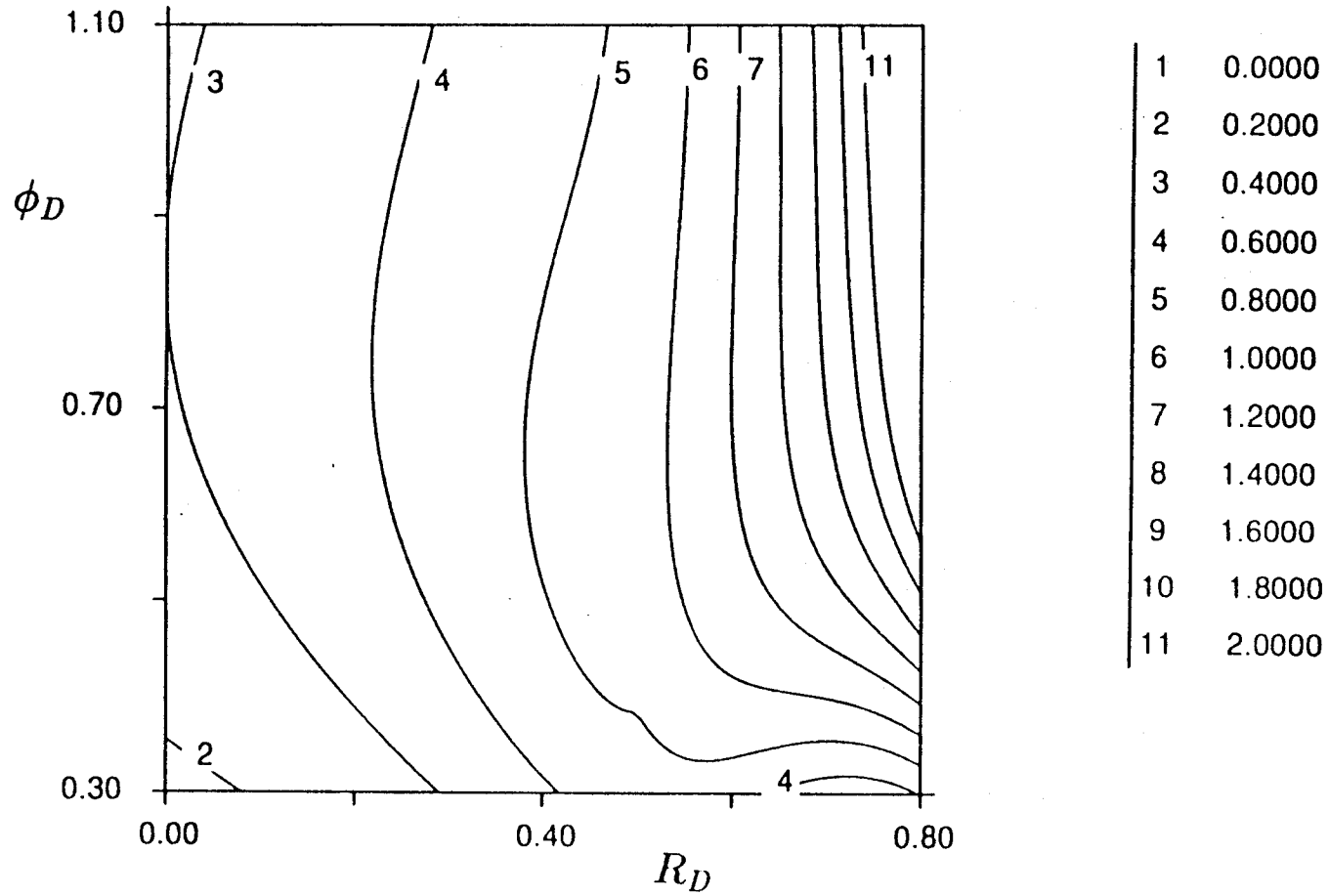

Fig 9.50 Same as 9.48, but $\frac{s}{b} = 0.5$

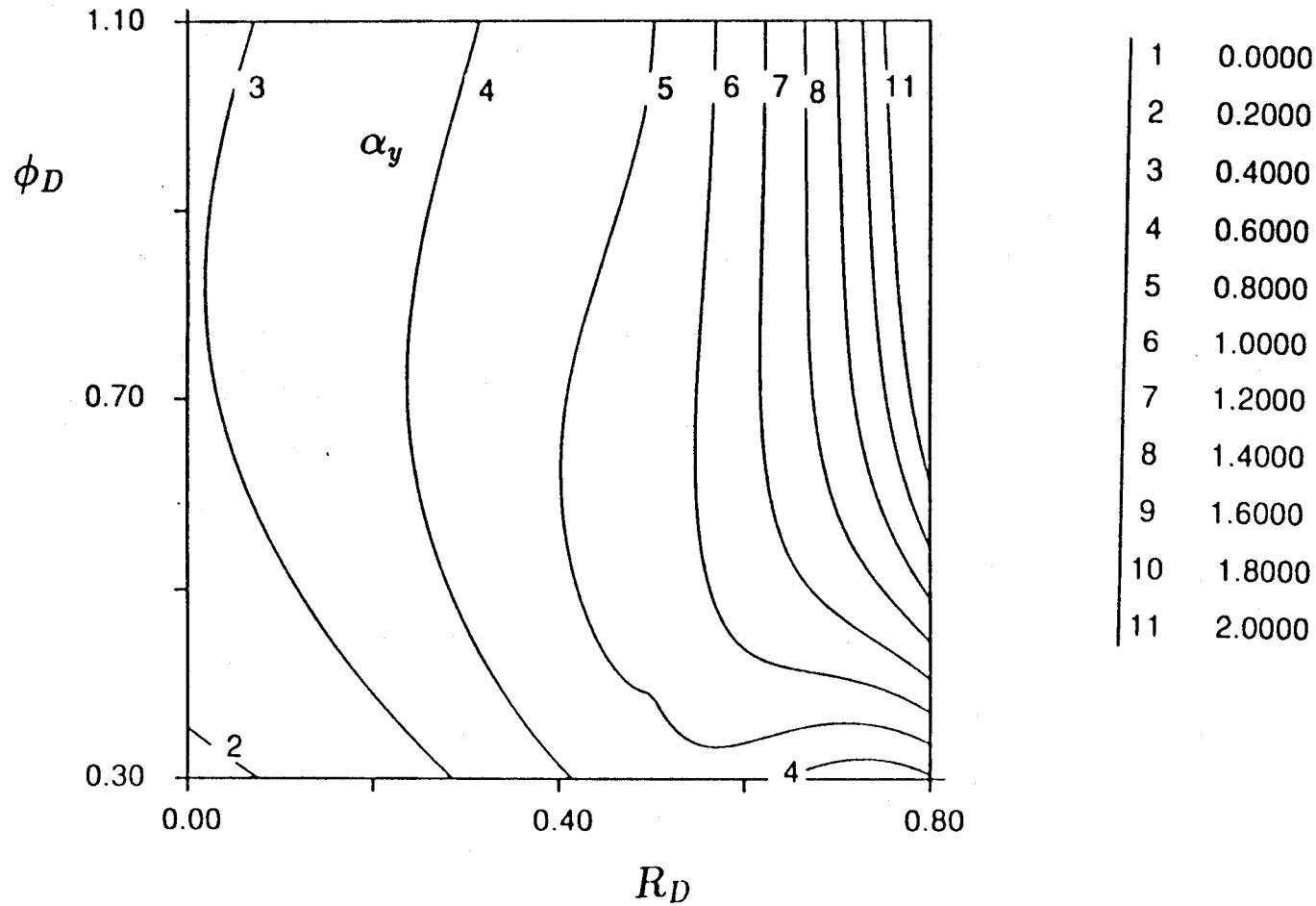

Fig 9.51 Same as 9.50, but $\frac{\bar{\delta}}{H} = 0.0187$

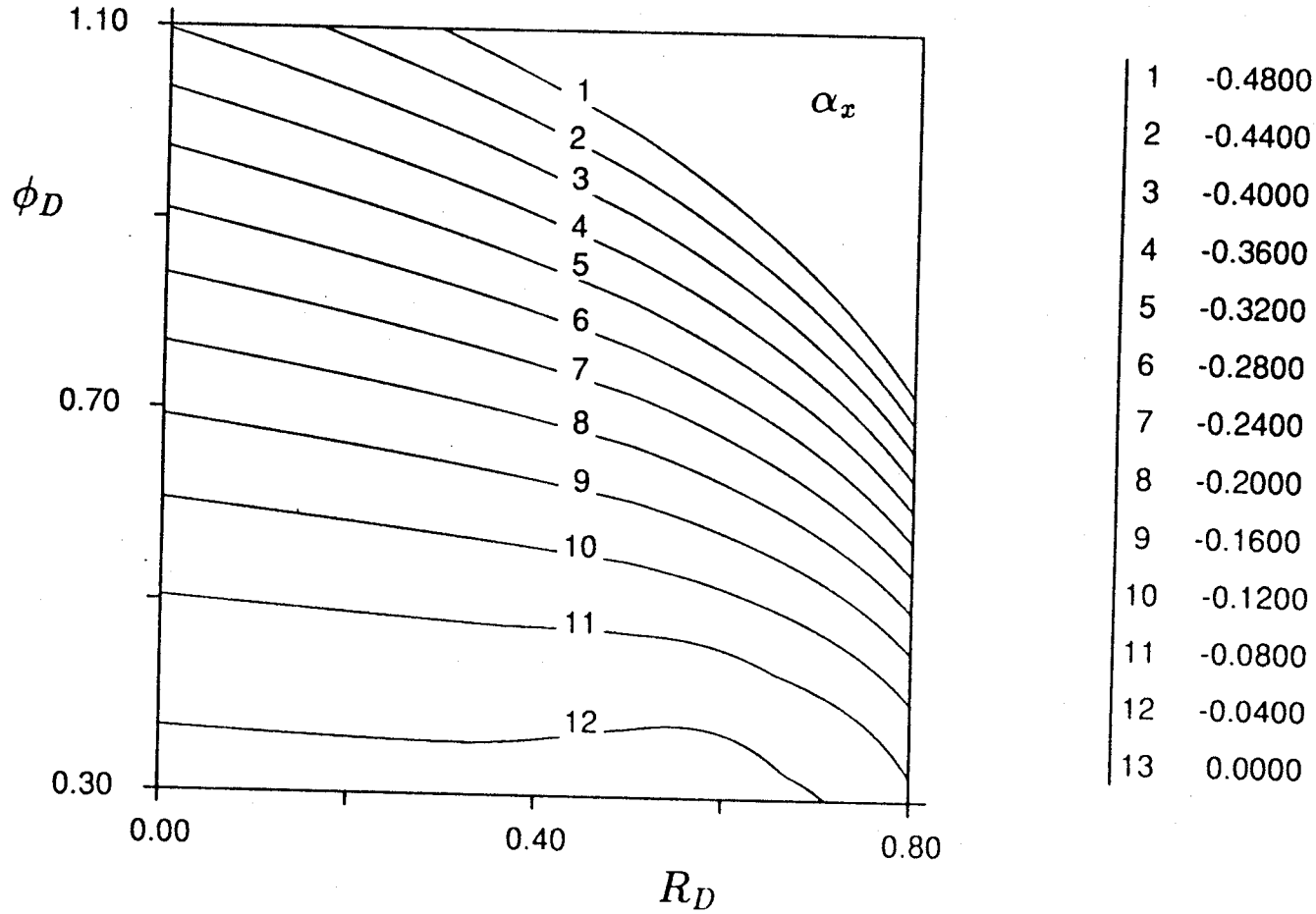

Fig 9.52 Parametric variations of the direct force coefficient.
$\frac{\bar{\delta}}{H} = 0.03,\ \frac{s}{b} = 1.0$

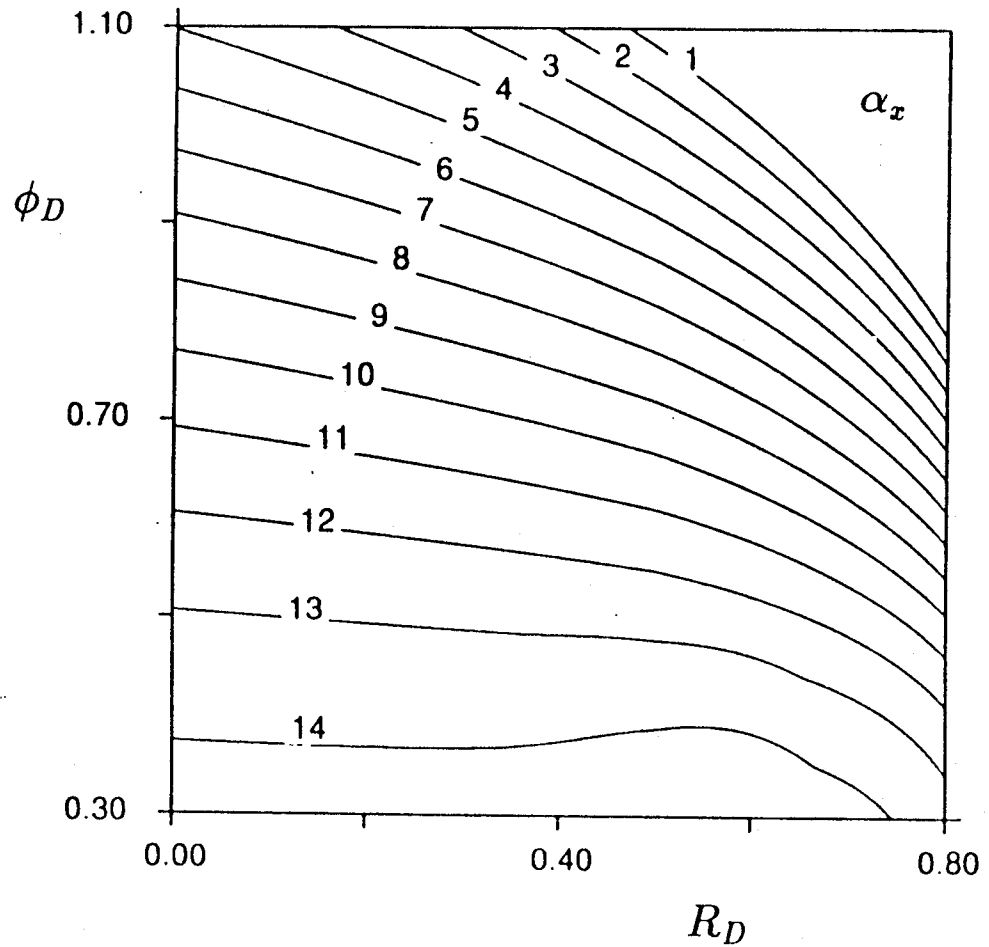

1	-0.5600
2	-0.5200
3	-0.4800
4	-0.4400
5	-0.4000
6	-0.3600
7	-0.3200
8	-0.2800
9	-0.2400
10	-0.2000
11	-0.1600
12	-0.1200
13	-0.0800
14	-0.0400
15	0.0000

Fig 9.53 Same as 9.52 but $\frac{\overline{\delta}}{H} = 0.0187$

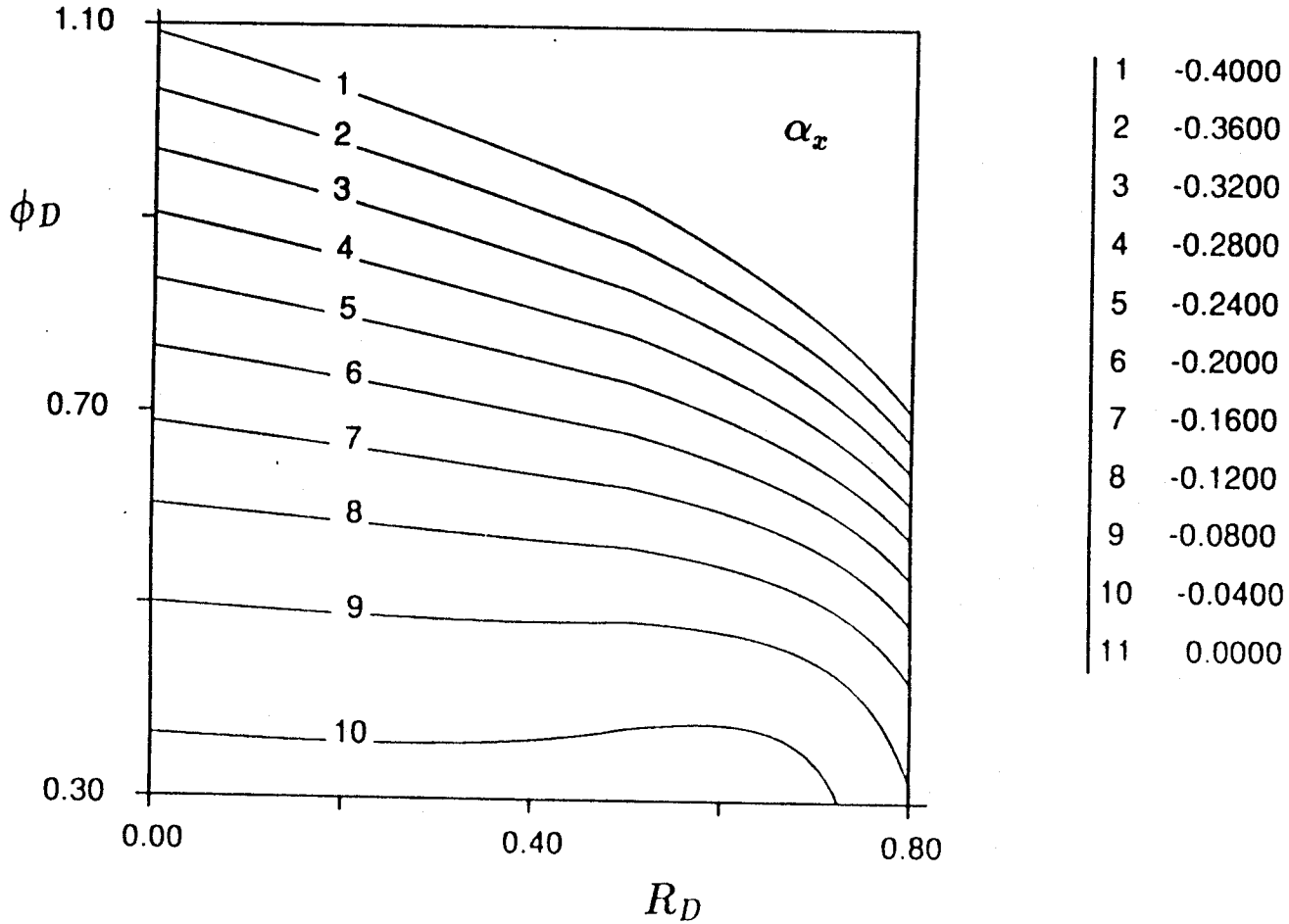

Fig 9.54 Same as 9.52 but $\frac{s}{b} = 0.5$

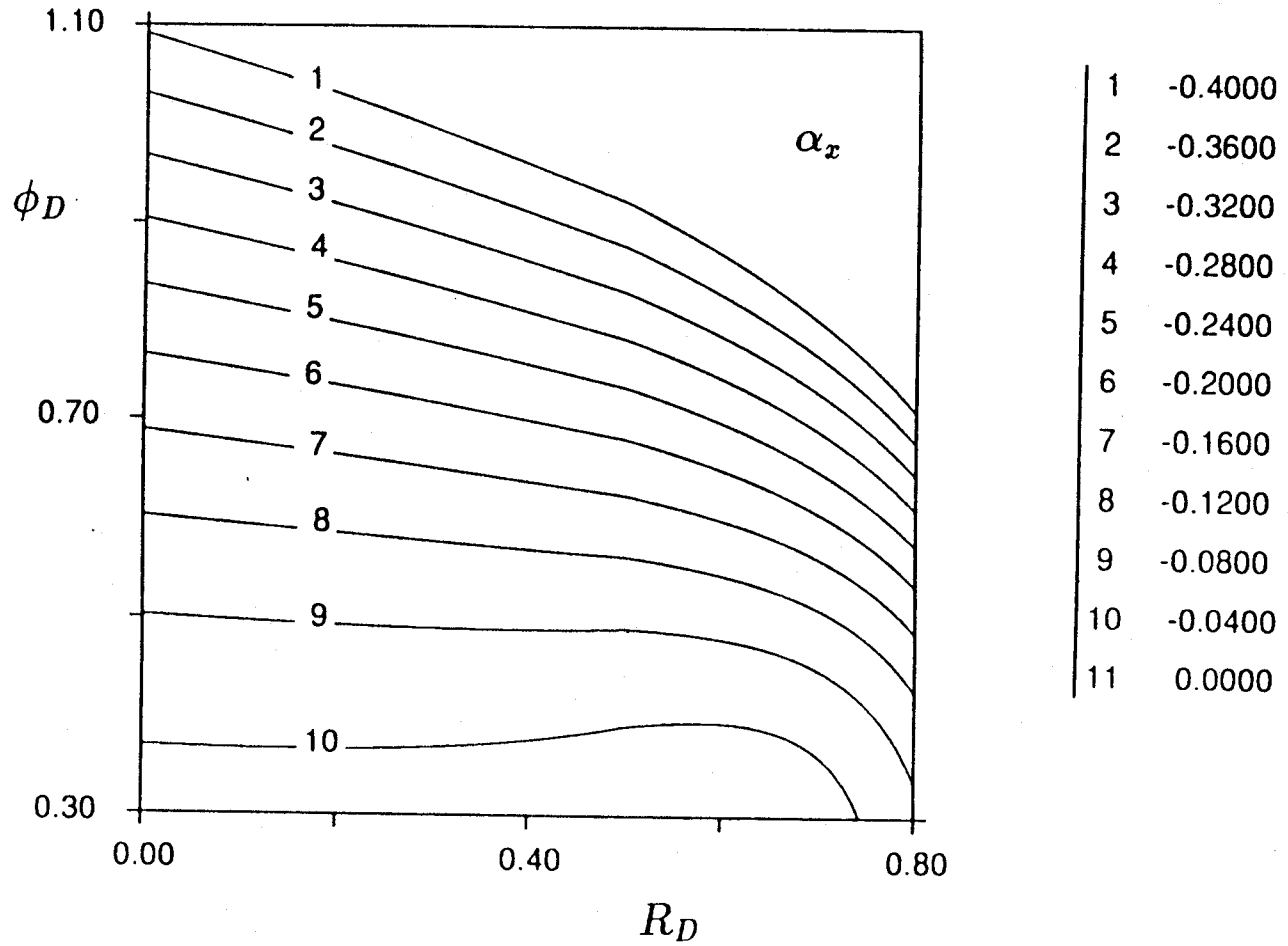

Fig 9.55 Same as 9.54 but $\frac{\bar{\delta}}{H} = 0.0187$

predicted cross-force Alford coefficient α_y from about 2.1 to around 0.7 at our design conditions. On the other hand, the data from the dynamometer (Sec. 4 and 5) indicate (a) levels of α_y (corrected for pressure effects) between 1.7 and 2.3 roughly, and (b) a trend to decrease α_y with the gap d' between the stator and rotor hubs, with perhaps a weaker trend to decrease as well with the distance d between stator and rotor blades. These experimental results, together with the theoretical understanding of the origin of the low predicted α_y, prompt us to a re-examination of the model assumptions. In particular:

(i) The calculation of stator pressure drop and stator exit tangential velocity in Sec. 9.2 is based on the radially redistributed velocities c_x^+, c_x^-. This is consistent with the "actuator disk" approach, which reduces all stage effects to the x=0 plane but, since the distance between stator and rotor blade centers is of the order of the blade height H, while the axial length for radial flow migration was found to be H/π, it is probably an unrealistic assumption. The separate velocities c_x^+, c_x^- should be adequate as mean <u>rotor</u> axial velocities, but the splitting must occur somewhere between rotor and stator, so that c_{x0} must be a more accurate representation at the stator. Notice this would be indeed redistributed in the tangential direction, however ($c_{x0} = c_{x0}(y')$). This modification should partially decouple the upstream pressure field from the rotor tip gap non-uniformity, and so reduce the extent of the XY redistribution and raise the predicted α_y.

(ii) For the hub gap values used (1.3 to 38% of chord), a relatively open communication exists between the rotor-stator space and the large volume enclosed by the stator hub cap (see Figs. 2.14 and 3.1, for example). This can create enough "breathing" in and out of the cavity to largely average out the static pressure in the space between stator and rotor blades. As a consequence, the upstream flow may become nearly uniform but, at the same time, the new flow injected into the interblade space (or the flow lost through the hub gap) will still have the effect of putting non-uniform flow through the rotor. It is not clear *a priori* to what extent these effects cancel each other. A further complication is that flow entering the interblade space will carry only small amounts of tangential momentum (c_{y2} between 0 and the wheel speed U,

compared to the $c_{y2} = c_{x0} \tan \alpha_2$ of the flow coming through the stator blades). On the other side of the perimeter, the flow lost through the gap is stator-guided flow, and therefore the perturbation force f_y' (y/R) due to this effect is non-sinusoidal. Also, since the radial flow velocity at the hub gap is proportional to the square root of the driving pressure difference, nonlinearity is introduced in an essential manner. In particular, a very small $\hat{p}_2(y)$ perturbation amplitude is sufficient to drive a proportionally much larger flow into and out of the hub cavity, while at the same time being too small to produce any significant $\hat{c}_{x_0}$ amplitude.

(iii) As implied by the discussion of (ii), increasing the axial hub clearance can be expected to reduce the pressure nonuniformity P_2' between the stator and the rotor. Since this perturbation is skewed azimuthally such as to provide a forward-whirling contribution to the cross-force F_y, there will be a corresponding reduction of this contribution when axial clearance increases. This third effect opposes those of (i) and (ii).

The first of these effects is very easy to incorporate into the analysis. All that is required is to replace c_x^+ or c_x^- in the stator by c_{x0}, while retaining them in the stator. This affects the calculation of P_2 (station 2 is between stator and rotor) and also of the turnings $c_{y_2}^+ - c_{y_3}^+$ and $c_{y_2}^- - c_{y_3}^-$ used in calculating W^+ and W^-, and therefore α_y.. As expected, this modification does reduce the flow redistribution and increase the predicted α_y. This is shown in Fig. 9.56, which refers to our own turbine, with a tip gap $\bar{\delta}/H = 0.03$. It can be seen that $|\hat{c}_{x_0}|$ is reduced by about 1/3, and its phase moves also further away from zero. The effect on α_y is shown in Fig. 9.57. This includes the 2-D predictions ($\alpha_y = w$), the 2-D predictions with "stratified" stator flow (i.e., using c_x^+ and c_x^- in the stator), and the 3-D predictions with radially uniform axial velocity, c_{x_0}. At the design condition, $\phi = 0.58$, α_y goes from 0.7 to 1.25 in the latter case. A similar increase in $|\alpha_x|$ is seen in Fig. 9.58.

Since the dynamic effects come entirely from the re-distribution in the R-scale, the modification to c_{x_0} at the stator can be expected to reduce these effects as well. Figure 9.59 shows α_y vs. normalized whirl speed, and should be compared to Fig. 9.48, where the stratified stator assumption was used. The modification to the level of α_y is at all Ω values about the same as at

$\Omega = 0$. This seems to indicate little change to the slope, or damping factor, although the fractional increase in ay is clearly higher at high Ω, where the stratified model predicted zero or negative α_y.

The hub gap is more difficult to account for properly. However, given the importance of the observed trend with d′, a simplified theory has been also developed for this purpose and is explained in Sec. 9.3.8.1. The direct contribution of the pressure modification (point (iii) above) has not to date been incorporated into the theory.

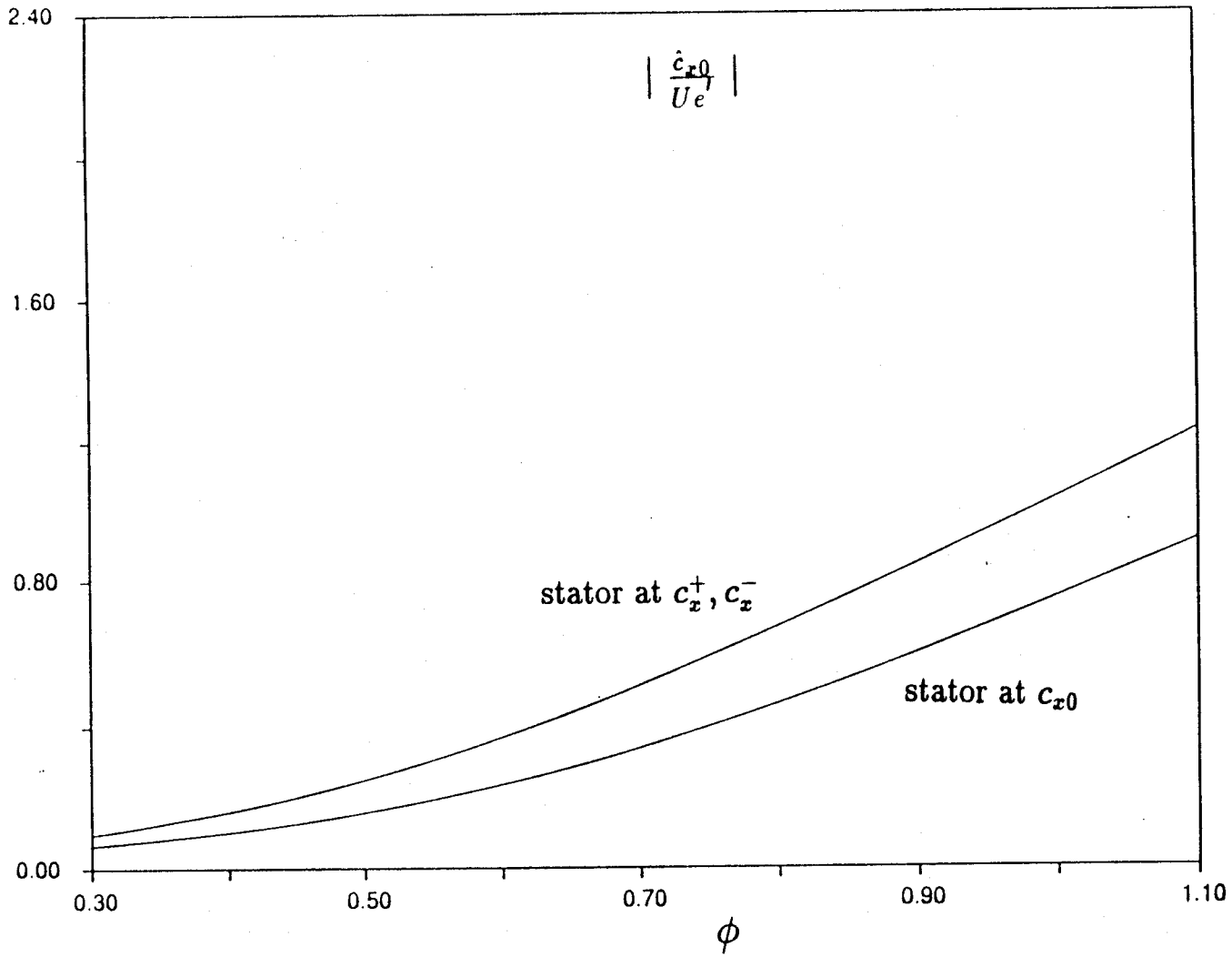

Fig 9.56a Effect on the upstream flow redistribution of changing from a stator flow stratified (c_x^+, c_x^-), to one radially uniform (c_{x0}). (Magnitude of $\frac{\hat{c}_{x0}}{Ue}$)

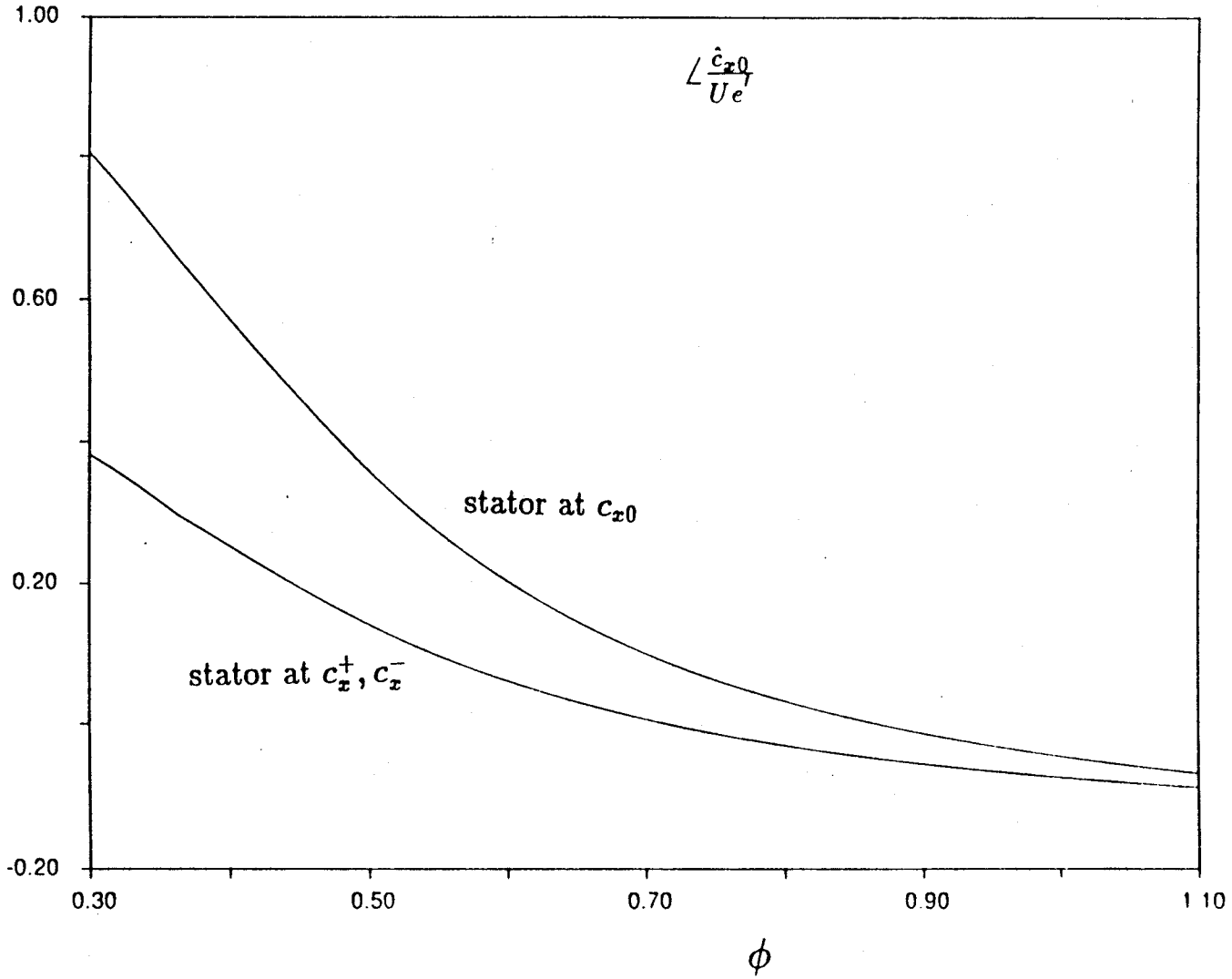

Fig 9.56b Same as 9.56a, but phase angle.

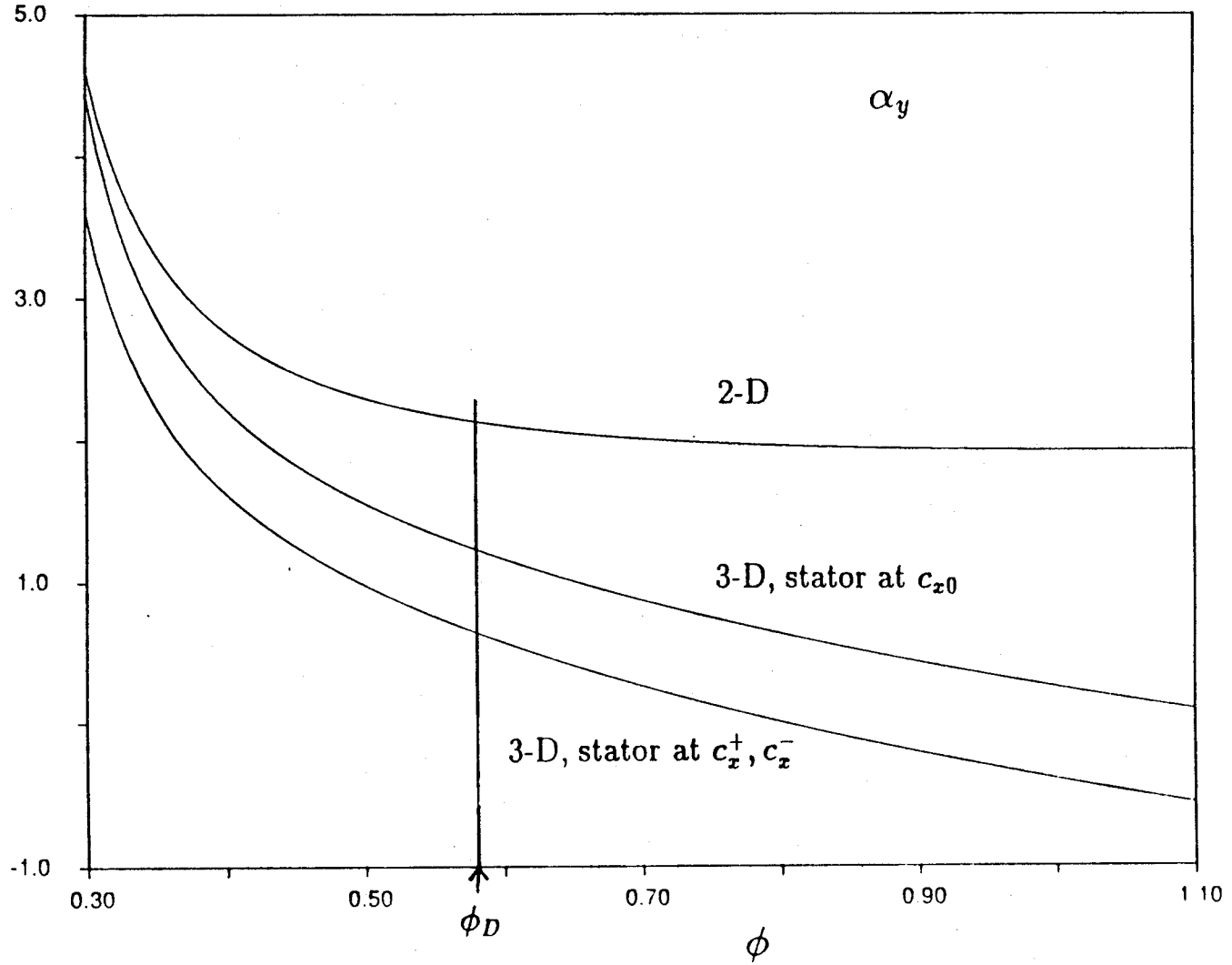

Fig 9.57 Effect on the cross-force coefficient of changing from stratified to uniform stator flow.
2-D result (no redistribution) included for comparison.

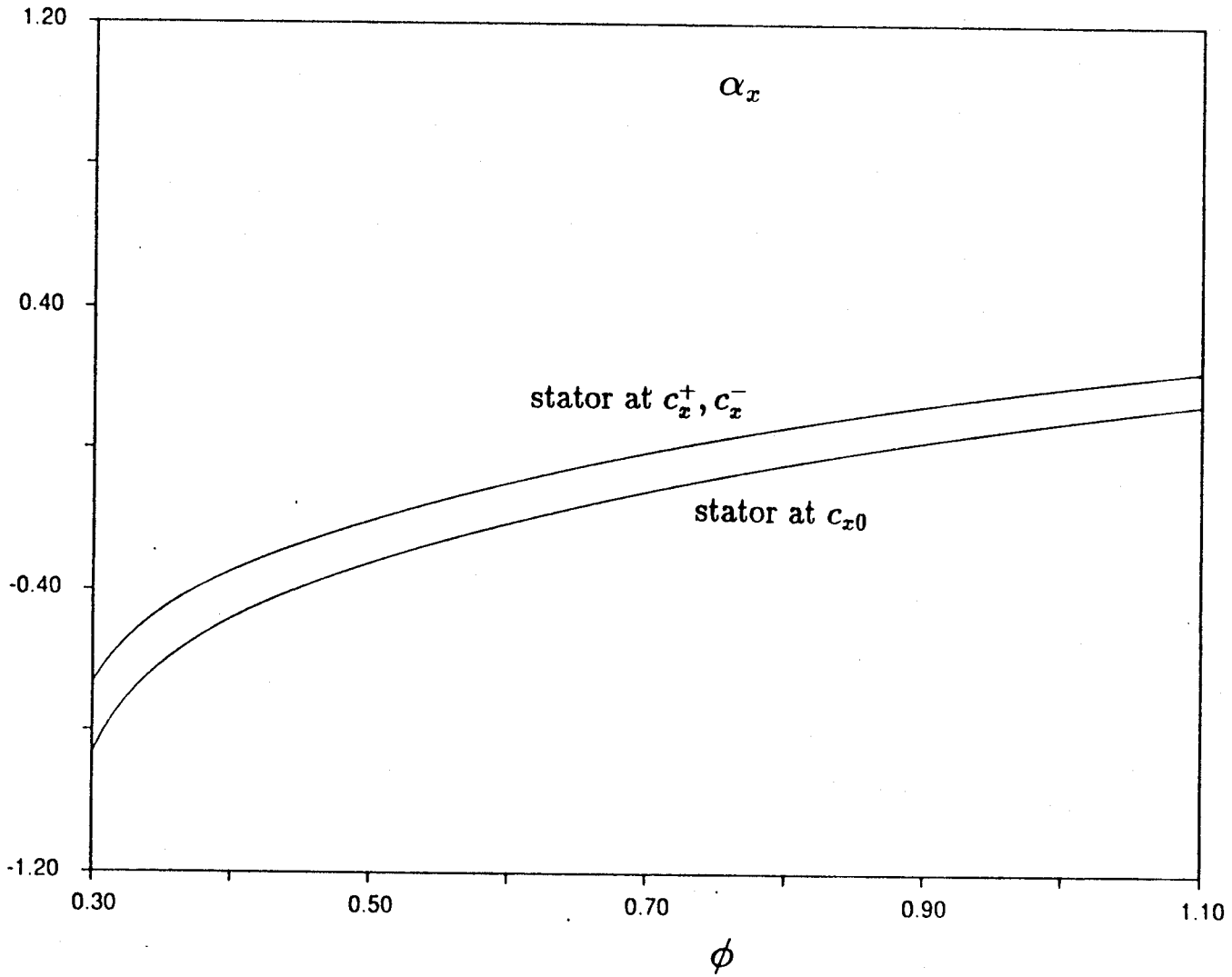

Fig 9.58 Effect of stator flow model on direct force coefficient.

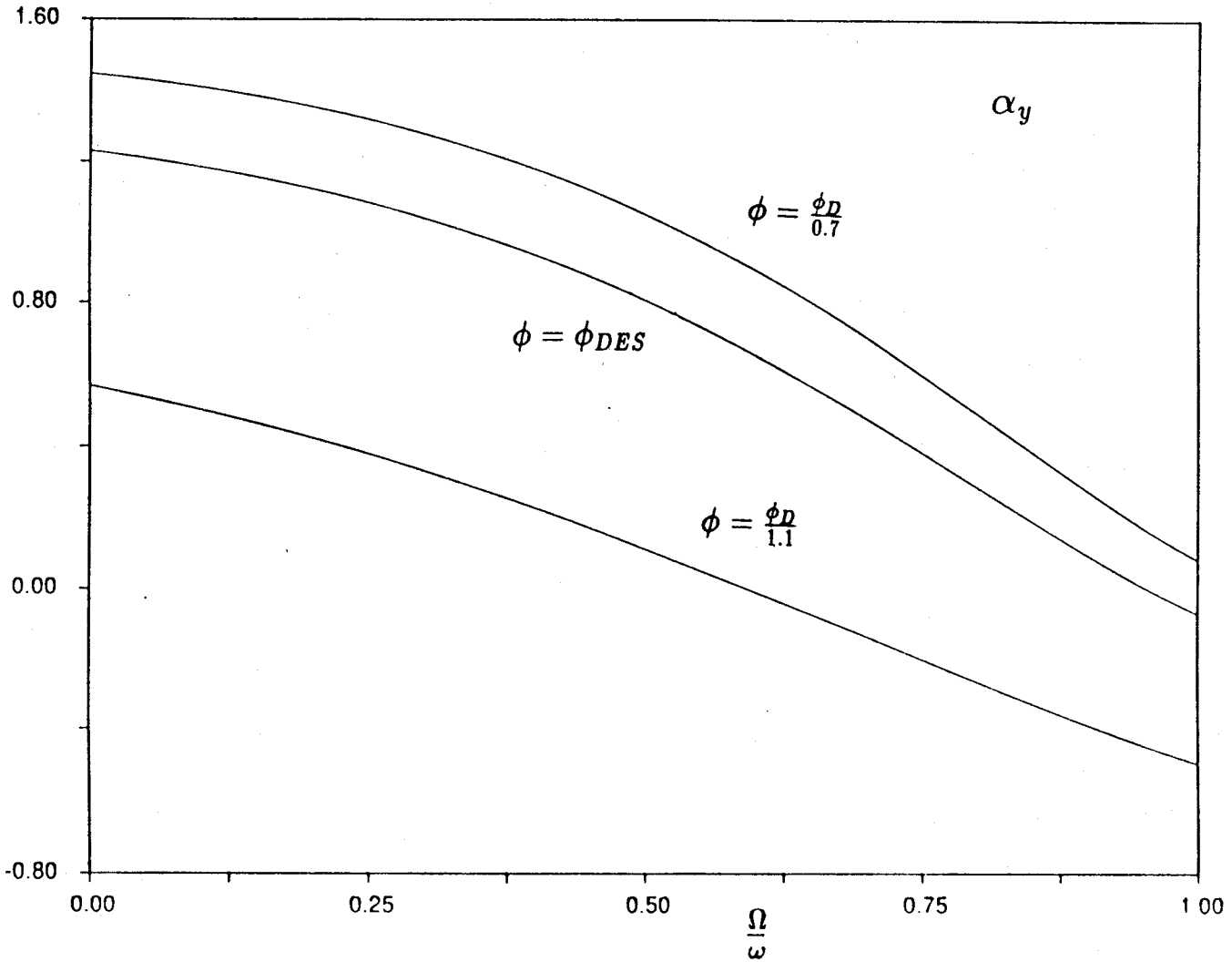

Fig 9.59 Dynamic effects on the cross-force coefficient using uniform stator flow. Compare to Fig 9.47b.

9.3.8.1 Analysis of Hub Gap Effects

Figure 9.60 shows the situation when the local pressure $P_2(y)$ between stator and rotor is below the mean value $\bar{P}_2$ prevailing in the hub cap volume. Some flow then comes from that volume and flows through the rotor disk. Let this be a fraction μ of the local incoming flow $m_o(y)$. As before, the fraction λm_o is underturned at the blade tips, and the rest (now $(1 - \lambda - \mu)$ m_o) constitutes the main flow. Of course, when $P_2(y) > \bar{P}_2$, the fraction μm_o of the stator flow will leave via the hub gap, so that the fractions λ and $1 - \lambda - \mu$ will fill the rotor passage.

The flow μm_o entering the passage from the hub volume will carry a tangential velocity c_y^a somewhere between zero and $U = \omega R$, as determined by frictional balance in the hub volume. This is much less than the c_y component of the stator-delivered main flow, and variations within the stated range will have secondary effects only. We will specify c_y^a by means of the parameter

$$a_y = \frac{c_y^a}{U} \qquad (0 < a_y < 1) \tag{9.127}$$

The axial velocity c_x^a of this flow fraction as it leaves the turbine rotor can be found by imposing that the rotor static pressure drop be the same for this stream as for the main flow:

$$\frac{1}{2}\left(c_x^- \tan\beta_3\right)^2 - \frac{1}{2}\left(c_x^- \tan\alpha_2 - U\right)^2 = \frac{1}{2}\left(c_x^a \tan\beta_3\right)^2 - \frac{1}{2}\left(c_y^a - U\right)^2 \tag{9.128}$$

which gives

$$c_x^a = \sqrt{\left(c_x^-\right)^2 + \left(c_{y_2}^a - c_x^- \tan\alpha_2 - 2U\right)\left(\frac{c_{y_2}^a - c_x^- \tan\alpha_2}{\tan^2\beta_3}\right)} \tag{9.129}$$

The velocities c_x^+ and c_x^- corresponding to the underturned and main streams at the rotor can be found by a simple extension of the arguments in Sec. 9.2.

Using $\lambda << 1$ and $\mu << 1$, we find (with either $\mu > 0$ or $\mu < 0$)

$$\frac{c_x^+}{c_{x_0}} = 1 - \lambda\frac{q}{2} + \mu \tag{9.130}$$

$$\frac{c_x^-}{c_{x_0}} = 1 + (1-\lambda)\frac{q}{2} + \mu \tag{9.131}$$

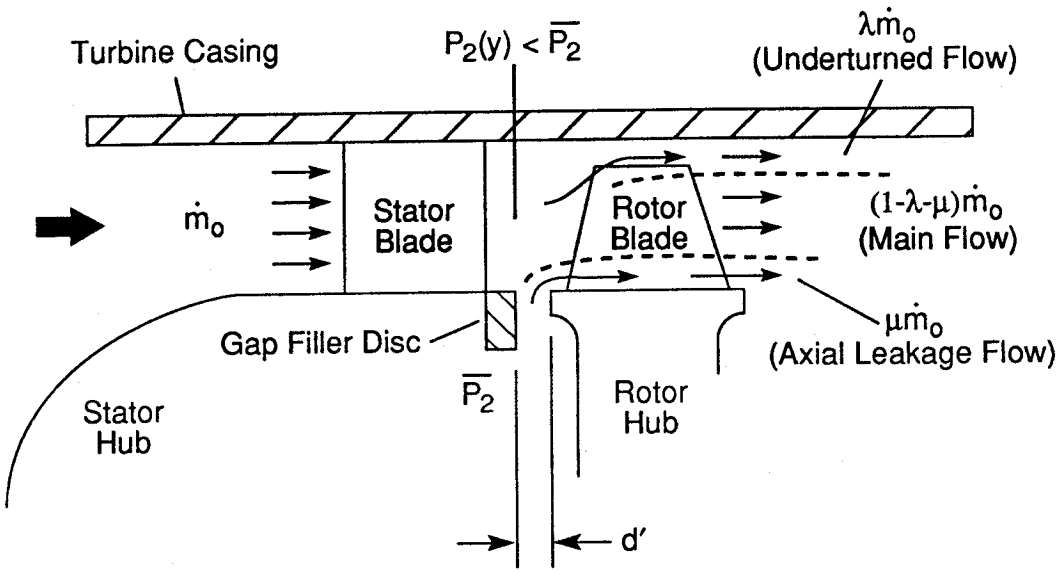

Fig. 9.60: Effect of a hub axial gap

which replace (9.46a,b). When these are substituted into the definition of the shear layer strength $Q = c_{x_0}^2 q$, the new quadratic equation for q differs from Eq. (9.104) only by small terms of order μ, which can be ignored as leading to 2nd order corrections only.

The pressure P_2 in the stator-rotor space is found from Bernoulli's equation. We now adopt the viewpoint that the stator flow is still radially uniform ($c_x = c_{x0}(y)$) and find

$$\frac{P_0 - P_2}{\rho} = \frac{\tan^2 \alpha_2}{2} \, c_{x_0}^2 \tag{9.132}$$

where P_0 itself may have a y-dependence, as in Sec. 9.3. For the steady-offset case, this dependence is also given by Bernoulli's equation, leading to

$$\frac{P_{-\infty} - P_2}{\rho} = \frac{1 + \tan^2 \alpha_2}{2} \, c_{x_0}^2 - \frac{1}{2} \bar{c}_{x_0}^2 \tag{9.133}$$

or, in coefficient form

$$c_{p_2} = \frac{P_{-\infty} - P_2}{\rho U^2} = \frac{1 + \tan^2 \alpha_2}{2} \, \phi^2 - \frac{1}{2} (\bar{\phi})^2 \tag{9.134}$$

The pressure drop between 2 and x >> H is the sum of P_2 - P_3 and P_3 - P_∞. The first of these can expressed as

$$\frac{P_2 - P_3}{\rho} = \frac{1}{2} \left(c_{x_0} \tan \beta_3 \right)^2 - \frac{1}{2} \left(c_{x_0} \tan \alpha_2 - U \right)^2 \tag{9.135}$$

while the second part is

$$\frac{P_2 - P_\infty}{\rho} = \frac{1}{2} \left(\bar{c}_{x_\infty} \right)^2 - \frac{1}{2} \left(\bar{c}_x \right)^2 \tag{9.136}$$

where, using $\eta = -\lambda(q/2) + \mu$, so that $\left(\bar{c}_x / c_{x_0} \right) = 1 + \eta$, we have $\bar{c}_{x_\infty} = 1 + 2\eta$. Therefore, again in coefficient form,

$$c_p^* \equiv \frac{P_3 - P_\infty}{\rho U^2} = \frac{\phi^2}{2} \tan^2 \beta_3 - \frac{1}{2} \left(\phi \tan \alpha_2 - 1 \right)^2 + \frac{\phi^2}{2} \eta \, (2 + 3\eta) \tag{9.137}$$

The radial in or out flow through the axial hub gap d′ is driven by the pressure differential P_2 - $\bar{P}_2$. After normalizing by the incoming mass flux, we obtain

$$\mu = \frac{\sqrt{2}}{\phi}\frac{d'}{H}\sqrt{\left|c_{p_2}'\right|}\ sg\left(c_{p_2}'\right) \tag{9.138}$$

where $c_{p_2}' = c_{p_2} - \bar{c}_{p_2}$ and $sg\left(c_{p_2}'\right) = +1$ or -1, depending on the sign of c_{p_2}', i.e. flow is out of the cavity ($\mu > 0$) when P_2 is less than $\bar{P}_2$ ($c_{p_2}' > 0$), and vice versa.

Notice the essential nonlinearity in Eq. (9.138). In order to proceed with our assumption of sinusoidally varying quantities, we need to neglect the higher harmonics of $\sqrt{\left|c_{p_2}'\right|}\ sg\left(c_{p_2}'\right)$ when c_{p_2}' itself is sinusoidal in y/R. Letting ϕ be the phase of c_{p_2}', namely, $c_{p_2}' = \mathrm{Re}\left[\hat{c}_{p_2} e^{i(y/R)}\right]$ and $\hat{c}_{p_2} = \left|\hat{c}_{p_2}\right| e^{i\phi}$, we obtain for the <u>first harmonic</u> of μ:

$$\hat{\mu}\left(1^{st}\text{Harmonic}\right) = 1.1128\frac{\sqrt{2}}{\phi}\frac{d'}{H}\sqrt{\left|\hat{c}_{p_2}\right|}\, e^{i\phi} \tag{9.139}$$

where the numerical factor is $\dfrac{\sqrt{2}}{3\pi^{3/2}}\Gamma^2\left(\dfrac{1}{4}\right)$.

In order to connect to the downstream flow without the complications of the multi-mode behaviors of the perturbed three-layer structure (underturned stream, main flow, and axially leaked flow), we now make use of one of the results obtained before, namely, that the downstream pressure nonuniformity is relatively unimportant (see Sec. 9.3.7). If we carry this behavior to the present analysis, and postulate that $P_\infty{}' \cong 0$, i.e. $c_{p_T}' \equiv c_{p_2}' + \left(c_p^*\right)' \cong 0$, we can close the problem and obtain its solution in relatively simple form. In linearized form (about azimuthally uniform flow), the above approximation amounts to

$$\left(\frac{\partial c_{p_T}}{\partial \phi}\right)_{\delta,\mu}\frac{\hat{c}_{x_0}}{U} + \left(\frac{\partial c_{p_T}}{\partial(\delta/H)}\right)_{\phi,\mu}\frac{e}{H} + \left(\frac{\partial c_{p_T}}{\partial \mu}\right)_{\delta,\phi}\hat{\mu} \cong 0 \tag{9.140}$$

where $c_{p_T} = c_{p_2} + c_p^* = \left(P_{-\infty} - P_\infty\right)\Big/\rho U^2$. This gives the upstream flow redistribution $\hat{c}_{x_0}$ in terms of eccentricity e/H and axial hub gap flow μ (actually, the amplitude $\hat{\mu}$ of its tangential variation). This quantity itself depends on $\hat{c}_{p_2}$ through Eq. (9.139), and $\hat{c}_{p_2}$ can be expressed as

$$\hat{c}_{p_2} = \left(\frac{\partial c_{p_2}}{\partial \phi}\right)_{\delta,\mu}\frac{\hat{c}_{x_0}}{U} + \left(\frac{\partial c_{p_2}}{\partial(\delta/H)}\right)_{\phi,\mu}\frac{e}{H} + \left(\frac{\partial c_{p_2}}{\partial \mu}\right)_{\delta,\phi}\hat{\mu} \tag{9.141}$$

where, if the stator is taken to have axial velocity c_{x_0}, we have (Eq. (9.134)) $\dfrac{\partial c_{p_2}}{\partial(\delta/H)} = \dfrac{\partial c_{p_2}}{\partial \mu} = 0$.

Elimination of $\hat{c}_{x_0}/U$ and $\hat{\mu}$ between Eqs. (9.139), (9.140), and (9.141) yields an equation

for $\hat{c}_{p_2}$:

$$\hat{c}_{p_2} = \left(- \frac{\partial c_{p_2}}{\partial \phi} \frac{\partial c_{p_T}/\partial \mu}{\partial c_{p_T}/\partial \phi} \right) \frac{k}{\phi} \left(\frac{d'}{H} \right) \sqrt{|\hat{c}_{p_2}|}\, e^{i\phi} + \left(- \frac{\partial c_{p_2}}{\partial \phi} \frac{\partial c_{p_T}/\partial (\delta/H)}{\partial c_{p_T}/\partial \phi} \right) \frac{e}{H} \tag{9.142}$$

where k = 1.57378.

So far, $\hat{c}_{p_2}$ has been taken to be a general complex quantity. However, Eq. (9.142) shows that it must be either real positive ($\phi = 0$) or real negative ($\phi = \pi$). Both possibilities can be accounted for if $\hat{c}_{p_2}$ is calculated as

$$\hat{c}_{p_2} = r^2 \, sg(C) \tag{9.143}$$

where $r = \sqrt{|\hat{c}_{p_2}|}$ obeys the quadratic equation

$$r^2 + B\, r - |C| = 0 \tag{9.144}$$

and B and C are

$$B = \frac{\partial c_{p_2}}{\partial \phi} \frac{\partial c_{p_T}/\partial \mu}{\partial c_{p_T}/\partial \phi} \frac{k}{\phi} \left(\frac{d'}{H} \right) \tag{9.145a}$$

$$C = \frac{\partial c_{p_2}}{\partial \phi} \frac{\partial c_{p_T}/\partial (\delta/H)}{\partial c_{p_T}/\partial \phi} \frac{e}{H} \tag{9.145b}$$

As before, sg(C) is the "sign" function, equal to +1 or -1, depending on the sign of C. The same meaning can be attached to the factor $e^{i\phi}$ in calculating $\hat{\mu}$ from Eq. (4.139). For all cases of interest, we find sg(C) = +1, or $\phi = 0$.

Equation (9.142) (or (9.144)) is clearly nonlinear in d'/H. Two limits of interest are:

(a) Very small axial hub gap, d'/H = 0. Then Eq. (9.139) gives $\hat{\mu} = 0$, and (9.140) and (9.142) show finite limits for $\hat{c}_{p_2}$ and $\hat{c}_{x_0}$. In particular, the latter is then

$$\frac{\hat{c}_{x_0}}{U} = - \frac{\partial c_{p_T}/\partial (\delta/H)}{\partial c_{p_T}/\partial \phi} \frac{e}{H} \tag{9.146}$$

Comparison to (9.112) shows that the present approximation is equivalent to retaining only the first term in the numerator and the first two in the denominator of the exact formula for $\hat{c}_{x_0}/U$.

(b) For relatively large hub axial gap, such that $B^2 >> 4\,|C|$ (Eqs. (9.145), the first term in

(9.144) becomes insignificant, so that $|\hat{c}_{p_2}| \equiv \left(\frac{|C|}{B}\right)^2 \sim \frac{1}{(d'/H)^2}$. Thus, the pressure becomes nearly uniform in the space between stator and rotor, but substitution into (9.139) shows that $\hat{\mu}$ tends then to a non-zero constant limit:

$$\hat{\mu} \rightarrow \frac{-\partial c_{p_T}/\partial(\delta/H)}{\partial c_{p_T}/\partial \mu} \frac{e}{H} > 0 \tag{9.147}$$

From Eq. (9.140) we then find that $\hat{c}_{x_0}/U$ also behaves as $1/(d'/H)^2$, and dies out at the same rate as $\hat{c}_{p_2}$ as the axial gap increases. Thus, the residual pressure nonuniformity, too small to induce appreciable upstream flow nonuniformity, can still drive leakage flows through the axial hub gap. This is due to the square root dependence of μ on $\bar{P}_2 - P_2$.

To complete the development, an expression is needed for the Alford coefficient α_y ($\alpha_x = 0$ now, since no rotation of the flow pattern occurs in this simplified model). The tangential force per unit length is now, when $\mu > 0$,

$$f_y = \rho c_{x_0} H \left[\lambda \left(c^+_{y_2} - c^+_{y_3}\right) + (1-\lambda)\left(c^-_{y_2} - c^-_{y_3}\right) + \mu \left(c^a_{y_2} - c^a_{y_3}\right)\right] \tag{9.148a}$$

When $\mu < 0$, only two streams occur in the rotor:

$$f_y = \rho c_{x_0} H \left[\lambda \left(c^+_{y_2} - c^+_{y_3}\right) + (1-\lambda+\mu)\left(c^a_{y_2} - c^a_{y_3}\right)\right] \tag{9.148b}$$

These forces are now projected as in Sec. 9.3.6 and integrated around the perimeter, the only difference being that Eqs. (9.148a) or (9.148b) must be used, depending on the sign of μ (positive from $-\pi/2$ to $+\pi/2$, negative in the rest). The result is a generalization of the previous results to the form

$$\alpha_y = -\frac{\hat{c}_{x_0}}{\bar{c}_{x_0}\left(\frac{e}{H}\right)} - \frac{\bar{\lambda}\left(\hat{c}^+_{y_2} - \hat{c}^+_{y_3}\right) + \hat{\lambda}\left[\left(\bar{c}^+_{y_2} - \bar{c}^+_{y_3}\right) - \left(\bar{c}^-_{y_2} - \bar{c}^-_{y_3}\right)\right] + (1-\bar{\lambda})\left(\hat{c}^-_{y_2} - \hat{c}^-_{y_3}\right) + \hat{\mu}\frac{\left(\bar{c}^a_{y_2} - \bar{c}^a_{y_3}\right) + \left(\bar{c}^-_{y_2} - \bar{c}^-_{y_3}\right)}{2}}{\left[\bar{\lambda}\left(\bar{c}^+_{y_2} - \bar{c}^+_{y_3}\right) + (1-\bar{\lambda})\left(\bar{c}^-_{y_2} - \bar{c}^-_{y_3}\right) + \hat{\mu}\frac{\left(\bar{c}^a_{y_2} - \bar{c}^a_{y_3}\right) - \left(\bar{c}^-_{y_2} - \bar{c}^-_{y_3}\right)}{\pi}\right]\frac{e}{H}} \tag{9.149}$$

The last term in the numerator deserves some comment. The new flow $\hat{\mu}$ introduced through the axial gap d' does work in proportion to $\bar{c}^a_{y_2} - \bar{c}^a_{y_3}$ over the half-perimeter where $\hat{\mu} > 0$, which is that surrounding the point of widest tip gap. Over the other half, near the minimum tip gap, there is a flow defect $|\hat{\mu}|$, and work is lost in proportion to $\bar{c}^-_{y_2} - \bar{c}^-_{y_3}$. Upon integration, these

two effects reduce the Alford force in proportion to the average of both tangential velocity changes.

This direct effect of the gap d′ (a reduction of α_y due to work done by the flow μm_0) is countered by the reduction of $\hat{c}_{x_0}$ which also occurs as d′ increases. This is clearest in the first term of Eq. (9.149), but it is also noticeable in the term $(1-\bar{\lambda})\left(\hat{c}_{y_2}^{-} - \hat{c}_{y_3}^{-}\right)$, because smaller $\hat{c}_{x_0}$ leads to smaller tangential velocities as well. The other terms in the numerator are minor. The new $\hat{\mu}$ term in the denominator is a shift of the mean force $\bar{f}_y$ due to the different amplitude of the f_y (y/R) curve vs. y/R over the two halves of the perimeter. Its effect is small.

9.3.8.2 Results and Discussion

For our design condition ($\phi = 0.58$, $\alpha_2 = 70°$, $\beta_3 = 60°$, s/b = 0.756, d/H = 0.03), and assuming the hub gap fluid is injected with $c_{y_2}^a = 0$, Table 9.5 shows calculated results. Notice that, because of the nonlinearity introduced by the hub gap, a particular rotor eccentricity ($e' = e/H = 0.01$) must be specified.

The first row in the table is for $d' = 0$, and would correspond to the previous theory, where no hub gap was allowed, except that the neglect of all downstream pressure nonuniformities has some distorting effects. In particular, the total α_y is calculated as 1.617, compared to about 1.25 (Fig. 9.56) from the full theory. Shown in that line are the upstream nonuniformity amplitude $\hat{c}_{x_0}/U$, the nonuniformity of pressure between stator and rotor $\left(\hat{c}_{p_2}\right)$, and the various contributions to α_y. The reducing effects of $\hat{c}_{x_0}$ on α_y are clearly seen in $(\alpha_y)_1$ and $(\alpha_y)_4$.

As the axial hub gap d′ is opened, we can see a rapid decrease in both $\hat{c}_{x_0}$ and $\hat{c}_{p_2}$, reflected directly in decrease in the negative α_y contributions $(\alpha_y)_1$, $(\alpha_y)_4$.. At the same, however, a negative contribution from the new injected flow (term $(\alpha_y)_5$) now appears. The net result is an increase in α_y. This increase is rapid for small d′, and tends to approach a limit at high d′ values. Half of the total increase is gained when $d'/H \cong 0.012$.

The sensitivity to the poorly known value of $c_{y_2}^a$ was tested and is shown in Table 9.6.

TABLE 9.5
CALCULATED RESULTS USING SIMPLIFIED THEORY
WITH AXIAL HUB GAP $d' \neq 0$ AND $e' = e/H = 0.01$

$\frac{\delta'}{H}$	$\frac{\hat{c}_{x_0}}{Ue'}$	$\frac{\hat{c}_{p_2}}{e'}$	$\hat{\mu}$	$(\alpha_y)_1$	$(\alpha_y)_2$	$(\alpha_y)_3$	$(\alpha_y)_4$	$(\alpha_y)_5$	$\alpha_y = \sum_{i=1}^{5} (\alpha_y)_i$
0	0.1258	0.6238	0	-0.2169	-0.0189	1.9598	-0.1066	0	1.6174
0.02	0.04395	0.2179	2.333×10^{-3}	-0.0758	-0.0075	1.9731	-0.0373	-0.1586	1.6940
0.05	0.01329	0.06588	3.483×10^{-3}	-0.0229	-0.0032	1.9781	-0.0113	-0.2180	1.7227
0.1	0.00390	0.01933	3.773×10^{-3}	-0.0067	-0.0018	1.9796	-0.0031	-0.2362	1.7315
0.2	0.00102	0.00506	3.862×10^{-3}	-0.0017	-0.0014	1.9800	-0.0008	-0.2418	1.7342
0.4	0.00026	0.00128	3.886×10^{-3}	-0.0004	-0.0013	1.9802	-0.0002	-0.2433	1.7348

Notes: $(\alpha_y)_1$ = contribution in Eq. (9.149) from term in $\hat{c}_{x_0}$

$(\alpha_y)_2$ = contribution in Eq. (9.149) from term in $\hat{c}^{+}_{y_3} - \hat{c}^{+}_{y_2}$

$(\alpha_y)_3$ = contribution in Eq. (9.149) from term in $\hat{\lambda}$

$(\alpha_y)_4$ = contribution in Eq. (9.149) from term in $\hat{c}^{-}_{y_3} - \hat{c}^{-}_{y_2}$

$(\alpha_y)_5$ = contribution in Eq. (9.149) from term in $\hat{\mu}$

TABLE 9.6: SENSITIVITY OF α_y (d′ LARGE) TO $c^a_{y_2}$

For all cases, α_y (d′ = 0) = 1.6174

$c^a_{y_2}/U$	α_y ($\delta'/H = 0.4$)
0.0	1.7348
0.5	1.7132
1.0	1.6662

It can be seen that, for $c^a_{y_2}/U$ up to about 0.5 (a likely limit), there is very limited sensitivity.

As noted, the d′/H effect introduces nonlinearity into the problem. To test whether this ought to be visible in the data, results are shown in Table 9.7 for α_y (e/H) at two different values of d′/H.

TABLE 9.7: LINEARITY CHECK VS. ROTOR OFFSET

e/H	0.002	0.005	0.01	0.015	0.02
α_y (d′/H = 0.02)	1.7002	1.6898	1.6799	1.6737	1.6694
α_y (d′/H = 0.4)	1.7121	1.7125	1.7132	1.7139	1.7146

A purely linear behavior would be indicated by a constant α_y when e/H varies. For a small axial gap (d′/H = 0.02), there is a slight "softening" type of nonlinearity but, interestingly, for a wider axial gap, this changes to a "hardening" type. Both are small, however, and would be within the error band of the experiments.

9.3.9 Summary of Redistribution Theory

The following points have been clarified by the theoretical developments in Sec. 9.3:

(a) In the absence of all axial gap effects, the flow responds strongly to the turbine offset, by migrating preferentially towards the location where the blade tip gap is widest.

(b) This migration alleviates substantially the Alford cross-force from its value predicted using a

purely local work loss coefficient.

(c) A second effect of the above redistribution is the prediction of substantial dynamic damping, which would be essentially absent in a purely local treatment.

(d) As a secondary effect, the non-symmetries of the downstream flow also introduce a direct (restoring) Alford force.

(e) Revision of the assumptions to limit the radial flow redistribution to the rotor only, and not the stator, reduces the upstream flow redistribution in the azimuthal direction, and increases the predicted α_y (by almost a factor of 2 at design conditions).

(f) Allowing the effect of flow injection from (or storage into) the hub cap volume, through the hub axial gap, further increases the predicted α_y. The increase nearly saturates when $d'/H \geq 5\%$.

(g) Additional work is required to integrate the direct effect of axial clearance on pressure-derived cross forces into a complete predictive scheme.

Appendix 9A: Disk versus Downstream Disturbances in Linearized Actuator Disk Theory

The linearized equation governing the streamline displacement $\tilde{z}$ in inverse coordinates is

$$\frac{1}{c_{x_o}^2}\tilde{z}_{xx} + \tilde{z}_{\Psi\Psi} = -\frac{\omega_y(\Psi)}{(c_{x_o}^3)} \tag{9A.1}$$

and $\omega_y \equiv 0$ for $x < 0$. The boundary conditions (Eq. 9.29) are all homogeneous. The right-hand side of (9A.1) will be written for short as $R(x,\Psi)$. To make it explicit that this must be replaced by zero for $x < o$, we introduce the unit step function $u(x)$ ($u=0$ for $x<0$, $u=1$ for $x>0$), and write

$$R(x,\psi) = r(\psi)\, u(x) \tag{9A.2}$$

where $r(\Psi) = -\omega_y(\Psi)/c_{x_o}^3$. The function $R(x, \Psi)$ can be decomposed into its even and odd parts with respect to x:

$$R(x, \Psi) = \frac{1}{2} r(\Psi) + \left[u(x) - \frac{1}{2}\right] r(\Psi) \tag{9A.3}$$

The solution $\tilde{z}$ can then be broken into the part $\tilde{z}_H$, which satisfies the homogeneous equation, plus the forced solution, which will itself have even and odd components $\tilde{z}_E$ and $\tilde{z}_0$, corresponding to the decomposition (9A.3). Imposing the homogeneous boundary conditions (Eq. (9.29)) on $\tilde{z}_H$ ensures that

$$\tilde{z}_H \equiv 0 \tag{9A.4}$$

The forced, even solution $\tilde{z}_E$ obeys (for <u>all</u> x)

$$\frac{1}{c_{x_o}^2}(\tilde{z}_E)_{XX} + (\tilde{z}_E)_{\Psi\Psi} = \frac{1}{2} R(\Psi) \tag{9A.5}$$

and can therefore be taken as a function of Ψ alone, which leads to immediate integration

$$\tilde{z}_E = \frac{1}{2}\int^{\Psi}\left(\int^{\Psi_1} R(\Psi_2)\, d\Psi_2\right) d\Psi_1 + A\Psi + B \tag{9A.6}$$

with A and B chosen to satisfy $\tilde{z}_E(x,o) = \tilde{z}_E(x, H\, c_{x_o}) = 0$.

The odd forced solution, $\tilde{z}_o$ must then be made to cancel $\tilde{z}_E(-\infty,\Psi)$:

$$\tilde{z}_0(-\infty,\Psi) = -\tilde{z}_E(\Psi) \tag{9A.7}$$

Therefore, at $x\rightarrow\infty$, $\tilde{z}_0(+\infty,\Psi) = +\tilde{z}_E(\Psi)$, and superimposing,

$$\tilde{z}_0(+\infty,\Psi) = 2\,\tilde{z}_E(\Psi) \tag{9A.8}$$

On the other hand, since $\tilde{z}_0(x,\Psi)$ is odd in x, we have $\tilde{z}_0(0,\Psi) = 0$, so that

$$\tilde{z}_0(0,\Psi) = \tilde{z}_E(\Psi) \tag{9A.9}$$

Comparison of (9A.8) and (9A.9) proves that the displacement of each streamline is twice as large far downstream as it is at the disk.

Appendix 9B: Definition of Parameters Used in the Analysis

For convenient reference, we collect in this Appendix a number of performance parameters whose definitions vary sometimes from author to author. The form given here was used throughout our calculations.

Flow Coefficient

$$\phi = \frac{c_{x_o}}{U} \tag{9B.1}$$

Work Coefficient

$$\psi = \frac{\text{Power}}{\dot{m}\, U^2} \tag{9B.2}$$

For nominal conditions (no gap),

$$\psi = \phi\left(\tan \alpha_2 + \tan \beta_3\right) - 1 \tag{9B.3}$$

and if there is zero exit swirl $\left(\phi = 1/\tan\ \beta_3\right)$, then

$$\psi = \frac{\tan \alpha_2}{\tan \beta_3} \tag{9B.4}$$

Degree of Reaction

$$R = \frac{\text{Pressure drop in rotor}}{\text{Pressure drop in stage}} \tag{9B.5}$$

For zero gap (from Eqs. (9.23), (9.24),

$$R = \frac{\tan^2 \beta_3 - \left(\tan\ \alpha_2 - 1/\phi\right)^2}{2\dfrac{\tan \alpha_2}{\phi} - \left(\dfrac{1}{\phi^2} - \tan^2 \beta_3\right)} \tag{9B.6}$$

and if the exit swirl is zero $\left(\phi\ =\ 1/\tan \beta_3\right)$, then

$$R = 1 - \frac{\tan \alpha_2}{2 \tan \beta_3} \tag{9B.7}$$

Zweifel Coefficient

$$ZW = \frac{\text{Tangential force per Blade}}{\text{(Tangential Projected Area) x (Relative Exit Dynamic Head)}} \qquad (9B.8)$$

For constant axial velocity,

$$ZW = 2 \left(\frac{s}{b}\right) \cos^2 \beta_3 \left(\tan \beta_2 - \tan \beta_3\right) \qquad (9B.9)$$

where s = Azimuthal blade spacing, and b = Axial depth of blading.

Blade Lift Coefficient

$$C_L = \frac{\text{Blade Lift}}{\text{(Blade Chord) x (Relative Inlet Dynamic Head)}} \qquad (9B.10)$$

The ratio of ZW to C_L is just the ratio of the reference dynamic heads:

$$C_L = (ZW) \left(\frac{\cos \beta_2}{\cos \beta_3}\right)^2 \qquad (9B.11)$$

10.0 Conclusions and Recommendations

10.1 Major Findings

This work has firmly established the reality of the destabilizing forces first postulated by Alford and Thomas. The general scaling and approximate order of magnitude is also consistent with their pioneering insights. Beyond this, however, we have found a number of effects and trends, some of which had not been previously reported. The most important of these are:

1) In addition to the Alford mechanism, namely the excess of turbine force generated on the narrow-gap side of a deflected turbine and vice versa, a significant contribution to the cross-forces comes from a nonuniform pattern of pressure which develops over the rotor area.
2) This pressure field is largely responsible for the existence of a direct force as well (along the turbine offset axis). The Alford mechanism also cooperates in creating these direct forces, because the pattern of turbine force per unit length is slightly shifted with respect to that of the gap width.
3) The larger part at least of the pressure nonuniformity pattern is found to extend over axial lengths of the order of the turbine diameter, starting at the stator exit and to be radially uniform. Thus, it cannot be explained as a local blade-tip effect (as, for example, associated with the leakage vortex), but must result from azimuthal flow redistributions, as predicted by our three-dimensional theory.
4) In addition to the large-scale pressure pattern, there are indications of localized effects occurring specifically in the narrow-gap region. This, plus the behavior of the cross-forces at small tip gap, strongly suggest the need to study carefully the viscous effects that may occur in the gap due to the opposing drives of the pressure gradient and the casing relative motion.
5) The direct and cross-forces increase substantially as the tip gap is reduced, confirming earlier findings in the German work on the topic. Furthermore, because this sensitivity is almost entirely absent in the inviscid theoretical treatment, it reinforces the notion of a strong role of viscosity at small gaps. This is despite the fact that cascade correlations would not indicate viscosity as a major factor, and could be due, as noted, to the relative casing motion.

10.2 Development of Analytical Models

A number of interrelated theoretical models were developed as tools for interpretation and extrapolation of data. They are capable of predicting most of the trends observed, but are not quantitatively accurate enough for design work. However, having established the important effects and the theoretical methods of attack, these models do offer good prospects for development into fully quantitative tools. Among the new achievements in the theoretical area are:

- A model which predicts efficiency and work losses from a uniform tip gap in situations such as a shrouded turbine, where the leaking fluid does no work.
- A modification of the above to account for the partial work done by the fluid leaking through the gap and by that rolling up with it into the leakage vortex.
- An extension of these models to include dynamically offset turbine locations, by exploiting the separation of radial and tangential scales. This allows predictions of flow redistribution and of damping.
- A simplified model for the effect of axially leaking fluid.

10.3 Recommendations

Our efforts in the area of dynamic Alford forces were not successful in obtaining quantitative damping data. This is due to the large inertial and vibratory forces which contaminate the data, particularly because of the need to extract the damping from forces along the shaking axis. The existence of large dry friction in the linear bearings supporting the turbine assembly was identified as the major source of the vibrations. A simple way to obtain at least one non-zero whirl speed data point is to leave the shaft centered, but mount the turbine eccentrically on it, so as to obtain simultaneous spin and whirl at the same frequency. This would have the advantage of putting the major inertial force on the radial axis, while fluid forces of interest are on the tangential axis.

A number of other remaining deficiencies have been mentioned in passing. In particular, we recommend that especial attention be paid to the study (both experimental and theoretical) of turbine (as opposed to compressor or fan) leakage flows and Alford forces with very small (less

6) We have obtained agreement between the trends of forces measured directly and those inferred from integration of local velocity triangles and pressure forces. The latter required extensive probing of the flow field, but the agreement constitutes strong support for the mechanisms discussed.

7) The cross forces are found to increase when the axial hub clearance and/or the axial stator-rotor distance *decreases*. This contradicts earlier findings by German workers. The effect appears to result from competition between opposing trends of the two contributions to cross forces: work defect nonuniformity (which would increase with increasing axial clearance) and pressure nonuniformity (which shows the opposite trend).

8) Separate experiments on labyrinth seals under circular whirl and rotation showed clearly that shroud seals do exhibit substantial cross-force damping. This damping is independent of inlet swirl or spin rate, and is a purely inviscid (kinematic) effect.

9) The direct forces on labyrinth seals with geometrically equal inlet and exit gaps can be attributed to the variation of the carry-over coefficient of the second gap to the gap width. This effect also increases noticeably the cross-forces.

10) Contrary to initial expectations, honeycomb lands have a minor effect only in seal cross-forces, although they do reduce substantially the direct forces. This appears to be related to interference with the carry-over effect.

11) Theory and data show a very large effect of the flow nonuniformities induced *upstream* of an offset labyrinth seal on those in the seal gland itself, and hence on the seal cross forces. The particular character of the upstream nonuniformities needs to be determined in each particular case.

12) The direct and cross forces on a shrouded turbine fitted with a one-cavity labyrinth can be calculated on the basis of a combination of seal theory (accounting for upstream nonuniformity) and a simple form of work-defect theory.

References

1. J.S. Alford,"Protecting Turbomachinery from Self-Excited Rotor Whirl". J. of Engineering for Power, October 1965, pp. 338-344.

2. H.J. Thomas, "Instabile Eigenschwingungen von Turbinenlaufern, Angefacht durch die Spaltstromungen Stopfbuschenung Beschanfelungen". AEG-Sonderdruck, 1958. Also "Unstable Oscillations of Turbine Rotors Due to Steam Leakage in the Clearance of the Sealing Glands and the Buckets", Bulletin Scientifique, A.J.M., Vol. 71, 1958, pp. 1039-1603.

3. Martinez-Sanchez-M., and Greitzer, E.M., "Turbine Blade-Tip Clearance Excitation Forces". Final Report on NSAS Contract No. NAS8-35018, June 7, 1985.

4. Martinez-Sanchez, M., and Jery, B., "Turbine Blade and Seal Tip-Clearance Excitation Forces". Phase II Report on NASA Contract No. NAS8-35018, January, 1990.

5. Urlichs, K., "Durch Spaltstromungen Hervorgerufene Querkrafte und den Läufern Thermischer Turbomaschinen". Dissertation, Technical University of Munich, 1975. Translated as NASA TM 77293, "Clearance Flow Generated Traverse Forces at the Rotors of Thermal Turbomachines", October, 1983.

6. Wohlrab, R., Experimentelle Ermittlung Spaltstromungsbedingter Drafte am Turbinenstuffen und Deren Einfluss auf die Laufstablitat Einfacher Rotoren". Dissertation, Technical University of Munich, 1975. Translated as NASA TM 77293, "Experimental Determination of Gap-Flow Conditioned Forces at Turbine Stages, and Their Effect on the Running Stability of Simple Rotors", October 1983.

7. Vance, J.M., and Laudadio, F.J., "Experimental Measurement of Alford's Force in Axial Flow Turbomachinery". ASME paper 84-GT-140, June, 1984.

8. Jery, B., "Experimental Study of Unsteady Hydrodynamic Force Matrices on Whirling Centrifugal Pump Impellers". Ph.D. Dissertation, California Institute of Technology, 1987.

9. Millsaps, K.T., "Analysis of Aero-Elastic Forces in Labyrinth Seals and the Design of an Experimental Facility to Measure Them". S.M. Thesis, Massachusetts Institute of Technology, August, 1986.

10. Millsaps, K.T., "The Impact of Unsteady Swirling Flow in a Single Gland Labyrinth Seal on Rotordynamic Stability: Theory and Experiment". Ph.D. Thesis, Massachusetts Institute of Technology, in preparation.

10b. Grant, Howard P., "Measuring Time-Averaged Stagnation Pressure in Pulsatile Flow", ISA 23rd International Instrumentation Symposium, Las Vegas, Nevada, May 1977.

11. Rains, D.A. "Tip Clearance Flows in Axial Flow Commpressers and Pumps". CALTECH, Hydrodynamics and Mech. Engineering Labs., Report No. 5, 1954.

12. Graham, J.A.H. "Investigation of a Tip Clearance Cascade in a Water Analogy Rig". ASME Paper 85-IGT-65, Beijing Intnl. Gas Turbine Symposium and Exposition, Beijing, P.R. of China, Sept. 1985.

13. Kostyuk, A.G. "A Theoretical Analysis of the Aerodynamic Forces in the Labyrinth Glands of Turbomachines". Teploenergetika, 1972, Vol. 19, No. 11, pp. 29-33.

14. Iwatsubo, T. "Evaluation of Instability Forces of Labyrinth Seals in Turbines or Compressors". NASA cp 2133, 1980, pp. 139-169.

15. Vermes, G., "A Fluid-Mechanics Approach to the Labyrinth Seal Leakage Problem". Jl. of Basic Engineering, Trans. ASMA, Series D, Vol. 82, No. 2, June 1960, pp. 265-275.

16. Erich, F. and Childs, S.D. "Self-Excited Vibrations in High Performance Turbomachinery". Mechanical Engineering, May 1984.

17. Qiu, Y., Martinez-Sanchez, M. and Greitzer, E.M. "The Prediction of Destabilizing Blade-Tip Forces for Shrouded and Un-Shrouded Turbines". Symposium on Instability of Rotating Machinery, Carson City, NV, June 1985.

18. Waterman, W.F. "Turbine Loss Correlation and Analysis". Lecture presented at the Workshop on Tip Clearance Effects in Axial Turbomachines, Penn State Univ., April 14-18, 1986.

19. Vavra, M.H. Aerothermodynamics and Flow in Turbomachines, John Wiley, Inc. 1960.

20. Lakshminarayana, B. "Methods of Predicting the Tip Clearance Effects in Axial Flow Turbomachinery". ASME Journal of Basic Engineering, Vol. 104, pp. 467-481, 1970.

21. Lakshminarayana, B. and Horlock, J.H. "Tip Clearance Flow and Losses for an Isolated Compressor Blade". ARC R&M 3316, 1962.

22. Lewis, R.I. and Yeung, E.H.C. "Vortex Shedding Mechanisms in Relation to Tip Clearance Flows and Losses in Axial Fans". ARC R&M 3829, 1977.

23. Adamczyk, J.J., Celestina, M.A., Beach, T.A. and Barnett, M. "Simulation of Three-Dimensional Viscous Flow Within a Multi-Stage Turbine". ASME Paper 89-GT-152, Toronto, CANADA, 1989.

24. Crook, A.J. "Numerical Investigation of Endwall/Casing Treatment Flow Phenomena". M.S. Thesis, Massachusetts Institute of Technology, Dept. of Aeronautics/Astronautics, August 1989.

25. Horlock, J.H., Actuation Disc Theory, McGraw-Hill, 2978.

26. Gauthier, Robert P., "An Investigation of Flow Field Perturbation Caused by Constant Bladle-Tip Clearance in a Turbine". M.S. Thesis, Massachusetts Institute of Technology, Dept. of Aeronautics/Astronautics, 1990.

27. Chen, G.T; Greitzer, E.M.; Tan, T.S. and Marble, F.E. "Similarity Analysis of Compressor Tip Clearance Flow Structure". To be presented at the 1990 ASME Gas Turbine Conference.

28. Benckert, H., and Wachter J. "Flow-Induced Spring Coefficients of Labyrinth Seals for application in Rotordynamics". NASA CP-2133, pp. 189-212.

29. Martinez-Sanchez, M., Lee, O.W.K., Czajkowski, E., "Prediction of Force Coefficients in Labyrinth Seals". NASA CP-2338, 1984, pp.235-256.

30. Scharrer, J.K. and Childs D.W., "Theory vs. Experiment for the Rotordynamic Coefficients of Labyrinth Gas Seals". Parts 1 and 2, ASME Jl. of Vibration, Accoustics, Stress, and Reliability in Design, Vol. 110, No. 3, pp. 270-287 (1989).

31. Kameoka, T. and Abe T. "A Theoretical Approach to Labyrinth Seal Forces", NASA CP-2338, pp. 28-30 (1984).

32. J.P. Den Hartog "Forced Vibrations with Combined Coulomb and Viscous Friction", Trans Am . Soc. Mech. Eng., Vol. 53, No. 9, pp. 107-123 (1931).